Cell death in the human malaria parasite: exploring autophagy as a drug target and early cellular events following drug perturbation

Ibrahim F. Ali

Ph.D. thesis

June, 2018

Keele University

DECLARATION

SUBMISSION OF THESIS FOR RESEARCH DEGREE

Part 1. DECLARATION by the candidate for a research degree

Degree for which thesis being submitted: Ph.D.

Title of thesis: **Cell death in the human malaria parasite: exploring autophagy as a drug target and early cellular events following drug perturbation**

Date of submission: **19.3.2018** Original registration date: **28.4.2014**

Name of candidate: **Ibrahim Faris Ali**

Research institute: **ISTM** Name of lead supervisor: **Prof. Paul Horrocks**

I certify that:

- **(a)** The thesis being submitted for examination is my own account of my own research.
- **(b)** My research has been conducted ethically. Where relevant a letter from the approving body confirming that ethical approval has been given has been bound into the thesis as an Annex.
- **(c)** The data and results presented are the genuine data and results actually obtained by me during the conduct of the research
- **(d)** Where I have drawn on the work, ideas and results of others this has been appropriately acknowledged in the thesis.
- **(e)** Where any collaboration has taken place with one or more other researchers, I have included within an 'Acknowledgements' section in the thesis a clear statement of their contributions, in line with the relevant guidance document.
- **(f)** The greater portion of the work described in the thesis has been undertaken subsequent to my registration for the higher degree for which I am submitting for examination
- **(g)** Where part of the work described in the thesis has previously been incorporated in another thesis submitted by me for a higher degree (if any), this has been identified and acknowledged in the thesis
- **(h)** The thesis submitted is within the required word limit as specified in the Regulations

Total words in submitted thesis (including text and footnotes, but excluding references and appendices) **55.188**

Signature of candidate …… Date: 19.3.2018

Abstract

The emergence and spread of resistance to antimalarial drugs has highlighted the demand to search for new drugs that target novel pathways in the human malaria parasite *Plasmodium falciparum*. This thesis explores the potential for targeting of the PfAtg8-PfAtg3 protein-protein interaction (PPI) that is required for lipidation of phosphatidylethanolamine (PE) within parasite autophagy pathway. Whilst *P. falciparum* lacks a complete cascade of the classical autophagy pathway, the homologues for key proteins such as PfAtg8 exist and have been shown to be involved in cellular processes such as vesicle trafficking and apicoplast biogenesis. Here, the antiplasmodial activity of a library of 131 compounds designed *in silico* to act as inhibitors of hLC3 (Atg8 homologue)-Atg3 interaction were evaluated. Two hits, SK1.47 and SK1.49, have been identified and shown to have moderate antiplasmodial activity (EC_{50} of 1-2 µM) against intraerythrocytic parasites, produce a rapid cytocidal activity against trophozoite stage parasites and have selectivity for the parasites over HepG2 cells. As a first proof of concept, both compounds inhibit the formation of PfAtg8-labelled vesicles, potential autophagosomes, induced by nutrient starvation. Computational modelling of SK1.47 and SK1.49 docking to PfAtg8 suggests that the naphthalene group binds to the W-pocket and the substituted phenyl binds to the L-pocket of the PfAtg3 interacting region of PfAtg8. This docking study also highlights aspects of the core structure of both molecules that should be further explored in terms of their antiplasmodial activity.

Ultrastructural changes and induction of biochemical markers of apoptotic cell death appear to suggest that SK1.47 and SK1.49 treated parasites do not undergo apoptotic cell death. This study was extended to exploit a bioluminescence assay of parasite viability

following exposure to a range of benchmark antimalarial drugs, which allows samples to be prepared that match a defined and titrated kill effect applied using drugs of different chemical classes. These established the conditions for a comparative study of apoptotic markers of early cell death using these different chemical classes, and also highlighted the central role of mitochondrial membrane potential collapse for the majority of drugs that explored and Ca^{2+} redistribution from the digestive vacuole following treatment with 4-aminoquinolines.

This study also highlights the opportunity of autophagy related proteins (Atg) of *P. falciparum* parasite as a novel target for drug development. Although SK1.47 and SK1.49 compounds are not considered as lead compounds for drug development due to lack the required potency with unfavourable physicochemical properties (high LogP), they are available now as chemical probes to explore the contested role of autophagy in malaria parasite homeostasis and response to drugs.

LIST OF CONTENTS

LIST OF FIGURES

LIST OF TABLES

Abbreviations

AIM	Atg8 family interacting motif
ACP	acyl-carrier protein
ACT	Artemisinin combination therapy
AQ	Amodiaquine
ARM	Artemether
Atg	Autophagy Related Protein
ATQ	Atovaquone
BRRoK	Bioluminescence Relative Rate of Kill
BDH	British Drug House
BSA	Bovine Serum Albumin
°C	Degree Celsius
CC_{50}	50% Cytotoxic Concentration
CCCP	Carbonyl Cyanide m-Chlorophenylhydrazine
CD36	Cluster determinant 36
CI	Confidence intervals
CM	Compete medium
CO_2	Carbon dioxide
CQ	Chloroquine
CR1	Complement receptor 1
CS	Circumsporozoite
CSA	Chondroitin sulfate A
CVT	Cytoplasm to vacuole targeting
3D	Three dimensions
DDT	Dichlorodiphenyltrichloroethane
DHA	dihydroartemisinin
DMSO	Dimethyl sulfoxide
DNA	Deoxyribonucleic Acid
DV	Digestive vacuole
EC_{50}	50% Effective Concentration

EDTA	Ethylene Diamine Tetra acetic acid
EMP1	Erythrocyte Membrane Protein 1
ER	Endoplasmic reticulum
FACS	Flow Cytometry Cell Sorting
FRRG	Phenylalanine-arginine-arginine-glycine
FSC	Forward scatter
GMEP	Global Malaria Eradication Program
HBA	H-bond acceptor
HBD	H-bond donor
HCl	Hydrochloric Acid
HepG2	Hepatic G2 cell line
hrs	Hours
ICAM1	Intercellular adhesion molecule 1
IFA	Immunofluorescence assay
iRBC	Infected Red Blood cell
IRS	Indoor residual spraying
ITNs	Insecticide-treated nets
KCl	Potassium Chloride
LD_{50}	50% Lethal Dose
LC3	Light Chain 3
LEU50	Leucine amino acid 50
LogP	Logarithm of octanol-water partition coefficient
RO5	Lipinski's rule-of-five
LLIN	Long-Lasting Insecticide-treated Nets
LUC	Luciferase
LYS48	Lysine amino acid 48
M	Molar
3-MA	3-methayl adenine
MCA1	Metacaspase genes
µg	Microgram
µL	Microliter

µm	Micrometre
ΔΨm	Mitochondrial outer membrane potential
MQ	Mefloquine
mTOR	Mammalian-target of rapamycin
MSF	Malaria SYBR Green I Fluorescence
MW	Molecular weight
N_2	Nitrogen
NaCl	Sodium Chloride
Na_2HPO_4	Disodium Hydrogen Phosphate
NaH_2PO_4	Monosodium Dihydrogen Phosphate
NaOH	Sodium Hydroxide
NROTB	Rotatable bonds
O_2	Oxygen
PAS	Phagophore assembly site
PBS	Phosphate Buffer Saline
PBD	Protein Data Bank
PCD	Programmed Cell Death
PE	Phosphatidylethanolamine
PEX	Peroxisomal Membrane Proteins
PPQ	Piperaquine
PG	Proguanil
pH	Potential of Hydrogen
PI	Phosphatidylinositol
PI3K	Phosphatidylinositol-3-kinase
PI3P	Phosphatidylinositol-3 phosphate
PPI	Protein-Protein Interaction
PV	Parasitophorous Vacuole
PVM	Parasitophorous Vacuole Membrane
PYR	Pyrimethamine
PYRD	Pyronaridine
QN	Quinine

RBCs	Red Blood cells
+ve	Positive control
-ve	Negative control
SD	Standard Deviation
sdH2O	Sterile deionized Water
SERCaP	Single Exposure Radical Cure and Prophylaxis
SDX	Sulphadoxine
SM	Starvation medium
SPR	Surface Plasmon Resonance
SNAP	S-nitroso-N-acetyl-penicillamine
SSC	Side scatter
TCP	Target Candidate Profiles
TOR	Target of rapamycin
TPP	Target product profiles
TPSA	Total Polar Surface Area
TSP	Thromobospondin
TUNEL	Terminal deoxynucleotidyl transferase (TdT)-mediated dUTP Nick End Labelling
TEM	Transmission Electron Microscopy
uRBCs	Uninfected red blood cells
v/v	Volume/volume
WHO	World Health Organisation
w/v	Weight/volume

ACKNOWLEDGMENTS

I would like first to express my sincere gratitude to my supervisor Professor Paul Horrocks for his continuous support of my Ph.D. research, for his patience, motivation, and immense knowledge. His guidance has helped me throughout my research and during the writing of this thesis. I could not have imagined having a better advisor and mentor for my Ph.D. study- an inspiring advisor and one of the most patient people I have ever worked with.

Also I would like to give special thanks to my sponsor, the Ministry of Higher Education and Scientific Research of Iraq and the Iraqi Cultural Attache in London, for the funding and the opportunity to complete my Ph.D. study.

It is also my pleasure to thank my advisor Dr. Helen Price for her suggestions, especially on my presentations during the weekly parasitology group meetings. I am grateful to Dr. Clare Hoskins, Dr. Anthony Curtis and Dr. Anja Winter for their valuable advice. I would also like to acknowledge Dr Reynisson for the supply of the chemical library used in the first part of this thesis as well as Prof. Paul Roepe for his assistance in developing the Immunofluorescence microscopy data reported in Chapter 3. I would also like to thank all my fellow Ph.D. students in the Institute for Science and Technology in Medicine and School of Life Sciences, who supported me and motivated me to strive towards my goal.

A special thanks to my family. Words cannot express how grateful I am to my mother, for all of the sacrifices that you have made on my behalf. Your prayer for me was what has sustained me thus far. At the end I would like express appreciation to my family, my beloved wife Sameera who spent sleepless nights with me and was always my support in

the moments when there was no one to answer my queries, and my children, Ahmed, Hasan and Zaid for their patience during my studies and whilst writing this thesis.

Chapter 1: General introduction

1.1 Malaria is a global disease

Malaria is a serious tropical parasitic disease with a global reach, affecting some 91 countries. According to the World Health Organisation Report (2016), approximately 212 million malaria cases with 429,000 deaths were reported in 2015 (WHO, 2016). The majority of this mortality occurs in African children aged under 5 years old. This estimation is likely lower than the actual malaria burden as most of countries affected by malaria have limited diagnostic resources, particularly in rural areas (Autino *et al.*, 2012), and often lack the potential to survey malaria distribution and mortality due to mass migration of human groups; especially in conflict regions (Pindolia *et al.*, 2014). The first global malarial risk map was produced by Lysenko and Semashko in 1960 (Fig. 1.1) (Dalrymple *et al.,* 2015). Here they describe four categories of endemicity depending on the proportion of the population that carry blood-stage parasites, termed the parasite rate (PR); hypoendemic region (<10%), mesoendemic region (≥10% <50%), hyperendemic region (≥ 50% <75%), holoendemic region (≥75%) (reviewed in Dalrymple *et al.,* 2015).

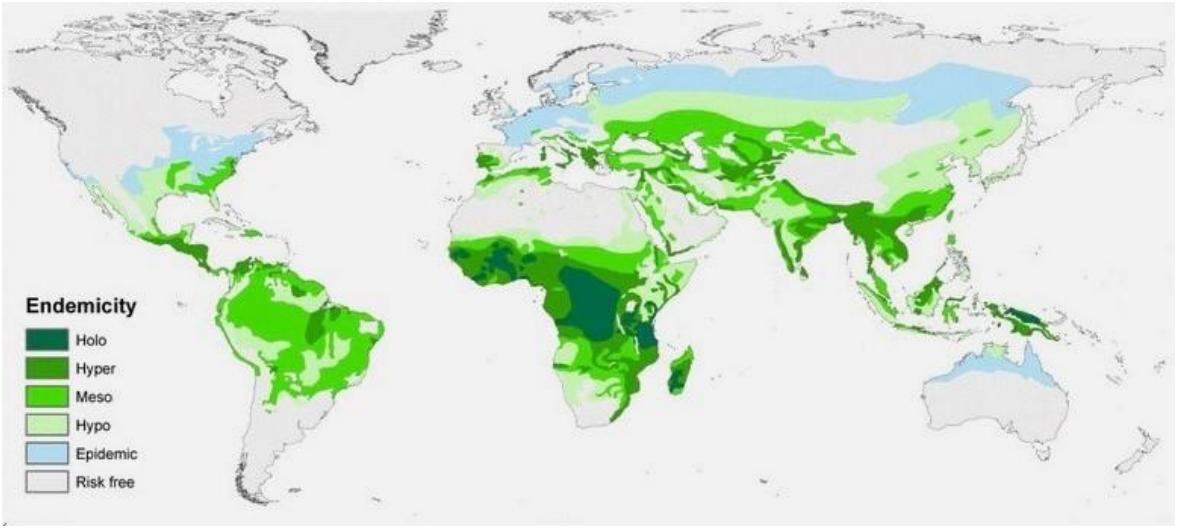

Fig. 1.1 A 'Lysenko' map of global malaria endemicity circa 1900. This historic map constructed by Lysenko and Semashko during the 1960s was based on a worldwide assembly of diverse malariometric data, simple climatic rules and expert opinion. The classic strata of malaria endemicity are described, each relating to infection prevalence (parasite rate, PR) in children: hypoendemic, PR <10 %; mesoendemic, PR ≥10 % and <50 %; hyperendemic, PR ≥50 % and <75 %; and holoendemic, PR ≥75 %. This is a reproduction of the map from Hay *et al.* (2004).

The causative agent of malaria in humans is protozoan parasites of the *Plasmodium* genus, with five species causing infections in humans (Kwenti *et al.,* 2017). Of these, *P. falciparum* is the most virulent species and is prevalent almost in all malaria endemic countries with its widest geographic range within Africa, and as a consequence the primary burden of mortality falling on this region (Fig. 1.2) (Gupta *et al.,* 1994). Recent emerging populations newly at risk of malaria are arising as a result of climate changes affecting the anthropogenic vector of *Plasmodium* spp. (Okonko *et al.*, 2009) as well as the emergence and spread of drug resistant parasites (White *et al.,* 2014) and insecticide resistant mosquitoes (Ranson *et al.,*2011).

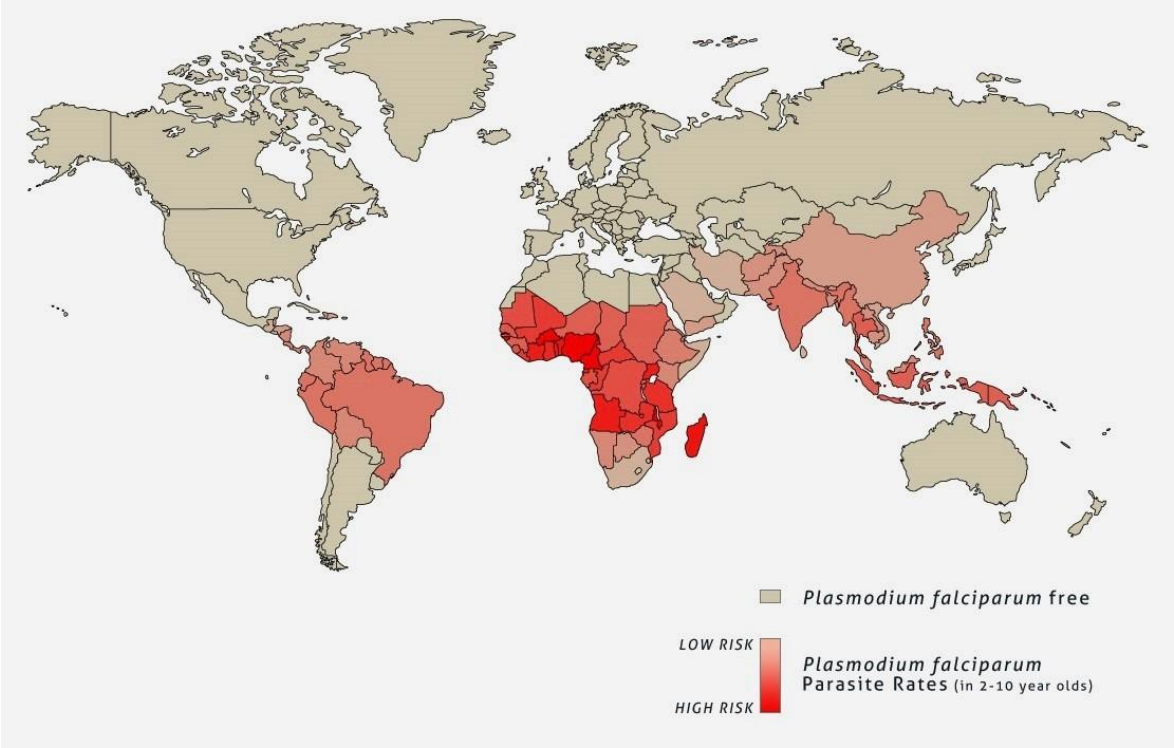

Fig. 1.2 The global map of *P. falciparum* parasite rates (proportion of population infected with blood-stage parasites) in 2010. Note the residual spatial distribution of high parasite rates in children in Sub-Saharan Africa (Source: Gething *et al.,* 2011).

The first regional eradication campaign for malaria was launched in the 1940s and represented a stationary base upon which the Global Malaria Eradication Program (GMEP) was launched in 1955 (Carter and Mendis, 2002). These elimination programmes utilised insecticide-treated nets (ITNs), the insecticide dichlorodiphenyltrichloroethane (DDT) for indoor residual spraying and mass administration of chloroquine (CQ) chemoprophylaxis. The success of this campaign resulted in the elimination of malaria from Europe, North America, the Caribbean and some parts of Asia and South-Central America (Carter and Mendis, 2002). Regretfully, a decline in global efforts to eliminate malaria between 1968 and 1991, due to economic, financial and institutional challenges (Mills *et al.,* 2008), in addition to spread evolution of antimalarial drug resistance led to resurgence in the malaria burden in sub-Saharan Africa (Plowe, 2005). The hope for

malaria elimination and eradication was revived following the declaration of the Roll Back Malaria initiative by the World Health Organisation (WHO) in 1998 (Tanner and Savigny, 2008). Despite progression in malaria control in Africa, resulting in falls of 21% in new cases of malaria and 31% in deaths between 2010 and 2015 (WHO, 2016), the challenge of malaria, particularly in Sub-Saharan Africa is still significant.

1.2 Parasite life cycle

Unicellular protists of the *Plasmodium* genus, the causative agent of malaria, are transmitted to humans through the bite of an infected female *anopheles* mosquito vector during the course of a blood meal. To date, five species of *Plasmodium* have been reported to cause clinical malaria, including; *P. falciparum, P. vivax, P. ovale* (there are two subspecies; *P. ovale curtisi* and *P. ovale wallikeri* (Sutherland *et al.* 2010), *P. malariae*, and *P. knowlesi*. For successful completion of the parasite complex multistage life cycle, two hosts are required, the human vertebrate and the mosquito invertebrate (Fig. 1.3 illustrates the life cycle of *P. falciparum*). The key stages of this life cycle are described below.

1.2.1 Parasite life cycle in the human host

1.2.1.1 Pre-erythrocytic phase or Hepatic schizogony phase

Hepatic schizogony of malaria parasites in human is characterised as an asymptomatic phase of infection (Derbyshire *et al.*, 2012). During this stage, intracellular and extracellular development of parasite occurs. Human infection is initiated by transmission of infectious sporozoites from the salivary glands of an infected female *Anopheles* mosquito into the subcutaneous tissues during a blood meal (Burkot *et al.,* 1986).

Sporozoites migrate though the bloodstream to the liver. During this migration, some sporozoites are engulfed by local macrophages and some migrate to the lymphatic system and induce protective immunity (Good and Doolan*,* 2007). In hepatocytes, exo-erythrocytic forms are created within a protective vacuole called the parasitophorous vacuole (PV). In order to establish infection within the hepatocytes, the PV and circumsporozoite surface (CS) proteins (surface proteins of sporozoites) isolate the parasites from the host cell cytoplasm and suppress pro-inflammatory cytokines production, respectively. These represent the key mechanisms of immune evasion in the hostile human environment (Eksi and Williamson, 2011; Singh *et al.,* 2007). In infected-hepatocytes, sporozoite development occurs over 5-16 days, depending on the parasite species, producing thousands of hepatic merozoites within a host-derived vesicle called merosome (Kebaier *et al.,* 2009). The liver-stage represents a key difference between *Plasmodium* spp. that infects humans. *P. vivax* and *P. malariae* infections can result in the formation of dormant forms termed hypnozoites (Collins, 2007). Delayed activation and maturation of these hypnozoites are related to relapsing malaria, which can occur several months to several years after the initial infection (Collins, 2007; Imwong *et al*., 2007; Siala *et al.,* 2005) and lead to a phenomenon termed post-treatment relapse (Greenwood *et al.,* 2008; Szmitko *et al.*, 2008; Theunissen *et al.,* 2009; Zenz *et al.,* 2000).

Following completion of hepatic development, the merosomes are released into circulatory system and burst in the pulmonary capillaries releasing thousands of hepatic-merozoites into the bloodstream to initiate the next step of asexual development of life cycle in humans, the intraerythrocytic phase, which is characterised by the patent pathophysiology of infected red blood cells (Fig. 1.3) (Chotivanich *et al.*, 2000).

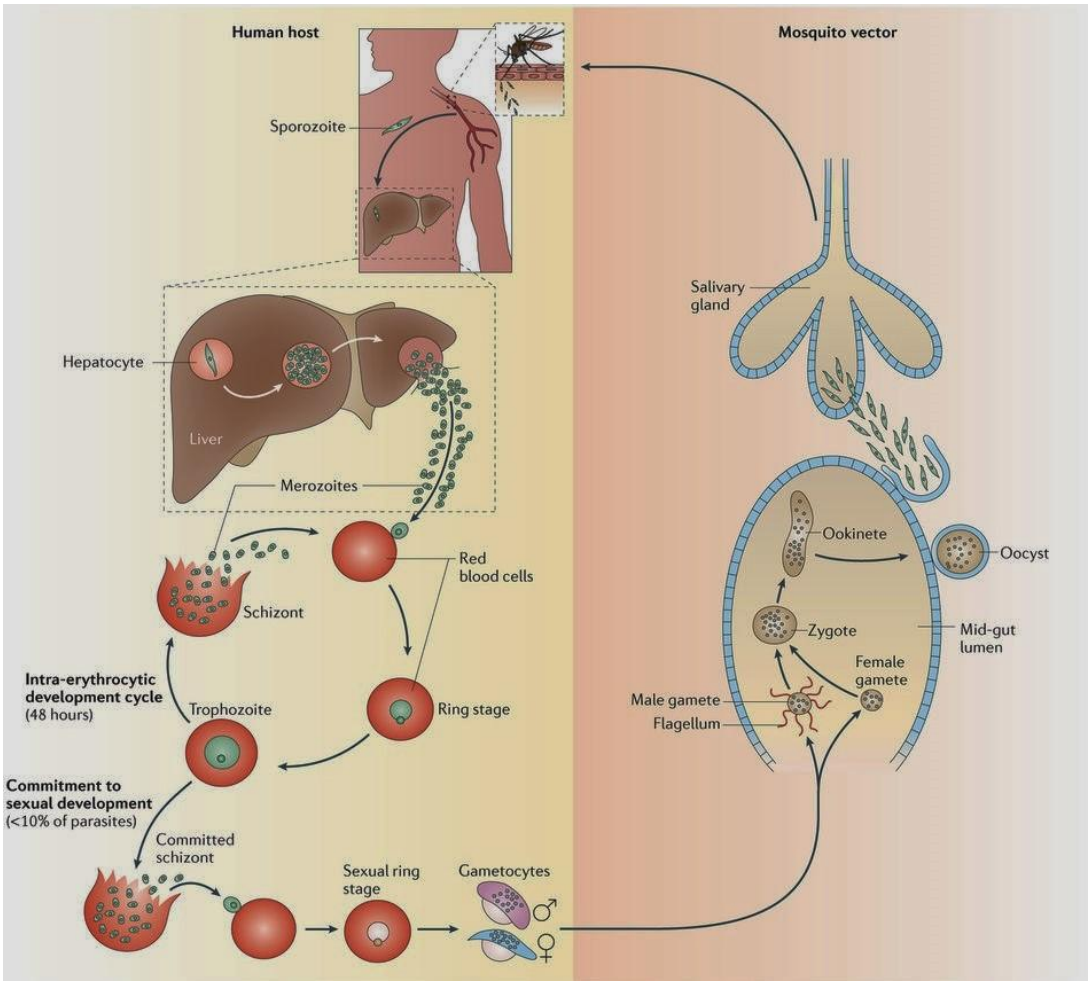

Fig. 1.3 The life cycle of *P. falciparum*. Infectious sporozoites are transferred to humans via the bite of an infected female *Anopheles* mosquito. The sporozoites migrate to, invade, and then replicate within hepatocytes, termed the exo-erythrocytic phase. After a clinical sub-patent period of some 10 days, tens of thousands of hepatic merozoites are released into the bloodstream. Here, the intraerythrocytic phase is established when red blood cells (RBCs) are infected by the merozoites. Parasites inside RBCs undergo several rounds of asexual multiplication (These include the well described morphological stages of ring, trophozoite and then schizont), with a release of merozoites after 48 hrs, which can reinitiate RBC infection – leading to development of high levels of parasitaemia and the pathophysiology of disease. A proportion of infected RBC commit to sexual differentiation instead of multiplication, producing micro- and macrogametocytes stages infectious to mosquitoes when taken up in a blood meal. Completion of sexual commitment and gamete fusion form the zygote and then ookinete in the mosquito midgut. Migration of the ookinete through the basement membrane of the gut to reside against the haemocoel results in the formation of oocyst. Here, meiotic division, followed by mitotic replication generates thousands of haploid sporozoites, which are released from ruptured oocysts. These sporozoites migrate to the salivary glands of the mosquito, where they become available to be transmitted to humans (Source: Josling and Llinas, 2015).

1.2.1.2 Intraerythrocytic schizogony – infection of the red blood cells

This phase is characterised by symptomatic features of infection and rapid expansion of the parasite burden. During this phase, growth within, and then release of new merozoites from infected red blood cells repeats over several cycles. The virulence of *P. falciparum* parasites depends, in part, on their ability to infect all RBCs, irrespective of their age (red blood cells circulate for approximately 120 days), using a range of variety receptor-ligand interactions (Cooke *et al.,* 2004) mediated through merozoite surface proteins and proteins released from organelles located at their apical end (Fig. 1.4). RBC age appears to play a critical role in determination of infection based on *Plasmodium* spp. infection, with *P. vivax* and *P. ovale* invasion restricted to young circulating age RBCs, also termed reticulocytes, and *P. malariae* invasion restricted to the oldest circulating red blood cells (McQueen and McKenzie, 2004).

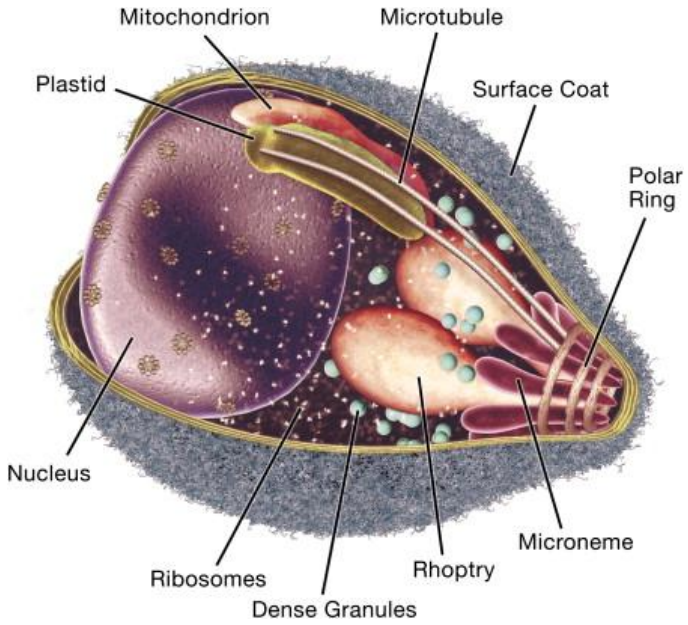

Fig. 1.4 Scheme illustration of a merozoite. The image highlights major organelles and cellular structures, with the penetrative organelles (micronemes, rhoptries and dense granules) located in the apical anterior end of merozoite (Source: Cowman and Crabb, 2006).

Following invasion of RBCs, a programme of architecture remodelling is launched including loss of penetrative organelles such as apical rings, conoid, rhoptries and micronemes and modification of the host erythrocyte to adapt to the new intraerythrocyte environment (Field and Shute 1956). Infected RBCs (iRBCs) undergo parasite-directed modifications to their cytoskeleton (increase their deformability), an increase in plasma membrane permeability to nutrients located in serum, as well as the export of proteins from the parasite to the erythrocyte surface. The latter proteins, such as Erythrocyte Membrane Protein 1 (PfEMP1), which located on electron-dense knobby structures are critical to the pathology of disease (Cooke *et al.*, 1998; Gruenberg *et al.*, 1983). PfEMP1 are critical to the ability of parasite to persist in red blood cells against the human immune response through clonal antigenic variation of PfEMP1 (Kyes *et al.,* 2007) and avoidance of splenic clearance by PfEMP1 binding to a wide of host receptors (Craig and Scherf, 2001).

Following infection of the red blood cell, the parasite undergoes a number of well-described morphological changes (Fig. 1.5) over the next 48 hrs (red blood cell development takes 24 hrs for *P. knowlesi* and 72 hrs for *P. malariae*). The first are the round and hollow cytoplasm shapes termed the ring stage. The ring stage is characterised by a low metabolic activity and minimal remodelling of iRBCs with the lack of any obvious cytoplasmic organelles (Spielmann *et al.*, 2006). Ring stage iRBC are often visualised in diagnostic microscopic tests as this stage of iRBC freely circulate in the bloodstream, lacking the surface expression of PfEMP1 that would be required to mediate sequestration of the iRBC in the microvasculature (Langreth and Peterson, 1985). In *P. falciparum,* this stage continues for approximately 24 hrs post infection with the size of the ring increasing as well as the thickness of the cytoplasmic ring (Bannister and

Mitchell, 2009). At this point, the parasite is typically termed trophozoites – the name derived from the parasite feeding (Greek trophe) on the RBC haemoglobin to provide both space and nutrients for growth and replication (Sherman, 2012). Trophozoites are highly metabolic active, with key activities including haemoglobin trafficking to the parasite acidic digestive vacuole (DV) and protein export, such as PfEMP1, to the erythrocyte surface. The trophozoite stage proceeds up to about 32 hrs post-invasion and is followed by the schizont stage. Within the schizont, multiple rounds of deoxyribonucleic acid (DNA) replication and cytoplasmic division result in the characteristic large and segmented morphology as new merozoites are formed (Bannister *et al.,* 2000). Several physical and biochemical events such as increases in intracellular pressure, destabilisation of iRBCs membrane integrity and proteolysis of the parasitophorous vacuole membrane (PVM) are thought to trigger RBCs rupture and release of between 16-32 new merozoites into the bloodstream. These merozoites are now available to reinvade uninfected erythrocytes (uRBCs), this process represents an exponential growth phase in parasite population (Glushakova *et al.*, 2005).

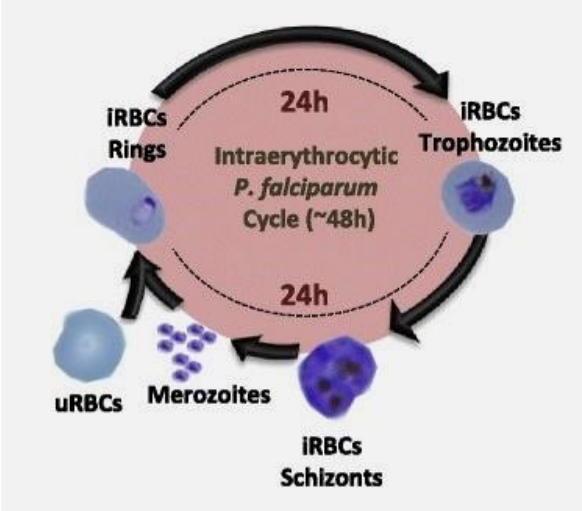

Fig. 1.5 The major morphological stages of intraerythrocytic development in *P. falciparum*. (Source: Mata-Cantero *et al.,* 2015).

1.2.2 Parasite life cycle in the mosquito host

Under conditions of stress such as those induced under high parasitaemia, nutrient-poor conditions or antimalarial drug exposure, a proportion of newly invaded RBCs trigger gametogenesis instead of entry in a new cycle of asexual intraerythrocytic development (Carter and Miller, 1979; Dyer and Day, 2002). Here, two types of gametocytes, termed microgametocytes (males) and macrogametocytes (females), are formed and complete development of several days before being taken up into a female *Anopheles* mosquito during a blood meal (see review by Josling and Llinas, 2015). During the growth and development of gametocytes, these iRBCs are primarily sequestered in bone marrow (Farfour *et al.,* 2012). Five distinct morphological forms or stages (stages I–V) were first described by Field and Shute (1956). Gametocyte stage-I is morphologically similar to an asexual trophozoite stage whilst the subsequent gametocyte stages can be microscopically differentiated and specifically recognized by a characteristic sickle-like shape. Gametocyte stage-V is the only infectious form for mosquito vector as it no longer sequesters in the bone marrow and can be found in peripheral blood (Carter and Miller, 1979). After being taking up by the mosquito, within the midgut both microgametocytes and macrogametocytes initiate the terminal developmental process producing flagellated microgametes and macrogametes, respectively. Fertilization of macrogametes by microgametes produces zygotes (diploid) which rapidly develop into a motile ookinete (Bennink *et al.,* 2016). Penetration the midgut wall of mosquito by ookinetes leads to them residing against the basement wall of the haemocoel, with ookinetes developing to oocysts. Oocysts undergo meiotic division to the haploid state and then undergo mitotic division to generate thousands of haploid daughter sporozoites within an oocyst.

Following rupture of the oocyst, sporozoites migrate through the haemocoel to the mosquito salivary glands to be available to infect a human host (Sinden, 1999).

1.3. Malaria pathogenesis

Although the liver stages of the life cycle plays a central role in infection by providing hepatic merozoites into the bloodstream, this stage of the infection is characterised by subclinical symptoms and is often termed the pre-patent period (Lindblade *et al.,* 2013). *P. falciparum*, the most virulent species of human malaria parasite, is highly endemic in sub-Saharan Africa, where infection correlates with severe malaria and mortality, particularly in children aged under 5 years (Nankabirwa *et al.,* 2014). Malaria pathogenesis is characterised by a complex network of host-parasite interactions (Acharya *et al.,* 2017). Differences in pathology depend on environmental factors (primarily related to conditions that favour the presence of the mosquito vector as well as local health infrastructure), host factors (history of exposure to parasite, immune status and presence of protective factors such as haemoglobinopathies) and parasite factors (expression of virulence proteins that interact with human host ligands and capacity to evade host immune response) (Schofield and Mueller, 2006). Pregnant women, particularly primigravida, represent a particular risk group due to their modified immune status and the existence of a novel organ, the placenta, for parasite sequestration (Uneke, 2007). This pre-symptom period of infection (incubation period) ranges between one to few weeks relying on the infecting *Plasmodium* spp., chemoprophylaxis therapy (Schlagenhauf-Lawlor, 2007) and immune response based on previous exposure to infection (White, 2009). Clinically, malaria is generally classified into two sub-groups

(uncomplicated and complicated or severe malaria) according to the clinical manifestation of the infection (Patel *et al.,* 2003).

1.3.1 Uncomplicated malaria

Uncomplicated malaria is characterized by a range of primary malaria symptoms. These are clinically similar to flu-like symptoms and include; mild fever, periodic chills, mild anaemia, nausea, headaches and fatigue (White *et al.,* 2014). The *Plasmodium* parasite obtains the majority of its synthetic nutritional requirements through digestion of 25 to 80% of host red blood cell haemoglobin during intraerythrocytic phase (Goldberg, 1993), a process that affects the osmotic balance within the host cell (Lew *et al.*, 2003). The release of free haem, which is toxic, is detoxified by the formation of an insoluble haem polymer called haemozoin crystals (Olivier *et al.,* 2014). Release of haemozoin during schizont rupture is considered the likely cause of fever through induction of a proinflammatory immune response. This proinflammatory response, however, is also likely contributed to by the recognition of free parasite DNA that may also be recognised by toll-like receptors on monocytes and dendritic cells (Parroche *et al.,* 2007). The fever is usually irregular at the beginning of a malaria infection, although the classical periodic appearance of fever occurs a few days later as a result of synchronised schizont rupture and development of parasite load within the patient (Bartoloni and Zammarchi, 2012).

1.3.2 Complicated or severe malaria

Efficient treatment of malaria can be achieved if the disease is diagnosed early and an effective drug given rapidly. Failing this, the disease may develop and the effect of the high parasite load on organs can occur leading to severe malaria. Severe malaria is defined as a complex multi-system disorder with several clinical manifestations. Critical to

this pathology, is the role of *P. falciparum* erythrocyte membrane protein 1 (PfEMP1) (Montgomery *et al.*, 2007). PfEMP1 is exported from the parasite to the surface of the erythrocyte infected by mature stages of parasite (trophozoite and schizont). PfEMP1-decorated infected erythrocytes are less available in peripheral blood due to their ability to cytoadhere to endothelial cells of host organs via a wide range of host receptors including; cluster determinant 36 (CD36), intercellular adhesion molecule 1 (ICAM1), thromobospondin (TSP), complement receptor 1 (CR1)and chondroitin sulfate A (CSA) (Chan *et al.,* 2014). Through this cytoadhesion process, the parasite sequesters itself in a low oxygen environment necessary to complete its development (it is a microaerophilic organism) and also provide protection to mature iRBCs from splenic clearance (Franke-Fayard *et al.,* 2010). PfEMP1 on the surface of iRBCs also have the ability to bind to other uRBCs, forming rosettes, or other iRBCs, forming clumps that are considered likely to block post-capillary venules and result in poor development of tissue and localised inflammatory hypoxia pathology (Newton *et al.*, 1994). PfEMP1 also has a second function, where clonal antigenic variation of the PfEMP1 expressed by the parasite population supports the establishment of a long-term chronic infection despite the host ability to generate antibodies against PfEMP1 on the surface of infected erythrocytes (Pasternak and Dzikowski, 2009).

Cerebral malaria cases are caused by parasite sequestration within the microvasculature of the brain and are particularly noted for their high mortality rates (MacPherson *et al.*, 1985). A more common pathology, particularly in young children, is severe malarial anaemia (SMA) (White *et al.,* 2014). A number of mechanisms contribute to this severe anaemia, including; splenic destruction of infected erythrocytes (Buffet *et al.*, 2009), macrophages phagocytosis of infected erythrocytes (Biemba *et al.*, 1998), infection and

destruction of erythrocytes during its normal intraerythrocyte development and suppression of bone marrow activity and dyserythropoiesis (Perkins *et al.*, 2011). Infection during pregnancy (congenital malaria) is caused by iRBCs binding to CSA on the surface of syncytiotrophoblasts in the placenta (Uneke, 2007). As a result localised proinflammatory responses decrease the function of the placenta and lead to low birth weight, premature delivery and may result in still birth (Steketee *et al.*, 2001).

1.4. Malaria prevention and control

Malaria control strategies have been successfully applied over the last fifteen years to reduce the overall global burden of this disease. These strategies rely on the treatment of infections by targeting the parasite using small molecule drugs, or through the use of insecticides to block the transmission by the *Anopheles* vector. Comparisons of malaria burden with and without these interventions over the last 15 years highlight the considerable success of transmission blocking interventions, primarily usage of ITNs, artemisinin combination therapy (ACT) and indoor residual spraying (IRS) of surfaces that mosquitoes rest on (Fig. 1.6).

Insecticide treated bed nets offer a simple, safe and environment friendly method to prevent malaria infection. These nets were introduced during World War II to protect soldiers against vector-borne diseases (specifically malaria and leishmaniasis) in Europe (Curtis *et al.*, 1990). Modern bed nets are treated with one or more pyrethroids and have been shown to efficiently protect against infection through repelling and actual killing of the mosquito vector (Curtis *et al.,* 1990). The use of more permanent insecticide treatment of the bed nets have created long-lasting insecticide-treated nets (LLIN) that are used in current malaria control strategies.

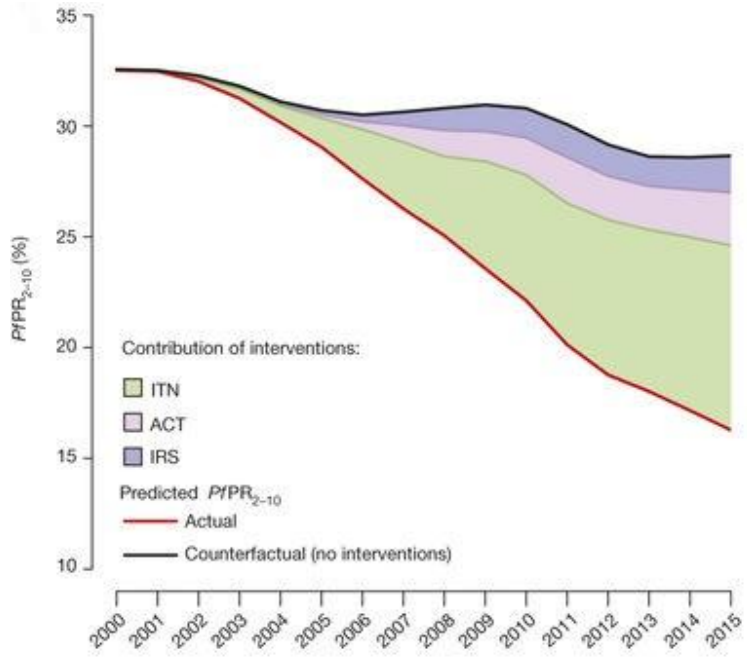

Fig. 1.6 Influence of different control tools on malaria burden in Africa from 2000 to 2015. Where percentage of parasite rate under three different malaria interventions including; insecticide treated bed nets (ITN), artemisinin combination therapy (ACT) and indoor residual spraying (IRS) as well as non-intervention were applied during study period (Source: Bhatt *et al.,* 2015).

According to a survey study done by Wanzira *et al.* (2016) in Uganda, a significant population coverage of LLIN contributed to a significant decrease of malaria infection in the study region and that the effectiveness of LLINs was raised when it is used in combination with IRS (Hailu *et al.*, 2016). Despite resistance to DDT being reported in some malaria endemic regions, the WHO strongly recommends using DDT-indoor residual spray in West and Central Africa due to the prolonged efficacy of DDT (approximately 12 months) compared to other insecticides such as pyrethroids (4–6 months), organophosphates or carbamates (2–6 months). Thus one spray cycle/year of DDT IRS reduces the total insecticide cost and also minimizes its level in environment (WHO, 2006).

In terms of vaccination against the malaria parasite, significant efforts have been focussed on the development of a vaccine to support malaria eradication. Despite decades of basic and clinical research, production of a cheap, safe and effective vaccine is still not promising (Ballou, 2009). There are a number of challenges that have obstructed progression in this field, including; the complexity of the parasite life cycle, extensive antigenic variation and polymorphic strains, as well as an incomplete understanding of what aspects of the host immune response actually provides the protection seen in people exposed to infections repeatedly by the malaria parasites (Langhorne *et al.*, 1989). The multistage life cycle of malaria parasite determines that there are three types of stage-based vaccines; pre-erythrocytic stage, intraerythrocytic stage and transmission blocking vaccines (Guilbride *et al.*, 2010; Hill, 2011). Currently, the target of the most active vaccine is the sporozoite surface protein of *P. falciparum*, CS protein (Gardner *et al.*, 2002). RTS, S/AS01, type of CS vaccine, is a pre-erythrocytic vaccine that is also called Mosquirix^{TM} and has been developed by GlaxoSmithKline (Kaslow and Biernaux, 2015). It is a formulation of repeated region of conserved motifs from CS incorporated with a C-terminal region that contains T cell epitopes from the surface protein of hepatitis B. An adjuvant AS01, consisting of a monophosphoryl lipid A fused with QS21, is added to enhance its overall immunogenicity (Stoute *et al.*, 1997). The RTS, S/AS01 vaccine can induce a short life protection in immunized children and is still under phase-III of clinical trials (Crompton *et al.*, 2010; WHO, 2017) with approval for larger field studies in 2017/18 (Han *et al.,* 2017). Further trials to improve the protection ability of RTS, S/AS01 using different adjuvants (Genton *et al.*, 2010) or a virus delivery vector are also ongoing (Walther *et al.*, 2006). Blood stage vaccines show less promise than CS-based vaccines due to high antigenic variation in the intraerythrocytic stage of malaria parasite (Takala *et*

al., 2009) and only modest antibody levels are reported even when incorporated with adjuvants (Ellis *et al.*, 2009). Suppression of parasite transmission through the use of transmission blocking vaccines have focussed on a prefertilization antigen of *P. falciparum* (Pfs48/45) expressed in gametocytes (Outchkourov *et al.,* 2008), with the number of oocysts dramatically reduced in mosquitoes fed with blood that contains antibodies obtained from immunized mice or monkeys (Chowdhury *et al.*, 2009). Importantly, the short half-life of potential malaria vaccines and appropriate means to deliver them where most needed in resource-poor areas, provide important challenges in the delivery of an efficient vaccine against malaria parasites (Crompton *et al.,* 2010; Hill, 2011).

1.4.1 Antimalarial drugs

Treatment of malaria currently relies upon small molecule drugs. The first antimalarial drug widely used was quinine (QN), originally isolated in 1820 from the bark of the Cinchona tree (Willcox *et al.,* 2004). The bark of this tree, termed "Jesuit's powder" was introduced to Europe, from South America, in the early 17th Century for the treatment of malarial fevers (Achan *et al.*, 2011). Despite emerging resistance to QN in some parts of world by 1910, it is still used widely and is a drug on the WHO list of essential medicines. The emergence of resistance as well as challenges in production of a cost-effective synthetic QN prompted the search for alternatives at the start of the 20th Century. This pattern of introduction of a new drug, use and then emergence of resistance was repeated several times during the 20th Century (Fig. 1.7) (Wells *et al.,* 2015). The development of CQ in 1934, the first of several 4-aminoquinolines introduced in this century, was eventually delivered widely as an antimalarial in 1945, replacing mepacrine based on its improved tolerability and safety profile (Famin and Ginsburg, 2002; Slater, 1993). However, the first case of CQ resistant *P. falciparum* was documented at the Thai-

Cambodian border in 1957 and was followed by the emergence of resistance in South America in 1959, with resistance eventually spreading to Africa in 1978 (Packard, 2014). Other quinoline-containing drugs such as amodiaquine (AQ) and mefloquine (MQ) were introduced in 1950 and 1977, respectively (Mein, 1951; MMV, 2015). Resistance to AQ, a 4-aminoquinoline, was reported in Thailand in 1975 (Hall *et al.,* 1975), while resistance to MQ, an aminoalcohol, reported in Asia in late 1990.

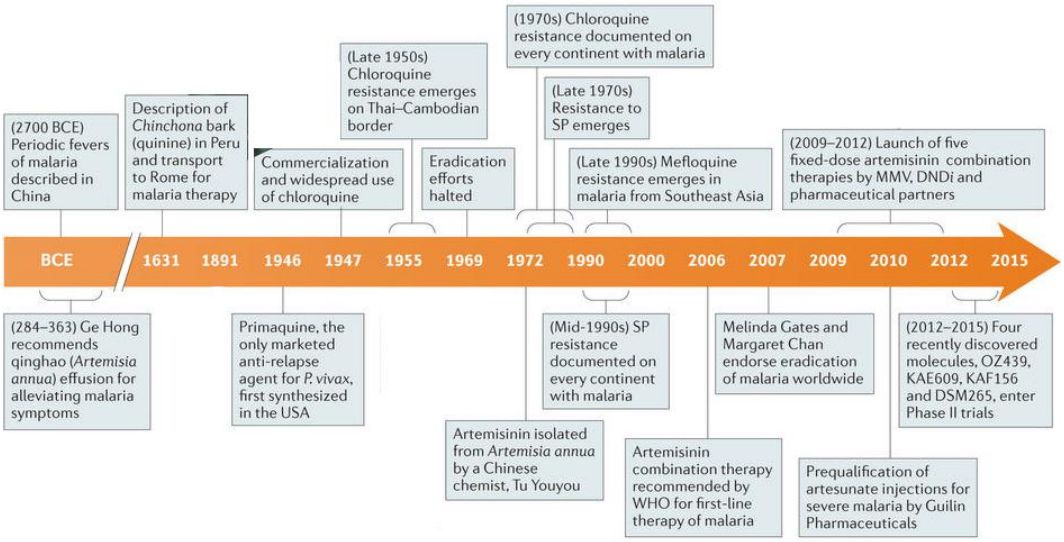

Fig. 1.7 A timeline of antimalarial drugs development and the emergence of resistance. Abbreviations: Sulphadoxine–Pyrimethamine (SP), Drugs for Neglected Diseases initiative (DNDi), World Health Organization (WHO), Medicines for Malaria Venture (MMV) (Source: Wells *et al.,* 2015).

The last new class of antimalarial, prior to artemisinins, was atovaquone (ATQ), a naphthoquinone that was combined with proguanil (PG) in the prophylactic drug malarone. Unfortunately, resistance to ATQ emerged almost immediately after its introduction (Vaidya and Mather, 2000).

The digestive vacuole (DV) is a key target for quinolone antimalarial drugs. The DV is an acidic lysosomal-like compartment within intraerythrocytic parasites which haemoglobin digestion takes place. As a result of haemoglobin digestion, the toxic haem moiety (ferriprotoporphyrin IX, FPIX) is released and is available to damage the DV membrane

(Leed *et al*., 2002; Sullivan *et al.,* 1996; Ginsburg *et al.,* 1998). FPIX is detoxified by biocrystalization to generate haemozoin, also termed malaria pigment, as well as by glutathione mediated degradation. Quinoline drugs, particularly the 4-aminoquinolines (including chloroquine, amodiaquine, pyronaridine and piperaquine) and aryl amino alcohol (including quinine and mefloquine, see Fig. 1.8) have a high affinity for FPIX, with the subsequent FPIX conjugate no longer being capable for biocrystalization. Thus, toxic levels of FPIX conjugate accumulate within the DV in the presence of quinolone drugs (reviewed in De Villiers and Egan, 2009). A key aspect of the targeted accumulation of quinolones is their weakly basic properties. In neutral conditions (outside of the DC), these molecules are neutral and have the capacity to readily transit membranes. However, within the acidic DV, these quinolines becomes protonated and this positive charge means that they are no longer capable of transiting membranes, accumulating to high concentrations with the consequential effect of generating toxic FPIX conjugates (Famin *et al,* 1999; Ginsburg *et al.,* 1998; Auparakkitanon *et al*., 2006; Fivelman *et al*., 2007; Warhurst *et al.,* 2007). Of note is that the aryl amino alcohols mefloquine and quinine are weaker basic properties and less affinity to FPIX, suggesting these drugs may also share additional modes of action (Foley and Tilly, 1997).

Of note is therapeutic potential of chloroquine against other conditions such as dermatological, immunological, rheumatological and infectious diseases (reviewed in Al-bari, 2015). Here the acidotropic properties of the weak base chloroquine has been noted to cause an accumulation in acidic lysosomes where it can interfere with antigen presentation on the surface of dendritic cells and/or block cytokine production by macrophages as well as inhibiting Ca^{2+} and Toll-like receptors signalling in B and T cells (Kyburz *et al.,* 2006; Ma *et al*., 2012). Similarly, a role for chloroquine as an adjunct for

cancer therapy has been previously reported to be associated with its ability to modulate the autophagy pathway (Farrow *et al.,* 2014) and/or induce apoptosis (Park *et al*., 2016).

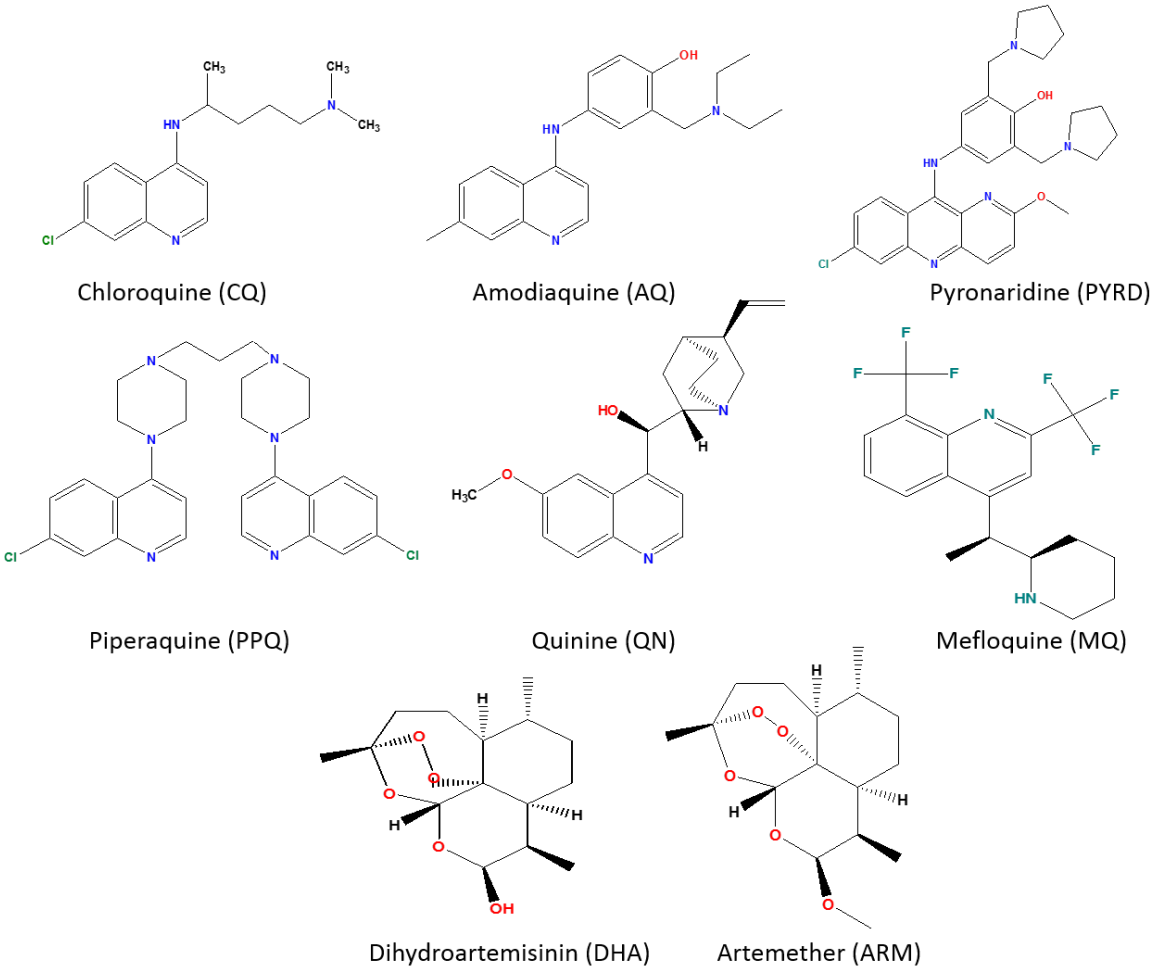

Fig. 1.8 Chemical structure of antimalarial drugs (Sours: Delves *et al.,* 2012).

Artemisinins, sesquiterpene lactones that contain an endoperoxide bridge, are the latest class of antimalarials to be introduced. Artemisinins were discovered in 1972 in China by a team led by Tu Youyou, research that led in 2015 to her being jointly awarded the Nobel Prize for Medicine or Physiology (Croft and Ward, 2015). Artemisinin are a natural product isolated from the plant *Artemisia annua*, a plant used in Chinese traditional medicine for the treatment of fevers. This natural product was isolated and modified by Tu's team to reduce its toxicity and improve its antimalarial efficiency (Miller and Su, 2011). Artemisinin and its derivatives became the first line for both uncomplicated and severe malaria infections at the start of the 21st Century (Maude *et*

al., 2010). Artemisinins' antimalarial action arises as a result of the scission of the endoperoxide bridge within artemisinin molecules by free iron or iron within FPIX to produce free radicals or reactive oxygen spices (ROS) (Antoine *et al.,* 2013; Meshnick *et al.,* 1993). During this process, ferrous iron binds with either oxygen in the bridge cleaving the endoperoxide bond producing oxygen radical intermediates, which then undergo rearrangement process producing carbon-centred radicals (Butler *et al.,* 1998). These carbon-centred radicals have high affinity to bind with macromolecules such as protein, lipid, DNA and carbohydrate. Given the wide range of apparent targets of action, treatment with artemisinins is characterized by a fast reduction of parasitaemia, their high potency and gametocytocidal effects (Balint, 2001). Artemisinin was originally introduced as a monotherapy, although concerns regarding 28-day clearance rates (a key concern given the short serum half-life of artemisinins) and the risks of drug resistance, led to the introduction of artemisinin combination therapies (ACT) and are now recommended by the WHO (Sagara *et al.*, 2012). ACT use an artemisinin in combination with a partner drug such as lumefantrine, piperaquine (PPQ) or pyronaridine (PYRD), with the latter drugs providing protection against recrudescence based on their longer serum half-lives (Eastman and Fidock, 2009; Henrich *et al.,* 2013). Unfortunately, recent reports describing the failure of ACT and the emergence of resistance to artemisinin, MQ and PPQ in South East Asia referring to a challenge to the future of this highly effective combination therapy (Dondorp *et al.,* 2009; Dondorp *et al.*, 2017; Na-Bangchang *et al.*, 2013; Saunders *et al.*, 2014).

1.4.2 The search for future antimalarial drugs

Although decades of the global efforts to combat malaria have led to the reduction of mortality and morbidity by 60% and 37%, respectively, emergence of resistance to ACT highlights the demand for new treatment strategies to face a future with widespread

multidrug resistant malaria parasites (Hemingway *et al.,* 2016). A global strategy has been set by the WHO, includes achieving a 90% reduction in malaria burden between 2016 and 2030 (WHO, 2016). To meet this ambitious strategy, the antimalarial drug community came together to describe two new antimalarial medicines; a single exposure radical cure and prophylaxis (SERCaP) for the treatment of malaria cases and a new prophylactic treatment that would be suitable for a mass drug administration (Burrows *et al.,* 2013). This work included the development of target product profiles (TPP) for each medicine; with target candidate profiles (TCP) indicating the ideal and minimal requirements for the different component parts of what will be a combination therapy drug. These TCP and TPP represent key platforms for antimalarial drug discovery and development, and this need to be renewed regularly according to changes in requirements that relate to the needs of patients and the current status of malaria parasite resistance (Burrows *et al.,* 2017). Four different therapeutic strategies have been proposed relating to the phase of parasite infection; (1) a liver stage therapy to target hepatic schizonts and dormant hypnozoites, (2) an intraerythrocytic stage therapy to target the parasite burden causing disease (3) a transmission blocking therapy to work either in humans or the mosquito and (4) production of small molecules that provide chemoprophylaxis in migrant population and asymptomatic cases suitable for mass distribution (Leroy *et al.,* 2014).

Based on these requirements, several TCPs were proposed (Fig. 1.9). These include; TCP1, this was previously used for rapid clearance of asexual blood stage parasites, although now also includes drugs with long duration of action through a long serum half-life (Flannery *et al.,* 2013a). This merging of two previous TCP addresses the need for a rapid elimination the majority of parasites from blood stream by a fast acting candidate with residual parasites being removed by the long duration of action of the partner candidate

potentially providing post-treatment prophylaxis. An additional candidate to be included in the combination therapy needs to target hepatic hypnozoites directly as well as preventing relapses, mainly *P. vivax*, from dormant hypnozoites. This was previously termed TCP3a and is now TCP3 and TCP4, respectively (Burrows *et al.,* 2017). The final human stage target are the gametocytes, the candidate previously called TCP3b, and now is TCP5 focusses on the blocking of malaria transmission through targeting the parasite gametocytes and TCP6, an endectocide molecule that blocks parasite transmission by targeting the insect vector (Burrows *et al.,* 2017).

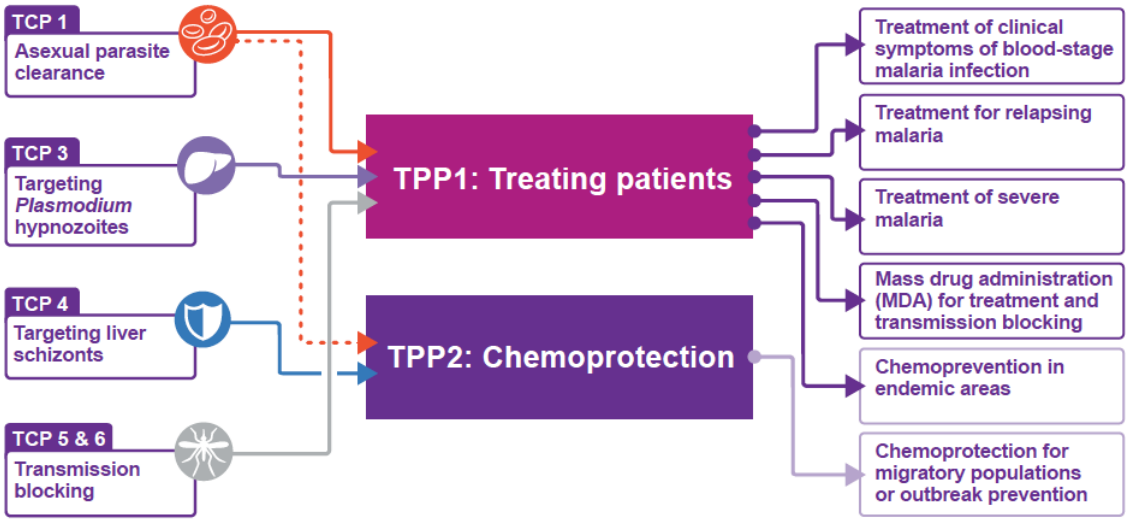

Fig. 1.9 Correlation between target product profiles (centre) and target candidate profiles (left) of the proposed combination therapies. The uses of each product were summarized on the right (Source: Burrows *et al.,* 2017).

Phenotypic screening of massive chemical libraries to date have explored the antimalarial activity of over six million compounds (Gamo *et al.,* 2010), identifying 20-30,000 compounds that exhibit sub-micromolar potency against the blood stage of malaria parasite *P. falciparum.* This search resulted in a significant progress over the past decade,

with many new chemicals entering the pipeline for antimalarial drug development (Wells *et al.,* 2015). To provide a sustainable pipeline, however, there remains a requirement to discover and develop new antimalarial chemotypes that have modes of action distinct to those that currently exist.

These distinct modes of action are typically attributed to biological processes that are both essential and unique to the parasite. Biological processes that occur in both mammalian and mosquito host are generally are less favourable, although parasite-specific differences may afford an opportunity to develop drugs that are more selective for the parasite over the host. Towards this end, my thesis explores the potential of a non-canonical autophagic pathway in *P. falciparum*. In addition, I explore here how a better understanding of how parasites die following drug perturbation may provide insights to a process of programmed cell death that may be exploited in the search for parasite-specific biological processes.

1.5 Programmed cell death

To support ongoing of antimalarial drug discovery, there is an urgent demand to explore novel modes of drug action. One opportunity depends on understanding the potential of programmed cell death (PCD). The existence, and indeed the role, of PCD within malarial parasites is controversial (discussed below), and although several recent reports have described features typical of apoptotic PCD following drug treatment (Ch'ng *et al.,* 2010, 2011; Gaviria *et al.,* 2013; Gunjan *et al.,* 2016; Meslin *et al.,* 2007, 2011a, b; Picot *et al.,* 1997; Rathore *et al.,* 2015; Roberts *et al.,* 2008), others do not (Nyakeriga *et al.* 2006; Porter *et al.,* 2008; Tomlins *et al.,* 2013; Totino *et al.,* 2008). These reports together do not currently provide a conclusive view on what features of cell death following drug

treatment could be attributed to PCD, or even a pathway that would link these features together. For example, the importance of PCD in parasite cell death, and the potential for such a pathway as a new drug target, represents a significant gap in our understanding of the malaria parasite.

1.5.1 The nomenclature of programmed cell death

Cellular death has an essential role in maintaining the morphological and physiological balance in health and disease (Fuchs and Steller, 2011). Hence, the study of phenotypic and biological changes that correlated with cell death are fundamental in disease control and treatment. The term of cellular death is complex, and has developed with increases in our understanding of the mechanisms by which cells die. Prior to 1970, all cell death was considered necrosis (accidental cell death) before the discovery of apoptosis, a PCD that forms a part of the normal function of the cells (Kerr *et al*., 1972). PCD can be triggered in both normal and infected cells, while necrosis just occurs in pathological cases (Nabben and Glatz, 2015; Kroemer *et al.*, 2009). However, it has since been proposed that two main categories of PCD exist; autophagic-like cell death and apoptotic-like cell death (formerly apoptosis) (Bursch *et al.,* 2000) (Fig. 1.10). PCD are regulated programmes of cell death that follow distinct pathways with both apoptosis and autophagy acting as positive or negative regulators in cell maintenance during health and disease (Dockrell, 2001; Shintani and Klionsky, 2004). Apoptosis (type I of PCD) can be a normal development response when death signals are received, or could results from trauma such as drug treatment (Sanz *et al.,* 2008). Apoptosis is characterised by specific features, such as; plasma membrane blebbing, collapse of the mitochondrial outer membrane potential (ΔΨm) and increase its permeability, nuclear compaction (pyknosis), DNA

fragmentation and caspase activation. The cells ultimately shrink and show signs of cytoplasmic and nuclear fragmentation. Autophagic cell death is a more recent classification of PCD (type II) and is often termed macroautophagy. This type of PCD is generally induced by nutrient starvation, but has been shown to result from normal cell differentiation (Nunes *et al.,* 2014), as well as pathological processes such as neurodegenerative disease and cancer (Levine and Kroemer, 2008). Cells undergoing autophagic-cell death show the development of large autophagosome structures that enclose part of cytoplasm and organelles, delivering and fusing them to lysosomes to degrade their contents.

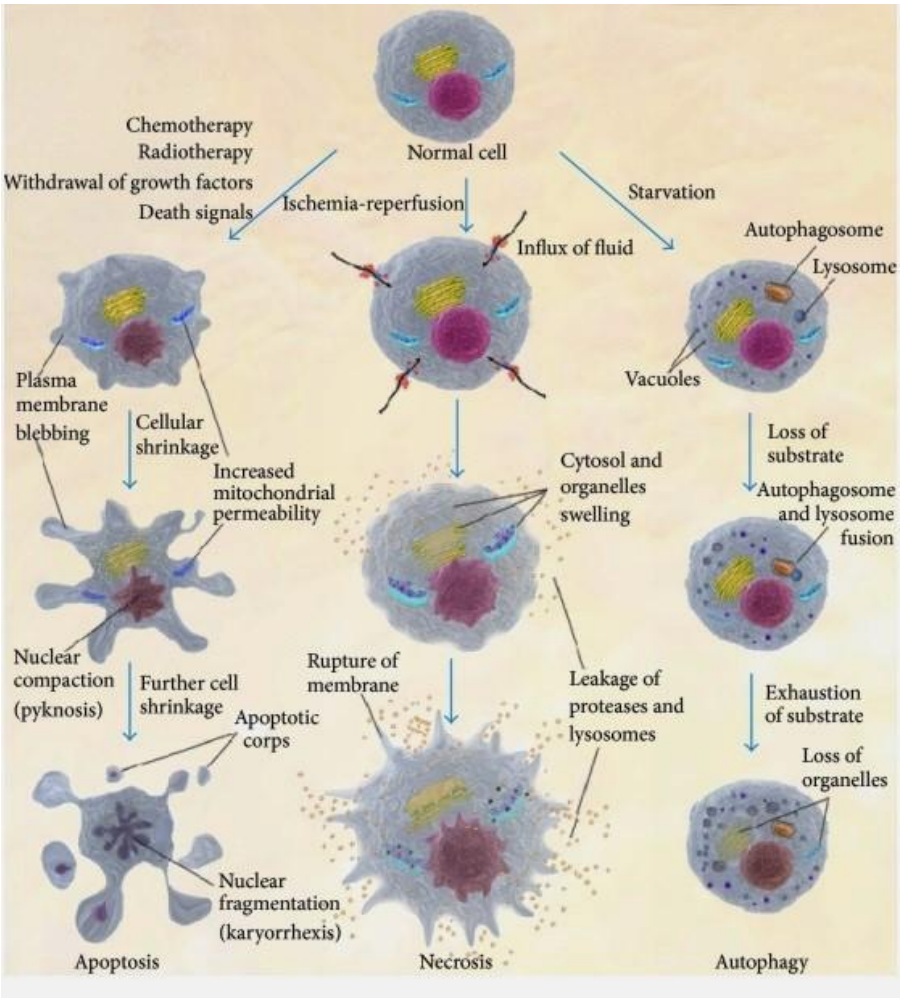

Fig. 1.10 Scheme illustrating morphological differences between necrosis, apoptosis and autophagy cell death in metazoan cells (Source: Nunes *et al.,* 2014).

1.5.2 Programmed cell death in malarial parasites

Whilst the study of cell death, and that of PCD, has primarily focussed on their effects in metazoans, features related to PCD have been increasingly observed in unicellular organisms including *Leishmania spp.,* trypanosomes, *S. cerevisiae*, *Trichomonas vaginalis* (Deponte, 2008) and *Toxoplasma gondii* (Ghosh *et al.,* 2012). The existence of PCD in *Plasmodium* spp. remains the subject of debate with some studies suggesting that PCD is apoptosis (Ch'ng *et al.,* 2010, 2011; Mutai and Waitumbi, 2010; Pattanapanyasat *et al.,* 2010), whilst others support the occurrence of autophagic-like cell death (Cervantes *et al.,* 2014; Eickel *et al.,* 2013; Gaviria *et al.,* 2013; Porter *et al.*, 2008; Totino *et al.*, 2008). Some studies favour the presence of both apoptosis and autophagic-like cell death (Engelbrecht and Coeltzer, 2013; Oakley *et al.*, 2007). Perhaps the most interest is why would a protozoan parasite undergo PCD? PCD is widely studied in metazoan organisms, where there PCD plays a critical role in development, normal homeostasis and response to environment or infective agents (Gavrilescu and Denkers, 2013). Looking at protozoan cell death using "language" developed for metazoans is likely the basis for this ongoing debate about whether true PCD exists in the malaria parasite. During evolution, however, the malaria parasite has selected a set of biological pathways to support its development. These would include many pathways that allow the parasite to infect, colonise and reproduce in two very different host environments (Coppens, 2011).

As well as the key morphological features described above, a critical molecular marker of autophagic-like cell death is the autophagy related protein 8 (Atg8), a protein located in the membrane of autophagosomes, whilst a key marker of apoptosis are caspase enzymes (the absence of a role of caspases in autophagic-like cell death has also led to this process being termed caspase-independent PCD). The molecular markers of

autophagy in *Plasmodium* are discussed in more detail below. However, true caspases have not been identified in *Plasmodium* parasite, although caspase-like cysteine proteases (metacaspases) found in plants, fungi, and protozoan, which also lack true caspases are found (Meslin *et al.,* 2011b).

Three metacaspase genes, PfMCA1 (PF13_0289), PfMCA2 (PF14_0363) and PfMCA3 (PF14_0160) have been found in the genome of *P. falciparum,* although the actual role(s) of these molecules has not been yet resolved (Meslin *et al.,* 2011b). The expression of PfMCA1 is limited to the intraerythrocytic stages of development (Meslin *et al*., 2011b), whereas expression of its homologue PbMCA1 in *P. berghei* was restricted to female gametocytes, oocysts and sporozoites, and did not correspond with significant observations of apoptosis (Le Chat *et al*., 2007). Some features of apoptotic-like cell death have been described in *P. falciparum* following stress although with only limited evidence of metacaspase activity (Ch'ng *et al.,* 2010, 2011; Eda and Sherman 2002; Picot *at al.,* 1997; Rathore *et al.,* 2011, 2015).

1.6 The autophagic pathway

Autophagy is a lysosome-mediated degradation pathway by which abnormal proteins and injured organelles can be recycled providing micromolecules, mainly amino acids, as an endogenous source of energy (Eskelinen and Saftig, 2009). This process supports cell survival during different cellular stresses such as nitrogen starvation (Angcajas *et al.,* 2014) or oxidative stress (Scherz-Shouval *et al.,* 2007). Additionally, information obtained via electron microscopic studies has shown that autophagy is part of developmental process supporting the life cycle of eukaryotic cells, where recycling of organelles by the autophagy machinery is a key response to deprivation of growth factors or nutrients (Lum *et al.,* 2005). These observations are supported by developmental phenotypic studies of

mammalian cells cultured under different conditions (Cecconi and Levine, 2008). These studies demonstrated that the autophagy pathway has an ability to mimic PCD in a caspase-independent manner, and is termed autophagic cell death or programmed cell death type II (PCD II). Accordingly, autophagy can play a negative or positive role in cell survival (Deretic, 2006). Moreover, genetic and phenotypic studies of malignant tumours indicated that disease progression is mediated by autophagy and thus provides a potential new therapeutic target for drug discovery (Rubinsztein *et al.,* 2012b; Sui *et al.,* 2013).

Autophagy was first described following the observation in the cytosol of cells of cytoplasmic content sequestrated by a double or multiple membrane structure that were then fused to lysosome. These double or multiple membrane structures, later termed autophagosomes, contained mitochondria, endoplasmic reticulum (ER) and lysosomal hydrolytic enzymes. Presenting autophagy in 1963 as the mechanism for the degradation and recycling of intracellular macromolecules by lysosomes, Christian de Duve opened up a new field of autophagy that has impacted significantly on our understanding of normal and pathological cell biology (Klionsky, 2008). The origin of autophagy is Greek: “auto” meaning self and “phagy” meaning eating and specifically refers to the recycling of cellular macromolecules or organelles under specific physiological or limited nutrient conditions (Reuck and Cameron, 1963).

Several broad patterns of autophagy have been identified based on the processes of cargo packaging and delivery to the lysosome (Glick *et al.,* 2010), and are broadly termed microautophagy, macroautophagy or chaperone-mediated autophagy (Fig. 1.11). In microautophagy, direct engulfment of targeted materials occurs by the lysosome

membrane. Macroautophagy refers to the process that includes autophagosome formation, where selected substances are processed, vesiculated and trafficked to lysosome for degradation (reviewed in Rigden *et al.,* 2009). While in chaperone-mediated autophagy, chaperone-tagged proteins are guided to interact selectively with chaperone receptors on the lysosome membrane following by transferring them through the lysosome membrane to the lysosome lumen to be degraded (Kaushik and Cuervo, 2012). However, alternative classifications of autophagy detail the type of cargo, including mitophagy, pexophagy, ribophagy and lipophagy for the degradation of mitochondria, peroxisomes, ribosomes and lipid droplets, respectively (He and Klionsky, 2009).

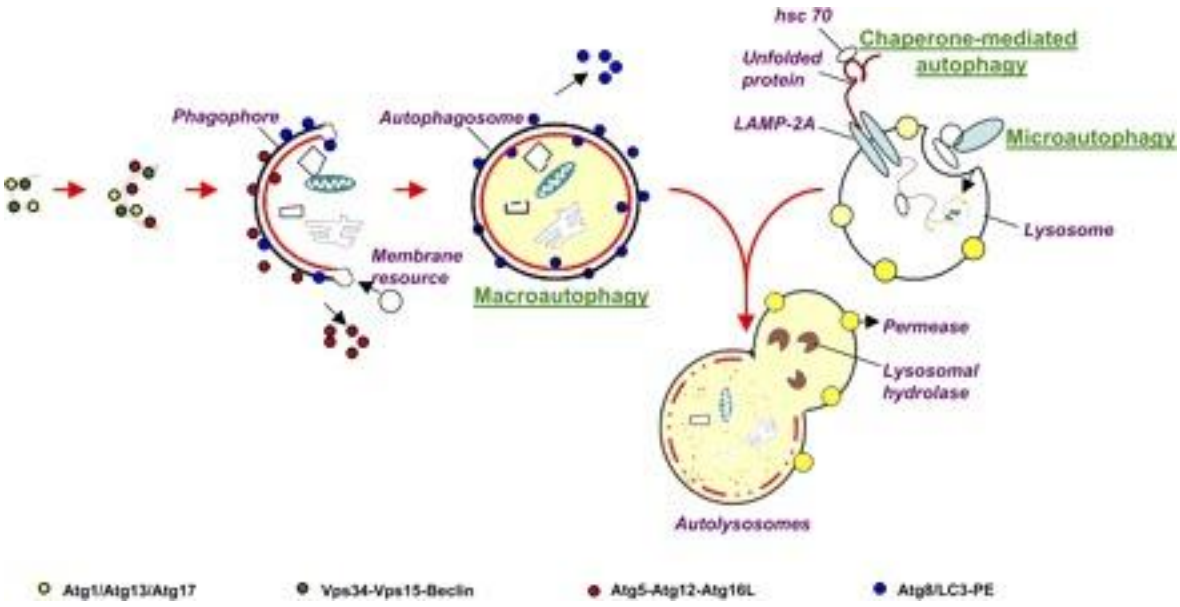

Fig. 1.11 Illustrates the different forms of autophagy. Microautophagy initiates with direct engulfment of the targeted materials at lysosome membrane followed by membrane invagination, protrusion and separation of contents into the lysosome lumen. Macroautophagy involves formation of C-shape double membrane structure (phagophore) that sequesters a portion of cytoplasm (or organelles) producing an autophagosome, which subsequently fuses with the lysosome membrane to produce an autolysosome. Chaperone-mediated autophagy is where the substrate-chaperone complex is driven to lysosome via lysosomal chaperone receptors LAMP-2A. The key refers to the involvement of different protein complexes during macroautophagy and are described further in the main text (Source: Periyasamy-Thandavan *et al.,* 2009).

Macroautophagy is characterised by the formation of a pre-autophagosomal structure termed the phagophore assembly site (PAS) (Mizushima *et al*., 2001; Suzuki *et al*., 2001). PAS grow and elongate to produce initial sequestering compartment, a double-membrane structure named phagophore. The targeted materials are enclosed by phagophore, with a range of organelles or plasma membrane thought to provide lipid membrane for its growth (Axe *et al.,* 2008; Hailey *et al*., 2010; Ravikumar *et al.,* 2010; Simonsen and Tooze, 2009). Although the exact origin of the phagophore in mammalian cells is questioned, the double membrane autophagosome is generated as a result of expansion and completion of the phagophore (Rubinsztein *et al*., 2012a). When the autophagosome docks with a lysosome, the outer membrane of the autophagosome fuses with the lysosome single membrane and its cargo along with the inner autophagosome vesicle are released into the lysosomal lumen to undergo digestion (reviewed in Duszenko *et al.,* 2011). The lysosome lumen provides an acidic environment with hydrolysis enzymes that digest the targeted proteins, lipids, carbohydrates and nucleic acids forming recyclable materials that are recycled back to the cytosol through transport proteins (permeases) located in the lysosome membrane (Russell *et al*., 2014). Both selective and non-selective autophagy of aggregated proteins and organelles has been described in eukaryotic cells (Kraft *et al.*, 2009). Selective autophagy is considered a receptor-based autophagy pathway, where a specific cargo (e.g. mitochondria, ribosome, nucleus) are tagged in response to internal signals derived from the cargo itself (Yu *et al.,* 2008).The alternate, non-selective autophagy, results when cytoplasmic components are randomly sequestrated by a phagophore in response to environmental signals such as nutrient starvation or hormone limitation (Kim and Klionsky, 2000; Yin *et al.*, 2010).

1.7 Regulation of the macroautophagy pathway

Investigation of response to nutrient depravation in the yeast *Saccharomyces cerevisiae* has proven critical in determining the regulated cascade of molecular events in macroautophagy (Inoue and Klionsky, 2010). The most common naming for the component parts of the macroautophagy system uses the prefix Atg, based on their homology to autophagy mutants originally described in *S. cerevisiae* (Rose *et al.,* 2006; Suzuki *et al.*, 2001). Biochemical and electron microscopy studies complement genetic and modern bioinformatics approaches to extend our understanding of how macroautophagy operates, allowing consensus aspects of this process to be described. These fall into six main steps, detailed below (He and Klionsky, 2009).

(i) Nutrient sensing and induction of autophagy*.*

Sensing and responding to nutrient availability is essential for cell viability. Under normal nutrient conditions, nutrient sensing pathways engage with biosynthesis and storage pathways of macromolecules, whilst under starvation conditions new micromolecule homeostasis mechanisms are required (Efeyan *et al.*, 2015). Nutrient-poor conditions promote cells to use autophagy to provide endogenous micromolecules. In starved cells, target of rapamycin (TOR)-dependent triggers are initiated as the first step of the autophagy pathway (Diaz-Troya *et al.*, 2008). TOR complexes are fundamental in maintaining a balance between biosynthetic and catabolic processes within cells. There are two multiprotein complexes of TOR; TOR complex 1 (TORC1) and TOR complex 2 (TORC2), both are implicated in the autophagy regulatory machinery (reviewed in Brennand *et al.*, 2011). Only TORC1 (mTOR1 in mammals) is sensitive to rapamycin antibiotic treatment (Loewith *et al.*, 2002). Under nitrogen-poor conditions, TORC2

through its downstream target protein kinase (Ypk1) inducing factor-2α (eIF2α) kinase (an amino acid sensor) to upregulate the macroautophagy pathway (Vlahakis *et al.*, 2014). TORC1 operates differently, and inhibits the eIF2α kinase which causes down regulation of macroautophagy under normal growth condition (Valbuena *et al.,* 2012). When nutrients become limited, or after exposure to rapamycin, macroautophagy is upregulated. Induction of this autophagy pathway follows from dephosphorylation of Atg13 that increases its affinity for the autophagy initiator protein (Atg1) (Puente *et al.,* 2016; Wu *et al.,* 2013). Under nutrient rich conditions, TORC1 blocks the autophagy process by hyperphosphorylation of Atg13 that inhibits the interaction between Atg1 and Atg13. As such, the Atg1-Atg13 complex is a key operator regulating these early initiator events (Kamada *et al*., 2000). The activity of Atg1-Atg13 complex is required for the formation of the phagophore in yeast, likely by guiding transmembrane protein Atg9 to accumulate at the PAS site to promote lipid collection to the expanding phagophore (He *et al.,* 2008; Simonsen and Tooze, 2009). Other Atg proteins are recruited to the PAS; the transmembrane protein (Atg18) contains a phenylalanine-arginine-arginine-glycine (FRRG) motif, which is essential for combination with phosphatidylinositol-3 phosphate (PI3P) and Atg18-Atg2. Atg18 serves as a platform for Atg8 translocation to the PAS, a key biomarker for autophagic activity, as well and protects it from the premature cleavage activity of Atg4 (Nair *et al.*, 2010).

(ii) Cargo selection and packaging

Although the term of autophagy often refers to non-selective degradation of cytoplasmic components by macroautophagy, specific selection of cargo to the PAS operates using receptor and adaptor proteins to specifically isolate a cargo. Our understanding of this selective targeting is based primarily on information obtained from studies of cytoplasm

to vacuole targeting (CVT) process originally described in yeast (Lynch-Day and Klionsky, 2010). Atg19 is a key protein in cargo selection in the CVT signalling route (Scott *et al.*, 2001). Association of Atg19 with precursor aminopeptidase I (PrApe1) and precursor α-manosidase I (PrAm1) produce the CVT complex, which binds later with Atg11. Both Atg19 and Atg11 work to drive CVT cargo to the PAS site. The Atg19 provides a binding site to Atg8-PE complex on the PAS (reviewed in Duszenko *et al.*, 2011) (Fig. 1.12). For more specific organelle cargo, a range of additional CVT proteins have been identified. These include Atg30, which has been identified as a central protein for pexophagy (Farre *et al.*, 2008). Selection of peroxisomes for degradation is mediated by two peroxisomal membrane proteins (PEX3 and PEX14). These proteins also participate in biogenesis of the peroxisomes. The phosphorylated form of PEX14 interacts with Atg30 to target peroxisomes and drive them to the PAS site (Manjithaya *et al.*, 2010). Furthermore, mitochondria can be targeted and degraded under low oxygen conditions, where yeast uses a fermentation process instead of a respiratory process. Both Atg32 and Atg33 proteins have been reported as essential proteins in mitochondria targeting in *S. cerevisiae* (Kanki *et al.,* 2009; Okamoto *et al.,* 2009).

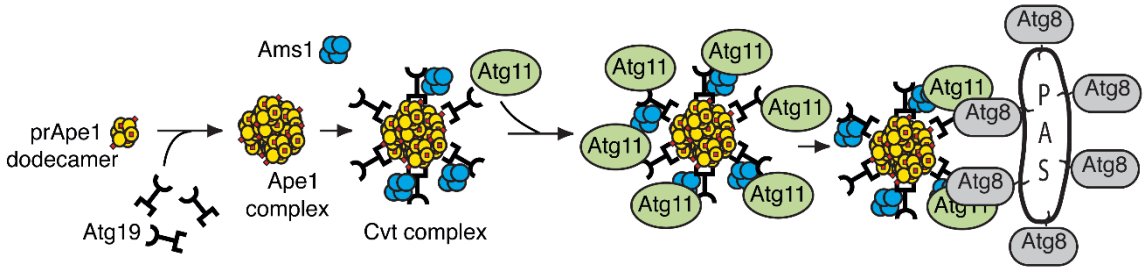

Fig. 1.12 Molecular events of cargo selection in the cytoplasm to vacuole targeting (CVT) pathway. Accumulation of precursor aminopeptidase I (prApe1) and Ams1 with Atg19 to produce the CVT complex, which combines with Atg11 to be transferred to Atg8 on the PAS site (Source: Klionsky, 2005).

(iii) Vesicle nucleation

Phosphorylation of PAS as a result of the activity of the phosphatidylinositol-3-kinase (PI3K)-III complex triggers the nucleation process. Initially, vacuolar protein sorting (Vps34) combines with the phagophore membrane following activation of Atg1 kinase (ULK1) (Itakura and Mizushima, 2010). Vps34 is a catalytic component of multiple protein complexes, some of which implicate in autophagy-independent machinery, whilst others are involved in the distinct stages of autophagy process (Koyama-Honda *et al.*, 2013) (Fig. 1.13). The PI3K-III complex is composed of Vps15, Vps34, Atg6 and Atg14 that converts phosphatidylinositol (PI) to PI3P on the PAS and this is followed by recruitment of Atg18, Atg2, Atg20, Atg21 and Atg24 (Obara *et al.,* 2008; Suzuki *et al.,* 2001). In addition, colocalization of At18 and Atg2 provides a binding site for other related proteins on the PAS and phagophore membrane (Burman and Ktistakis, 2010). Activation of Atg9 is required to modify PAS to the phagophore membrane during initiation step of macroautophagy. The Atg9 also serves as platform for binding At18-Atg2 complex to the PAS (Nair *et al*., 2010). Webber *et al* (2007) confirmed that mammalian Atg9 (mAtg9) traffic between Golgi complex and endosomes suggesting involvement of Golgi complex in autophagy pathway.

(iv) Vesicle maturation and completion

During this step, maturation of the phagophore membrane is completed producing an autophagosome (Fig. 1.13). Two complexes belong to families of ubiquitin-like proteins participate in this process; the Atg12-Atg5 conjugation system and the Atg8-PE conjugation system (Geng and Klionsky, 2008; Nakatogawa *et al*., 2009). In the first system (the Atg12-Atg5 complex), the activity of Atg7 and Atg10, which represent E1-like

activating enzyme and E2-like ligase enzyme, respectively, are required for covalent conjugation between Atg12 and Atg5 (Walczak and Martens, 2013). Dimerizing two molecules of Atg16 causes non-covalent interactions between Atg16 and Atg12-Atg5 producing the Atg12-Atg5-Atg16 complex (E3-like ligase enzyme). In the second conjugation system, Atg4 cleaves the Atg8 to expose its C-terminal glycine which allows Atg8, through the action of Atg7 (an E1-like activating enzyme), to bind covalently to Atg3 (an E2-like ligase enzyme) producing Atg8-Atg3 complex. The Atg12-Atg5-Atg16 complex now acts on the Atg8-Atg3 complex to add phosphatidylethanolamine (PE) to Atg8 and deposit the Atg8-PE within the phagophore membrane (Nakatogawa, 2013). It has been shown that the Atg8-PE complex localizes on both the outer and inner membranes of phagophore, whilst the Atg12-Atg5-Atg16 complex is only placed on the outer membrane (Brennand *et al.,* 2011).

In human cells, hLC3 (Light Chain 3) (Atg8 homologue) is reported in most cells as being in an inactivated form. During induction of autophagy, proteolysis of the LC3 substrate by the Atg4 cleavage enzyme produce LC3-I, which is reprocessed to LC3-II by Atg7 and Atg3 activities. In order to find a foothold on the phagophore membrane, the LC3-II conjugates with PE (Barth *et al.,* 2010). After completion of the autophagosome, reprocessing of the Atg8-PE complex by the Atg4 activity is required to deconjugate the Atg8 from the outer membrane of autophagosome and that facilitates maturation of this structure into fusion-capable autophagosome (Yu *et al.,* 2012), whilst a minor population of the Atg8 remains linked with the inner surface of autophagosome until it is fused with the lysosome. Thus Atg8 is considered as a core marker in identification of the autophagy machinery (Fig. 1.13) (reviewed in Duszenko *et al*., 2011).

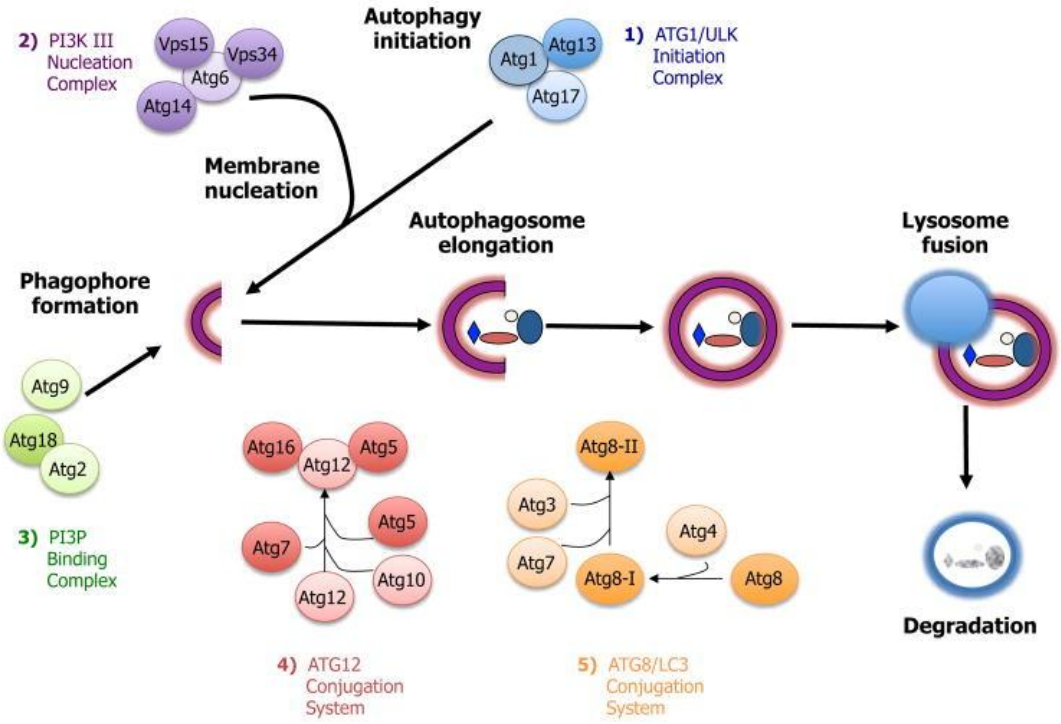

Fig. 1.13 Molecular events during autophagosome formation. Formation of the double-membrane bound autophagosome involves a sequential series of steps from induction, membrane nucleation, phagophore formation and autophagosome elongation to form the complete autophagosome. These steps are controlled by at least five different functional groups of proteins: 1) The Atg1/ULK1 initiation complex; 2) the PI3-kinase nucleation complex; 3) the PI3P-binding complex; 4) the Atg5-Atg12 conjugation system; and 5) the Atg8/LC3 conjugation system (Source: Gelino and Hansen, 2012).

(v) Trafficking, docking and fusion to the lysosome

Atg proteins which are involved in the earlier steps of autophagosome formation are deconjugated and relocalized to be reused in a new cycle of autophagy. Accordingly, Atg8, Atg5, Atg12 and Atg16 leave the outer membrane of the autophagosome or CVT vesicle and recycled in order to be used in a new autophagy cycle (Legakis *et al.,* 2007; Nakatogawa *et al*., 2007). The autophagosome, with its cargo, is now ready to fuse with the lysosome with Atg8 and Rab7 acting as key regulators in this trafficking. Although direct fusion between the autophagosome and lysosome to produce an autolysosome is the most common outcome, in mammalian cells the autophagosome under unknown

conditions can also combine with late endosomes to generate an amphisome, which subsequently fuses with the lysosome to form an autolysosome (Klionsky and Schulman, 2014).

(vi) Vesicle breakdown within the lysosome

Acidic hydrolysis degrades the autophagosome cargo components during this last step of the autophagy process. As described earlier, the autophagosome docks to lysosome and the outer membrane of the autophagosome fuses with the lysosome single membrane and its cargo along with the inner autophagosome vesicle are released into the lysosomal lumen to undergo digestion (reviewed in Duszenko *et al.,* 2011). The membrane of the internalized autophagosome undergoes delipidation and proteolysis through the action of lipase Atg15 and peptidase B in order to release the cargo and consume its components. As a final step, the Atg22 efflux system, which is found in the lysosome/ vacuole membrane, is responsible for the transport of amino acids (the end products of autophagy process) into the cytosol (Yang *et al.,* 2006).

1.8 The role of autophagy in *Plasmodium* parasites

Recent studies over the last 2 decades have provided evidence of autophagy-like trafficking in apicomplexan parasites (for reviews see Besteiro, 2017; Hain and Bosch, 2013; de Late *et al.,* 2017; Mizushima and Sahani, 2014). Autophagic vesicles have been described under conditions of nutrient starvation in *T. gondii* (Besteiro *et al.,* 2011) and *P. falciparum* (Tomlins *et al.,* 2013). However, the (i) lacking of full components (Atg proteins) of the canonical autophagy cascade (see below), (ii) as well as these parasites both being predominantly obligate intracellular parasites, and (iii) the lacking of lysosomes (the DV has been proposed to be the site of autophagosome targeting in *P.*

falciparum) have led some authors to suggest an alternative or additional roles for components of the classical autophagy pathway remaining in these parasites (reviewed in Besteiro, 2017). These alternatives explore the role of autophagy in the significant morphological changes of *P. falciparum* and apicoplast biogenesis (an organelle essential for parasite viability). It may well be that autophagy in *P. falciparum*, and other apicomplexan parasites, has been developed to have catabolic roles (cell cycle morphology changes and nutrient stress) as well as a role in maintaining an apicoplast and controlling its inheritance into daughter cells (Fig. 1.14). Importantly, from this figure, we see a key role for the autophagy biomarker Atg8 in all autophagy processes.

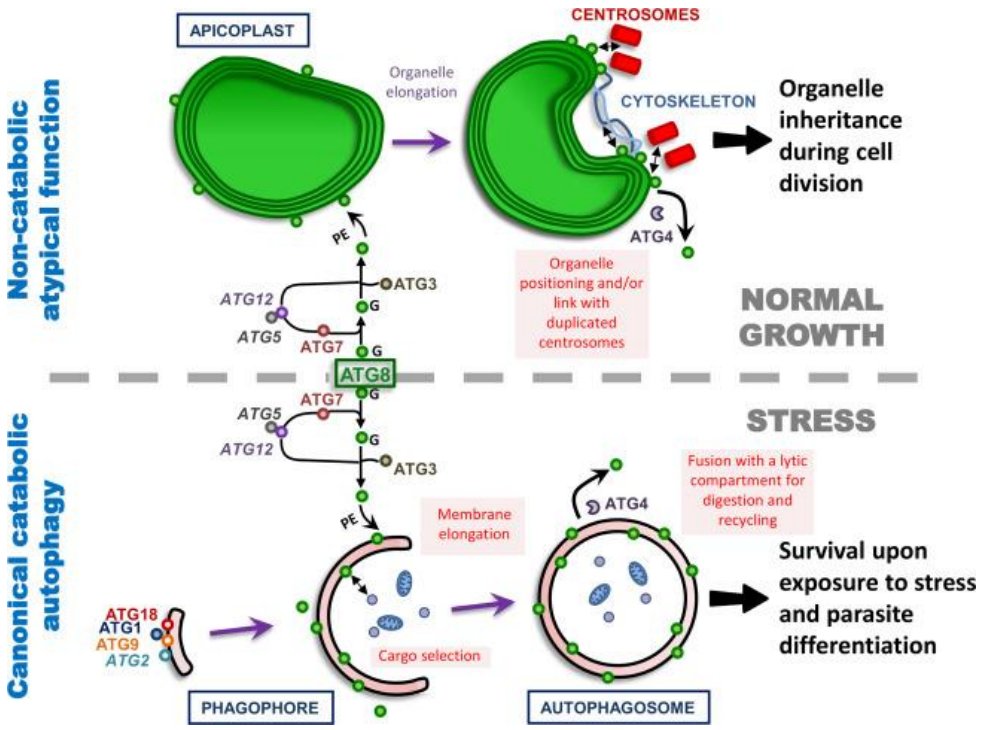

Fig. 1.14 Scheme illustrating the central role for the Atg8 autophagy marker in formation of the autophagosome and in apicoplast maintenance in apicomplexan parasites (Source: Besteiro, 2017).

1.8.1 Trafficking vesicles to the digestive vacuole

A role for the autophagy pathway during endocytic transport of *P. falciparum* has been explored by employing two different stress conditions. CQ perturbation and nutrient starvation have been used to study endocytosis in *Plasmodium* species (Gaviria *et al.,* 2013; Hoppe *et al.,* 2004). CQ is a lysosomotropic agent that blocks fusion between autophagosomes and the DV in *P. falciparum* causing an accumulation of endocytic vesicles in the parasite cytoplasm (Roberts *et al.,* 2008). Disruption of endocytic trafficking and accumulation of PfAtg8-decorated vesicles in the cytoplasm of *P. falciparum* challenged with CQ has been reported (Gaviria *et al.,* 2013). Cervantes *et al.* (2013) also observed involvement of PfAtg8 in both cytoplasmic vacuolation and apicoplast segmentation in *P. falciparum* treated with two lysosomotropic agents (CQ and bafilomycin A). Furthermore, immunofluorescence and ultrastructural studies suggested the role of Rab7a in endocytic vesicle trafficking in *P. falciparum* and *P. berghei* (Krai, 2013; Lopes da Silva *et al.,* 2012; Tomlins *et al.,* 2013). Similarly, Rab membrane markers such as Rab4, Rab5 and Rab11 in *Trypanosoma brucei* (Pal *et al*., 2002), Rab5 in *T. gondii* (Robibaro *et al.,* 2002) and Rab7 in L*eishmania donovani* (Patel *et al.,* 2008) have been reported to be associated with intracellular trafficking of autophagosome-like vesicles in these protozoan parasites.

1.8.2 Clearance of organelles

Metamorphosis in *Plasmodium* parasites follows successful infection and development in different host cells (Coppens, 2011). After the penetration of hepatocytes, the *Plasmodium* parasite undergoes morphological and physiological changes transforming from a motile and elongated form (sporozoite) to a non-motile and round-shaped form

(hepatic schizont) (Jayabalasingham *et al.,* 2010). During this transformation, clearance of organelles such as the inner membrane complex, rhoptries and micronemes occur (Jayabalasingham *et al.,* 2010). Two autophagy-mediated pathways are hypothesized to be involved in this organelle recycling, either organelle expulsion (exophagy) or vacuolar degradation of organelles (endophagy). Jayabalasingham *et al.* (2010) reported engulfment of micronemes and they were subsequent transported to the parasitophorous vacuole for expulsion. Immunofluorescence and fluorescence tagging studies indicates that micronemes expulsion was most likely included Atg8 proteins involvement (Coppens, 2011). This expulsion mechanism is widely reported in metazoans, including the maturation of RBCs, where the reticulocyte nucleus is expelled into bone marrow by an exosome-mediated pathway (Blanc *et al.,* 2005). During sporozoite metamorphosis, the biosynthetic organelles (e.g. ER, mitochondria and apicoplast) appear the only organelles protected from autophagic degradation (Coppens, 2011). Ultrastructural and biochemical studies of *P. berghei* liver stages revealed that PbAtg8-decorated vesicles in the parasite cytoplasm contain micronemes. Despite cytoplasmic vacuolation being shown in *P. berghei* following rapamycin treatment, the existence of PbAtg8-mediated mitophagy is still questioned (Eickel *et al.,* 2013). In *T. gondii,* starvation-induced mitophagy can be blocked by exposing parasites to the autophagy inhibitor 3-methayl adenine (3-MA), suggesting a similar role for autophagy in this parasite transformation (Ghosh *et al.,* 2012).

1.8.3 Apicoplast maintenance

The apicoplast is a non-photosynthetic plastid related to parasite survival in apicomplexan parasites, where it is involved in the synthesis of fatty acid, isoprenoid and iron-sulphur

clusters (Lim and McFadden, 2010). In *P. falciparum*, upregulation of Atg8 proteins during apicoplast biogenesis and partial localization with an apicoplast marker, acyl-carrier protein (ACP) suggesting a role of Atg8 in apicoplast maintenance (Kitamura *et al.,* 2012; Tomlins *et al.,* 2013). These observations were supported in a study performed by Cervantes *et al.*, where Atg8-labeled vesicles detected in both the cytoplasm of the intraerythrocytic stage of *P. falciparum* as well localized onto the apicoplast organelle (Cervantes *et al.,* 2014). Challenging parasites with the lysosomotropic agents CQ and bafilomycin A blocked endocytosis and caused apicoplast fragmentation supporting the proposed dual role of autophagy in degradation of intracellular proteins and biogenesis of apicoplast organelle (Cervantes *et al.,* 2014).

1.9 *P. falciparum* lacks a complete set of canonical autophagy proteins

Bioinformatic analyses of the *P. falciparum* genome, like other apicomplexan parasites, shows that whilst homologues of some members of the canonical autophagy pathway are present, many are not (Cervantes *et al.,* 2014; Hain and Bosch, 2013; Navale *et al.,* 2014). The apparent lack of some components, particularly those for induction and cargo selection, underpin arguments that autophagy as a response to nutrient stress may not be a key function for these parasites. That said, components for PAS formation specially Atg9 and autophagosome expansion exist, and support electron micrographs of these structures, particularly in *T. gondii* (Nguyen *et al.,* 2017), but not in *P. falciparum* (Cervantes *et al.,* 2014; Navale *et al.,* 2014). The presence or absence of these components is reviewed below.

Autophagy is typically induced by nutrient starvation or rapamycin treatment, but *P. falciparum* apparently lacks TOR proteins and hence this would explain the lack of

induction of autophagy in rapamycin treated *P. falciparum* parasite (Cervantes *et al.,* 2014). However, genes associated with phagophore expansion and vesicle completion have been found (Cervantes *et al.,* 2014). These analyses reveals that *P. falciparum* also lacks Atg13 and its C-terminal binding site on Atg1 (Hain and Bosch, 2013). This evidence together with distribution of autophagosome-like vesicles in the parasite cytoplasm suggests the existence of an Atg1-independent induction of autophagy in *P. falciparum*. The observation of autophagic vesicles in Atg knockout mice suggests that not all steps of the autophagy cascade are necessary (Mizushima and Levine, 2010). To date, a number of putative Atg homologues have been identified in malaria parasites (Hain and Bosch, 2013). See Fig. 1.15 for a summary. These include; Atg1 and Atg17 of the Atg1 complex (Navale *et al.,* 2014); Vps15, Vps34 (Navale *et al.,* 2014), Atg6 and Atg14 of the PI3K-III complex (Cervantes *et al.,* 2014); Atg18 and Atg2, but not Atg9, of the Atg9 cycling system (Cervantes *et al.,* 2014); Atg12, Atg5 and Atg16, but not Atg10, of the Atg12 ubiquitin-like conjugation system (Cervantes *et al.,* 2014) as well as all components (Atg8, Atg3, Atg4 and Atg7) of the Atg8-PE ubiquitin-like conjugation system (Cervantes *et al.,* 2014; Hain and Bosch, 2013; Navale *et al.,* 2014). More recently, putative homologues of additional Atg1 complex members (e.g. Atg29 and Atg31 genes) have not observed in whole genome sequences of *P. falciparum* (de Late *et al.,* 2017). Despite Atg6 but not Atg14 has been detected in *T. gondii* (de Late *et al*., 2017) it seems that both of these proteins are existed in autophagy cascade of *P. falciparum* (Cervantes *et al.,* 2014). Moreover, it has been proved that homologue of Atg18 and its motif FRRG (the binding site of P3K and Atg2) are expressed by in *P. falciparum*. Based on above, existence of PI3K enzyme and Atg2 homologues have been suggested in *P. falciparum* (Hain and Bosch, 2013). Altogether,

unlike higher eukaryotes and *T. gondii, P. falciparum* lacks critical proteins of nutrient sensing and induction of regular autophagy process (Cervantes *et al*., 2014) (Table 1.1).

Process	Atg gene	Navale *et al.* (2014)	Hain and Bosch (2013)	Cervantes *et al.* (2014)
Nutrient sensing and induction	Atg1	✓	✓	-[2]
	Atg13	✗	✗	-
	Atg17	✓	P[1]	-
	Atg29	-	P	-
	Atg31	-	P	-
Cargo selection	Atg11	✓	-	-
	Atg19	✗	-	-
Vesicle nucleation	Vps15	✓	✓	-
	Vps34	✓	✓	✓
	Atg6	✗	✗	✓
	Atg14	✗	✓	✓
Vesicle expansion and completion	Atg3	✓	✓	✓
	Atg4	✓	P	✓
	Atg5	✓	✓	✓
	Atg7	✓	✓	✓
	Atg8	✓	✓	✓
	Atg10	✗	✗	
	Atg12	✓	✓	✓
	Atg16	✗	✗	✓
	Atg21	✗	-	-
Trafficking, docking and fusion to the lysosome	Rab7	✓	✓	-
	Ykt6	-	✓	-
	VAMP8	-	✓	-
Vesicle breakdown	Atg15	✓	✗	✓
	Atg22	✓	✓	-
	Prb1	-	✗	-
Others	Atg2	✓	P	✓
	Atg9	✗	✗	✗
	TG18	✓	✓	✓
	Atg23	✓	-	-
	Atg24	✗	-	-

Table 1.1 The plasmoDB (*Plasmodium* Database) identifier for *P. falciparum* homologues described in three genome wide researches (Cervantes *et al*., 2014; Hain and Bosch, 2013; Navale *et al.,* 2014) are shown against the different steps of the autophagy cascade, induction, cargo selection, nucleation, expansion and completion, docking and fusion, vesicle degradation and others. Note P[1] indicates that the gene probably exists, while -[2] indicates that the gene was not checked in the study.

In *P. falciparum*, PfAtg8 is a part of membranous system under normal growth conditions. The exposed C-terminal glycine of the PfAtg8 covalently attaches to PfAtg7 through a thioester bond (Tomlins *et al.,* 2013). PfAtg7 transfers PfAtg8 to PfAtg3 to form another thioester bond before binding to PE on the phagophore membrane (Yamaguchi *et al.*, 2010). Hain *et al*. (2014) reported that inhibition of the PfAtg8 and PfAtg3 interaction prevents PE lipidation of the PfAtg8 and blocking of phagophore development. To date, an Atg10 homologue in *Plasmodium* parasite, which would normally participate in of the binding of Atg12 to Atg5, has not been found (Cervantes *et al*., 2014; de Late *et al*., 2017). Additionally, unlike *S. cerevisiae* and mammalian cells, the binding site of PfAtg5 (glycine residue) required for interaction with PfAtg12, is lacking in *P. falciparum* (Navale *et al.,* 2014). A set of endosomal markers belonging to the Rab protein family have been described in apicomplexan members (Langsley *et al*., 2008; Quevillon *et al.*, 2003). In higher eukaryotes, Rab7 and Atg8 with other trafficking proteins guide the autophagosome to the lysosome membrane for fusion (Wang *et al.*, 2011). It is therefore likely, like in *S. cerevisiae*, PfRab7 is involved in trafficking and fusion of autophagosome-like vesicles with the DV which would act as a lysosome given the absence of these structures in *P. falciparum* (Teter *et al.*, 2001). The *Plasmodium* parasite also has a homologue of Atg15 lipase. So, DV may have function similar to that of lysosome in eukaryotic cells (Navale *et al.* 2014) Interestingly, a homologue for Atg22, an efflux pump for recycled amino acids has been identified in *P. falciparum* genome (Yang *et al.,* 2006), although the DV also has the capacity to export amino acids derived from the digestion of haemoglobin.

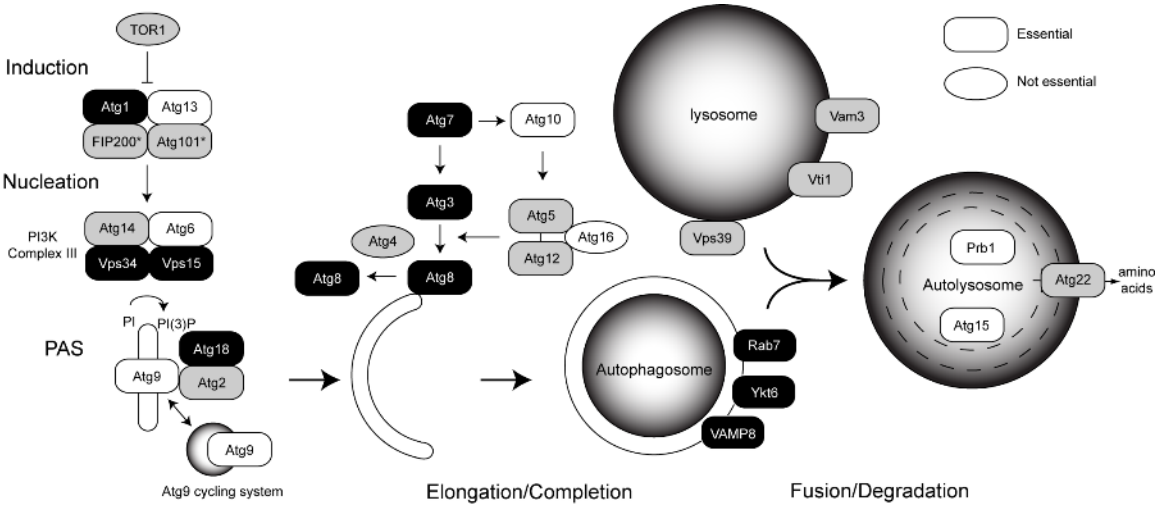

Fig. 1.15 Conservation of the canonical autophagy pathway in *Plasmodium.* Proteins essential for macroautophagy in other eukaryotic systems are depicted as rounded rectangles. Ovals represent proteins whose essentiality is not known. Black filling indicates strong evidence for homology in *P. falciparum*, where grey filling indicates where homology is weaker. White filled boxes indicate where no homologue was identified. *Human proteins FIP200 and Atg101 thought to be functional homologues of yeast Atg31/Atg17Atg29. (Source: Hain and Bosch, 2013).

1.10 Atg8-Atg3 Protein-Protein Interaction (PPI) as a target for small inhibitor molecules in *P. falciparum*

Recently, the Atg8-Atg3 PPI in *P. falciparum* has been given more attention as a target for new antimalarial drug development due to its potential in parasite survival (Hain *et al.,* 2016). Atg8 (which is already produced in an active form) is attached covalently with PE on the phagophore membrane initiating autophagosome formation (Walker *et al.,* 2013). As mentioned previously, this process (Atg8-PE interaction) occurs through serial reactions of Atg7 (E1-like activating enzyme) and Atg3 (E2-like ligase enzyme) and eventually involved by action of Atg12-Atg5 (E3-like ligase enzyme) to lipidate Atg8 with PE (Fig. 1.16) (Suzuki and Ohsumi, 2007).

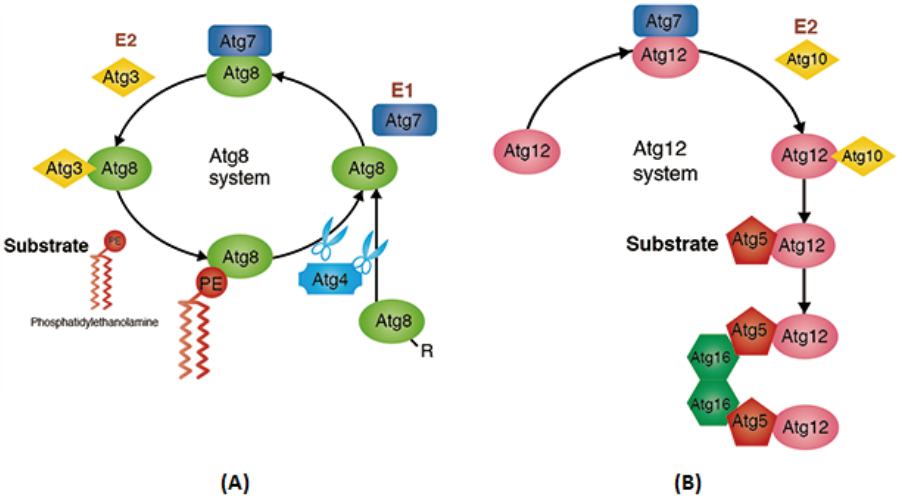

Fig. 1.16 Illustrating Atg8-PE conjugation system (A) and Atg12-Atg5 conjugation system (B) in *P. falciparum* parasite (Source**:** http://ruo.mbl.co.jp/bio/g/product/autophagy/article/Atg.html).

Co-crystallization of PfAtg8-PfAtg3 molecules has been performed by Hain *et al.* (2012), where they described the PfAtg3 binding site on the surface of PfAtg8 molecule as follows: two hydrophobic pocked named W and L-pockets which are occupied by the tryptophan and proline amino acids of the PfAtg3 peptide, respectively. The space between W and L-pockets seems to be important in this interaction. Furthermore, PfAtg8 has an extra pocket, named the A-pocket, created by the A-loop which is specific to apicomplexan species. X-ray crystallography of PfAtg8-PfAtg3, however, offers opportunities to explore specific selectivity for compounds that specifically inhibit this interaction in *P. falciparum* (a wider discussion of these in the introduction to chapter 4). In this context, a library of Medicines for Malaria Venture (MMV) compounds were screened against the blood stage of *P. falciparum* parasite to evaluate their autophagy inhibitory potential using Malaria SYBR Green I Fluorescence (MSF) and Surface Plasmon Resonance (SPR) assays as well as docking-based virtual screening against a PfAtg8 crystal structure (Hain *et al.,* 2014). Interestingly, MSF assay showed inhibition of parasite

growth after treatment with compound 1 (IC_{50}= 1.4 µM) and that was supported by significant decrease in PfAtg8 lipidation at 50 µM of the same compound using immunoblot assay. Additionally, the molecular model docking showed consistent docking mode of compound 1 (Fig. 1.17) across PfAtg3 binding site on surface of PfAtg8 molecule (Hain *et al.,* 2014).

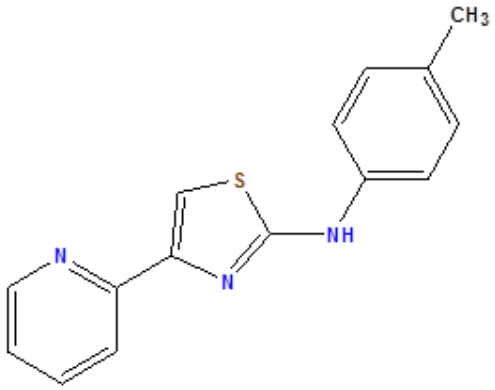

Fig. 1.17 Chemical structure of compound 1 (MMV007907) compound.

In 2016, a virtual library of synthetic compounds was screened against blood and liver stages of *P. falciparum* parasite. The outcome data indicated inhibition of parasite growth in both blood and liver stages upon drug treatment. There was a shift from lipidated PfAtg8 to unlipidated PfAtg8 level indicating decrease in the interaction between PfAtg8 and PfAtg3 molecules under drug treatment. In blood stage of 3D7 *P. falciparum* parasite, the best compound (ALC25) (Fig. 1.18) reported IC_{50}= 18.5 µM and 19.0 µM by MSF and SPR assays, respectively. Interestingly, cross reaction with other apicomplexan species such as *Eimeria, Toxoplasma, Neospora, Cryptosporidium, Theileria,* and *Babesia* were predicted using bioinformatics. Accordingly, the potential of small molecules to inhibit this novel target (protein-protein interaction) may offer a route forward for antimalarial drug development.

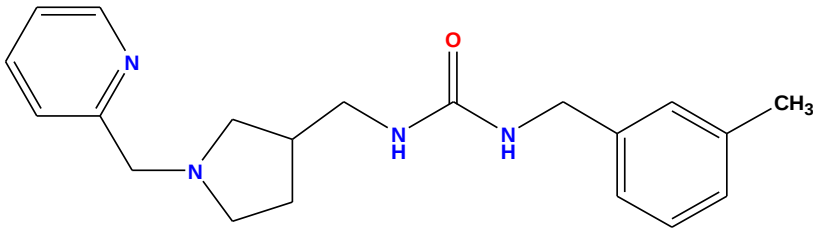

Fig. 1.18 Chemical structure of ALC25 compound.

1.11 Objectives of this study

The role of autophagy in *P. falciparum* is relatively poorly understood. Whilst key proteins in the canonical pathway exist, whether autophagy, as described in other eukaryotes, is used by the parasite as a response to nutrient stress and/or a potential mechanism for programmed cell death is debateable. The potential for small molecule inhibitors of the PfAtg8-PfAtg3 interaction as a new target for antiplasmodial action is of particular interest given the current demand for new target pathways for future antimalarial drug development.

This project therefore set out with two key objectives. The first was to evaluate a library of compounds, provided through collaboration with Dr Johannes Reynisson of the University of Auckland, New Zealand, that had been shown to modulate autophagy in cancer cell lines, with one mode of action predicted to be through inhibition of the Atg3-Atg8 interaction. This study screened the library against *P. falciparum* intraerythrocytic stages, identified and characterised leads, and explore their potential as small molecule inhibitors of PfAtg8- PfAtg3 interaction.

These hits were taken forward into a second part of the study. The objective of this second part was to explore early morphological and biochemical events in *P. falciparum* cell death, correlating the data from these putative autophagy inhibitors against a range

of current antimalarial compounds. A critical aspect of this second part of the study is that the use of a genetically modified *P. falciparum* that expresses a luciferase reporter gene (Wong *et al.*, 2011), allowed us to assay parasites that had been subject to a known cytocidal effect (Ullah *et al.,* 2017). Thus, parasite cultures were exposed to a concentration of compound that caused a 50% reduction in viability within a fixed timeframe, 6 hrs, and were compared against each other to determine what early events in cell death were common following drug treatment, and whether there were features of cell death that are specific to the autophagy inhibitor or antimalarial drug being tested.

The objectives above were listed here as follow:

1. Evaluation of antiplasmodial activity of a library of putative autophagy inhibitors, selecting the most potent hits to explore their selectivity against intraerythrocytic parasites, their rate of kill and timing of action.
2. Model the interaction of the putative autophagy inhibitors against the Atg8 of *P. falciparum* to explore any potential of structure activity relationships.
3. Perform a comparative study of drug action against the intraerythrocytic trophozoite stage of *P. falciparum* to explore whether ultrastructural or biochemical markers can be attributed to a programmed cell death phenotype.

Chapter 2: Materials and methods

2.1 Stocks and reagents

Note: Unless otherwise indicated, the materials were provided as follows; chemicals from *Sigma-Aldrich* Company Ltd., cell culture reagents from Gibco-Thermo Fisher Scientific, Abcam/UK and Millipore/*USA*, laboratory plasticware from Star lab Ltd, Greiner Bio-One/UK and Sarstedt/GmbH-*Germany*.

Complete growth medium

500 mL of RPMI (Roswell Park Memorial Institute)-1640 medium was supplemented with 10 mM D-glucose solution, 5 mM Sodium Hydroxide (NAOH), 2 mM glutamine, 100 µM hypoxanthine, 25 µg/mL gentamycin sulphate and 37.5 mM (4-(2-hydroxyethyl)-1-piperazine-ethanesulfonic acid (HEPES) buffer. This was further supplemented with 0.25% (w/v) albumax-II and 5% (v/v) heat-deactivated human serum.

Incomplete growth medium

This medium is prepared as per instructions for complete growth medium. The albumax-II and heat-deactivated human serum are omitted from this buffer.

Albumax-ll solution

5% (w/v) albumax-II solution was achieved by dissolving 25 g albumax-II powder (Thermo Fisher Scientific, UK-Invitrogen) in a total of 500 mL of incomplete growth medium. The albumax-ll solution was sterilized by filtration (0.45 µm filter) and aliquots were stored at -20 °C.

Blasticidin S HCl stock

To make 10 mg/mL Blasticidin S HCl, 50 mg of Blasticidin S HCl (Thermo Fisher Scientific, UK-Invitrogen) were dissolved in 5 mL of incomplete growth medium. The aliquots were stored at -20 °C. The complete growth media of $Dd2^{luc}$ parasite cultures were supplemented with 2.5 µg/mL of Blasticidin S HCl solution.

D-glucose solution

45% (w/v) D-glucose solution was prepared by adding 225g D-glucose to a total of 500 mL sdH_2O. The solution was sterilized (0.2 µm filter). The aliquots were stored at 4 °C.

Embedding Agar

3% (w/v) embedding agar was prepared by dissolving 0.3 g of agar powder (BDH, UK) in 10 mL of sdH_2O. The agar was allowed to cool to approximately 30-40 °C before being used.

Glycerolyte freezing solution

57 g glycerol, 1.6 g sodium lactate, 300 mg KCl, 124 mg disodium phosphate (Na_2HPO_4) and 51 mg monosodium phosphate (NaH_2PO_4) were dissolved into 80 mL of sdH_2O. The pH was adjusted to 6.8. The volume made up 100 mL with sdH_2O, filter sterilised (0.2 µm filter) and stored at 4 ˚C.

Hoechst 33342 nucleic acid stain

A 10 µg/mL Hoechst 33342 working reagent was prepared by dilution 1 µL of 10 mg/mL Hoechst 33342 (Thermo Fisher Scientific, UK) in to 1 mL of complete medium. The reagent was prepared immediately prior to use.

Hypoxanthine solution (1 M)

1 M hypoxanthine stock solution was prepared by dissolving 544.4 mg hypoxanthine in 40 mL of 1N NaOH. The solution was sterilised (0.2 µm filter) and aliquots stored at -20 ℃.

Malaria SYBR Green I Fluorescence (MSF) lysis buffer

10XMSF lysis buffer stock was prepared as Tris (200 mM, pH 7.6), EDTA (50 mM), saponin (0.08%, w/v) and Triton-X 100 (0.8%, v/v) in sdH_2O and stored at room temperature. Immediately prior to use, this was diluted to 1XMSF lysis buffer in sdH_2O.

Paraformaldehyde solution

To prepare 1 L of 4% (w/v) paraformaldehyde, 800 mL of 1XPBS was added into a glass beaker on a magnetic stirrer inside a fume cabinet. Heating and stirring was applied up to 60 °*C* following by addition 40 g of paraformaldehyde (Sigma-Aldrich, UK) to the heated 1XPBS. 1N NaOH was added drop by drop until the solution became clear. The volume was made up to 1 L by 1XPBS and pH adjusted at 7.4 using HCl. The solution was filtered, aliquoted and stored at -20 ℃ (Ljungström *et al.,* 2008).

Saponin lysis buffer

10% (w/v) saponin lysis buffer was prepared by adding 10 g of saponin (Thermo Fisher Scientific, UK) into a total of 100 mL 1XPBS. The lysis buffer was filter sterilized (0.2 µm filter) and stored at 4 ℃.

Sorbitol lysis buffer

5% (w/v) sorbitol lysis buffer was made by dissolving 5 g of D-sorbitol in a total of 100 mL sdH_2O. The buffer was filter sterilised (0.2 µm filter). The solution was aliquoted and stored at 4 °C.

Tris-HCl buffer (0.5 M)

0.5 M Tris-HCl buffer was prepared by dissolving 60.6 g Trizma base into 800 mL of sdH_2O and pH adjusted to 7.6 using concentrated HCl. The buffer volume was made up to 1000 mL using sdH_2O and stored at room temperature (Dawson *et al.,* 1986).

WR99210 stock

A long-term stock (25 mM) of WR99210 drug was made by dissolving 50 mg WR99210 (kindly provided by D. Fidock, Columbia University) in 1 mL of dimethyl sulfoxide (DMSO) (Sigma-Aldrich, UK) and kept at -20 ℃. Further dilution at 1:1000 was made in incomplete growth medium as a 25 µM working stock. The complete growth media of $NF54^{luc}$ parasite cultures were supplemented with 5 nM of WR99210.

2.2 *P. falciparum* cell culture methods

2.2.1 Human blood and serum preparation

Leukocyte-depleted human blood type ORh^+ and human serum were provided by the National Blood and Transfusion Services (Bristol, UK). All blood samples are stored, used and disposed of according to the Human Tissue Licence (HTA 12349) held by Keele University. All work using human blood products with *P. falciparum* were performed in Health and Safety Executive approved Biological Containment 3 (derogated based on the

non-aerosol nature of work) facilities according to Standard Operating Procedures detailing training and work practices in these facilities.

Leukocyte-filtered blood was aliquoted in to 50 mL tubes and refrigerated at 4 ℃ up to three weeks. For parasite cultivation, a 50% haematocrit stock was prepared by first collecting the RBC by centrifugation at 1520 g for 8 min at room temperature. The upper serum phase was removed and stored as collected pooled samples for use in supplementing complete growth medium. The RBC pellet was washed using 1 volume of incomplete cell culture medium, mixing and collection of RBC by centrifugation at 850 g for 5 min at room temperature. This process was repeated twice. The pelleted RBC were suspended in one volume of incomplete growth medium and stored at 4 ℃ for up to 2 weeks.

For human serum preparation, serum was collected from the blood deliveries or provided as a separate product. Serum was heat-deactivated at 56 °C for 30 min in a water bath before being aliquoted as 40 mL samples and stored at -20 °C. These serum samples were used in the preparation of complete growth medium.

2.2.2 *In vitro* continuous culture of *P. falciparum*

Three clones of *P. falciparum*; namely 3D7, NF54^{Luc} (kindly provided by Muqdad Hmoud, Keele University) and Dd2^{luc} (Wong *et al*., 2011) were used in this study. The intraerythrocytic stages were cultured continuously in human RBC (typically between 1-2% parasitaemia and 2% haematocrit) in complete growth medium at 37 °C under 1% oxygen, 3% carbon dioxide and 96% nitrogen atmosphere (BOC, UK) (Trager and Jensen, 1976). The parasite was sub-cultured with daily replacement of complete growth medium and addition of fresh uninfected RBC. Light microscopic determination of the

parasitaemia and staging of iRBCs were performed using Giemsa (10%, v/v) stained thin blood smears of methanol-fixed iRBCs (Petithory *et al.,* 2005).

2.2.3 Synchronization of *in vitro* parasite cultures by the sorbitol-lysis method

P. falciparum cultures were synchronized according to the protocol of Lambros and Vanderberg (1979). Light microscopy was used to determine a predominance of ring stage parasites suitable for this synchronization process. IRBCs were collected by centrifugation at 830 g for 5 min at room temperature. These were suspended in five volumes of pre-warmed (37 ˚C) 5% sorbitol. After 5 min incubation at 37°C, iRBCs were collected by centrifugation as above. The upper sorbitol phase was discarded and the pelleted iRBCs (containing viable ring stage parasite only) suspended in complete growth medium (2% haematocrit). The culture was gassed and returned into the incubator at 37 ˚C.

2.2.4 Cryostorage of *P. falciparum* intraerythrocytic culture

Liquid nitrogen provides an environment for long-term preservation of ring stage *P. falciparum*. Intraerythrocytic cultures were enriched (5-10 % parasitaemia of which >80% were ring stage) and the iRBCs collected by centrifugation at 850 g for 5 min at room temperature. Three volumes of iRBCs were mixed with 5 volumes of glycerolyte freezing solution. This was completed in two stages. For the first stage, one volume of glycerolyte freezing solution was added drop by drop to collected iRBC, with continual mixing before being left standing upright to equilibrate over 5 min at room temperature. This process is repeated, again drop by drop, with the remaining four volumes of glycerolyte freezing solution. The iRBCs/glycerolyte freezing mixture was then divided into 1 mL aliquots in

labelled cryotubes. The cryotubes were transferred to -80 ˚C for at least 24 hr before being stored in liquid nitrogen for long term storage.

To thaw *P. falciparum* parasite cultures, cryotubes were taken out from liquid nitrogen storage and defrosted at 37 ˚C in the culture incubator. The thawed iRBCs (typically between 0.8-1 mL) were placed in a 50 mL centrifuge tubes. A one-fifth volume of 12% (w/v) NaCl was slowly added, drop by drop with gentle mixing, and then the mixture left for 5 min at room temperature. Next, ten volumes of 1.8% (w/v) NaCl is added, one volume at a time with gentle mixing. After an additional 5 min equilibration at room temperature, ten volumes of 0.9% (w/v) NaCl and 0.2% (w/v) D-glucose was added, one volume at a time with gently mixing. The iRBCs were collected by centrifugation at 850 g for 5 min at room temperature. The iRBCs were resuspended in complete culture medium and fresh RBCs, typically to a 2% haematocrit. The flask was gassed and placed into the incubator at 37 ˚C with examination of the success of thawing demonstrated by trophozoite stage culture 24 hrs later.

2.3 Drug assays

2.3.1 Compound library screening

For the initial screening of the LC3 (Atg8)-Atg3 PPI, all 131 compounds were tested at 2, 10 and 50 µM concentrations. Each experiment was carried out as a technical duplicate, with three biological replicates (n=6 total). To prepare this five-fold serial drug dilution, 125 µL of complete growth medium was placed into starting wells in the first column of a 96-multiwell clear tissue culture plate, with the adjacent two wells loaded with 100 µL of complete growth medium. 2.5 µL of 5 mM stock solution of the compound to be tested was added into the starting well in the first column providing a 100 µM concentration of

this compound. This was carefully mixed by repeated pipetting and 25 µL transferred from the starting well across the next two wells, with complete mixing in each well. 25 µL of the last well contents was discarded to provide three wells, each containing 100 µL of a five-fold dilution of compound. 100 µL of an iRBC mastermix (1% parasitaemia, predominantly early to mid-trophozoite, 4% haematocrit) was added into each wells, effectively having the drug concentration in each well as well as the haematocrit (final was 2%). Three wells containing 100 µL of iRBC mastermix with 100 µL of complete growth medium served as a control positive (+ve) (no drug), whilst an additional three wells containing 100 µL of iRBC exposed to a 10 µM supralethal concentration of CQ served as a negative (-ve) control (no viable parasites). The 96-well tissue culture plates were placed in a humidified airtight box under a low oxygen atmosphere 1% O_2, 3% CO_2 and 96% N_2 (BOC, UK) at 37 ˚C for 48 hrs.

A standard MSF assay (Smilkstein *et al*., 2004) was used to determine the inhibitory effect of the compounds tested. After the incubation period, 100 µL of parasite cultures were mixed with equal volume of 1XMSF lysis buffer supplemented with 1X SYBR Green I (supplied as a 5000x stock by Invitrogen, UK) on a black 96-well tissue culture plate and incubated for 1 hr at room temperature in the dark. The fluorescent signal was measured using the blue fluorescence module (excitation λ= 490 nm, emission λ= 570 nm) in a Glomax-Multi Detection System (Promega, UK). Growth following exposure was determined as a proportion of the untreated (no drug) control (i.e. 100%), with a background subtraction using the negative control (supralethal CQ) (i.e. 10 µM) applied. The % relative growth was calculated as follows:

$$\text{Relative Growth (\%)} = \frac{\mu_{(S)} - \mu_{(-)}}{\mu_{(+)} - \mu_{(-)}} \text{ X 100}$$

Where $\mu_{(S)}$, $\mu_{(+)}$ and $\mu_{(-)}$ represent the means for the sample in question and positive (100%) and negative (0%) controls, respectively.

2.3.2 Determination of 50% Effective Concentration (EC_{50})

Following an initial screen, compounds of interest were taken forward for nine concentrations (2-fold dilution) to enable the EC_{50} to be determined. These 96-multiwell plates were set up using a variation of the experiment shown above – with plates formatted as shown in Fig. 2.1. Triplicate serial compound dilutions in complete growth medium were made across the 96-multiwell plates – with two compounds being tested on each plate. Starting wells contain 200 µL of the initial drug dilution, with 100 µL of mixed well contents moved across the plate to produce a 2-fold dilution between each column. 100 µL of the final well volume was discarded. 100 µL of iRBC mastermix (1% parasitaemia at early to med trophozoite stage, 4% haematocrit) was added into each well. As a control positive (+ve), 100 µL complete growth medium plus 100 µL of iRBC mastermix (no drug) was used whilst iRBCs exposed to a 10 µM supralethal concentration of CQ served as a negative (-ve) control (no viable parasites). The 96-multiwell tissue culture plates were placed in a humidified airtight box under a low oxygen atmosphere 1% O_2, 3% CO_2 and 96% N_2 (BOC, UK) at 37 ˚C for 48 hrs.

After incubation, the fluorescence signal from a standard MSF assay was determined for each well and the mean % relative growth determined as described above in 2.3.1. To determine the EC_{50}, a non-linear regression (log_{10}-concentration versus normalised-

response) was analyzed using GraphPad Prism5 v5.0 software (GraphPad Software, Inc., San Diego, California, USA). At least 3 different biological replicates with triplicate technical repeated were used to provide the mean and standard deviation for this regression analysis. This analysis provides the EC_{50} and the 95% confidence intervals (95% CI) reported in this study.

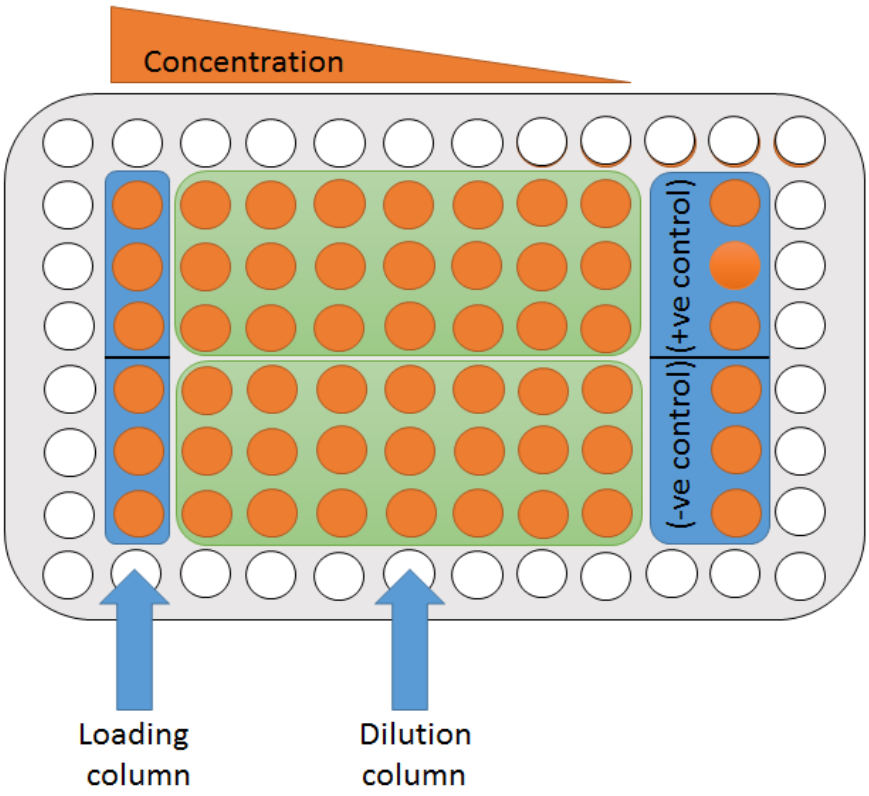

Fig. 2.1 Schematic of a 96-multiwell plate used to determine EC_{50}. Compounds are added into the loading column in triplicate, two compounds are therefore tested per plate. The dilution columns provide for a two-fold serial dilution of the compound being tested. Positive controls (+ve) consist of mastermix exposed to no compound (100% relative growth) and the negative control (-ve) wells each contain a supralethal dose of chloroquine (10 µM). Outer wells are filled with incomplete medium to reduce edge-effects from evaporation during incubation.

2.3.3 Determination of 50% Lethal Dose (LD_{50})

Estimation of a 50% Lethal Dose (LD_{50}) were carried out according to the bioluminescent protocol reported in Ullah *et al.* (2017) based on those originally described by Paguio *et al*. (2011) using a fluorescent reporter system. In the Ullah *et al.* (2017) report, it was

demonstrated that a 6 hrs exposure to compound, followed by immediately reading the residual bioluminescence signal, provided equivalent data to a 6 hrs drug bolus followed by washing and re-culture for 42 hrs. Assays were set up in the same way as those for the determination of the EC_{50} (*2.3.2*) although with a higher staring concentration. The same controls were used throughout. The residual bioluminescence signal was measured using the simple one-step lysis protocol described originally by Hasenkamp *et al.* (2012). Briefly, 40 µL samples of culture were transferred to a white 96-multiwell plate and 10 µL of passive lysis buffer (Promega, UK) added and mixed by pipetting. 50 µL of luminogenic substrate (Promega, UK) was mixed with the lysed parasites and the bioluminescence signal measured for 2 sec in a Glomax-Multi Detection System (Promega, UK). Data were collected and analysed using Instinct software (Promega) and the LD_{50} estimated from non-linear regression (log_{10}-concentration *versus* normalised-response) using GraphPad Prism5 v5.0 software (GraphPad Software, Inc., San Diego, California, USA). At least 3 different biological replicates were performed for each compound, with each experiment using three technical repeats (n=9).

2.3.4 Bioluminescence Relative Rate of Kill (BRRoK) assay

The BRRoK assay was carried out as originally described by Ullah *et al.* (2017). Trophozoite-stage cultures of $Dd2^{luc}$ or $NF54^{luc}$ (100 µL, 2% parasitaemia, 4% haematocrit, n= 3) were added to 96-multiwell plates containing 100 µL of pre-dosed (final three-fold EC_{50} dilution series from 9 to 0.33x EC_{50}) complete culture medium and mixed by pipetting (see plate set up in Fig. 2.2). The 96-multiwell plate was then incubated for either 3, 6 or 48 hrs at 37 °C. The bioluminescent signal measured using the luciferase single-step lysis protocol described by Hasenkamp *et al.* (2012) as described above in

2.3.3. Controls in each biological replicate consisted of trophozoite stage culture with no drug added (100%) or uninfected erythrocytes (0%). The mean and standard deviation (SD) of bioluminescence data from three independent biological repeats were expressed as a proportion of the untreated control (100%) and reported as the % normalized bioluminescence signal.

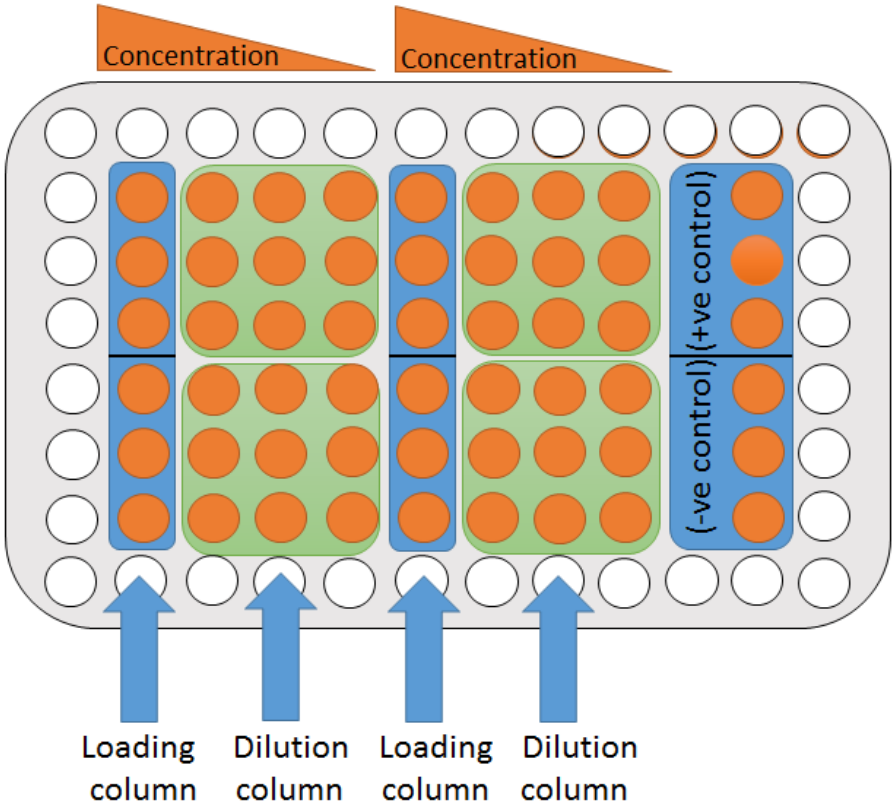

Fig. 2.2 Schematic of a 96-multiwell plate used to measure BRRoK. Compounds are seeded into the loading column in triplicate at a final 9xEC_{50} concentration; four compounds are tested per plate. The dilution columns provide for a three-fold serial dilution of the compound being tested. Positive controls consist of mastermix exposed to no compound or control positive (+ve) and the negative control (-ve), wells each contain uninfected erythrocytes (0% relative growth). Outer wells are filled with incomplete medium to reduce edge-effects from evaporation during incubation.

2.3.5 Time course-exposure assay

To investigate the effect of compounds on different intraerythrocytic stages of Dd2^{luc} *P. falciparum* parasite, highly synchronized early ring stage (up to 10 hrs post infection) or early trophozoite (20 to 26 hrs post infection) were prepared as follows; a 1% parasitaemia, 2% haematocrit, culture was exposed to a 50% kill concentration of CQ and the two most potent autophagy inhibitors, SK1.47 and SK1.49. After 6 hrs of incubation with drug/compound, the samples were divided to two equal portions. The first portion was washed with ten volumes incomplete growth medium three times, with collection of the iRBC pellet by centrifugation (1800 g, 5 min), to remove the drug/compounds. In the second portion, the drug/compound was maintained in the culture medium. For both experiments, thin blood smears were prepared after 16, 24 and 48 hrs incubation, Giemsa stained and examined by light microscopy to stage the culture and monitor presence of abnormal iRBC morphology. To capture images, slides were observed using a LETZ Dialux 20 EB microscope (x100 oil immersion objective lens) coupled with a digital camera system (Wetzlar, Germany).

2.4 Cytotoxicity assays using HepG2 cell lines

HepG2 (ATCC HB-8065) cell lines were cultured in Dulbecco Modified Eagle Medium (DMEM, Invitrogen, Gibco-BRL 11995-065) supplemented with 10% (v/v) fetal bovine serum and 0.2% (v/v) penicillin/streptomycin solution (Invitrogen). The culture flasks were incubated for 3 days at 37 °C in a 5% CO2 incubator. The culture medium was replaced every 2-3 days. Cells were harvested following aspiration the supernatant and addition of 10 mL 1XPBS to wash the residual cell culture medium from the HepG2 monolayer and followed by addition of 2.5 mL of 0.2% Trypsin-EDTA (5 mM) for 5 min at

37 °C. After trypsinization, 6 mL of DMEM culture medium was added to the cells, mixed and the released HepG2 collected by centrifugation (590 g for 3 min at room temperature). A HepG2 cell suspension at $1X10^5$ cells/mL was prepared as a mastermix for the cytotoxicity assay. To determine the effect of the putative autophagy inhibitors on HepG2 viability, a triplicate of 100 µL serial drug dilutions in DMEM medium were performed in 96-multiwell plates and followed by addition 100 µL of the HepG2 mastermix into each well (see Fig. 2.1 to illustrate how serial dilution plates are set up). The wells without compounds served as positive controls (+ve) and for negative controls (-ve), 2 µL of 50 µM actinomycin-D was added to provide a 500 nM final concentration (supralethal dose). After incubation for 48 hrs at 37 °C, 20 µL of Alamar Blue cell viability reagent (Thermo Fisher Scientific, UK) was added into each well, incubated at 37 °C for 6 hrs to allow a colour change across the serial compound dilution. The fluorescent signal was measured using the blue fluorescence module (excitation λ= 490 nm, emission λ= 570 nm) in a Glomax-Multi Detection System (Promega, UK). The 50% cytotoxic concentration (CC_{50}) of compounds was determined using the same non-linear $\log_{10}$ concentration-normalised response method described in 2.3.1. At least three different biological replicates were obtained for each compound, with each experiment having three technical repeats (n=9).

2.5 Molecular docking study

Computational docking of a ligand into putative binding site of the target protein can be applied as a useful tool in the structure-based drug design. In this study, X-ray crystallography of PfAtg8 protein was obtained from the database of Protein Data Bank (PBD ID 4EOY) (www.rcsb.org/pdb/home/home.do). This molecule is usually provided as

a co-crystallized form with its regulator (PfAtg3 protein) which occupied W and L pockets on the surface of PfAtg8 (Fig. 2.3), thus a single 3D crystal model of PfAtg8 was prepared using UCSF Chimera 1.11.2 software (www.cgl.ucsf.edu/chimera/) and this single chain of PfAtg8 molecule saved as a PDB file format for following molecular docking.

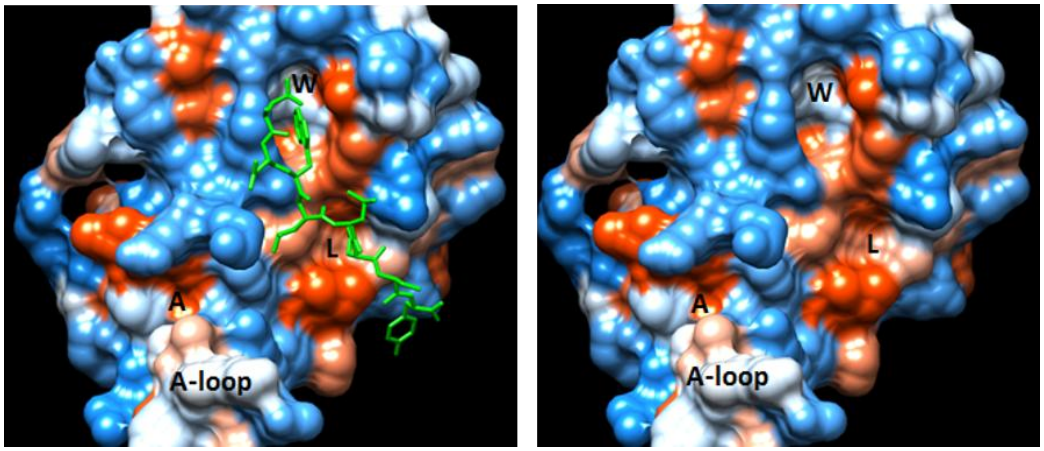

Fig. 2.3 The left image indicates 3D co-crystal structure of PfAtg8 (homologue of Human LC3) and PfAtg3 which represented as a stick model in green (PDB ID 4EOY) in *P. falciparum*. Two hydrophobic pockets W and L on the anterior surface of PfAtg8 represent a functional parts of PfAtg8 which occupied by PfAtg3 peptide inducing lipidation of PfAtg8 molecule and resumption phagophore development to autophagosome. In addition, Apicomplexan members have extra pocket called A-pocket on the posterior surface of Atg8 which is generated by A-loop. Right image displays single model of PfAtg8 prepared after removing PfAtg3 using UCSF Chimera *1.11.2* software to be applied as a receptor for ligand in computational molecular docking assay.

The SMILES (Simplified Molecular Input Line Entry System) of interested compounds were determined by ChemDraw Ultra 7.0 software and saved for later docking steps. Ligand-PfAtg8 molecular docking was obtained using Mcule software package (www. mcule.com). Initially, the ligand was figured by ChemWriter^{TM} 2.15.2 screen of the Mcule software using ligand SMILES and this followed by upload PfAtg8 molecule as a receptor which already saved as a PDB file format as described above. The PfAtg8 PDB file format is automatically added into the Mcule software database by which allowed to be requested in future docking assays. The two putative binding centres [Lysine 48 (LYS48)

and Leucine 50 (LEU50) amino acids] as well as LYS47 amino acid within PfAtg8 molecule were predicted according to the previous studied (Hain *et al*., 2014; Dr Johannes Reynisson's group, unpublished data) and also via molecular visualisation of PfAtg8 protein surface features (Fig. 2.4).

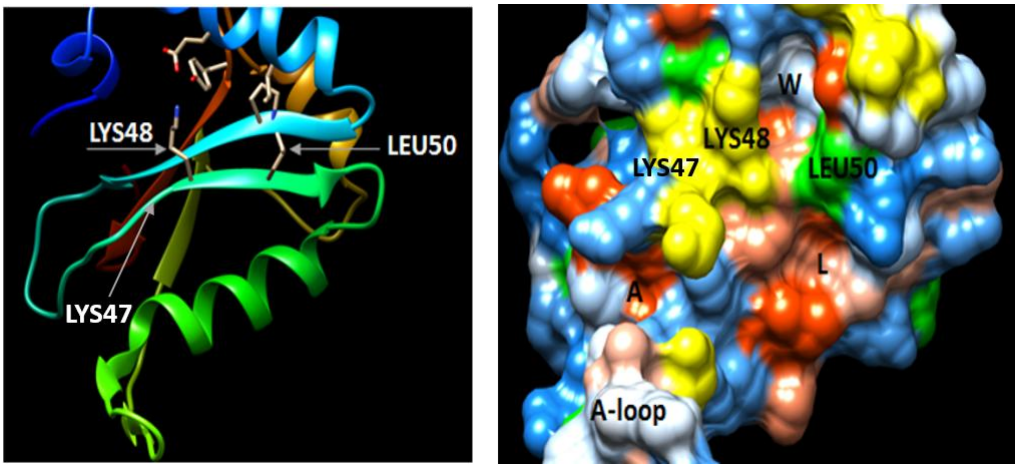

Fig. 2.4 The overall structure of PfAtg8 in *P. falciparum*. Left image, a ribbon structure of PfAtg8, displays two amino acid residues (LYS48 and LEU50) of PfAtg8 molecule which putatively contribute in H-bond generation with PfAtg3 molecule in the cargo binding site of PfAtg8. LYS48 and LEU50 as well as LYS47 were selected as biding centres according to the previous studies (Hain *et al.* (2014); Dr Johannes Reynisson's group, unpublished data) and molecular visualisation of PfAtg8 protein surface features. Right image, surface presentation of PfAtg8 showing three hydrophobic pockets (W, L and A-site) with LYS48 and LEU50 positions presented as yellow and green areas, respectively. LYS48 is located next to W pocket while LEU50 residue is near to space between W and L-pocket of PfAtg8.

Hit/lead optimization is required in order to improve the docking score, which is usually given by negative values and high negative scoring represents high binding affinity. Once the docking centre was specified, the scheme applied for ligand-protein molecular docking of 5 more potent compounds (putative autophagy inhibitors) and 2 compounds (structurally related) added for comparative analysis. 7-8 binding points (7-8 atoms) for LYS48, LYSY47 and LEU50 binding centres with 4 docking poses of each binding point were assayed by Mcule software (www. mcule.com). All docking poses were visualised by Mcule before being saved as PDB file format for further analysis. The docking outcome

data was analyzed by UCSF Chimera 1.11.2 software and ligand-PfAtg8 restricted H-bonds viewed.

2.6 Transmission Electron Microscopy (TEM)

To study ultrastructure changes in intraerythrocytic stages of *P. falciparum* under drug stress, early trophozoite stages (20 to 26 hrs post invasion) at ~10% parasitaemia and 4% haematocrit were exposed to 50% lethal concentrations of 4-aminoquinolines (CQ, AQ, PYRD, and PPQ), amino alcohols (QN and MQ), artemisinins (dihydroartemisinin, DHA, and artemether, ARM), DBeQ and 2 putative autophagy inhibitory compounds (SK1.47 and SK1.49) for 6 hrs at 37 °C. All samples imaged underwent a bioluminescence assay to determine the actual reduction in viability achieved in each experiment (See section 2.3.3). Cultures were harvested by centrifugation at 1800 g for 5 min at room temperature. The harvested cells were resuspended in 1XPBS and pelleted using the same centrifugation conditions above. Washing process was repeated two more times and the collected red blood cells lysed in 0.1% (w/v) saponin solution (1:20 volume) for 1 min on the ice following by centrifugation at 400 g for 10 min at 4 °*C* as described previously (Totino *et al.,* 2008). Fixation of parasites was performed using a protocol described originally by Beaumelle *et al.* (1987). Briefly, the released parasites were washed twice in 10 volumes of 1XPBS, with centrifugation (400 g for 10 min at 4 °*C*) used to collect the parasite pellet. These were then fixed with 2% (w/v) glutaraldehyde/1XPBS overnight at 4 °*C* and then washed twice with 0.1 M cacodylate buffer in 0.2% CaCl2 using centrifugation (400 g for 10 min at room temperature) to collect the parasite pellet. The pellet was gently resuspended in 100 µL of 1% (w/v) osmium tetroxide for 1 hr at room temperature before being embedded in 3% (w/v) agar (*Agar* Scientific Ltd., UK). For

dehydration, a graded ethanol series was used on the fixed parasites before being embedded in Spurr resin overnight at 60 °*C*. Ultrathin sections (80-90 nm thickness) were prepared using a Reichert-JUNG Ultracut E microtome (Leica-Microsystems, Wetzlar, Germany). The ultra-sections were loaded on 200-mesh thin bar grids-copper (Agar Scientific Ltd, UK) and air dried. With support from the Keele Electron Microscopy Unite, sections were stained with uranyl acetate dye and imaged using a Transmission Electron Microscope (JEOL-1230, USA).

2.7 Biochemical methods

2.7.1 Mitochondrial outer membrane potential (ΔΨm) assay

To evaluate effect of drug/compound on the ΔΨm, the MitoProbe cell-permeable lipophilic JC-1 dye **(**5,5′,6,6′-Tetrachloro-1,1′,3,3′-tetraethylbenzimidazolocarbocyanine iodide (Thermo Fisher Scientific, UK) was used with different techniques (Fluorescence microscope, plate reader and flow cytometry) to monitor fluorescence signal. The cytoplasmic monomeric form of JC-1 has maximum emission wavelength at 525 nm (green fluorescence) whilst functional mitochondria accumulate an aggregated JC-1 dye which emits red fluorescence at 590 nm. The ratio between red and green fluorescence was used as an indicator of ΔΨm. A low ratio of red/green reflects loss of the ΔΨm. In all experiments, the ionophore carbonyl cyanide m-chlorophenylhydrazine (CCCP), that rapidly collapses the ΔΨm was used as a control negative (-ve) whilst untreated samples served as a positive control (+ve). As mitochondrial depolarisation is described as an early feature of apoptosis, parasite cultures were exposed to concentrations of drug/compounds being tested that achieved 25%, 50% and 90% loss of viability over 6 hrs

at 37 ℃ (see 2.3.1). All experiments were prepared in triplicate and at least three biological replicates performed (n=9).

2.7.1.1 ΔΨm assay using fluorescence microscopy

Fluorescence microscopy analysis of ΔΨm was obtained according to manufacturer's instructions and as described previously by Pasini *et al.* (2013). Cell suspensions ($1X10^6$ iRBCs/mL) were mixed with a 2 µM final concentration of JC-1 for 30 min at 37 °C in the dark. Post-stained cells were washed twice with ten volumes of 1XPBS and the iRBCs collected by centrifugation (400 g for 10 min at room temperature). The nucleic acid of iRBCs were stained with Hoechst 33342 (Thermo Fisher Scientific, UK) at a 1 µg/mL final concentration for 10 min at 37 °C. Stained iRBCs were collected by centrifugation (400 g for 10 min at room temperature) and then suspended in anti-fade mounting solution (Vectashield) before being mounted on microscopic slides. The iRBCs were covered with a coverslip, sealed using nail varnish and stored in the dark at 4 *°C* prior to imaging (performed the same day). The cells were microscopically visualised and counted using 100X objective lens of EVOS microscope (EVOS® Cell Imaging Systems, Life Technologies, Carlsbad, CA, USA) with appropriate filters (DAPI filter for blue Hoechst fluorescence signal: excitation/emission λ= 357 nm/447 nm, and the GFP filter for JC-1 green fluorescence signal: excitation/emission λ= 470 nm/525 nm, RFP filter for JC-1 red fluorescence signal: excitation/emission λ= 531 nm/593 nm). 60-70 iRBCs/sample were counted for each replicate, with three biological repeats performed.

2.7.1.2 ΔΨm assay using a fluorescence plate reader

An early trophozoite stage (20 to 26 hrs post invasion) of parasite culture was exposed to drugs/compounds in 96-multiwell plate for 6 hrs at 37 °C. After this incubation period, the

96-well plates were centrifuged (400 g for 10 min at room temperature) and the supernatant discarded. The treated iRBCs were washed twice with 100 µL of 1X PBS followed by centrifugation as above. The collected iRBCs ($1x10^6$ iRBCs/mL) were mixed with 2 µM final concentration of freshly prepared JC-1 regent using instructions provided by the manufacturer and modified by Pasini *et al.* (2013). The 96-well plates were incubated for 30 min at 37 °C in the dark. For the controls, 200 µM final concentration of CCCP was added for 1 hr at 37 °C (Porter, 2007) as a negative control (-ve) whilst untreated iRBCs represented a positive control (+ve). These controls were treated, washed and stained as above. The fluorescence signals were measured using the GloMax-Multi Detection System (Promega, UK) with appropriate filters for red fluorescence (excitation/emission λ= 525/590 nm) and green fluorescence (excitation/emission λ= 490/520 nm) used sequentially.

2.7.1.3 ΔΨm assay using fluorescence flow cytometry

For assessment of ΔΨm by fluorescence flow cytometry, 6 hrs drug-treated samples were washed twice with 10 volumes of 1X PBS using centrifugation (500 g for 5 min at room temperature) to collect iRBCs. Suspensions ($1x10^6$ iRBCs/mL) of drug-treated, positive and negative control samples were prepared in 1.5 mL microculture tubes and JC-1 (2 µM final concentration) loaded for 30 min at 37 °C in the dark. The stained iRBCs were washed twice with 10 volumes of 1X PBS using centrifugation (400 g for 10 min at room temperature) to collect iRBCs. Following the respective incubation and staining period, cell suspensions (≤ 500 cells/µL) were prepared in 1XPBS for flow cytometry analysis.

Flow cytometry analysis was initiated by determination forward scatter (FSC) *versus* side scatter (SSC) of treated and untreated iRBCs. 100,000 RBCs/sample were analyzed using

FL1 for JC-1 green fluorescence (excitation/emission λ= 488nm/525nm*)* and FL2 for JC-1 red fluorescence (excitation/emission λ= nm535/575nm) using Beckman *Coulter* FC500 Flow Cytometry (Beckman Coulter*,* Inc. 250 S. Kraemer Blvd. Brea, CA 92821 USA). The data was analyzed and plotted using Flowing software 2.5.1.

2.7.2 *In Situ* DNA fragmentation assay

2.7.2.1 *In Situ* DNA fragmentation assay by flow cytometry cell sorting

This assay is called also Terminal deoxynucleotidyl transferase (TdT)-mediated dUTP nick end labelling (TUNEL) assay. Drug-induced DNA fragmentation in $Dd2^{luc}$ and $NF54^{luc}$ of *P. falciparum* parasites were investigated based on labelling of DNA strand breaks using the commercial *In Situ* Cell Death Detection Kit*,* Fluorescein (Sigma-Aldrich*,* UK). In drug-treated groups, concentrations required to achieve 50% and 90% kill in 6 hrs were determined using the bioluminescence-based assay described above (see 2.3.3). Both treated and untreated groups of iRBCs were analysed at three different time points; 6, 24 and 48 hrs following drug exposure, to assess DNA fragmentation at single-cell level as assessed by flow cytometry. Drug was washed off tested iRBCs using 10 volumes of 1XPBS and iRBCs collected by centrifugation (500 g for 5 min at room temperature). The subsequent TUNEL assay was carried out according to instructions provided by the manufacturer as modified by Oakley *et al* (2007). Briefly, one volume (50 µL) of $1X10^6$ iRBCs suspension was mixed with three volumes (150 µL) of fixative (4%, w/v, paraformaldehyde/ 0.015%, w/v, glutaraldehyde) for 1 hr at 4 *°C*. Post-fixed iRBCs were washed twice with 1XPBS and collected by centrifugation (400 g for 10 min at 4 *°C*). The iRBCs were permeabilized by the addition of 100 µL of 0.1% (w/v) Triton X-100 and incubated for 3 min on ice. The Triton X-100/iRBCs were washed twice with 1XPBS and

collected by centrifugation (400 g for 10 min at 4 °C). 50 µL of permeabilized iRBCs were mixed with an equal volume of labelling solution of TUNEL kit (prepared freshly for each experiment) following by incubation for 1 hr at 37 °C in the dark. The sample tubes were gently flicked twice during the incubation period to suspend any settled iRBCs. To provide a positive control (+ve), 50 µL of fixed and permeabilized iRBCs were mixed with an equal volume of 50U/mL DNase I (Invitrogen) in 50 mM Tris-HCl pH 7.5, containing 1 mg/mL bovine serum albumin (BSA) (Sigma-Aldrich, UK) (see Totino *et al.,* 2008) and incubated for 20 min at room temperature to artificially induce DNA-nicks. DNase I-treated cells were washed and subjected to TUNEL staining as described above.

Treated iRBC suspensions (≤ 500 cells/µL) were prepared in 1XPBS with the samples kept away from direct light until analysed by flow cytometry cell sorting (FACS) machine. A sample was removed from the original iRBCs used at the start of the experiment to determine parasitaemia with SYBR Green I dye. Parasitaemia was determinate according to protocol initially developed by Jang *et al*. (2014), where 10,000X SYBR Green I dye (Invitrogen) was freshly diluted with 10% ethanol/ 1X PBS (1:1000 ratio) and 125 µL of untreated iRBCs in complete growth medium (4% haematocrit) were mixed with same volume of this 1:1000 SYBR Green working solution for 30 min at room temperature in the dark.

Forward scatter (FSC) *versus* side scatter (SSC) of treated and untreated iRBCs were found (Fig. 2.5) and following by adjustment appropriate filters, where Green-Blue (GRN-B) filter used for TUNEL green fluorescence signal, whilst Yellow-Blue (YEL-B) filter used for red fluorescence of SYBR Green I. 20,000 cells were analysed for each sample. The data was

analysed and graphed using Guava EasyCyte^{TM} HT System and GuavaSoft 3.1.1 software (Millipore, USA).

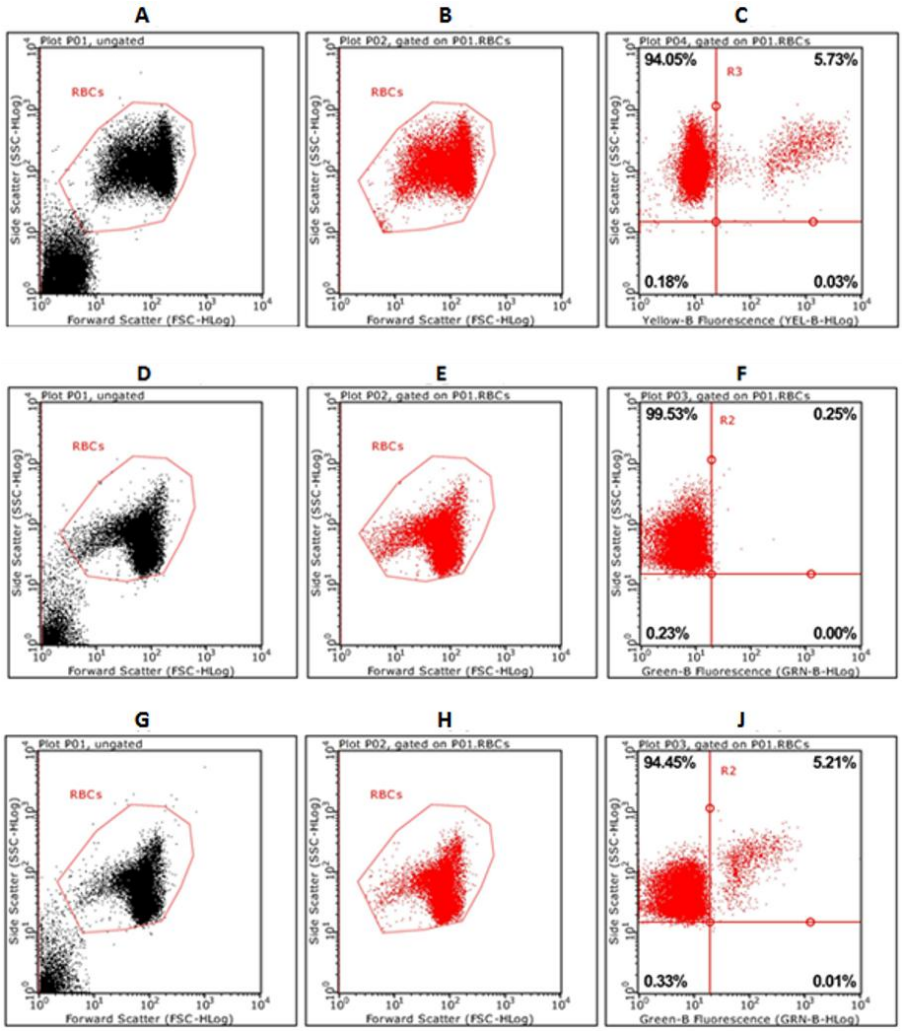

Fig. 2.5 Flow cytometry dot plot graphs of DNA fragmentation assay (TUNEL assay) using *In Situ* Cell Death Detection Kit, Fluorescein. Top row represents drug-untreated iRBCs sample and stained with SYBR Green I only to identify parasitaemia percentage. Middle row indicates drug-untreated sample loaded with TUNEL labelling solution only to identify DNA fragmentation. The bottom row shows DNase-treated sample (control positive) and stained also with TUNEL labelling solution only. 20,000 cells of both infected and uninfected RBCs were gated and labelled as RBCs (A, D and G), and the remaining particles represent debris and components of destroyed cells. B, E and H represent gated RBCs only. R3 in the dot plot graph (C) indicates percentage of parasitaemia at 6 hrs of experiment period, R2 in graph (F) represents percentage of TUNEL positive cells in drug-untreated sample while R2 in graph (J) shows TUNEL positive cells in DNase I-treated sample.

2.7.2.2 *In Situ* DNA fragmentation by fluorescence microscope

Fluorescence microscopic analysis of the TUNEL-treated iRBCs was also carried out. After TUNEL staining (*2.7.2.1*), samples were stained with a 0.5 µg final concentration of Hoechst 33342 (Thermo Fisher Scientific, UK) for 10 min at 37 °C. Stained iRBCs were collected by centrifugation (400 g for 10 min at room temperature) and then suspended in 1XPBS before been placed on microscopic slide. The iRBCs were covered with a coverslip, sealed using nail varnish and stored in the dark at 4 *°C* prior to imaging (performed the same day). The iRBCs were visualised and counted using an EVOS microscope (EVOS® Cell Imaging Systems, Life Technologies, Carlsbad, CA, USA) using 100X objective lens with appropriate filters (DAPI filter for blue Hoechst fluorescence signal: excitation/emission λ= 357 nm/447 nm, and the GFP filter for TUNEL-green fluorescein fluorescence signal: excitation/emission λ= 470 nm/525 nm). A least 60 cells/ sample were counted with all experiments sat up in triplicate with three independent biological replicates (n=9).

2.7.3 Caspase-like cysteine protease activation assay

2.7.3.1 Caspase-like cysteine protease activation assay by flow cytometry

To investigate caspase activation in drug-treated *P. falciparum* intraerythrocytic stages, the CaspaTag Pan-Caspase *In Situ* Assay Kit, Sulforhodamine kit (Millipore, USA) was used. Sulforhodamine-labelled caspase inhibitor (SR-VAD-FMK) is cell permeable, non-toxic and covalently binds to the active site cysteine of caspase heterodimer. Bound reagent, indicating the presence of caspases, is retained in the cell on washing. The protocol used below was based on that originally described in Ch'ng *et al* (2010).

Infected iRBCs were exposed to 50% and 90% kill concentrations as determined from bioluminescence assay (see 2.3.3*J*. Drug-treated and untreated cells were loaded with freshly prepared SR-VAD-FMK reagent according to manufacturer instructions. In brief, trophozoite stage (20-26 hrs post-invasion) parasite cultures ($1X10^6$ cells/300 µL) were mixed with 7 µL of a freshly prepared 30X stock of SR-VAD-FMK reagent for 1 hr at 37 °C in the dark (Ch'ng *et al.,* 2010). The tubes were gently flicked twice during incubation period to suspend settled cells. Post-stained cells were washed twice with 1XPBS and the iRBCs collected by centrifugation (400 g for 10 min at room temperature). The iRBCs were resuspended in 1 mL of 1XPBS (≤ 500 cells/µL) for flow cytometry analysis. To determinate the parasitaemia, SYBR Green I-stained sample of the initial RBC mastermix was done as described above (see 2.7.2.1). The green fluorescence signal of SYBR Green I was being detected using the Green-Blue (GRN-B) filter, whilst the red fluorescence signal of CaspaTag was detected using the Yellow-Blue (YEL-B) filter. For each sample, 20,000 total erythrocytes were required. Analysis and plotting data were carried on via Guava easyCyte™ HT System and GuavaSoft 3.1.1 software, respectively (Millipore, USA).

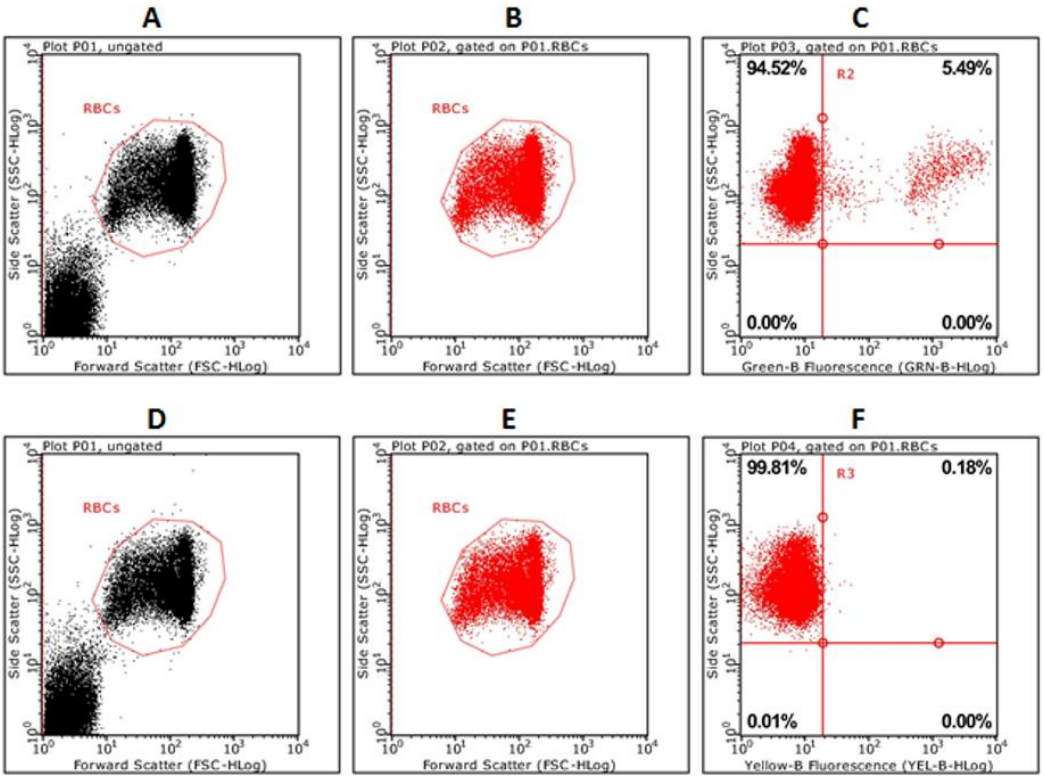

Fig. 2.6 Flow cytometry analysis data of caspase-like cysteine activation assay enzyme using CaspaTag Pan-Caspase *In Situ* Assay Kit, Sulforhodamine kit (Millipore, USA). The top row indicates drug-untreated cells which stained with SYBR Green I only as indicator of iRBCs to calculate parasitaemia percentage (see section 2.7.2.1). The bottom row displays drug-untreated and SR-VAD-FMK-labelled sample as indicator of caspase-like enzyme activation. Forward scatter and side scatter were obtained and overall, 20.000 of infected and uninfected cells were gated and labelled as RBCs (A and D). B and E indicates isolated-RBCs only. Parasitaemia was calculated using SYBR Green-labelled iRBCs [C (R2)] whilst (R3) in (F) represents CaspaTag-positive cells as an indicator of caspase-like enzyme activation in *P. falciparum* trophozoite stage.

2.7.3.2 Caspase-like cysteine protease activation assay by fluorescence microscope

Further analysis of caspase-activation was also done by florescence microscopy, where treated and untreated cell groups were stained with SR-VAD-FMK as described above. After staining, samples were stained with a 1 µg/mL final concentration of Hoechst 33342 (Thermo Fisher Scientific, UK) for 10 min at 37 °C. The iRBCs were visualised and counted by EVOS microscope using 100X objective lens with appropriate filters (DAPI filter for blue Hoechst fluorescence signal: excitation/emission λ= 357 nm/447 nm, and the RFP filter for CaspaTag-red fluorescence signal: excitation/emission λ= 531 nm/593 nm). A least 60-

70 cells/sample were counted with all experiments sat up in triplicate with three independent biological replicates (n=9).

2.7.4 Intracellular calcium distribution assay

The dynamics of intracellular calcium localization following drug/compound treatment was investigated using the protocols originally described by Ch'ng *et al* (2011). Early trophozoite stage (20 to 26 hrs post invasion) parasites were challenged with 25%, 50% and 90% kill concentrations of each drug for 6 hrs. After drug treatment, the samples were washed twice in 10 volumes of 1XPBS and collected by centrifugation (500 g for 5 min at room temperature). The treated and untreated iRBCs were loaded with 2 µM of green fluorescence calcium indicator (Fluo-4 AM, freshly was prepared using the instructions provided by Thermo Fisher Scientific) following by incubation for 30 min at 37 ℃ in the dark. Post-stained cells were washed twice with ten volumes of 1XPBS and the iRBCs collected by centrifugation (400 g for 10 min at room temperature). The nucleic acid of iRBCs were stained with Hoechst 33342 (Thermo Fisher Scientific, UK) at a 1 µg/mL final concentration for 10 min at 37 ℃. The dye-stained samples were washed and mounted on a microscopic slide as described above (see section 2.7.1.1). The stained iRBCs were observed using the 100X objective of an EVOS microscope using a DAPI fluorescence filter for blue Hoechst fluorescence signal (excitation/emission λ= 357 nm/447 nm) and GFP fluorescence filter for Fluo-4 AM-green fluorescence signal (excitation/emission λ= 470 nm/525 nm). At least 60-70 cells/sample were quantified for each sample. All experiments were obtained from triplicate technical replicates from three biological replicates (n=9).

2.7.5 Phosphatidylserine detection using the FITC-Annexin V assay

Fluorescence microscopic analysis of phosphatidylserine (PS) exposed on the iRBC surface following different stress conditions in trophozoite stage (20-26 hrs post-invasion) *P. falciparum* were performed using a commercial FITC-Annexin V kit (Abcam, UK). The experiments were established using antimalarial drug stress (50% and 90% kill concentrations) as well as exposure to febrile temperature (40 ℃).

2.7.5.1 Phosphatidylserine detection following drug-induced stress

After 6 hrs of drug treatment that induced 50% and 90% kill, $1X10^5$ iRBCs were suspended in 500 µL of 1X binding buffer provided with the kit. 5 µL of freshly prepared FITC-Annexin V reagent according to manufacturer's instructions and as originally described by Totino *et al* (2011) with 1 µg/mL final concentration of Hoechst 33342 were added to the iRBCs/binding buffer and incubated for 30 min at 37 ℃ with protection from light. The iRBC were washed twice in 10 volumes of 1XPBS with iRBCs collected by centrifugation (400 g for 10 min at room temperature). The iRBCs were visualised and counted by an EVOS microscope using 100X objective lens with appropriate filters (DAPI filter for blue Hoechst fluorescence signal, excitation/emission λ= 357 nm/447 nm, and the FITC filter for FITC-Annexin V fluorescence signal, excitation/emission λ= 494 nm/518 nm). A least 60 cells/ sample were counted with all experiments sat up in triplicate with three independent biological replicates (n=9).

2.7.5.2. Phosphatidylserine detection following heat stress

The effect of febrile temperature on PS localization was investigated using a protocol originally described by Engelbrecht and Coetzer (2013). Experiments were initiated by

incubating trophozoite stage (20-26 hrs post-invasion) iRBCs for 2, 4 or 8 hrs in a water bath at 40 ℃. Parasite viability was measured following these three time points using the bioluminescence-based assay (See section 2.3.2). After heat shock, samples were returned to 37 ℃ and incubated until 48 hrs after the start of the experiment. The heat-shocked iRBC cultures were stained with FITC-Annexin V reagent and Hoechst 33342 dye and visualised as described above (see section 2.7.5.1).

Chapter 3: Screening for potential inhibitors of the PfAtg8-PfAtg3 protein-protein interaction (PPI)

3.1 Introduction

Autophagy offers a potential drug target due to its central role in the maintenance of cellular homeostasis in both normal and pathological situations. Drug development programmes have been linked a diverse range of diseases such as cancer, neurodegeneration and cardiac disorders (Levine and Kroemer, 2008; Rubinsztein *et al.,* 2012b). As such, a range of drugs and compounds have been identified that modulate the function of proteins within the autophagy cascade (Chuo *et al.,* 2011; Hain *et al.,* 2012; Mizushima *et al.,* 2001; Liu *et al.,* 2011; Powis *et al.,* 1994; Wu *et al.,* 2010). Examples of these compounds are shown in Fig. 3.1 and the site of action for a number of autophagy inhibitors in a classical autophagic cascade in Fig. 3.2.

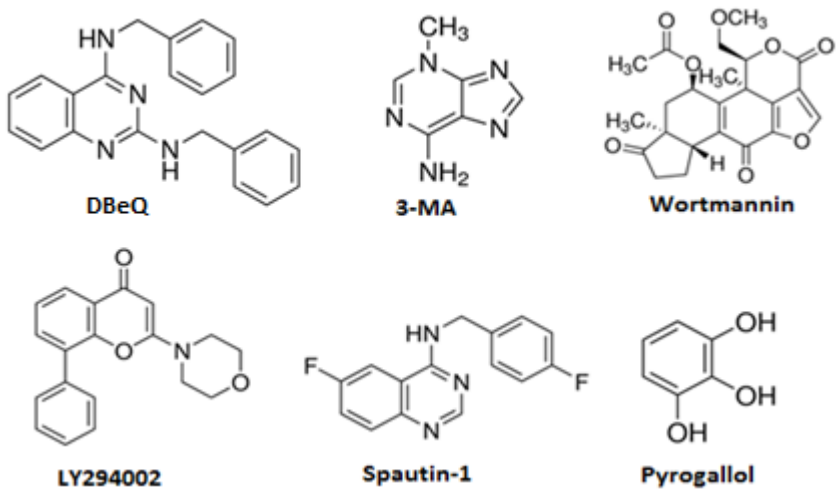

Fig. 3.1 Examples and structures of exemplar autophagy inhibitors.

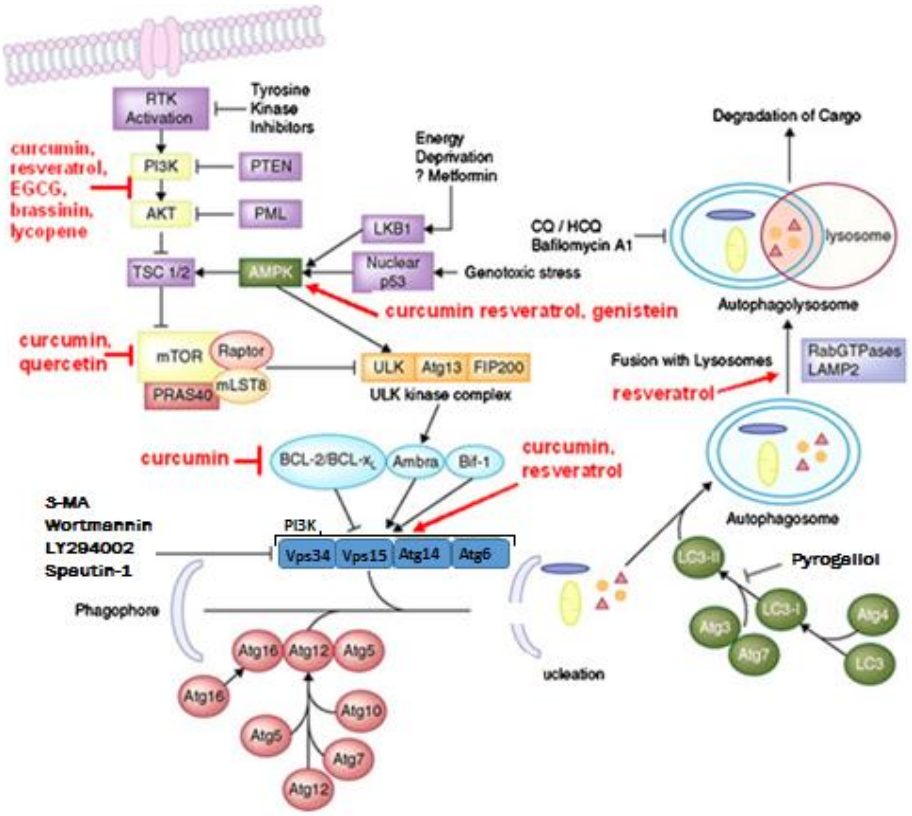

Fig. 3.2 Sites of action for autophagy inhibitors. A generic macroautophagy cascade is shown with key regulatory steps in initiation (mTOR, PI3K signalling), phagophore maturation, autophagosome formation and trafficking to the Lysosome. Compounds that inhibit autophagy (black) and drugs under development (red) are indicated against where they act in this cascade. (Source: Feitelson *et al.,* 2015).

A number of these inhibitors have been assessed for their antiplasmodial effects against the intraerythrocytic stages of *P. falciparum*. Exposure to 5 mM of 3-MA, which inhibits autophagosome formation by targeting PI3K, leads to a small reduction in Atg8 levels assessed using western blotting and immunofluorescence assays (Navale *et al.,* 2014). Wortmannin, which also targets PI3K activity, has an EC_{50} of between 40-70 µM (Tomlins *et al.* 2013), although exposure to 10 µM of wortmannin for 6 hrs did not affect the localization or production of Atg8 in pre-starved *P. falciparum*. Increasing the concentration to 100 µM for a 1.5 hr pulse reduced PI3K activity by 58%. The accumulation of autophagosome-like vesicles containing undigested haemoglobin in the

cytoplasm of *P. falciparum* parasites pre-treated with 3 μM wortmannin suggests that PI3K involves in *P. falciparum* in autophagosome formation and the subsequent trafficking of these vesicles to the DV (Vaid *et al.,* 2010). The same trafficking disruption was observed in this same study using a second PI3K inhibitor LY294002 (50 μM) which has an apparent EC_{50} of 26 μM against intraerythrocytic parasites.

In 2012, Hain *et al.* determined the structure of PfAtg8 from a co-crystal with the Atg8 family interacting motif (AIM) of PfAtg3. This structure revealed some distinct features of PfAtg8 distinct to the LC3 homologue found in humans. These included a change in the orientation and distribution of charge over the Atg3 interacting region of Atg8, a shallow cleft that contains two hydrophobic pockets termed W and L (based on the proximity of tryptophan and leucine residues). The implications of these structural differences and compound docking are developed in the next chapter. PfAtg8 also includes an A-loop, with an adjacent A-pocket, that result from an insertion of 9 amino acids that is found in the Atg8 of a range of apicomplexan parasites. In this study, the authors screened a small fragment library to determine their ability to block an interaction between PfAtg8 and the PfAtg3 AIM as detected by SPR. Here they showed that 1,2,3-trihydroxybenzene (common name is pyrogallol) inhibited this interaction with an $EC_{50.SPR}$ of 150 μM. A second related compound, 1,2,4-trihydroxybenzene, also inhibited the same interaction although with a much higher $EC_{50.SPR}$ potency of 1 mM.

The potential for the PfAtg8-PfAtg3 protein-protein interaction as a novel target for drug development was developed by the same team when they reported a SPR screen of the open access MMV Malaria Box resource (Hain *et al.,* 2014). Here they report three structurally related hits with $EC_{50.SPR}$ ranged between 6.0-18.1 μM that appear to act in a

concentration-dependant manner. The best hit, compound 1 (MMV007907) [common scaffold is a 4-pyridin-2-yl-1,2-thiazol-2-amine (PTA)], that has an EC_{50} against intraerythrocytic stages between 1.4 µM and against the liver stage of approximately 30 µM. In the latter case, this concentration of the PTA did not appear to affect the human liver cell line used in the *in vitro* assay. *In silico* docking studies suggest that PTA, with three structures tested, block the PfAtg8-PfAtg3 protein-protein interaction when they bind at the W and L-pocket sites. Increasing concentrations of compound 1 result in an accumulation of the unlipidated PfAtg8 as assessed by western blot, supporting the role of PfAtg8-PfAtg3 in the cascade that adds phosphatidylethanolamine to PfAtg8. Two years later, a second report outlined a similar approach to the discovery of potential PfAtg8-PfAtg3 protein-protein interaction inhibitors (Hain *et al.,* 2016). Here the team used an initial virtual screen between approximately 370,000 structures in the ChemBridge chemical library and PfAtg8. Thirteen hits were validated using the SPR assay to show inhibition of PfAtg8-PfAtg3 interaction. One compound, ALC25 (1-[(3-methylphenyl) methyl]-3-([1-(pyridine-2-ylmethyl) pyrrolidin-3-yl] methyl) urea, proved to inhibit intraerythrocytic growth, but not liver stages, with an EC_{50} of 19 µM and result in the accumulation of unlipidated PfAtg8. *In silico* docking studies suggested, however, that ALC25 interactions were more likely occurring at the A-pocket on PfAtg8.

Through collaboration with Dr Johannes Reynisson, a molecular modeller and computational chemist from the University of Auckland, New Zealand, a library of compounds related to molecules that modulate autophagy in human cell lines were provided to our research team. In addition to this library, Dr Anthony Curtis (Keele University) added additional compounds that he has synthesised for a research project with Dr Alan Richardson (Keele University) for his research project on autophagy

inhibitors in human ovarian cell cancer lines. These compounds are considered likely to act as protein-protein interaction inhibitors in the Atg8 and/or Atg12 cascade. Here I provide a report of the antiplasmodial screening of these compounds against the intraerythrocytic stages of *P. falciparum*, with an initial characterization of the pharmacodynamic and toxicity properties of two hits that were taken forward, in collaboration with Professor Roepe (Georgetown University) to provide initial evidence for their potential as inhibitors of PfAtg3-PfAtg3 interaction.

3.2 Results

3.2.1 Screening the compound library for activity against intraerythrocytic asexual stages

A chemical library of 131 compounds was provided by Dr Johannes Reynisson from Auckland University, New Zealand, and Dr Anthony Curtis from the School of Pharmacy School at Keele University. Appendix 1 provides a table of their ID number and chemical structure. Antiplasmodial activity was determined against intraerythrocytic trophozoite stages of *P. falciparum* over 48 hrs using a MSF assay. Serial drug dilution provided a screen at three concentrations (2, 10 and 50 µM), with technical duplicates and three biological replicates (n=6) were performed. The fluorescence data was normalized against untreated controls and a mean ± SD of n=6 of relative growth (%) plotted (Fig. 3.3 and 3.4). The compounds were provided in two tranches, the first 64 compounds (Fig. 3.3) were screened against 3D7 (CQ sensitive, CQS, laboratory clone) then switched to $Dd2^{luc}$ (CQ resistance, CQR, laboratory clone) for the remaining 67 compounds (Fig. 3.4). This switch was done as it was decided that the subsequent assays would be done using the $Dd2^{luc}$ line for the relative rate of kill assays.

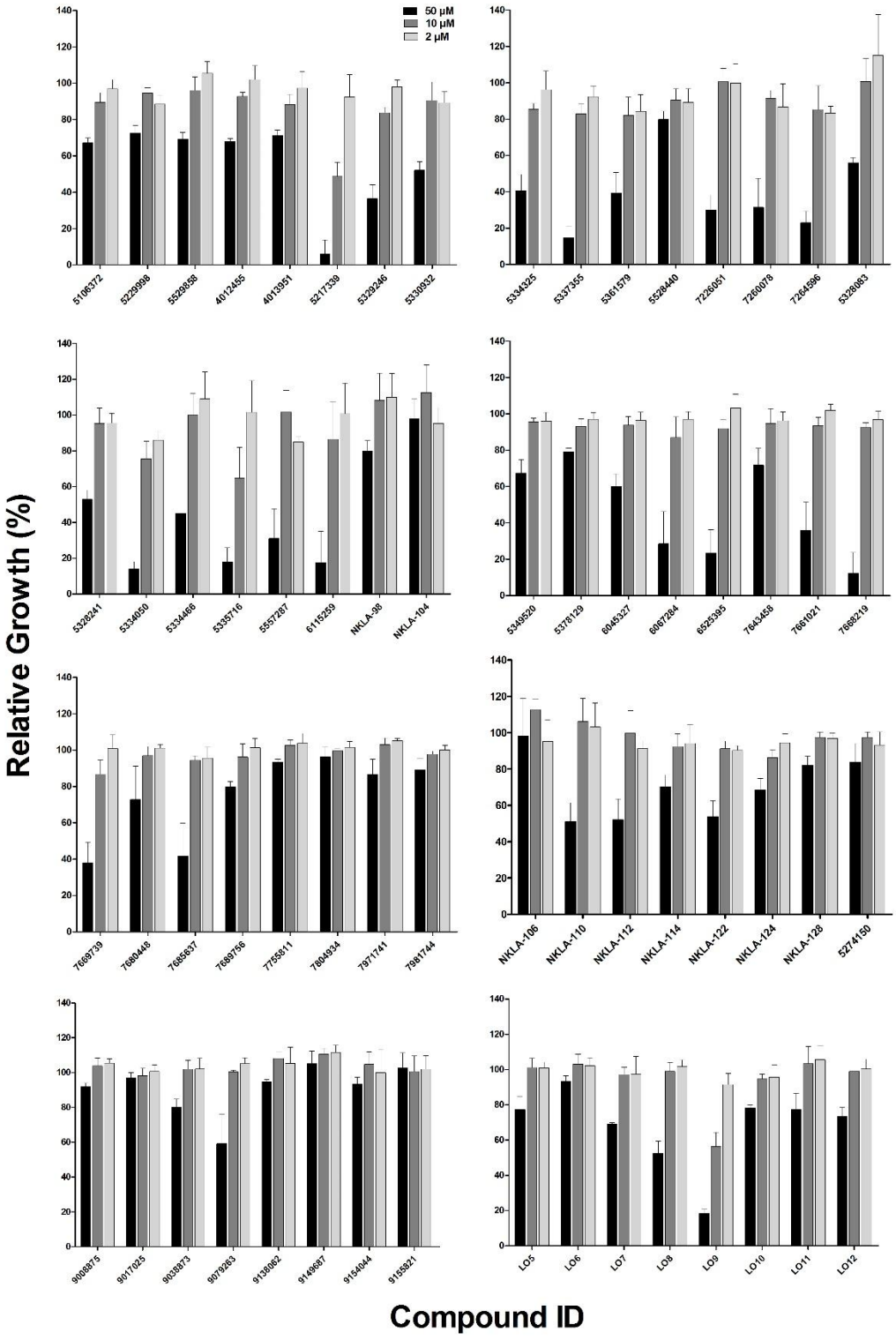

Fig. 3.3 Initial screening data for the 64 potential autophagy inhibitors at 2, 10, 50 µM (see key for labelling) after 48 hrs exposure of intraerythrocytic trophozoite stages of 3D7 clone using the MSF growth assay. The data shown is a normalised growth, compared to untreated controls, with the mean ± SD (n= 6) shown. See appendix 1 for chemical structures for the ID shown on the x-axis.

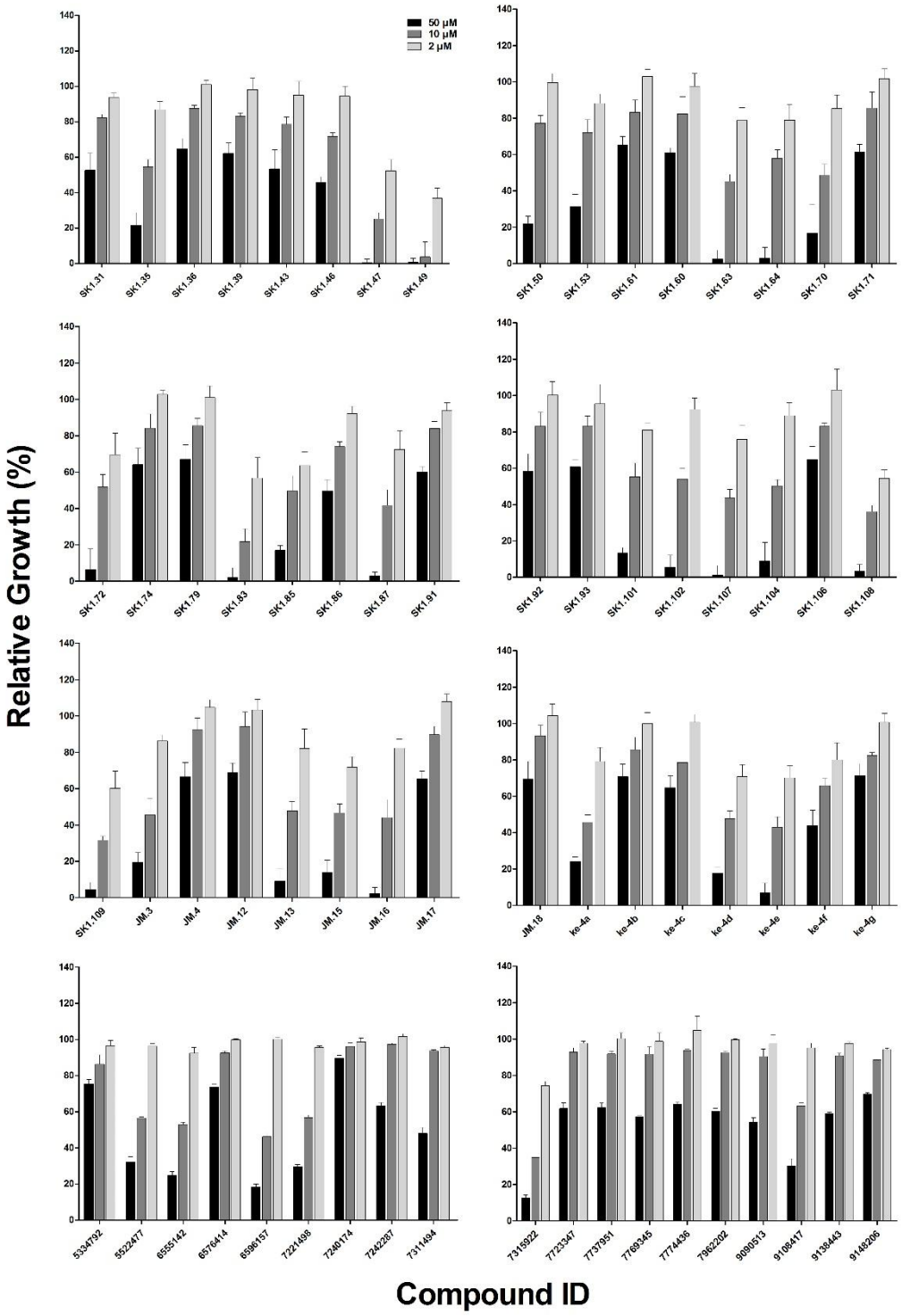

Fig. 3.4 Initial screening data for the 67 potential autophagy inhibitors at 2, 10, 50 µM (see key for labelling) after 48 hrs exposure of intraerythrocytic trophozoite stages of Dd2^{luc} clone using the MSF growth assay. The data shown is a normalised growth, compared to untreated controls, with the mean ± SD (n= 6) shown. See appendix 1 for chemical structures for the ID shown on the x-axis.

3.2.2 Determination of the 50% effective concentration (EC_{50})

The screen identified 56 compounds that showed > 50% reduction in relative growth at the highest concentration 50 µM. Of these, 18 showed a >50% reduction at 10 µM with only two, SK1.47 and SK1.49, showing the same reduction in relative growth at 2 µM. The EC_{50} of these 56 compounds was determined using the MSF assay using a two-fold drug dilution series, each experiment done as a technical triplicate with three biological repeats (n=9). The EC_{50} was first done in either 3D7 and $Dd2^{luc}$ clones depending on the initial tranche of compound library screened. However, compounds with EC_{50} <10 µM in either tranche were repeated in the other parasite clone. Eight most potent compounds therefore had their EC_{50} determined in both CQS (3D7) and CQR ($Dd2^{luc}$) parasites (Fig. 3.5, Table 3.1) (See appendix 2 for more information about EC_{50} for tested compounds). The EC_{50} determined in both 3D7 and $Dd2^{luc}$ were similar. A linear correlation of these values revealed a strong correlation (r^2= 0.9, P < 0.0001), although the slope of 1.6±0.15 suggests a slightly higher in EC_{50} value in the CQR clone $Dd2^{luc}$ (Fig. 3.6). This is unlikely to reflect a cross resistance to existing drug resistance in $Dd2^{luc}$ compared to 3D7 as the resistance index (EC_{50} in $Dd2^{luc}$/3D7) is low (1.4-1.6) and in several cases the 95% CI for EC_{50} in the two strains overlap or are very close (Table 3.1).

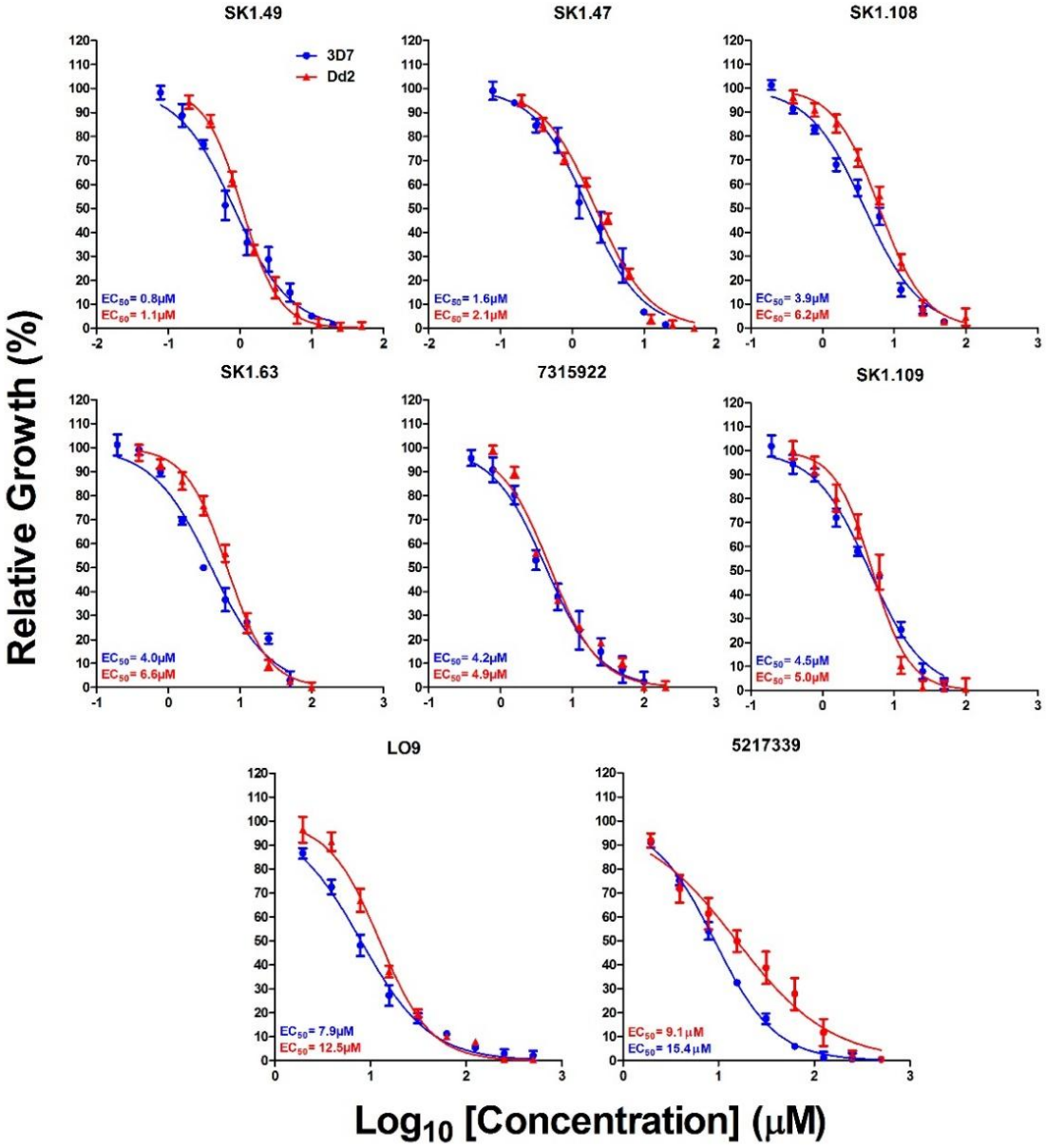

Fig. 3.5 Log_{10} concentration-normalised response curves for the eight most potent compounds against 3D7 (blue) and $Dd2^{luc}$ (red). The mean and SD are represented by dots and error bars, respectively. The estimated EC_{50} values are shown on each graph (see table 3.1).

Compound ID	EC_{50} (µM) in 3D7 (95% CI)	EC_{50} (µM) in $Dd2^{luc}$ (95% CI)	Chemical structure
SK1.49	0.8 (0.6 to 1.0)	1.1 (1.0 to 1.1)	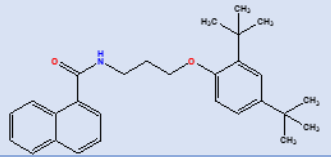
SK1.47	1.6 (1.3 to 2.0)	2.1 (1.7 to 2.6)	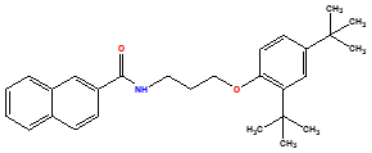
SK1.108	3.9 (3.0 to 5.0)	6.2 (5.4 to 7.1)	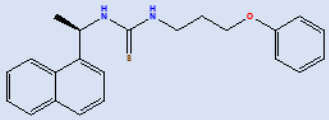
SK1.63	4.0 (3.0 to 5.2)	6.6 (5.9 to 7.3)	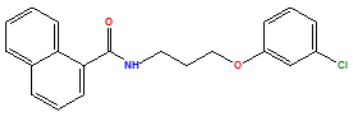
7315922	4.2 (3.3 to 5.3)	4.9 (3.6 to 6.5)	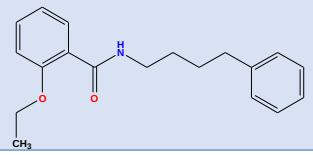
SK1.109	4.5 (3.5 to 5.6)	5.0 (4.0 to 6.0)	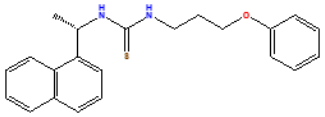
LO9	7.9 (7.0 to 8.9)	12.5 (10.9 to 14.2)	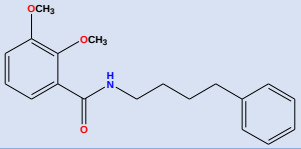
5217339	9.1 (8.6 to 9.5)	15.4 (11.8 to 20.0)	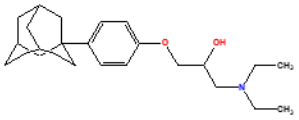

Table 3.1 Estimated EC_{50} values of the eight most potent compounds in 3D7 and $Dd2^{luc}$ clones of *P. falciparum* parasite.

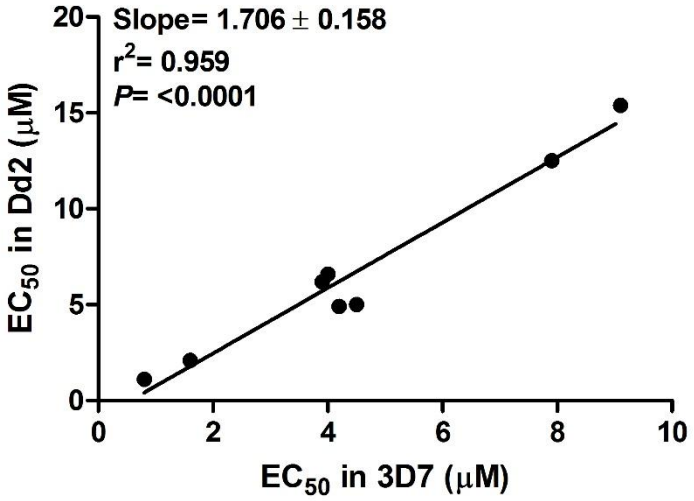

Fig. 3.6 Correlation of the mean EC_{50} values determined for the eight most potent compounds in 3D7 and $Dd2^{luc}$. Results of a linear regression are shown on the graph.

A selected range of commercially available autophagy inhibitors were also screened to compare their antiplasmodial effects. These autophagy inhibitors include; DBeQ (p97 ATPase inhibitor) (Chou *et al.,* 2011), pyrogallol (LC3-Atg3 inhibitor) (Hain *et al.,* 2012), 3-MA, wortmannin, LY294002 (PI3K inhibitors) (Curran and Smith, 2014) and spautin-1 (PI3K inhibitor) (Shao *et al.,* 2014). EC_{50} values of these autophagy inhibitors were determined in $Dd2^{luc}$ using the MSF assay for 48 hrs (n=9) (Fig. 3.7). Except for DBeQ, they all showed a low antiplasmodial potency which correlates with previously described observations (Hain *et al.,* 2012; Navale *et al.,* 2014; Shao *et al.,* 2014; Tomlins *et al.* 2013; Vaid *et al.,* 2010) although these studies used a range of techniques such as SPR and PI3K activity assays. Only DBeQ was taken forwarded as a described autophagy inhibitor for comparison due to its low-micromolar (1.7 μM) EC_{50} value.

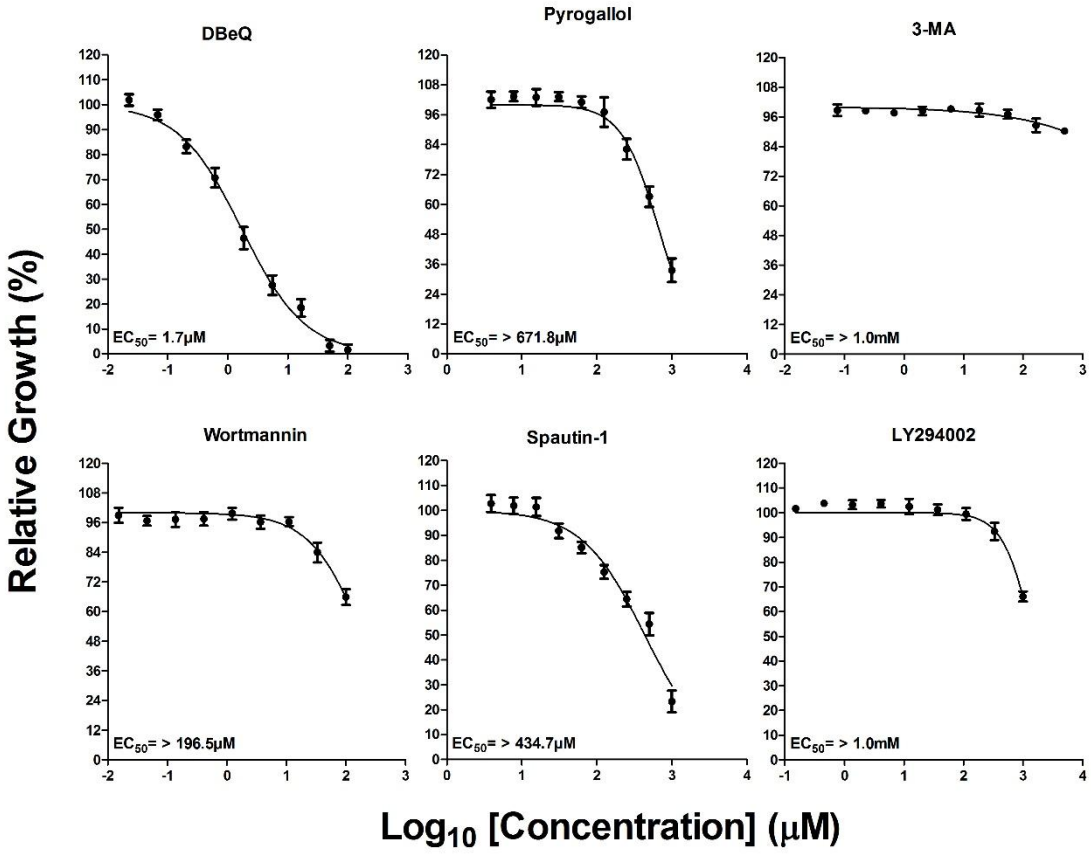

Fig. 3.7 Log_{10} concentration-normalised response curves for the commercial autophagy inhibitors against $Dd2^{luc}$. The mean and SD are represented by dots and error bars, respectively. The estimated EC_{50} values are shown on each graph.

3.2.3 *In vitro* determination of estimated 50% lethal dose (LD_{50}) in $Dd2^{luc}$

The EC_{50} data provides a key pharmacodynamic property of a compound over 48 hrs, but does not explain initial activity of the compound in terms of whether it is cytostatic or cytocidal. This killing effect can be determined using a lethality assay developed originally by Paguio *et al.* (2011). This assay is based on a modified MSF assay, but requires a complex procedure including drug bolus, washing and regrowth to determine the lethal effect after 48 hrs of additional growth in the absence of drug. However, a bioluminescence assay developed in our laboratory by Ullah *et al.* (2017) provides the ability to measure the viability of cells immediately after the 6 hrs drug-bolus treatment,

removing the need for washing and regrowth, with data from this simpler assay was shown to correlate with the 48 hrs MSF/wash-off assay. This parameter, termed here the 50% Lethal dose (LD_{50}), was determined for a range of benchmark antimalarial drugs which reflect distinct classes of chemical structure and mode of actions. These included; 4-aminoquinolines (CQ, AQ, PYRD and PPQ), amino alcohols (QN and MQ), artemisinin derivates (DHA and ARM) and ATQ. These data will be compared against those for the eight most potent compounds from the library with four additional library compounds selected that share structural similarities to one or more of these original eight, as well as DBeQ as a described autophagy inhibitor.

The assay was performed as originally described (Ullah *et al.* 2017), measuring the remaining luciferase activity after 6 hrs exposure to a serial two-fold dilution of drugs/compounds (Fig. 3.8 and 3.9). The data shown are the mean ± SD of three independent experiments, each with three technical replicates (n=9). For comparison, the previous EC_{50} determination after 48 hrs using the MSF assay is plotted on the same graph.

The LD_{50} of seven of the benchmark antimalarial drugs (Fig. 3.8) used were previously reported (Ullah *et al.* 2017) and are in close agreement with those obtained in this study using the same $Dd2^{luc}$ clone. The data clearly show the expected right-shift of the LD_{50} curves compared to the EC_{50} curve, a result of the effect of the drug/compound being exposed for different lengths of time. A similar right-shift of the LD_{50} curves was observed for a majority of the library compounds (Fig. 3.9). All LD_{50} values are reported in Table 3.2.

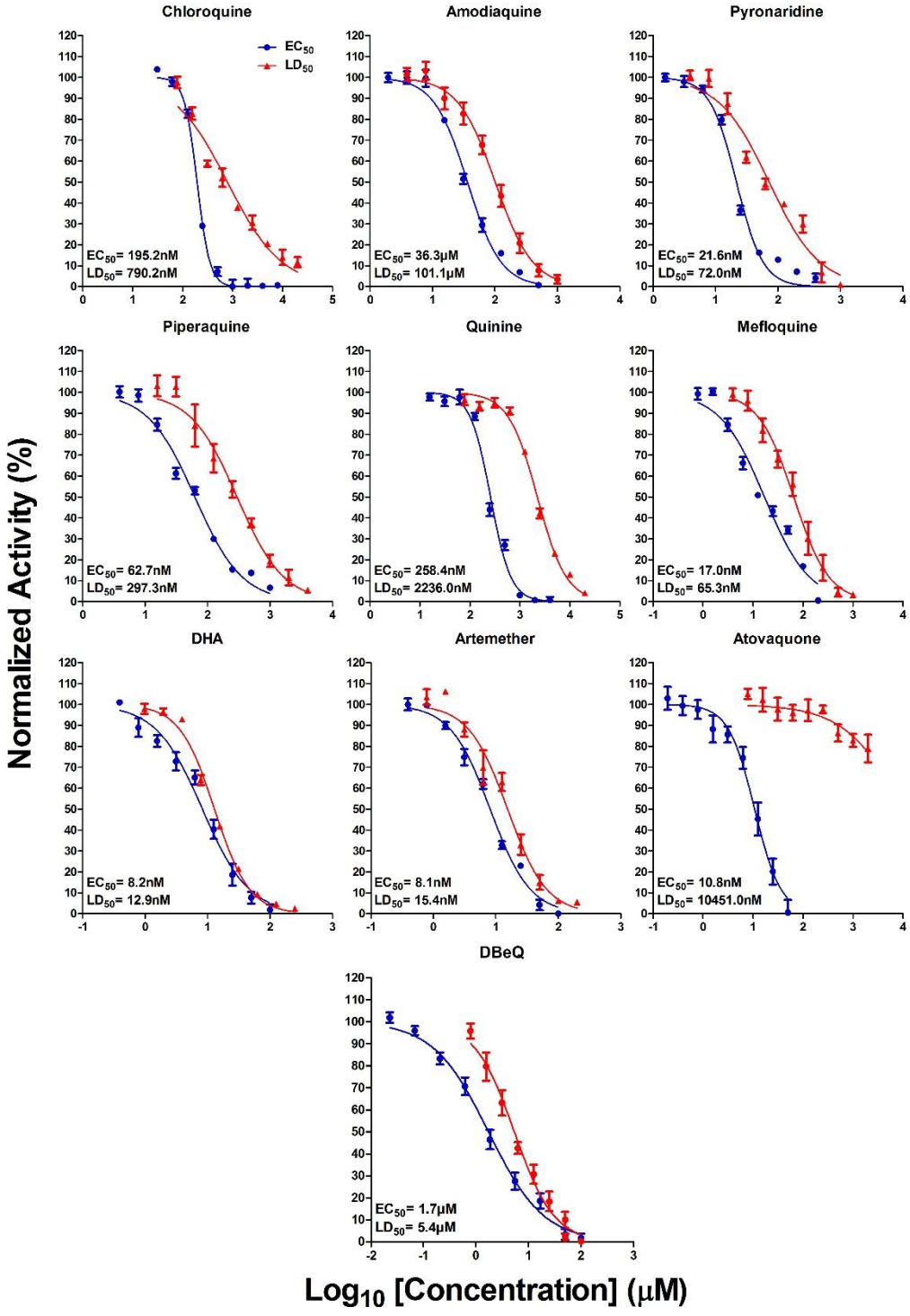

Fig. 3.8 Log_{10} concentration-normalised response curves for benchmark antimalarial drugs and DBeQ. The normalised response curves provide either the LD_{50} from a 6 hrs bioluminescence assay (red lines) or the EC_{50} from a 48 hrs MSF assay (blue lines). All values are reported on the graphs and in Table 3.2. The mean and SD (n=9) are represented by dots and error bars, respectively.

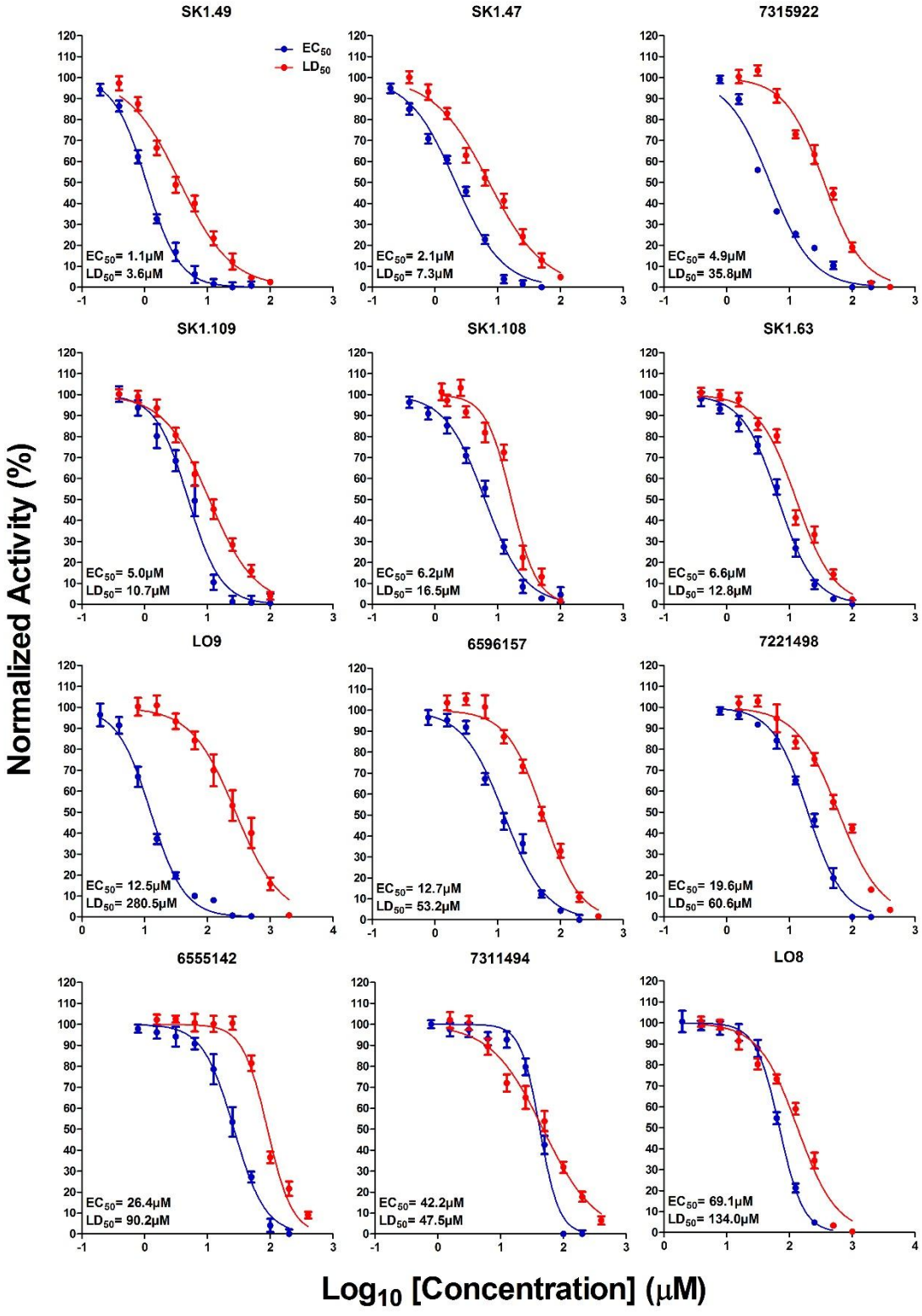

Fig. 3.9 Log_{10} concentration-normalised response curves for 12 library compounds. The normalised response curves provide either the LD_{50} from a 6 hrs bioluminescence assay (red lines) or the EC_{50} from a 48 hrs MSF assay (blue lines). All values are reported on the graphs and in Table 3.2. The mean and SD (n=9) are represented by dots and error bars, respectively.

The rank order of the LD_{50} shift appears to show artemisinins < 4-aminoquinolines < amino alcohols < ATQ. This is interesting as is an exact inverse correlation of the same rank order when considering their relative rate of kills (Ullah *et al.* 2017). Here the rapid cytocidal action known for artemisinins and 4-aminoquinolines over the first 6 hrs provides a small shift (see Table 3.2 for the LD_{50}/EC_{50} ratio) and contrasts with the initial cytostatic effect of ATQ over the first cycle of cell growth, termed a lag-phase, which would be captured in the 6 hrs assay performed here. The LD_{50}/EC_{50} ratio for the majority of library compounds is between 2 and 4, ratios that would include the rapid initial cytocidal activity of artemisinins and 4-aminoquinolines. Of note is that the autophagy inhibitor DBeQ has a ratio of 3.2, well within the range that would suggest a rapid cytocidal effect.

Compound ID	EC_{50} (nM) in $Dd2^{luc}$	LD_{50} (nM) In $Dd2^{luc}$	LD_{50}/EC_{50} Ratio
DHA	8.2	12.9	1.6
ARM	8.1	15.4	1.9
AQ	36.3	101.1	2.8
PYRD	21.6	72.0	3.3
MQ	17.0	65.3	3.8
CQ	195.2	790.2	4.0
PPQ	62.7	297.3	4.7
QN	258.4	2236.0	8.6
ATQ	10.8	10451	967.7
Compound ID	**EC_{50} (µM) in $Dd2^{luc}$**	**LD_{50} (µM) In $Dd2^{luc}$**	**LD50/EC_{50} Ratio**
7311494	42.2	47.5	1.1
SK1.63	6.6	12.8	1.9
LO8	69.1	134	1.9
SK1.109	5.0	10.7	2.1

SK1.108	6.2	16.5	2.7
7221498	19.6	60.6	3.1
DBeQ	1.7	5.4	3.2
SK1.49	1.1	3.6	3.3
SK1.47	2.1	7.2	3.4
6555142	26.4	90.2	3.4
6596157	12.7	53.2	4.2
7315922	4.9	35.8	7.3
LO9	12.5	280.5	22.4

Table 3.2 LD_{50} and EC_{50} values and their ratios of the benchmark antimalarials and library compounds.

3.2.4 *In vitro* determination of Bioluminescence Relative Rate of Kill (BRRoK)

The BRRoK assay was developed in our laboratory to provide an indication of the initial RoK (Ullah *et al.,* 2017). Using fold-EC_{50} concentration exposures between 0.3 to 9x EC_{50} provides a series of curves that demonstrate the initial concentration-dependant killing effect of the drug/compound tested. Comparison of these effects, using these equipotent concentrations, allows the relative initial killing effects for different drugs/compounds to be determined, particularly when benchmarked against antimalarial drugs for which other *in vitro* and *in vivo* RoK data is available. Given the suggestion from the LD_{50} assessment that the library compounds may exhibit an initial rapid cytocidal effect, the BRRoK assay was used to confirm this observation.

The BRRoK assay was done as previously described (Ullah *et al.,* 2017), although here three endpoints to the assay were determined; 6 hrs (as in the original report) as well as 3 hrs and 48 hrs. Four of the benchmark antimalarials were used; DHA, CQ, QN and ATQ as these represent the full range of initial RoK previously demonstrated (Fig. 3.10). The same assay was performed under the same conditions for the 12 library compounds for which

the LD_{50} data was done (Fig. 3.11). In all experiments each timepoint was performed as three technical replicates, with three biological repeats (n=9). The bioluminescence signal was normalised in all experiments against an untreated control at the same timepoint.

Comparing of the 6 hrs benchmark antimalarials (Fig. 3.10) to data published by Ullah *et al*. (2017), our data provided the same rank order in terms of speed of action as follows; DHA > CQ > QN > ATQ. As well as a concentration-dependant effect on parasite viability, data here also shows a time-dependant effect. Interestingly, when ATQ is exposed for 48 hrs, the lag-phase finished and the killing effect of ATQ becomes apparent. The prediction that DBeQ would have a rapid initial cytocidal affect is demonstrated here, with it appearing to have an initial rate of kill between DHA and CQ.

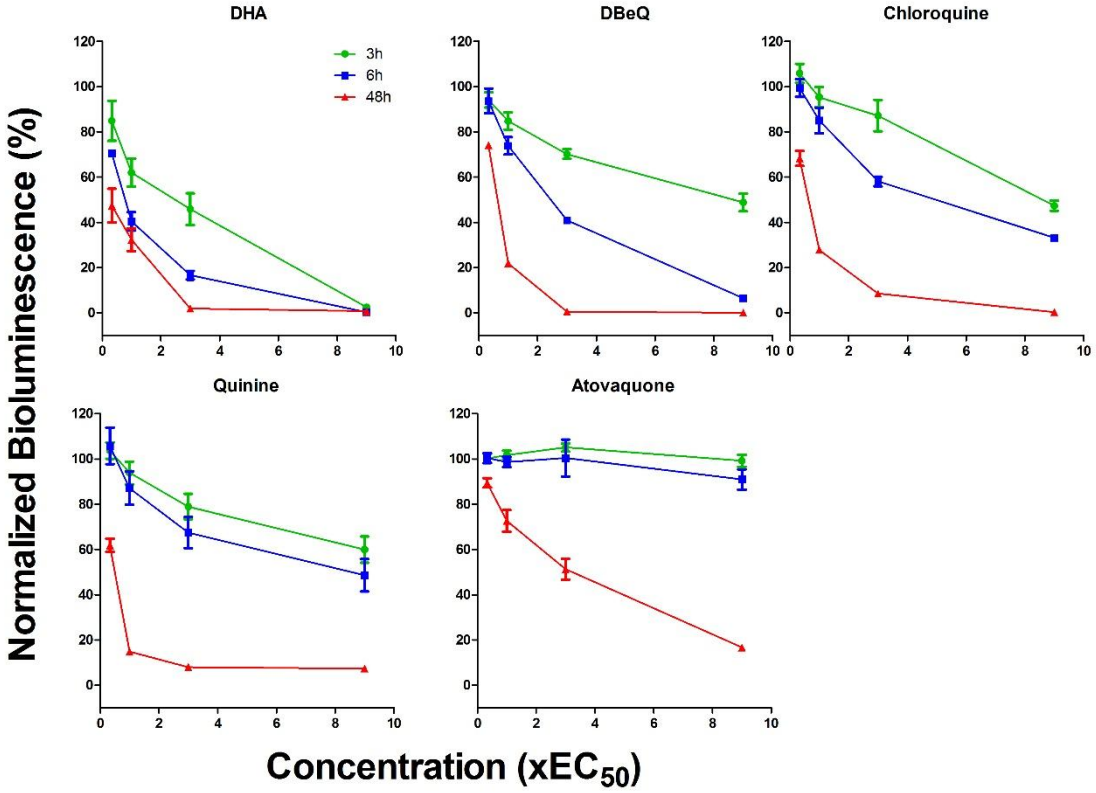

Fig. 3.10 BRRoK assay curves representing concentration (x-axis) and time-dependant (see key) killing effects for benchmark antimalarials and DBeQ. The mean and SD (n=9) normalised bioluminescence signal are represented by dots and error bars, respectively.

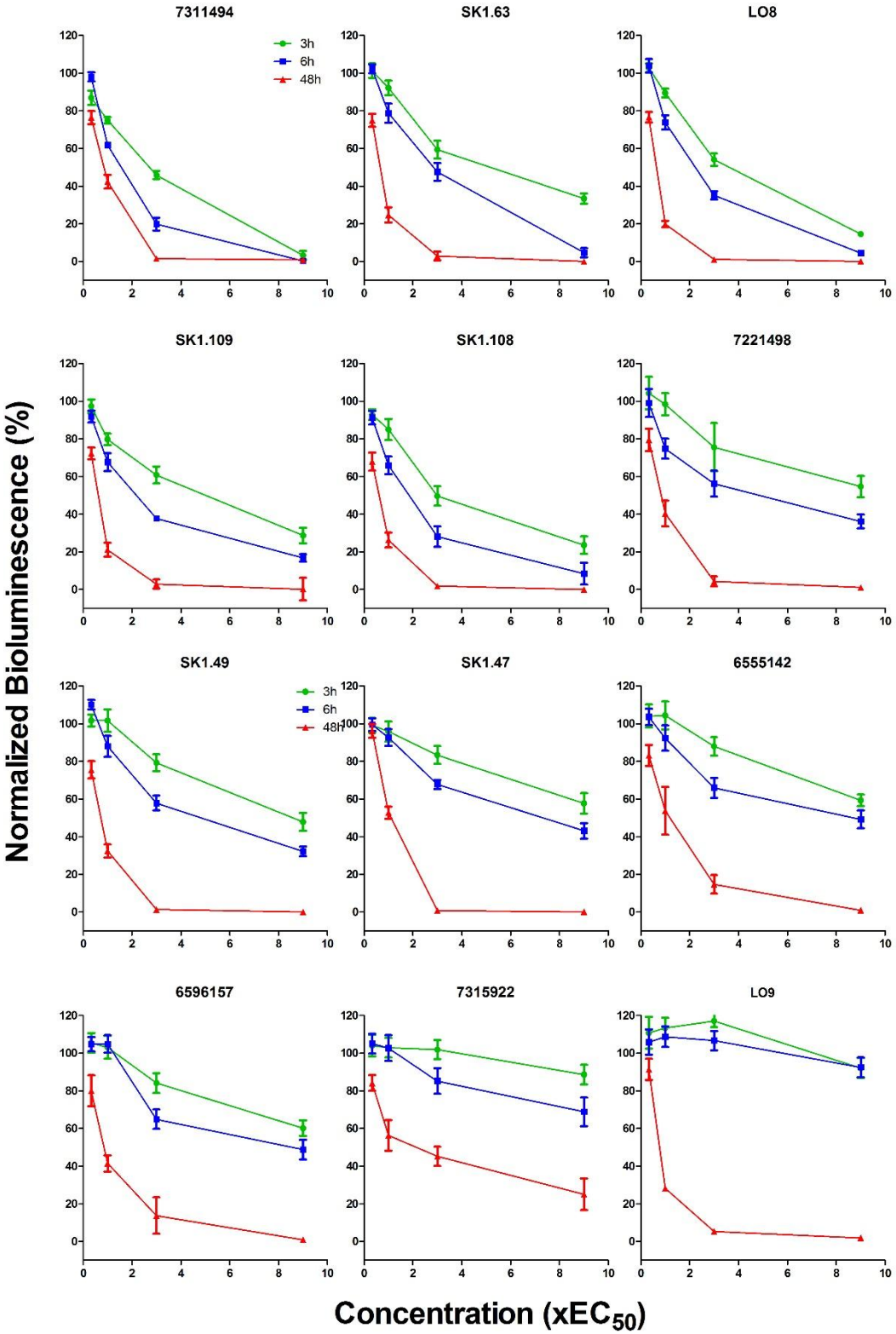

Fig. 3.11 BRRoK assay curves representing concentration (x-axis) and time-dependant (see key) killing effects for 12 library compounds. The mean and SD (n=9) normalised bioluminescence signal are represented by dots and error bars, respectively.

A similar time and concentration-dependent killing effect was observed for all the library compounds. The rank order ranged from 7311494 with an initial cytocidal effect most similar to that of DHA to LO9 which appear to be initially cytostatic with its lethal effect only appear after 48 hrs, essentially similar to that of ATQ (Fig. 3.11). This gross ranking agrees with the prediction based on the LD_{50}/EC_{50} ratios (Table 3.2). The majority of the 12 compounds, however, appear to share similar BRRoK profiles that suggest an initial rate of kill similar to that of CQ. This similarity may reflect that these compounds may also share a similar mode of action – at least with each other, if not with CQ. A more complete analysis between the structures of these compounds with their BRRoK data will follow in the discussion.

3.2.5 *In vitro* determination of cytotoxic effects against the human HepG2 cell line

Two of the eight best library compounds contain a thiourea motif, a known toxicity risk (Pingaew *et al.,* 2013). To explore this as well as any potential toxicity risks in the other library compounds, an initial toxicity assay was performed using the human HepG2 cell line. This assay could only be done using six of the eight compounds as 7315922 and 5217339 were not available. The toxic effect on HepG2 was assessed using the Alamar blue assay that relies on viable cells producing NADPH, NADH and FADH which can reduce the oxidized and non-fluorescent Alamar blue dye to a pink fluorescent state (Rampersad, 2012). HepG2 cells were exposed to a 2-fold serial compound dilution in triplicate for 48 hrs, with three biological replicates done. The fluorescence data was normalized against an untreated control and the mean ± SD (n=9) of relative growth plotted (Fig. 3.12). Log concentration-response curves were produced and the 50% cytotoxic concentration

(CC_{50}) estimated, on all graphs the EC_{50} of the same compound against *P. falciparum* (3D7) are also shown.

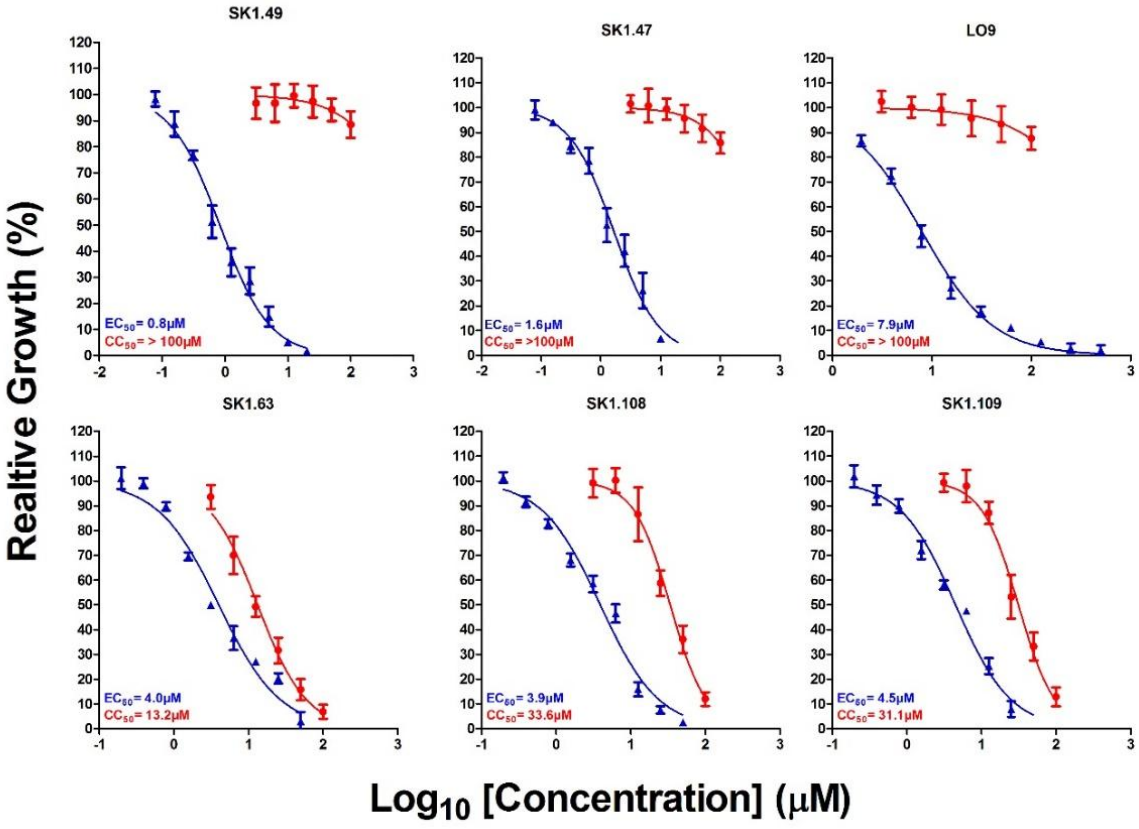

Fig. 3.12 Cytotoxic effects of library compounds against the HepG2 cell line using the Alamar blue assay. The log concentration-normalised growth curves were fitted (red line) and the CC_{50} estimated (shown on each graph). The log concentration-normalised growth curves for antiplasmodial action (blue lines) are also shown along with the EC_{50} from3D7.

The relative selectivity of these compounds against *P. falciparum* when compared against the HepG2 line was determined to provide the selectivity index (SI) (Table 3.3). Here, the SI is CC_{50} in HepG2/EC_{50} in 3D7. Interestingly, the two most potent antiplasmodial compounds, SK1.47 and SK1.49, also showed a high selectivity; SI > 90.9 and > 47.6, respectively, given their low cytotoxic effect against HepG2. For compound LO9, the SI can only be determined at > 8.0 given the maximum concentration HepG2 were exposed

to. As expected, the thiourea motif-contained compounds, SK1.108 and SK1.109 both showed high toxicity and low selectivity as a result. Surprisingly, SK1.63 showed the most cytotoxic effect against HepG2, despite its structural similarity to SK1.47 and SK1.49.

Compound ID	CC_{50} in HepG2 (µM)	EC_{50} in $Dd2^{luc}$ (µM)	Selectivity Index (SI)
SK1.49	> 100	1.1	> 90.9
SK1.47	> 100	2.1	> 47.6
SK1.108	33.6	6.2	5.4
SK1.109	31.1	5.0	6.2
SK1.63	13.2	6.6	2.0
LO9	> 100	12.5	> 8.0

Table 3.3 CC_{50} HepG2 and EC_{50} values for *P. falciparum* 3D7 parasites. Selectivity index (SI) determined as CC_{50}/EC_{50}.

3.2.6 Prediction of bioavailability from physicochemical properties

The oral bioavailability of drugs can be predicted from their molecular properties. A range of observations established by Lipinski *et al.* (1997) and Veber *et al.* (2002), called Lipinski's rule-of-five (RO5) and Veber's rules, respectively, explored the correlation between physicochemical properties of molecule and its determined bioavailability. According to RO5, four physicochemical criteria best describe a compound likely to give a chance for achieving a high oral bioavailability. These include; (i) the number of H-bond donor (HBD) ≤ 5, (ii) the number of H-bond acceptor (HBA) ≤ 10, (iii) the molecular weight (MW) ≤ 500 and (iv) a LogP (octanol-water partition coefficient) of ≤ 5. Veber's rules are similar, and include two additional criteria; (i) the number of rotatable bonds (NROTB) as ≤ 10 and (ii) that the total polar surface area (TPSA) should be ≤ 140 $Å^2$. These

physicochemical properties were determined for the 56 library compounds that were initially demonstrated to show some antiplasmodial effect (i.e. > 50% reduction in growth at 50 µM) using ChemDraw Ultra 7.0 and Molinspiration software (www.molinspiration.com) computational tools. The combined data for each compound was compared to the RO5 and Veber's rules (Table 3.4). Of the top eight compounds, four compounds failed the RO5 test due to their high lipophilicity (LogP > 5) suggesting that they would likely have low absorption and distribution in an aqueous phase. Generally, the majority of the rest of the compounds have a high LogP (> 4), reflecting a common structure around hydrophobic moieties connected with alkyl chains (Fig. 3.13)

Compound ID	MW[1]	HBA[2]	HBD[3]	LogP[4]	TPSA[5] (Å^2)	NROTB[6]	Vol.[7] (Å^3)	Lipinski's RO5	Veber's rule
SK1.49	**417.5**	**3**	**1**	**7.5**	**38.3**	**8**	**422.5**	**Fail**	**Pass**
SK1.47	**417.5**	**3**	**1**	**7.6**	**38.3**	**8**	**422.5**	**Fail**	**Pass**
7315922	**297.4**	**3**	**1**	**4.6**	**38.3**	**8**	**296.3**	**Pass**	**Pass**
SK1-109	**364.5**	**3**	**2**	**5.3**	**33.2**	**9**	**344.8**	**Fail**	**Pass**
SK1.108	**364.5**	**3**	**2**	**5.3**	**33.2**	**9**	**344.8**	**Fail**	**Pass**
SK1.63	**339.8**	**3**	**1**	**4.9**	**38.3**	**6**	**303.7**	**Pass**	**Pass**
LO9	**313.4**	**4**	**1**	**4.1**	**47.5**	**8**	**305.1**	**Pass**	**Pass**
6596157	**299.3**	**4**	**2**	**4.3**	**58.5**	**6**	**287.3**	**Pass**	**Pass**
SK1.70	309.4	3	1	3.7	38.3	6	302.6	Pass	Pass
SK1.104	346.4	5	2	3.3	51.7	10	318.6	Pass	Pass
JM.16	334.4	3	1	3.7	32.3	4	329.1	Pass	Pass
5217339	358.5	3	2	1.8	33.8	8	369.3	Pass	Pass
SK1.64	384.2	3	1	5.0	38.3	6	308.1	Fail	Pass
ke-4a	325.4	3	2	3.5	27.2	7	310.8	Pass	Pass
SK1.107	360.4	5	2	3.6	51.7	10	335.4	Pass	Fail
JM3	346.4	5	1	2.9	58.6	6	310.7	Pass	Pass
SK1.83	381.2	3	1	4.1	38.3	6	270.2	Pass	Pass
SK1.50	365.4	5	1	4.2	56.8	8	341.3	Pass	Pass
SK1.87	347.8	4	1	4.6	55.4	8	324.8	Pass	Pass
SK1.102	300.4	3	2	3.6	33.2	9	284.3	Pass	Pass
SK1.72	315.3	5	1	3.6	56.8	8	297.3	Pass	Pass
7221498	295.4	2	1	5.2	29.1	6	304.0	Fail	Pass
ke-4d	339.5	3	2	4.1	27.2	7	327.4	Pass	Pass

JM-15	330.4	3	1	4.1	32.3	4	316.7	Pass	Pass
SK1.35	331.4	2	1	5.8	29.1	7	331.4	Fail	Pass
ke-4e	375.5	3	2	4.7	27.2	7	354.8	Pass	Pass
SK1.85	321.4	5	1	3.0	64.6	8	284.2	Pass	Pass
JM-13	330.4	4	1	3.3	49.4	5	301.8	Pass	Pass
SK1.53	365.4	5	1	4.3	56.8	8	341.3	Pass	Pass
6555142	311.4	3	1	5.2	38.3	7	312.7	Fail	Pass
SK1.101	286.4	3	2	3.3	33.2	8	267.5	Pass	Pass
6115259	239.3	2	1	3.4	29.1	5	237.2	Pass	Pass
5522477	283.3	3	1	3.7	38.3	7	279.5	Pass	Pass
9108417	297.4	3	1	4.2	38.3	6	295.9	Pass	Pass
9090513	267.3	2	1	4.3	29.1	6	270.6	Pass	Pass
7311494	281.4	2	1	4.9	29.1	6	287.1	Pass	Pass
7737951	299.3	4	1	3.8	47.5	7	288.3	Pass	Pass
LO8	313.4	4	1	4.3	47.5	8	305.1	Pass	Pass
9148206	329.8	5	1	3.5	56.8	8	313.8	Pass	Pass
5335716	271.3	2	1	3.8	29.1	6	258.9	Pass	Pass
7661021	373.9	4	1	4.4	55.4	6	313.2	Pass	Pass
5337355	287.8	2	1	4.4	29.1	6	267.5	Pass	Pass
5334050	332.2	2	1	4.5	29.1	6	271.9	Pass	Pass
7226051	322.2	2	1	5.1	29.1	6	281.1	Fail	Pass
7264596	322.2	2	1	4.9	29.1	6	281.1	Pass	Pass
7668219	401.5	6	1	3.8	71.0	8	370.8	Pass	Pass
5361579	306.5	4	1	2.9	35.9	6	316.1	Pass	Pass
7260078	287.8	2	1	4.3	29.1	6	267.5	Pass	Pass
5557287	322.2	2	1	5.1	29.1	6	281.1	Fail	Pass
6525395	381.4	5	1	3.6	61.7	6	346.6	Pass	Pass
7669739	443.6	6	1	3.4	78.8	6	384.9	Pass	Pass
5334466	287.8	2	1	4.3	29.1	6	267.5	Pass	Pass
7685637	368.9	4	0	4.9	32.7	2	328.5	Pass	Pass
5334325	191.2	3	2	1.1	49.3	4	184.4	Pass	Pass
5329246	271.3	2	1	3.8	29.1	6	258.9	Pass	Pass
6067284	439.3	6	2	2.2	65.9	6	343.7	Pass	Pass

Table 3.4 Physicochemical properties of 56 library compounds. These Include; [1]Molecular weight (MW), [2] H-bond acceptors (HBA), [3]H-bond donors (HBD), [4]Log partition coefficient, a measure of lipophilicity (LogP), [5]Total polar surface area (TPSA),[6]Number of rotatable bond (NROTB), [7]molecular volume. The final two columns indicate whether they meet the RO5 or Veber's rules criteria for predicted bioavailability. The eight compounds explored in this study head the list in bold.

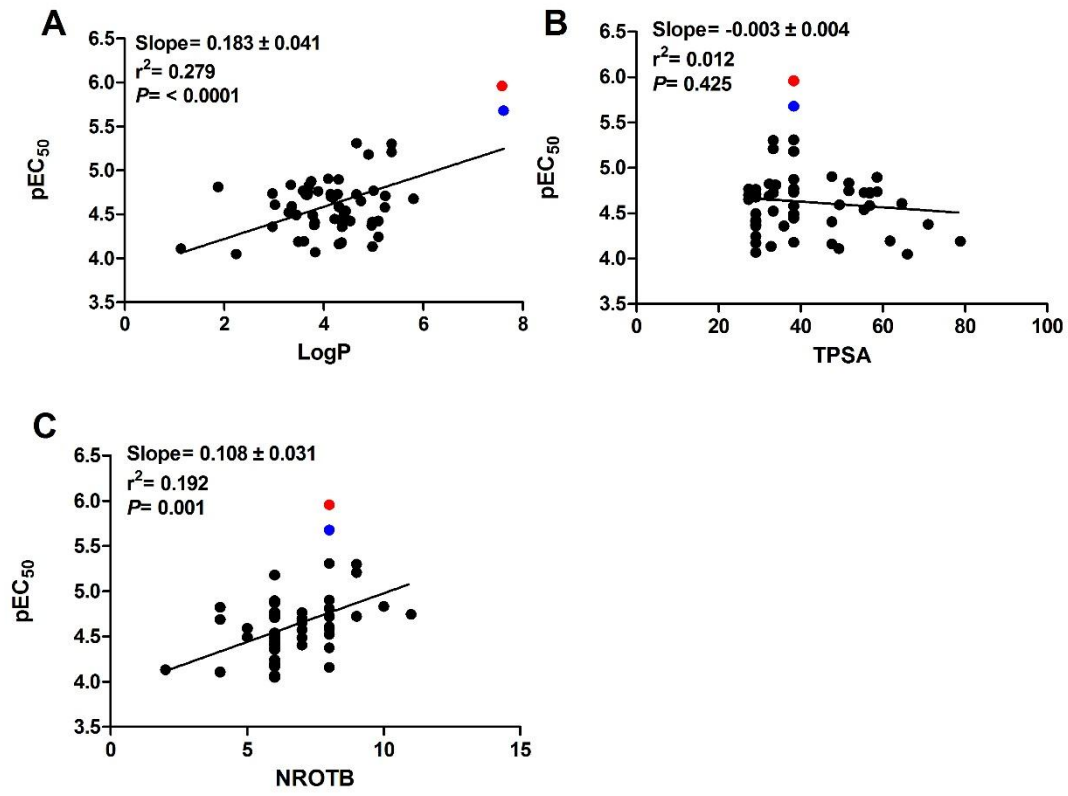

Fig. 3.13 Illustrating the correlation between compounds' antiplasmodial potency and their physicochemical properties. These were represented by pEC_{50} versus Log partition coefficient (LogP, A), total polar surface area (TPSA, B) and number of rotatable bonds (NROTB, C). For ease, SK1.49 (red dot) and SK1.47 (blue dot) are highlighted on each graph.

Given the importance of the total polar surface area (TPSA) and number of rotatable bonds (NROTB), in addition to LogP, in terms of defining the likely bioavailability, the correlation of these parameters with antiplasmodial activity were also explored (Fig. 3.13B and C). Like LogP, no direct correlation was observed (regression lines show negligible slope or are not significant).

3.2.7 *In vitro* assessment of serum albumin-drug binding for SK1.47 and SK1.49

The prediction of SK1.47 and SK1.49 being highly hydrophobic (LogP > 7) would suggest that they would have low distribution in aqueous phase and that within blood they would likely bind and sequester to serum albumin. To explore this potential serum binding effect, the EC_{50} of SK1.47 and SK1.49 in $Dd2^{luc}$ was repeated in a culture medium lacks

human serum (i.e. contained only 0.25% albumax as the 5% human serum would be omitted). We predicted that if a compound has affinity to bind with human serum, it should result in left shift in concentration-response curve (lower EC_{50}) when the majority of the serum albumin was removed. The EC_{50} were determined in both normal (NS; 0.25% albumax and 5% human serum) and low serum (LS; contains 0.25% albumax only) growth media. SK1.47 and SK1.49 were tested along with CQ (LogP=5) as well as two additional compounds SK1.104 and SK1.107from the library with LogP values of 3.3 and 3.6, respectively. Each experiment was controlled against untreated parasites grown in the same medium, with each performed as technical triplicates and three biological repeats (n=9). The Log concentration-normalised response curve was plotted and the EC_{50} estimated (Fig. 3.14).

All compounds had lower EC_{50} values in LS medium, suggesting that more compounds were available to exert their effect in a low serum environment. The ratio of EC_{50} in NS/LS was determined for each compound (Table 3.5). Comparison of the LogP of the library compounds against this ratio supported a prediction that reduced lipophilicity, leading to reduced serum binding, would result in more compounds to affect the parasite. That is, the difference in EC_{50} NS/LS is higher for SK1.47 and SK1.49, with an almost 50% lower $EC_{50.}$ This correlation does not hold as true when CQ, with an intermediate LogP, is included although CQ has a distinct chemical structure to the library compounds.

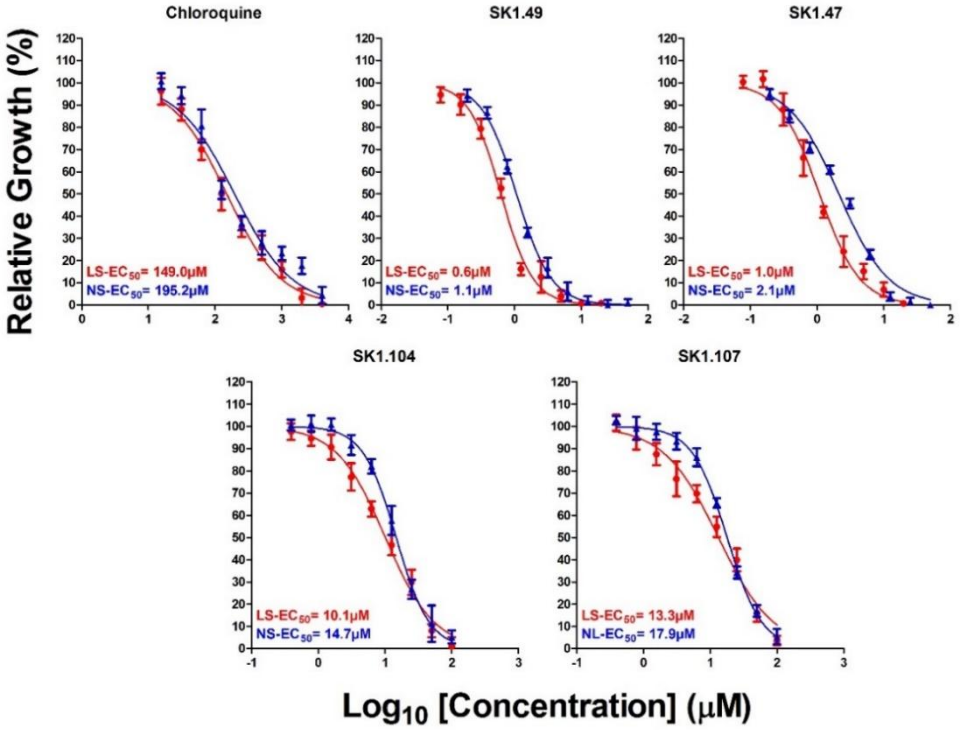

Fig. 3.14 Log_{10} concentration-normalised response curves in either Normal Serum (NS, blue lines) or Low Serum (LS, red lines). The mean and SD (n=9) of growth relative to a matched untreated NS or LS control are represented by dots and error bars, respectively.

Compound ID	EC_{50} (LS)	EC_{50} (NS)	Ratio of EC_{50} (NS/LS)	LogP
CQ	149	195.2	1.31	5.0
SK1.49	0.6	1.1	1.83	7.5
SK1.47	1.0	2.1	2.1	7.6
SK1.104	10.1	14.7	1.45	3.3
SK1.107	13.3	17.9	1.35	3.6

Table 3.5 Reports EC_{50} values of the indicated compounds in Low Serum (LS) or Normal Serum (NS) as well as their ratio and the LogP value of each compound.

3.2.8 *In vitro* stage-dependant effects of SK1.47 and SK1.49 against asexual intraerythrocytic *P. falciparum*

Thus far we have demonstrated that SK1.47 and SK1.49 are the most potent inhibitors of intraerythrocytic growth, exerting a rapid cytocidal effect that appears to be selective for the parasite. To establish at what stage(s) during the intraerythrocytic cycle that these compounds exert this cytocidal effect, a light microscopic visualising was employed. Microscopic observation provides an appropriate tool to understand drug susceptibility on the different developmental stages of the parasite (Rosenblatt *et al*., 2002). The experiment plan contains four treatment courses;

Troph-A; commencing in mid-trophozoites (24-28hr post invasion), the parasites were exposed to a continuous concentration of compound that would elicit a 50% kill in 6 hrs (the LD_{50}) over 48 hrs to complete one cell cycle.

Troph-B; commencing in mid-trophozoites, the parasites were exposed to 6 hrs bolus at a LD_{50} concentration after which the parasites are washed to remove the drug and allowed to complete one cell cycle.

Ring-A; commencing in mid-rings (6-12 hrs post invasion), the parasites were exposed to a continuous concentration of the trophozoite LD_{50} over 48 hrs to complete one cell cycle.

Ring-B; commencing in mid-rings, the parasites are exposed to 6 hrs bolus at the trophozoite LD_{50} concentration after which the parasites are washed to remove the drug and allowed to complete one cell cycle.

These treatment courses are summarised in Fig. 3.15. This approach allows the stage specific effect of SK1.47 and SK1.49 to be determined from the A-treatments, but also whether a developmental stage is also unaffected from the B-treatments. The latter is a characteristic property of CQ. CQ primarily exerts its effect on trophozoite stage parasites

but not ring stages (Gligorijevic *et al.,* 2008; Yayon *et al.,* 1983). Exposure of ring stage parasites to a CQ drug bolus that is removed, allows the parasites to continue developing normally into the trophozoite stages (Paguio *et al.* 2011). As such, CQ was included in this experimental plan as well as untreated parasites. Each treatment was carried out in triplicate, starting with appropriate stage synchronised cultures of a 1-2% parasitaemia. Thin blood smears were collected at the start, and then after 16 hrs, 24 hrs and 48 hrs and Giemsa stained. At least 100 infected erythrocytes were staged at each time point. Fig. 3.16 shows examples of stained parasites defined as ring, trophozoite or schizont stages as well as those determined to be abnormal (dead or dying) following drug/compound treatment.

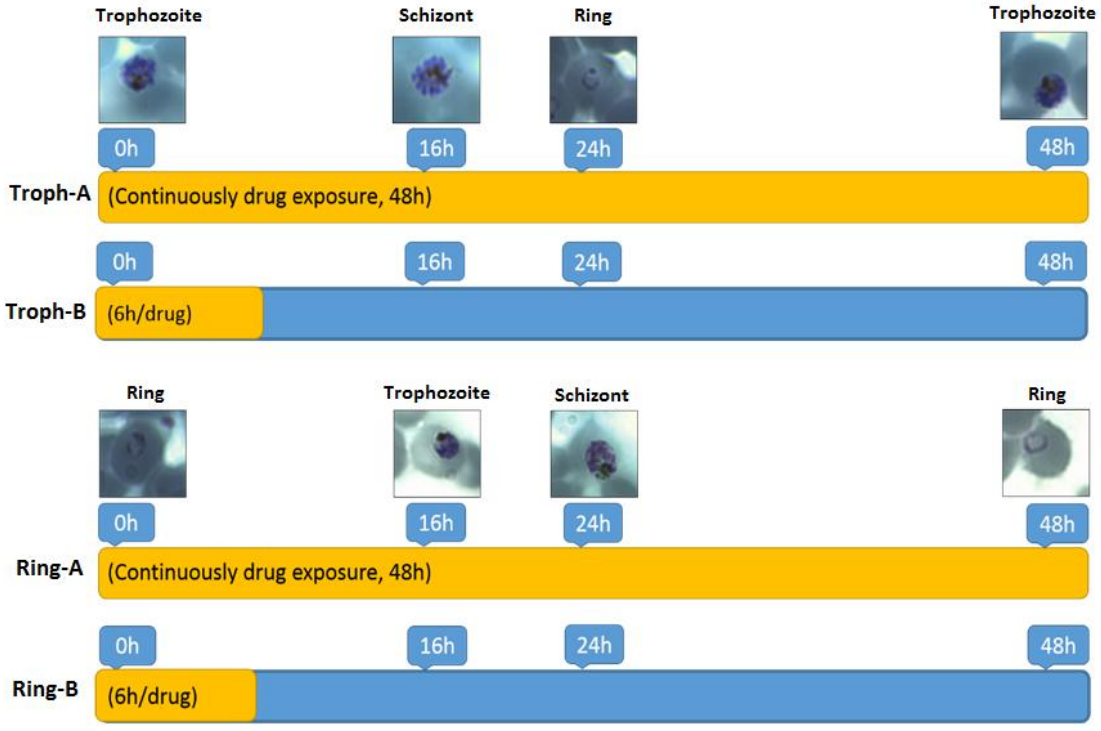

Fig. 3.15 Experimental plan to determine the stage-dependent effects of SK1.47 and SK1.49. Each experiment is represented as a bar, with yellow indicating when the parasites were exposed to SK1.47 and SK1.49 or CQ and blue where these had been removed by washing after 6 hrs of exposure. The timepoints for microscopic examination are indicated above each line, as are examples of parasites that are untreated and show expected progression of development.

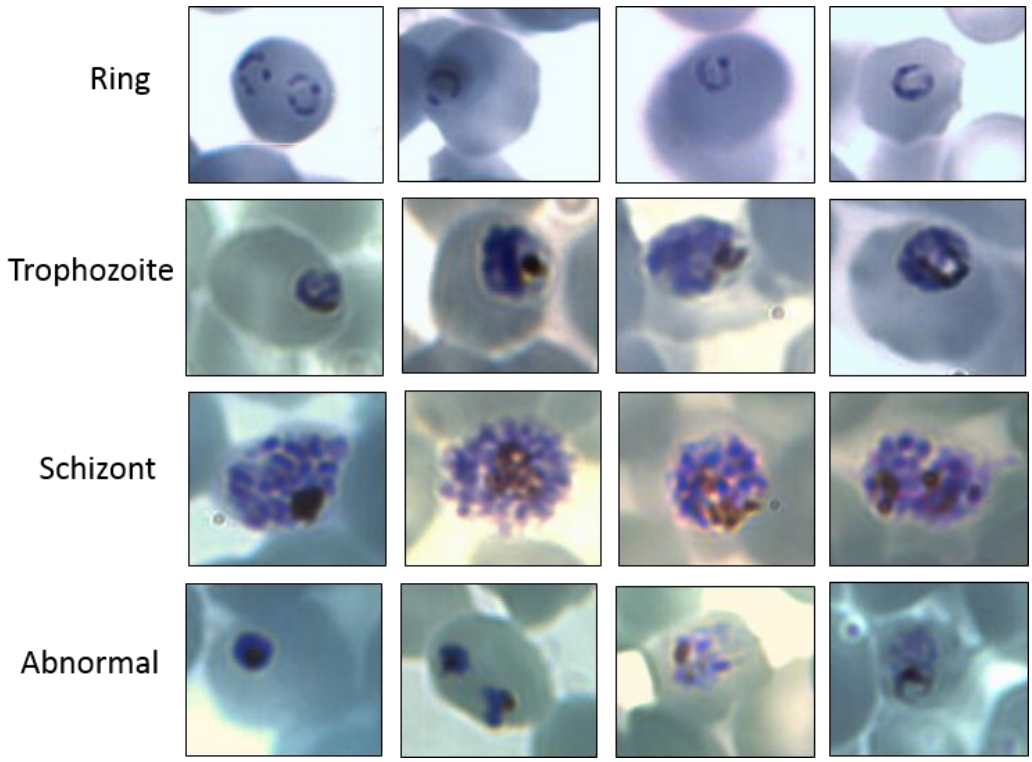

Fig. 3.16 Giemsa-stained images of ring, trophozoite and schizont intraerythrocytic parasites as well as those defined as abnormal (shrunken, uneven shape etc.).

Two biological repeats of all treatments were carried out, with the data presented separately in Fig. 3.17 and Fig. 3.18 As these experiments were carried out on different days, there were likely differences in the relative proportion of age of ring and trophozoite synchronised cultures.

In both biological repeats the expected development of untreated parasites was as expected 16 hrs, 24 hrs and 48 hrs following the start of the experiment, with the same stage at the start of the experiment the predominant stage after 48 hrs (Fig. 3.17 and 3.18). The CQ gave results that were expected, specifically;

(i) In Troph-A, there was no apparent progression to schizonts, with the proportion of abnormal parasites increasing, eventually to 100%, over the course of the experiment.

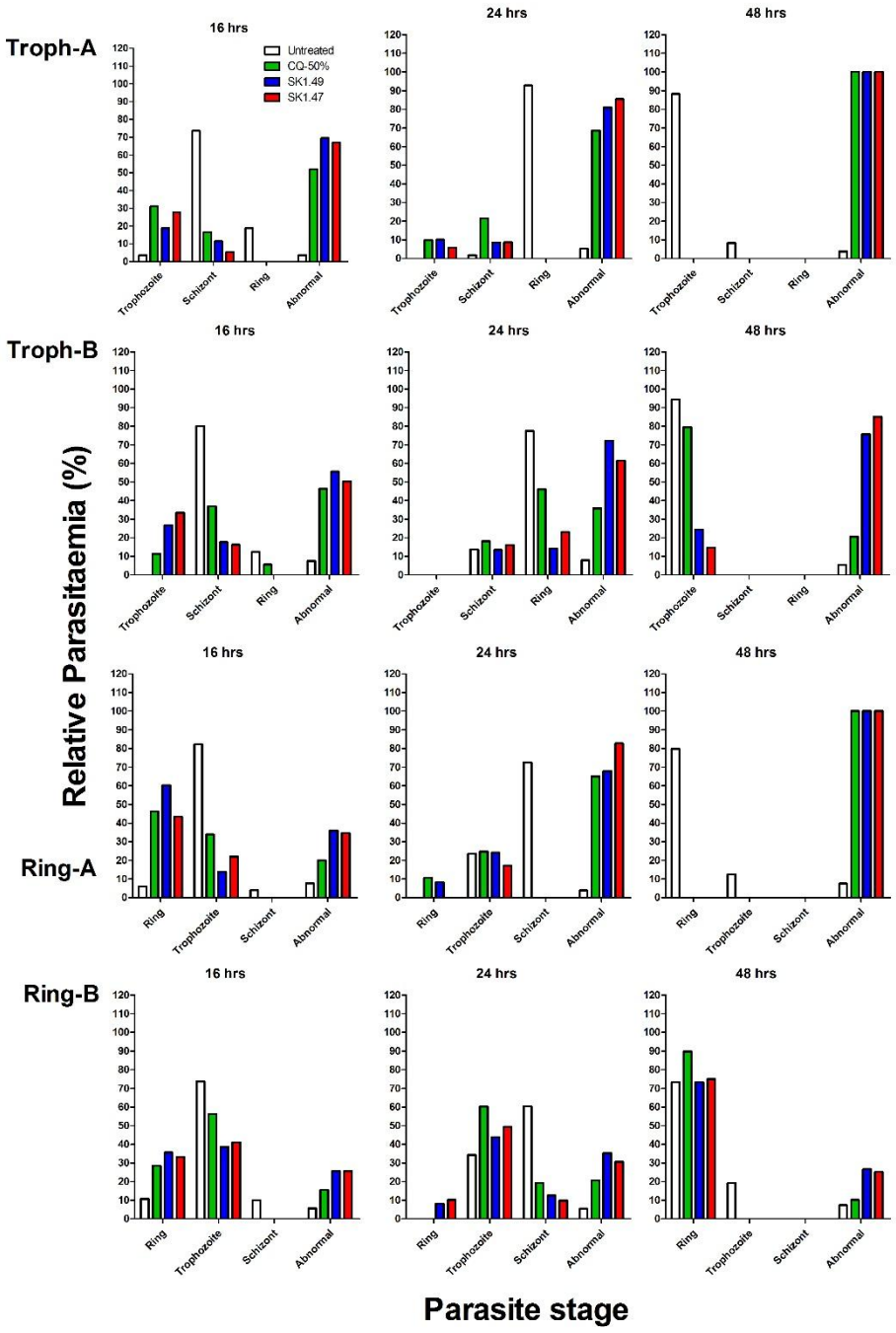

Fig. 3.17 Stage-dependent effects of SK1.49, SK1.47 and CQ on synchronised intraerythrocytic parasites (see key). See Fig. 3.15 for a description of treatments used for Troph-A, Troph-B, Ring-A and Ring-B. The relative proportion of intraerythrocytic stage determine from Giemsa-stained slides taken at the indicated timepoint is shown. This panel represents data from the first biological replicate.

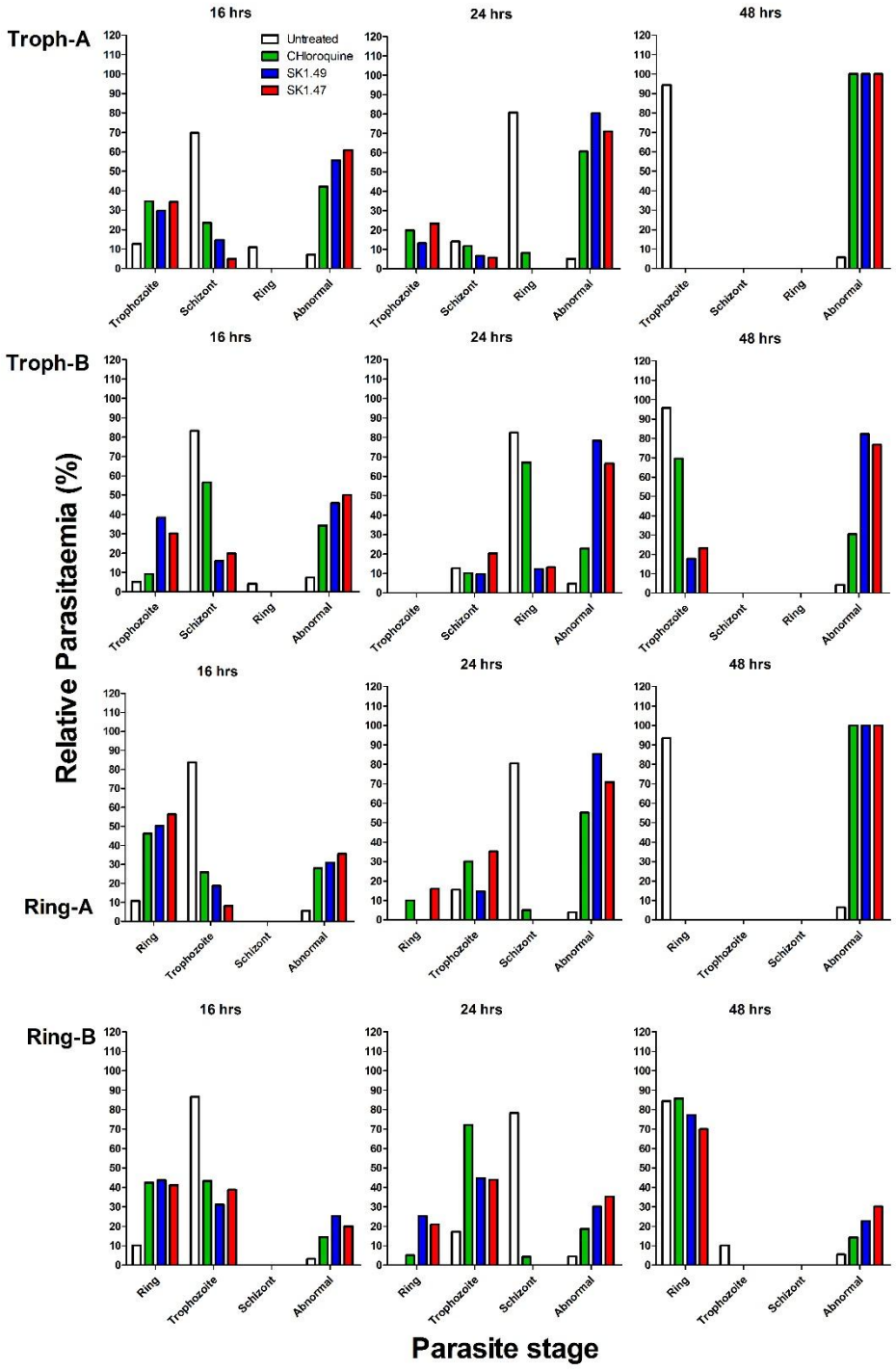

Fig. 3.18 Stage-dependent effects of SK1.47, SK1.49 and CQ on synchronised intraerythrocytic parasites. See also legend for Fig. 3.17. This panel represents data from the second biological replicate of this experiment.

(ii) Continuous exposure of rings to CQ in Ring-A results in a delayed progression into trophozoites. After 24 hrs, no schizonts are apparent and the proportion of abnormal cells increases, with 100% abnormal after 48 hrs.

(iii) Trophozoites that are exposed to a pulse of CQ (Troph-B) appear delayed after 16 hrs, with abnormal cells apparent. There is, however, progression into newly invaded rings after 24 hrs and trophozoites are the predominant stage at 48 hrs. The reduction in proportion of abnormal cells would result from the increase in healthy parasite stages after reinvasion.

(iv) Rings that are exposed to a pulse of CQ (Ring-B) appear delayed after 16 hrs, but with many less abnormal cells apparent when compared to the trophozoite pulse. After 48 hrs, ring stage parasites are the predominant stage.

Together, these data indicate that CQ primarily kills trophozoite stage parasites, with some effect on delaying both rings and trophozoites when provided as a pulse. However, removal of CQ allows the ring stages to progress, with the proportion of unaffected trophozoites also being capable of reinvasion.

Exposure to SK1.47 and SK1.49 shows clear evidence of trophozoite kill following both continuous and pulse exposure. The effect of SK1.47 and SK1.49 contrasts with the effect of CQ following a pulse treatment (Troph-B), however, where we see in both biological replicates an absence of reinvasion and > 80% of abnormal cells, compared to < 30% after CQ treatment. This difference could be accounted by SK1.47 and SK1.49 having a more profound killing effect, although the BRRoK data would suggest they have similar RoK within the 6 hrs pulse. Alternatively, it could be that SK1.47 and SK1.49 are less efficiently removed by the washing protocol used in the pulse experiment. The ring stage

treatments suggest this is also unlikely. SK1.47 and SK1.49, like CQ, delay ring stage development and ultimately kills the trophozoites when continuously exposed (Ring-A). However, that SK1.47 and SK1.49 can be washed out appears to be evidenced in both Ring-B experiments, where a delay in development was evident, but ultimately ring stage parasites predominate after 48 hrs, albeit with higher proportions of abnormal cells.

This phenomenon was further investigated using a bioluminescence based assay. SK1.47, SK1.49 and CQ were exposed to $Dd2^{luc}$ for 6 hrs at an LD_{50} dose. After which, the culture was split, one half maintaining exposure to the drug/compound and the other washed before being allowed to continue growth for a further 42 hrs to allow one complete cycle of growth. Bioluminescence signals, relative to a matched untreated control, were measured immediately after the drug bolus and at both 48 hrs endpoints. The experiment was carried out as a technical triplicate with two biological repeats (n=6) with the mean ± SD plotted (Fig. 3.19).

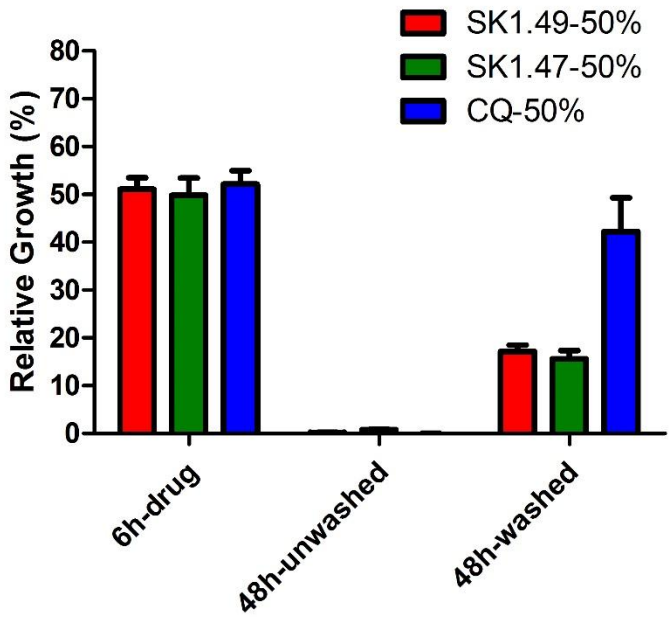

Fig. 3.19 Bioluminescence assay data of trophozoite parasites treated with 50% kill concentration of CQ, SK1.49 and SK1.47 for 6 hrs. Following the pulse, bioluminescence was determined at 48 hrs following continuous exposure (unwashed) or after wash and regrowth (washed). The data represents mean activity ± SD normalised to an untreated control (n=6).

Comparison of the bioluminescence signals after the drug bolus reveals the expected 50% loss in bioluminescence signal following exposure to a LD_{50} concentration. Similarly, after a continuous exposure of drug/compound for 48 hrs, no bioluminescent signal is evident as all the parasites are dead. The pulse/wash with CQ provides a mean signal slightly less than that immediately after the pulse, but does suggest that parasites not killed within the first 6 hrs are viable 42 hrs later as the CQ has been effectively removed. The same is not apparent for SK1.47 and SK1.49 which both show < 20% of parasites survived the pulse/wash. The implications of this are discussed in the discussion.

3.2.9 Proof-of-concept: SK1.47 and SK1.49 exposure affects the distribution of PfAtg8-labelled vesicles in starved intraerythrocytic parasites

Declaration: note that the spinning disk confocal immunofluorescence microscopy assay in this section was kindly carried out by Paul Roepe's group of Georgetown University, USA. I contributed to the planning of the experiment and the analysis of data, but did not perform the spinning disk confocal microscopy or prepare the figures.

A characteristic morphological feature of autophagy in eukaryotes is the redistribution of Atg8 upon starvation (Shpilka *et al.,* 2011). Upon starvation, Atg8 is reorganised from a separated localization within the cytoplasm to form widely distributed puncta throughout the cell, these puncta representing the Atg8-labelled autophagosomes containing cargo for recycling under nutrient stress. Gaviria *et al*. (2013) showed a similar reorganisation of PfAtg8 in infected erythrocytes grown in starvation medium (SM) (depleted of amino acids). Here, immunofluorescence assay (IFA) microscopy of parasites grown in complete medium (CM) show a single point of PfAtg8 labelling within the parasite cytoplasm with a

small number of discrete puncta located elsewhere in the infected erythrocyte. Following starvation, large numbers of dispersed separate puncta of Atg8-labelled are located throughout the infected erythrocyte (see Fig. 3.20 for examples). Gaviria *et al*. (2013) were also able to show that (i) infected erythrocytes grown in complete medium exposed to increasing concentrations of CQ accumulated more PfAtg8-labelled puncta, corresponding to a proposed role of lethal concentrations of CQ in inducing an autophagosomal-like response and thus a potential mechanism of cell death, and (ii) that the number of PfAtg8-labelled puncta in starved cells decreases when exposed to the PI3K inhibitor 3-MA (although the concentration of 3-MA is not described). Thus, IFA of PfAtg8 (using an antibody originally raised against the similar Atg8 from *T. gondii*) imaged using a spinning disk confocal fluorescence microscopy, allows measurements of the distance of PfAtg8-labelled puncta from the DV (those > 3.5 μm from DV counted) to determine the effect of drugs on PfAtg8 redistribution.

SK1.47 and SK1.49 were provided to the research team of Professor Roepe at Georgetown University where the Gaviria study was originally done (Gaviria *et al.* 2013). Using their IFA approach on HB3 (CQS strain), they imaged the effect of these library compounds on PfAtg8 redistribution in parasites grown in complete medium (CM) and starvation medium (SM). Images were provided to me for analysis. Initial analysis of PfAg8 distribution in CM and SM showed the expected results (Fig. 3.20) with parasites grown in SM revealing large numbers of discrete puncta. Similarly, parasites grown in CM and exposed to increasing concentrations of CQ show a significant and concentration-dependant effect (Fig. 3.21) as originally reported by Gaviria *et al.* (2013).

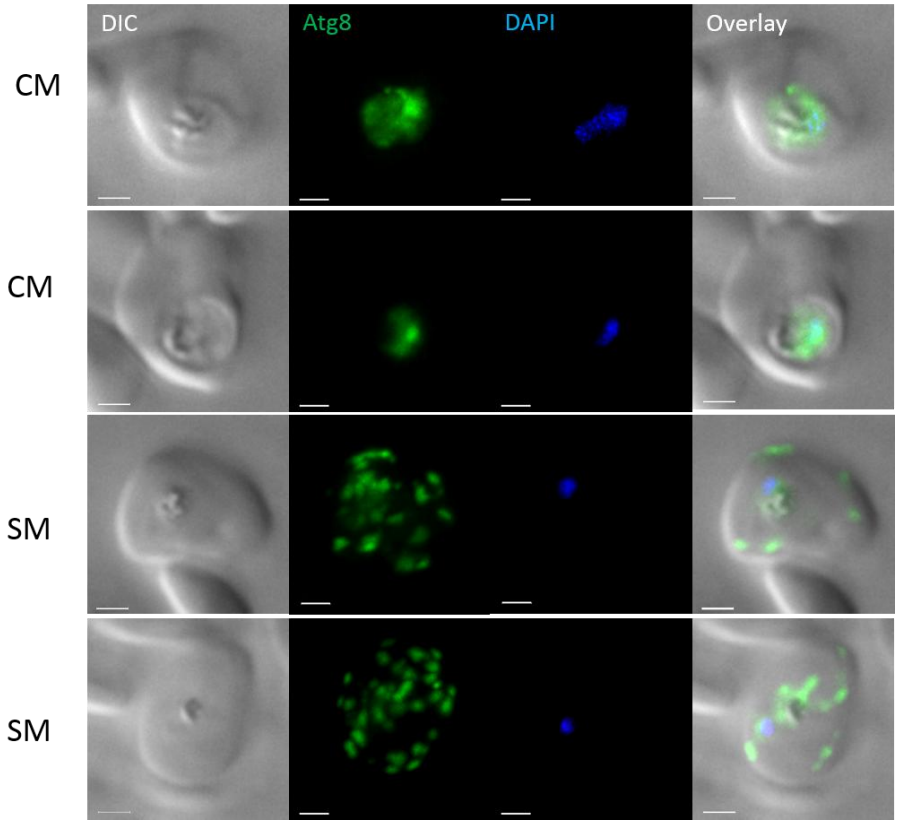

Fig. 3.20 PfAtg8 redistribution and localisation in HB3 clone of *P. falciparum* cultured in complete (CM) and starvation medium (SM) for 6 hrs. The first column from left is Differential Interference Contrast (DIC, brightfield imaging), the second column from left (green) is florescent-tagged α- TgAtg8 antibody, the third column (blue) is DAPI-stained nucleus and the last column is overlay of DIC, Atg8 and DAPI.

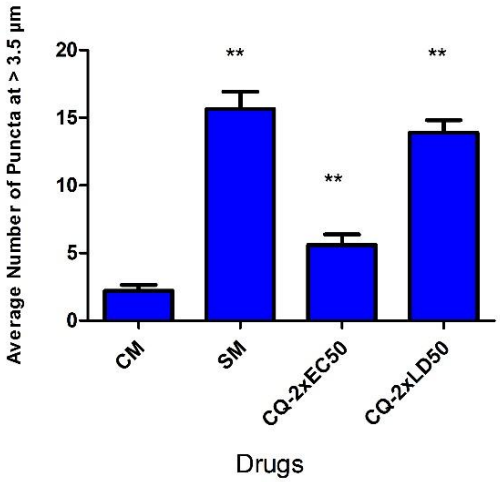

Fig. 3.21 Distribution of PfAtg8 puncta for HB3 strain of *P. falciparum* parasite cultured in complete medium (CM), starvation medium (SM) or CM with increasing concentrations of CQ (counts are from 20 cells/sample). CQ exposure at $2xEC_{50}$ lead to a significant increase in distributed puncta ($p<0.05$, ANOVA) compared to untreated CM, increasing the concentration to $2xLD_{50}$, again leads to a significant increase in puncta numbers ($P < 0.05$, ANOVA) compared to

untreated and 2xEC_{50} CQ. Note, these data are consistent with observations by Gaviria *et al.* (2013).

Exposure of HB3 infected erythrocytes, grown in CM, to 10xEC_{50} SK1.47 and SK1.49 (roughly equivalent to a 2xLD_{50}) did not result in an increase in PfAtg8-labelled puncta numbers or distribution (Fig. 3.22 and Fig. 3.23), an observation distinct to that of CQ. Exposure of infected erythrocytes to 6 hrs of SM was next done in the presence of increasing concentrations (2xEC_{50} and 10xEC_{50}) of SK1.47 and 1.49. Here we were able to show that both library compounds significantly reduce ($P < 0.05$, ANOVA) the numbers of PfAtg8-labelled puncta compared to SM parasites alone in a concentration-dependant manner (Fig. 3.23, Fig. 3.24 and Fig. 3.25).

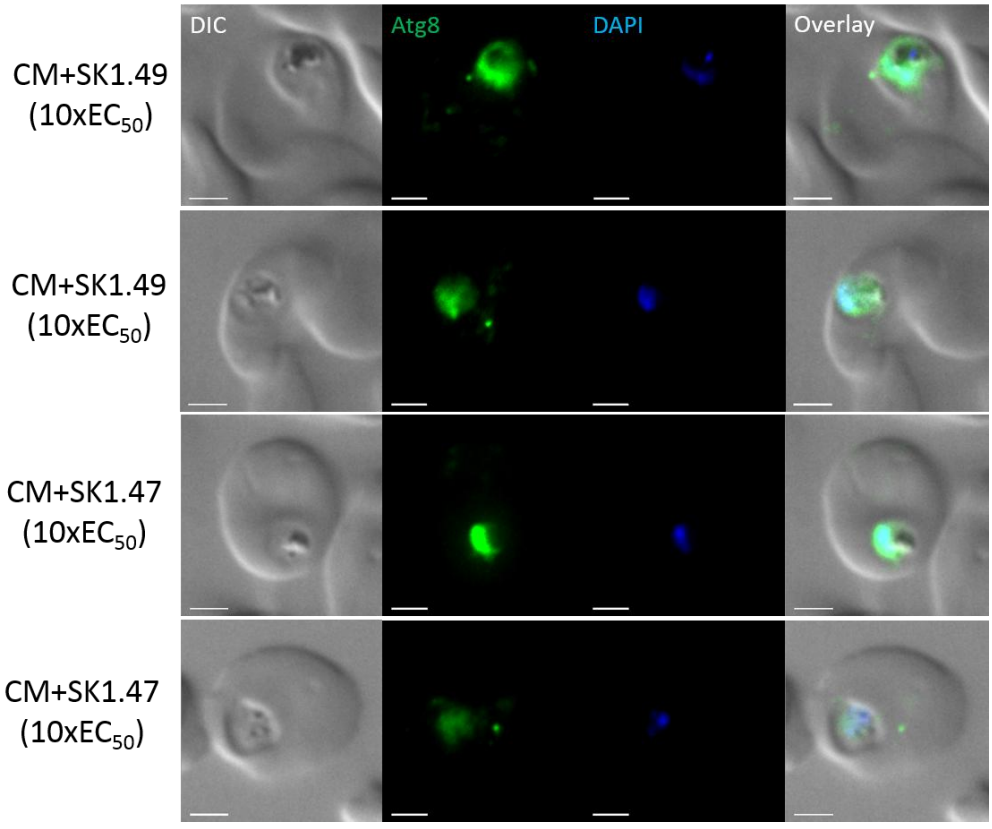

Fig. 3.22 PfAtg8 redistribution and localisation in HB3 clone of *P. falciparum* cultured in complete medium (CM) for 6 hrs in the presence of 10xEC_{50} of SK1.47 and SK1.49. Panels arranged as per Fig. 3.20.

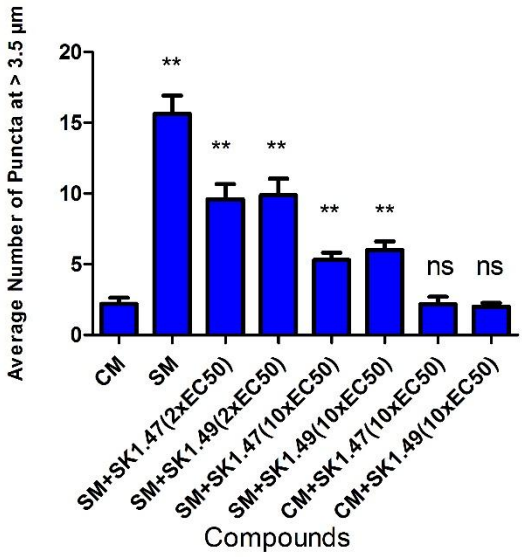

Fig. 3.23 Distribution of PfAtg8 puncta for HB3 strain of *P. falciparum* parasite cultured in complete medium (CM) or starvation medium (SM) with increasing concentrations of SK1.47 and SK1.49 (counts are from 20 cells/sample). Library compound exposure at both $2xEC_{50}$ and $10XEC_{50}$ in SM leads to a significant decrease in distributed puncta ($P < 0.05$, ANOVA) in comparison to SM only, but no significant effect on parasites grown in compound-containing CM in comparison to CM only ($P < 0.05$, ANOVA).

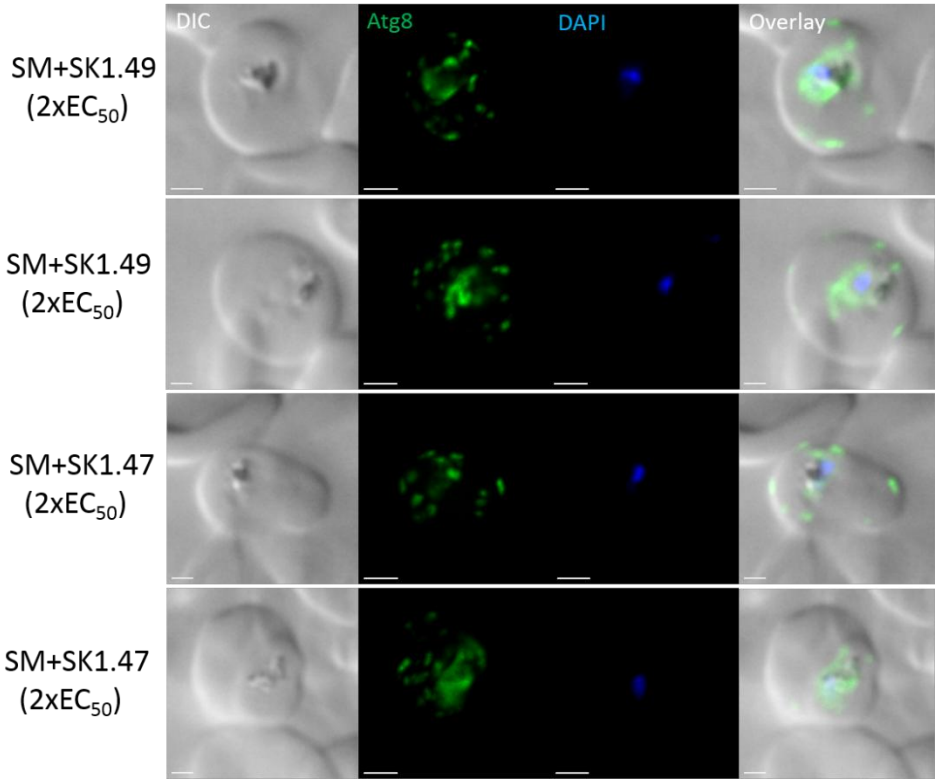

Fig. 3.24 *Pf*Atg8 redistribution and localisation in HB3 clone of *P. falciparum* cultured in starvation medium (SM) for 6 hrs in the presence of $2xEC_{50}$ of SK1.47 and SK1.49. Panels arranged as per Fig. 3.20.

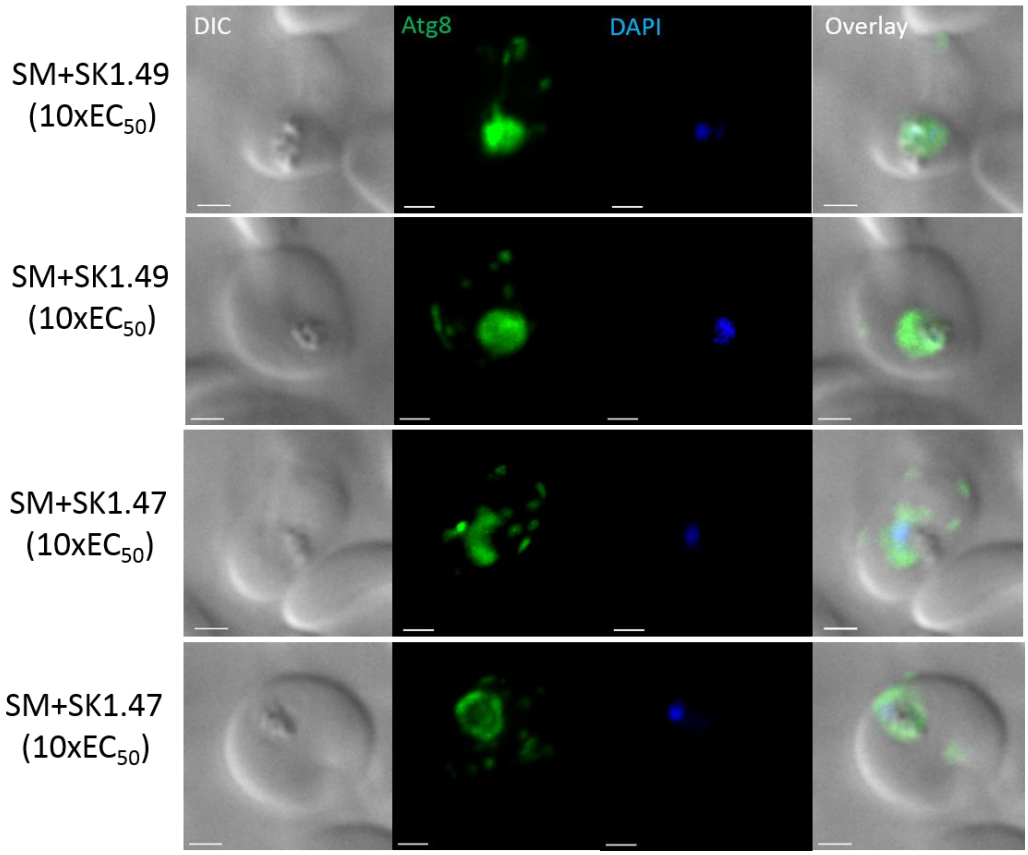

Fig. 3.25 PfAtg8 redistribution and localisation in HB3 clone of *P. falciparum* cultured in starvation medium (SM) for 6 hrs in the presence of 10xEC$_{50}$ of SK1.47 and SK1.49. Panels arranged as per Fig. 3.20.

The same methodology was also used to explore the effect of the commercial autophagy inhibitor DBeQ, a compound thought to modulate autophagy through the inhibition of the p97 ATPase associated with the proteasome (Fig. 3.26). Although insufficient numbers of images were available for a quantitative analysis, a qualitative analysis of the IFA reveal that DBeQ appears to similarly reduce the numbers of PfAtg8-labelled puncta in starved parasites in a concentration-dependant manner

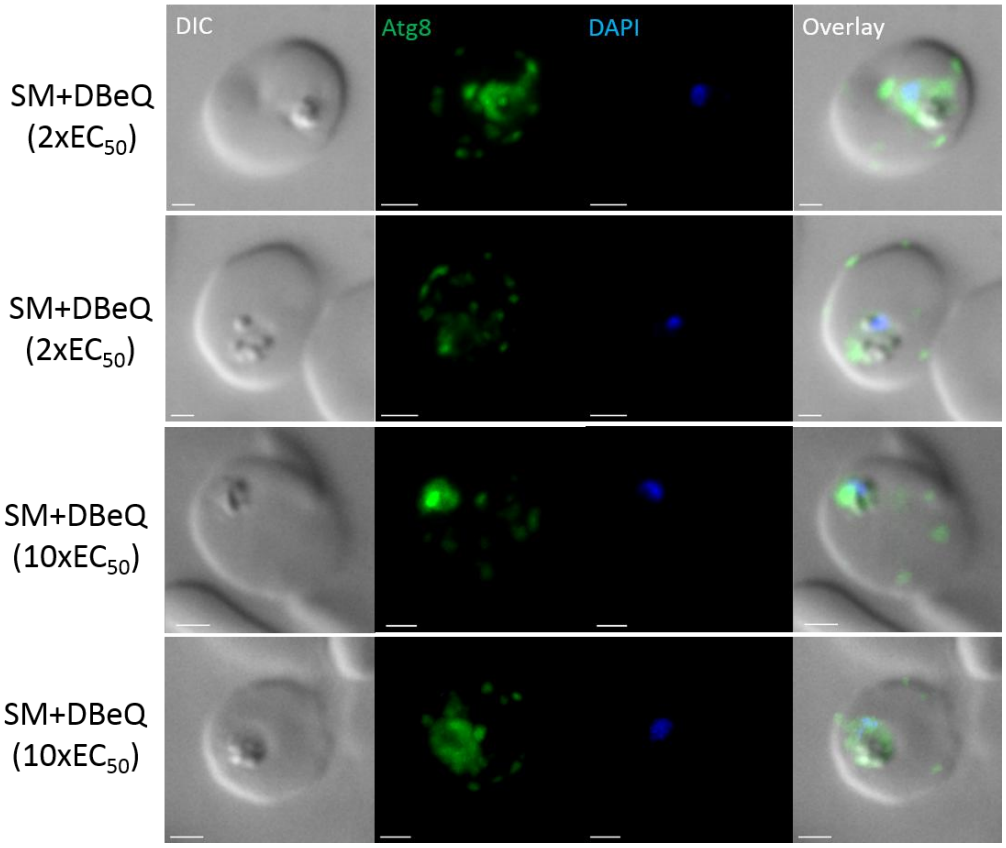

Fig. 3.26 PfAtg8 redistribution and localisation in HB3 clone of *P. falciparum* cultured in starvation medium (SM) for 6 hrs in the presence of increasing concentrations ($2xEC_{50}$ and $10xEC_{50}$) of DBeQ. Panels arranged as per Fig. 3.20.

3.3 Discussion

Here we describe the screening and initial characterisation of the antiplasmodial activity of a library of 131 compounds developed as potential modulators of autophagy in human cell lines (Reynisson and Richardson, *pers. comm*.). One specific proposed mode of action is that they would interfere with the interaction between Atg8 and Atg3, resulting in a reduction of the levels of lipidated Atg8 and affect the function and/or distribution of Atg8. Initial screening of the 131 compounds focussed on the identification of compounds that have an effect against intraerythrocytic stages, in two genetically different CQS and CQR parasite lines and have limited, or no, evidence of toxicity in HepG2. This screen provided two initial hits, SK1.47 and SK1.49, which share a similar structure (Fig. 3.27),

low µM potency against intraerythrocytic parasites irrespective of their CQ resistance phenotype (Fig. 3.5), good selectivity against HepG2 (Fig. 3.12) as well as a rapid cytocidal action (Fig. 3.11) against trophozoite stage of parasites (Fig. 3.17). Both compounds also appear to modulate the distribution of PfAtg8 when the parasites are exposed to starvation conditions (Fig. 3.23).

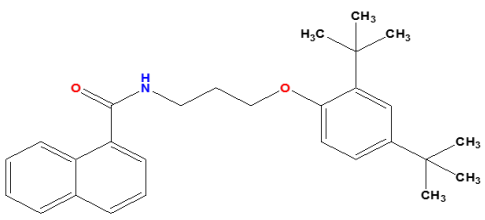

SK1.49

Naphthalene-1-carboxylic acid [3-(2,4-di-tert-butyl-phenoxy)-propyl]-amide

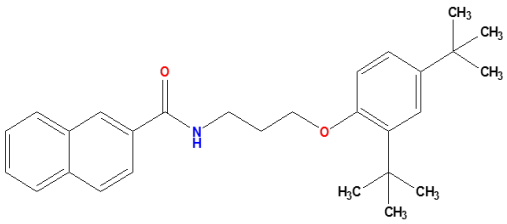

SK1.47

Naphthalene-2-carboxylic acid [3-(2,4-di-tert-butyl-phenoxy)-propyl]-amide

Fig. 3.27 Structures of SK1.49 and SK1.47.

SK1.47 and SK1.49 share structural features with other library compounds identified a potential priorities based on their low EC_{50} against intraerythrocytic stage of parasite (Appendix 1). Specifically, the compounds share two hydrophobic ring moieties, linked with an alkyl chain (preferably 6 or more heavy atoms in length) that contains either an amide or thiourea group. Based on modelling of compounds predicted to block PfAtg8-PfAtg3 interactions (Hain *et al.,* 2014, 2016), this structure would make some sense. The hydrophobic ends would be available to dock within the W and L hydrophobic pockets across the PfAtg3 interaction region of PfAtg8, with the alkyl linker providing the length and flexibility for these ends to dock as well as the amine or thiourea moiety available to form hydrogen bonds. This molecular modelling is explored in the next chapter.

We have been cautious in how these library compounds are described – avoiding the term “autophagy inhibitor”. This is because classical autophagy, or macroautophagy, may

not be a normal function in the protozoan *P. falciparum*. Whilst features like autophagy have been described in *P. falciparum* (Gaviria *et al*. 2013), and are perhaps illustrated here with the increased number and distribution of Atg8-labelled vesicles on starvation (Fig. 3.23)- these Atg8-labelled puncta may not be autophagosomes (containing cytoplasmic cargo for recycling as part of a stress response) as classically described. It is clear that parts of the canonical autophagy components can still be found in the parasite genome, it may be, however, that the remaining processes have been retained for an alternative function. These have been suggested to include apicoplast function and biogenesis, recycling of organelles no longer required (reviewed in Besteiro *et al.,* 2011) or the trafficking of lipid bound cargo through the parasite (Walczak *et al.,* 2018). Based on these potential functions in the normal growth and development of the parasite, compounds SK1.47 and SK1.49 may kill the parasites by interfering with the regulation of PfAtg8-PE levels required for these processes rather than inducing autophagic cell death.

The IFA data provided from our collaboration with Professor Roepe provided proof-of-concept for SK1.47 and SK1.49 interfering with PfAtg8 redistribution. These data showed that, unlike CQ, SK1.47 and SK1.49 treatment did not result in an accumulation of PfAtg8-labelled puncta in parasites grown in complete medium. Here, CQ is thought to either interfere directly with the trafficking of PfAtg8-labelled vesicles to the DV or by preventing their fusion as CQ accumulation within the DV leading to increases the pH and blocks this process (Gaviria *et al.,* 2013). This is perhaps expected as SK1.47 and SK1.49 are predicted to prevent the lipidation of PfAtg8 by PfAtg3 – therefore blocking the early stage of the cascade before formation of the PfAtg8-labelled puncta. That there was no effect compared to untreated cells in complete medium may be because the fluorescent imaging assay did not readily allow any potential changes in levels of PfAtg8 to be

detected. This instead would require a western blot – although these are challenging with PfAtg8 as you are comparing lipidated versus unlipidated forms, and such assays presented in published papers (Hain *et al.,* 2014, 2016) are of low resolution. Instead, it was clear that when PfAtg8-labelled puncta are induced by starvation, the formation of these is reduced by SK1.47, SK1.49 and DBeQ. Although all of the components of autophagy cascade in *P. falciparum* have not been discovered yet, features that related to autophagy are proposed, i.e. the puncta, on starvation do exist. Whilst not explored in this study, it may be that the parasite has conserved some capacities to undergo some forms of autophagy when amino acids are limiting. Such hypothesis has been suggested in non-unikont parasites under starvation in which autophagy pathway can be induced in Atg1-independent manner (Földvári-Nagy *et al.,* 2014). As SK1.47 and SK1.49 would block PfAtg8 lipidation which required in formation of these puncta, their effect in reducing the numbers of them is seen here (see Fig. 3.28 for model that integrates the IFA observations). Interestingly, the Gaviria *et al*. (2013) study also reports that 3-MA inhibits PI3K activity that required to initiate autophagosome nucleation, also reduces the number of PfAtg8-labelled puncta in starved parasites. The function of DBeQ in the same effect is less clear. DBeQ is an inhibitor of the p97 ATPase associated with the proteasome degradation pathway (Chou *et al.,* 2011) and one of its effects include reduction the levels of lipidated Atg8. A similar or related effect in *P. falciparum* may also reduce the levels of lipidated PfAtg8 and thus block the synthesis of the PfAtg8-labelled puncta.

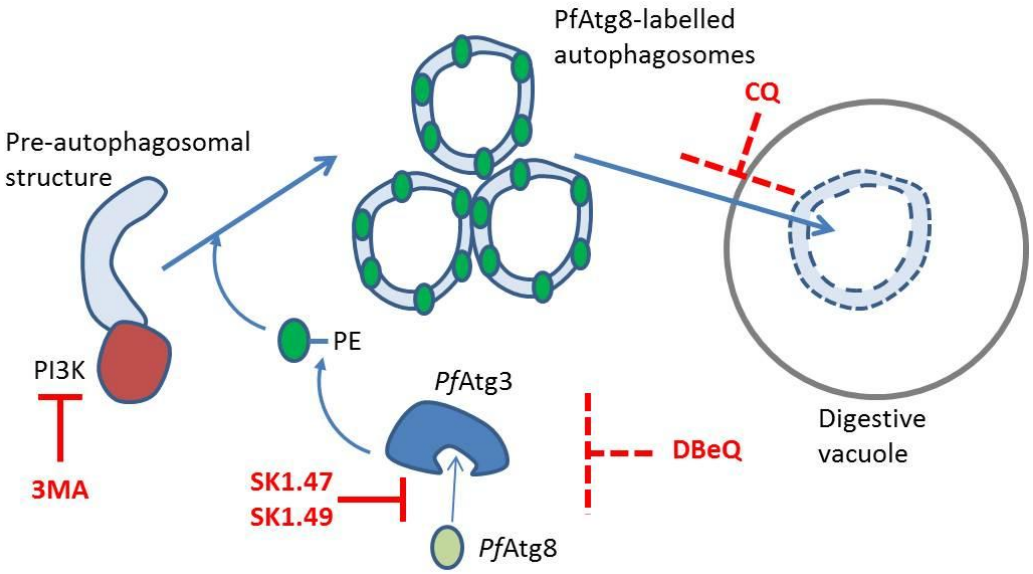

Fig. 3.28 Model of action of SK1.47, SK1.49, 3-MA, DBeQ and CQ in modulating the distribution of PfAtg8-labelled puncta in *P. falciparum* under normal and starvation stress conditions. Under conditions of nutrient stress, structures that may be PfAtg8-labelled autophagosomes would be induced and trafficked to the digestive vacuole for lysis of their contents. Under normal growth conditions, PfAtg8-labelled structures may function in the normal development to turn over organelles or traffic materials such as haemoglobin to the digestive vacuole. Under these normal conditions, the site of action of CQ in blocking transport or fusion of PfAtg8-labelled structures to the digestive vacuole would result in their accumulation – and thus result in the observed accumulation of dispersed PfAtg8-labelled puncta. SK1.47 and SK1.49 are predicted to act before the formation of these structures, and would therefore not be seen. Under conditions of nutrient stress where the number and distribution of PfAtg8-labelled puncta increase, the action of 3-MA (Gaviria *et al.,* 2013) on the phosphatidylinositol 3-kinase (PI3K), SK1.47 and SK1.49 on PfAtg8-PfAtg3 and DBeQ (modulating PfAtg8 levels through the inhibition of the P97 ATPase) in blocking the formation of these structures would result in the observed concentration-dependant reduction of their number and distribution.

Definitive proof for the action of SK1.47 and SK1.49 in inhibiting the interaction between PfAtg8 and PfAtg3 are not provided by the data shown here. Attempts to gain support were done by providing Dr Jürgen Bosch (lead author of the Hain *et al*. studies) with these compounds for SPR. Unfortunately issues in his laboratory prevented these studies to be completed. He did respond to say that the initial studies suggested that the interaction of the PfAtg3 AIM domain with PfAtg8 was reduced in the presence of both SK1.47 and SK1.49. However, he also noted that the compounds also inhibited PfAtg8 dimerization in a control well. This could be the result of these compounds binding to PfAtg8 and altering

their conformation, which may in turn affects PfAtg3 binding. This may be relevant *in vivo* of the action of PfAtg8-PfAtg3 is act as a multimeric complex, noting that the crystal structure of PfAtg8 and AIM of PfAtg3 was a trimer (Hain *et al.,* 2012). Dr Jürgen Bosch personal communications with us indicated this looked promising, but the data was not sufficient to demonstrate SK1.47 or SK1.49 binding to PfAtg8. Attempts to repeat these experiments during the course of this study did not succeed.

An alternative approach that could be adopted here is a genetics approach following drug-selection pressure to generate a resistance phenotype (Flannery *et al.,* 2013b, Cowell *et al.,* 2018). Here, whole genome sequencing of sensitive and resistant phenotype parasites offers the opportunity to identify potential targets based on association with mutations in the resistant parasite genome. Validation of the causative nature of these mutations in generating the resistant phenotype would require the specific introduction of this mutation into the sensitive parasite genotype, an editing technology now supported by the introduction of CRISPR-Cas9 into *P. falciparum* (Crawford *et al.,* 2017*;* LaMonte *et al*., 2016).

The rate of kill studies used here took advantage of our laboratory specific work in understanding how quickly drugs kill parasites (Ullah *et al*., 2017). That the compounds in the library were synthesised to explore their action in inhibiting protein-protein interactions in autophagy, this was an opportunity to explore whether structurally related compounds, predicted to share the same or a similar mode of action, would provide a similar rate of kill. Comparison of the reduction in bioluminescence after 6 hrs against the benchmark antimalarials shows that SK1.47 and SK1.49 have a relative initial rate of kill similar to that of CQ (Fig. 3.29). This is promising for a component of a future antimalarial combination therapy that would have to quickly reduce the parasite burden, defined in

Target Candidate Profile 1 (Burrows *et al.,* 2013). Here, SK1.47 and SK1.49 meet the minimum essential criteria of a rate of kill at least as good as CQ. The majority of the compounds tested also share the same kill profile to SK1.47 and SK1.49. The exceptions are, however, quite interesting. SK1.108 and SK1.109, both containing the toxic thiourea group, both appear to have a more rapid initial rate of kill, closer to artemisinin (the ideal TCP criteria reference) than CQ (Fig. 3.29). Another pair of related structures that share a similar rate of kill is 6596157 and 6555142, differing only by the 2-O-methyl substitution to a phenyl ring.

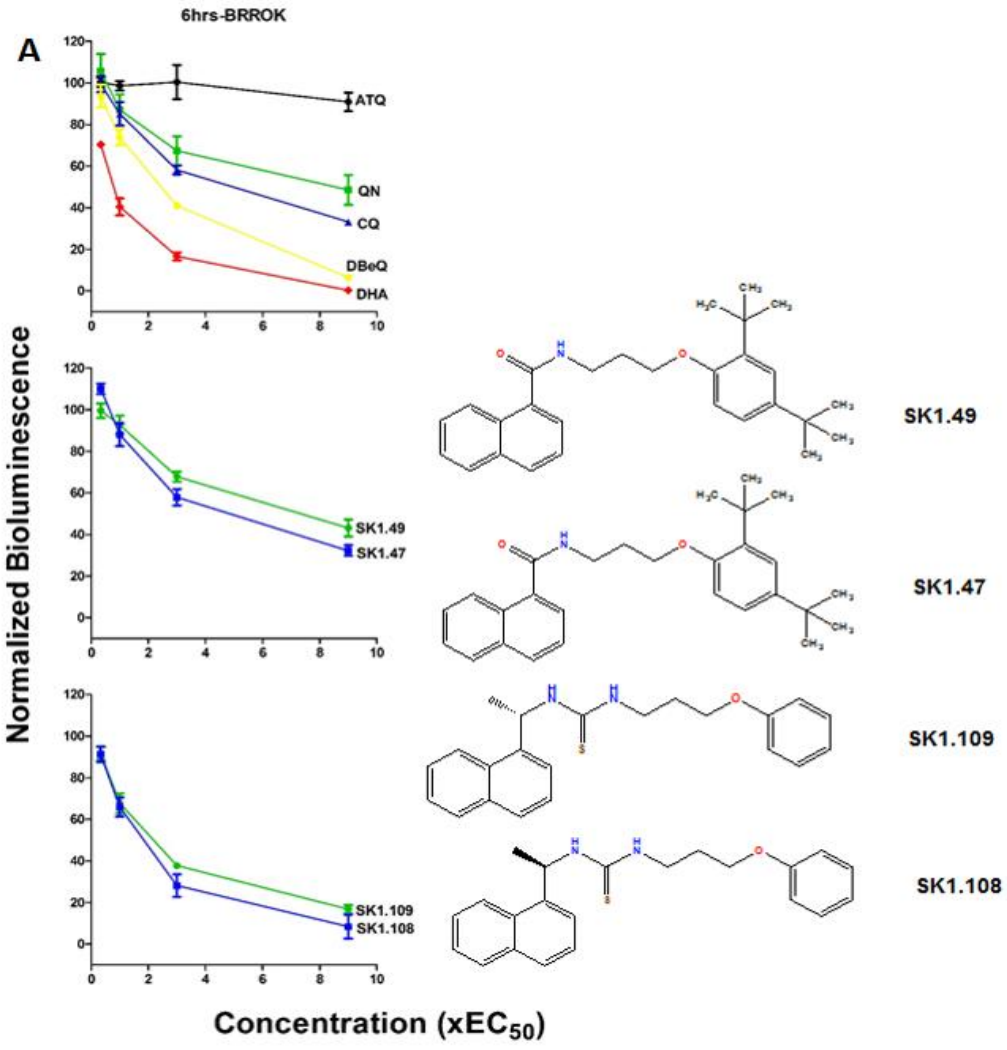

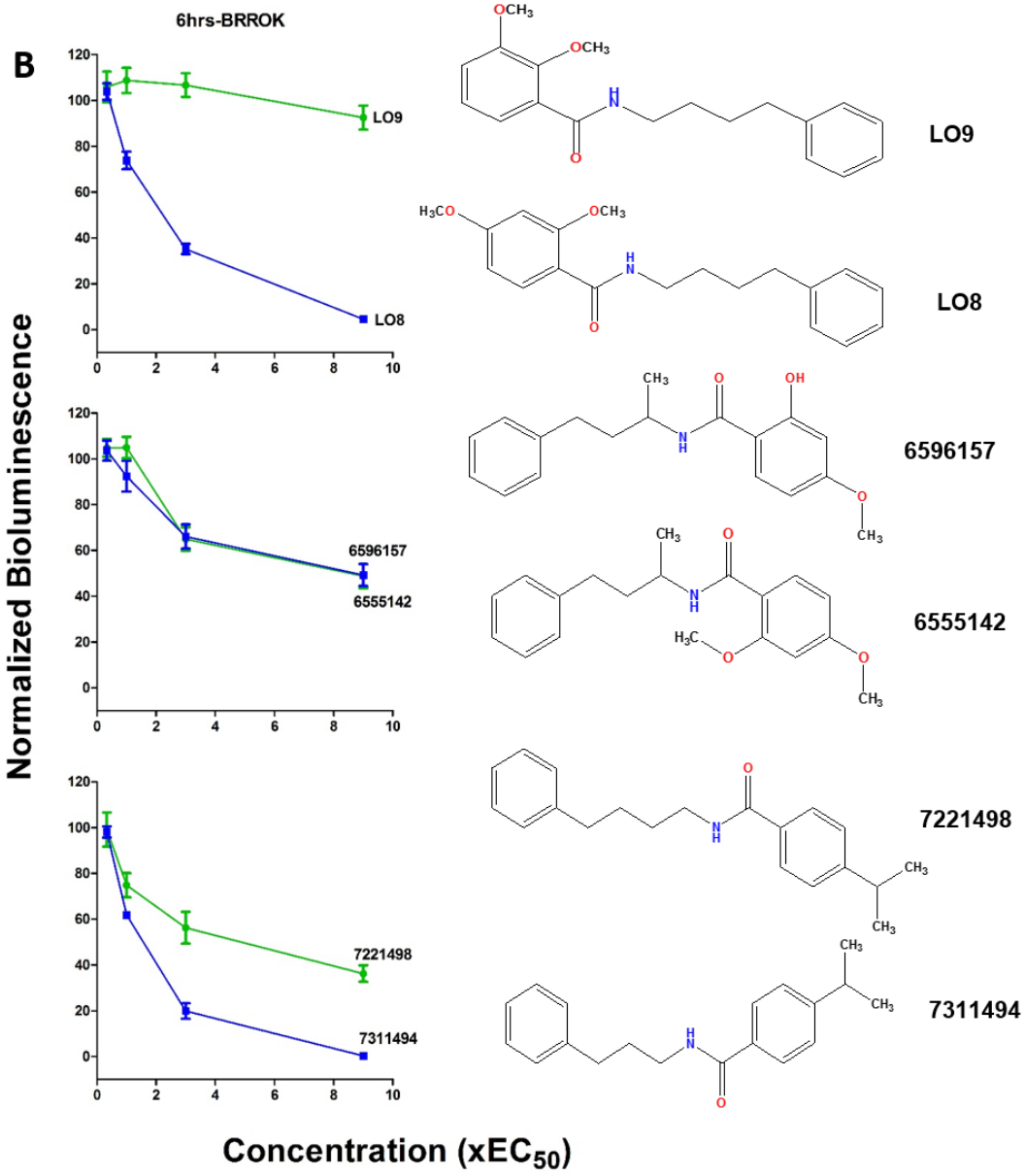

Fig. 3.29 Comparison of 6 hrs BRRoK data for structurally related library compounds. The top panel illustrates the 6 hrs BRRoK data for benchmark antimalarials. The subsequent panels illustrate the similar or differences in initial rates of kills for the indicated structurally-similar compounds.

From this comparison, that closely related structures share the same rate of kill does not appear to be true all the time. Comparison of the rates of kill of LO8 and LO9, with a small difference in the 2,3 versus 2,4 organisation of the O-methyl substitutions to a phenyl

ring, reveal a dramatic difference in rate of kill (Fig. 3.29). LO8 has a rate of kill more comparable to artemisinins, with LO9 essentially being cytostatic over the first 6 hrs. Similarly, although without as large a difference in the rate of kill, is a comparison of 7221498 (similar to CQ) and 7311494 (similar to artemisinin) where the compounds differ by the difference of one carbon length in the alkyl linker (Fig. 3.29). This may be a useful observation if taken forward to develop modifications to these compounds to improve their activity. Currently, only SK1.47 and SK1.49 have been shown to affect PfAtg8 distribution. It would be interesting to see whether compounds that have a different rate of kill, e.g. LO8 and LO9, also similarly affect PfAtg8 redistribution. If it were the case that they did not, then it would be relatively easy to screen both the EC_{50} and BRRoK activity of many derivatives, with the BRRoK assay acting as a simpler marker of what could be expected from the more complex PfAtg8 IFA.

SK1.47 and SK1.49 appear to have trophozoite stage-dependent effects, suggesting that a target of normal PfAtg8 function exists at this stage. This may correlate with a role in increased vesicular trafficking in the growing trophozoite or an additional demand for fatty acids or isoprenoids from the apicoplast, all presumably requiring PfAtg8. The observation that a pulse of either compound at trophozoites is not reversible, or at least not as much as that from a pulse of CQ, is interesting. This could be due to both compounds not being readily removed by washing. Although more lipophilic, these compounds could be removed after a pulse in ring stages. Perhaps then, the effect of these compounds in the 6 hrs exposure is more rapid than that of CQ – but this is not really evident from the BRRoK assay data. This non-reversible effect cannot be readily explained either by its structure – with no moiety that could lead to a covalent bond forming to the target, in the same way that artemisinin forms covalent adducts when the

endoperoxide bond is broken. Whilst it is clear that SK1.47 and SK1.49 preferably kill the trophozoite stages, more work in identifying potential targets from transcriptomic, proteomic and metabolic approaches are needed to try and understand the mode of action at this stage.

At the moment, we would suggest that SK1.47 and SK1.49 are very preliminary hits. They show only moderate potency against intraerythrocytic stages- but this activity is also rapidly cytocidal, reasonably selective and shown to affect PfAtg8 redistribution (a novel target). These compounds are perhaps best described as “chemical probes” that could be exploited at this stage to explore the function of PfAtg8 – particularly to define whether autophagy-like processes are active in the normal development of parasites. The role of PfAtg8 in apicoplast function and whether autophagic processes turnover specialist organelles after invasion would be obvious initial targets for these chemical probes. In terms of drug development, the high LogP is a particular risk for these compounds, restricting its bioavailability. Exploring how modifications can be made to the hydrophobic ends (e.g. how hydrophobic do they need to be?) or modifications to the alkyl linker may offer the opportunity to reduce the LogP, potentially increasing the potency and provide a hit to be taken forward for proper development.

Chapter 4: Molecular Modelling to explore ligand docking to PfAtg8

4.1 Introduction

Lipidation of Atg8 with phosphatidylethanolamine (PE) in eukaryotes requires an interaction with the ubiquitin-like conjugating enzyme Atg3 (Brennand *et al.,* 2011; Hayat, 2014; Nakatogawa *et al*. 2009; Xie and Klionsky, 2007). This interaction takes place between the Atg8 family interacting motif (AIM) of Atg3 and a conserved docking surface of Atg8 that contains two deep hydrophobic pockets, the W and L-pockets. The conservation of these features in *P. falciparum* was confirmed by X-ray crystallography of a PfAtg3 AIM peptide docking to PfAtg8 (Hain *et al.,* 2012).

Despite the only 54% conservation of amino acids between PfAtg8 and the human homologue (microtubule-associated protein 1A/1B-light chain 3, hLC3), there is a broad secondary and tertiary structural similarity between these proteins (Fig. 4.1). Importantly, the PfAtg3 AIM docking region is consistent with that of hLC3 in terms of existence the W and L-pockets, within a positively charged electrostatic surface (Fig. 4.2). Whilst there are structural similarities, several differences are found;

(i) The amino acids that form the PfAtg3 AIM docking regions are distinct between PfAtg8 and hLC3.

(ii) The size of Atg3 AIM docking pocket is larger in PfAtg8 at 511Å^3 compared to 403 Å^3 in hLC3. This is reflected in a larger W and L-pocket of PfAtg8, which are 377 Å^3 and 271 Å^3 in size, respectively.

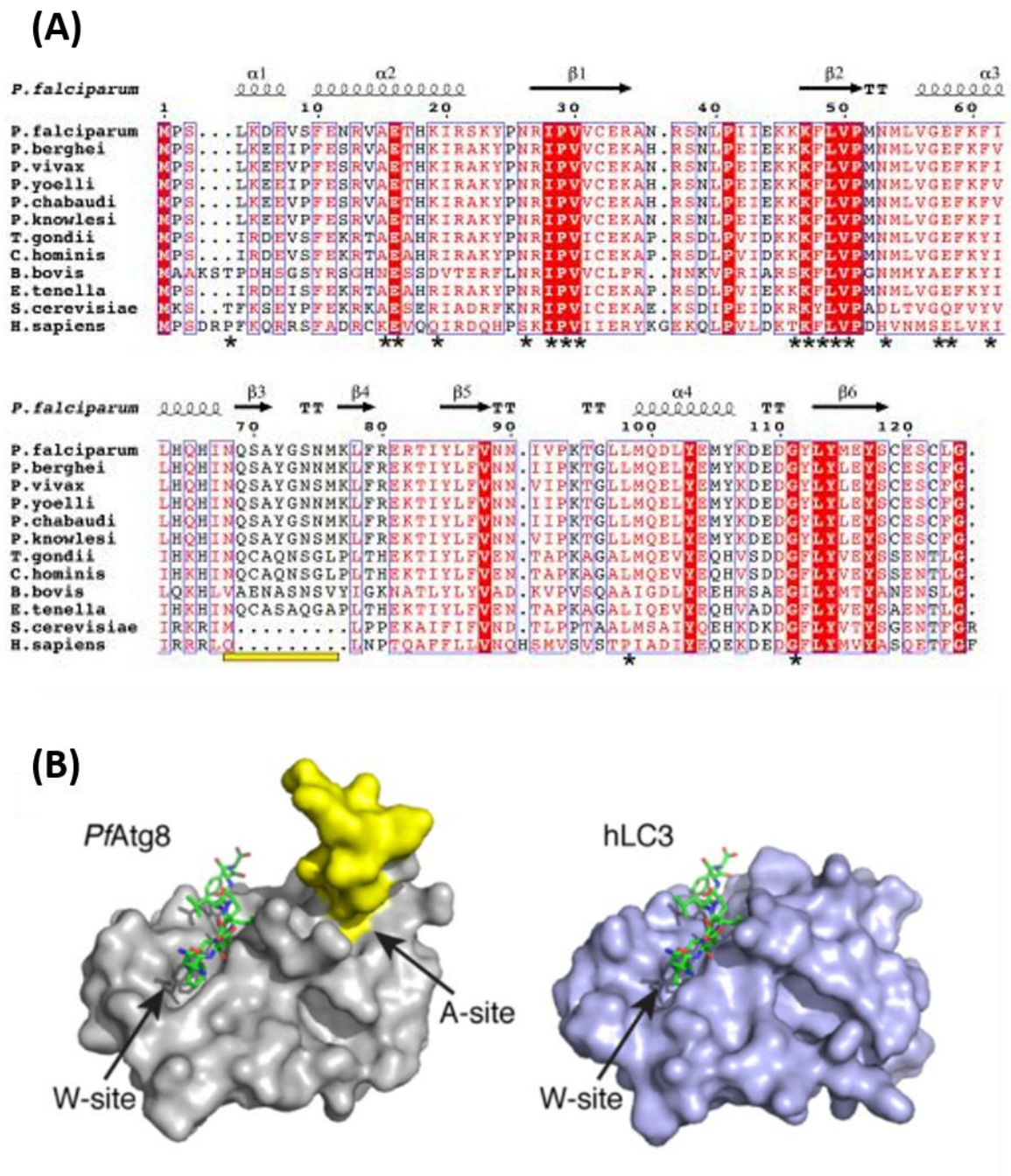

Fig. 4.1 Conservation between PfAtg8 and the human hLC3 homologue. (A) Sequence alignment of the primary and secondary structures of 10 apicomplexan Atg8 with homologues from human and budding yeast illustrates the conservation of secondary structural features amongst these Atg8 proteins. The position of alpha-helices and beta-sheets are shown over the primary sequences, Note the yellow highlighted insertion – termed the Apicomplexan loop found only in the apicomplexans in the alignment. (Source: Hain *et al.*, 2012). (B) Comparison of the tertiary structure illustrates the structural similarity between PfAtg8 and hLC3 (with the Atg3 AIM illustrates as a green stick projection. Note the A-loop insertion (yellow) forms a novel tertiary structure in PfAtg8 features, forming an adjacent novel A-loop pocket (A-site) (Source: Hain *et al.,* 2016).

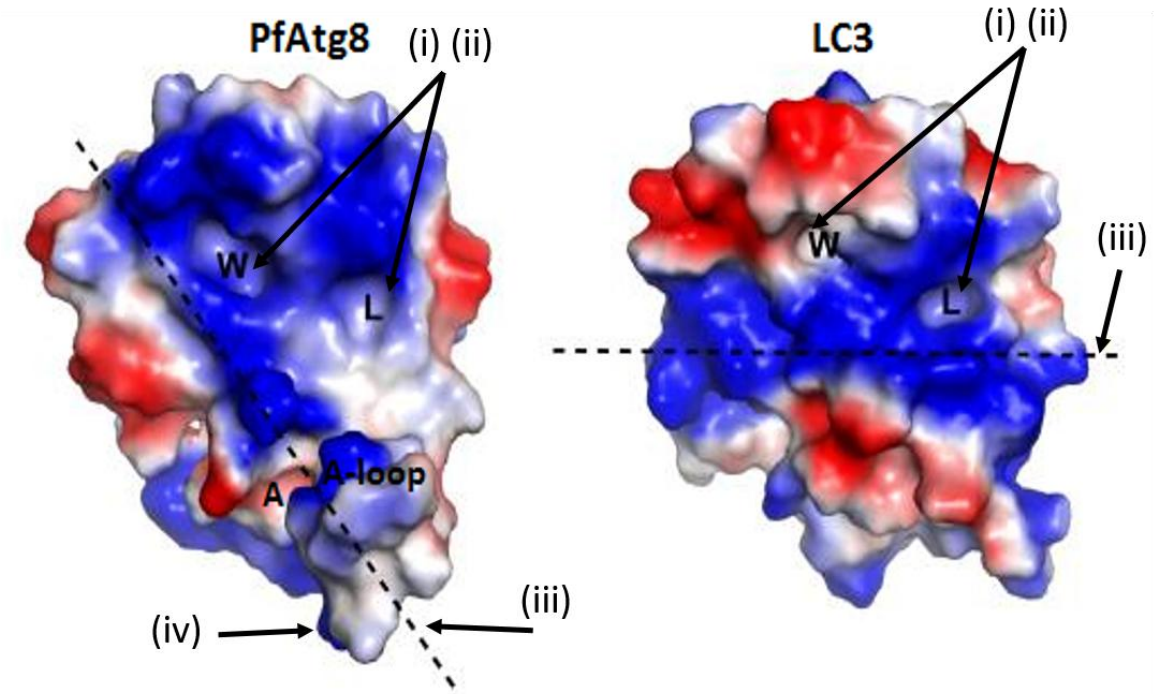

Fig. 4.2 Structural models of *P. falciparum* Atg8 (PfAtg8) and human LC3 (hLC3). The images in the top panel were generated here using the UCSF Chimera 1.11.2 software (www.cgl.ucsf.edu/chimera/) and are compared here to images illustrating the positive electrostatic charge (blue) found around the W and L-pockets in both PfAtg8 and hLC3 from Hain *et al.* (2012). The electrostatic surface potential indicates that a positively charged band in PfAtg8 is tilted by 56° compared to only 2° in hLC3.

(iii) There is a significant difference in the tilt of the positively charged band over the Atg3 AIM docking region.

(iv) The existence of the A-loop in PfAtg8, a critical region for PfAtg3 AIM docking (Hain *et al*., 2012), which is not located within the docking region, creates a large (513Å^3) A-loop pocket next to this projection. This A-loop is lacked in the hLC3.

The amino acid residues of the PfAtg3 AIM lay over the docking region, with the side chain of tryptophan 105 (TRP105) projecting into the W-pocket and the side chain of proline 108 (PRO108) projecting into the L-pocket (Fig. 4.3). These interactions are

stabilised by hydrogen bonds to lysine 48 (LYS48) and leucine 50 (LEU50) of PfAtg8 (Hain *et al.,* 2012).

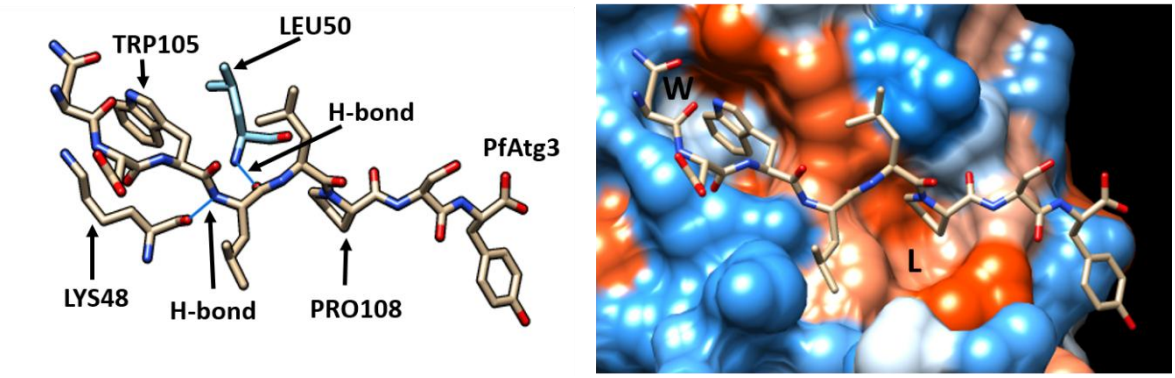

Fig. 4.3 Modelling the interaction of PfAtg3 AIM into its docking site on PfAtg8. On the left, the hydrogen bonds (H-bond) formed between LYS48 and LEU50 of PfAtg8 (brown sticks) with the PfAtg3 AIM (blue sick) are illustrated. On the right, the X-ray crystallography of PfAtg8 with PfAtg3 AIM (stick form), the projection of the side chains of TRP105 and PRO108 of PfAtg3 AIM into the W and L-pockets of PfAtg8, respectively, as illustrated. Both images prepared using UCSF Chimera 1.11.2 software (www.cgl.ucsf.edu/chimera/).

Disruption of protein-protein interaction (PPI) using small molecules or peptides have been demonstrated to modulate biochemical pathways and has some therapeutic potential (Sable and Jois, 2015; Scott *et al.,* 2016). This approach is usually supported by X-ray crystallography of the target protein to explore its structure and determine putative binding residues (or binding centres) for ligands which can be then exploited using computational analysis methods (Capra *et al.,* 2009). PfAtg8-PfAtg3 interaction is an example for this approach, where reported by Hain *et al.* (2016) using the ChemBridge library. Here, they identified ALC25 compound which binds to the A-pocket of PfAtg8 (Fig. 4.4). Previous work by this research team had also screened the MMV Malaria Box to identify MMV007907 (termed in their study compound 1) which binds across the PfAtg3 AIM docking site, with a pyridine moiety docked into the L-pocket and a methylbenzene group bound into the W-pocket (Fig. 4.5) (Hain *et al.,* 2014).

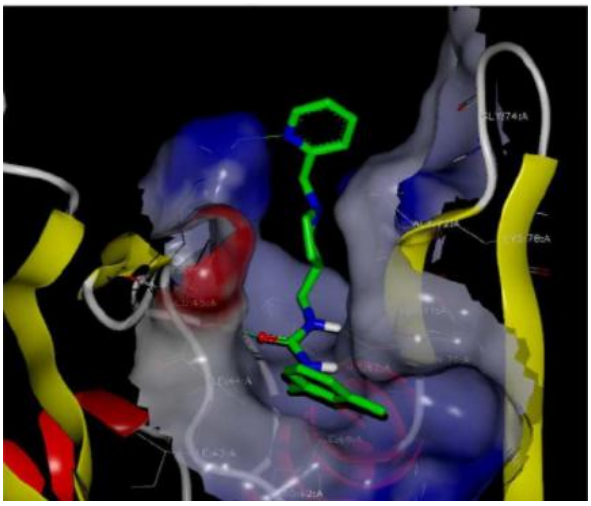

Fig. 4.4 Modelling of ACL25 docking into the A-pocket of PfAtg8. (Source: Hain *et al.*, 2016)

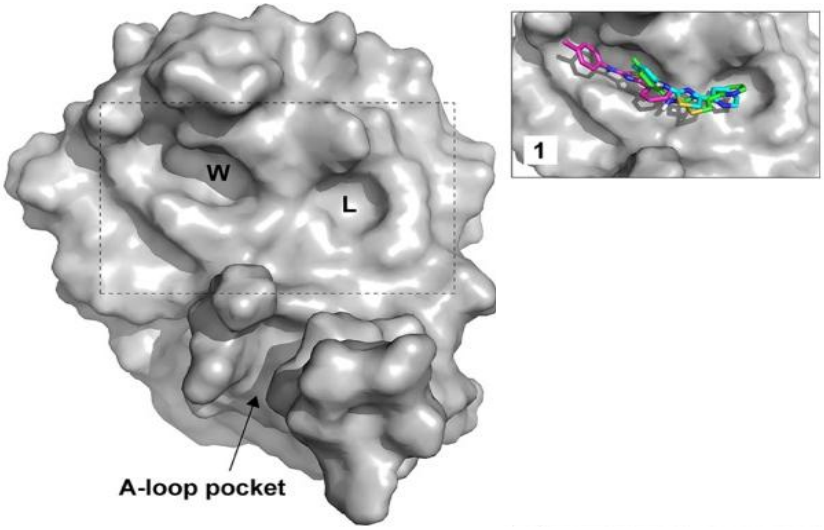

Fig. 4.5 Modelling of compound 1 docking into the W and L-pockets of PfAtg8. Note that alternative docking simulations are shown in the inset in different colours, This model developed by constraining the modelling through selecting LYS47 of PfAtg8 as a binding centre for ligand (Source: Hain *et al.*, 2014)**.**

Based on availability of the crystal structure of PfAtg8, the opportunity to model hits from the compound library against this target was attempted here. It was decided to use a commercially available online drug discovery platform called Mcule software (Mcule.com). This is an accessible molecular docking program, supported with online tutorials and was available for a paid licence fee. The aim of the study is to explore how modelling of interactions between our hits and PfAtg8 would provide information about

docking status of these compounds. This information would then be used to look at the antiplasmodial activity data for the compounds screened in chapter 3 and start to explore how the structure of the compounds can be exploit to define the interaction between compound and PfAtg8. This probably allows understanding how the structure is potentially related to the activity of the compounds screened.

4.2 Results and discussion

4.2.1 Workflow for modelling studies and initial validation

The Mcule docking models of the small molecules against protein targets are provided in a Protein Data Bank (PDB) format. PDP files for PfAtg8 and hLC3 were available in PDB files 4EOY and 2ZJD, respectively. For both of these files, the respective protein structures are available as multimers – PfAtg8 bound to the AIM of PfAtg3 is present as a trimer (Fig. 4.6) and hLC3 bound to p62 is present as a dimer. By using the free online software UCSF Chimera 1.11.2 (www.cgl.ucsf.edu/chimera/), these PDB could be imaged and peptide chains that not required were removed and a single chain of PfAtg8 and hLC3 saved and uploaded into the Mcule database as a new PDB files.

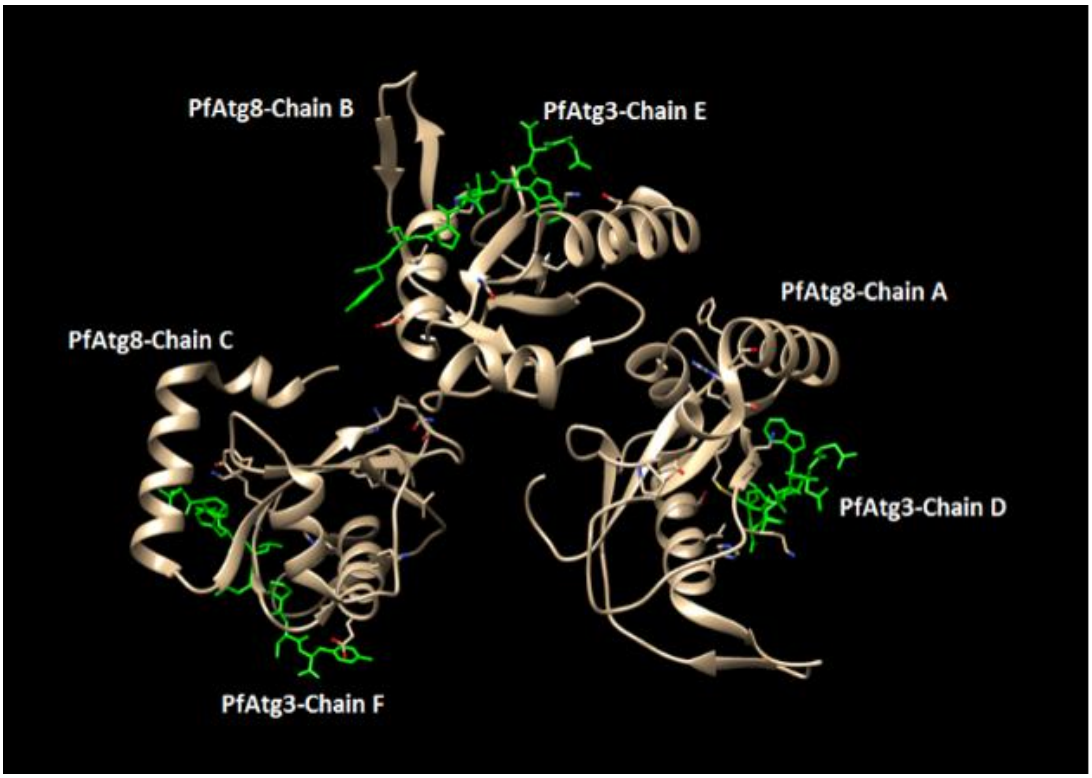

Fig. 4.6 PDB file 4E0Y shown using UCSF Chimera 1.11.2 imaging tool. Here the PfAtg8-PfAtg3 AIM complex represents 6 chains in which 3 chains of each molecule were co-crystallized. Three PfAtg3 chains and two PfAtg8 chains are removed to prepare the final PDB file of PfAtg8 for the Mcule software.

The structures of the library compounds to be explored in the modelling were provided as Simplified Molecular entry Input Lines Entry System (SMILES) formats produced using the ChemWriter^{TM} 2.15.2 screen of the Mcule software. Mcule requires the selection of binding centres to restrain the docking simulation; these binding centres are amino acids in the protein structure (PfAtg8) (Fig. 4.7). For this study, three binding centres were selected based on the current knowledge about the PfAtg3 AIM binding with PfAtg8. These were included; LYS48 and LEU50 based on their formation of hydrogen bonds to the PfAtg3 AIM peptide and LYS47 based on its formation of hydrogen bonds to compound 1 (Hain *et al*., 2012, 2014). Each of these binding centres contains a number of

binding points – heavy atoms within the chain that may act as hydrogen bond donors or acceptors. Lysine amino acid contains eight binding points, and leucine has seven (Fig. 4.8).

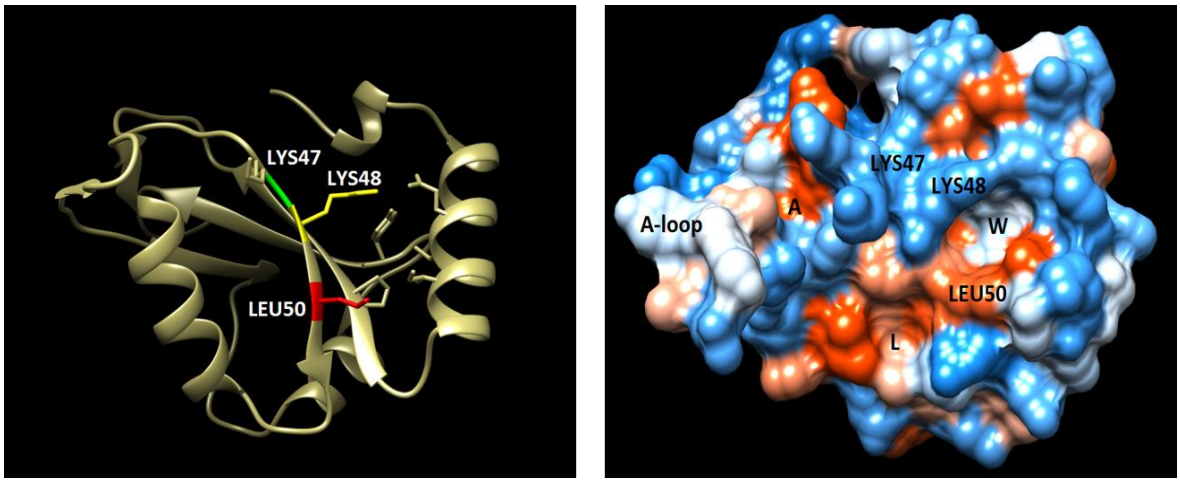

Fig. 4.7 Selection of amino acids within PfAtg8 as binding centres for Mcule docking simulations. The image on the left is a ribbon representation of PfAtg8, with the three binding centres of as lysine 47 (LYS47, green), lysine 48 (LYS48, yellow) and leucine 50 (LEU50, red). The space occupying model to the right shows the position of these binding centres relative to the W and L-pockets.

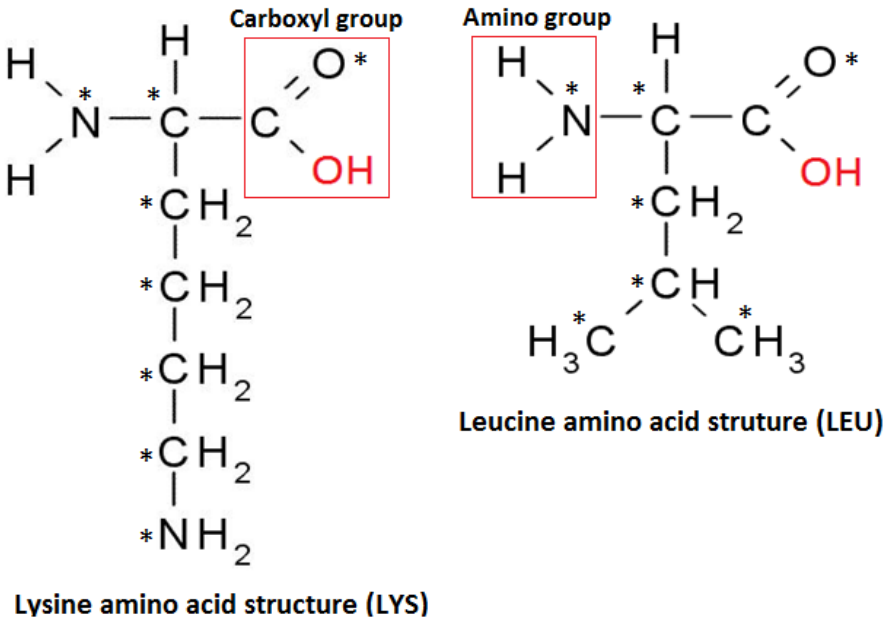

Fig. 4.8 Chemical structure of lysine (LYS) and leucine (LEU) amino acids. The eight or seven heavy atom binding points within LYS and LEU, respectively, are identified with black stars.

With three binding centres providing a total of 23 binding points, the Mcule software predicts for each binding point four top poses (Fig. 4.9), providing 92 docking simulations for each compound over these three binding centres. Each simulation provides a docking score – this is a score of predicted binding affinity of the ligand to PfAtg8 using an energy component method which attempts to minimise the energy required for this interaction, an approach widely used in docking simulation software (Kroemer, 2007). As such, the lower score meaning the more likely that interaction occurs as modelled.

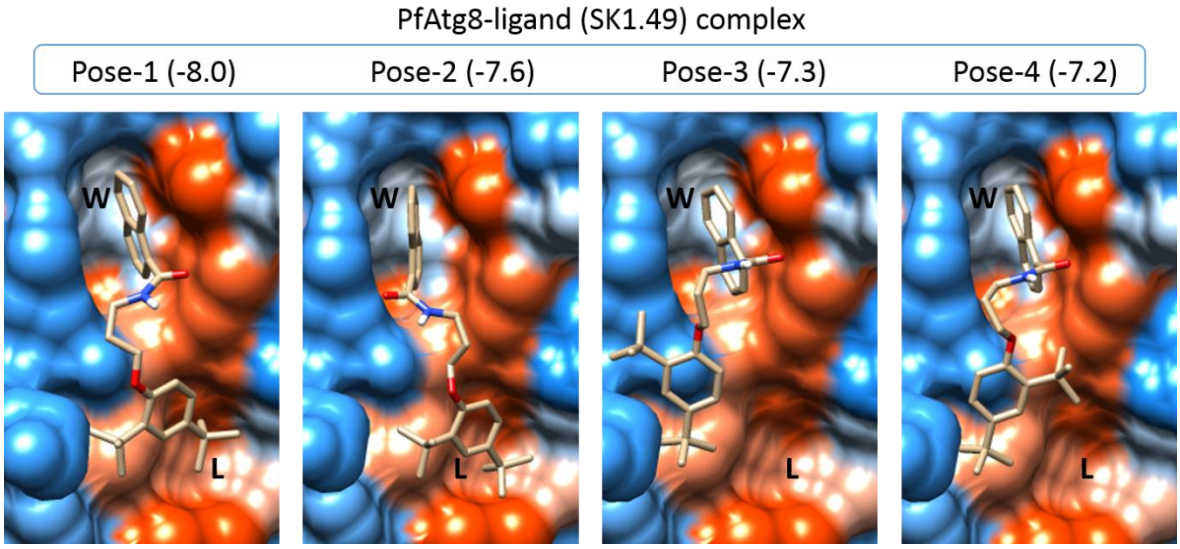

Fig. 4.9 Example docking of SK1.49 to the C385 binding point of LYS48 within PfAtg8. The images represent the top four ranked docking poses for SK1.49 to this binding point on LYS48. The poses are ranked in their relative docking score rank, with pose 1 the highest ranked, and pose 4 the lowest ranked.

The pose of the ligand provided the following data that was recorded in appendix 3. These are included; the docking score, the potential to form a hydrogen bond (and to which binding centre) as well as a pose prediction in terms of docking into the W and L-pockets. As an example in Fig. 4.9, poses 1 and 2 dock within both pockets (W and L-pockets), whereas poses 3 and 4 only docking within the W-pocket. Docking Simulations were carried out for (i) SK1.47 and SK1.49 as the best hits in the compound library, (ii)

SK1.108 and SK1.109 as whilst toxic, they were potent inhibitors of intraerythrocytic growth and share the naphthalene moiety with SK1.47 and SK1.49, (iii) SK1.63 is also moderately potent (EC_{50} of 4 µM) against intraerythrocytic stages and also shares a naphthalene moiety and (iv) compound 1 from the Hain *et al.* (2014) study that was predicted to bind into the PfAtg3 AIM docking site. The highest scoring pose (i.e. best docking score) of the 92 simulations performed for each compound, are shown in Fig. 4.10. In addition, molecular docking of SK1.49 and compound 1 with hLC3 were performed against the equivalent binding centres in hLC3. Together, over 1100 docking simulations are reported here.

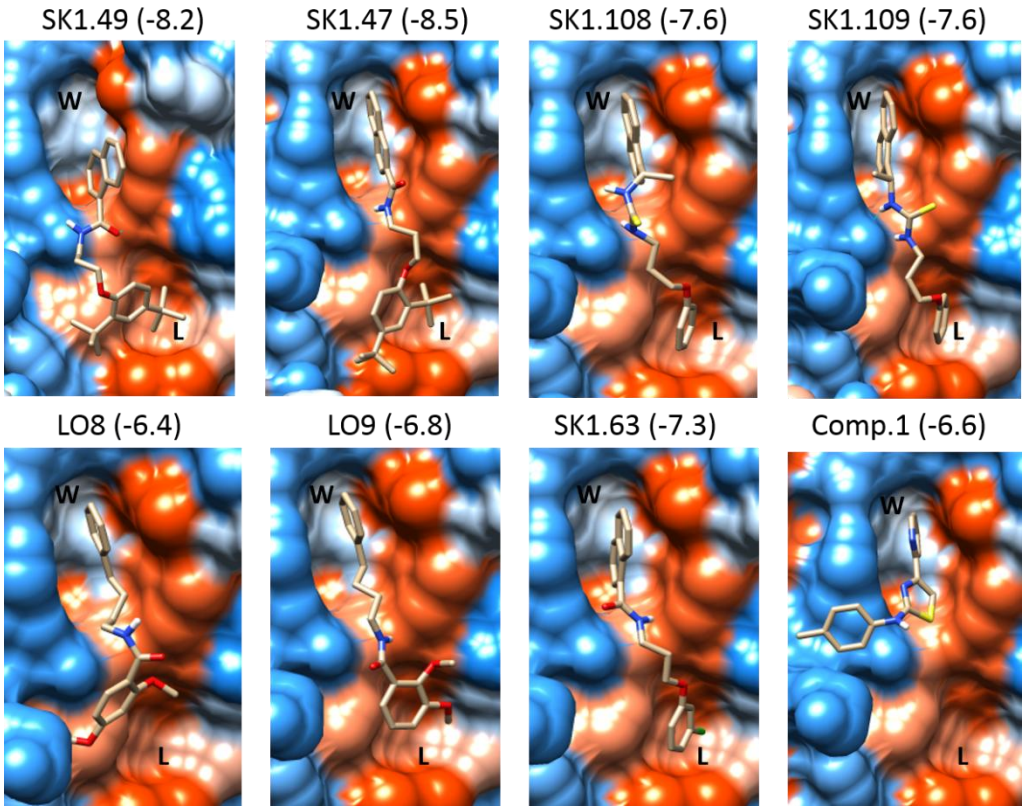

Fig. 4.10 The top scoring docking pose for the compounds modelled for binding to PfAtg8. Note the docking score is provided in brackets for each compound.

Compound 1 was included as previous modelling of its interaction with PfAtg8 had been reported (Hain *et al.*, 2014) using the OpenEye software package. In this work, the

prediction of compound 1 to interact with PfAtg8 (bound to the LYS47 binding centre) reports that the pyridine ring of compound 1 is occupied the L-pocket, the methylbenzene group lies across the W-pocket and the thiazole ring is positioned between the 2 pockets as a bridge. This simulation is not the best docking pose that predicted using Mcule package (Fig. 4.10), where the pyridine ring of compound 1 placed in the W-pocket and the methylbenzene group projects away towards the A-pocket. The Mcule prediction, however, of the top score docking poses provided alternative docking simulation to that described by Hain *et al*. (2014), and the OpenEye prediction is one of the lower ranked Mcule poses using the LYS47 binding centre (Fig. 4.11). Also, another slight difference is that whilst the OpenEye software predicts a H-bond to LYS47 using this amino acid as the binding centre, Mcule, using the same binding centre, instead predicts two H-bond – neither to LYS47, instead these forming with LYS48 and LEU50 (Fig. 4.12). These data suggest that similar modelling data can be obtained with Mcule in modelling compound 1 interaction with PfAtg8 – but also a need to recognise that these are models and that modification within these models need to be considered carefully in any discussion about ligand interactions with PfAtg8.

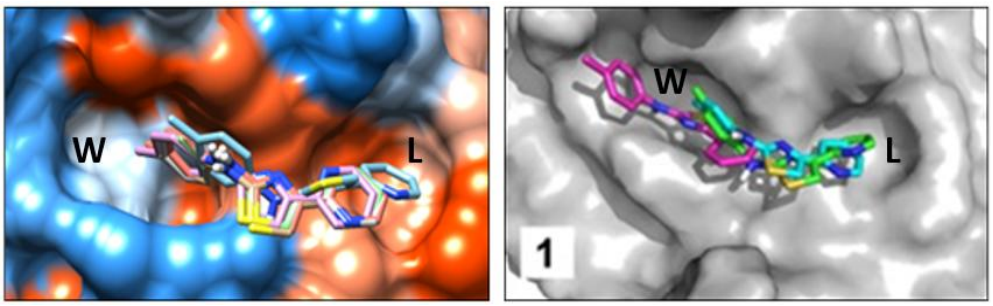

Fig. 4.11 Comparison of docking models from Mcule (left) and OpenEye (right; Hain *et al.,* 2014) for compound 1 interaction across the W and L-pockets of PfAtg8. Note that whilst the OpenEye data are the best docking scores for the LYS47 binding centre, those for Mcule on the right are not.

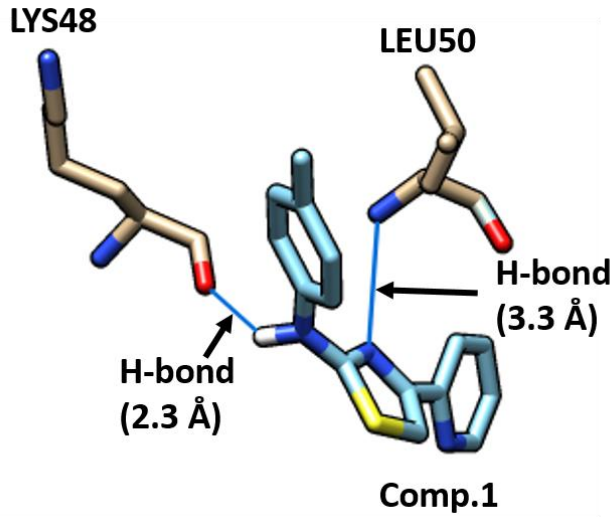

Fig. 4.12 Stick model projection of the H-bond predictions of Mcule docking of compound 1 to PfAtg8. H-bonds to compound 1 from O383 and N400 binding points of carbonyl and amino groups of LYS48 and LEU50 binding centres, respectively. This pose developed using the O374 binding point of the LYS47 binding centre- the equivalent centre that predicts a H-bond to LYS47 using the OpenEye software by Hain *et al.,* (2014).

4.2.2 Ligand docking to PfAtg8

As indicated earlier, 92 docking poses are available for each compound docked to PfAtg8. These are the top four scoring docking poses for each binding point within the three binding centres that chosen. For each pose, the docking score, the potential to form a H-bond and whether the ligand docked within the W and L-pockets were recorded (see appendix 3). Given the number of docking poses available, the data presented for each ligand here is the top scoring docking pose for the eight binding points in LYS47 and LYS48 and the seven binding points for LEU50. These are presented as stick images, without PfAtg8, to allow variations in ligand position to be clearly seen (see Fig. 4.13 as an example). To provide context, the final merged image of all the top scoring docking poses includes X-ray crystallography of PfAtg8, with the W-pocket at the top of the images and the L-pocket at the bottom. In these images, the A-pocket would be located to the left. A

summary schematic is used to present what is the most common orientation of the ligand with respect to the W and L-pockets based on all the docking poses available.

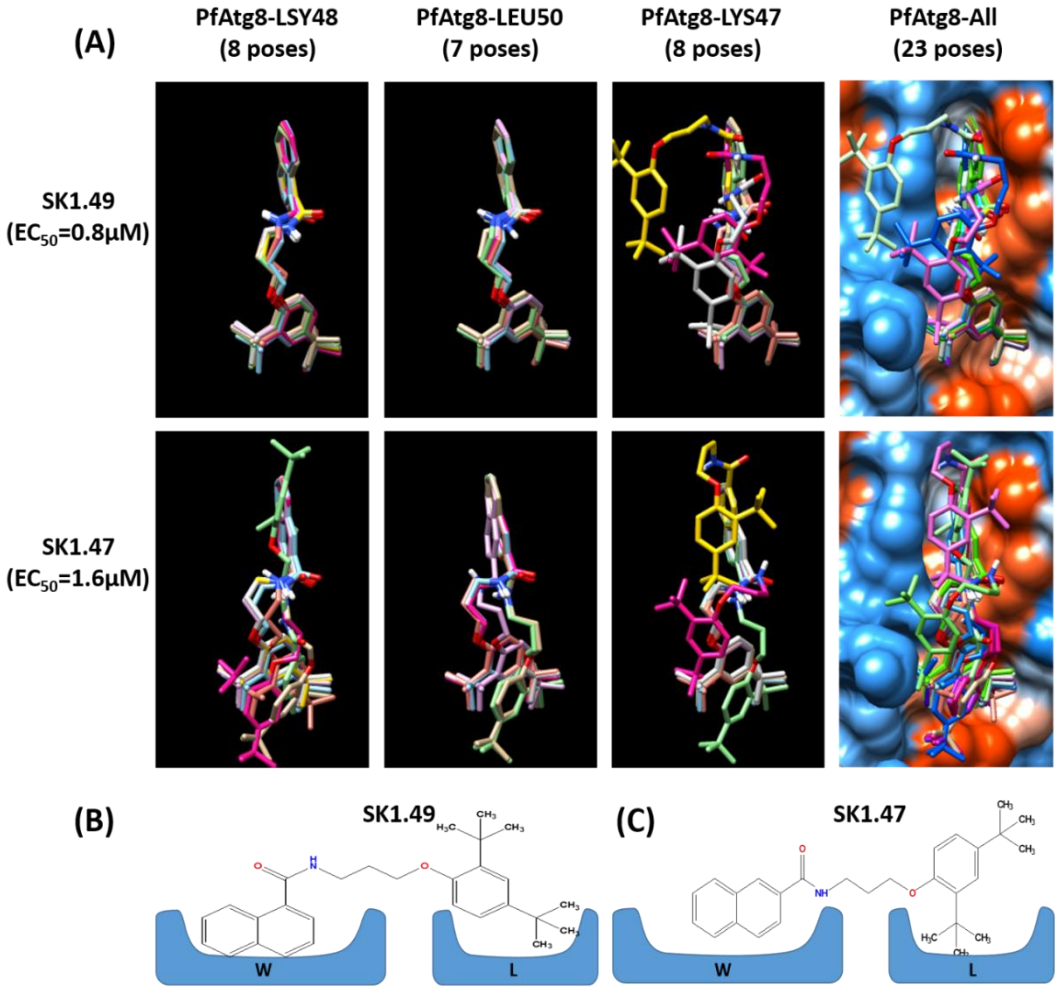

Fig. 4.13 SK1.49 and SK1.47 docking to PfAtg8. (A) Panels left to right represent the top scoring docking pose to the eight or seven binding points present in LYS47/48 or LEU50, respectively, for the indicated compound (with EC_{50} also indicated). For each binding centre these are shown separately, with a final merged image that includes the model of PfAtg8. The W-pocket at the top and the L-pocket at the bottom. (B) and (C) Show a schematic representing the apparent preferred docking of the ligands to the W and L-pockets.

SK1.47 and SK1.49 provide the most consistent ligand docking poses using the LYS48 and LEU50 binding centres with all poses docking closely together. This was more clearly for the more potent, SK1.49 (Fig. 4.13). This molecular docking predicted that the naphthalene group docks within the larger W-pocket, with the amine/alkyl chain forming

a bridge between two hydrophobic pockets, whilst L-pocket occupied by the trimethyl substitution of the phenyl ring. For SK1.49, the 4-trimethyl substitution is clearly preferred, with a slight preference in SK1.47 for the 2-trimethyl substitution positioned in the L-pocket. This would suggest that the difference in spacing which is provided by the α or β naphthalene in SK1.49 and SK1.47, respectively, determines how the 2, 4-trimethyl substitutions present in both molecules docks into the L-pocket. Additionally, the amine group, in both cases, forms a H-bond to LYS48, although not consistently for all the docking poses.

Docking of the next two most potent compounds, SK1.108 and SK1.109, supports the previous preference for positioning of the naphthalene group in the W-pocket, with both compounds sharing an α naphthalene group (Fig. 4.14). The unsubstituted phenyl group at the other end of the ligands is typically positioned in the L-pocket. The data showed that formation of H-bond by both amine groups within the thiourea of the linker region is specified to LYS48. A third library compound containing an α naphthalene group, SK1.63 (EC_{50} of 4 μM), was also modelled to explore this preferential location of the naphthalene group in the W-pocket (Fig. 4.15). Interestingly, this preference here was less clear, with variation in the orientation at high scoring docking poses producing a new docking simulation by which 3-chlorophenyl group positioned into the W-pocket. This alternate orientation may reflect that the modelling is attempting to fit the large 3-chlorophenyl group in the larger W-pocket. Interestingly, where the 3-chlorophenyl group is docked in the W-pocket, the naphthalene group is rarely located in the L-pocket, suggesting this large group may not fit in this smaller pocket (L-pocket).

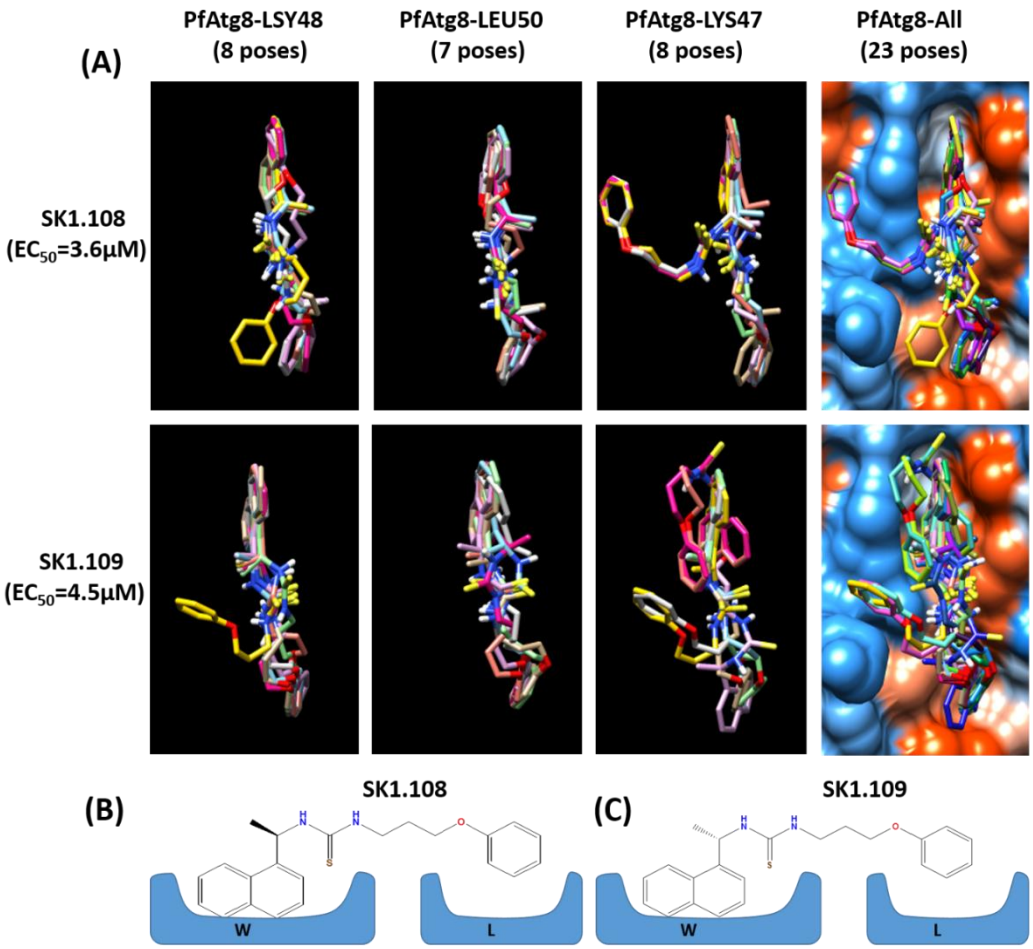

Fig. 4.14 SK1.108 and SK1.109 docking to PfAtg8. (A) Panels left to right represent the top scoring docking pose to the eight or seven binding points present in LYS47/48 or LEU50, respectively, for the indicated compound (with EC_{50} also indicated). For each binding centre these are shown separately, with a final merged image that includes the model of PfAtg8. The W-pocket at the top and the L-pocket at the bottom. (B) and (C) Show a schematic representing the apparent preferred docking of the ligands to the W and L-pockets.

Analysis of the top scoring docking poses of compound 1 (MMV007907) identified from a screen of the MMV Malaria Box (Hain *et al.*, 2014) shows a consistent orientation of the pyridine ring in the W-pocket and the docking of the 4-methylphenyl group away from the L-pocket (Fig. 4.15). This group, 4-methylphenyl, is now orientated towards the A-pocket. Such orientation was observed by Hain *et al.* (2016) in a subsequent study, where they identified ACL25 compound that is predicted to bind within this A-pocket. These

observations lead us to suggest that linking of these two compounds together may provide a highly specific inhibitor of the PfAtg8-PfAtg3 interaction.

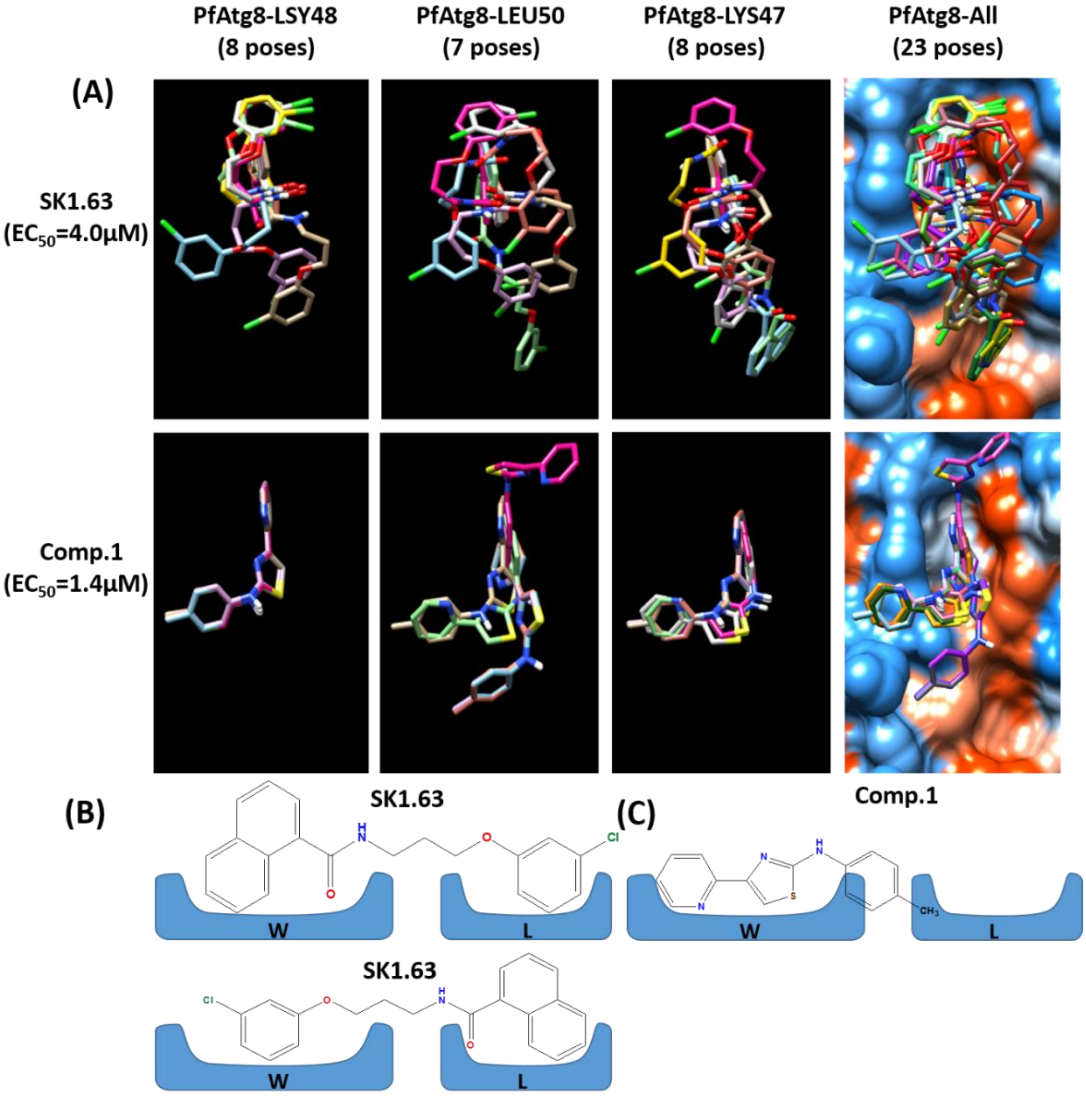

Fig. 4.15 SK1.63 and Compound (Comp.) 1 docking to PfAtg8. (A) Panels left to right represent the top scoring docking pose to the eight or seven binding points present in LYS47/48 or LEU50, respectively, for the indicated compound (with EC_{50} also indicated). For each binding centre these are shown separately, with a final merged image that includes the model of PfAtg8. The W-pocket at the top and the L-pocket at the bottom. (B) and (C) Show a schematic representing the apparent preferred docking of the ligands to the W and L-pockets. Note for SK1.63 that the 3-chlorophenyl group may occupy either the W or L-pocket. For Comp.1, the 4-methylphenyl group is positioned away from the L-pocket, and is now orientated towards the A-pocket.

The last two compounds docked were LO8 and LO9 (Fig. 4.16). Although these two compounds differ just on the basis of the position of one O-methyl substitution, with 2,4-O-methyl in LO8 and 2,3-O-methyl in LO9, were shown in chapter 3 to have very distinct potencies against the intraerythrocytic trophozoite stages and initial kill dynamics.

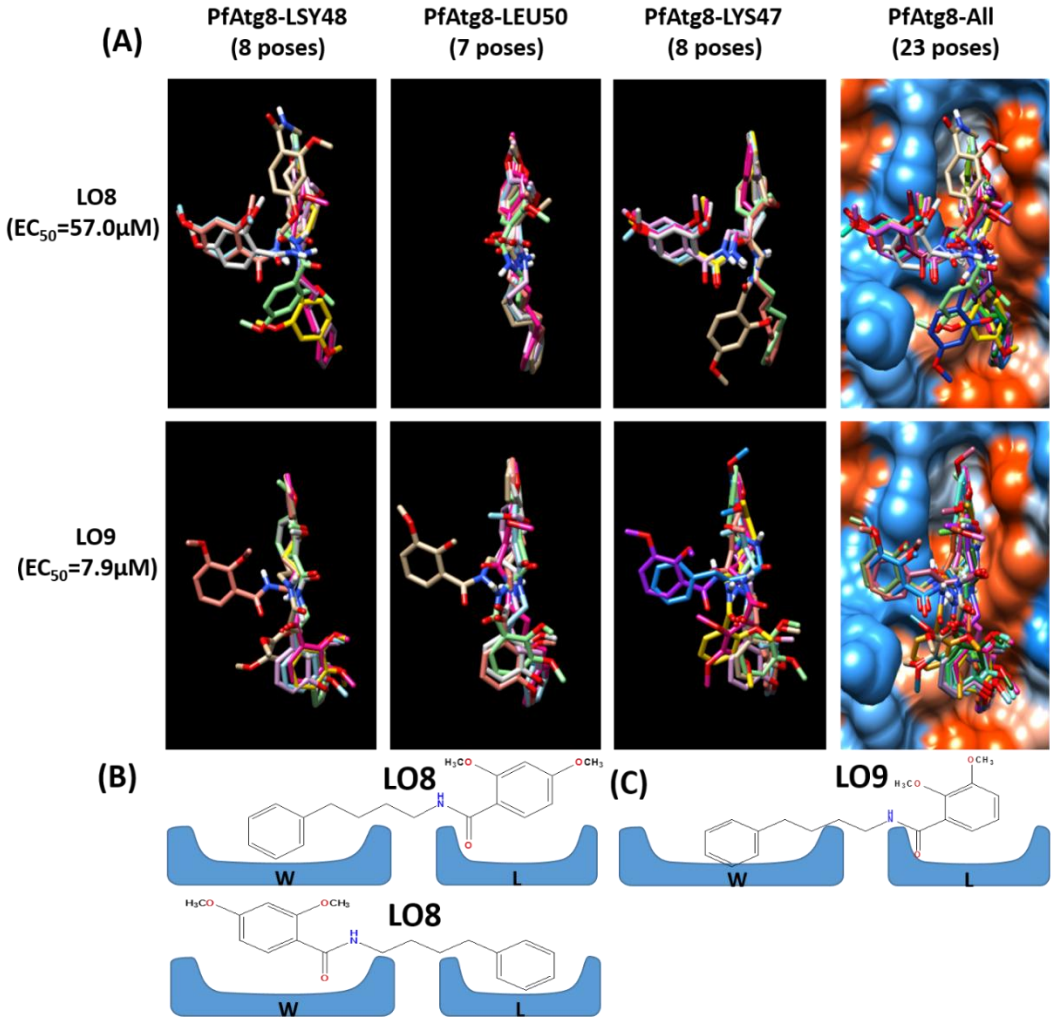

Fig. 4.16 LO8 and LO9 docking to PfAtg8. (A) Panels left to right represent the top scoring docking pose to the eight or seven binding points present in LYS47/48 or LEU50, respectively, for the indicated compound (with EC_{50} also indicated). For each binding centre these are shown separately, with a final merged image that includes the model of PfAtg8. The W-pocket at the top and the L-pocket at the bottom. (B) and (C) Show a schematic representing the apparent preferred docking of the ligands to the W and L-pockets. Note for LO8 that the 2,4-O-methyphenyl group may occupy either the W or L-pocket. However, for LO9 the 2,3-O-methylphenyl is preferentially located in the L-pocket.

This molecular modelling revealed that the less potent LO8 adopted two main orientations, with the O-methyl substituted and unsubstituted phenyl groups located in either of the W and L-pockets. This docking simulation, however, was not observed in LO9, where the 2, 3-O-methyl phenyl group predicted to bind with L-pocket only. This suggests that steric hindrance based on the move from the meta to the para position for one of the O-methyl substitutions may play a role in how these molecules dock with PfAtg8.

So far the analysis of docking data has explored how these ligands may interact with the PfAtg3 AIM docking region of PfAtg8, particularly with respect to the W and L-pockets. Each docking simulation also produces a docking score. Whilst recognising the evidence that agreements between docking score and compound activity rarely correlate (Grinter and Zou, 2014; Liu *et al.,* 2013; Sakano *et al.,* 2016), this was observed here for the compounds that structurally related. Table 4.1 reports the top docking score for each binding point for the three binding centres chosen (this data summarised from appendix 3). In addition, the top scoring docking poses that include evidence of H-bond formation were highlighted in green. Interestingly, this highlighting clearly shows the lack of correlation between predicted H-bond formation and compound activity. For example, whilst SK1.47 and SK1.49 are the most potent compounds, but they provided the lowest scoring of H-bond formation. Contrastingly, this feature was greater with lower potent compounds such as SK1.108 and SK1.09. This may be due to exist thiourea group, and with two hydrogen bonds donating amines are more likely to be predicted to form H-bonds. The same is also seen for compound 1 which includes more hydrogen donating and accepting groups than both SK1.47 and SK1.49. To simplify this analysis, only the mean of top scoring for each of the three binding centres was chosen (Table 4.2).

(A) Target (PfAtg8)																						
	Binding points in LYS48								Binding points in LEU50							Binding points in LYS47						
Comp. ID	N-380	C-382	O-383	C-384	C-385	C-386	C-387	N-388	N-400	C-402	O-403	C-404	C-405	C-406	C-407	N-371	C-373	O-374	C-375	C-376	C-377	C-378	N-379
SK1.49	-7.9	-7.9	-7.9	-7.9	-8.0	-7.9	-7.9	-7.9	-7.9	-7.9	-7.8	-7.9	-7.9	-8.0	-8.0	-7.9	-7.9	-7.9	-7.7	-7.9	-7.6	-7.1	-7.3
SK1.47	-8.3	-8.3	-8.5	-8.2	-7.8	-8.5	-8.3	-8.3	-8.5	-8.0	-8.1	-8.5	-8.3	-8.3	-8.0	-8.3	-8.3	-8.3	-8.4	-8.3	-7.9	-7.5	-6.1
SK1.108	-7.2	-7.6	-7.4	-7.3	-7.4	-7.4	-7.4	-6.8	-7.4	-7.0	-7.4	-7.3	-7.4	-6.8	-7.3	-7.6	-7.2	-7.4	-7.0	-7.2	-7.1	-7.2	-6.2
SK1.109	-7.0	-7.6	-7.4	-7.2	-7.2	-7.5	-7.5	-6.8	-7.2	-7.2	-7.5	-7.4	-7.6	-7.0	-7.4	-7.2	-7.5	-7.1	-7.5	-5.8	-5.6	-5.9	-6.8
SK1.63	-6.7	-6.7	-6.3	-6.3	-6.2	-6.1	-6.2	-6.1	-6.6	-6.4	-6.3	-7.3	-6.2	-6.3	-6.2	-6.1	-6.8	-6.5	-6.6	-6.2	-6.6	-6.3	-6.5
LO9	-6.6	-6.5	-6.4	-6.6	-6.6	-6.6	-6.6	-6.8	-6.5	-6.4	-6.5	-6.1	-6.8	-6.8	-6.2	-6.5	-6.6	-6.1	-6.0	-6.0	-6.1	-6.4	-6.2
LO8	-5.6	-6.2	-6.4	-6.2	-6.2	-5.8	-6.2	-5.2	-6.1	-5.8	-6.3	-6.1	-6.4	-6.3	-6.0	-6.3	-5.8	-6.0	-6.0	-5.2	-6.0	-5.4	-5.2
Comp.1	-6.5	-6.3	-6.3	-6.3	-6.4	-6.3	-6.4	-6.5	-6.4	-6.0	-5.9	-5.9	-6.0	-5.9	-5.9	-6.3	-6.4	-6.6	-6.4	-6.4	-6.0	-6.0	-6.4
	(B) Target (human LC3)																					
	Binding points in LYS51								**Binding points in LEU53**							**Binding points in LYS49**						
Comp. ID	N-429	C-431	O-432	C-433	C-434	C-435	C-436	N-437	N-449	C-451	O-452	C-453	C-454	C-455	C-456	N-413	C-415	O-416	C-417	C-418	C-419	C-420	N-421
SK1.49	-6.8	-7.3	-7.3	-7.3	-6.7	-7.3	-7.0	-6.8	-7.6	-7.6	-7.5	-7.3	-7.4	-7.0	-7.0	-7.0	-7.4	-6.6	-7.3	-7.3	-7.2	-6.6	-6.4
Comp.1	-6.8	-6.7	-6.8	-6.7	-6.5	-6.6	-6.6	-6.7	-6.7	-6.2	-6.7	-6.4	-6.7	-6.7	-6.6	-6.7	-6.4	-5.9	-6.7	-6.7	-6.6	-5.5	-5.5

Table 4.1 Summary of top docking scores for each binding point within the three binding centres chosen for modelling of ligand interaction with (A) PfAtg8 and (B) hLC3. Where the top docking pose for the respective binding centre also includes the formation of a H-bond, the docking score is highlighted in green.

Comp. ID	EC_{50} (µM) in 3D7	LYS48	LEU50	LYS47
SK1.49	0.8	-7.91	-7.91	-7.66
SK1.47	1.6	-8.27	-8.24	-7.88
SK1.109	4.5	-7.27	-7.32	-6.67
SK1.108	3.9	-7.31	-7.22	-7.11
SK1.63	4.0	-6.32	-6.47	-6.45
LO8	57.0	-5.97	-6.14	-5.73
LO9	7.9	-6.58	-6.47	-6.23
Comp.1	1.4	-6.37	-6.01	-6.31

Table 4.2 Shows the mean of top scoring for each of the three docking centres for ligand docking to PfAtg8. The EC_{50} values used for the subsequent correlation were from the 3D7 strain of *P. falciparum*.

In Fig. 4.17, a clear trend between the docking score and the *in vitro* activity against intraerythrocytic parasites for the library compounds can be seen. The most potent compounds, SK1.47 and SK1.49, have lower docking scores, indicating better predicted docking, than the less potent LO8 and LO9. This is encouraging, as it suggests that there are correlation between docking score and antiplasmodial activities. Caution in over-interpreting due to that this trend comes from (i) the relatively few compounds were used to explore this trend and (ii) that compound 1 does not follow this trend. Compound 1 has lower docking scores, but has an *in vitro* potency similar to that of SK1.47 and SK1.49 and although it is clearly distinct in its structure compared to the library compounds explored.

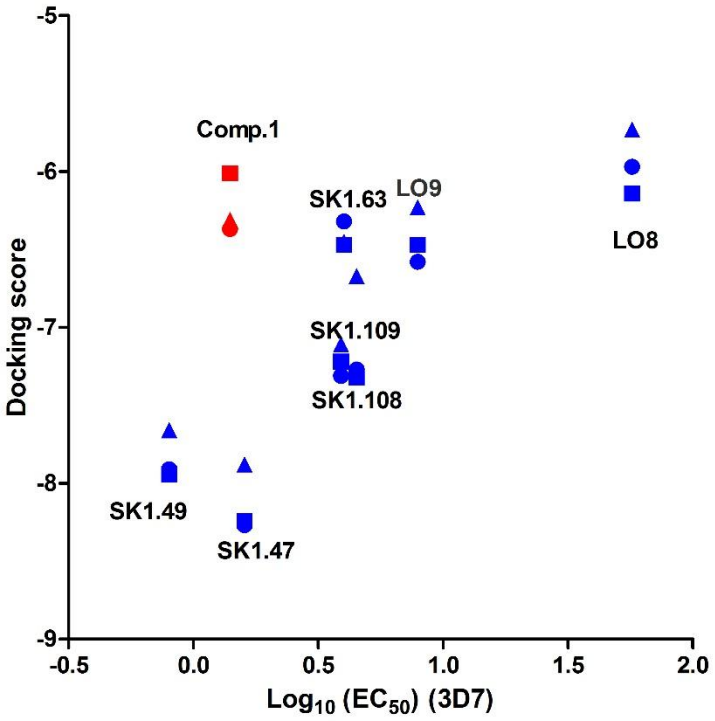

Fig. 4.17 Exploring the correlation between the mean of top scoring for each of the three docking centres and the intraerythrocytic potency of the modelled library compounds. The top docking scores for the three binding centres (LYS47, triangle; LYS48, circle and LEU50, square) used for each compound are plotted against the Log10 of their EC50 determined against intraerythrocytic trophozoites of the 3D7 strain of *P. falciparum*.

4.2.3 Docking SK1.49 and Compound 1 to hLC3

Both SK1.49 and compound 1 show some selectivity in intraerythrocytic parasites over human HepG2 cell lines (Chapter 3 for SK1.49 and Hain *et al*., 2014 for compound 1). To provide an initial exploration of how this selectivity may arise, and given the apparent differences in the Atg3 AIM docking regions between PfAtg8 and hLC3, the molecular docking were repeated using hLC3, with the homologous binding centres in hLC3 (LYS49, LYS51 and LEU53) for those originally selected in PfAtg8. As with PfAtg8, docking scores, orientation over the W and L-pockets and H-bond predictions were recorded in appendix 3 with the top docking scores summarised in Table 4.1. The same method of showing the

top scoring for docking poses for binding points in the LYS49, LYS51 and LEU53 binding centres was used here – with panels comparing the docking simulations for each compound against PfAtg8 and hLC3 shown over each other (Fig. 4.18 and 4.19).

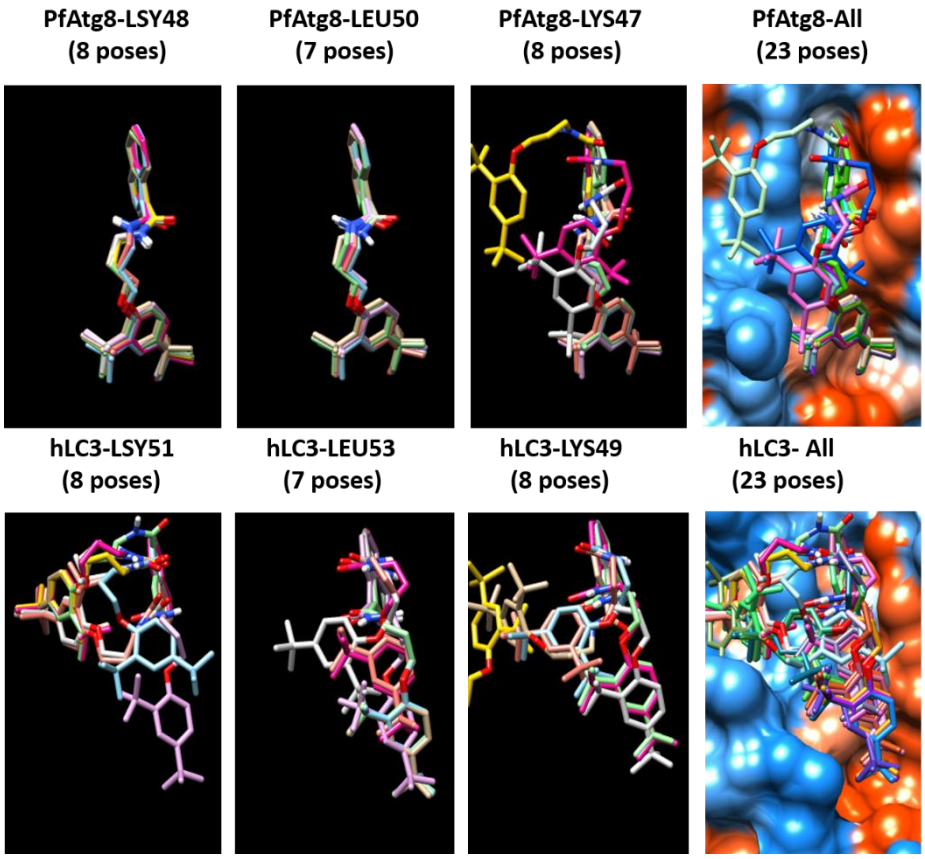

Fig. 4.18 Docking of SK1.49 to PfAtg8 (top panels) and hLC3 (bottom panels). Panels left to right represent the top scoring docking pose to the eight or seven binding points present in LYS47/48 and LEU50 for PfAtg8 and their homologous binding centres LYS49/41 and LEU53 in hLC3. A final merged image that includes the model of PfAtg8 or hLC3. The W-pocket at the top and the L-pocket at the bottom.

Docking of SK1.49 to hLC3 suggested that whilst the naphthalene group is still preferentially located in the W-pocket, the 2,4,-trimethyl substituted phenyl group did not consistently occupied the L-pocket as like as PfAtg8 (Fig. 4.18). Instead, across all binding centres, the top scoring docking poses for each binding point adopt a range of

conformations, and these all have a lower docking score than the comparable binding points in PfAtg8 (Table 4.1). It appears that the differences in this Atg3 AIM docking region between PfAtg8 and hLC3 could be potentially exploited to provide selectivity for inhibition of the parasite PfAtg8-PfAtg3 interaction.

Molecular modelling with compound 1, similarly reveal interesting differences (Fig. 4.19). Hain *et al*., 2014, report a selectivity index of 13.0 for this compound. According to their study, the pyridine group of compound 1 docks into the L-pocket of PfAtg8 and the 4-methylphenyl group projects into the W-pocket. Interestingly, a similar docking simulation for compound 1 against hLC3 was obtained, where the 4-methylphenyl group appear to tend to dock into the W-pocket, with the pyridine group orientated towards the L-pocket. Whilst the docking scores for the top docking poses for each binding points in PfAtg8 and hLC3 do not show the same clear difference that they do for SK1.49 (Table 4.1). The very different predictions of orientation of binding between SK1.49 and compound 1 may provide the basis for selectivity of compound 1 against *P. falciparum* over HepG2.

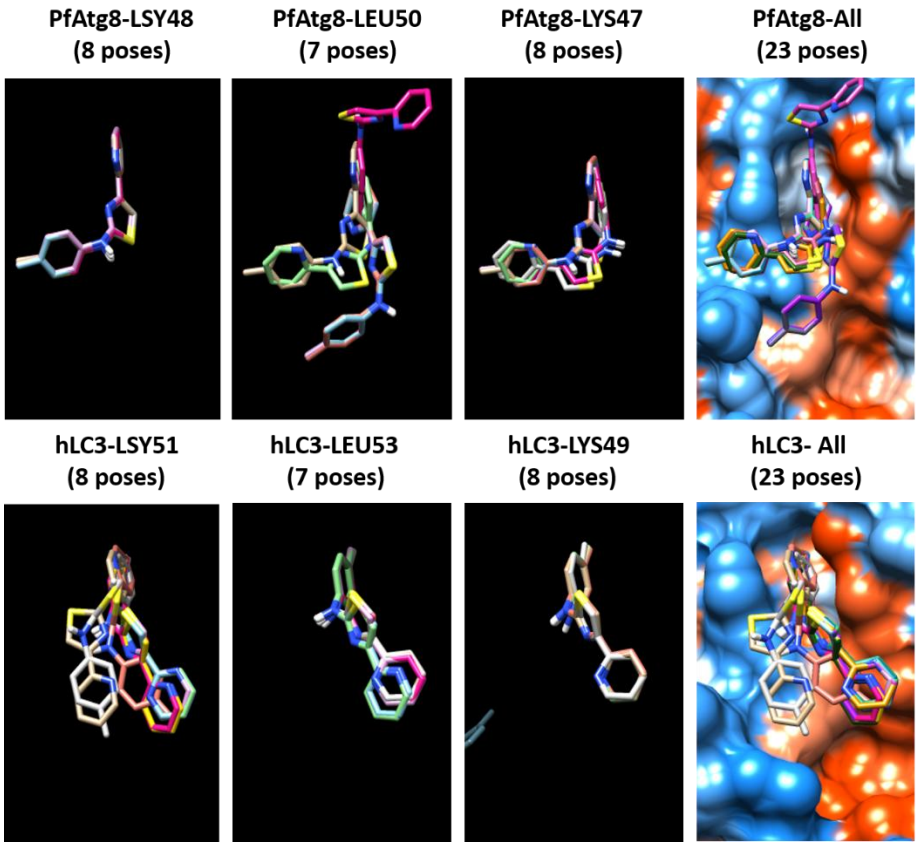

Fig. 4.19 Docking of compound 1 to PfAtg8 (top panels) and hLC3 (bottom panels). Panels left to right represent the top scoring docking pose to the eight or seven binding points present in LYS47/48 and LEU50 for PfAtg8 and their homologous binding centres LYS49/51 and LEU53 in hLC3. A final merged image that includes the model of PfAtg8 or hLC3. The W-pocket at the top and the L-pocket at the bottom.

4.3 Conclusions

The docking simulations of the library compounds over the PfAtg3 AIM docking region of PfAtg8 were assayed based on the hypothesis that these compounds bind within this region and act as protein-protein inhibitors. These docking models have provided information about the likely orientation of these compounds across the W and L-pockets within PfAtg3 AIM region of PfAtg8, a suggestion of a correlation between better docking scores and *in vitro* antiplasmodial activity as well as alternative models of ligands docking to hLC3 that may reflect the selectivity against *P. falciparum*. This observations, however, need to be supported by further analysis using either pull-down assays or SPR to explore

whether these compounds compete with PfAtg3 AIM peptide to interact with PfAtg8 (Hain *et al*., 2012; 2014; 2016). Initials support that the Mcule software developed ligand binding models comparable to those used in previous studies using the alternative software package OpenEye (Hain *et al*., 2014) suggested that comparable, but not exact, models could be developed. These library compounds were provided to our research team by Dr Johannes Reynisson, an expert in molecular modelling. To provide additional support for our key predictions about the location and orientation of library compound binding to PfAtg8, his team provided models of SK1.49 and SK1.109 binding to the PfAtg3 AIM docking region of PfAtg8 using a third ligand docking software, GOLD (Fig. 4.20).

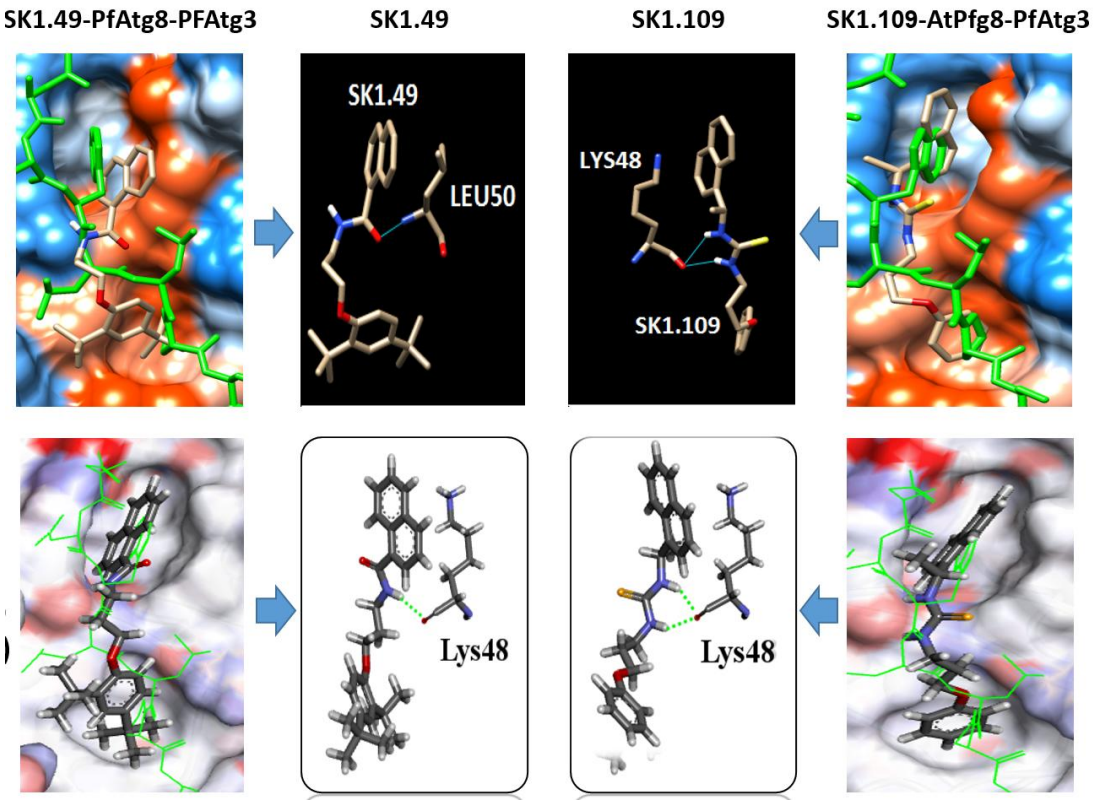

Fig. 4.20 Comparison of Mcule (upper panels) and GOLD (lower panels) models of SK1.49 and SK1.109 docking to PfAtg8. The upper panels are data developed in this study, the lower panel images provided by Dr. Reynisson's team. To the left are docking predictions with SK1.49 and to the right simulations with SK1.109. In each case, the docking of the compound to the W and L-pockets is shown with the PfAtg3 AIM peptide in green. The central panels show only a stick form of the compound, with predicted H-bonds to the indicated binding centre of PfAtg8.

Interestingly, the molecular docking in GOLD using SK1.49 and SK1.109 showed similar simulation to that obtained by Mcule. These include the docking of the naphthalene group into the large W-pocket for both molecules, while a trimethyl group from SK1.49 projected into the L-pocket, and the amine groups form H-bonds with the indicated binding centres (although as shown for SK1.49 these H-bonds do not always go to the same binding centre) (Fig. 4.20).

These modelling predictions can now be used to explore the relative activity of related compounds screened in Chapter 3. Hopefully, we be able to determine information which can be used subsequently to make structural modifications to optimize binding and enhance activity. The first aspect of this structure activity relationship is the length of amine/alkyl linker region between the two hydrophobic ends with prediction that these hydrophobic ends to dock into the W and L-pockets. This was clearly observed when compare four pairs of related compounds that differ only in the length of linker region (Fig. 4.21). In all cases, the compound with the longer linker region was more potent than the shorter counterpart. These data suggest that the linker region needs to be of sufficient length to provide efficient orientation for the hydrophobic ends to dock into the W and L-pockets.

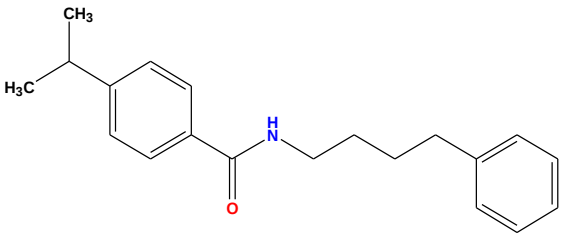

7221498 (Dd2 EC_{50}= 19.6 µM)

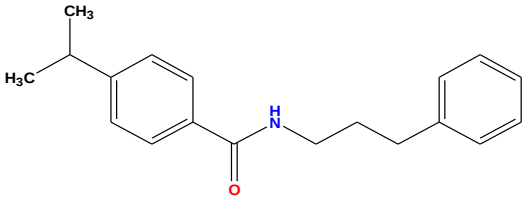

7311494 (Dd2 EC_{50}= 42.2 µM)

(6 atoms linker > 5 atoms linker)

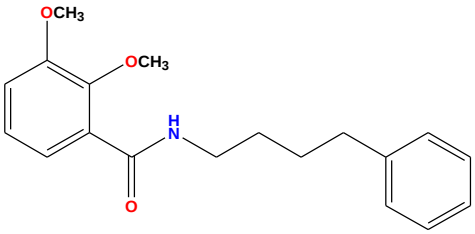

LO9 (Dd2 EC_{50}= 12.5 µM)

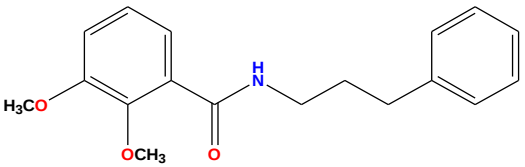

7737951 (Dd2 EC_{50}= 39.3 µM)

(6 atoms linker > 5 atoms linker)

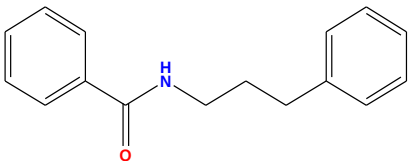

6115259 (3D7 EC_{50}= 42.3 µM)

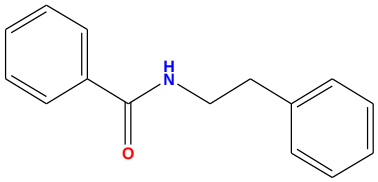

NKLA-98 (3D7 EC_{50}= > 50 µM)

(5 atoms linker > 4 atoms linker)

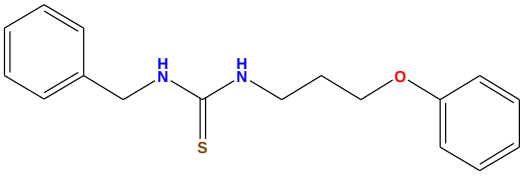

SK1.102 (Dd2 EC_{50}= 18.9 µM)

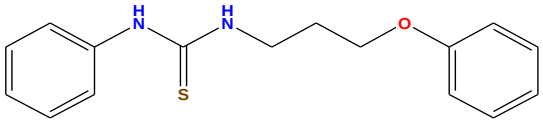

SK1.101 (Dd2 EC_{50}= 29.9 µM)

(8 atoms linker > 7 atoms linker)

Fig. 4.21 Exploring the structure activity relationship of alkyl linker length. Structure of compound with antiplasmodial activity (EC50) are reported.

The docking data for SK1.63 indicated that the role of a halogen substitution on the phenyl group apparently competing in the docking predictions with the naphthalene group for the W-pocket. The compound library contained a number of related halogen substituted compounds which can be used to explore the potential effect of steric hindrance of the halogen substitutions in docking into the W and/or L-pockets. The

following three compounds (Fig. 4.22) all share a halogen substitution at the same para-position on the phenyl group closest to the amine group in the linker. There is an inverse relationship between the size of the halogen substitution (F, 19.0 < Cl, 35.4 < Br 79.9) and their potency, which may reflect that the smaller halogens are able to fit into the W or L-pocket of PfAtg8.

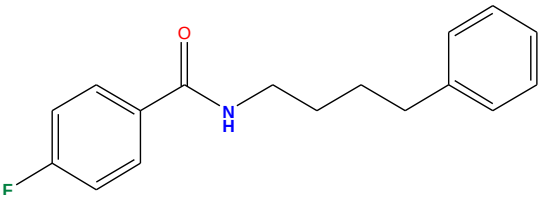

5335716 (3D7 EC_{50}= 17.3 µM)

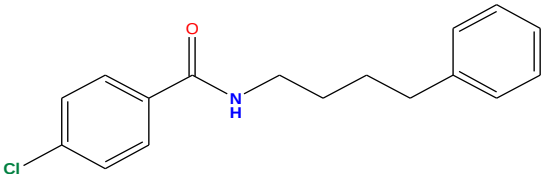

5337355 (3D7 EC_{50}= 32.2 µM)

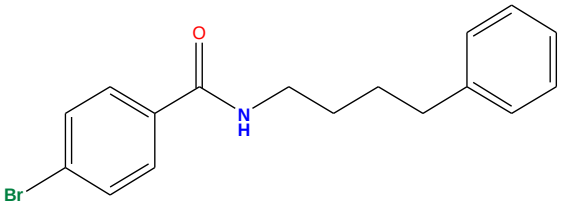

5334050 (3D7 EC_{50}= 37.8 µM)

(para-fluorophenyl > para-chlorophenyl > para-promophenyl)

Fig. 4.22 Exploring the structure activity relationship of para-substituted halogens. Structure of compound with antiplasmodial activity (EC_{50}) are reported.

This potential for steric hindrance in docking to the W and L-pockets is also reflected in comparisons of the next three groups of related halogen substituted phenyl rings (Fig. 4.23). All the three compounds share a bromo-substituted phenyl group, although the position of this substitution is different.

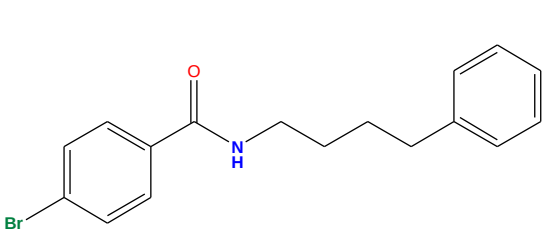

5334050 (3D7 EC_{50}= 37.8 µM)

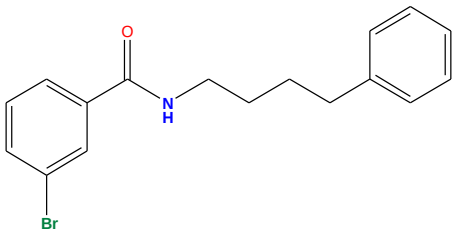

5328241 (3D7 EC_{50}= > 50 µM)

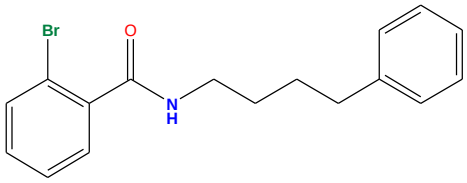

5328083 (3D7 EC_{50}= > 50 µM)

(para-bromophenyl > meta-bromophenyl > ortho-bromophenyl)

Fig. 4.23 Exploring the structure activity relationship of the position of bromo substitutions. Structure of compound with antiplasmodial activity (EC_{50}) are reported.

Here the para-orientation may be considered to be more likely to fit into the W-pocket, with the ortho- and meta-orientations less active if the position of the halogen group offers some steric hindrance to this docking. This observation is also apparent in two additional pairs of compounds (Fig. 4.24), all of which show greater potency when the halogen is placed at the para position.

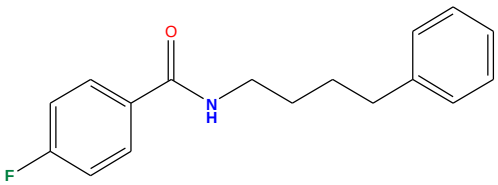

5335716 (3D7 EC_{50}= 17.3 µM)

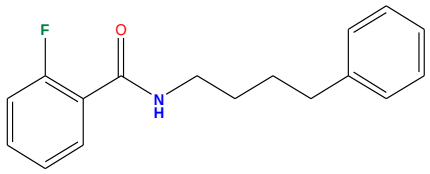

5329246 (3D7 EC_{50}= 85.6 µM)

(para-fluorophenyl > meta-fluorophenyl)

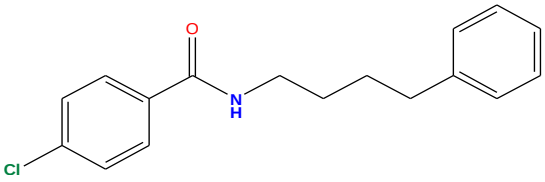

5337355 (3D7 EC_{50}= 32.2 µM)

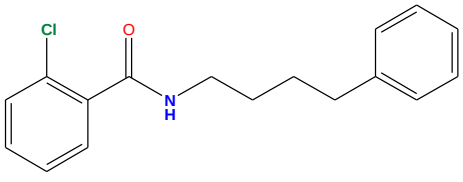

7260078 (3D7 EC_{50}= 44.0 µM)

(para-chlorophenyl > meta-chlorophenyl)

Fig. 4.24 Exploring the structure activity relationship of the position of fluoro and chloro substitutions. Structure of compound with antiplasmodial activity (EC_{50}) are reported.

In terms of project a naphthalene group into the W-pocket, there appears to be a preference for the α-naphthalene over the β-naphthalene, as illustrated best between SK1.49 and SK1.47 (Fig. 4.25). The other active compounds, SK1.108, SK1.109 and SK1.63 all share the same α-naphthalene orientation. One additional pair of structurally related compounds, SK1.50 and SK1.53, that differ only in the orientation of the naphthalene group also demonstrate a slightly higher potency for the α-naphthalene orientation.

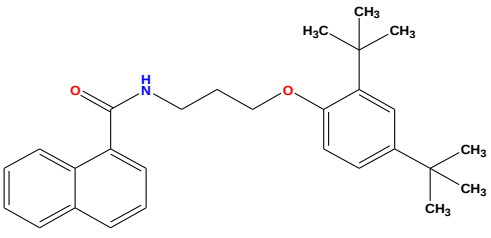

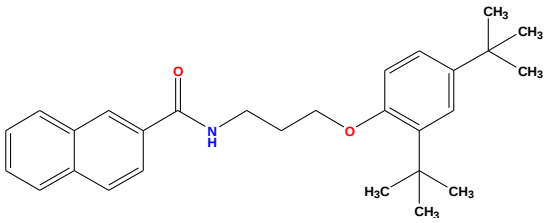

SK1.49 (Dd2 EC_{50}= 1.1 µM) **SK1.47** (Dd2 EC_{50}= 2.1 µM)

SK1.49 (3D7 EC_{50}= 0.8 µM) **SK1.47** (3D7 EC_{50}= 1.6 µM)

(α- naphthalene > β-naphthalene)

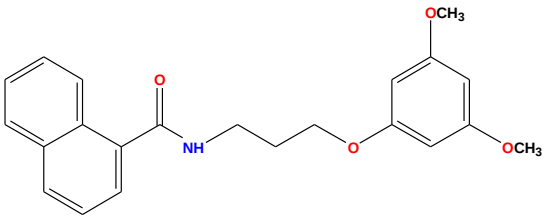

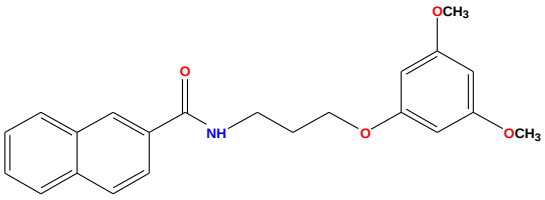

SK1.50 (Dd2 EC_{50}= 18.7 µM) **SK1.53** (Dd2 EC_{50}= 26.1 µM)

(α- naphthalene > β-naphthalene)

Fig. 4.25 Exploring the structure activity relationship of α and β-naphthalene moieties. Structure of compound with antiplasmodial activity (EC_{50}) are reported.

From modelling above, it appears that need to design compounds with two hydrophobic ends and linker regions to interact across PfAtg3 AIM binding site on PfAtg8. Comparison of the antimalarial activities of SK1.49 and SK1.70 suggests that modifications to the hydrophobicity or substitution of phenyl ring may increase potency of compound. SK1.70 lacks the trimethyl substitutions to the phenyl group that found in SK1.49 – and as such has a LogP of 3.7 compared to a LogP of 7.5 in SK1.49 (Fig. 4.26). It may be that the increased hydrophobicity of the phenyl group in SK1.49 – along with the projection of the hydrophobic trimethyl group deep into the L-pocket is important for the higher potency of this compound.

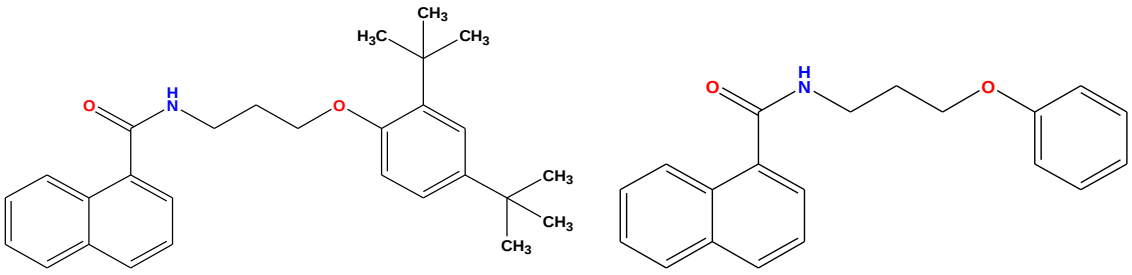

SK1.49 (Dd2 EC_{50}= 1.1 µM)

SK1.70 (Dd2-EC_{50}= 13.4 µM)

Fig. 4.26 Exploring the structure activity relationship of trimethyl substitutions. Structure of compound with antiplasmodial activity (EC_{50}) are reported.

SK1.108 and SK1.109 are stereoisomers (enantiomeric forms) with the stereocenter located over the carbon immediately next to the naphthalene group (Fig. 4.27). Apparently there is no effect of this stereoisomerism on the compound potency.

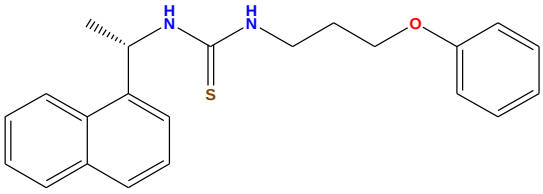

SK1.109 (Dd2 EC50= 5.0 µM)

SK1.109 (3D7 EC50= 4.5 µM)
(S-enantiomeric form)

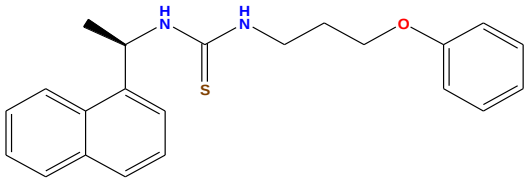

SK1.108 (Dd2 EC50= 6.2 µM)

SK1.108 (3D7 EC50= 3.9 µM)
(R-enantiomeric form)

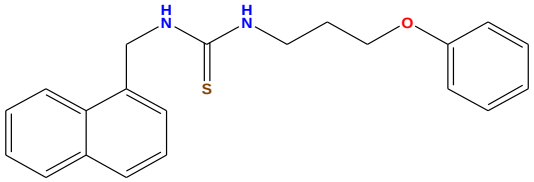

SK1.106 (Dd2 EC50= > 50 µM)

(Non-enantiomeric form)

Fig. 4.27 Exploring the structure activity relationship of enantiomeric compounds. Structure of compound with antiplasmodial activity (EC_{50}) are reported.

However, comparison of these compounds with the non-enantiomeric SK1.106 does suggest that some modification of the carbon next to the naphthalene group increase the potency of the compound. In this context, all the most active compounds (SK1.47, SK1.49 and SK1.63) in the library have a keto- group arranged over this position. Whilst no modelling data of SK1.106 was developed here, the potential for the importance of this position is noted.

Considering these observations all together, a summary of the key observations can be suggested (Fig. 4.28) and these include;

(i) Use naphthalene, or other large hydrophobic centre, is used to occupy the W-pocket.

(ii) The length of alkyl linker between amine group and O atom is preferably greater than 3 carbons in length provides effective occupation to the region between the W and L-pockets.

(iii) The amino group within the linker is important for H-bond formation.

(iv) The carbon link between the naphthalene group and the amine group needs to explore the nature of substitutions here (R) noting the potential to form a stereocenter at this position.

(v) The role of the oxygen at the end of the linker chain needs to be carefully considered as it may affect the angle at which a R1 substituted phenyl group will approach the L-pocket.

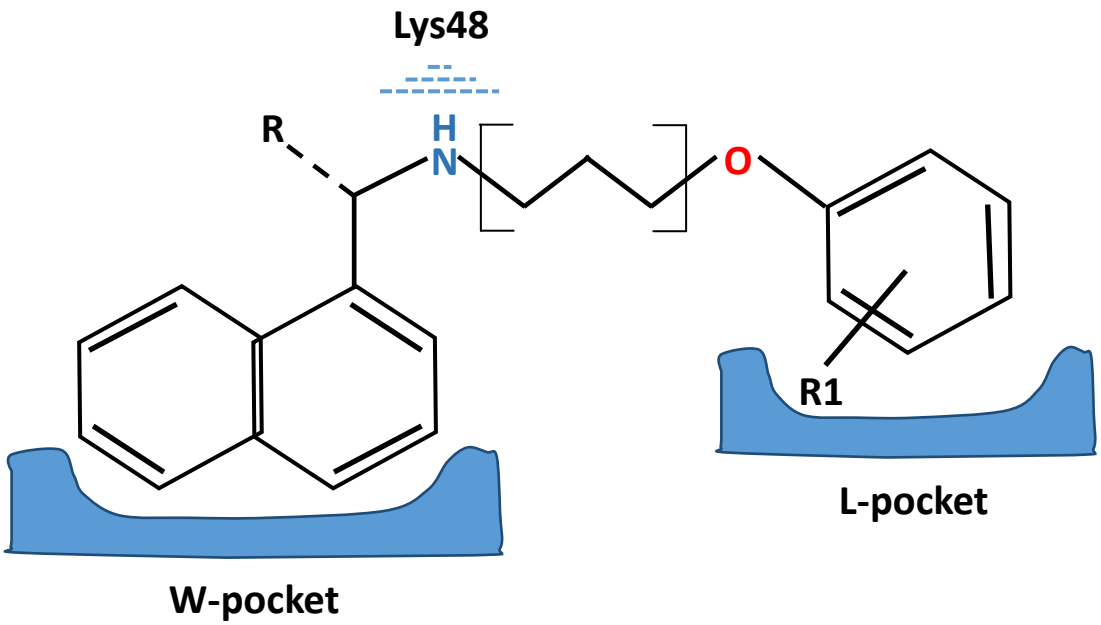

Fig. 4.28 Schematic illustrating key structure activity relationship data developed in this study. A generic lead compound is docked into the W and L-pockets of PfAtg8 with H-bond being made to the LYS48 residue. R and R1 represent positions that require additional study (see main text).The enclosed region of the alkyl linker is considered the minimum to enable docking of the hydrophobic ends into the W and L-pockets.

(vi) The role of O that is closest to phenyl group may determine the angle of projection of this end (phenyl ring) into L-pocket.

(vii) The hydrophobicity and position of substitutions on the phenyl group need to be explored in terms of their potential to dock into the L-pocket.

These observations can be used to support a new way forward to developing a compound that could be considered a lead for development. Based on this information, *in silico* modifications to this scaffold can be generated, with potentially thousands of compounds screened in molecular docking studies. The principle for the success of this approach was demonstrated by Hain *et al*. (2016) who used such an approach to screen the ChemBridge library to discover ACL25. The distinction here is that we would have a core scaffold against which to make modifications.

Small modifications on the scaffold above were performed to explore the potential of this approach. As a result, four compounds were generated *in silico* (Fig. 4.29). These modifications were included a slightly increase in the length of linker chain and addition of a pyridine ring within the linker which may enhance the binding ability of new compounds by reduction the of routable bonds and providing additional hydrogen donating site as well as halogenation of phenyl ring using trifluoromethyl which contributed in reduction of the LogP of the compounds to < 5 to follow Lipinski's RO5 (Table 4.3). These compounds were also assayed to explore the effect of the positioning of a trifluoromethyl substitution on the phenyl group – and how this would affect docking into the L-pocket.

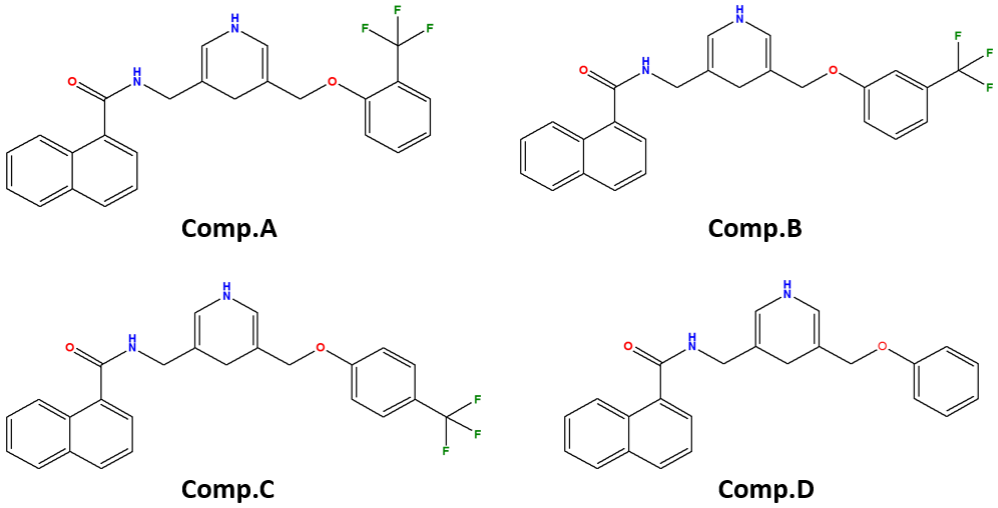

Fig. 4.29 Test series of compounds designed *in silico* using the generic template.

Importantly, all the physicochemical properties of these test compounds suggested that they all contain drug-like properties (Table 4.3). LogP of all compounds were lowered from 7.5, which found in SK1.49, to 4.8 or lower. The molecular weight remained under 500, whereas NBA and NBD are both under 5. Additionally, the NROTB and TPSA are ≤ 10 and ≤ 140 $Å^2$, respectively. Interestingly, these features are all in agreement with Lipinski's RO5 and Veber's rules (Table 4.3) (Lipinski *et al.*, 1997; Veber *et al.*, 2002).

Compound ID	MW[1]	HBA[2]	HBD[3]	LogP[4]	TPSA[6] ($Å^2$)	NROTB[7]	Vol.[8] ($Å^3$)	Lipinski's RO5	Veber's rules
Comp.A	438.4	4	2	4.8	50.3	7	377.9	Pass	Pass
Comp.B	438.4	3	1	4.8	50.3	8	377.9	Pass	Pass
Comp.C	438.4	4	2	4.8	50.3	7	377.9	Pass	Pass
Comp.D	370.4	4	2	3.8	50.3	6	346.6	Pass	Pass

Table 4.3 Physicochemical properties of 4 new suggested compounds (A, B, C and D). These include; [1]Molecular weight (MW), [2]Number of H-bond acceptor (HBA), [3]Number of H-bond donor (HBD), [4]Log partition coefficient, a measure of lipophilicity (LogP), [5]Total polar surface area (TPSA),[6]Number of rotatable bond (NROTB), [7]Molecular volume. The final two columns indicate whether they meet the RO5 or Veber's rules criteria for predicted bioavailability.

Each compound was docked in Mcule against PfAtg8 using only the LYS48 binding centre for this short evaluation – although all binding points were tested (8 binding points) (Fig. 4.30). The orientation of the top scoring docking poses for each binding point reveal that compounds C and D always placed by their naphthalene groups in the W-pocket – however, the positioning of the trifluoromethyl group at either the ortho- or meta-positions potentially obstructed the insertion of this group into the L-pocket (which is always clearly observed for the para-position) and led to the substituted phenyl groups being positioned in the W-pocket. This data suggests that compound C may bind more consistently in the same orientation in the docking simulations and this, as well as the better docking scores for compound C (Table 4.4), would suggest this compound would be of the most interest in these four for synthesis and testing in *in vitro* assays.

Target (PfAtg8)									
Binding points in LYS48									
Comp. ID	N-380	C-382	O-383	C-384	C-385	C-386	C-387	N-388	Mean
Comp.A	-8.9	-9.0	-8.9	-8.9	-8.9	-8.8	-8.6	-8.5	-8.81
Comp.B	-8.8	-8.6	-8.8	-8.5	-8.6	-8.7	-8.3	-8.2	-8.56
Comp.C	-9.2	-8.9	-9.0	-9.2	-8.9	-8.9	8.6	8.5	-8.90
Comp.D	-7.6	-7.9	-7.8	-7.7	-7.6	-7.9	-7.5	-7.6	-7.70

Table 4.4 Docking scores of the top docking poses for Compounds A, B, C and D using the LYS48 binding centre in PfAtg8. Note that poses that predict a H-bond are highlighted in green.

Whilst only a short evaluation, the intention was to demonstrate how the generic predicted scaffold for the interaction of these library compounds with PfAtg8 could be adapted to explore issues around hydrophobicity, linker length and positioning of substitutions to the phenyl ring can be explored relatively quickly. Certainly, a high

throughput modelling exercise could be used to consider a larger number of binding centre as well as greater modifications to the generic scaffold. In addition, and exploiting the idea of Hain *et al.* (2016), exploring how compounds may be developed that bridge to the A-pocket from the Atg3 AIM binding sites may lead to potent and selective compounds that block PfAtg3-PfAtg8 interactions.

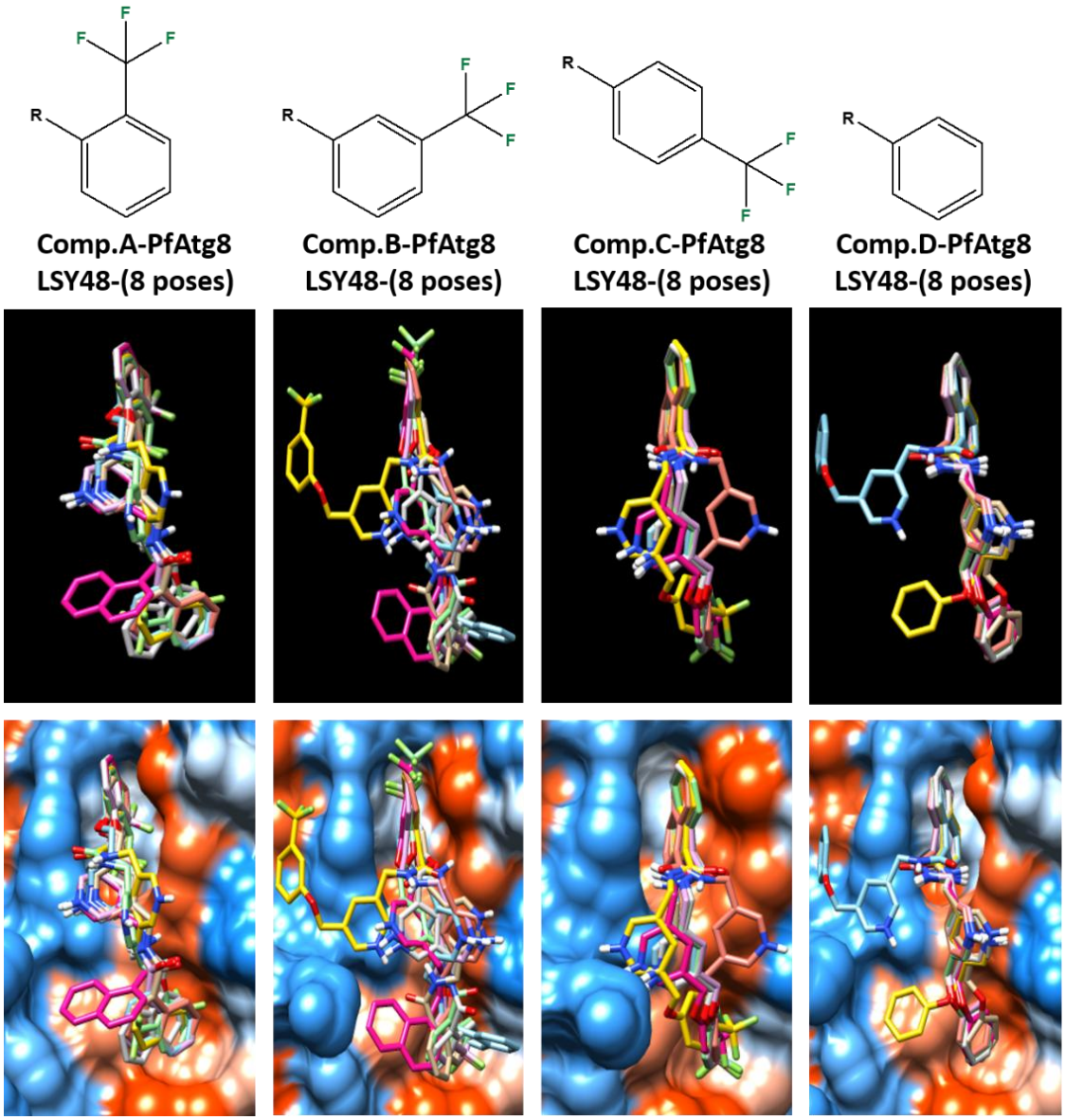

Fig. 4.30 Docking of compounds A to D against PfAtg8. Molecular docking of each compound with the eight highest top scoring docking poses for binding points in LYS48 are projected. Top panels show the ligands in stick form with PfAtg8 omitted, this is then added in the lower panel to show the W-pocket at the top and L-pocket at the bottom.

Chapter 5: Exploring changes to the ultrastructure of intraerythrocytic P. falciparum following an equipotent drug challenge

5.1 Introduction

Improvement in the ultrastructural imaging techniques such as cryo-electron microscopy, atomic force microscopy and technical protocols in processing time-lapse data over the last ten years allows to widely study the development of *P. falciparum* following drug treatment (Cyrklaff *et al*., 2017; Johnson *et al*., 2017; Riglar *et al.,* 2011). Studies of drug action against intraerythrocytic parasites using TEM have been used for some thirty years – with Table 5.1 highlighting a number of these studies. TEM analysis of ultrastructural changes under normal and drug stress have provided insights into consecutive events that occur on action site of drugs which can be assisted to explore the mechanism of action of antimalarial drugs at the cellular level (Ch'ng *et al.,* 2011; del Pilar Crespo *et al.* 2008; Hoppe *et al.,* 2004; Chen *et al.,* 2000; Roberts *et al.,* 2008; Sachanonta *et al.,* 2011).

These studies of drug action are typically compared against untreated parasites, and usually focus on the trophozoite stage (Fig. 5.1 and 5.2). Here, the dominant feature of the parasite is the DV which has a uniform electron density, with evident electron dense puncta representing haemozoin (Hz) crystals within a continuous membrane. The cytoplasm of the parasite is heavily decorated with a dotted appearance, representing extensive arrangements of ribosomes throughout the cytoplasm. The nucleus typically has the same electron density as like as the cytoplasm, and is determined by its nuclear membrane (Fig. 5.1).

Author	Parasite strain/stage[1]	Method	Stimulus (Concentration/Time)	Key features
Zhang and Just (1987)	FCB strain / trophozoite	TEM	CQ (10µM/45min) Ammonium chloride (20mM/2hrs)	Accumulation of endocytic vesicles (EV) only inside digestive vacuole (DV), alkalization of DV, CQ did not interfere with haemozoin (Hz) formation at high concentration. CQ-like effects showed by ammonium chloride.
Wu *et al.* (1988)	NIH-7G8 strain / trophozoite	TEM	PYRD (1µM/ 30min/24hrs)	Accumulation of EV inside DV (membranous whorls), DV was devoid of Hz crystals, swollen mitochondria and endoplasmic reticulum (ER), ribosomal depletion and necrotic features in some cells were observed.
Kawai *et al.* (1996)	SGE1 / trophozoite propagated in owl monkey	TEM	PYRD (40mg/kg of body weight) 4-6hrs	Significant changes in DV size, reduction of Hz crystals, mitochondrial dilation and accumulation of undigested EV inside DV.
Chen *et al.* (2000)	ANKA strain of *P. berghei* / hepatic stages	TEM	DHA (ED_{50}/4-8hrs)	Loss in DV membrane integrity, EV numbers slightly increased, evidence of ribosomal depletion, reduction in mitochondrial membrane integrity.
Hoppe *et al.* (2004)	D10 strain / trophozoite	FITC-dextran and anti-haemoglobin using phase-contrast Microscopy and TEM	CQ (120nM) QN (1µM) Artemisinin (110nM) MQ (60nM) Ammonium chloride (20mM) For 8hrs	All treatments caused loss in DV membrane integrity, an increase in number of cytoplasmic located EV by CQ and Ammonium chloride treatment, whilst QN, MQ and artemisinin treatment reduced EV numbers.
Porter *et al.* (2008)	CSC1 strain/ trophozoite	TEM	40 ℃ (6hr) CQ (100µM/4hrs) Staurosporine (5µM/5hrs)	Swelling of DV in all treated samples, increase in translucent cytoplasmic EV and accumulation of undigested EV inside DV in CQ-treated samples.

Roberts *et al*. (2008)	3D7 strain / trophozoite	Anti-haemoglobin using immunofluorescence microscopy	CQ AQ QN MQ (all 5XIC$_{50}$/8hrs)	Increase of EV numbers in CQ and AQ-treated samples, reduction of EV in QN, MQ-treated samples. Increase of haemoglobin level in CQ-treated sample while reduced in other drug-treated samples.
del Pilar Crespo *et al.* (2008)	D10 strain / ring and trophozoite	TEM	Artemisinin 40XIC$_{50}$/8hrs in trophozoite stage Artemisinin 2XIC$_{50}$/24hrs in ring	Both treatments caused loss in DV membrane integrity, EV and Hz crystal numbers unchanged after 8 hrs, slight increase in numbers of EV and reduction in Hz level after 24 hrs.
Totino *et al.,* 2008	PSS1 strain/ trophozoite	TEM	CQ (180nM) SNAP (360µM) Staurosporine (4µM) For 24hrs	All drugs showed increase of EV in the parasite cytoplasm.
Sachanonta *et al.* (2011)	AK121 strain / trophozoite	TEM	Artesunate (60mg/mL) QN (300mg/mL) PPQ (300mg/mL) (4-8hrs)	Swelling of DV in PPQ-treated parasites, whereas relatively small DV in artesunate-treated parasites, reduction of Hz crystals with ribosomal depletion in all treated samples, swollen mitochondria in QN-treated sample only, and EV vesicles accumulated inside DV in PPQ-treated sample, dilation of PV in artesunate-treated samples.
Ch'ng *et al.* (2011)	3D7 strain / trophozoite	TEM	CQ (3µM/4hrs)	Intact DV membrane with discrete Hz crystals and undigested EV accumulated inside DV. Some cells showed disruption in DV membrane and Hz crystals being dispersed into cytoplasm.
Klonis *et al.* (2011)	3D7 strain / trophozoite	FITC-dextran using immunofluorescence microscopy and FACS	Artemisinin (IC50= 95nM/24hrs) (1µM/24hrs)	EV reduced in parasite cytoplasm. Haemoglobin uptake reduced.

Tomlins *et al* (2013)	3D7 D10 Strains of *P. falciparum*/ trophozoite	Fluorescence microscopy, western blot and immuno-TEM	Starvation	Number of PfAtg8 puncta and EV increased
Eickel *et al.* (2013)	ANKA strain of *P. berghei/* Liver stages	Fluorescent microscopy and TEM	Rapamycin (0.5µM)	Number of PfAtg8 puncta did not change, but EV number increased.

Table 5.1 Studies that have explored ultrastructural changes of *P. falciparum* parasite challenged with antimalarial drugs at different concentrations and exposure times. Endocytic vesicle (EV), digestive vacuole (DV), haemozoin (Hz), endoplasmic reticulum (ER), transmission electron microscopy (TEM). [1] unless otherwise indicated, these are studies reported in *P. falciparum.*

Other features include; spherical electron-dense vesicles located within the cytoplasm, and usually termed endocytic vesicles (EV) were observed (del Pilar Crespo *et al.,* 2008). Mitochondria, when observed, are elongated tubes with no evidence of cristae (Fig. 5.1).

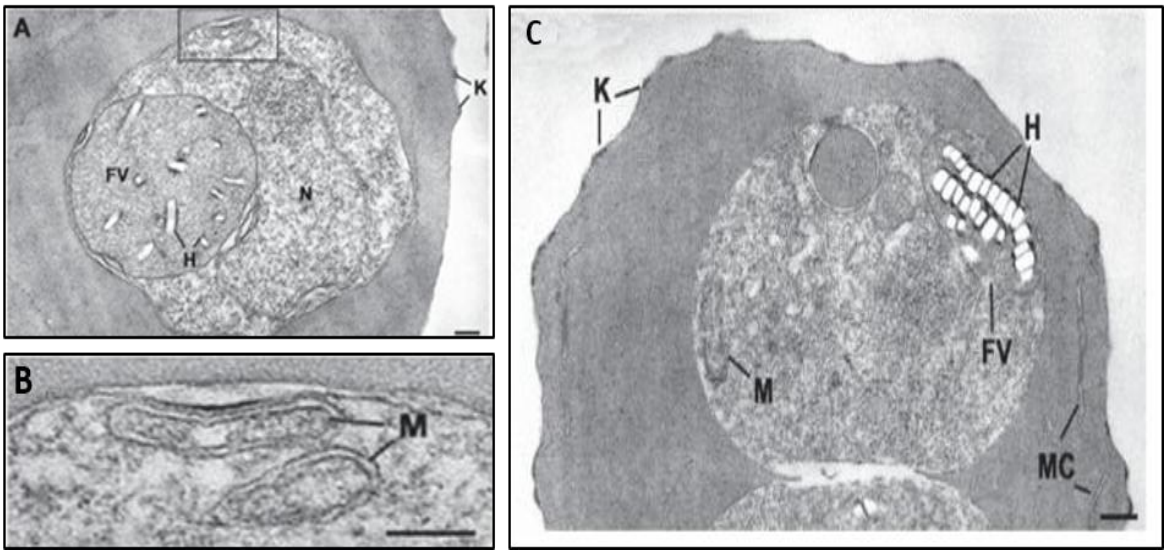

Fig. 5.1 Ultrastructural morphology of untreated trophozoite stage of *P. falciparum*. These include; digestive vacuole (termed food vacuole FV here, **A** and **C**) containing haemozoin crystals (H, **A** and **C**), nucleus (N, **A**), elongated mitochondria (M ,**B** and **C**). Parts **A** and **C** also show Maurer's clefts (MC) under RBC plasma membrane and knobs (K) on the exofacial surface of iRBC (Source: Sachanonta *et al.,* 2011). The bar in 200nm.

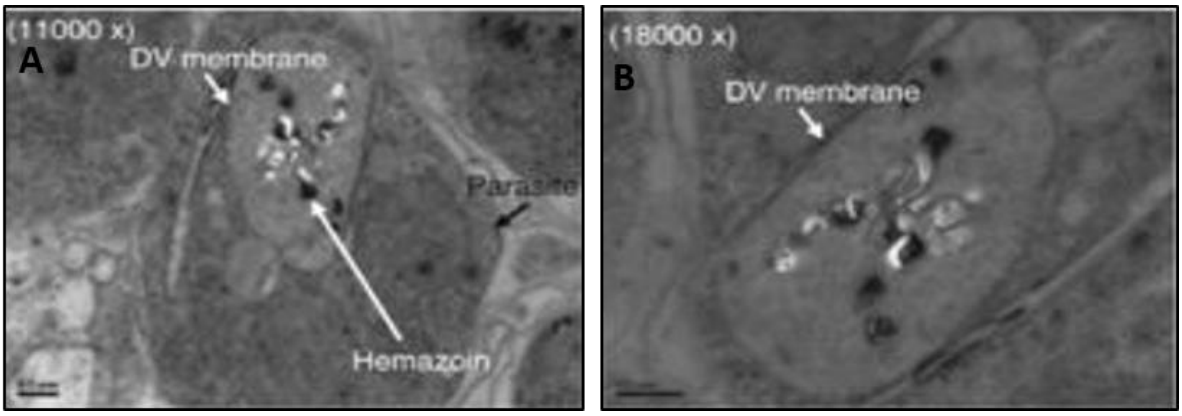

Fig. 5.2 TEM micrographs of untreated trophozoite stage of *P. falciparum* (A) and (B) illustrating intact digestive vacuoles (DV) membranes enveloping a uniformly dense compartment decorated with haemozoin crystals. The scale bars show 0.5 µm units for X11,000 and X18,000 magnifications (Source: Ch'ng *et al.,* 2011).

Although studies of ultrastructural changes following drug-treatment provide various outcomes in the observations seen (Table 5.1), they do agree on one key point – there is no evidence of necrotic, or unregulated, cell death following drug treatment. This is due to the absence of gross swelling of organelles, no gross loss of structural integrity including blebbing and not complete loss of membrane bound structures in all the studies undertaken. Furthermore, there is no consistent evidence of apoptotic cell death. Totino *et al* (2008) used CQ, staurosporine (as an inducer of apoptosis) as well as a nitric oxide donor S-nitroso-N-acetyl-penicillamine (SNAP) to induce cell death and explored whether the changes in nuclear morphology consistent with chromatin condensation (i.e. changes in nucleus shape, size or uniformity in electron density) occur. This study did not indicate the observations above, although cytoplasmic vacuolation (the name endocytic vesicle also used, and used in this thesis) was shown in all three treatments, with cytoplasmic vacuolation consistently described in a number of studies using CQ (Hoppe *et al.,* 2004; Ch'ng *et al.,* 2011; Porter *et al.,* 2008; Zhang and Just 1987). On this basis, Totino *et al* (2008) suggested that all these treatments resulted in a similar autophagic-like cell death. However, a different study that included staurosporine and CQ treatments did not report any changes in cytoplasmic vacuolation, but instead reporting that both treatments resulted in DV swelling and, in somecases, rupture (Porter *et al.* 2008).

Ultrastructural studies have mainly focussed on the action of CQ, and its effects on the DV in particular (Ch'ng *et al.,* 2011; Hoppe *et al.,* 2004; Porter *et al.,* 2008; Totino *et al.,* 2008; Zhang and Just 1987). Together these studies provided some consistent observations (Fig. 5.3). CQ exposure results in an increase in the number of cytoplasmically located endocytic vesicles. These vesicles can sometimes be observed in the DV where they termed membranous whorls (Fig. 5.4). Within the DV, haemozoin crystals become less

defined and are reduced in number, with breaches of the DV membrane occasionally observed leading to leackage of the less electron-dense DV contents into the more electron-dense cytoplasm (Fig.5.4) (Ch'ng *et al.,* 2011).

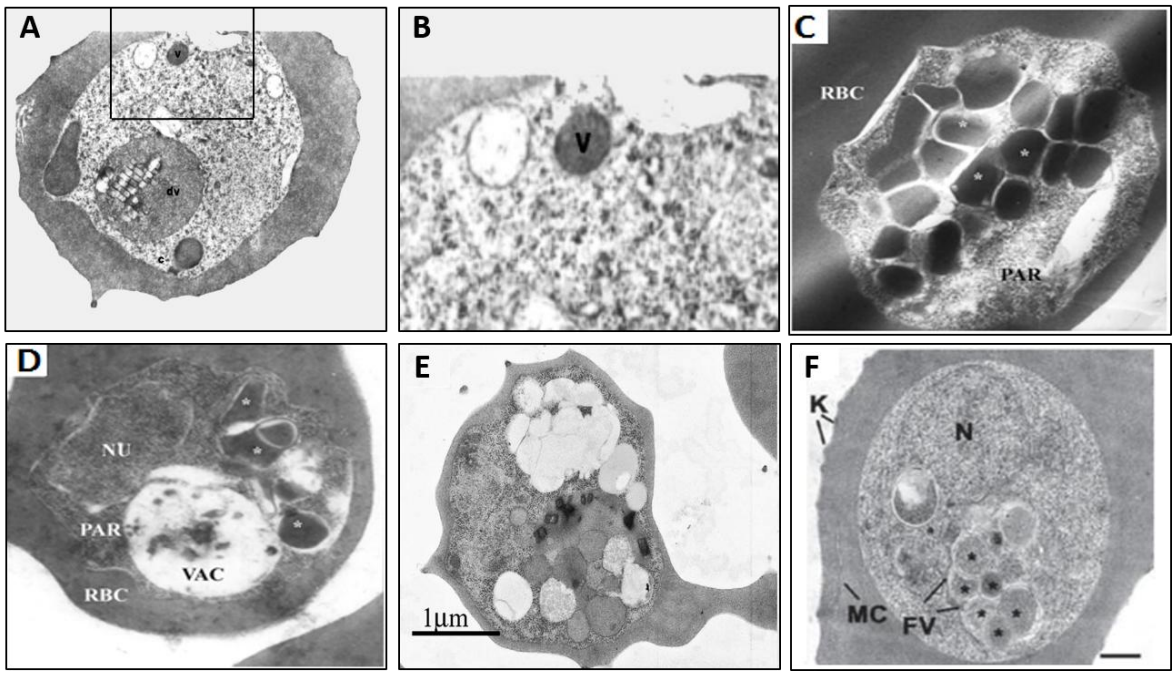

Fig. 5.3 Transmission electron micrographs of untreated and drug-treated trophozoite stages of *P. falciparum*. (A) and (B) Untreated trophozoite stages of *P. falciparum* exhibits digestive vacuole (dv) and within the inset a higher magnification of a cytoplasmic vesicle (v) thought to contain haemoglobin from the host erythrocyte. This structure sometimes referred to as a cytosome. (Source: Goldberg *et al*., 1990). (C) and (D) CQ-treated parasites (120nM/12hrs) shows electron-dense vesicles (white stars) distributed in the parasite cytoplasm (Source: Hoppe *et al.,* 2004). (E) CQ-treated parasite (100µM/4hrs) shows translucent vesicles (white vesicles) distributed in the parasite cytoplasm with electron-dense vesicles (grey vesicles) located within the DV. (Source: Porter *et al*., 2008). (F) PPQ-treated parasite (300mg/mL for 8hrs) shows the same accumulation of electron-dense vesicles in the DV (*). Note also the Maurer's cleft (MC) and knobs (K) under iRBC plasma membrane and on the surface of iRBC, respectively, and the nucleus (N). (Source: Sachanonta *et al.,* 2011).

Perhaps the best quantitative study of morphological changes is that performed by Sachanonta *et al.* (2011). Here, *P. falciparum* were exposed to artesunate, QN or PPQ at concentrations typically found in human serum– with 300 micrographs analysed for each drug treatment. Features common to all treatments included a reduction in haemozoin

crystal counts and patches of apparently ribosome-free cytoplasm (now appear as electron-translucent areas) (Fig. 5.3F). These observations were previously indicated by Wu *et al.* (1988) in PYRD-exposed parasites. A marked observation was the extensive accumulation of membranous whorls in the DV of PPQ-treated parasites (Fig. 5.3F), similar to those seen when trophozoites are exposed to high concentrations of CQ (Fig. 5.3E), although without the accompanying electron-translucent vesicles in the cytoplasm. A specific effect of artesunate treatment was a swelling of the parasitophorous vacuole, with clear space defined between the parasite and the host erythrocyte cytoplasm (Fig. 5.5).

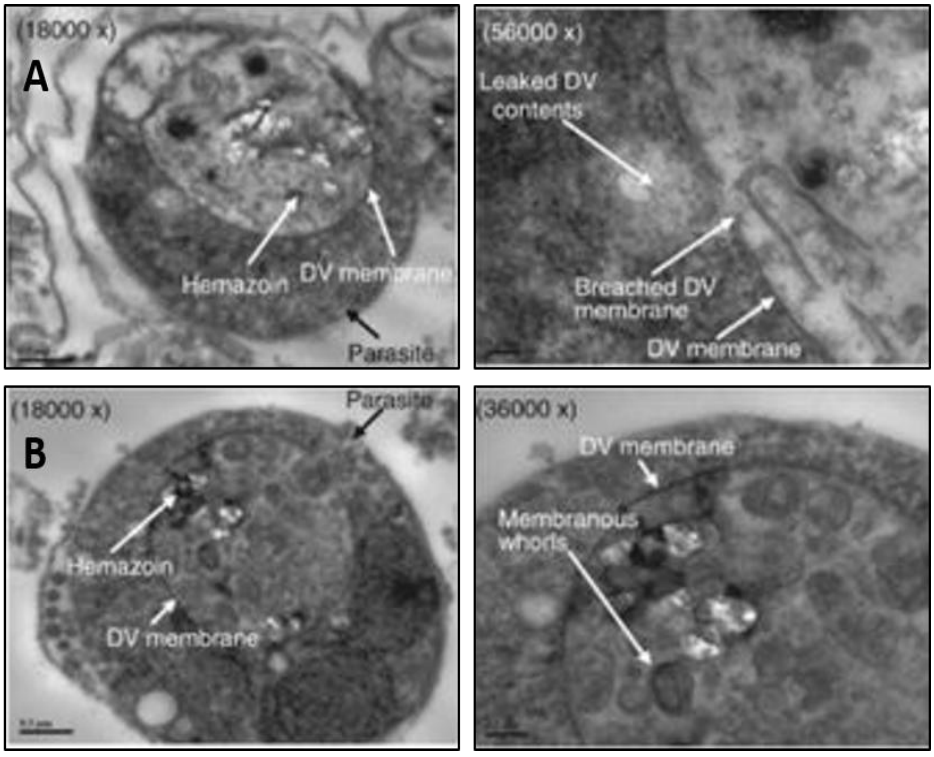

Fig. 5.4 Transmission electron micrographs of intraerythrocytic trophozoite stages of *P. falciparum* challenged with 3 µM CQ for 4 hrs. (A) Shows reduced levels of haemozoin crystals and compromise to the DV membrane leading to leak of DV materials into the cytoplasm (shown in more detail to the inset image on right). (B) Shows an intact DV membrane, less discrete haemozoin crystals and an accumulation of membranous whorls in the DV (see inset to right).). The scale bars show 0.5 µm unit for X18,000 magnification, 0.2 µm unit for X36,000 magnification and 0.1 µm unit for X56,000 magnification (Source: Ch'ng *et al.,* 2011).

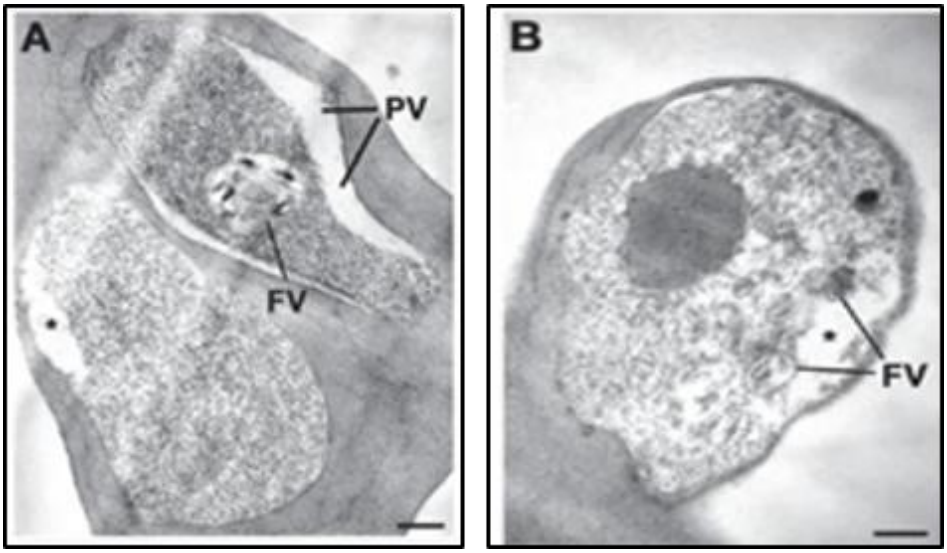

Fig. 5.5 Ultrastructural micrographs of artesunate-treated intraerythrocytic trophozoite stages of *P. falciparum*. (A) and (B) show food vacuoles (FV) containing reduced numbers of haemozoin crystals. (A) illustrates a dilated parasitophorous vacuole (PV) with the same micrograph showing regions of the cytoplasm depleted of ribosomes (*). The bar is 200 nm (Source: Sachanonta *et al.,* 2011).

An overview of these studies reveal a number of issues; (i) they are heavily bias on using one drug – chloroquine, (ii) whilst some inferences can be drawn from the different studies reporting the effect of CQ on the progress of ultrastructural changes, variations in parasite strain, the concentrations of CQ used and the length of exposure are all confounding factors, and (iii) no real attempts, beyond that of Sachanonta *et al.* (2011) have been made to do a comparative study of these treatments and then quantify these structural changes. The key issue in such comparative studies using different drugs is how to define a similar endpoint for the comparative study using drugs with different potencies and different rates of kill. The work done by Ullah *et al.* (2017) in correlating loss of bioluminescence signal with loss of parasite viability has been exploited here to overcome the issue of defining a similar endpoint, and thus facilitating a comparative study of ultrastructure changes. Here, a concentration of drug/compound has been determined that leads to a 50% reduction in parasite viability in 6 hrs. This has been

exploited here to do a comparative study of ultrastructural changes in the early stages of cell death for a range of drugs, including at least two drugs of each class for internal comparison, with these then compared to parasites exposed to SK1.47, SK1.49 and DBeQ under the same conditions.

5.2 Results

5.2.1 Experiment set up and initial observations

Eight benchmark antimalarial drugs were selected for this study including; the 4-aminoquinolines CQ and AQ and their related analogues PPQ and PYRD, the arylamino alcohols (QN and MQ) and artemisinins (DHA and ARM). From work described here in chapter 3 and linking to that performed by Ullah *et al*. (2017), estimation of the concentration of drug to reduce parasite viability by 50% in 6 hrs (LD_{50}) were available. Initial experiments for preparation volumes of culture necessary for fixation and staining using these concentrations did not consistently provide a 50% reduction in bioluminescence. This more likely due to an increase in parasitaemia and haematocrit in the cultures used for electron microscopy in comparison to the microwell plate assays. Thus, empirical increases in the LD_{50} concentrations were tested until a range of concentrations were determined (Table 5.2). For each of the two biological repeats reported here, samples were prepared over this range and that with the remaining bioluminescent signal closest to 50% selected for preparation of electron micrographs (Fig. 5.6).

Drug	LD_{50}	50% kill (nM)
CQ	790.2	900-1000
AQ	101.1	120-140
PPQ	297.3	350-390
PYRD	72.0	100-120
QN	2236.0	2500-3000
MQ	65.3	80-100
DHA	12.9	20-25
ARM	15.4	20-25
Compound	**LD_{50}**	**50% kill (µM)**
DBeQ	5.4	7-8.5
SK1.47	7.2	9-10
SK1.49	3.6	5-6.5

Table 5.2 LD_{50} values (from section 3.2.3) and range of 50% kill concentrations used to provide samples with a 50% reduction of viability after treatment.

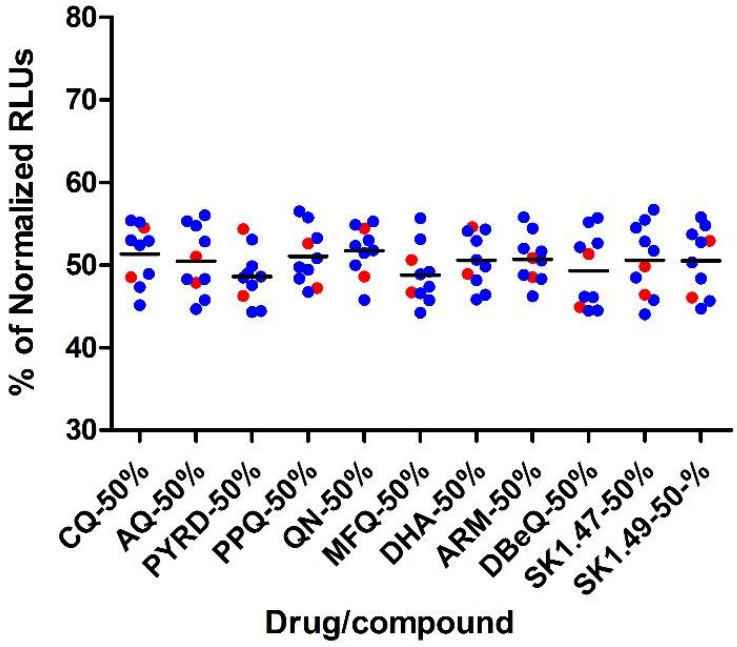

Fig. 5.6 Bioluminescence signals (normalised to untreated control) following treatment with the indicated drug/compound to derive samples that have a 50% loss in viability. Each dot represents one experiment (with the majority from experiments in chapter 6) with the line representing the mean, those highlighted in red for samples used to produce electron micrographs.

Saponin-enriched trophozoites were prepared for transmission electron microscopy based on the protocol originally described by Beaumelle *et al.* (1987) (see section 2.6). In

brief, parasites were cultured to achieve a ~ 10% parasitaemia and either exposed to drug or left untreated as a control. After treatment, the iRBCs were lysed in 0.1% (w/v) saponin and the released parasites were fixed overnight in 2% (w/v) glutaraldehyde. The pre-fixed parasites were stained with 1% (w/v) osmium tetroxide following by embedding in agar before dehydration and embedding in Spurr resin. Ultra-sections (80-90 nm thickness) were obtained and then stained with uranyl acetate. Ultrastructural images were captured using a Transmission Electron Microscope (JEOL-1230, USA).

Transmission electron micrographs of untreated trophozoite parasites confirmed the success of the protocol and electron microscopy facilities, where features expected of trophozoite stage parasites observed (Fig. 5.7 and 5.8). These observations include; (i) a clearly defined DV, which is surrounded by a continuous membrane that clearly stained and enveloping Hz crystals, (ii) the presence of electron-dense vesicles (termed here endocytic vesicles, EV) distributed in the parasite cytoplasm, (iii) an electron-dense cytoplasm enriched with ribosomes, (iv) a membrane bound nucleus that shares a similar electron density to the cytoplasm, (v) the presence of elongated mitochondria with a less electron-dense matrix and (vi) a parasitophorous vacuole (PV), a space between plasma membrane of the parasite and cytoplasm of iRBC, surrounding by PV membrane. Together, these observations suggest that the protocol employed is capable of producing the resolution of images to carry out the comparative study of changes to morphology following drug/compound treatment.

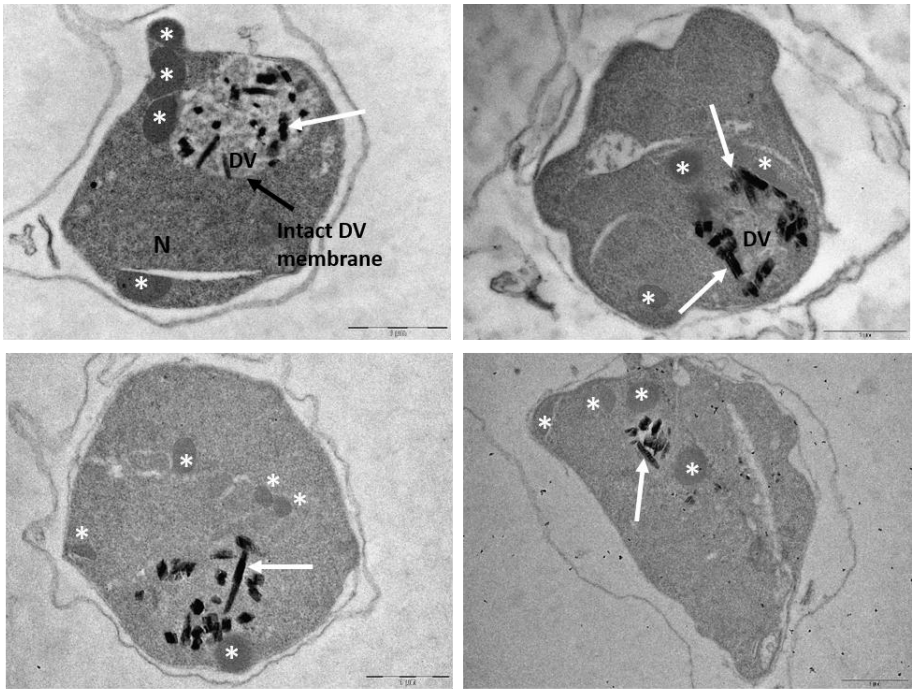

Fig. 5.7 Ultrastructural morphology of untreated trophozoite intraerythrocytic stages of *P. falciparum.* The images show observations previously described**,** including; intact membrane of digestive vacuole (DV) enveloping haemozoin crystals (white arrows), several electron-dense endocytic vesicles (EV) distributed in the parasite cytoplasm (white stars). Note that the parasite nucleus labelled by N. The scale bar shows 1 µm unit for X 30,000 magnification.

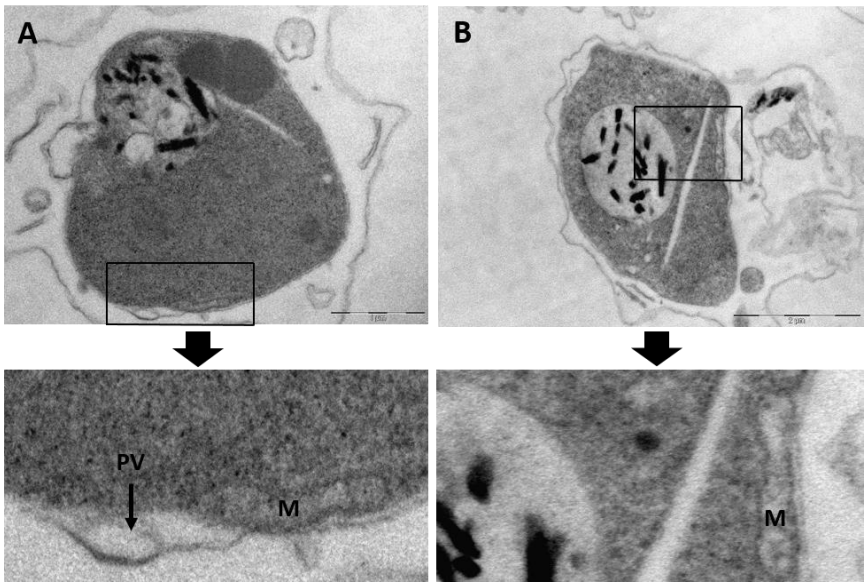

Fig. 5.8 Ultrastructural morphology of mitochondria and parasitophorous vacuole membrane in trophozoite intraerythrocytic stages of *P. falciparum.* (A) and (B) with their associated insets below each panel, show single elongated mitochondrion (M) placed under parasite plasma membrane as well as parasitophorous vacuole (PV) in (A) that is restricted between the parasite plasma membrane and parasitophorous vacuole membrane. The scale bar shows 1 µm unit for X 30,000 magnification.

5.2.2 Qualitative analysis of transmission electron micrographic observations.

5.2.2.1 Concentration-dependant effects on the ultrastructural morphology of CQ-treated parasites.

Whilst CQ is the most used drug in electron microscopic studies of *P. falciparum*, comparisons between the effects of different concentrations, for different lengths of time in different strains affect the interpretation that can be made. Here, to illustrate the utility of defined endpoints determined using bioluminescence, trophozoites were exposed to concentrations of CQ that cause a 25%, 50% or 100% loss in luciferase signal over 6 hrs. These reductions in bioluminescence are the result of 300-450 nM, 900-1000 nM and 8-10 μM concentrations of CQ.

Representative images of parasites from each treatment are shown in Fig. 5.9. Features previously reported following CQ treatment are all found. Specifically;

(i) An accumulation of electron-dense EV in the parasite cytoplasm. Here we observe a concentration-dependent effect, where more EV are observed as the kill effect is increased from 25% to 50% (Fig. 5.9). In contrast, the number of cytoplasmic electron-dense EV are reduced in parasites exposed to a concentration that kills 100%, with swollen DV filled with vesicles previously been termed membranous whorls. Additionally, similar translucent vesicles to those indicated by Porter *et al.,* (2008) following treatment with supralethal dose of CQ now appeared in the parasite cytoplasm.

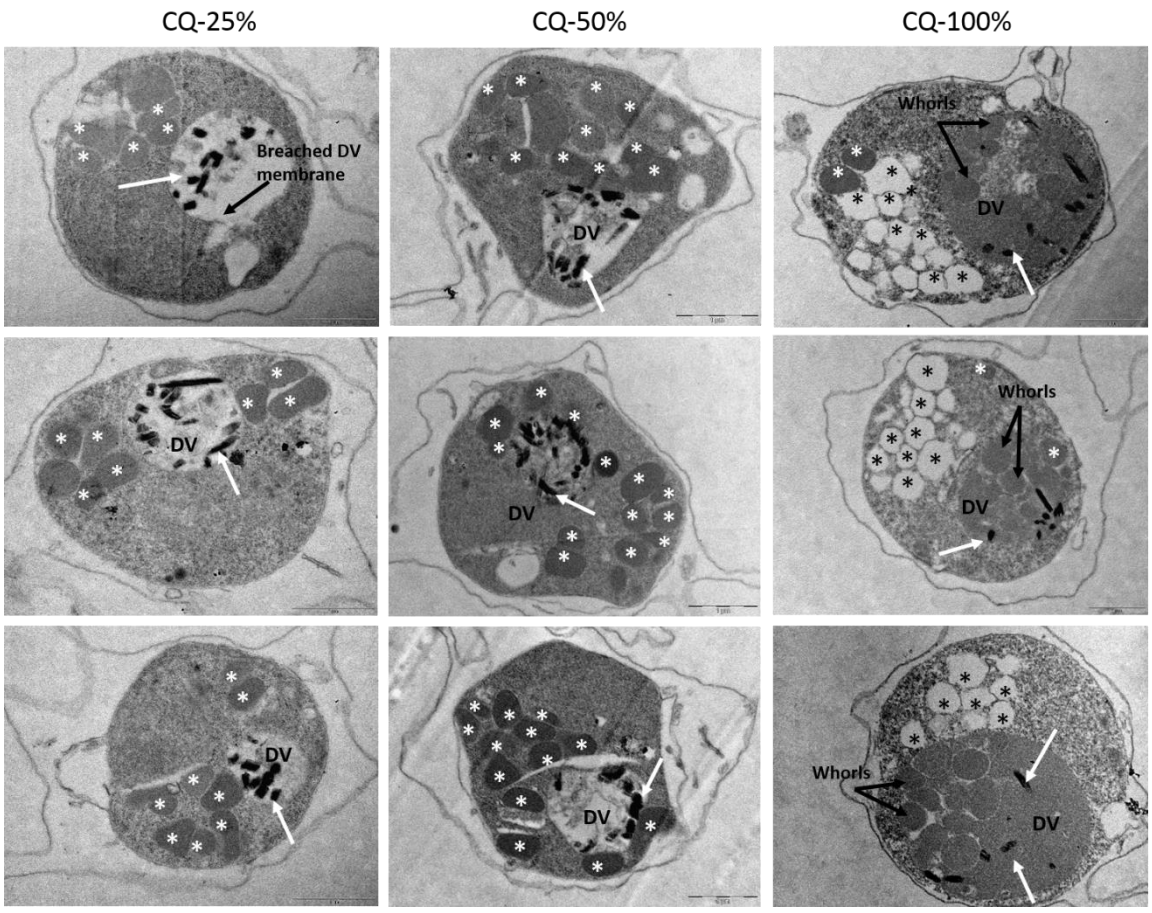

Fig. 5.9 Ultrastructural morphology of CQ-treated intraerythrocytic trophozoite parasites after exposure to increasing concentrations resulting in 25%, 50% or 100% loss of parasite viability. Common features include cytoplasmic located endocytic vesicles (EV) (white stars), membranous whorls inside swollen DV and haemozoin crystals (white arrows). In addition, for CQ-100% clearly apparent electron-translucent vesicles (black stars) are instead found in the cytoplasm of parasites. The scale bar shows 1 µm unit for X 30,000 magnification.

(ii) Swelling of the DV, particularly when exposed to a 100% kill concentration, an apparent reduction in the presence of haemozoin crystals with evidence of a breach of the DV in some cases.

(iii) Regions of the cytoplasm that are apparently depleted of ribosomes. These are distinct from membrane bound regions due to their irregular shape.

Whilst these features have all been previously described, the data here does seem to suggest an emerging pattern. At the lowest level of CQ, the inhibition of EV trafficking to

the DV with cytoplasmic vacuolation phenomenon were observed (Fig. 5.9). Some DV function in haemoglobin digestion is evident from the formation of Hz crystals. As the concentration of CQ increases to produce a 50% kill, there are many more EV apparent with the initial emergence of the electron-translucent vesicles in the parasite cytoplasm. The highest concentration of CQ results in a reduction of cytoplasmic EV, with vesicles of the same electron density now filling an enlarged DV. These findings follow those of Hoppe *et al*. (2004) who developed a novel endocytic trafficking assay based on the uptake of fluorescently labelled dextrans from the RBC cytoplasm. They also showed an accumulation of cytoplasmic EV upon CQ treatment, suggesting disrupture of fusion between EV and DV membrane. However, here, we see that exposure to the highest concentration of CQ may not block the delivery of EV to the DV, based on the similarity in appearance between the cytoplasmic EV and intra-DV membranous whorls, but instead prevent their breakdown and thus the delivery of haemoglobin to the DV for digestion. This latter observation correlates with Porter *et al* (2008) study in that CQ treatment causes the accumulation of undigested vesicles in the DV of the parasite. Inhibition of haemozoin formation by CQ was reported to be a concentration-dependent effect using β-haematin inhibitory activity assay (Combrinck *et al.,* 2012; Omodeo-Sale *et al.,* 2009).

5.2.2.2 Exploring the ultrastructural morphology of parasites exposed to the same endpoint treatment of antimalarial drugs and the putative autophagy inhibitors SK1.47 and SK1.49.

Using the LD_{50} concentrations of each drug, the same 50% loss of viability (based on a 50% reduction in bioluminescence) was achieved across treatments with the antimalarial

drugs and the putative autophagy inhibitors. Taking the putative autophagy inhibitors SK1.47, SK1.49 and DBeQ first, it is readily apparent that they all share a very similar morphology (Fig. 5.10).

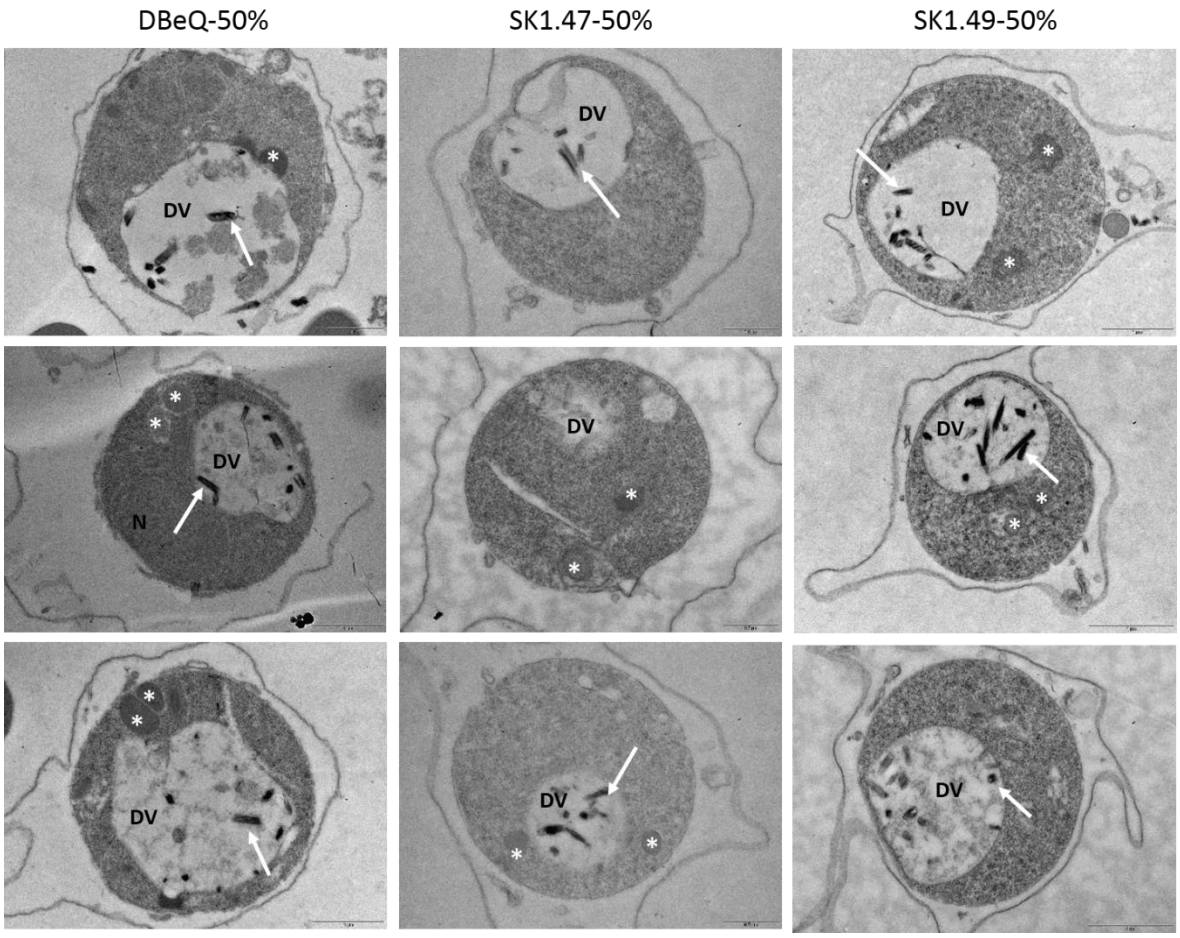

Fig. 5.10 Ultrastructural morphology of intraerythrocytic trophozoite stages exposed to 50% kill concentrations of the putative autophagy inhibitors DBeQ, SK1.47 and SK1.49. Features marked include cytoplasmic endocytic vesicles (EV) (white stars), digestive vacuole (DV), and haemozoin crystals (white arrows). The scale bar shows 1 µm unit for X 30,000 magnification.

The most surprising feature is the appearance of the DV. This appears less dense than those of untreated parasites, more swollen and contains few haemozoin crystals. In some images, and particularly those from parasites treated with DBeQ, some vesicles can be seen within the DV. These vesicles appear distinct than those observed in CQ-treated

parasites as they are less electron dense and less regular in appearance. Cytoplasmic EV are apparent, but there is no evidence of accumulation of them on compound treatment. Other potential observations such as ribosome free areas, swollen mitochondria (although mitochondria only visible in a very small proportion of all images taken) or compromised DV membranes were not features observed following treatments with these compounds.

The 4-aminoquinoline AQ and the related PPQ and PYRD analogues share some morphological changes observed using high concentration of CQ (Fig. 5.11). Of these, the presence of electron-dense vesicles inside the DV is of particular note. Whilst several examples of this observation are noted in PYRD and AQ treated parasites, the transmission electron micrographs of PPQ-treated parasites uniformly show the presence of large numbers of these intra-DV vesicles. Similar feature of PPQ treatment has been previously reported by Sachanonta *et al.* (2011). Here, the DV were often observed to be swollen and contained the intra-DV vesicles and with fewer haemozoin crystals. AQ and PYRD also reported induction of swelling of DV, although recognition a clear reduction in haemozoin crystals is more challenging.

The most distinguishing feature between AQ, PPQ and PYRD-treated parasites compared to CQ-treated parasites is the absence of EV in the cytoplasm of these parasites. Treatment with the 4-aminoquinoline CQ results in a large increase in EV accumulation, and may have been similarly expected here based on the shared chemical class. In these parasites, however, the numbers of EV were not significantly different to untreated parasites, where typically ranged from one to three (Fig. 5.11).

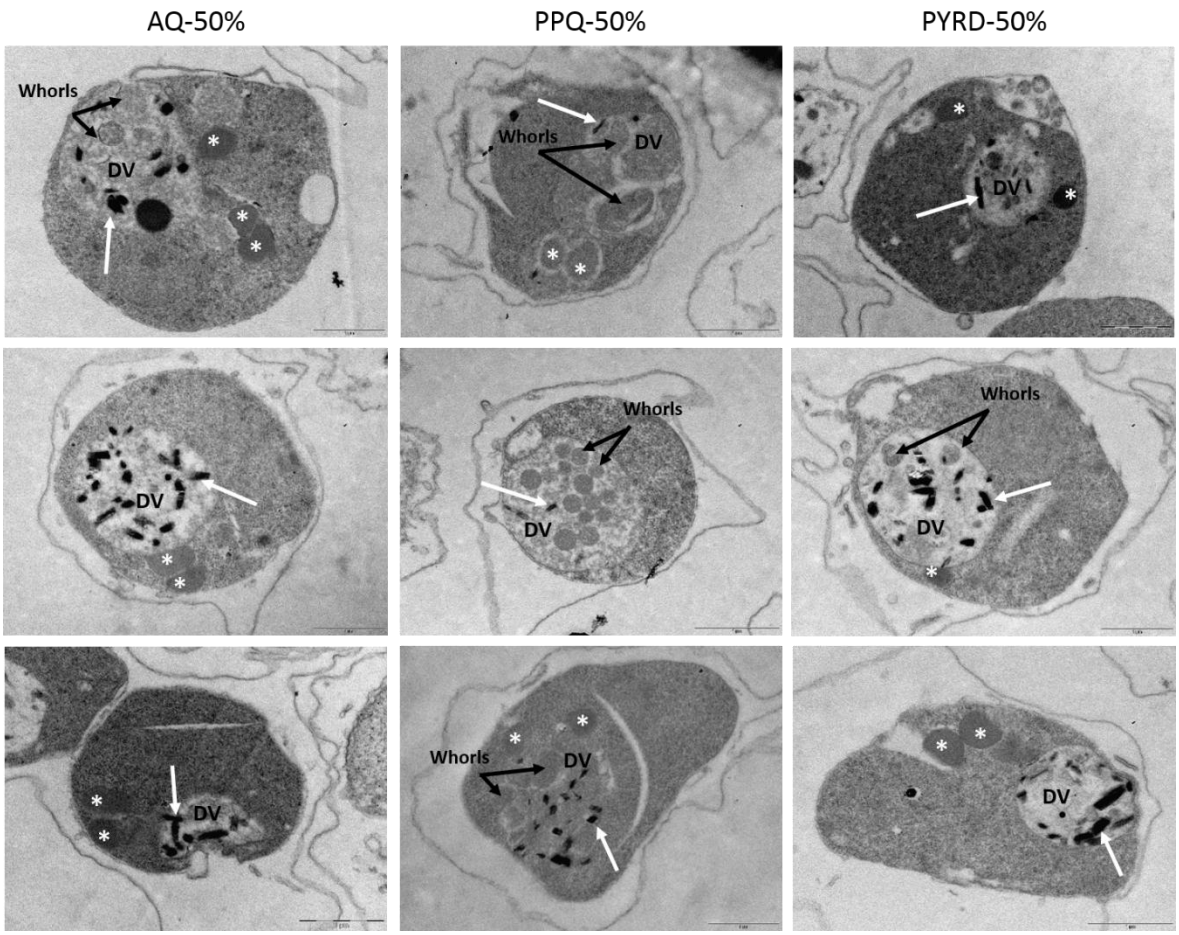

Fig. 5.11 Ultrastructural morphology of intraerythrocytic trophozoite stages exposed to 50% kill concentrations of amodiaquine (AQ), piperaquine (PPQ) and pyronaridine (PYRD). Features marked include cytoplasmic endocytic vesicles (EV) (white stars), digestive vacuole (DV), haemozoin crystals (white arrows) and membranous whorls (black arrows). The scale bar shows 1 µm unit for X 30,000 magnification.

For the arylamino alcohols (QN and MQ)-exposed parasites, transmission electron micrographs revealed ultrastructural morphology similar to that reported of AQ and PYRD. These changes include; no apparent change in the number of cytoplasmic EV, a dilated and apparently more electron translucent DV containing few Hz crystals (Fig. 5.12). The low numbers of cytoplasmic EV agrees with the reduced levels of FITC-dextran endocytic transport, in QN and MQ-treated parasites compared to CQ treatment (Hoppe *et al*., 2004). Similarly, QN and MQ-treated parasites were shown to have reduced levels of haemoglobin in the parasite cytoplasm using anti-haemoglobin antiserum (Roberts *et*

al., 2008). Comparison of the QN-treated group from this study to those obtained by Sachanonta *et al.* (2011) provides agreement on all these features. The latter study also reported swollen mitochondria, this could not be confirmed here as so few mitochondria were imaged to make that judgement possible.

The final comparison is for the artemisinins DHA and ARM (Fig.5.13). The TEM micrographs reveal few morphological changes compares to untreated controls. These included, no apparent difference in the number of cytoplasmic EV, the DV appears to have an unchanged density, no intra-DV vesicles and large numbers of haemozoin crystals are evident. Similar observations were indicated by Chen *et al.* (2000) and Haynes *et al.* (2013) using TEM and β-haematin inhibitory activity assay, respectively. By contrast, these findings are clearly distinct to those reported by Sachanonta *et al*. (2011) and del Pilar Crespo *et al*. (2008). Sachanonta *et al*. (2011) reported a complete loss of distinct organelle structure and its replacement with a dense amorphous material. This study, however, exposed the parasites to 20 μM of artesunate, some 1000X the concentration applied here. del Pilar Crespo *et al*. (2008) reported loss of DV membrane integrity and release of haemozoin into the cytoplasm using artemisinin, with them using 40X the concentration applied here.

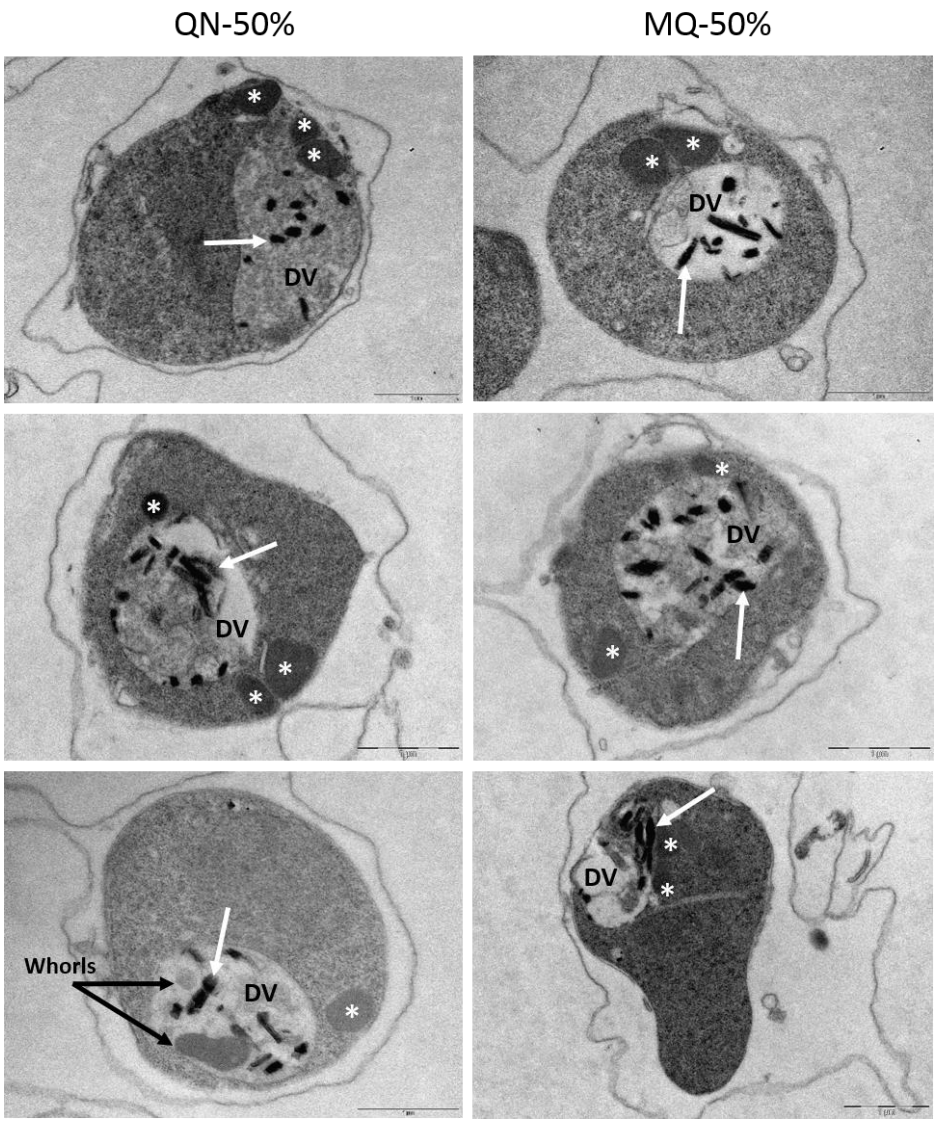

Fig. 5.12 Ultrastructural morphology of intraerythrocytic trophozoite stages exposed to 50% kill concentrations of quinine (QN) and mefloquine (MQ). Features marked include cytoplasmic endocytic vesicles (EV) (white stars), digestive vacuole (DV), haemozoin crystals (white arrows) and membranous whorls (black arrows). The scale bar shows 1 µm unit for X 30,000 magnification.

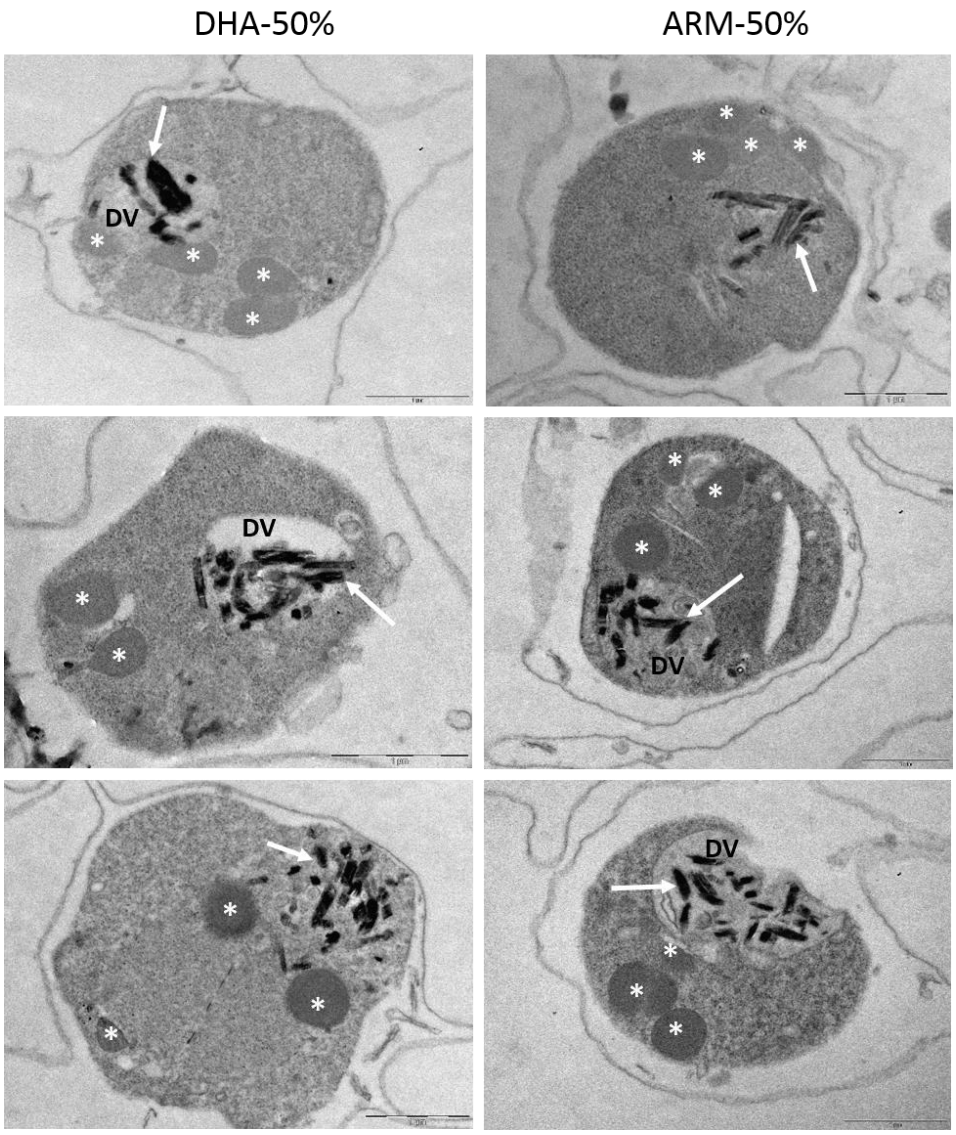

Fig. 5.13 Ultrastructural morphology of intraerythrocytic trophozoite stages exposed to 50% kill concentration of dihydroartemisinin (DHA) and artemether (ARM). Features marked include cytoplasmic endocytic vesicles (EV) (white stars), digestive vacuole (DV) and haemozoin crystals (white arrows). The scale bar shows 1 µm unit for X 30,000 magnification.

5.2.3 Quantitative analysis of transmission electron micrographic observations

The common assay endpoint employed here allowed us to compare how the morphology of drug-treated parasites changed when exposed to different drugs. The previous section highlighted qualitative changes seen for the different classes of drugs studied – and how related drugs/compounds provide similar outcomes. For each treatment, 70-80 TEM

images were available for a quantitative assessment of specific morphological features. Those chosen were;

(i) The number of electron-dense cytoplasmic EV. These varied dramatically in the CQ-treated parasites and may have some role in the delivery of haemoglobin to the DV for digestion.

(ii) The ratio between the DV and the parasite cytoplasm – this being used to make an assessment of DV swelling.

(iii) The number of haemozoin crystals in the DV.

These variables were selected as these features are present in almost all the imaged TEM graphs as well as being simple criteria to measure. Exploring the effect on mitochondria morphology, for example, could not be done due to few images showed recognisable mitochondria. Similarly, whilst ribosome depleted regions within the cytoplasm were observed, there were also the electron-translucent vesicles observed upon CQ treatment. Their morphologies are distinct, but is based on a judgement of how regular the shape is – and this subjectivity could be an issue. Other events, such as DV breach and dispersed Hz in the parasite cytoplasm are both rarely observed and subjective.

5.2.3.1 Quantitative analysis of endocytic vesicles.

Fig. 5.14 illustrates the quantitative assessment used. EV are defines as cytoplasmic located, spheroid and contain electron-dense materials. Counts of the actual number of EV within each parasite were made (Fig. 5.15 and Table 5.3). In addition, based on the distribution of the EV count, the proportions of cells with ≥ 2 EV were also determined (Hoppe *et al.,* 2004) (Fig. 5.16). The analysis first revealed a concentration-dependent effect of CQ on EV numbers. As the concentration increases to achieve a 50% kill, there is

a significant increase in the number of EV. This is similarly seen when the proportion of cells that have ≥ 2 EV increased from 11.4% in the untreated sample to 22.8 and 43.2% in 25% and 50% kill dose of CQ, respectively (Fig. 5.16).

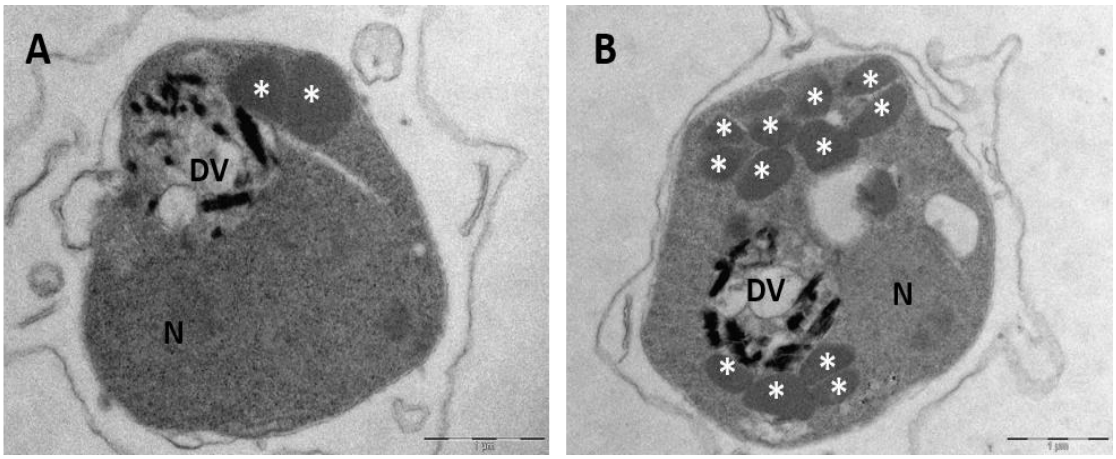

Fig. 5.14 Ultrastructural micrographs of trophozoite stage of *P. falciparum.* The numbers of endocytic vesicles (white stars) within the parasite cytoplasm were counted. Examples here show 2 EV in an untreated control (A) and 12 EV in 50% kill dose CQ-treated parasites (B). Note the parasite nucleus (N) and digestive vacuole (DV). The scale bar shows 1 µm unit for X 30,000 magnification.

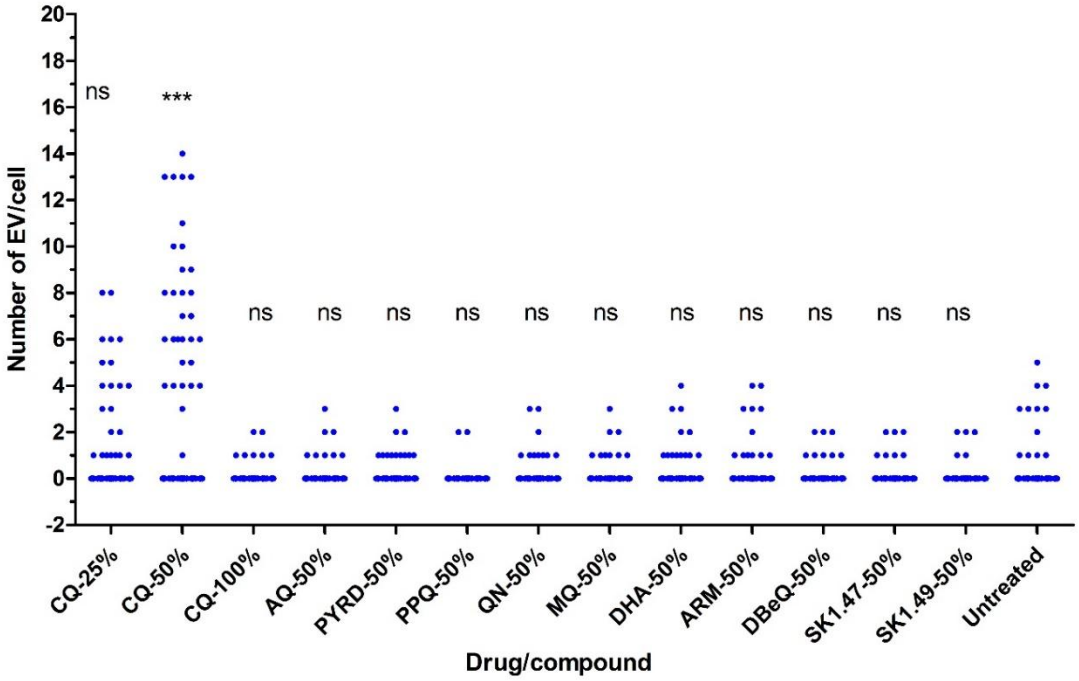

Fig. 5.15 Distribution of EV count per cell according to the kill effect and antimalrial drug/compound used. One-way ANOVA with a Dunnet post-test comparison to the untreated group. Ns, not significant; ***, p<0.0001.

The 100% kill dose CQ-treated parasites showed no significant difference in EV number compared to the untreated control and the proportion of cells that contained ≥ 2 EV falls to 2.8% (Fig. 5.16). This striking difference matches the qualitative observation (Fig. 5.9), that showed the electron-dense vesicles are instead located in the DV and those vesicles still present in the cytoplasm are electron-translucent and not counted here.

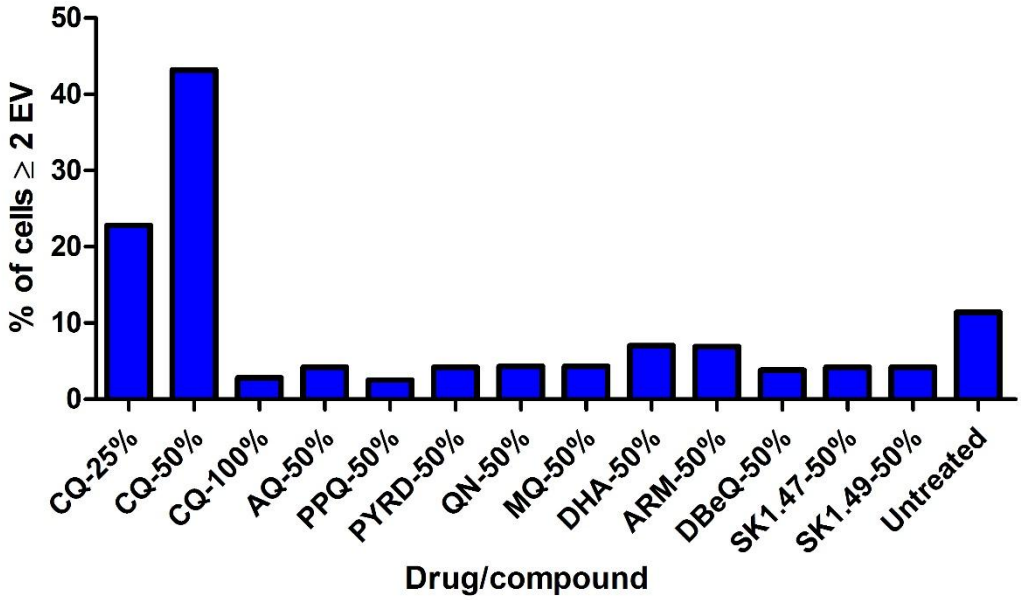

Fig. 5.16 Bar chart representing the proportion of cells that contain ≥ 2 endocytic vesicles (EV) in the parasite cytoplasm following each treatment or in an untreated control. Note there are no error bars as all TEM images within each group (70-80images) are included in this analysis.

Analysis of the distribution of EV count in all other drug treatments reveal no significant difference, matching the qualitative assessment in the previous section that suggested there were no apparent changes in EV numbers. Interestingly, the mean numbers of EV/cell are similar when grouped according the the class of drug/compound; i.e. SK1.49 and SK1.47 at 0.11-0.14 EV/cell, DHA and ARM at 0.31 EV/cell and QN and MQ at 0.19-0.21 EV/cell (Table 5.3). The distribution of data and the numbers of counts performed do

not make this a statistically relevant observation. Unlike CQ, all other treatments resulted in a lower proportion of cells with 2 or more EV, which together with the mean count and lower maximum numbers of EV counted suggests that whilst a significant difference cannot be dteremined based on the distribution of EV counts here – additional work to explore this effect is warranted.

Drug/Compound	Mean of EV	SD	Max. # EV
CQ-25%	1.12	2.09	8
CQ-50%	3.24	4.38	14
CQ-100%	0.13	0.41	2
AQ-50%	0.17	0.53	3
PYRD-50%	0.23	0.57	3
PPQ-50%	0.05	0.31	2
QN-50%	0.21	0.61	3
MQ-50%	0.19	0.54	3
DHA-50%	0.31	0.79	4
ARM-50%	0.31	0.92	4
DBeQ-50%	0.14	0.45	2
SK1.47-50%	0.14	0.45	2
SK1.49-50%	0.11	0.43	2
Untreated	0.44	1.22	5

Table 5.3 Report of the mean, standard deviation (SD) and maximum (Max.) number of cytoplasmic located endocytic vesicles (EV) per cell.

5.2.3.2 Quantitative analysis of DV/cytoplasm ratio.

To explore the qualitative observation that some treatments appear to lead to DV swelling, the ratio of the widest point of the DV compared to the widest point of the parasite cytoplasm was determined. Given that some images were captures at different magnifications and that DV size does change during normal parasite development, this normalisation was used to try and minimize the effect of these factors. Lengths were determined as pixel counts and used as follows (Fig. 5.17):

$$\text{Ratio of DV/cytoplasm} = \frac{\text{Length of longest width of DV (blue arrow)}}{\text{Length of longest width of cytoplasm (red arrow)}} \times 100$$

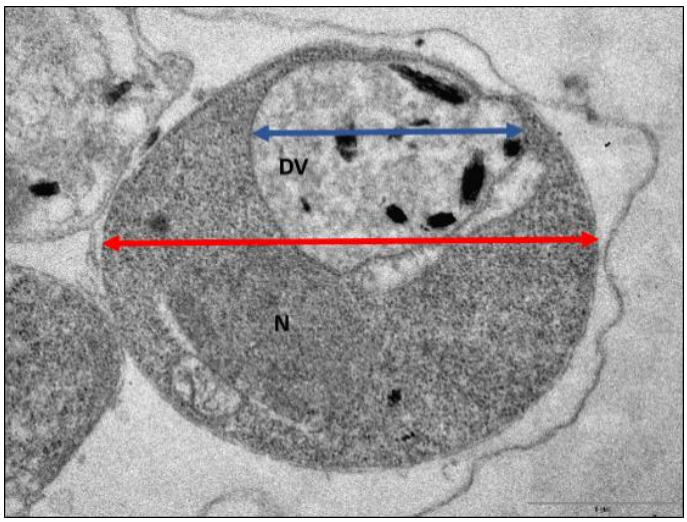

Fig. 5.17 Ultrastructural image of trophozoite stage of *P. falciparum* challenged with 50% kill dose of SK1.49 to illustrate how the ratio of DV/cytoplasm is calculated. DV/cytoplasm ratio represents the length of longest width of DV (blue arrow)/ the length of longest width of parasite cytoplasm (red arrow), using online pixel ruler (https://www.rapidtables.com/web/tools/pixel-ruler.html). The scale bar shows 1 µm unit for X 30,000 magnification.

Given the datasets for each treatment consist of 70-80 images, these have been analysed as one dataset. To ensure whether this approach is statistically acceptable for data developed on different days, the DV ratio count for the two CQ treatments from two

different days were compared. T-tests of each pair of data showed no siginificant difference between DV ratios developed from TEM produced on two different days (Fig. 5.18).

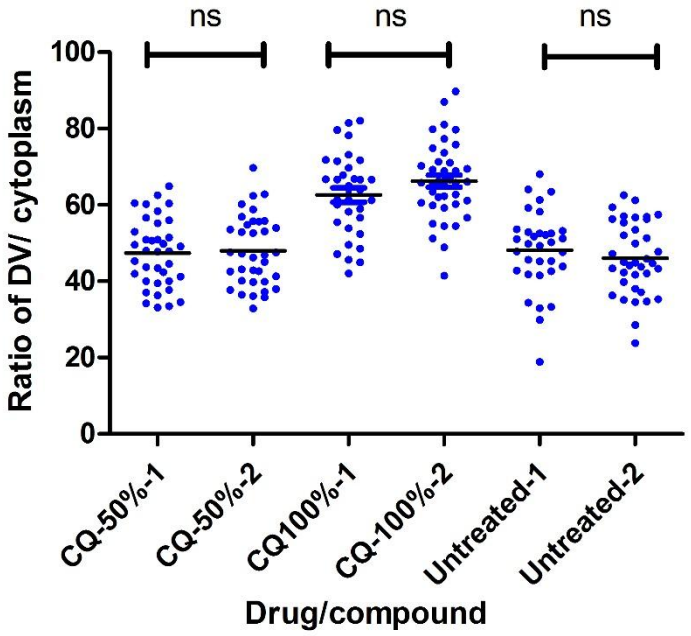

Fig.5.18 Shows ratio of DV/cytoplasm of trophozoite stage of *P. falciparum* following 50% and 100% of CQ treatment as well as an untreated control. Columns marked 1 and 2 represent two different biological replicates. Comparison of these pairs reveals no significant (ns) difference between them.

A plot of the distribution of the DV ratio for each treatment shows the wide distributions of DV ratio that were expected based on the potential distribution of maturation of parasites photographed and that sections may captured through parasites at different points in the DV (Fig. 5.19). CQ did not show a concentration-dependant increase in DV ratio, with the DV ratio apparently unchanged and not significantly different to that of untreated parasites. The DV ratio of the 100% kill treatment is significantly larger ($P < 0.0001$) (one-way ANOVA with a Dunnett post-test) – and this result of packing with vesicular structures. AQ at 50% kill does provide a significant increase, although a small

increase, in DV ratio. This contrasts with the 50% CQ treatment where this effect was not observed. PYRD treatment provided no significant difference in DV ratio compared to an untreated control, although PPQ treatment does – and again is apparently associated with the presence of large numbers of intra-DV vesicles. Treatment with the arylamino alcohols QN and MQ both led to a significant increase in the DV ratio, with a DV swelling effect comparable to that found in AQ-treated parasites. Of particular note is that treatment with neither artemisinin derivatives led to an increase in the DV ratio compared to untreated controls.

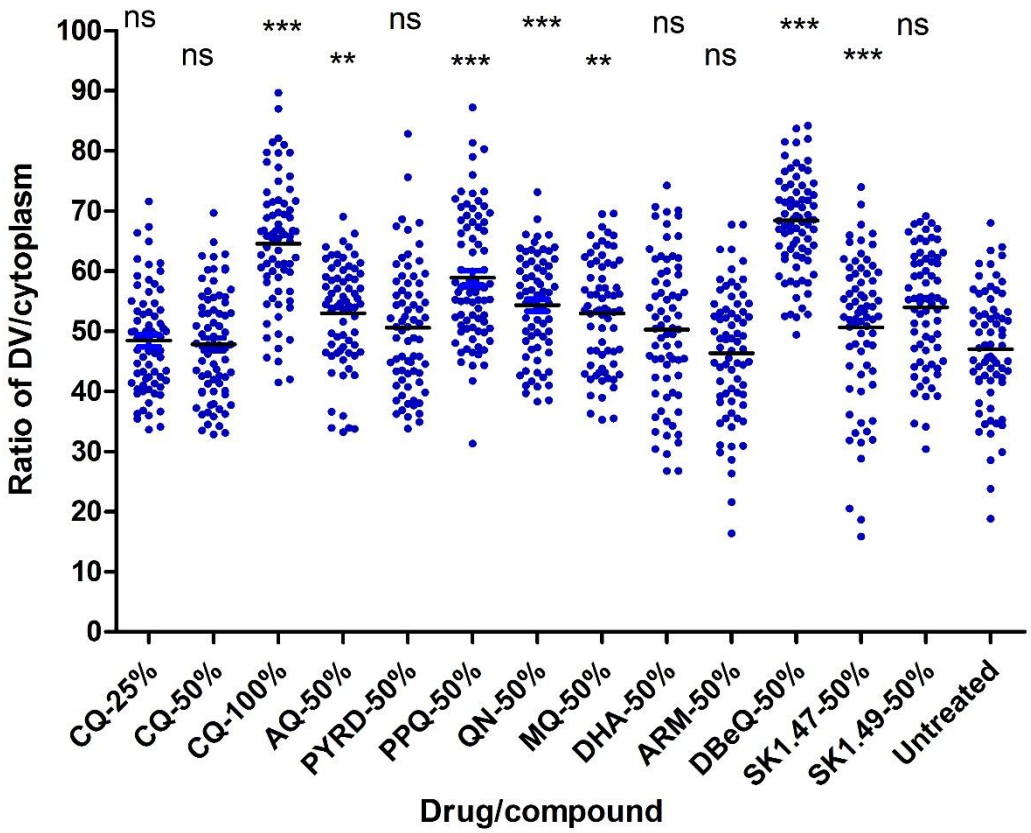

Fig. 5.19 Scatterplot of the ratio of DV/cytoplasm in drug-treated and untreated parasites. Each dot represents the measurement from one cell. Horizontal lines represent the mean. One-way ANOVA with a Dunnet post-test comparison to the untreated group was done for all samples. Ns, not significant; **, $p<0.01$; ***, $p<0.0001$.

The putative autophagy inhibitor DBeQ showed a large and significant change in DV ratio (Fig. 5.19), reflecting the massive swelling for DV (Fig. 5.10). A DV swelling effect for SK1.49 is also evident, although not as great as that of DBeQ. Whilst there is a slightly increase in the mean DV ratio for SK1.47, there is no significant difference in the distribution of DV ratio compared to an untreated control.

5.2.3.3 Quantitative analysis of haemozoin crystals.

A manual counting of haemozoin crystals was done for all treatments with Fig. 5.20 illustrating examples images and the count of haemozoin crystals.

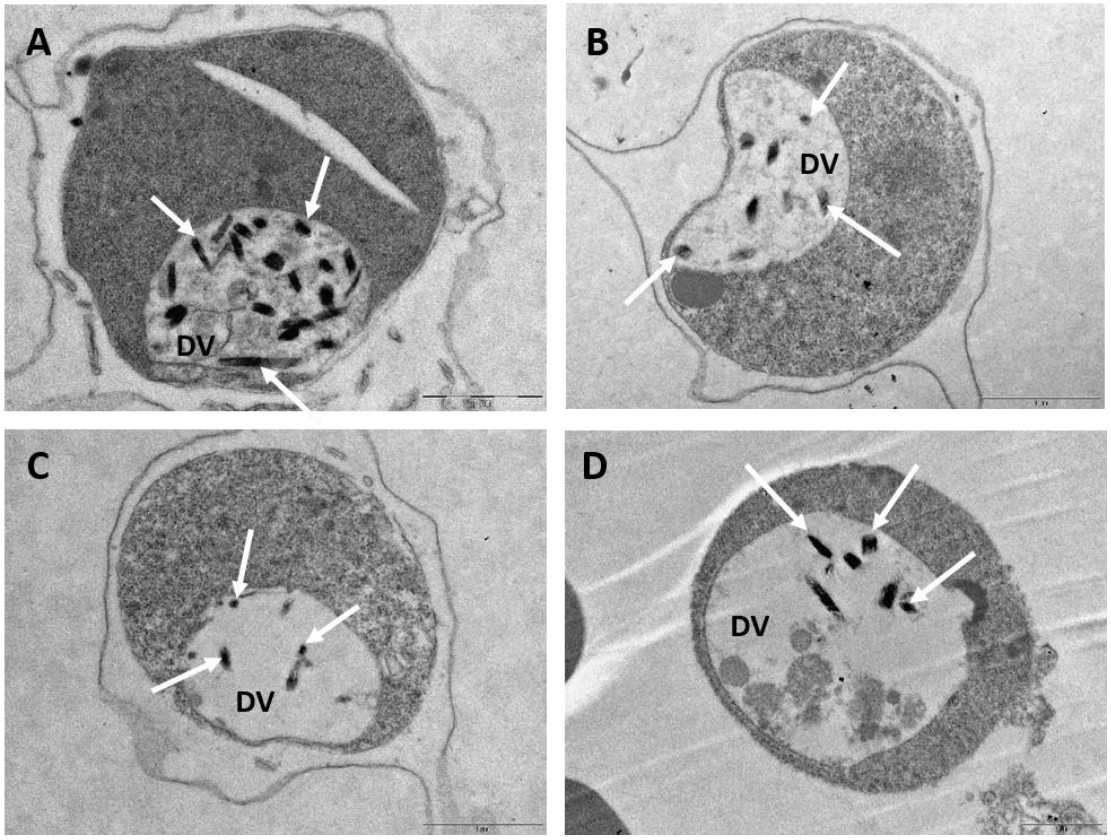

Fig. 5.20 Ultrastructural image of trophozoite stage of *P. falciparum* challenged with 50% kill dose of putative autophagy inhibitors to illustrate haemozoin crystal counting. (A) Untreated (20 crystals), (B) SK1.47 (8 crystals), (C) SK1.49 (6 crystals) and (D) DBeQ-treated (7 crystals) parasites. Note that Hz crystals are marked by white arrows and digestive vacuole (DV). The scale bar shows 1 µm unit for X 30,000 magnification.

A scatterplot was prepared to illustrate the distribution of haemozoin crystal counts for each treatment (Fig. 5.21). One-way ANOVA with a Dunnett post-test explored whether a significant difference in the distribution of haemozoin crystal counts compared to the untreated sample existed in any treatment. As expected, based on the well-established effect of CQ in inhibition of haemozoin formation (Combrinck *et al.,* 2012), a concentration-dependent reduction in haemozoin crystal counts were observed.

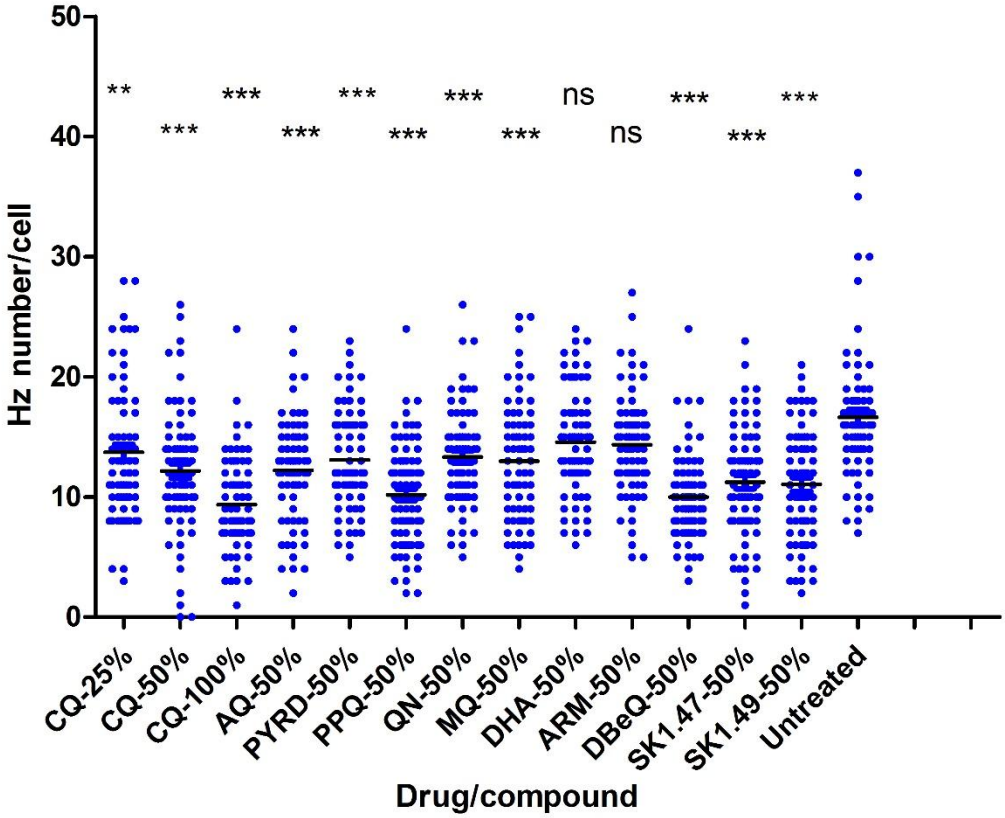

Fig. 5.21 Scatterplot of haemozoin crystal counts in drug-treated and untreated parasites. Each dot represents the measurement from one cell. Horizontal lines represent the mean. One-way ANOVA with a Dunnet post-test comparison to the untreated group was done for all samples. Ns, not significant; **, $p<0.01$; ***, $p<0.0001$.

All treatments, except for the artemisinins, significantly reduced the haemozoin crystal count. That artemisinins did not is likely due to have no effect on haem biocrystalization

(Chen *et al.,* 2000; Haynes *et al.,* 2003). Of note is that of the four most effective compounds in reducing haemozoin crystal count after exposure of a 50% kill concentration, three were the putative autophagy inhibitors with PPQ, with the DV instead filled with electron-dense vesicles.

5.3 Discussion

We describe here a comparative study of ultrastructural changes following exposure to a number of antimalarial drugs that achieve a 50% reduction in parasite viability within 6 hrs exposure time. The ability to measure a defined endpoint using a simple and quick assay across a range of drugs, as well as vary the concentration to achieve a different killing effect, offers a distinct advantage over previous attempts to carry out comparative studies. This is exemplified here using the 25%, 50% and 100% killing concentrations for CQ – an approach that is adopted more widely in the next chapter. The processing of samples to produce sufficient images for analysis, with over 1000 TEM images analysed here, restricted the extent to which this "dial a death" approach could be extended beyond CQ in the time available. All the phenotypes found here, however, were previously described, although the electron translucent cytoplasmic EV following exposure to high concentrations of CQ are rarely commented on, we would suggest that our data helps to explore the links between the observations previously made.

Different ultrasturatural studies on *P. falciparum* parasites have described morphological changes that considered the parasite DV as the initial site for action for many blood stage antimalarial drugs (Ch'ng *et al.,* 2011; del Pilar Crespo *et al.* 2008; Chen *et al.,* 2000; Roberts *et al.,* 2008; Sachanonta *et al.,* 2011). In addition, inhibition of haemoglobin capture and trafficking to the DV via endocytic vesicles have been previously described in

P. falciparum exposed to quinolines and artemisinin (Hoppe *et al.,* 2004; Kawai *et al.,* 1996). Our observations of the effect of CQ with increasing concentrations mapped to their killing effect, potentially brings together these observations. As the CQ concentration increases up to the 50% kill, the proportions of cells with more EV increases. This was significantly higher compared to 25% of CQ and untreated parasites. This is similar to what has been found previously in D10 strain of *P. falciparum* following 12 hrs post exposure of $4XIC_{50}$ of CQ (Hoppe *et al.,* 2004). This accumulation of EV may be due to lysosomotropic feature of CQ, where accumolation of drug within the DV raise the its pH and prevents fusion between the EV and DV membrane (Gaviria *et al.,* 2013). Alterations in the action of CQ at much higher concentration (e.g. 100% kill dose) included accumalation of EV (based on their similar size and density to cytoplasmic EV) inside a swollen DV is probably due to involve other targets such as the vacuolar phospholipase that may be responsible for digestion of EV membranes allowing their contents to be digested (Yayon and Ginsburg, 1983; Waite *et al.,* 1976; Van den Bosch, 1980). Correlating with these structural features is that high concentrations of CQ result in the accumulation of undigested haemoglobin in the treated parasite (Hoppe *et al.,* 2004; Roberts *et al.,* 2008). These reports would correlate with our observations of the DV/cytoplasm ratio and the count of haemozoin crystals, suggesting that haemoglobin within these vesicles are not available for digestion and as a consequence no haem is released for polymerization. One potentially novel feature here that needs further investigation is the accumulation of the electron-translucent vacuoles at the highest concentration of CQ – specifically whether they reflect a defect in haemoglobin feeding from the host erythrocyte at high concentrations of CQ. Similarly, additional studies are required to explore the nature of the electron dense EV induced upon exposure to CQ. In particular,

the use of immuno-TEM with antibodies to Atg8 – these studies attempting to correlate whether the Atg8 labelled puncta described in Chapter 3 are the same as the EV structures described in the TEM studies in this chapter. An interesting control here may be to extend the immuno-TEM to include imaging of parasites subjected to starvation conditions; conditions known to induce the distribution of Atg8 labelled puncta.

Another objective of the comparative study was to determine ultrastructural changes following exposure to SK1.47, SK1.49 and DBeQ. Interestingly, they all have similar effects, and clearly distinct from those for the classes of antimalarial drugs tested. Treatment with these putative modulators of autophagy led to;

(i) Swollen digestive vacuoles (although data for SK1.47 no significant), that have a reduced electron density staining with remnants of Hz crystals. Some electron-dense vesicles are observed in the DV of DBeQ treated parasites, although they do not share the same morphology as those found in PPQ and CQ treated parasites. No evidence of DV membrane breaches.

(ii) No significant changes in cytoplasmic EV compared to untreated controls. The mean EV count and proportion of cells with 2 or more EV were actually lower than those of untreated cells for SK1.47, 1.49 and DBeQ, but did not reach significance in our analysis.

The slight reduction in EV numbers following treatment with SK1.47, 1.49 and DBeQ, and their correspondingly high numbers in CQ treated parasites shares similarities with the numbers of Atg8-labelled vesicles in SK1.47, 1.49 and CQ treated parasites cultured in complete medium (as they are here for the TEM study) and imaged using immunofluorescence microscopy (Chapter 3). If these EV are the same as Atg8-labelled

vesicles, then we can start to interpret our ultrastructure findings on SK1.47, 1.49 and DBeQ treatment. Based on the putative function of SK1.47, 1.49 and DBeQ, by inhabitation the normal formation of the Atg8-labelled vesicles/EV, then we would expect to see less of them. Currently, there is an apparent reduction in the mean number of EV (75% reduction, Table 5.3), although there is insufficient data to say this is a significant effect. The reduced levels of Atg8-labelled vesicles/EV would reduce the amount of haemoglobin delivered to the DV, causing decrease of Hz count due to reduction of free haem that release from haemoglobin digestion. Interestingly, MQ inhibits endocytosis of FITC-dextran, although not via the same mechanisms as CQ. Hoppe *et al.* (2004) discussed how the inhibition of haemoglobin delivery is distinct between CQ and MQ, with MQ reducing haemoglobin delivery as a result of the inhibition of the formation of EV rather than blocking their fusion to the DV. This is probably due to the ability of MQ to bind with cytoplasmic phospholipids that are required for the formation of EV membrane. Such mechanism has also been suggested for QN and AQ, but not for CQ (Barroso *et al.,* 2015; Chevli *et al.,* 1982; Ginsburg and Krugliak, 1988; Roberts *et al.,* 2008). If SK1.47, SK1.49 and DBeQ similarly inhibit EV formation, and these are no longer trafficking haemoglobin, then the corresponding observations of a swollen, less electron-dense DV with reduced haemozoin crystal count for MQ, QN, SK1.47, SK1.49 and DBeQ may all be related. That SK1.47and SK1.49 may interfere with haemoglobin trafficking is certainly a hypothesis to follow up, with a research plan that aims to explore whether EV observed under TEM are the same as the PfAtg8-labelled puncta in immunofluorescence microscopy. If this hypothesis was true, then one aspect of SK1.47 and SK1.49 action may well be starvation of macromolecules that needed for growth, specifically in trophozoite stage parasites. In addition, these observations have been based only looking at the morphological changes

associated with a 50% kill, and yet the potential to explore the evolution of morphological changes using a phased 25%, 50% and 100% kill has been demonstrated here for CQ. The same phased 25%, 50% and 100% kill for SK1.47, SK1.49 and DBeQ to prepare TEM micrographs to compare to those produced in the same way for QN, MQ and perhaps AQ treatment may provide a start in exploring whether inhibiting EV formation is a target of action for these compounds.

Chapter 6: Monitoring biochemical markers of regulated cell death in intraerythrocytic P. falciparum exposed to antimalarial drugs, SK1.47 and SK1.49

6.1 Introduction

In the last 2 decades, there was debate about whether *P. falciparum* undergoes programmed cell death (reviewed in Deponte and Becker, 2004; Taylor-Brown and Hurd, 2013; Sow *et al.,* 2015). The first description on apoptotic features of *P. falciparum* cell death after exposure to CQ, specifically DNA fragmentation, was made by Picot *et al.* (1997). Later work in *P. berghei* described how apoptotic features such as chromatin condensation, DNA fragmentation and externalization of phosphatidylserine (PS) appears to be associated with self-limiting infections of the mosquito midgut (Al-Olayan *et al.,* 2012). Over this period of time there have been a range of studies (Table 6.1) investigating the presence of apoptotic features in intraerythrocytic *P. falciparum* exposed to a range of drug or febrile temperature stresses. Together, these reports described features such as chromatin condensation, DNA fragmentation, PS externalization, $\Delta\Psi m$ collapse, Ca^{2+} redistribution and activation of Clan CA cysteine protease activity (Ch'ng *et al.,* 2010, 2011; Nyakeriga *et al.,* 2006; Meslin *et al.,* 2007). There have also, however, been reported that these apoptotic features are not evident following drug treatment (Nyakeriga *et al.,* 2006; Porter *et al.,* 2008) or that the features of cell death observed were more typical of autophagic-like cell death (Eickel *et al.,* 2013; Gaviria *et al.,* 2013; Totino *et al.,* 2008).

Author	Parasite strain (sensitivity to CQ)/stage	Method	Stimulus (Concentration/Time)	Key features
Picot *et al.* (1997)	3D7 strain (CQS) Lili strain (CQR) of *P. falciparum*/ Trophozoite	Western blot (Agarose Gel Electrophoresis)	CQ (IC_{50}= 40nM/6hrs) (IC_{50}= 360 nM/6hrs)	Only 3D7 strain showed positive DNA laddering.
Nyakeriga *et al* (2006)	F32 strain (CQS) of *P. falciparum/* Trophozoite	FACS ($DiOC_6$(3) kit) Western blot (Agarose Gel Electrophoresis)	CQ (20nM) ATQ (2.7µM) SNAP (600 mM) Etoposide (6.8µM)	20 min drug exposure did show ΔΨm depolarisation, except ATQ showed rapid decrease in ΔΨm. 24 hrs drug exposures did not show DNA positive laddering in all treatments.
Meslin *et al.* (2007)	3D7 strain (CQS) 7G8 strain (CQR) of *P. falciparum/* Trophozoite	Fluorescence microscopy (JC-1/TUNEL-Kit)	CQ (IC_{90}=55nM /18hrs) (IC_{90}=55nM/36hrs) (IC_{90}=1400nM/18hrs) (IC_{90}=1400nM/36hrs)	 ~20% of JC-1 positive cells ~60% of TUNEL positive cells ~12% of JC-1 positive cells ~18% of TUNEL positive cells
Porter *et al.* (2008)	CSC-1 strain (CQR) of *P. falciparum*/Mature blood stages	FACS ($DiOC_6$-Kit) Western blot (Agarose Gel Electrophoresis)	40 °C (24hrs) CQ (100µM/8hrs) Staurosporine (5µM/8hrs)	All treatments caused depolarisation in ΔΨm. No DNA laddering, but reduction in the caspase positive cells was detected in all treatments.
Oakley *et al.* (2007)	3D7 strain (CQS) of *P. falciparum*/ Schizont	Fluorescence microscopy (TUNEL kit)	41°C (2hrs)	60% TUNEL positive cells
Ch'ng *et al.* (2010)	3D7 strain (CQS) of *P. falciparum*/ Late ring	FACS (JC-1/ TUNEL/ CaspaTag kit)	CQ (30µM/8hrs) Staurosporine (10µM/8hrs)	31% and 25% depolarisation in ΔΨm, respectively. 27% and 56% TUNEL positive cells, respectively. 34% and 32% of caspase positive cells, respectively.
Ch'ng *et al.* (2011)	3D7 strain (CQS) 7G8 strain (CQR) K1 strain (CQR) of *P. falciparum*/ Late ring	Fluorescence microscopy (Fluo-4 AM kit)	CQ (3µM/4hrs)	~66%, 62% and 25% cytoplasmic redistribution of Ca^{2+} were reported in 3D7, 7G8 and K1, respectively.

Pattanapany-asat *et al.* (2010)	TM267 strain of *P. falciparum*	FACS (FITC-Annexin V kit)	38.5-39.0 °C Ring stage (18hrs/PI) Trophozoite (32h/PI) Schizont (42hrs/PI)	50.2%, 55.8% and 63.6% of PS externalization, respectively.
Matthews *et al.* (2012)	ANKA strain of *P. berghei/*Ookinete	Fluorescence microscope (JC-1/CaspaTag/ /TUNEL/FITC-Annexin V kit)	CQ (1mM/2h) Staurosporine (15µM/30min)	No change in ΔΨm in both treatments. 34% and 28% of TUNEL positive cells, respectively. 55.8% and 30% of caspase positive cells, respectively. 58% PS positive cells only in CQ-treated parasites in comparison with untreated control (30%).
Engelbrecht and Coeltzer (2013)	3D7 strain (CQS) of *P. falciparum*/Trophozoite	FACS ($DiOC_6$(3)/TUNEL/ Caspase kit)	41°C (24hrs)	Slightly increase in depolarised mitochondria, TUNEL positive cells and phosphatidylserine externalization.
Rathore *et al.* (2015)	3D7 strain (CQS) of *P. falciparum*/Ring stage	Fluorescence microscopy(JC-1/ TUNEL /CaspACE/Mag-Fluo-4 AM)	MG-132 (EC_{50}= 50nM/6hrs)	0.39 red/green ratio of JC-1. 43.8% and 35% of TUNEL and caspase positive cells, respectively.
Gunjan *et al.* (2016)	3D7 strain (CQS) of *P. falciparum*/ Late ring	FACS/ Fluorescence microscopy(JC-1/ TUNEL /EnzChek Caspase kit)	MQ (100nM/24hrs)	Ratio of red/green JC-1 reduced from 6.1 in untreated control to 1.85 in MQ-treated cells. Slightly increase in TUNEL-positive cells from 26% to 37%. 76% of caspase positive cells were observed.
Totino *et al.* (2008)	SPP1 stain (CQR) of *P. falciparum/*Trophozoite	FACS (Rhodamine-123/ TUNEL/Z-VAD-fmk-caspase inhibitor)	CQ (180nM/24hrs) Staurosporine (4µM/24hrs) SNAP (360 µM/24hrs)	All drugs showed loss of ΔΨm, 5-9% of TUNEL positive cells with absence of Caspase-like activity.

Table 6.1 Summary of the literature describing apoptotic features in *P. falciparum*. Chloroquine (CQ), atovaquone (ATQ), mefloquine (MQ), S-nitro-N-acetyl-D, L-penicillamine (SNAP), Fluorescence-activated cell sorting (FACS), mitochondrial outer membrane potential (ΔΨm), post infection (PI) and phosphatidylserine (PS).

One issue within the debate is the use of language and terms associated with regulated cell death such as necrosis, apoptosis and autophagic. The Nomenclature Committee of Cell Death (NCCD) provides specific definitions for these various pathways (Galluzzi *et al.,* 2012; 2015). In a recent review (Proto *et al.,* 2013), the term "unregulated cell death" was suggested for unicellular protozoan instead of these NCCD definitions which cannot be reached by these organisms. Sow *et al.* (2015) have countered this by saying that the NCCD terminology is based on observations of cell death in metazoans and the same criteria cannot be used to exclude the existence of regulated cell death pathways in unicellular protozoa. For example, the absence of a caspase in *P. falciparum* would prevent the classical definition of apoptosis, although a metacaspase PfMCA1 has been described by Meslin *et al.* (2007) which could act as an initiator of apoptosis through the conserved Ca^{2+} dependant membrane targeting and caspase recruitment domains (Meslin *et al.,* 2011; Le Chat *et al.*, 2007). An alternative protease, Clan CA cysteine proteases, activating apoptosis in *P. falciparum* has also been suggested (Ch'ng *et al.,* 2010).

Perhaps the best described research in this area has been authored by Ch'ng from the Tan laboratory in Singapore. They have published a series of papers that specifically investigate cell death after exposure to high concentration of CQ (concentrations at µM level which is more similar to lethal doses than inhibitory doses) and use a range of approaches to study biochemical and structural features of apoptotic cell death. The first report, Ch'ng *et al.* (2010), described how the high concentrations of CQ triggers the activity of Clan CA proteases, which probably induce permeabilization of the outer membrane of the mitochondria leading to $\Delta\Psi m$ collapse, with DNA fragmentation as the final effect. This action following CQ treatment, however, is activated by verapamil and was reduced in CQR parasites which led the authors to suggest that the digestive vacuole

is likely the source of the Clan CA proteases. This study was followed, Ch'ng *et al.* (2011), by reports describing a rapid and intensive permeabilization of the digestive vacuole membrane, although not always ruptured, similarly a lysosome-mediated cell death mechanism found in metazoans (Boya and Kroemer, 2008). Observation of Ca^{2+} redistribution from the digestive vacuole following this permeabilization was companied by upregulation of the Clan CA protease activity. The potential release of Clan CA proteases, such as falcipains as well as plasmepsin IV from the digestive vacuole was suggested when high concentrations of CQ used (Ch'ng *et al.*, 2011, 2014). A summary of this cascade of events following exposure to high concentrations of CQ is shown in Fig. 6.1.

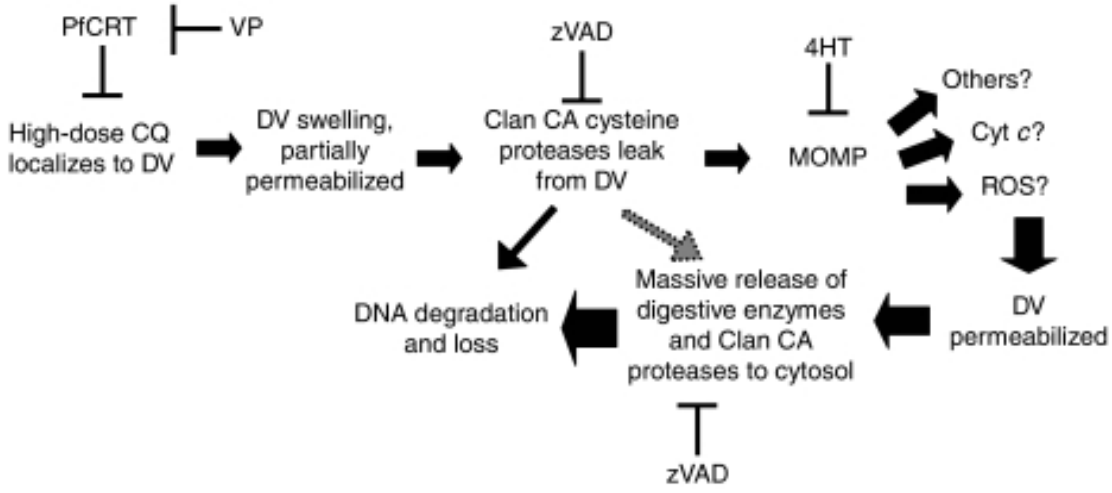

Fig. 6.1 Cascade of biochemical markers following exposure of intraerythrocytic *P. falciparum* to high concentrations of CQ. High doses of CQ cause swelling and permeabilization of the digestive vacuole (DV) to release Clan CA cysteine proteases. These lead to mitochondrial outer membrane permeabilization (MOMP) that triggers (through potentially a range of mechanisms) the complete permeabilization of the DV and a large increase in protease activity which ultimately leading to DNA damage. The position of inhibitors (VP, verapamil; zVAD, a cysteine protease inhibitor; 4HT, 4-hydroxytamoxifen) used in the characterization of this cascade are shown. (Source: Ch'ng *et al.,* 2010).

These studies also highlight two interesting features. First, the use of high concentrations of chloroquine to trigger cell death, and not inhibition, correlates with the work of Paul

Roepe who suggests that CQ action at inhibitory doses is different to that when used at lethal doses (reviewed in Roepe, 2014), although he implicates high concentrations of CQ in autophagic-like cell death (Gaviria *et al*., 2013). The second is the apparent role of ΔΨm collapse during programmed cell death, an observation that has also been linked with the triggering of apoptosis by etoposide, reactive oxygen species, staurosporine and heat shock (Meslin *et al.,* 2007; Oakley *et al.,* 2007; Porter *et al.,* 2008; Ch'ng *et al.,* 2010). Rathore *et al.* (2011) also showed that disruption of the ΔΨm led to trigger apoptotic cell death as suggested by an increase in protease activity and DNA fragmentation. These studies led Ch'ng *et al.* (2013) to suggest that a "powerless" mitochondria may be early and common trigger of apoptotic cell death which may providing a new antimalarial drug target.

These reports provide an experimental framework that describes a range of biochemical markers implicated in apoptosis following exposure to high concentrations of CQ. This framework has been exploited here for a comparative study of these same biochemical markers for a wider range of antimalarial drug classes. Based on the loss of bioluminescence following 6 hrs of exposure to these different drugs, we aim to obtain concentrations that cause 25%, 50% or 90% loss of viability for each drug. This approach allows a more effective comparison of the effects between these compounds as they have all been used to achieve the same endpoint in the reduction of parasite viability. The

same drug classes used for the ultrastructure studies in chapter 5 have been used here and this also similarly included SK1.47, SK1.49 and DBeQ to further explore their action against the intraerythrocytic trophozoite stage of *P. falciparum*.

6.2 Results

6.2.1 Determining the loss of viability endpoints using bioluminescence assay

To prepare samples for processing for biochemical markers of apoptosis, we first explored the concentrations of drugs/compounds to be used to achieve a 25%, 50% or 90% reduction in bioluminescence signal. This then being defined as the kill effect. Due to variation in the age of erythrocytes, parasitaemia, haematocrit, and synchronicity of culture…etc. it was found that the best way to achieve the matched kill effect for processing is using 3-4 samples for each kill effect with range of concentrations reported in table 6.2. The sample that provided the loss of bioluminescence closest to that required was taken for processing. Fig. 6.2 illustrates the normalised (against untreated controls) luciferase signal of ten of these experiments taken for processing in the work described in this chapter. All comparisons of drug/compound data within the same kill effect (e.g. all those that produce a 25% kill) are not significant, where all comparisons between the different kill effects for each drug/compound (e.g. 25% v. 50% v. 90%) are significant (one-way ANOVA, Bonferroni post-tests, all $p < 0.001$).

Drug	LD_{50}	25% kill (nM)	50% kill (nM)	90% kill (nM)
CQ	790.2	150-250	600-900	3000-4000
AQ	101.1	20-35	70-100	300-450
PPQ	297.3	50-80	200-300	800-1200
PYRD	72.0	15-30	60-90	300-400
QN	2236.0	400-700	1800-2200	5000-7000
MQ	65.3	15-25	50-80	250-350
DHA	12.9	3-5	10-15	50-80
ARM	15.4	4-7	15-20	60-80
Compound	**LD_{50}**	**25% kill (µM)**	**50% kill (µM)**	**90% kill (µM)**
DBeQ	5.4	1-2	5-8	25-40
SK1.47	7.2	1-3	6-9	30-45
SK1.49	3.6	0.8-2	4-6	20-30

Table 6.2 LD_{50} values (from section 3.2.3) and the range of concentrations of drug/compound used to provide samples with a 25%, 50% and 90% reduction of viability after treatment.

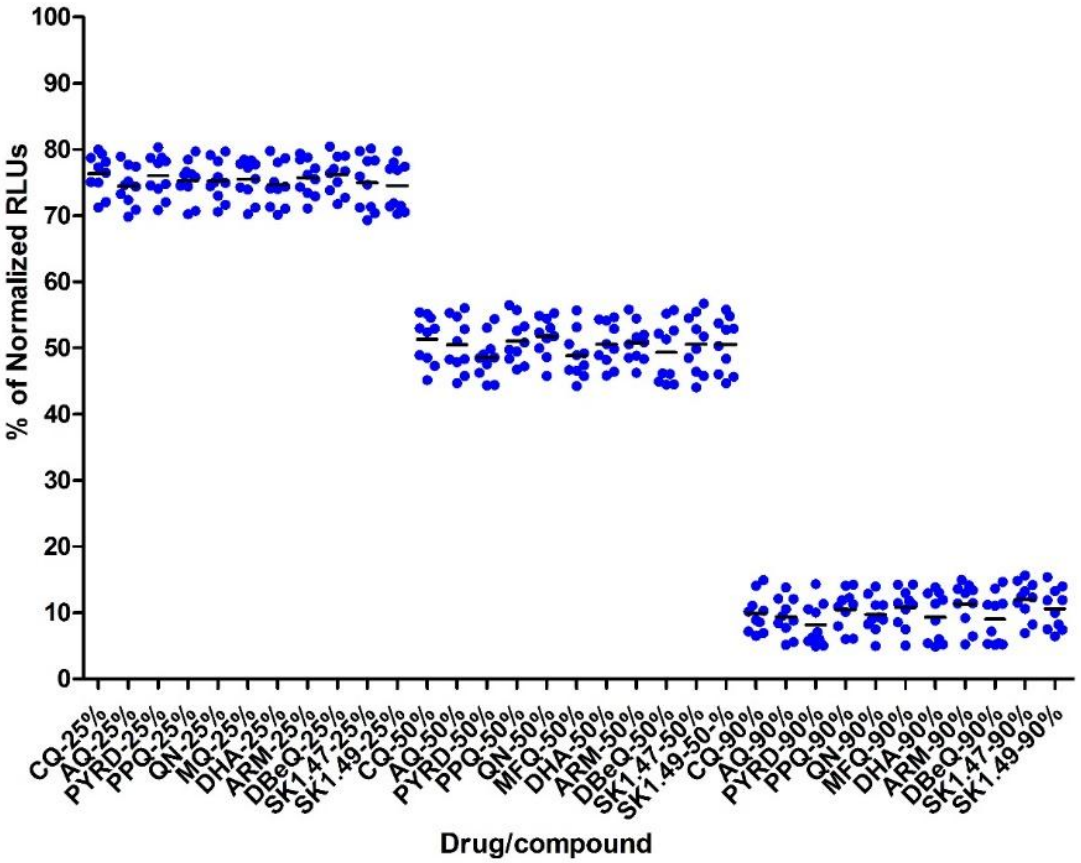

Fig. 6.2 Loss of normalised bioluminescence signals used to provide matched samples of 25%, 50% and 90% kill (see X axis for compound and the kill effect achieved) for intraerythrocytic *P. falciparum* used for studies of apoptotic markers. Data from ten experiments for each treatment are plotted with the mean indicated by a black bar.

6.2.2 Monitoring of mitochondrial outer membrane potential (ΔΨm) collapse following drug/compound treatment

Exposing intraerythrocytic stage of *P. falciparum* to a range of antimalarial drugs induced a collapse of the ΔΨm (Ch'ng *et al.,* 2010; Gunjan *et al.,* 2016; Meslin *et al.,* 2007; Porter *et al.,* 2008; Totino *et al.,* 2008). This feature has been assessed using both fluorescence microscopy and flow cytometry with range of fluorescent markers of ΔΨm, including the MitoProbe JC-1, $DiOC_6(3)$ and rhodamine 123. Here, we used the membrane-permeable fluorescent JC-1 dye, this provides a potential-dependant accumulation in the mitochondrial membrane, where accumulation results in an emission shift from green (~530 nm) to red (~590 nm). Collapse of the ΔΨm and subsequently increase in mitochondrial membrane permeabilization reduce the accumulation of JC-1, which leading to reduction of the red fluorescent signal. As a control in these experiments, the ionophore carbonyl cyanide m-chlorophenyl hydrazine (CCCP) was added at final concentration 200 µM. At this concentration a rapid collapse of ΔΨm represented by reduction of red/green fluorescence ratio was found (Porter, 2007).

Initial experiments were performed using fluorescence microscopy to monitor the loss of a punctate red fluorescent signal (the mitochondria marker). Untreated intraerythrocytic cultures show a bright punctate red signal, associated with the mitochondria, and a green fluorescent signal associated with accumulation of lower concentrations of JC-1 in the cytoplasm (Fig. 6.3). In cultures exposed to CCCP (as a negative control), loss the punctate red signal, with observation of a green signal in the cytoplasm were found (Fig. 6.3). Exposure to increasing concentrations of CQ, similarly to that reported by Ch'ng *et al.* (2010), caused in a reduction and then complete loss of the red fluorescence signal (Fig. 6.3). Three independent experiments were carried out, with 60-70 iRBCs/sample were

counted for each of the three kill effects (25%, 50% and 90%) for all 11 drugs/compounds. The mean ± SD of the iRBCs lacking a red fluorescent signal were counted and are reported in Fig. 6.4.

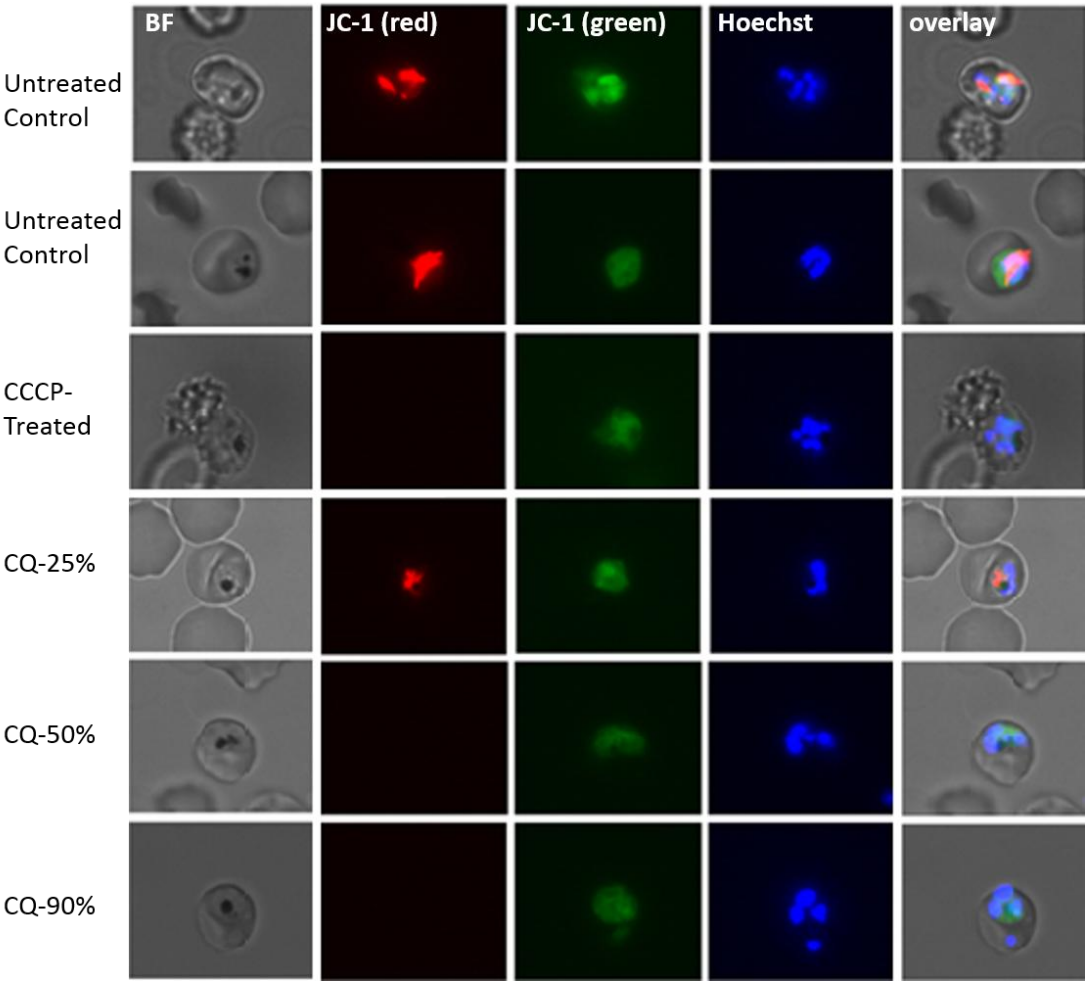

Fig. 6.3 JC-1 fluorescence assay to monitor ΔΨm collapse following exposure to increasing concentrations of CQ. The panels illustrate the brightfield (BF), red and green fluorescence signals associated with aggregate and monomer JC-1 forms respectively, nuclear staining (blue) using a Hoechst 33342 dye, and a final merge overlay for an iRBC. The y-axis indicates the treatment (or untreated control) applied to the culture. The increasing concentration of CQ applied reflects the increasing kill effect achieved within 6 hrs.

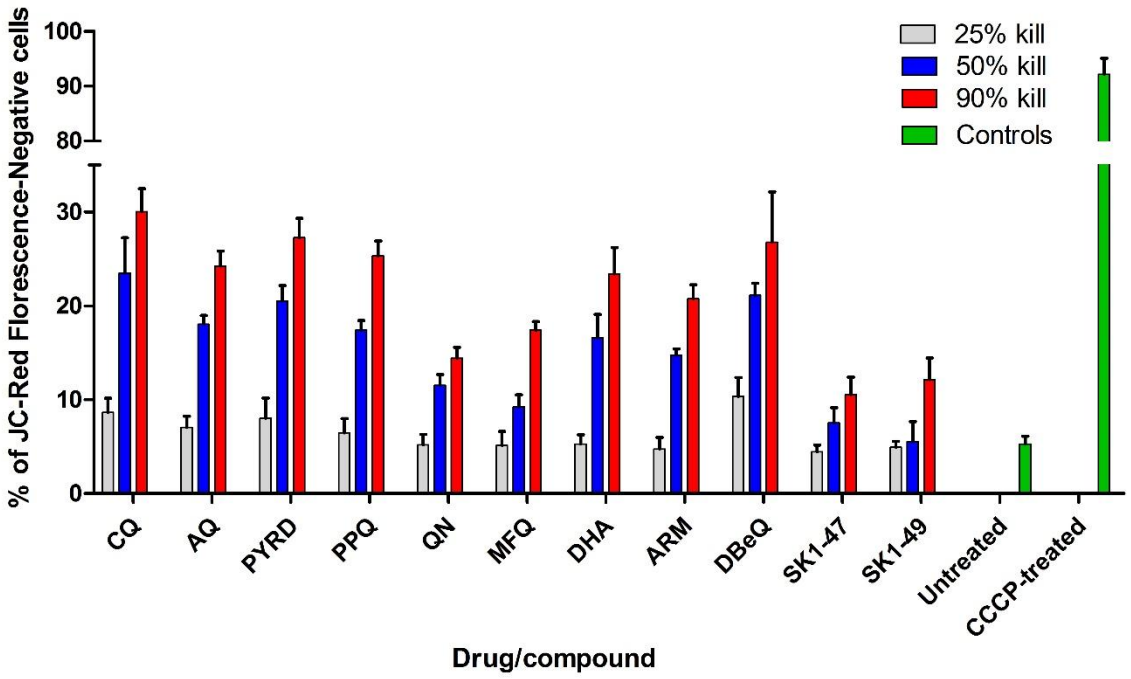

Drug/Comp.	CQ	AQ	PYRD	PPQ	QN	MQ	DHA	ARM	DBeQ	SK1.47	SK1.49
25%											
50%											
90%											

Fig. 6.4 Bar chart reporting the counts of infected erythrocytes (iRBCs) with a collapsed ΔΨm (lacking red fluorescent signal from JC-1 aggregate) following exposure to the indicated drug/compound. The key reports the kill effect achieved by the increasing concentrations of the drug/compound used. The bars report the mean of three independent counts, with the error bars reporting the SD. Below the chart is a table providing a heat map of the statistical test (one-way ANOVA, with Dunnett post-test) of the difference compared to the untreated control. The coloured boxes in which red, orange and yellow refer to $P < 0.0001$, 0.001 and 0.05, respectively, whilst a white box represents no significant difference with the untreated control.

This chart provides a series of expected results, Specifically; (i) the CCCP treatment results in the collapse of ΔΨm in the majority (> 90%) of iRBCs (Porter, 2007; Coronado *et al.* 2016), noting that a red signal will disappear or typically very small compared to the untreated control, (ii) a small proportion of untreated cells lack a red fluorescent signal, this has previously been reported (Ch'ng *et al.,* 2010; Totino *et al.,* 2008) and (iii)

Concentration-dependent effect for CQ, where increasing the concentration of CQ results in increase proportion of cells lacking red signal.

For all drugs/compounds tested, the proportion of cells with a ΔΨm collapse increased as the concentration of compound/drug increases, although the range of this increase is clearly different. ΔΨm collapse following exposure to 90% kill dose for drugs/compounds was much more significant than those exposed to 25% kill dose (all $P < 0.05$ using a Bonferroni post-test of ANOVA), although the same is not true for all compounds when comparing the ΔΨm collapse between the 90% and 50% kill. Comparison of the significance of the proportion of parasites showing collapse of ΔΨm for all drugs/compounds treatments at three kill effects against the untreated control (one-way ANOVA with a Dunnett post-test) are shown as a heat map in Fig. 6.4. The data suggests that the extent of the ΔΨm collapse as the concentration of the drug/compound is increased shows a trend, where the 4-aminoquinolines and the related PPQ and PYR, artemisinins and DBeQ > arylamino alcohols > SK1.47 and SK1.49.

Inconsistent effects on ΔΨm following treatment with putative autophagy inhibitors were observed. These differences are illustrated in Fig. 6.5, where representative fluorescence images are shown for DBeQ, SK1.47 and SK1.49, indicating lacking of concentration-dependent collapse of ΔΨm with the latter two compounds.

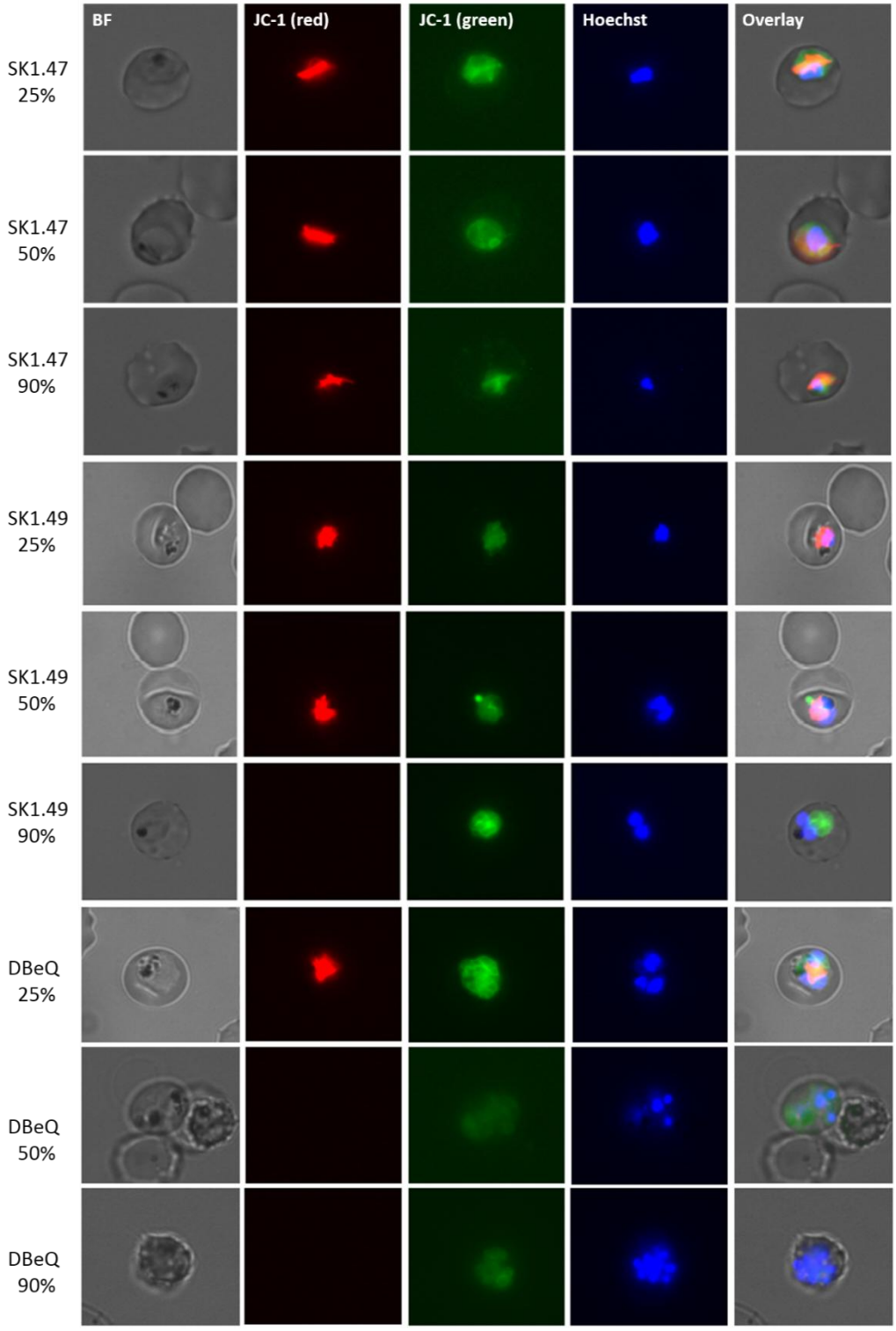

Fig. 6.5 JC-1 fluorescence assay to monitor ΔΨm collapse following exposure to increasing concentrations of SK1.47, SK1.49 and DBeQ by fluorescence microscopy. The panels illustrate the brightfield (BF), red and green fluorescence signals associated with aggregate and monomer JC-1 forms respectively, nuclear staining (blue) using a Hoechst 33342 dye, and a final merge overlay for an iRBC. The y-axis indicates the compound and the kill effect applied to the culture.

Exploring ΔΨm collapse using flow cytometry offers the opportunity to monitor the red/green fluorescence intensity for thousands of iRBCs (Nyakeriga *et al.,* 2006; Porter, 2008; Ch'ng *et al.*, 2010; Engelbrecht and Coeltzer, 2013). This was applied here, with samples treated as above and then processed for flow cytometry. For each sample, 100,000 cells include infected and uninfected erythrocytes were analysed.

Forward and side scatter were used to gate a population of erythrocytes and the proportion of green (excitation/emission λ= 488/525nm) and red (excitation/emission λ= 535/575nm) fluorescent cells in this gated population determined (Fig. 6.6). Thresholds for the green and red fluorescence were established using the untreated and CCCP controls. The threshold captures the green fluorescent population (all iRBCs) in the region H2 for untreated cultures. The same threshold used to monitor red fluorescent population in region H3 and this captures the majority of the same population as H2 in untreated cells (red fluorescence intensity is less than that of green). The H3 red fluorescent population was dramatically reduced in CCCP-treated cultures. Using this approach, the proportion of red/green cell counts are used to determine the proportion of iRBCs labelled with the JC-1 aggregate (or red signal) as an indicator of normal ΔΨm. The cell count v fluorescence intensity plots for cultures exposed to increasing concentrations of CQ (Fig. 6.6). As expected, as the concentration of CQ increases the proportion of cells gated in H3 (red fluorescence-labelled cells) decreases, reporting an increase in proportion of cells with ΔΨm collapse.

The counting of the proportion of iRBCs with a red fluorescence signal following exposure to three kill concentrations (25%, 50% and 90%) of each drug are plotted in Fig. 6.7. The untreated control suggests approximately 5% of the parasites lack a red signal, in agreement with the direct counts by microscopy. The CCCP treated cultures report

around 17% of iRBCs with JC-1 red fluorescence. This appears to be an issue with the ratio relying on changes to the green fluorescence signal irrespective of the treatment provided. Whilst it is clear that exposure to lower concentrations of compounds has a minimal effect on the proportion of green fluorescent parasites compared to the untreated control, increasing concentrations of all compounds affects the accumulation of JC-1 monomers and thus reduces the proportion of green fluorescent parasites. This means that some caution needs to be applied in interpreting Fig. 6.7.

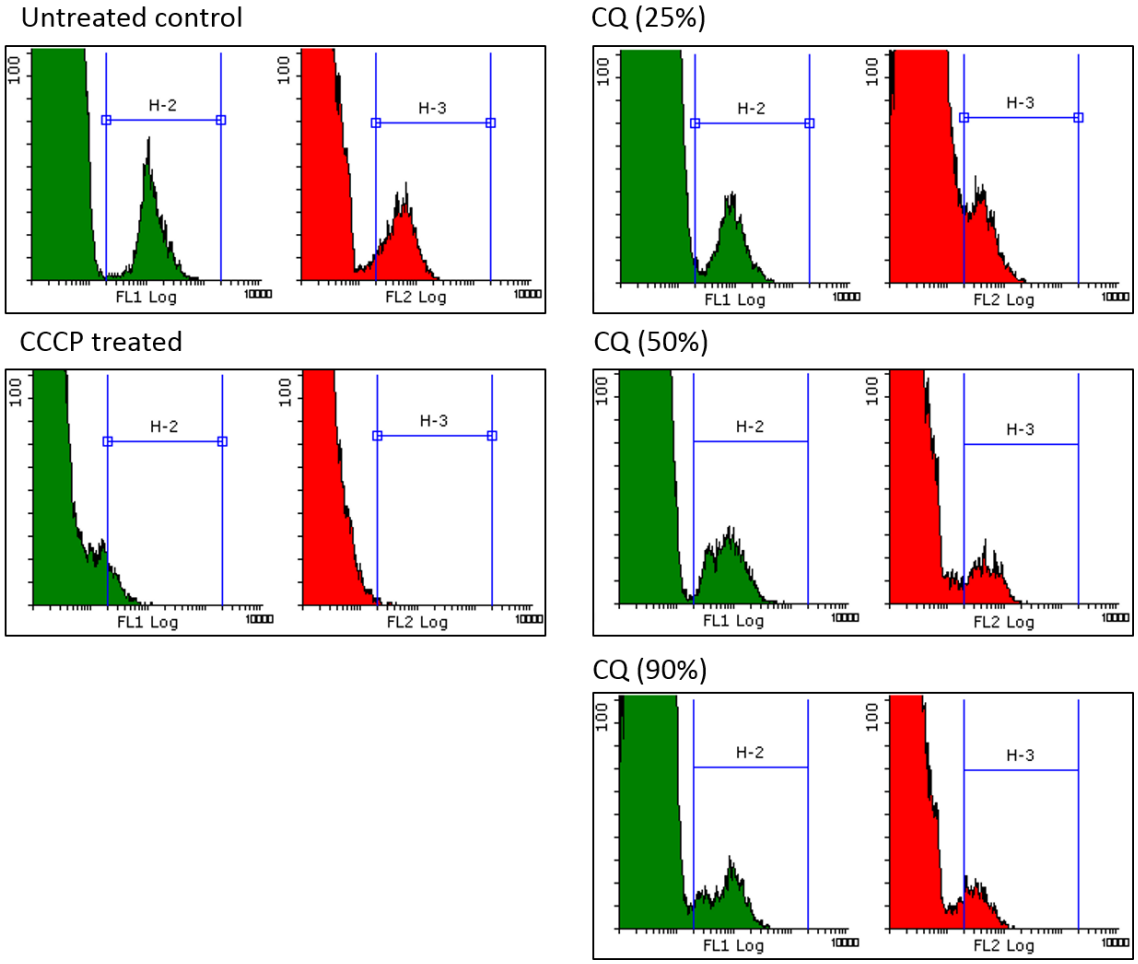

Fig. 6.6 Defining the thresholds H2 (green JC-1 monomer) and H3 (red JC-1 aggregate) used to monitor ΔΨm collapse by flow cytometry. Plots of event counts (y axis) versus green and red Log_{10} fluorescence intensity (x-axis) for a gated erythrocyte/infected erythrocyte population stained with JC-1. The gates used to count the green (H2) and red (H3) fluorescent cells (events) are indicated on each graph along with the treatment applied. Note – CCCP treatment, as well as preventing JC-1 aggregate formation (red fluorescence) also affects the accumulation of JC-1 monomers (green fluorescence) as reflected in the left shift in the fluorescence intensity in this population.

It appears that SK1.47 and SK1.49 have a minimal effect on ΔΨm, with no significant differences between all concentrations used compare to untreated control. A significant difference between the proportions of red/green fluorescent cells in untreated cultures versus cultures exposed to the highest concentrations of 4 amino-quinolines, artemisinins and DBeQ was also evident (Fig. 6.7). These findings agree with those of the direct observation of treated parasites by microscopy.

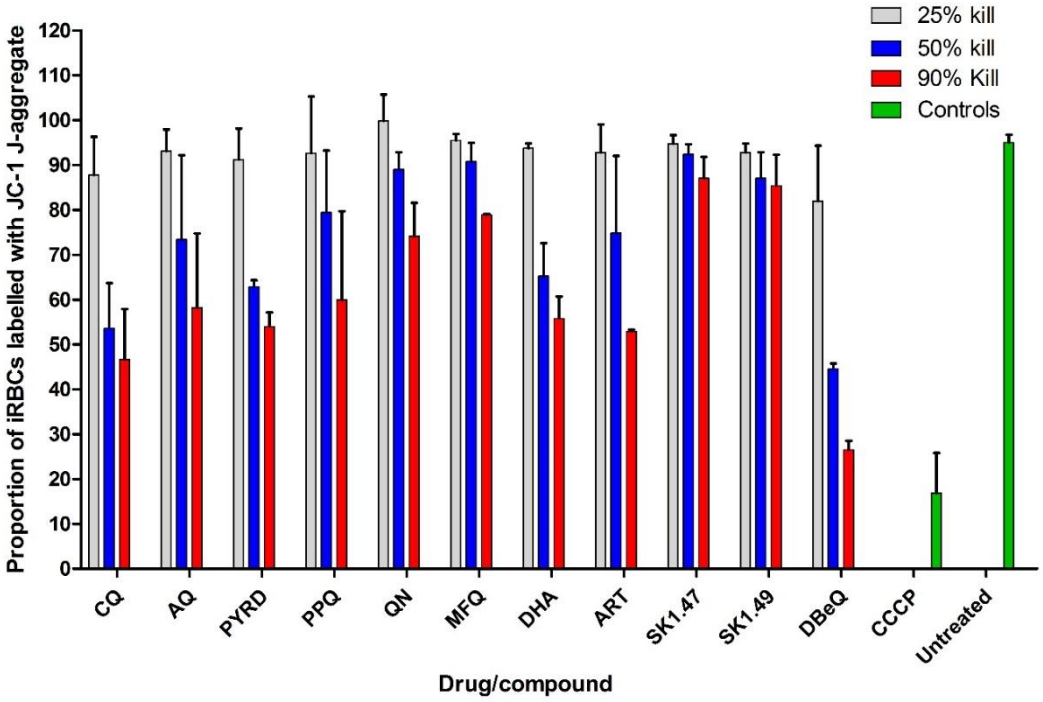

Drug/Comp.	CQ	AQ	PYRD	PPQ	QN	MQ	DHA	ARM	DBeQ	SK1.47	SK1.49
25%											
50%											
90%											

Fig. 6.7 Bar chart reporting the proportion of intraerythrocytic parasites retaining a red JC-1 fluorescence signal following drug/compound exposure by flow cytometry. The y-axis reports the proportion of JC-1 red/green labelled iRBCs from analysis of flow cytometry data. The means of three independent experiments are shown with error bars reporting the SD. The key indicated the kill effect achieved for each of the drugs/compounds tested. Below the chart is a table providing a heat map of the statistical test (one-way ANOVA, with Dunnett post-test) of the difference compared to the untreated control. The coloured boxes in which red, orange and yellow refer to $P < 0.0001$, 0.001 and 0.05, respectively, whilst a white box represents no significant difference with the untreated control.

One potential issue with the scoring system used for fluorescence microscopy is that any red punctate signal is scored as a parasite with unaffected mitochondria. This was not the case, and is illustrated in Fig. 6.3 where the CQ-25% treated parasite has a smaller red punctate signal than an untreated control. This was also an issue with the flow cytometry, where exposure to higher concentrations of drugs/compounds (and CCCP) affected both the green and red fluorescence intensity, taking events below the threshold applied to be determined as positive for green or red fluorescence. To overcome this limitation, we applied a "population" rather than a "individual" cell-based approach and monitored the red and green fluorescence of the whole population of treated parasites using a fluorescence plate reader. Using a 96-well microplate format, three technical repeats of each treatment were done, with three biological repeats for each plate (n=9). The red fluorescence signal from the CCCP-treated parasites was used as a baseline with the subsequent mean of the red/green fluorescence ratio determined as 1 for untreated parasites. Thus, a reduction in the relative green/red fluorescence ratio would report a loss of red fluorescence signal and thus ΔΨm collapse.

As above, all compounds/drugs at all concentrations were applied and the mean ± SD of the relative red/green fluorescence ratios plotted (Fig. 6.8). A concentration-dependant ΔΨm collapse was evident for all compounds tested except SK1.47 and SK1.49. Whilst exposure to the highest concentration of SK1.49 produced a significant difference in the relative red/green ratio compared to an untreated control, this was only a small difference. These results, in terms of the differences achieved and their significance, are more comparable to the direct counts from microscopy. However, taken together, all the results for the JC-1 assays similarly report;

(i) An apparent concentration-dependent effect on ΔΨm collapse for all drugs/compounds used except SK1.47 and SK1.49.

(ii) Minimal effects on ΔΨm when exposed to concentrations of compounds/drugs that result in a 25% kill over 6 hrs.

(iii) SK1.47 and SK1.49 appear to have a minor effect on ΔΨm even when used at highest concentrations (90%) – an observation that is very different to that for DBeQ.

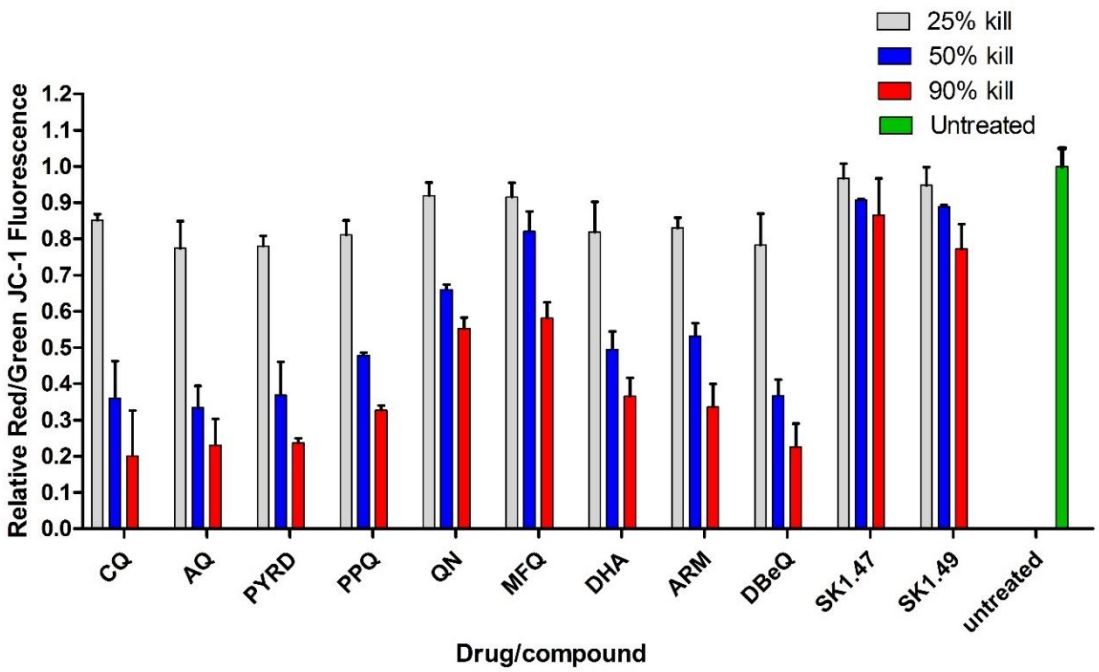

Drug/Comp.	CQ	AQ	PYRD	PPQ	QN	MQ	DHA	ARM	DBeQ	SK1.47	SK1.49
25%											
50%											
90%											

Fig. 6.8 Bar chart reporting the Relative Red/Green Fluorescence JC-1 Ratio in intraerythrocytic parasites exposed to the indicated treatment using plate reader. The means (n=9) are shown with error bars reporting the SD. The key indicates the kill effect achieved for each of the drugs/compounds tested. Below the chart is a table providing a heat map of the statistical test (one-way ANOVA, with Dunnett post-test) of the difference compared to the untreated control. The coloured boxes in which red, orange and yellow refer to $P < 0.0001$, 0.001 and 0.05, respectively, whilst a white box represents no significant difference with the untreated control.

(iv) There appears to be a consistent rank order in the effect of the chemical classes used in causing ΔΨm collapse, where 4-aminoquinolines, artemisinins and DBeQ > arylamino alcohols > SK compounds.

6.2.3 Monitoring DNA fragmentation following drug/compound exposure

Evidence to support existence of apoptotic-like cell death in *Plasmodium* parasites includes the detection of DNA fragmentation using the Terminal deoxynucleotidyl transferase dUTP Nick End Labelling (TUNEL) assay (Ch'ng *et al.,* 2010; Meslin *et al.,* 2007). This assay is based on the incorporation of a fluorescein-dUTP (green fluorescence) by a terminal deoxynucleotidyl transferase to the free 3' OH ends of genomic DNA created by double-strand breaks during apoptotic cell death (Ribeiro *et al.,* 2017). DNase I-treated iRBCs served as a control positive. Principally, DNase I induces break in DNA double strand that can be labelled (Fig. 6.9), noting that the colocalization of the green TUNEL and blue genomic DNA fluorescence signals was dependent for the cells that counted as TUNEL-positive cells.

Initial experiments (data not shown) showed only a very small proportion of TUNEL-positive cells following exposure to high concentrations of CQ over 6 hrs. As this was the case, the experiment was modified to only use concentrations of drugs/compounds that killed 50% and 90% of the parasite cultures in 6 hrs. In addition, only one drug from each class were selected for the analysis; CQ as a 4-aminoquinoline, QN as the arylamino alcohol and DHA for the artemisinin. Compounds SK1.47, SK1.49 and DBeQ were also included in all assays. The length of exposure to each concentration used was, however, extended to include time points at 6, 24 and 48 hrs based on previous work by Ch'ng *et al.* (2010) that would suggest that DNA fragmentation is a late stage in apoptotic cell death.

The first analysis scored TUNEL-positive cells by fluorescence microscopy. Fig. 6.9 illustrates how this scoring was applied using CQ exposure as an example. TUNEL-positive cells were defined as having a distinct punctate (not dispersed) green fluorescent signal that overlapped with the blue fluorescence stain of genomic DNA by Hoechst 33342.

Experiments were done in triplicate, with the proportion of TUNEL-positive cells from counts of 60-70 iRBCs for each drug/compound treatment scored and the mean ± SD plotted (Fig. 6.10). As expected, > 90% TUNEL-positive cells following DNase I treatment were reported. This is similar to previous work by others (Engelbrecht *et al.,* 2012). A small proportion of untreated cells was also labelled by a green fluorescence – these reflecting either a background of dead or dying cells or an artefact of labelling in parasites undergoing DNA replication. The data shows a time-dependant effect, with the highest proportions of TUNEL-positive cells found after 48 hrs (Fig. 6.10). Concentration-dependant effect, however, is lacking in this assay as comparison of the proportions of TUNEL-positive cells at equivalent timepoints for two concentrations of drugs/compounds are not significantly different (ANOVA, Bonferroni post-test). Comparison of TUNEL labelling of all samples against the untreated control only reveal a significant difference after 48 hrs for CQ, DHA, DBeQ and SK1.49, with the latter having the lowest proportion of TUNEL-labelled cells in this group (Fig. 6.10).

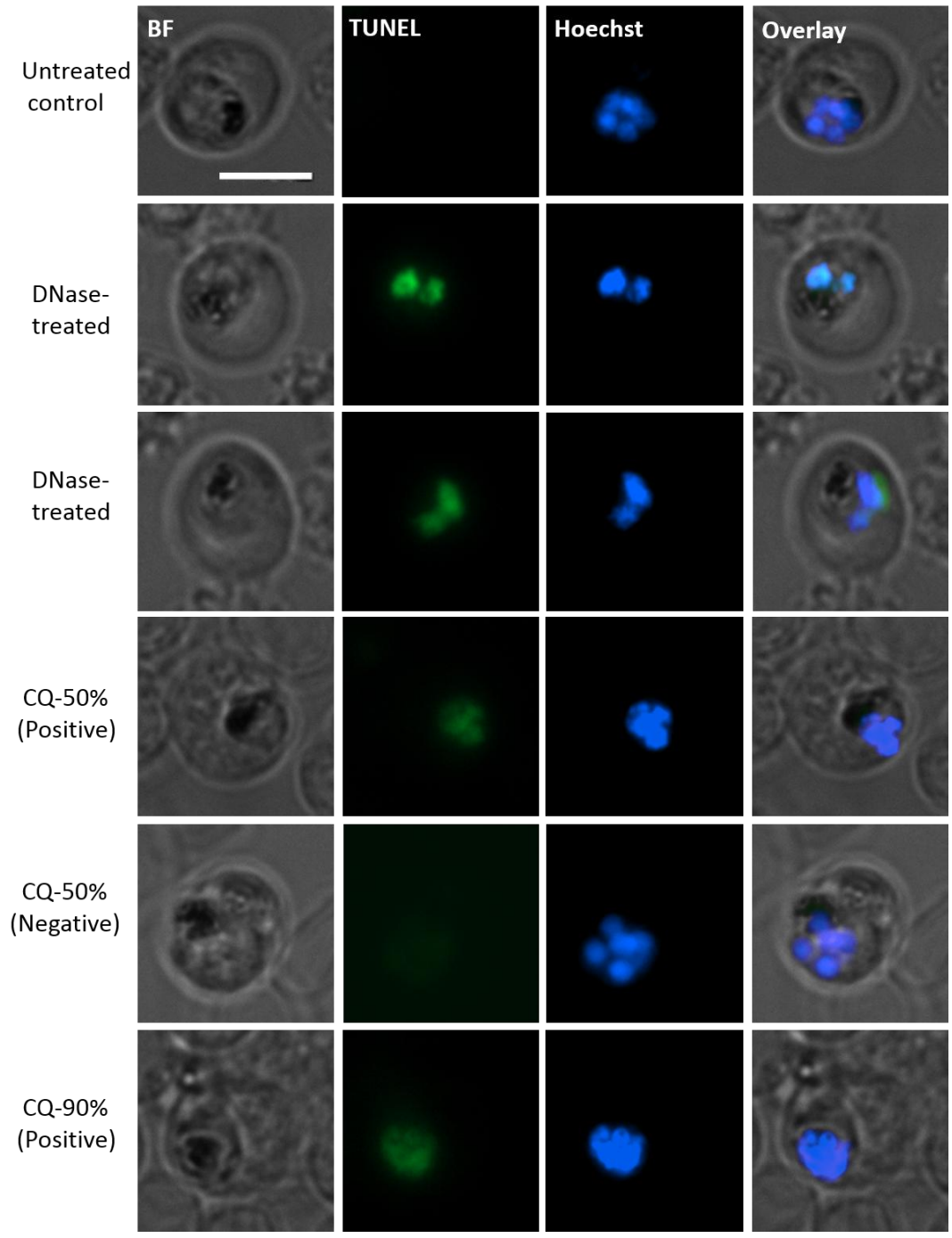

Fig. 6.9 TUNEL assay of *P. falciparum* infected RBCs exposed to 50% and 90% kill concentrations of CQ for 6 hrs using fluorescence microscopy. Panels show brightfield (BF), green fluorescein labelling by the TUNEL assay, nuclear DNA staining using Hoechst 33342 (blue fluorescence) and a merged overlay of these images. The bar in the first panel is 5 µm in size.

To increase the numbers of events monitored, the assays were repeated and TUNEL-positive iRBCs scored using flow cytometry. The assay was repeated three times, with the parasitaemia at the start of each experiment being determined using SYBR Green I

staining and counting by flow cytometry (Fig. 6.11). Counterstaining of the TUNEL assays with SYBR Green I was not possible as both depending on detection of green fluorescence. Using the forward/side scatter, the population of erythrocytes (infected and uninfected) were gated and the green fluorescence intensity versus side scatter plotted (Fig. 6.11). A fixed quadrant was established and threshold selected based on the detection of SYBR Green I stained iRBCs (Fig. 6.11C) and a minimum background for TUNEL-stained parasites in an untreated parasite culture (Fig. 6.11F).

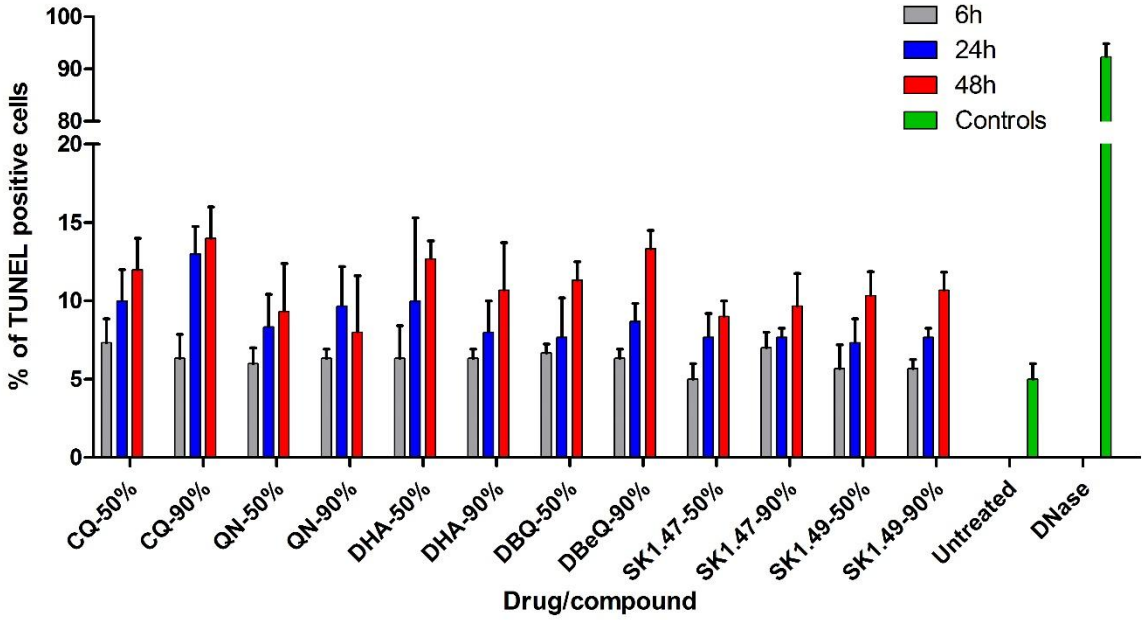

Drug /Comp.	CQ-50%	CQ-90%	QN-50%	QN-90%	DHA-50%	DHA-90%	DBQ-50%	DBeQ-90%	SK1.47-50%	SK1.47-90%	SK1.49-50%	SK1.49-90%
6hrs												
24hrs												
48hrs												

Fig. 6.10 TUNEL assay of DNA fragmentation in intraerythrocytic *P. falciparum* exposed to timecourse treatment of CQ, QN, DHA and putative autophagy inhibitors using fluorescence microscopy. The mean proportion of TUNEL-positive infected erythrocytes (iRBCs) scored is shown with ± SD (n=3). The key provides information of the length of exposure of cultures to the indicated drug/compound at the concentration that kills 50% and 90% of parasites after 6 hrs. Below the chart is a table providing a heat map of the statistical test (one-way ANOVA, with Dunnett post-test) of the difference compared to the untreated control. The coloured boxes in which red, orange and yellow refer to $P < 0.0001$, 0.001 and 0.05, respectively, whilst a white box represents no significant difference with the untreated control.

These parameters were used to confirm the detection of a high proportion of TUNEL-positive parasites treated with DNase I (Fig. 6.11G). Additionally, the proportion of TUNEL-positive cells following 50% (Fig. 6.11H) and 90% (Fig. 6.11I) concentrations of CQ were reported. These parameters were saved and used to determine the proportion of all iRBCs (determined using SYBR Green I) and TUNEL-positive cells following exposure to 50% and 90% kill concentrations of the drugs/compounds for 6, 24 and 48 hrs (Fig. 6.12).

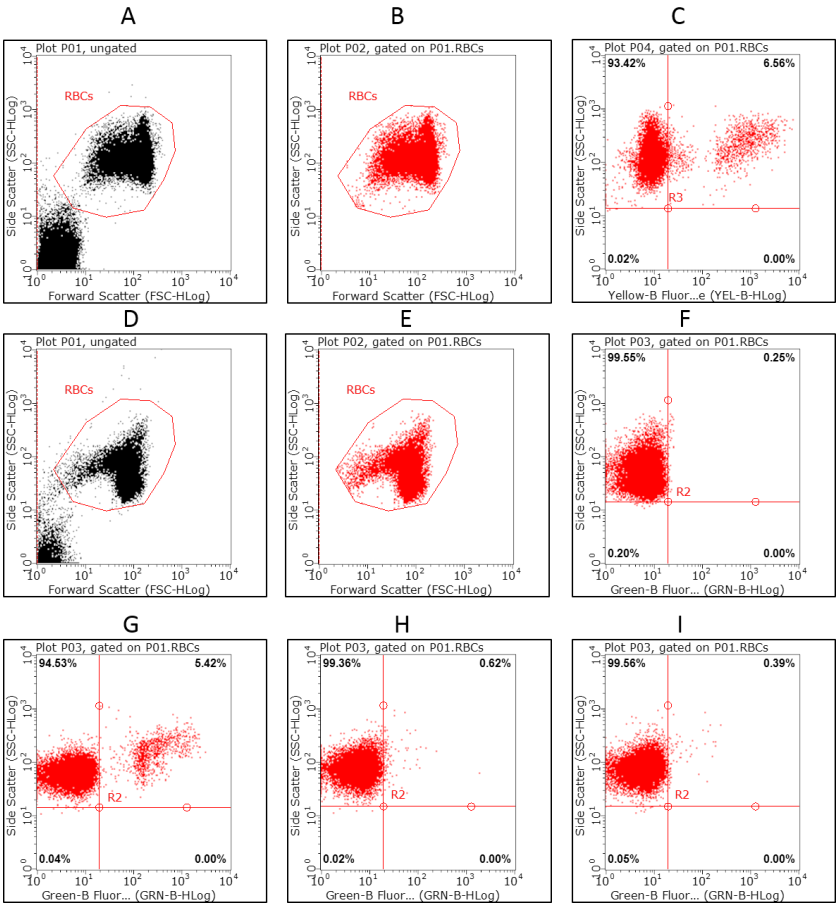

Fig. 6.11 Establishing the parameters for monitoring DNA fragmentation in compound/drug treated intraerythrocytic *P. falciparum* using the TUNEL assay using flow cytometry. A and **D** are forward and side scatter plots of untreated *P. falciparum* culture used to select the indicated gated region which is then highlighted in panels **B** and **E**, respectively. The events in the gated region of **B** are then plotted in **C** showing the fluorescence signal from SYBR Green I staining – this establishes the parasitaemia at 6.56%. The events in the gated region of **E** are similarly plotted in **F** to monitor the green fluorescence from the TNEL assay. Here –indicates that 3.8% (0.25/6.56) of the untreated parasites are TUNEL-positive. A similar plot of DNase treated parasites in **G** indicates that 82.6% (5.42/6.56) of the iRBCs are TUNEL-positive. Panels **H** and **I** represent the outcome following exposure to 50% (9.5%) and 90% (5.9%) of CQ for 6 hrs. 20,000 events are analysed in each experiment.

The controls in the flow cytometry analysis of TUNEL-staining provided almost identical results for the untreated and DNase treated controls in the direct microscopy count. Statistical analysis using ANOVA with a Bonferroni post-test revealed no significant differences when comparisons were made to explore a concentration-dependant effect of each compound/drug (compare matched timepoints between the 50% and 90% kill) or a time-dependant effect (compare timepoint data for each concentration of compound/drug). This outcome reflects the range of TUNEL-positive data between 5-15%, with comparisons against the untreated control revealing no consistent pattern of significant differences on treatment with different drugs/compounds over different timepoints (Fig. 6.12).

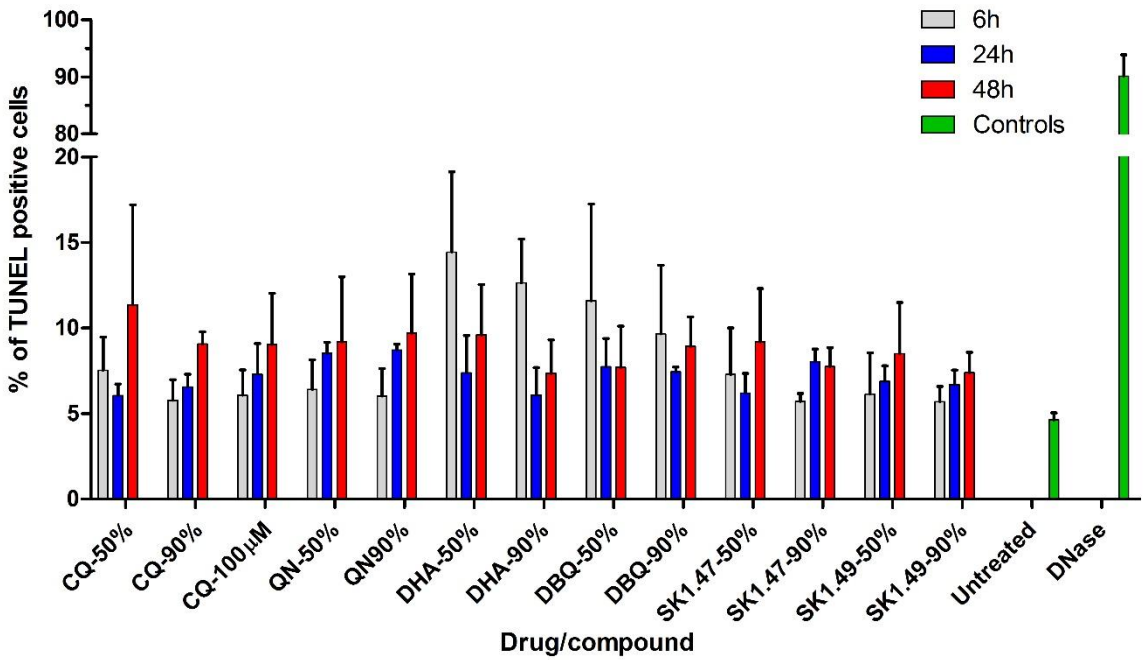

Drug /Comp.	CQ-50%	CQ-90%	CQ-100µM	QN-50%	QN-90%	DHA-50%	DHA-90%	DBQ-50%	DBeQ-90%	SK1.49-50%	SK1.49-90%	SK1.47-50%	SK1.47-90%
6hrs													
24hrs													
48hrs													

Fig. 6.12 TUNEL assay of DNA fragmentation in intraerythrocytic *P. falciparum* exposed to timecourse treatment of CQ, QN, DHA and putative autophagy inhibitors using flow cytometry.

The mean proportion of TUNEL-positive infected erythrocytes (iRBCs) scored by flow cytometry is shown with ± SD (n=3). The key provides information of the length of exposure of cultures to the indicated drug/compound at the concentration that kills the indicated % of parasites after 6 hrs. Below the chart is a table providing a heat map of the statistical test (one-way ANOVA, with Dunnett post-test) of the difference compared to the untreated control. The coloured boxes in which red, orange and yellow refer to $P < 0.0001$, 0.001 and 0.05, respectively, whilst a white box represents no significant difference with the untreated control.

The outcome reflects no clear evidence of DNA fragmentation following exposure to CQ, and this correlates with Totino *et al.* study (2008), although differs from Ch'ng *et al.* (2010). Given the potential that the lethal effect even at concentrations that kill 90% of parasites in 6 hrs was not enough, the analysis was repeated using a supralethal dose of 100 µM (Fig. 6.12). Again, no significant differences in TUNEL-positive cells compared to an untreated control were found. Resetting the fluorescence thresholds used to determine TUNEL-positivity cells did not change these observations (data not shown).

6.2.4 Monitoring protease activity following drug/compound exposure

Ch'ng *et al.* (2010, 2011) reported an increase in a Clan CA cysteine protease activity in intraerythrocytic trophozoite stage of *P. falciparum* following exposure to high concentrations of CQ, with similar observations of increased protease activity in mefloquine-treated parasites (Gunjan *et al.,* 2016). Again, there are also reports that described the absence of protease activity in CQ-treated parasites (Nyakeriga *et al.,* 2006; Porter *et al.,* 2008; Totino *et al.*, 2008). Clan CA cysteine protease activity was defined by Ch'ng *et al.,* (2010) based on the use of different inhibitors of protease classes. Typically, a CaspaTag-Pan Caspase assay employs a sulforhodamine-labelled peptide inhibitor (SR-VAD-FMK) of the caspase enzyme complex (typically a dimer). Irreversible binding of the inhibitor to the proteolytic cleavage site keeps the sulforhodamine-labelled peptide inhibitor in the cell after a series of wash steps (Fig. 6.13). The fluorescent signal being

monitored using a range of techniques include; fluorescence microscopy and flow cytometry. The caspase assay typically used in *P. falciparum* is the CaspaTag Pan-Caspase *In Situ* – a general assay format that does not readily distinguish between cysteine protease classes.

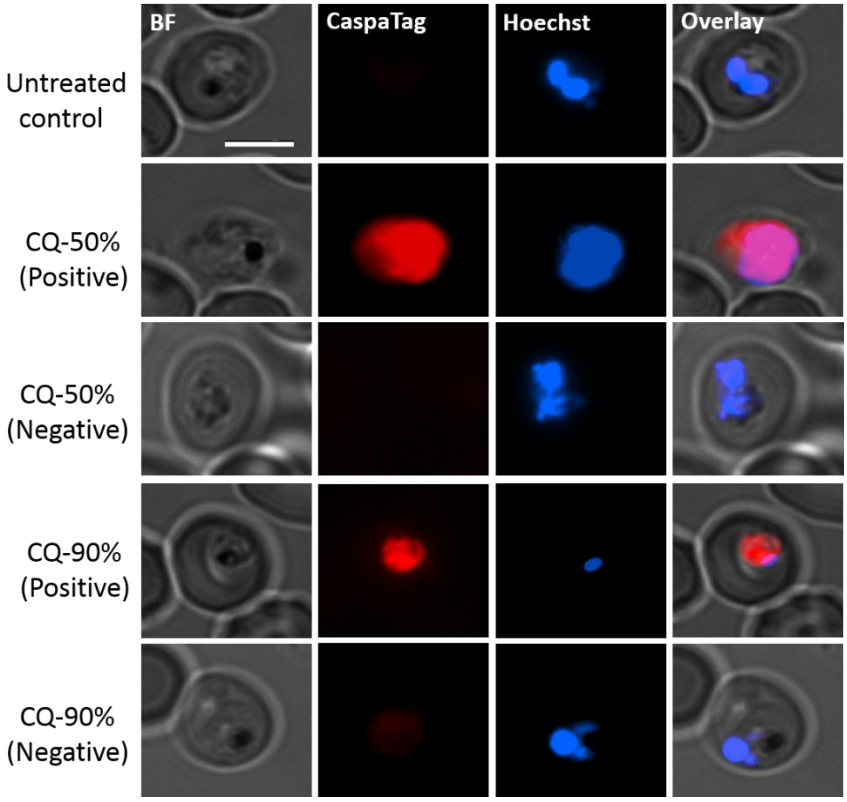

Fig. 6.13 CaspaTag staining of intraerythrocytic trophozoite stage of *P. falciparum* exposed to CQ. The panels show brightfield (BF), CaspaTag (red fluorescence from sulforhodamine), Hoechst 33342 (nuclear stain) and a merged overlay. The y axis indicates either the untreated control or experiments using concentrations of CQ that provide a 50% or 90% kill. Next to each line is whether this would be determined as a CaspaTag-labelled cell or not. Row from the top, untreated control, CQ-50% and CQ-90% treated parasites for 24 hrs. The bar is 5 µm.

However, to explore the action of protease activity following exposure to these drugs/compounds, the same CaspaTag Pan-Caspase *In Situ* assay format, utilising a sulforhodamine (red) fluorescent marker was employed. As with the TUNEL assay, initial data suggested low levels of proteases activity (Fig. 6.14). As such, the same approach

was adopted; using CQ and QN at 50% and 90% kill concentrations, but the time of assay extended to monitor effects at 6, 24 and 48 hrs. Three independent experiments, each counting approximately 60-70 iRBCs/sample, were done, with the mean ± SD of CaspaTag-positive cells plotted (Fig. 6.14).

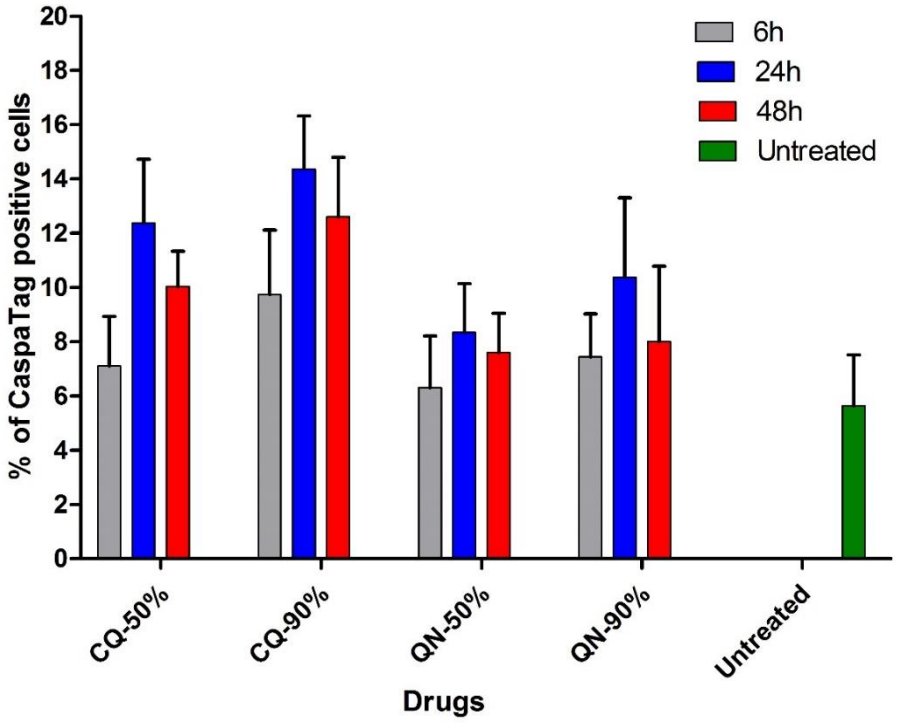

Drug	CQ-50%	CQ-90%	QN-50%	QN-90%
6hrs				
24hrs				
48hrs				

Fig. 6.14 Timecourse of CaspaTag staining of intraerythrocytic *P. falciparum* exposed to CQ and QN. The mean proportion of CaspaTag-positive cells (n=3) are shown with the SD as error bars. The key indicates the timepoint the determination presented was done. Below of the chart is a table providing a heat map of the statistical test (one-way ANOVA, with Dunnett post-test) of the difference compared to the untreated control. The coloured boxes in which red, orange and yellow refer to $P < 0.0001$, 0.001 and 0.05, respectively, whilst a white box represents no significant difference with the untreated control.

Whilst the overall proportion of CaspaTag-labelled parasites is low, a slight trend using CQ does emerge. Exposure to a higher concentration of CQ or for a longer time does result in a higher proportion of CaspaTag-labelled parasite, although the variance in data means not significant for all comparisons. These trends are not evident using QN. Comparison of the CaspaTag labelling to an untreated control does not reveal a consistent pattern of significant time-dependant labelling.

For further exploring of protease activity, CaspaTag assay was repeated for one antimalarial drugs in each class (CQ, QN and DHA) as well as included DBeQ, SK1.47 and SK1.49 using flow cytometry. As with the TUNEL assay, the parasitaemia of the untreated parasite culture was determined using SYBR Green I fluorescence staining (Fig. 6.15). By using the similar forward and side scatter parameters, the population of infected and uninfected erythrocytes were gated and counts of the SYBR Green I or sulforhodamine fluorescent parasites determined to provide a determination of the proportion of CaspaTag-labelled parasites (Fig. 6.15).

The mean proportion of CaspaTag-labelled cells from three independent experiments was plotted (Fig. 6.16). Our analysis suggests that assays performed at 48 hrs tend to have more CaspaTag-labelled parasites than those determined after only 6 hrs, although the variance in the data doesn't allow a significant trend to be established for all treatments. The data also shows that the highest concentrations of QN and the two SK compounds at 48 hrs exposure have significantly higher proportions of CaspaTag-labelled parasites compared to the untreated control. This observation, however, is balanced by the inconsistencies in the same data for DHA, where a longer incubation results in a decrease in the proportion of CaspaTag-labelled parasites. Again, based on the work of Ch'ng *et al.* (2010), we also included a supralethal concentration (100 µM) of CQ which again did not

provide any evidence of an appreciable change in the proportion of CaspaTag-labelled parasites at any timepoint. Readjustment the thresholds again did not provide any evidence of consistent trends.

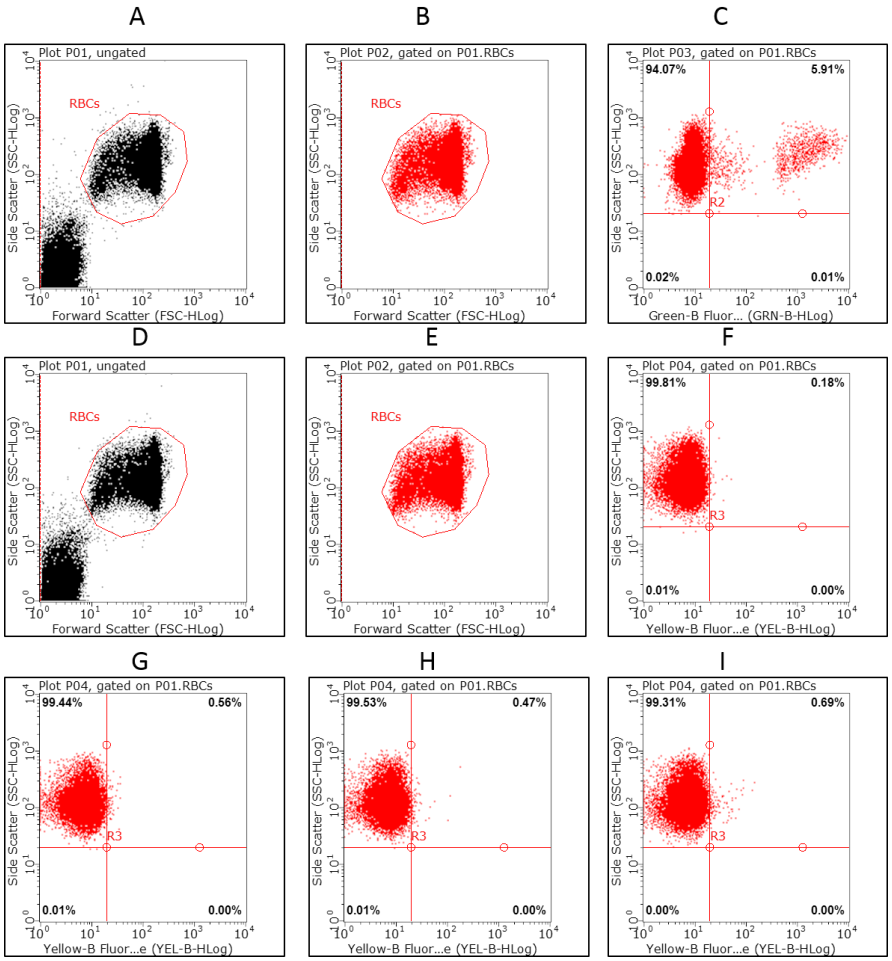

Fig. 6.15 Establishing the parameters for monitoring cysteine protease activity in compound/drug treated intraerythrocytic trophozoite stage of *P. falciparum* using the CaspaTag assay. A and **D** are forward and side scatter plots of untreated *P. falciparum* culture used to select the indicated gated region which is then highlighted in panels **B** and **E**, respectively. The events in the gated region of **B** are then plotted showing the fluorescence signal from SYBR Green I staining – this establishes the parasitaemia at 5.9%. The events in the gated region of **E** are similarly plotted in **F** to monitor the red fluorescence from the CaspaTag assay. Here this indicates that 3% (0.18/5.91) of the untreated parasites are CaspaTag-positive. Panels **G**, **H** and **I** represent the outcome following exposure to 50% (9.5%) and 90% (8.0%) of CQ or 90% (11.7%) of QN, kill effects respectively. 20,000 events are analysed in each experiment.

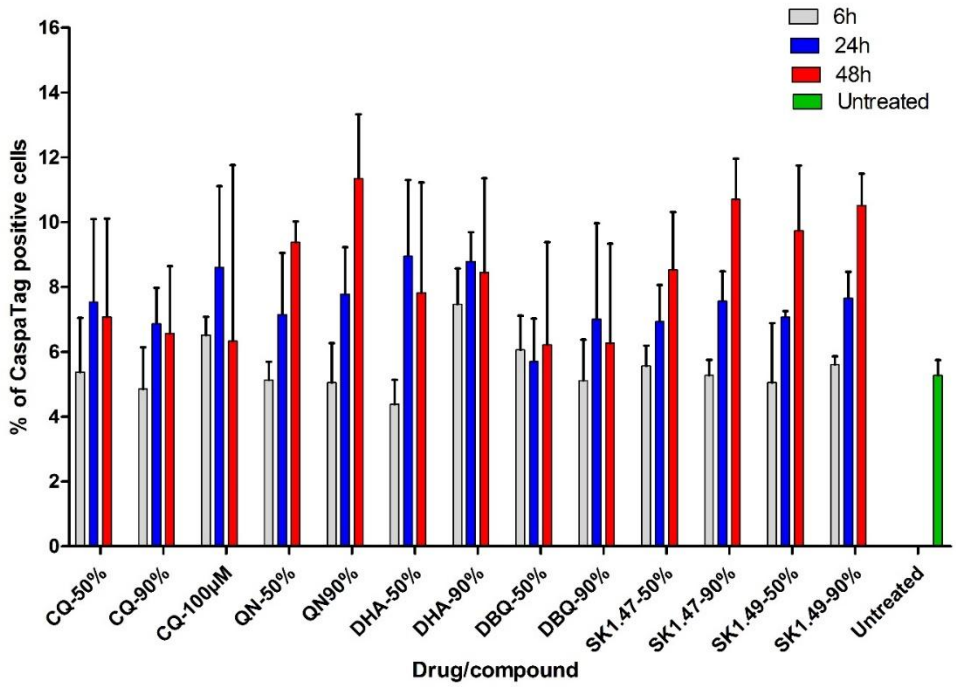

Drug /Comp.	CQ-50%	CQ-90%	CQ-100µM	QN-50%	QN-90%	DHA-50%	DHA-90%	DBQ-50%	DBeQ-90%	SK1.49-50%	SK1.49-90%	SK1.47-50%	SK1.47-90%
6hrs													
24hrs													
48hrs													

Fig. 6.16 CaspaTag assay of cysteine protease activity in intraerythrocytic *P. falciparum* exposed to timecourse treatment of CQ, QN, DHA and putative autophagy inhibitors. The mean proportion of CaspaTag-positive infected erythrocytes (iRBCs) scored by flow cytometry is shown with ± SD (n=3). The key provides information of the length of exposure of cultures to the indicated drug/compound at the concentration that kills the indicated % of parasites after 6 hrs. Below the chart is a table providing a heat map of the statistical test (one-way ANOVA, with Dunnett post-test) of the difference compared to the untreated control. The coloured boxes in which red, orange and yellow refer to $P < 0.0001$, 0.001 and 0.05, respectively, whilst a white box represents no significant difference with the untreated control.

6.2.5 Assessment of Ca^{2+} redistribution following drug/compound exposure

The parasite digestive vacuole provides a dynamic store of Ca^{2+} in intraerythrocytic trophozoite stages of *P. falciparum* and plays a critical role in parasite development by controlling intracellular Ca^{2+} signalling (Biagini *et al.,* 2003). Ch'ng *et al.* (2011) suggested that the high concentration of CQ causes partial permeabilization of the digestive

vacuole, leading to a redistribution of Ca^{2+} from this compartment into the parasite cytoplasm which may acts as a trigger for subsequent apoptotic processes. Similarly, Caridha *et al.* (2008) demonstrated a redistribution of Ca^{2+} in mammalian cells following exposure to MQ. To explore the early effects of antimalarial drugs/compounds on Ca^{2+} distribution, the Ca^{2+} indicator Fluo-4-AM was used with fluorescence microscopy. Parasite cultures were initially exposed to 25%, 50% and 90% kill concentrations of CQ and the distribution of the green fluorescent Fluo-4-AM dye monitored by fluorescence microscopy (Fig. 6.17). Untreated control parasites have a punctate green fluorescent signal, spatially separated from the nucleus that represents the concentration of Ca^{2+} stores in the digestive vacuole (Biagini *et al.,* 2003; Ch'ng *et al.,* 2011) as visualised with the dense hemozoin material in the brightfield image. In exposure to increasing concentrations of CQ, this Ca^{2+} store is redistributed to the cytoplasm, losing its distinct punctate distribution that does not overlap with the nucleus, where often an unlabelled space representing the position of the digestive vacuole is left. At the highest concentrations of CQ, this latter unlabelled compartment was lost in small proportion of iRBCs, suggesting that complete permeabilization of the digestive vacuole occurred and the Ca^{2+} distributed throughout the parasite cytoplasm.

Using the same protocol and scoring process, the distribution of Ca^{2+} following treatment with 25%, 50% and 90% kill concentrations of the benchmark antimalarials and putative autophagy inhibitors was assayed. The mean proportion of digestive vacuole and cytoplasm that stained with Fluo-4-AM or unlabelled (i.e. nuclear stain only observed) for three independent experiments is shown (Fig. 6.18). The untreated sample predominantly consists of digestive vacuole labelling (mean of 85%), with smaller proportions showing cytoplasmic staining (9%) or unlabelled (5%). As expected from the work reported by

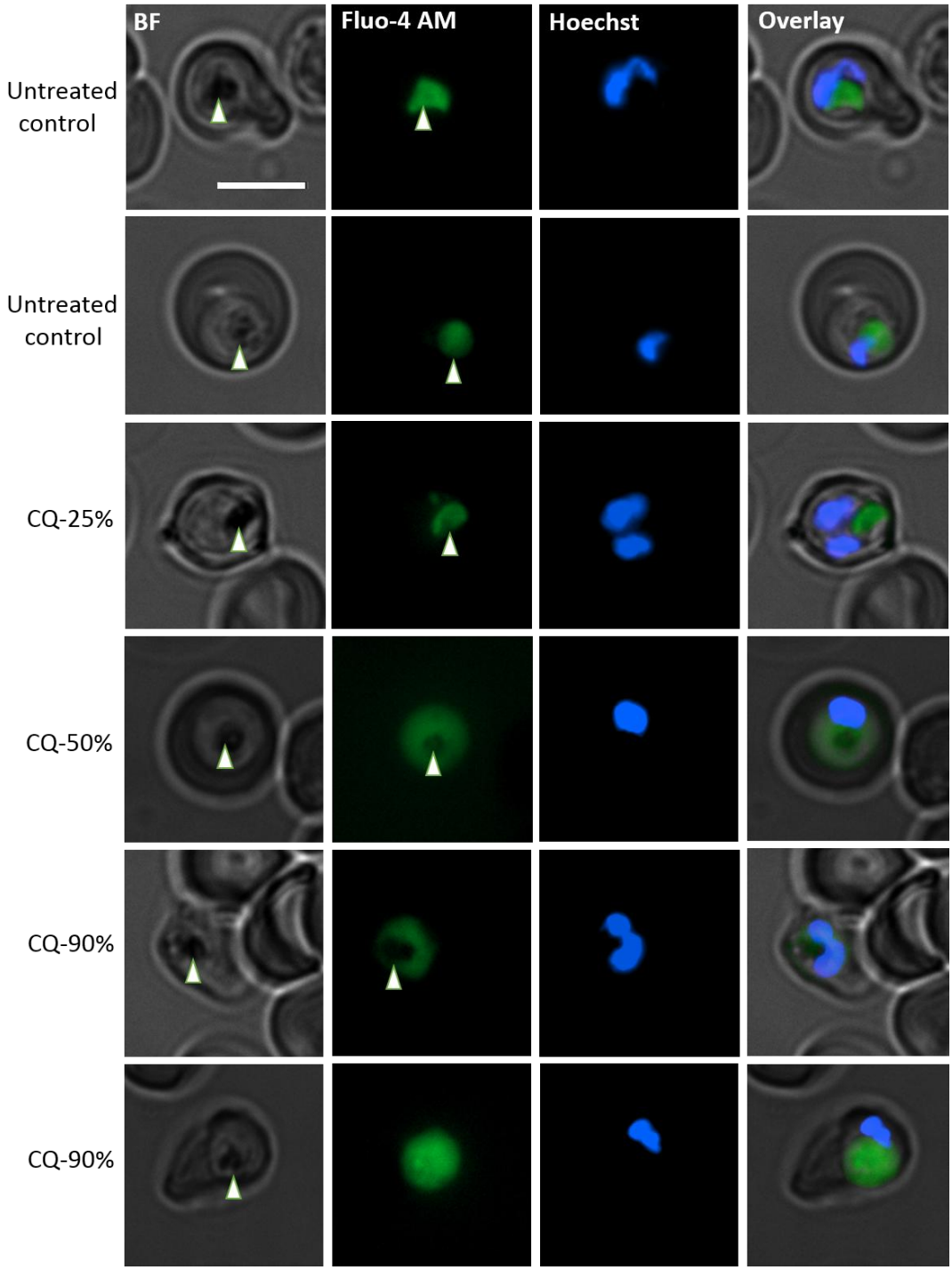

Fig. 6.17 Monitoring of Ca^{2+} distribution in intraerythrocytic *P. falciparum* exposed to 25%, 50% and 90% kill concentration of CQ. Panels show brightfield (BF), Fluo-4 AM (green) fluorescence located either as a punctate signal collocated with the hemozoin of the digestive vacuole (white arrows) in untreated or 25% CQ killed parasites or distributed throughout the cytoplasm (CQ>50% kill), Hoechst 33342-stained nucleus (blue fluorescence) and a merged overlay. The bar is 5 µm.

Ch'ng *et al.* (2011), a cytoplasmic redistribution of Ca^{2+} appears to follow a concentration dependent trend. This appears to be feature for the 4-aminoquinolines CQ, AQ, PPQ and PYRD treatment (Fig. 6.18), but less obviously for the other drugs/compounds tested.

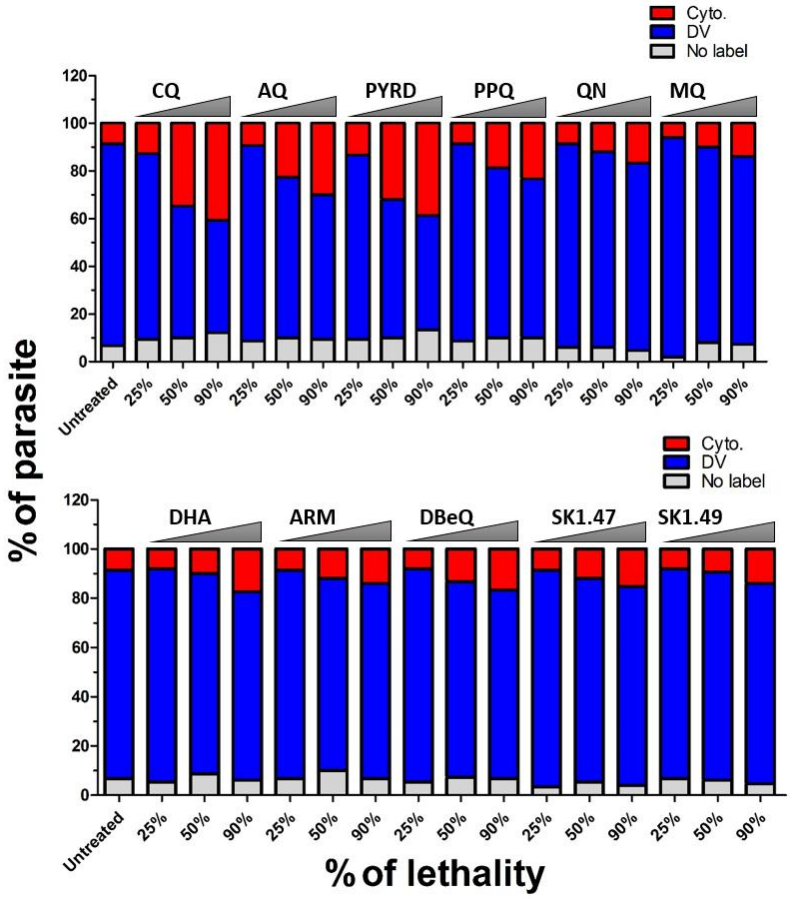

Fig. 6.18 Monitoring of Ca^{2+} distribution in intraerythrocytic *P. falciparum* following exposure to benchmark antimalarials and putative autophagy inhibitors. The mean proportion of parasites exhibiting either cytoplasmic (red bar), digestive vacuole (blue bar) or no Fluo-4-AM staining (grey bar) are reported. The indicated kill concentration used is indicated on the x-axis for the indicated drug/compound. Data represent means from three replicate experiments, each counting 60-70 infected erythrocytes (iRBCs).

To explore this trend, the mean ± SD of the cytoplasmic distribution of Ca^{2+} were plotted separately and a statistical analysis (one way-ANOVA with a Dunnett post-test) of these data, compared to the untreated control done (Fig. 6.19). The data indicates a clear evidence of statistically significant concentration-dependent redistribution of Ca^{2+} into

the cytoplasm at 50% and 90 kill concentrations for the 4-aminoquinolines tested. The significant difference in the redistribution of Ca^{2+} into the cytoplasm are only otherwise observed for the highest concentrations of DHA, although the extent of this redistribution is much lower than that observed for the 4-aminoquinolines (Fig. 6.19).

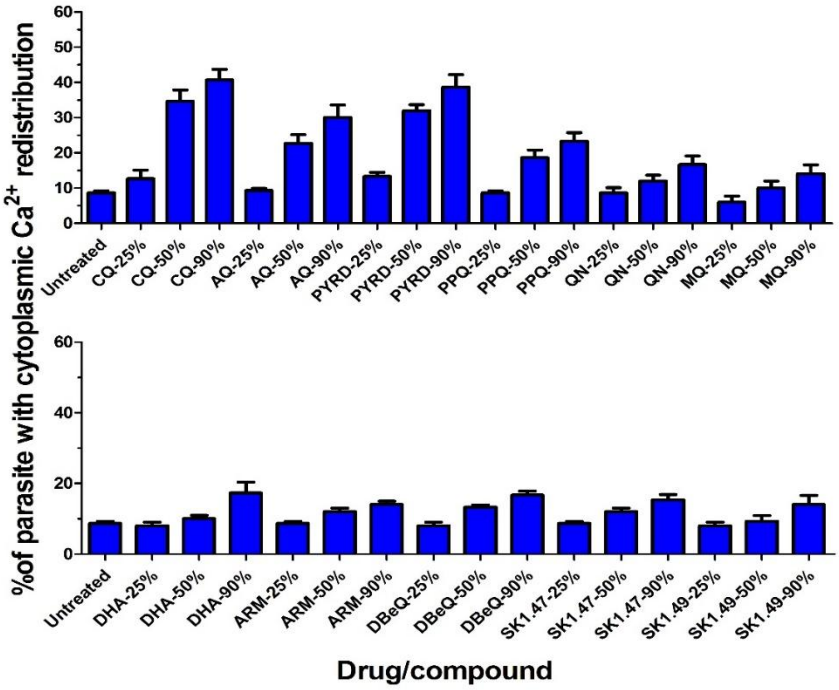

Drug/Comp.	CQ	AQ	PYRD	PPQ	QN	MQ	DHA	ARM	DBeQ	SK1.47	SK1.49
25%											
50%											
90%											

Fig. 6.19 Proportion of intraerythrocytic parasites showing cytoplasmic redistribution of Ca^{2+} following drug/compound treatment. Note this data is a subgroup of that presented in Fig. 6.18 and reports the mean proportion ± SD of infected erythrocytes with cytoplasmic distribution of Fluo-4-AM green fluorescence. Below the chart is a table providing a heat map of the statistical test (one-way ANOVA, with Dunnett post-test) of the difference compared to the untreated control. The coloured boxes in which red, orange and yellow refer to $P < 0.0001$, 0.001 and 0.05, respectively, whilst a white box represents no significant difference with the untreated control.

6.2.6 Assessment of phosphatidylserine externalization following compound/drug treatment

A well described feature of apoptosis in higher eukaryotes is the externalization of phosphatidylserine (PS), normally restricted to the inner surface of a lipid layer, to act as a signal for a damaged cell to be phagocytosed. Whilst the redistribution of PS onto the exofacial surface of iRBCs was not specifically studied in the Ch'ng *et al.* (2010, 2011, 2013) studies, this phenomenon has been described in *P. falciparum* following heat shock (Pattanapanyasat *et al.,* 2010; Engelbrecht and Coetzer, 2013) or in *P. berghei* ookinetes within the mosquito midgut under normal growth condition (Al-Olayan *et al.,* 2012). Externalization of PS was assayed in iRBCs following drug and heat stresses using a FITC-labelled Annexin V, a protein with a high binding affinity for PS, with fluorescence microscopy. Initial experiments were done using 50% and 90% kill concentrations of CQ, QN, DHA and DBeQ.

Two independent experiments were imaged using these conditions, with the fluorescence microscopy revealed no evidence of FITC-Annexin V staining of infected erythrocytes. Fig. 6.20 illustrates images collected for CQ and QN treatments, with that for DBeQ and DHA not shown. Quantitative analysis was not done as there is no evidence of PS externalization.

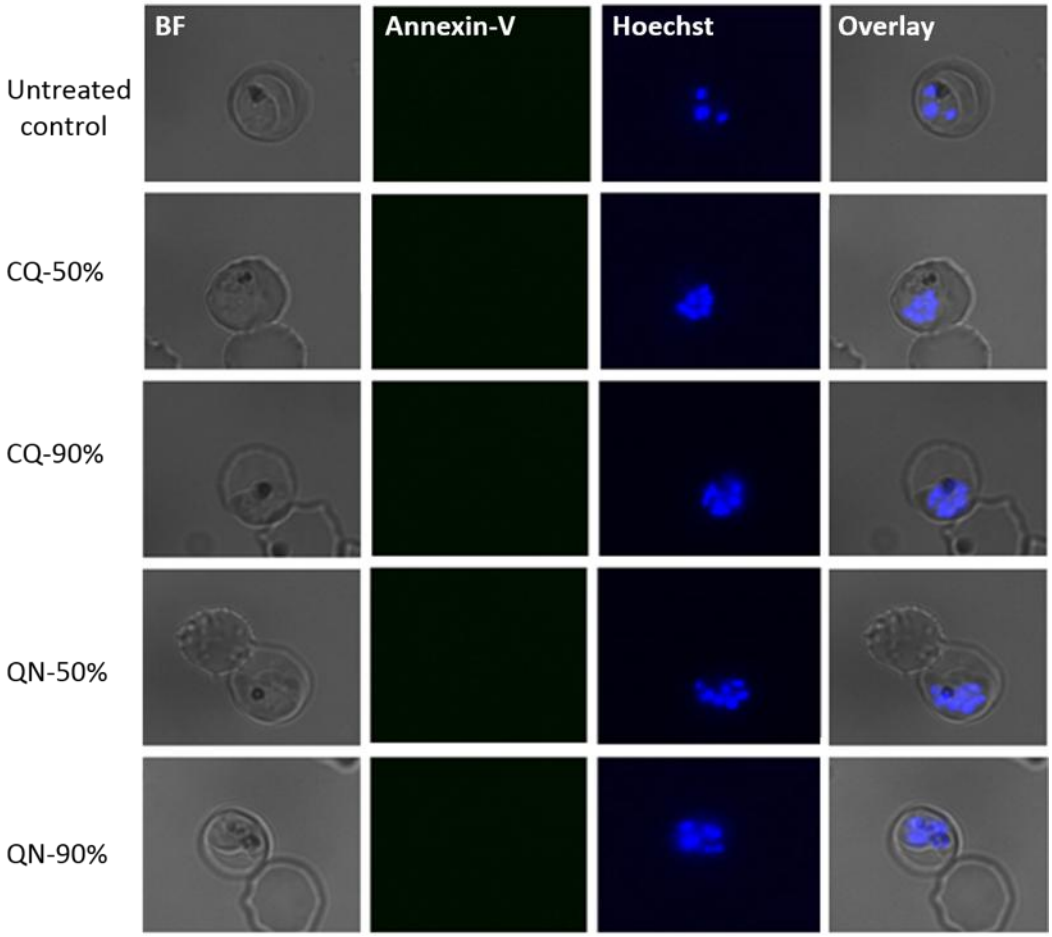

Fig. 6.20 Fluorescent microscopy of CQ and QN treated intraerythrocytic parasites to monitor phosphatidylserine (PS) externalization. Panels illustrate untreated and treated cultures (see y-axis for drug and concentration used) as brightfield (BF), FITC-Annexin V (green fluorescence) and Hoechst 33343 nuclear stain as well as a merged overlay.

For further exploring, the assay was repeated using a heat shock treatment previously reported to induce PS externalization from mature intraerythrocytic trophozoite parasites using flow cytometry (Engelbrecht and Coetzer, 2013). Trophozoite parasites were exposed to 40 °C for 2, 4 or 8 hrs and replaced at 37 °C. Imaging of PS externalization was performed at 8 or 48 hrs timepoint to explore whether this was an early or late effect of cell death. Both timepoints did not show any evidence of PS externalization (Fig. 6.21 and Fig. 6.22), despite the bioluminescence assay clearly showing both treatments provide a time-dependant loss of parasite viability (Fig. 6.23).

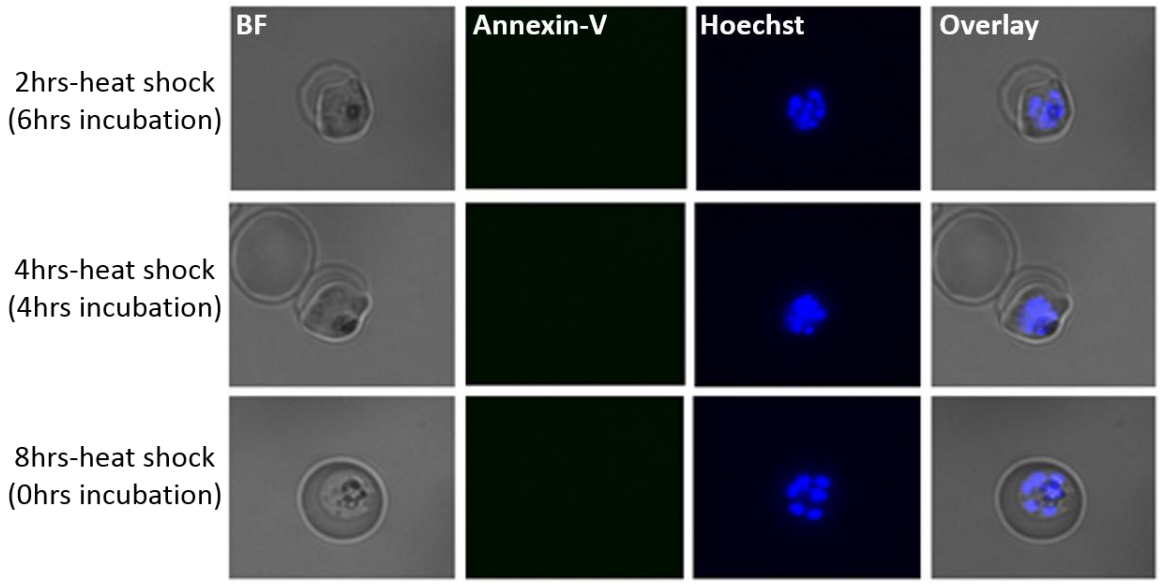

Fig. 6.21 Fluorescent microscopy of heat-shock treated intraerythrocytic parasites to monitor phosphatidylserine (PS) externalization at 8 hrs timepoint. Panels illustrate untreated and treated cultures (see y-axis for drug and concentration used) as brightfield (BF), FITC-Annexin V (green fluorescence) and Hoechst 33343 nuclear stain as well as a merged overlay. Cultures were exposed to 40 °**C for the indicated time and returned to** 37 °**C for the time indicated in brackets. All images were developed after 8 hrs.**

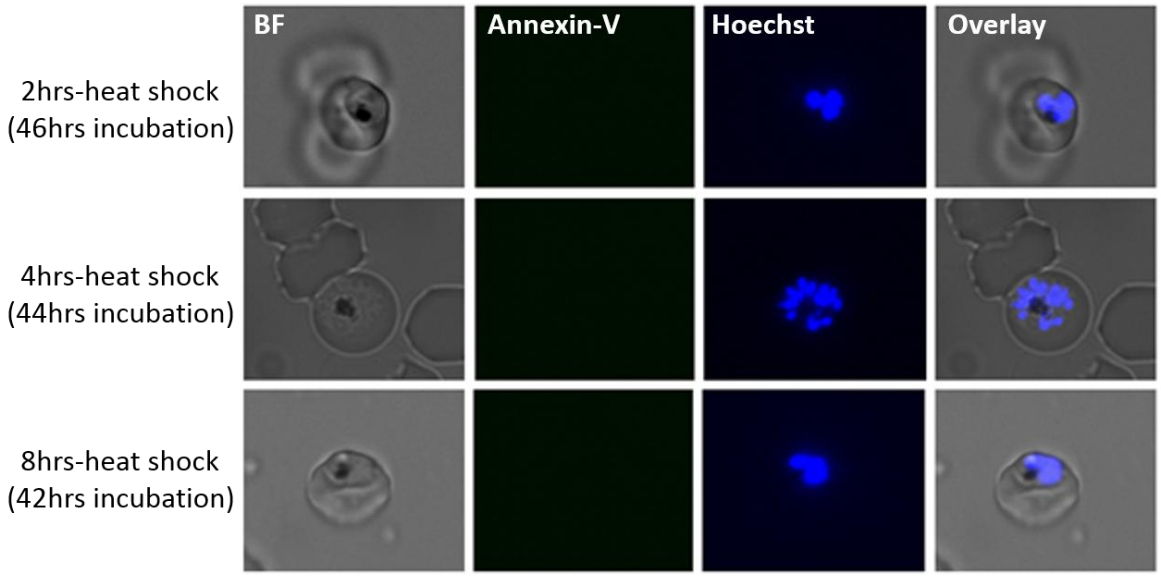

Fig. 6.22 Fluorescent microscopy of heat-shock treated intraerythrocytic parasites to monitor phosphatidylserine (PS) externalization at 48 hrs timepoint. Panels illustrate untreated and treated cultures (see y-axis for drug and concentration used) as brightfield (BF), FITC-Annexin V (green fluorescence) and Hoechst 33343 nuclear stain as well as a merged overlay. Cultures were exposed to 40 °**C for the indicated time and returned to** 37 °**C for the time indicated in brackets. All images were developed after 8 hrs.**

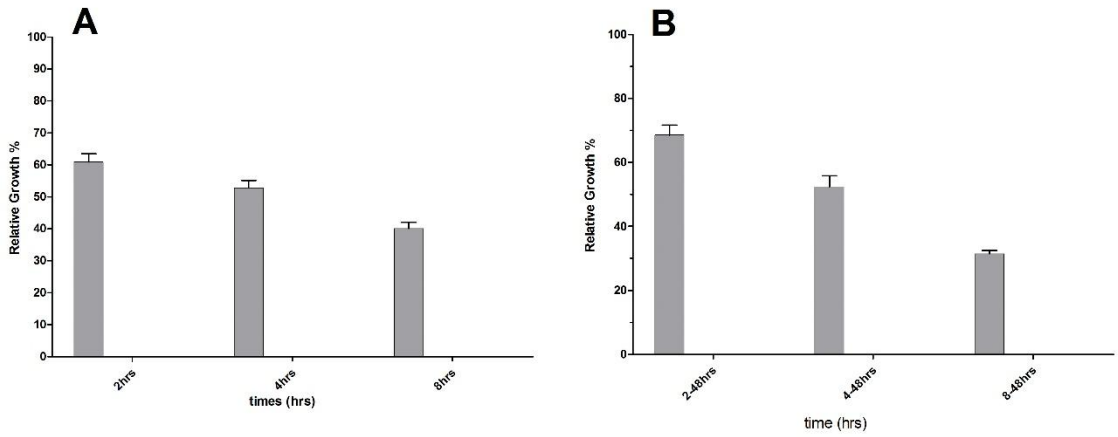

Fig. 6.23 Relative growth of trophozoite stage of *P. falciparum* following heat shock (40°*C*). Relative growth (treated versus control maintained at 37 °C) following heat shock (40 °C) for 2, 4 or 8 hrs and assessment at (A) 8 hrs or (B) 48 hrs after the start of the experiment. Heat-shocked cultures were returned to 37 °C after heat shock until the assay period. Mean ± SD of three independent replicates.

6.3 Discussion

The research in this chapter was based on the experimental framework proposed by Ch'ng *et al.* (2010; 2011) to explore apoptotic features in trophozoite stages of 3D7 (CQS) *P. falciparum* exposed to high concentrations of CQ. Some of their observations were described here in Dd2 (CQR), specifically;

(i) That high concentrations of CQ result in a significant concentration-dependant collapse of ΔΨm.

(ii) That high concentrations of CQ result in a significant concentration-dependant redistribution of Ca^{2+} from the DV into the parasite cytoplasm, indicating a partial permeabilization of the DV membrane.

The evidence that support an increase in Clan CA cysteine protease activity or DNA fragmentation was less clear. In both cases, the fluorescence microscopy data suggested that the highest levels of both was achieved using the highest concentration of CQ for the

longer period of time, although the flow cytometry data did not report any significant evidence for this trend. The absence of these observations here is supported by that originally reported by Nyakeriga *et al.* (2006) who argued for the absence of apoptotic cell death following CQ treatment, although the concentrations we use here are much higher than the 20 nM that used in their study. In our study, using a different strain that is CQR should not be a contributing factor to these differences as the concentrations of CQ that used are high – and were shown to be able to kill 50% and 90% of the parasites. Of note, however, is that drawing a comparison to Ch'ng *et al.* (2010; 2011) has to be done carefully as their reports do not describe the kill effects they achieved in the CQS 3D7 parasite strain used – although 3 μM should kill at least 90% of this strain. For both the CaspaTag and TUNEL experiments a supralethal dose of CQ (100 μM) was also used in $Dd2^{luc}$, and this did not change the observations of the low levels of cysteine protease or DNA fragmentation activities. These data was again agreed with those obtained by Porter *et al.* (2008) using supralethal dose (100 μM) of CQ for 8 hrs. The effects explored here were established to specifically examine early cell death effects, i.e. most assays were carried out within 6 hrs. The CaspaTag and TUNEL assays were extended to 48 hrs, as these effects may be later events in cell death, but again these did not provide high statistically significant evidence of cysteine protease activity or DNA fragmentation beyond the trend outlined above. Based on these factors, it seems that there is no evidence of apoptotic features of cysteine protease activity or DNA fragmentation following treatment with high concentration of CQ.

It is perhaps important to explore the potential limitations of the framework of experiments used here. Ch'ng *et al.* (2011 and 2012) explore the CQ concentration-dependant collapse of $\Delta\Psi m$ using the JC-1 dye. Whilst JC-1 accumulation within discrete

cellular compartments, the mitochondria, is evident in imaging assays, there is likely membrane-potential accumulation of JC-1 due to membrane potential over the parasite's plasma membrane (Antoine *et al*., 2013). Indeed, Figure 6.3 and 6.5 illustrate some accumulation across the parasite cytoplasm (green fluorescence signal) after the JC-1 dye has been removed by washing. This green fluorescence signal may mask low levels of JC-1 accumulation in the mitochondria following drug exposure. Thus, addition of a specific inhibitor of vacuolar-type (H+)-ATPases that generate the plasma membrane potential, using bafilomycin A1 or concanamycin A (Antoine *et al*., 2013), could be considered here. Similarly, fluorescent imaging studies of sub-cellular compartments, particularly the digestive vacuole with Fluo-4 AM based dyes needs to recognise that haem may quench fluorescence emissions below 600 nm (Esposito *et al.,* 2008).

Perhaps the most novel aspect of this study was the use of the bioluminescence assay of parasite viability to provide samples exposed to concentrations of different benchmark antimalarial drugs that provide a comparable kill. This comparison is drawn out in the next conclusions chapter as it allows the electron micrographic study of ultrastructural changes to be integrated. That said, one point that is worth mentioning here is that the analysis of the different biochemical markers of parasites exposed to a 25% kill indicated, in general, showed no significant difference compare to the untreated control. Whilst the 25% kill concentrations used were the lowest of the three tested, they are close to the EC_{50} concentrations. This observation seems to agree with the key point that Ch'ng and his colleagues were made, including that high concentrations of the drug are required to trigger biochemical markers associated with apoptotic cell death, with lower concentrations, more similar to EC_{50} concentrations unlikely to trigger apoptosis.

The including of SK1.47 and SK1.49 in this chapter was done to explore whether their action was linked to apoptotic markers of cell death, and how distinct their features were to those of CQ. The data for both compounds indicated;

(i) Neither compound appeared to provide for a significant concentration-dependant collapse of ΔΨm.

(ii) Neither compound appeared to provide for a significant concentration-dependant redistribution of Ca^{2+} from the DV into the parasite cytoplasm, indicating no apparent effect on DV membrane permeabilization.

(iii) Neither compound provided evidence of induction of cysteine protease activity or DNA fragmentation. Although these features were not evident for antimalarial drug treatment as well.

This would suggest that the rapid cell death triggered by exposure to high concentrations of SK1.47 or SK1.49 does not share hallmark features of apoptosis and appear to undergo a mechanism of cell death distinct from the benchmark antimalarial drugs that tested here. Perhaps not unexpected as we would support a role for these compounds in inhibiting autophagy, but this need not necessarily implicate autophagic cell death as the route of cell death using these compounds. This is perhaps is more interesting when comparing the results of SK1.47 and SK1.49 with those of DBeQ. The ultrastructure studies suggested that these three compounds share same effects, where all resulted in a swollen DV, no increase in EV vesicles and a decrease in Hz crystals in the DV. Yet here we see that DBeQ does cause a significant concentration-dependant collapse of ΔΨm with the highest concentration appearing to double the proportion of TUNEL-positive cells after 48 hrs. Interestingly, like SK1.47 and SK1.49, there was no apparent evidence of Ca^{2+}

redistribution following DBeQ treatment, despite the electron micrographs suggesting that the DV were swollen. It appears that swelling of the DV not include loss in their membrane integrity as this was supported by no significant evidence of Ca^{2+} redistribution, instead this being a feature of the 4-aminoquinolines and closely related drugs.

The absence of PS externalization following drug/compound exposure required a positive control of the assay to confirm that the Annexin V assay was working. This, we thought, would be provided by the heat shock experiment. Yet, despite evidence that the heat shock conditions used, the same as previously reported by Engelbrecht and Coetzer (2013), provided a time-dependant loss of parasite viability, no evidence of PS externalization was observed in our study. One observation made during the fluorescent microscopy did support that the assay was functional. For a small proportion of parasites, marked with the Hoechst (a DNA dye), a green fluorescent signal was seen – although brightfield examination indicated that these parasites were not intracellular (Fig. 6.24). Here the brightfield image along with the propidium iodide staining of the parasite nucleus clearly demarcates three parasites within a membrane stained with FITC-Annexin V. Principally, for propidium iodide to stain the parasite nucleus, the host erythrocyte membrane must be compromised (Mendiratta *et al.,* 2006). This would similarly suggest that Annexin V has access to internal PS labelled membranes. This was also shown by extensive Annexin V staining following treatment of a culture with 1% (w/v) saponin (data not shown). We would suggest that the methodology of the Annexin V assay needs to carefully consider whether it could lead to access of the stain into the infected erythrocyte – for example by exposure to potential hypotonic shock during staining or shear pressure during flow cytometry. Where fluorescent microscopy has been used to

report Annexin V staining of infected erythrocytes elsewhere (Pattanapanyasat *et al.,* 2010), comparison of these images with our own suggest that these may not be intraerythrocytic parasites (Note in lower panel B of Fig. 6.24 that the indicated trophozoite stage parasite is imaged next to an out of focus erythrocyte).

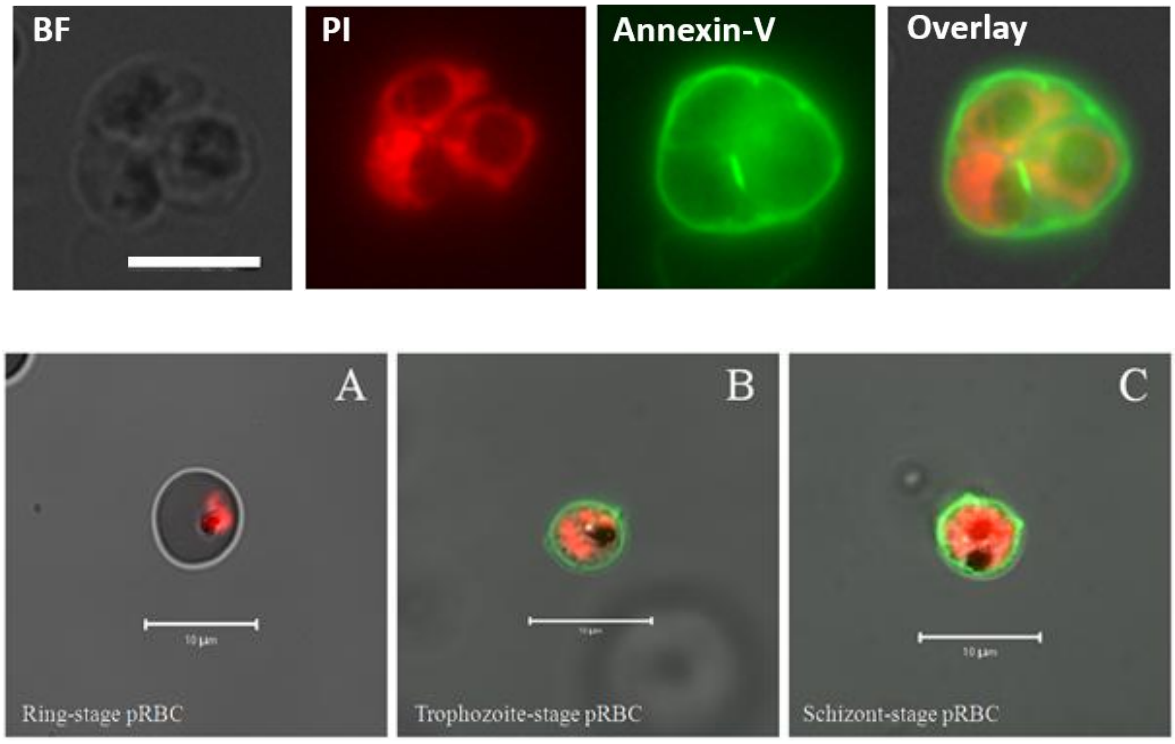

Fig. 6.24 Fluorescent microscopy of PS staining. The top panels represent images developed in this study showing brightfield (BF), red fluorescent propidium iodide (PI)-stained nucleus, green fluorescent Annexin V-stained phosphatidylserine and overlay. Note that images in the bottom panels represent red fluorescent propidium iodide and green fluorescent Annexin V staining of (A) ring, (B) trophozoite and (C) schizont stage of intraerythrocytic parasites (Pattanapanyasat *et al.,* 2010) prepared for flow cytometry. Note the size of the erythrocyte in panel B and the presence of haemozoin stained DV in the ring stage parasite (panel A).

Whilst PS externalization is not a marker of cell death in *P. falciparum*, data presented here suggests that the comparative approach adopted here has some potential in exploring the potential for a time-dependant cascade of biochemical markers of cell death – with ΔΨm collapse as a key initial marker of this event. Additional timepoints before and after the 6 hrs used here would be useful. In addition, exploring the effect of

these benchmark antimalarial drugs, particularly the 4-aminoquinolines in a CQS strain would be interesting (M. Hmoud has created a $NF54^{luc}$ strain (CQS) in our laboratory using the same luciferase reporter cassette used to genetically modify the $Dd2^{luc}$ strain that used here). Particularly to explore whether the same concentration dependant effects on $\Delta\Psi m$ collapse and Ca^{2+} redistribution happen in CQR and CQS parasites exposed to concentrations of CQ that produce the same kill effect in both parasite strains. In the same way, altering the expression of the luciferase reporter gene to take place in ring stage parasites would extend the comparative analysis into explore whether cell death markers are evident following high concentration exposure of antimalarial compounds, with artemisinins of particular interest here.

Chapter 7: Moving forward

This study set out with the aim to explore whether the PfAtg8-PfAtg3 interaction that provides for the phosphatidylethanolamine labelling of PfAtg8 offers some potential as a drug development target. A compound library was designed to act as inhibitors of autophagy protein-protein interaction in human cells were screened and two structurally related hits, SK1.47 and SK1.49, were identified. The key observations following treatment with these two hits included;

(i) Both compounds inhibit intraerythrocytic development in both CQR and CQS *P. falciparum* with a moderate EC_{50} potency of 1-2 µM.

(ii) Both compounds produce a cytocidal kill rate comparable to that of CQ, which achieving the minimal rate of kill criteria for TCP1.

(iii) Both compounds revealed trophozoite stage-dependent effects, although delays in ring stage development were evident.

(iv) Both compounds appear to have promising selectivity for intraerythrocytic parasites when compared to HepG2.

(v) Inhibition the numbers and distribution of starvation-induced PfAtg8-labelled is a key proof of concept data that indicates these compounds inhibit the phosphatidylethanolamine labelling of PfAtg8.

(vi) Modelling of the potential interaction of both compounds to the PfAtg3 interaction region of PfAtg8 indicates that the naphthalene group docks into the W-pocket with the 2,4,-trimethyl substituted phenyl group docking into the L-pocket. This modelling also suggests key aspects of the SAR of the screened library compounds with respect to docking into the W and L-pockets.

(vii) Absence of ultrastructural and biochemical evidences of apoptotic and necrotic-cell death following treatment with both compounds were indicated.

The role of the incomplete canonical autophagy cascade in *P. falciparum* is the subject of debate (Cervantes *et al.,* 2014; Gaviria *et al.,* 2013; Kitamura *et al.,* 2012; Navale *et al.,* 2014; Tomlins *et al.,* 2013; Walczak *et al.,* 2018). Our study, with its focus on only the potential of inhibition of PfAtg8-PfAtg3 as a drug target does not provide evidence for the presence or absence of autophagy. Induction of PfAtg8-labelled vesicles formation in starved parasites, suggesting that this feature may represent a type of adaptation to nutrient stress with autophagosome-like vesicle could be produced (Gaviria *et al.,* 2013). To well define whether this cytoplasmic vacuolation represent macroautophagy or not, the contents of PfAtg8-labelled vesicles need to be determined. For example, recycling of cytoplasm components of the parasite as nutrients via these vesicles would proof that. In addition, whilst the very preliminary observation indicated that PfAtg3 AIM peptides bind less well to PfAtg8 in the presence of SK1.47 and SK1.49 (Jürgen Bosch, *pers.* comm.), this is not suggesting that SK1.47 and SK1.49 bound with PfAtg3 binding region of PfAtg8 and blocked this interaction. This still requires biophysical data to support the modelling data reported in this thesis.

SK1.47 and SK1.49 do offer, however, chemical probes to explore the action of PfAtg8 in *P. falciparum* and, given the apparent structural similarity of Atg8 amongst apicomplexan parasite (Hain *et al.,* 2016), and more widely for other parasite systems. These chemical probes, complemented by compound 1 (MMV007907) and ACL25 (Hain *et al.,* 2014, 2016), could be used to explore better the apparent recycling of invasion organelles following the sporozoite invasion of hepatocytes (Jayabalasingham *et al.,* 2010; Meis *et al.,* 1985), the trafficking of vesicles within the intraerythrocytic stages (Gaviria *et al.,*

2013), the role of Atg8 in function and biogenesis of apicoplast (Cervantes *et al.,* 2014; Kitamura *et al.,* 2012) as well as whether the PfAtg8-labelled vesicles induced on starvation do indeed represent autophagosomes (Tomlins *et al.,* 2013). The current moderate antiplasmodial activity of SK1.47 and SK1.49 as well as their high lipophilicity mean that they are not realistic leads for further development. For this reason, additional studies need to take them forward for a more comprehensive evaluation of toxicity, serum stability and proof-of-concept in a murine malaria model were not considered here. In chapter 4, however, it has been illustrated how these compounds (SK1.47 and SK1.49) could be taken forward. Much like Hain *et al.* (2016), the potential for *in silico* modelling of interactions of small molecules to the PfAtg3 interacting region of PfAtg8 could be exploited here. Chapter 4 concludes with an analysis of the core SK1.47 and SK1.49 scaffold, suggesting the opportunities to modify this scaffold based on the SAR of the data developed in this study. This can readily exploit to generate *in silico* thousands of virtual analogues that can be docked against PfAtg8, noting that benchmark docking scores and EC_{50} activities for a range of analogues of SK1.47 and SK1.49 exist. This work would provide a library of compounds that would warrant synthesis to allow, (i) confirmation of more potent antiplasmodial activity, (ii) confirmation of proof-of-principle of action using the PfAtg8 immunofluorescence assay following starvation and (iii) comparison their relative rate of kill against SK1.47 and SK1.49 as changes in the relative rate of kill may suggest changes in the mode of action (DBeQ is a good example of this – a potential autophagy inhibitor that has distinct rate of kill dynamics as well as differences in the induction of biochemical markers of cell death) and (iv) materials for potential SPR, isothermal colorimetry and X-ray crystallography to explore the physical interaction with PfAtg8.

A second major part of my research explored the comparative effect of high concentrations of antimalarial drugs during early cell death events. This study was supported by a framework of studies using a high concentration of CQ to induce a temporal cascade of apoptotic markers (Ch'ng *et al.,* 2010, 2011). This study was supported by a bioluminescence- based assay for parasite viability, initially developed in our laboratory by Ullah *et al.* (2017). Importantly, this assay allowed different concentrations of different drugs to be compared against a defined and titratable, killing effect with 25%, 50% and 90% kill effect were dependent. This provides a novel tool to explore the effect of different drugs (as well as SK1.47, SK1.49 and DBeQ) at the same endpoint, providing the means to carry out a potential comparative analysis. In this way, I was able to explore the effect of CQ, and compare it to what has previously been reported by Ch'ng *et al.* (2010, 2011). This approach also allowed to use other 4-aminoquinolines AQ and related analogues, PPQ and PYRD as well as pairs of compounds from two other major classes of antimalarial drugs; the arylamino alcohols MQ and QN and the artemisinins DHA and ARM.

Fig. 7.1 provides a simplified traffic light (Red-Amber-Green) rating of the observations made by Ch'ng *et al.* (2010; 2011) compared to their model of the predicted apoptotic cascade (Ch'ng *et al.,* 2010). Where green indicates there is absolute correlations with our datasets reported in chapters 5 and 6 and red indicates no correlation, while amber means existence an intermediate correlation. As discussed in chapters 5 and 6, 50% and 9%-100% kill concentrations provided ultrastructural evidence of digestive vacuole swelling, and potentially leakage of DV contents into the cytoplasm, and biochemical evidence for the release of Ca^{2+} stores from the digestive vacuole and $\Delta\Psi m$ collapse. The

absence of an increase in cytoplasmic Clan CA cysteine protease activity and DNA fragmentation has already been discussed in chapter 6.

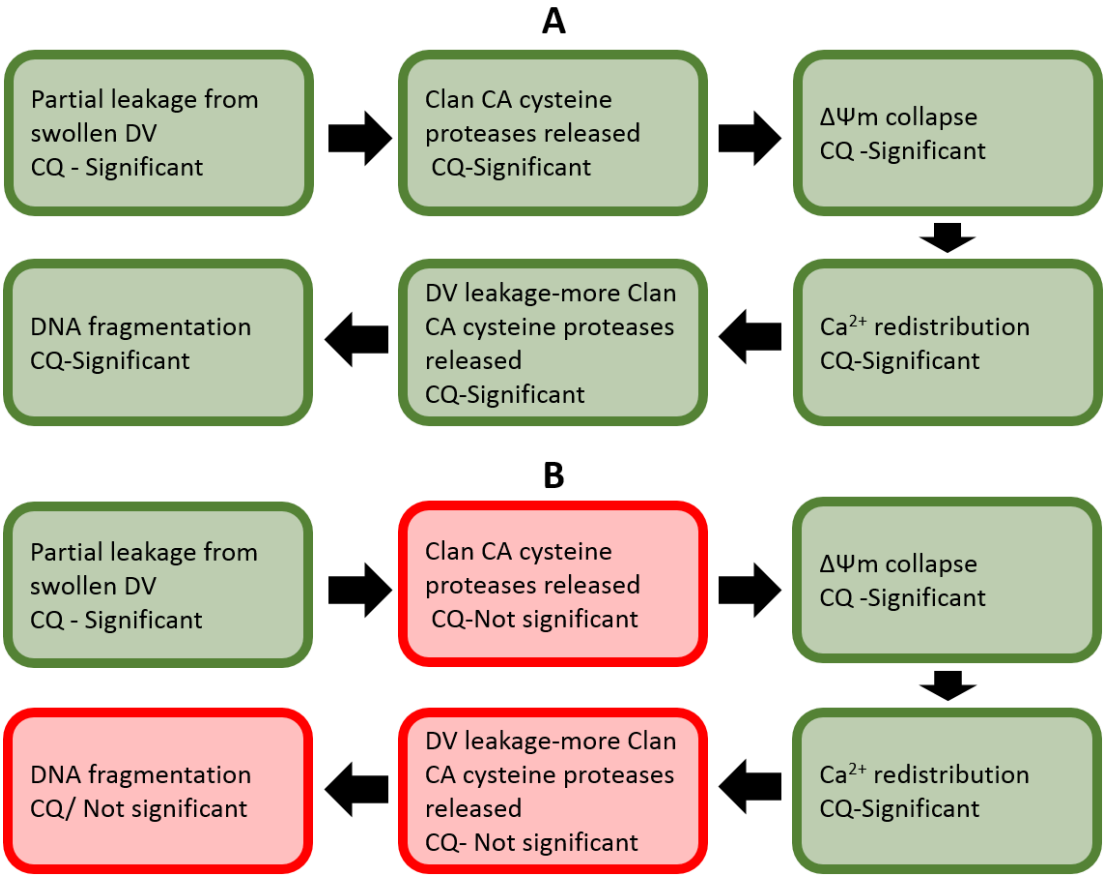

Fig. 7.1 Traffic light analysis comparing the observations linked to the (A) Ch'ng *et al.* (2010) model describing an apoptotic cascade in intraerythrocytic *P. falciparum* following exposure to high concentrations of CQ and (B) observations reported in this thesis using 50% and 90% kill concentrations of CQ modelled onto this framework.

The same traffic light analysis of the high concentration of CQ framework has been applied for the remaining 4-aminoquinolines and related analogues (Fig. 7.2A), arylamino alcohols (Fig. 7.2B), artemisinins (Fig. 7.2C) and the putative autophagy inhibitors (Fig.7.3). This analysis allows the following features to be identified;

(i) The analysis included pairs of closely related compounds predicted to share the same mode of action. These included QN and MQ, DHA and ARM and SK1.47 and

SK1.49. For all pairs of compounds the same pattern of ultrastructural and biochemical marker changes were observed. This provides some additional confidence in the observations made and the conclusions that can be drawn from them.

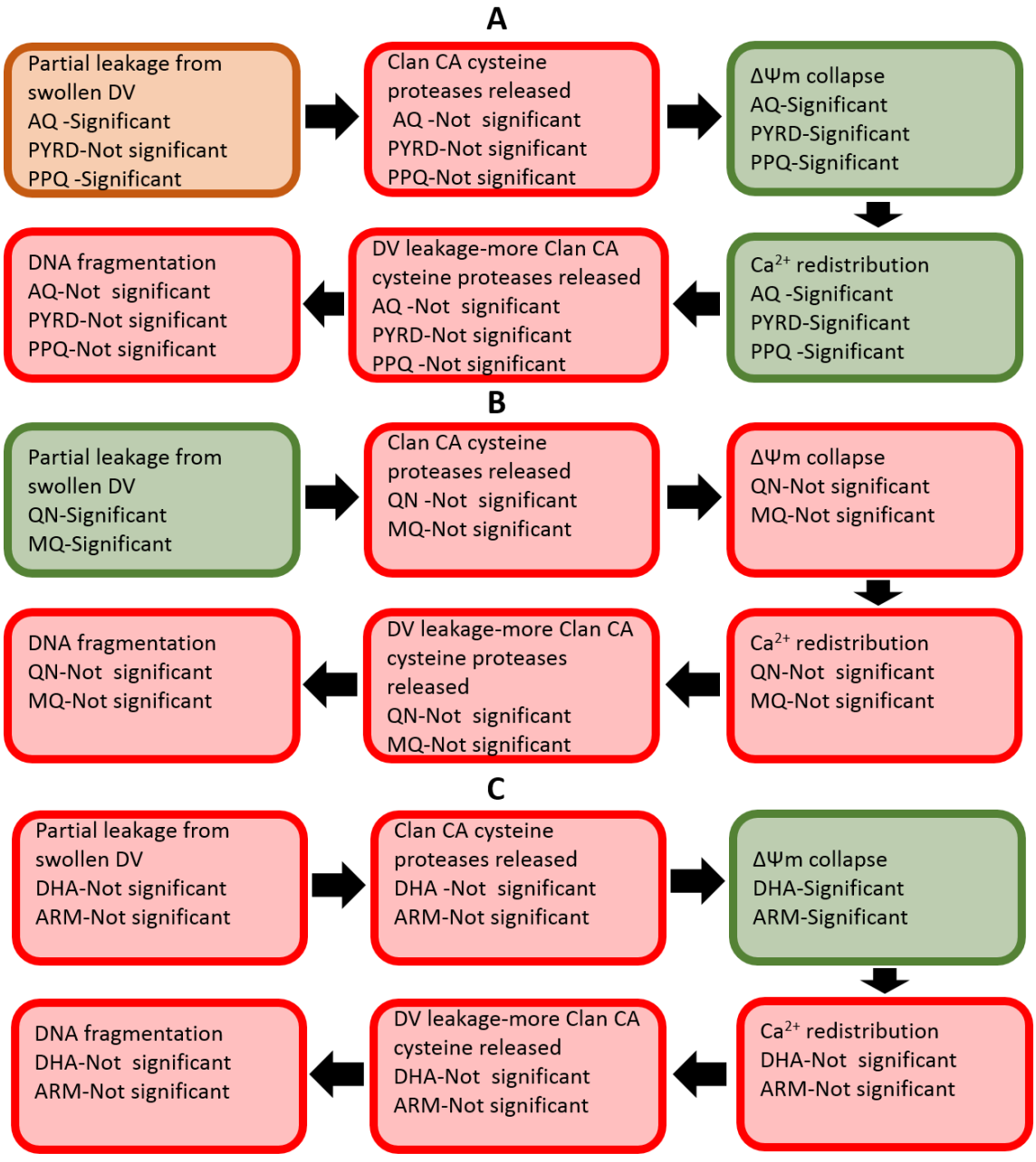

Fig. 7.2 Traffic light analysis comparing the observations linked to the Ch'ng *et al.* (2010) model describing an apoptotic cascade in intraerythrocytic *P. falciparum* following exposure to high concentrations of CQ. (**A**) Comparison using high concentrations of the 4-aminoquinolines AQ, PYRD and PPQ. (B) Comparison using high concentrations of the arylamino alcohols QN and MQ. (C) Comparison using high concentrations of the artemisinins DHA and ARM.

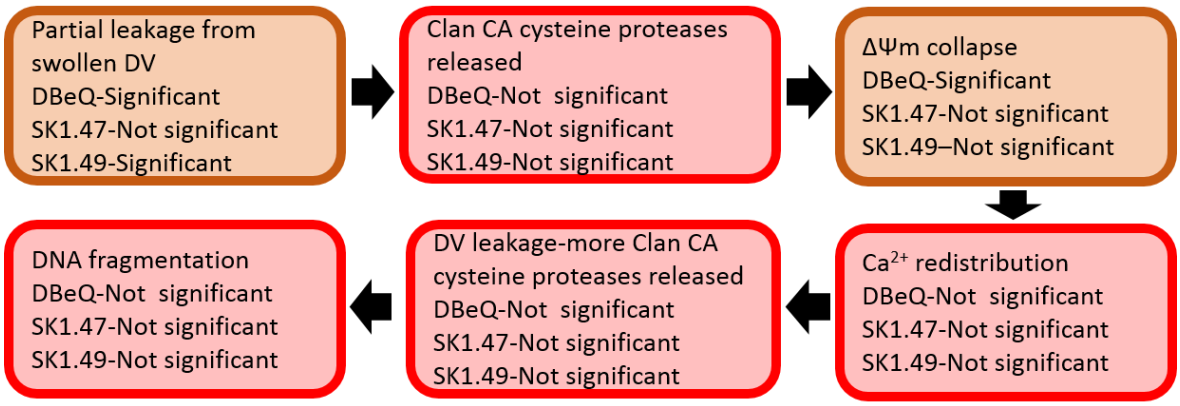

Fig. 7.3 Traffic light analysis comparing the observations linked to the Ch'ng *et al.* (2010) model describing an apoptotic cascade in intraerythrocytic *P. falciparum* following exposure to high concentrations of CQ using the potential autophagy inhibitors SK1.47, SK1.49 and DBeQ.

(ii) There are some speculations regarding to the targets of AQ, PPQ and PYRD, although based on their structural similarity to CQ this is predicted they likely inhibit haem polymerization (Combrinck *et al.,* 2012; Omodeo-Sale *et al.,* 2009). Targeting the digestive vacuole is clearly featured from the ultrastructural changes to digestive vacuole following AQ and PPQ treatment, but not for PYRD over the 6 hrs timeframe. This is also case for all of these drugs with a concentration-dependent redistribution of Ca^{2+} stores from the digestive vacuole to the cytoplasm. These drugs also shared a concentration-dependent ΔΨm collapse as like as CQ.

(iii) Interestingly, ultrastructural changes to the digestive vacuole, such as significant swelling in the case of QN, MQ, SK1.49 and DBeQ, did not result in its permeabilization as suggested by the lack of a significant concentration-dependent redistribution of Ca^{2+} stores from the digestive vacuole into the cytoplasm. Thus, evidence of ultrastructural changes to the digestive vacuole

(swelling) cannot be assumed to be a marker of digestive vacuole membrane damage.

(iv) It appears that ΔΨm collapse has a central role in cell death. This potential has previously been explored by Pasini *et al.* (2013) who developed an antiplasmodial growth assay using JC-1 fluorescence to estimate EC_{50}. This study specifically used ARM and CQ (as done here), but also included atovaquone which was not included here as it was considered unlikely to see markers of cell death within 6 hrs given the apparent lag phase for the action of this drug (Sanz *et al.,* 2012; Ullah *et al.,* 2017). Interestingly, whilst we may conclude that ΔΨm collapse may be a common marker of drug-induced cell death in intraerythrocytic *P. falciparum*, and by extension that this cell death is related to a form of apoptosis, this is indeed not true for SK1.47 and SK1.49. Thus, we see some markers of apoptotic cell death following treatment with some compounds and we never see ultrastructural features that would be characteristic of necrotic cell death.

Together, the comparative approach adopted here and the observations made provide what may be a start to a description of cell death phenotypes in *P. falciparum* that could start to systematically address the debate between apoptotic cell death and incidental cell death (Deponte and Becker, 2004; Proto *et al.,* 2012; Taylor-Brown and Hurd, 2013; Sow *et al.,* 2015). To take this work forward, I would suggest; (i) that the better differentiation of cell death events using high concentrations of drugs/compounds could focus on 50%, 75%, 90% and 99-100% kill concentrations (based on the absence of any evidence of changes at 25% kill concentrations), (ii) In addition, this study was limited by the stage-specific expression of the luciferase reporter gene within the trophozoite stages of intraerythrocytic development (Wong *et al.*, 2011; Ullah *et al*., 2017), (iii) To explore

longer exposures to drug/compound or even their effects in intraerythrocytic ring or other life cycle stages, the luciferase reporter cassette would need to be modified to create new genetically modified strains for study. Finally, the utility of the comparative ultrastructural and biochemical marker studies used here could be dramatically extended by the incorporation of more advanced post-genomic approaches such as transcriptomic (Birkholtz *et al.,* 2008; Natalang *et al.,* 2008; Mok *et al.,* 2014; Shaw *et al.,* 2015) proteomics (Gisselberg *et al.,* 2017; Ismail *et al.,* 2016; Mogire *et al.,* 2017; Wright *et al.,* 2014) and metabolomics (Allman *et al.,* 2016; Cowell *et al.,* 2018; Creek *et al.,* 2016 Tewari *et al.,* 2017).

References list

Achan, J., Talisuna, A.O., Erhart, A., Yeka, A., Tibenderana, J.K., Baliraine, F.N., Rosenthal, P.J. and D'Alessandro, U., 2011. Quinine, an old anti-malarial drug in a modern world: role in the treatment of malaria. *Malaria Journal*, *10*(1), p.144.

Acharya, P., Garg, M., Kumar, P., Munjal, A. and Raja, K.D., 2017. Host–Parasite Interactions in Human Malaria: Clinical Implications of Basic Research. *Frontiers in microbiology*, *8*, p.889.

Al-Bari, M.A.A., 2015. Chloroquine analogues in drug discovery: new directions of uses, mechanisms of actions and toxic manifestations from malaria to multifarious diseases. *Journal of Antimicrobial Chemotherapy*, *70*(6), pp.1608-1621.

Allman, E.L., Painter, H.J., Samra, J., Carrasquilla, M. and Llinás, M., 2016. Metabolomic profiling of the malaria box reveals antimalarial target pathways. *Antimicrobial Agents and Chemotherapy*, *60*(11), pp.6635-6649.

Al-Olayan, E.M., Williams, G.T. and Hurd, H., 2002. Apoptosis in the malaria protozoan, *Plasmodium berghei*: a possible mechanism for limiting intensity of infection in the mosquito. *International Journal for Parasitology*, *32*(9), pp.1133-1143.

Angcajas, A.B., Hirai, N., Kaneshiro, K., Karim, M.R., Horii, Y., Kubota, M., Fujimura, S. and Kadowaki, M., 2014. Diversity of amino acid signaling pathways on autophagy regulation: a novel pathway for arginine. *Biochemical and Biophysical Research Communications*, *446*(1), pp.8-14.

Antoine, T., Fisher, N., Amewu, R., O'neill, P.M., Ward, S.A. and Biagini, G.A., 2013. Rapid kill of malaria parasites by artemisinin and semi-synthetic endoperoxides involves ROS-dependent depolarization of the membrane potential. *Journal of Antimicrobial Chemotherapy*, *69*(4), pp.1005-1016.

Auparakkitanon, S., Chapoomram, S., Kuaha, K., Chirachariyavej, T. and Wilairat, P., 2006. Targeting of hematin by the antimalarial pyronaridine. *Antimicrobial agents and chemotherapy*, *50*(6), pp.2197-2200.

Autino, B., Noris, A., Russo, R. and Castelli, F., 2012. Epidemiology of malaria in endemic areas. *Mediterranean Journal of Hematology and Infectious Diseases*, *4*(1), e2012060.

Axe, E.L., Walker, S.A., Manifava, M., Chandra, P., Roderick, H.L., Habermann, A., Griffiths, G. and Ktistakis, N.T., 2008. Autophagosome formation from membrane compartments enriched in phosphatidylinositol 3-phosphate and dynamically connected to the endoplasmic reticulum. *The Journal of Cell Biology*, *182*(4), pp.685-701.

Balint, G.A., 2001. Artemisinin and its derivatives: an important new class of antimalarial agents. *Pharmacology & Therapeutics*, *90*(2), pp.261-265.

Ballou, W.R., 2009. The development of the RTS, S malaria vaccine candidate: challenges and lessons. *Parasite immunology*, *31*(9), pp.492-500.

Bannister, L.H. and Mitchell, G.H., 2009. The malaria merozoite, forty years on. *Parasitology*, *136*(12), pp.1435-1444.

Bannister, L.H., Hopkins, J.M., Fowler, R.E., Krishna, S. and Mitchell, G.H., 2000. A brief illustrated guide to the ultrastructure of *Plasmodium falciparum* asexual blood stages. *Parasitology today*, *16*(10), pp.427-433.

Barroso, R.P., Basso, L.G. and Costa-Filho, A.J., 2015. Interactions of the antimalarial amodiaquine with lipid model membranes. *Chemistry and Physics of Lipids*, *186*, pp.68-78.

Barth, S., Glick, D. and Macleod, K.F., 2010. Autophagy: assays and artifacts. *The Journal of Pathology*, *221*(2), pp.117-124.

Bartoloni, A. and Zammarchi, L., 2012. Clinical aspects of uncomplicated and severe malaria. *Mediterranean Journal of Hematology and Infectious Diseases*, *4*(1), e2012026.

Beaumelle, B.D., Vial, H.J. and Philippot, J.R., 1987. Revaluation, using marker enzymes, of the ability of saponin and ammonium chloride to free *Plasmodium* from infected erythrocytes. *The Journal of Parasitology*, pp.743-748.

Bennink, S., Kiesow, M.J. and Pradel, G., 2016. The development of malaria parasites in the mosquito midgut. *Cellular microbiology*, *18*(7), pp.905-918.

Besteiro, S., 2017. Autophagy in apicomplexan parasites. *Current Opinion in Microbiology*, *40*, pp.14-20.

Besteiro, S., Brooks, C.F., Striepen, B. and Dubremetz, J.F., 2011. Autophagy protein Atg3 is essential for maintaining mitochondrial integrity and for normal intracellular development of *Toxoplasma gondii* tachyzoites. *PLoS Pathogens*, *7*(12), p.e1002416.

Bhatt, S., Weiss, D.J., Cameron, E., Bisanzio, D., Mappin, B., Dalrymple, U., Battle, K.E., Moyes, C.L., Henry, A., Eckhoff, P.A. and Wenger, E.A., 2015. The effect of malaria control on *Plasmodium falciparum* in Africa between 2000 and 2015. *Nature*, *526*(7572), pp.207-211.

Biagini, G.A., Bray, P.G., Spiller, D.G., White, M.R. and Ward, S.A., 2003. The digestive food vacuole of the malaria parasite is a dynamic intracellular Ca^{2+} store. *Journal of Biological Chemistry*, *278*(30), pp.27910-27915.

Biemba, G., Gordeuk, V.R., Thuma, P.E., Mabeza, G.F. and Weiss, G., 1998. Prolonged macrophage activation and persistent anaemia in children with complicated malaria. *Tropical Medicine & International Health*, *3*(1), pp.60-65.

Birkholtz, L., Van Brummelen, A.C., Clark, K., Niemand, J., Maréchal, E., Llinas, M. and Louw, A.I., 2008. Exploring functional genomics for drug target and therapeutics discovery in Plasmodia. *Acta Tropica*, *105*(2), pp.113-123.

Blanc, L., De Gassart, A., Géminard, C., Bette-Bobillo, P. and Vidal, M., 2005. Exosome release by reticulocytes—an integral part of the red blood cell differentiation system. *Blood Cells, Molecules, and Diseases*, *35*(1), pp.21-26.

Boya, P. and Kroemer, G., 2008. Lysosomal membrane permeabilization in cell death. *Oncogene*, *27*(50), pp.6434-6451.

Brennand, A., Gualdrón-López, M., Coppens, I., Rigden, D.J., Ginger, M.L. and Michels, P.A., 2011. Autophagy in parasitic protists: unique features and drug targets. *Molecular and Biochemical Parasitology*, *177*(2), pp.83-99.

Buffet, P.A., Safeukui, I., Milon, G., Mercereau-Puijalon, O. and David, P.H., 2009. Retention of erythrocytes in the spleen: a double-edged process in human malaria. *Current Opinion in Hematology*, *16*(3), pp.157-164.

Butler, A.R., Gilbert, B.C., Hulme, P., Irvine, L.R., Renton, L. and Whitwood, A.C., 1998. EPR evidence for the involvement of free radicals in the iron-catalysed decomposition of qinghaosu (artemisinin) and some derivatives; antimalarial action of some polycyclic endoperoxides. *Free radical research*, *28*(5), pp.471-476.

Burkot, T.R., Graves, P.M., Cattan, J.A., Wirtz, R.A. and Gibson, F.D., 1987. The efficiency of sporozoite transmission in the human malarias, *Plasmodium falciparum* and P. vivax. *Bulletin of the World Health Organization*, *65*(3), pp.375-380.

Burman, C. and Ktistakis, N.T., 2010. Regulation of autophagy by phosphatidylinositol 3-phosphate. *FEBS Letters*, *584*(7), pp.1302-1312.

Burrows, J.N., Duparc, S., Gutteridge, W.E., van Huijsduijnen, R.H., Kaszubska, W., Macintyre, F., Mazzuri, S., Möhrle, J.J. and Wells, T.N., 2017. New developments in anti-malarial target candidate and product profiles. *Malaria Journal*, *16*(1), p.26.

Burrows, J.N., van Huijsduijnen, R.H., Möhrle, J.J., Oeuvray, C. and Wells, T.N., 2013. Designing the next generation of medicines for malaria control and eradication. *Malaria Journal*, *12*(1), p.187.

Bursch, W., Ellinger, A., Gerner, C.H., Fröhwein, U. and Schulte-Hermann, R., 2000. Programmed cell death (PCD), apoptosis, autophagic PCD, or others?. *Annals of the New York Academy of Sciences*, *926*(1), pp.1-12.

Capra, J.A., Laskowski, R.A., Thornton, J.M., Singh, M. and Funkhouser, T.A., 2009. Predicting protein ligand binding sites by combining evolutionary sequence conservation and 3D structure. *PLoS Computational Biology*, *5*(12), p.e1000585.

Caridha, D., Yourick, D., Cabezas, M., Wolf, L., Hudson, T.H. and Dow, G.S., 2008. Mefloquine-induced disruption of calcium homeostasis in mammalian cells is similar to that induced by ionomycin. *Antimicrobial Agents and Chemotherapy*, *52*(2), pp.684-693.

Carter, R. and Mendis, K.N., 2002. Evolutionary and historical aspects of the burden of malaria. *Clinical Microbiology Reviews*, *15*(4), pp.564-594.

Carter, R.I.C.H.A.R.D. and Miller, L.H., 1979. Evidence for environmental modulation of gametocytogenesis in *Plasmodium falciparum* in continuous culture. *Bulletin of the World Health Organization*, *57*(Suppl), pp.37-52.

Cecconi, F. and Levine, B., 2008. The role of autophagy in mammalian development: cell makeover rather than cell death. *Developmental Cell*, *15*(3), pp.344-357.

Cervantes, S., Bunnik, E.M., Saraf, A., Conner, C.M., Escalante, A., Sardiu, M.E., Ponts, N., Prudhomme, J., Florens, L. and Le Roch, K.G., 2014. The multifunctional autophagy

pathway in the human malaria parasite, *Plasmodium falciparum*. *Autophagy*, *10*(1), pp.80-92.

Chan, J.A., Fowkes, F.J. and Beeson, J.G., 2014. Surface antigens of *Plasmodium falciparum*-infected erythrocytes as immune targets and malaria vaccine candidates. *Cellular and Molecular Life Sciences*, *71*(19), pp.3633-3657.

Chen, P.Q., Yuan, J., Du, Q.Y., Chen, L., Li, G.Q., Huang, Z.Y., Yang, D.D. and Wu, L.N., 2000. Effects of dihydroartemisinin on fine structure of erythrocytic stages of *Plasmodium berghei* ANKA strain. *Acta Pharmacologica Sinica*, *21*(3), pp.234-238.

Chevli, R. and Fitch, C.D., 1982. The antimalarial drug mefloquine binds to membrane phospholipids. *Antimicrobial Agents and Chemotherapy*, *21*(4), pp.581-586.

Ch'ng, J.H., Kotturi, S.R., Chong, A.G., Lear, M.J. & Tan, K.S. (2010). A programmed cell death pathway in the malaria parasite *Plasmodium falciparum* has general features of mammalian apoptosis but is mediated by clan CA cysteine proteases. *Cell Death & Disease*, *1*(2), e26.

Ch'ng, J.H., Lee, Y.Q., Gun, S.Y., Chia, W.N., Chang, Z.W., Wong, L.K., Batty, K.T., Russell, B., Nosten, F., Renia, L. and Tan, K.S., 2014. Validation of a chloroquine-induced cell death mechanism for clinical use against malaria. *Cell Death & Disease*, *5*(6), p.e1305.

Ch'ng, J.H., Liew, K., Goh, A.S., Sidhartha, E. & Tan, K.S. (2011). Drug-induced permeabilization of parasite's digestive vacuole is a key trigger of programmed cell death in *Plasmodium falciparum*. *Cell Death & Disease*, *2*(10), e216.

Ch'ng, J.H., Yeo, S.P. and Tan, K.S.W., 2013. Can a single “powerless” mitochondrion in the malaria parasite contribute to parasite programmed cell death in the asexual stages?. *Mitochondrion*, *13*(3), pp.254-256.

Chotivanich, K., Udomsangpetch, R., Simpson, J.A., Newton, P., Pukrittayakamee, S., Looareesuwan, S. and White, N.J., 2000. Parasite multiplication potential and the severity of *falciparum* malaria. *The Journal of Infectious Diseases*, *181*(3), pp.1206-1209.

Chou, T.F., Brown, S.J., Minond, D., Nordin, B.E., Li, K., Jones, A.C., Chase, P., Porubsky, P.R., Stoltz, B.M., Schoenen, F.J. and Patricelli, M.P., 2011. Reversible inhibitor of p97, DBeQ, impairs both ubiquitin-dependent and autophagic protein clearance pathways. *Proceedings of the National Academy of Sciences*, *108*(12), pp.4834-4839.

Chowdhury, D.R., Angov, E., Kariuki, T. and Kumar, N., 2009. A potent malaria transmission blocking vaccine based on codon harmonized full length Pfs48/45 expressed in *Escherichia coli*. *PloS One*, *4*(7), p.e6352.

Collins, W.E., 2007. Further understanding the nature of relapse of *Plasmodium vivax* infection. *The Journal of Infectious Diseases, 195*(7), 919-920.

Combrinck, J.M., Mabotha, T.E., Ncokazi, K.K., Ambele, M.A., Taylor, D., Smith, P.J., Hoppe, H.C. and Egan, T.J., 2012. Insights into the role of heme in the mechanism of action of antimalarials. *ACS Chemical Biology*, *8*(1), pp.133-137.

Cooke, B.M., Mohandas, N. and Coppel, R.L., 2004, April. Malaria and the red blood cell membrane. In *Seminars in Hematology*, *41*(2), pp. 173-188.

Cooke, B.M., Nicoll, C.L., Baruch, D.I. and Coppel, R.L., 1998. A recombinant peptide based on Pf EMP-1 blocks and reverses adhesion of malaria-infected red blood cells to CD36 under flow. *Molecular Microbiology*, *30*(1), pp.83-90.

Coppens, I., 2011. Metamorphoses of malaria: the role of autophagy in parasite differentiation. *Essays in Biochemistry*, *51*, pp.127-136.

Coronado, L.M., Montealegre, S., Chaverra, Z., Mojica, L., Espinosa, C., Almanza, A., Correa, R., Stoute, J.A., Gittens, R.A. and Spadafora, C., 2016. Blood Stage *Plasmodium falciparum* Exhibits Biological Responses to Direct Current Electric Fields. *PloS One*, *11*(8), p.e0161207.

Cowell, A.N., Istvan, E.S., Lukens, A.K., Gomez-Lorenzo, M.G., Vanaerschot, M., Sakata-Kato, T., Flannery, E.L., Magistrado, P., Owen, E., Abraham, M. and LaMonte, G., 2018. Mapping the malaria parasite druggable genome by using *in vitro* evolution and chemogenomics. *Science*, *359*(6372), pp.191-199.

Cowman, A.F. and Crabb, B.S., 2006. Invasion of red blood cells by malaria parasites. *Cell*, *124*(4), pp.755-766.

Craig, A. and Scherf, A., 2001. Molecules on the surface of the *Plasmodium falciparum* infected erythrocyte and their role in malaria pathogenesis and immune evasion. *Molecular and Biochemical Parasitology*, *115*(2), pp.129-143.

Crawford, E.D., Quan, J., Horst, J.A., Ebert, D., Wu, W. and DeRisi, J.L., 2017. Plasmid-free CRISPR/Cas9 genome editing in Plasmodium falciparum confirms mutations conferring resistance to the dihydroisoquinolone clinical candidate SJ733. *PloS one*, *12*(5), p.e0178163.

Creek, D.J., Chua, H.H., Cobbold, S.A., Nijagal, B., MacRae, J.I., Dickerman, B.K., Gilson, P.R., Ralph, S.A. and McConville, M.J., 2016. Metabolomics-based screening of the Malaria Box reveals both novel and established mechanisms of action. *Antimicrobial Agents and Chemotherapy*, *60*(11), pp.6650-6663.

Croft, S.L. and Ward, S., 2015. The Nobel Prize in Medicine 2015: Two drugs that changed global health. *Science Translational Medicine, 7*(316), pp. 316ed 14.

Crompton, P.D., Pierce, S.K. and Miller, L.H., 2010. Advances and challenges in malaria vaccine development. *The Journal of Clinical Investigation*, *120*(12), pp.4168-4178.

Curran, E. and Smith, S.M., 2014. Phosphoinositide 3-kinase inhibitors in lymphoma. *Current Opinion in Oncology*, *26*(5), pp.469-475.

Curtis, C.F., Lines, J.D., Carnevale, P., Robert, V., Boudin, C., Halna, J.M., Pazart, L., Gazin, P., Richard, A., Mouchet, J. and Charlwood, J.D., 1990. Impregnated bednets and curtains against malaria mosquitoes. *Appropriate Technology in Vector Control*, pp.5-46.

Cyrklaff, M., Frischknecht, F. and Kudryashev, M., 2017. Functional insights into pathogen biology from 3D electron microscopy. *FEMS Microbiology Reviews*, *41*(6), pp.828-853.

Dalrymple, U., Mappin, B. and Gething, P.W., 2015. Malaria mapping: understanding the global endemicity of *falciparum* and *vivax* malaria. *BMC Medicine*, *13*(1), p.140.

Dawson, R. M. C., Elliott, D. C., Elliott, W. H. & Jones, K. M., 1986. Data for Biochemical Research, 3rd Ed. Oxford University Press.

de Late, P.L., Pineda, M., Harnett, M., Harnett, W., Besteiro, S. and Langsley, G., 2017. Apicomplexan autophagy and modulation of autophagy in parasite-infected host cells. *Biomedical Journal*, *40*(1), pp.23-30.

del Pilar Crespo, M., Avery, T.D., Hanssen, E., Fox, E., Robinson, T.V., Valente, P., Taylor, D.K. and Tilley, L., 2008. Artemisinin and a series of novel endoperoxide antimalarials exert early effects on digestive vacuole morphology. *Antimicrobial Agents and Chemotherapy*, *52*(1), pp.98-109.

Deponte, M. and Becker, K., 2004. *Plasmodium falciparum*–do killers commit suicide? *Trends in Parasitology*, *20*(4), pp.165-169.

Deponte, M., 2008. Programmed cell death in protists. *Biochimica et Biophysica Acta (BBA)-Molecular Cell Research*, *1783*(7), pp.1396-1405.

Derbyshire, E.R., Prudêncio, M., Mota, M.M. and Clardy, J., 2012. Liver-stage malaria parasites vulnerable to diverse chemical scaffolds. *Proceedings of the National Academy of Sciences*, *109*(22), pp.8511-8516.

Deretic, V., 2006. Autophagy in immunity and infection: a novel immune effector. John Wiley & Sons.

De Villiers, K.A. and Egan, T.J., 2009. Recent advances in the discovery of haem-targeting drugs for malaria and schistosomiasis. *Molecules*, *14*(8), pp.2868-2887.

Diaz-Troya, S., Pérez-Pérez, M.E., Florencio, F.J. and Crespo, J.L., 2008. The role of TOR in autophagy regulation from yeast to plants and mammals. *Autophagy*, *4*(7), pp.851-865.

Dockrell, D.H., 2001. Apoptotic cell death in the pathogenesis of infectious diseases. *Journal of Infection*, *42*(4), pp.227-234.

Dondorp, A.M., Nosten, F., Yi, P., Das, D., Phyo, A.P., Tarning, J., Lwin, K.M., Ariey, F., Hanpithakpong, W., Lee, S.J. and Ringwald, P., 2009. Artemisinin resistance in *Plasmodium falciparum* malaria. *New England Journal of Medicine*, *361*(5), pp.455-467.

Dondorp, A.M., Smithuis, F.M., Woodrow, C. and von Seidlein, L., 2017. How to contain artemisinin-and multidrug-resistant *falciparum* malaria. *Trends in Parasitology*, *33*(5), pp.353-363

Duszenko, M., Ginger, M.L., Brennand , A., Gualdron-Lopez, M., Colombo, M.I., Coombs, G.H., Copens, I., Jayabalasingham, B., Langsley, G., Castro, S.L., Menna-Barreto, R., Mottram, J.C., Navarro, M., Rigden, J.D., Romano, P.S., Stoka, V., Turk, B. and Michels, A.M., 2011. Autophagy in Protists. *Autophagy, 7*(2), pp.127-158.

Dyer, M. and Day, K.P., 2003. Regulation of the rate of asexual growth and commitment to sexual development by diffusible factors from *in vitro* cultures of *Plasmodium falciparum. The American Journal of Tropical Medicine and Hygiene*, *68*(4), pp.403-409.

Eastman, R.T. and Fidock, D.A., 2009. Artemisinin-based combination therapies: a vital tool in efforts to eliminate malaria. *Nature reviews. Microbiology*, *7*(12), pp.864-874.

Eda, S. and Sherman, I., 2002. Cytoadherence of malaria-infected red blood cells involves exposure of phosphatidylserine. *Cellular Physiology and Biochemistry*, *12*(5-6), pp.373-384.

Efeyan, A., Comb, W.C. and Sabatini, D.M., 2015. Nutrient sensing mechanisms and pathways. *Nature*, *517*(7534), pp.302-310.

Eickel, N., Kaiser, G., Prado, M., Burda, P.C., Roelli, M., Stanway, R.R. and Heussler, V.T., 2013. Features of autophagic cell death in *Plasmodium* liver-stage parasites. *Autophagy*, *9*(4), pp.568-580.

Eksi, S. and Williamson, K.C., 2011. Protein targeting to the parasitophorous vacuole membrane of *Plasmodium falciparum*. *Eukaryotic cell*, *10*(6), pp.744-752.

Ellis, R.D., Mullen, G.E., Pierce, M., Martin, L.B., Miura, K., Fay, M.P., Long, C.A., Shaffer, D., Saul, A., Miller, L.H. and Durbin, A.P., 2009. A Phase 1 study of the blood-stage malaria vaccine candidate AMA1-C1/Alhydrogel® with CPG 7909, using two different formulations and dosing intervals. *Vaccine*, *27*(31), pp.4104-4109.

Engelbrecht, D. and Coetzer, T.L., 2013. Turning up the heat: heat stress induces markers of programmed cell death in *Plasmodium falciparum in vitro*. *Cell Death & Disease*, *4*(12), p.e971.

Engelbrecht, D., Durand, P.M. and Coetzer, T.L., 2012. On programmed cell death in *Plasmodium falciparum*: status quo. *Journal of Tropical Medicine*.

Eskelinen, E.L. and Saftig, P., 2009. Autophagy: a lysosomal degradation pathway with a central role in health and disease. *Biochimica et Biophysica Acta (BBA)-Molecular Cell Research*, *1793*(4), pp.664-673.

Famin, O. and Ginsburg, H., 2002. Differential effects of 4-aminoquinoline-containing antimalarial drugs on hemoglobin digestion in *Plasmodium falciparum*-infected erythrocytes. *Biochemical Pharmacology*, *63*(3), pp.393-398.

Famin, O., Krugliak, M. and Ginsburg, H., 1999. Kinetics of inhibition of glutathione-mediated degradation of ferriprotoporphyrin IX by antimalarial drugs. *Biochemical pharmacology*, *58*(1), pp.59-68.

Farfour, E., Charlotte, F., Settegrana, C., Miyara, M. and Buffet, P., 2012. The extravascular compartment of the bone marrow: a niche for *Plasmodium falciparum* gametocyte maturation? *Malaria journal*, *11*(1), p.285.

Farre, J. C., Manjithaya, R., Mathewson, R. D. and Subramani, S., 2008. PpAtg30 tags peroxisomes for turnover by selective autophagy. *Developmental Cell, 14*(3), pp.365-376.

Farrow, J.M., Yang, J.C. and Evans, C.P., 2014. Autophagy as a modulator and target in prostate cancer. *Nature reviews Urology*, *11*(9), p.508.

Feitelson, M.A., Arzumanyan, A., Kulathinal, R.J., Blain, S.W., Holcombe, R.F., Mahajna, J., Marino, M., Martinez-Chantar, M.L., Nawroth, R., Sanchez-Garcia, I. and Sharma, D.,

2015, December. Sustained proliferation in cancer: Mechanisms and novel therapeutic targets. In *Seminars in Cancer Biology*, 35, pp. S25-S54..

Field, J.W. and Shute, P.G., 1956. The Microscopic Diagnosis of Human Malaria. II. A Morphological Study of the Erythroeytic Parasites. *The Microscopic Diagnosis of Human Malaria. II. A Morphological Study of the Erythroeytic Parasites.*, (24).

Field, M.C. and Carrington, M., 2004. Intracellular membrane transport systems in *Trypanosoma brucei*. *Traffic*, *5*(12), pp.905-913.

Fivelman, Q.L., Adagu, I.S. and Warhurst, D.C., 2007. Effects of piperaquine, chloroquine, and amodiaquine on drug uptake and of these in combination with dihydroartemisinin against drug-sensitive and-resistant *Plasmodium falciparum* strains. *Antimicrobial agents and chemotherapy*, *51*(6), pp.2265-2267.

Flannery, E.L., Chatterjee, A.K. and Winzeler, E.A., 2013a. Antimalarial drug discovery—approaches and progress towards new medicines. *Nature Reviews Microbiology*, *11*(12), pp. 849-862.

Flannery, E.L., Fidock, D.A. and Winzeler, E.A., 2013b. Using genetic methods to define the targets of compounds with antimalarial activity: miniperspectives series on phenotypic screening for antiinfective targets. *Journal of medicinal chemistry*, *56*(20), pp.7761-7771.

Földvári-Nagy, L., Ari, E., Csermely, P., Korcsmáros, T. and Vellai, T., 2014. Starvation-response may not involve Atg1-dependent autophagy induction in non-unikont parasites. *Scientific Reports*, *4*, p.5829.

Foley, M. and Tilley, L., 1997. Quinoline antimalarials: mechanisms of action and resistance. *International journal for parasitology*, *27*(2), pp.231-240.

Franke-Fayard, B., Fonager, J., Braks, A., Khan, S.M. and Janse, C.J., 2010. Sequestration and tissue accumulation of human malaria parasites: can we learn anything from rodent models of malaria?. *PLoS Pathogens*, *6*(9), p.e1001032.

Fuchs, Y. and Steller, H., 2011. Programmed cell death in animal development and disease. *Cell*, *147*(4), pp.742-758.

Galluzzi, L., Bravo-San Pedro, J.M., Vitale, I., Aaronson, S.A., Abrams, J.M., Adam, D., Alnemri, E.S., Altucci, L., Andrews, D., Annicchiarico-Petruzzelli, M. and Baehrecke, E.H., 2015. Essential versus accessory aspects of cell death: recommendations of the NCCD 2015. *Cell Death and Differentiation*, *22*(1), pp.58-73.

Galluzzi, L., Vitale, I., Abrams, J.M., Alnemri, E.S., Baehrecke, E.H., Blagosklonny, M.V., Dawson, T.M., Dawson, V.L., El-Deiry, W.S., Fulda, S. and Gottlieb, E., 2012. Molecular definitions of cell death subroutines: recommendations of the Nomenclature Committee on Cell Death 2012. *Cell Death and Differentiation*, *19*(1), pp.107-120.

Gamo, F.J., Sanz, L.M., Vidal, J., de Cozar, C., Alvarez, E., Lavandera, J.L., Vanderwall, D.E., Green, D.V., Kumar, V., Hasan, S. and Brown, J.R., 2010. Thousands of chemical starting points for antimalarial lead identification. *Nature*, *465*(7296), pp.305-310.

Gardner, M.J., Hall, N., Fung, E., White, O., Berriman, M., Hyman, R.W., Carlton, J.M., Pain, A., Nelson, K.E., Bowman, S. and Paulsen, I.T., 2002. Genome sequence of the human malaria parasite *Plasmodium falciparum*. *Nature*, *419*(6906), 498-511.

Gaviria, D., Paguio, M.F., Turnbull, L.B., Tan, A., Siriwardana, A., Ghosh, D., Ferdig, M.T., Sinai, A.P. and Roepe, P.D., 2013. A process similar to autophagy is associated with cytocidal chloroquine resistance in *Plasmodium falciparum*. *PloS One*, *8*(11), p.e79059.

Gavrilescu, L.C. and Denkers, E.Y., 2003. Apoptosis and the balance of homeostatic and pathologic responses to protozoan infection. *Infection and Immunity*, *71*(11), pp.6109-6115.

Gelino, S. and Hansen, M., 2012. Autophagy-an emerging anti-aging mechanism. *Journal of Clinical & Experimental Pathology*, Suppl 4, pii.006.

Geng, J., and Klionsky, D.J., 2008. The Atg8 and Atg12 ubiquitin-like conjugation systems in macroautophagy. *EMBO Reports, 9*(9), pp.859-864.

Genton, B., D'Acremont, V., Lurati-Ruiz, F., Verhage, D., Audran, R., Hermsen, C., Wolters, L., Reymond, C., Spertini, F. and Sauerwein, R., 2010. Randomized double-blind controlled Phase I/II a trial to assess the efficacy of malaria vaccine PfCS102 to protect against challenge with *P. falciparum*. *Vaccine*, *28*(40), pp.6573-6580.

Gething, P.W., Patil, A.P., Smith, D.L., Guerra, C.A., Elyazar, I.R., Johnston, G.L., Tatem, A.J. and Hay, S.I., 2011. A new world malaria map: *Plasmodium falciparum* endemicity in 2010. *Malaria Journal*, *10*(1), p.378.

Ghosh, D., Walton, J.L., Roepe, P.D. and Sinai, A.P., 2012. Autophagy is a cell death mechanism in *Toxoplasma gondii*. *Cellular Microbiology*, *14*(4), pp.589-607.

Ginsburg, H. and Krugliak, M., 1988. Effects of quinoline-containing antimalarials on the erythrocyte membrane and their significance to drug action on *Plasmodium falciparum*. *Biochemical Pharmacology*, *37*(10), pp.2013-2018.

Ginsburg, H., Famin, O., Zhang, J. and Krugliak, M., 1998. Inhibition of glutathione-dependent degradation of heme by chloroquine and amodiaquine as a possible basis for their antimalarial mode of action. *Biochemical pharmacology*, *56*(10), pp.1305-1313.

Gisselberg, J.E., Zhang, L., Elias, J.E. and Yeh, E., 2017. The prenylated proteome of *Plasmodium falciparum* reveals pathogen-specific prenylation activity and drug mechanism-of-action. *Molecular & Cellular Proteomics*, *16*(4 suppl 1), pp.S54-S64.

Glick, D., Barth, S. and Macleod, K.F., 2010. Autophagy: cellular and molecular mechanisms. *The Journal of Pathology*, *221*(1), pp.3-12.

Gligorijevic, B., Purdy, K., Elliott, D.A., Cooper, R.A. and Roepe, P.D., 2008. Stage independent chloroquine resistance and chloroquine toxicity revealed via spinning disk confocal microscopy. *Molecular and Biochemical Parasitology*, *159*(1), pp.7-23.

Glushakova, S., Yin, D., Li, T. and Zimmerberg, J., 2005. Membrane transformation during malaria parasite release from human red blood cells. *Current Biology*, *15*(18), pp.1645-1650.

Goldberg DE, Slater AF, Cerami A, Henderson GB, 1990. Haemoglobin degradation in the malaria parasite *Plasmodium falciparum*: an ordered process in a unique organelle. Proceedings of the National Academy of Sciences, 87(8), pp.2931-2935.

Goldberg, D.E., 1993, October. Hemoglobin degradation in *Plasmodium*-infected red blood cells. In *Seminars in Cell Biology*, *4*(5), pp. 355-361.

Good, M.F. and Doolan, D.L., 2007. Malaria's journey through the lymph node. *Nature Medicine*, *13*(9), pp.1023-1024.

Greenwood, T., Vikerfors, T., Sjöberg, M., Skeppner, G. and Färnert, A., 2008. Febrile *Plasmodium falciparum* malaria 4 years after exposure in a man with sickle cell disease. *Clinical Infectious Diseases*, *47*(4), pp.e39-e41.

Grinter, S.Z. and Zou, X., 2014. Challenges, applications, and recent advances of protein-ligand docking in structure-based drug design. *Molecules*, *19*(7), pp.10150-10176.

Gruenberg, J., Allred, D.R. and Sherman, I.W., 1983. Scanning electron microscope-analysis of the protrusions (knobs) present on the surface of *Plasmodium falciparum*-infected erythrocytes. *The Journal of Cell Biology*, *97*(3), pp.795-802.

Guilbride, D.L., Gawlinski, P. and Guilbride, P.D., 2010. Why functional pre-erythrocytic and bloodstage malaria vaccines fail: a meta-analysis of fully protective immunizations and novel immunological model. *PLoS One*, *5*(5), p.e10685.

Gunjan, S., Singh, S.K., Sharma, T., Dwivedi, H., Chauhan, B.S., Siddiqi, M.I. and Tripathi, R., 2016. Mefloquine induces ROS mediated programmed cell death in malaria parasite: *Plasmodium*. *Apoptosis*, *21*(9), pp.955-964.

Gupta, S., Hill, A.V., Kwiatkowski, D., Greenwood, A.M., Greenwood, B.M. and Day, K.P., 1994. Parasite virulence and disease patterns in *Plasmodium falciparum* malaria. *Proceedings of the National Academy of Sciences*, *91*(9), pp.3715-3719.

Hailey, D.W., Rambold, A.S., Satpute-Krishnan, P., Mitra, K., Sougrat, R., Kim, P.K. and Lippincott-Schwartz, J., 2010. Mitochondria supply membranes for autophagosome biogenesis during starvation. *Cell*, *141*(4), pp.656-667.

Hailu, A., Lindtjørn, B., Deressa, W., Gari, T., Loha, E. and Robberstad, B., 2016. Equity in long-lasting insecticidal nets and indoor residual spraying for malaria prevention in a rural South Central Ethiopia. *Malaria Journal*, *15*(1), p.366.

Hain, A.U. and Bosch, J., 2013. Autophagy in *Plasmodium*, a multifunctional pathway? *Computational and Structural Biotechnology Journal*, *8*(11), pp.1-9.

Hain, A.U., Bartee, D., Sanders, N.G., Miller, A.S., Sullivan, D.J., Levitskaya, J. and Bosch, J., 2014. Identification of an Atg8-Atg3 protein-protein interaction inhibitor from the Medicines for Malaria Venture Malaria Box active in blood and liver stage *Plasmodium falciparum* parasites. *Journal of Medicinal Chemistry, 57*, pp.4521-4531.

Hain, A.U., Miller, A.S., Levitskaya, J. and Bosch, J., 2016. Virtual screening and experimental validation identify novel inhibitors of the *Plasmodium falciparum* Atg8–Atg3 protein–protein interaction. *Journal of Medicinal Chemistry*, *11*(8), pp.900-910.

Hain, A.U., Weltzer, R.R., Hammond, H., Jayabalasingham, B., Dinglasan, R.R., Graham, D.R., Colquhoun, D.R., Coppens, I. and Bosch, J., 2012. Structural characterization and inhibition of the *Plasmodium* Atg8–Atg3 interaction. *Journal of Structural Biology*, *180*(3), pp.551-562.

Hall, A.P., Segal, H.E., Pearlman, E.J., Phintuyothin, P. and Kosakal, S., 1975. Amodiaquine resistant *falciparum* malaria in Thailand. *The American Journal of Tropical Medicine and Hygiene*, *24*(4), pp.575-580.

Han, L., Hudgens, M.G., Emch, M.E., Juliano, J.J., Keeler, C., Martinson, F., Kamthunzi, P., Tegha, G., Lievens, M. and Hoffman, I.F., 2017. RTS, S/AS01 malaria vaccine efficacy is not modified by seasonal precipitation: results from a phase 3 randomized controlled trial in Malawi. *Scientific Reports*, *7*(1), p.7200.

Hasenkamp, S., Wong, E.H. and Horrocks, P., 2012. An improved single-step lysis protocol to measure luciferase bioluminescence in *Plasmodium falciparum*. *Malaria Journal*, *11*(1), p.42.

Hay, S.I., Guerra, C.A., Tatem, A.J., Noor, A.M. and Snow, R.W., 2004. The global distribution and population at risk of malaria: past, present, and future. *The Lancet Infectious Diseases*, *4*(6), pp.327-336.

Hayat, M.A. ed., 2014. *Autophagy: Cancer, Other Pathologies, Inflammation, Immunity, Infection, and Aging: Volume 4-Mitophagy*. Academic Press.

Haynes, R.K., Monti, D., Taramelli, D., Basilico, N., Parapini, S. and Olliaro, P., 2003. Artemisinin antimalarials do not inhibit haemozoin formation. *Antimicrobial Agents and Chemotherapy*, *47*(3), pp.1175-1175.

He, C. and Klionsky, D.J., 2009. Regulation mechanisms and signalling pathways of autophagy. *Annual Review of Genetics, 43*, 67-93.

He, C., Baba, M., Cao, Y. and Klionsky, D.J., 2008. Self-interaction is critical for Atg9 transport and function at the phagophore assembly site during autophagy. *Molecular Biology of Cell, 19*(12), pp.5506-5516.

Hemingway, J., Shretta, R., Wells, T.N., Bell, D., Djimdé, A.A., Achee, N. and Qi, G., 2016. Tools and strategies for malaria control and elimination: what do we need to achieve a grand convergence in malaria? *PLoS Biology*, *14*(3), p.e1002380.

Henrich, P.P., O'Brien, C., Saenz, F.E., Cremers, S., Kyle, D.E. and Fidock, D.A., 2013. Evidence for Pyronaridine as a Highly Effective Partner Drug for the Treatment of Artemisinin-Resistant Malaria in a Rodent Model. *Antimicrobial Agents and Chemotherapy*, *58*(1), pp.183-195.

Hill, A.V., 2011. Vaccines against malaria. *Philosophical Transactions of the Royal Society of London B: Biological Sciences*, *366*(1579), pp.2806-2814.

Hoppe, H.C., van Schalkwyk, D.A., Wiehart, U.I., Meredith, S.A., Egan, J. and Weber, B.W., 2004. Antimalarial quinolines and artemisinin inhibit endocytosis in *Plasmodium falciparum*. *Antimicrobial Agents and Chemotherapy*, *48*(7), pp.2370-2378.

Imwong, M., Snounou, G., Pukrittayakamee, S., Tanomsing, N., Kim, J.R., Nandy, A., Guthmann, J.P., Nosten, F., Carlton, J., Looareesuwan, S. and Nair, S., 2007. Relapses of

Plasmodium vivax infection usually result from activation of heterologous hypnozoites. *The Journal of Infectious Diseases*, *195*(7), pp.927-933.

Inoue, Y. and Klionsky, D.J., 2010, September. Regulation of macroautophagy in *Saccharomyces cerevisiae*. In *Seminars in cell & developmental biology*, *21*(7), pp.664-670.

Ismail, H.M., Barton, V., Phanchana, M., Charoensutthivarakul, S., Wong, M.H., Hemingway, J., Biagini, G.A., O'Neill, P.M. and Ward, S.A., 2016. Artemisinin activity-based probes identify multiple molecular targets within the asexual stage of the malaria parasites *Plasmodium falciparum* 3D7. *Proceedings of the National Academy of Sciences*, *113*(8), pp.2080-2085.

Itakura, E. and Mizushima, N., 2010. Characterization of autophagosome formation site by a hierarchical analysis of mammalian Atg proteins. *Autophagy*, *6*(6), pp.764-776.

Jang, J.W., Kim, J.Y., Yoon, J., Yoon, S.Y., Cho, C.H., Han, E.T., An, S.S.A. and Lim, C.S., 2014. Flow cytometric enumeration of parasitemia in cultures of *Plasmodium falciparum* stained with SYBRgreen I and CD235A. *The Scientific World Journal*.

Jayabalasingham, B., Bano, N. and Coppens, I., 2010. Metamorphosis of the malaria parasite in the liver is associated with organelle clearance. *Cell Research, 20*, pp.1043-59.

Johnson, R., Rawson, S., McPhillie, M., Fishwick, C. and Muench, S., 2017. The Growing Role of Electron Microscopy in Anti-parasitic Drug Discovery. *Current Medicinal Chemistry*.

Josling, G.A. and Llinas, M., 2015. Sexual development in *Plasmodium* parasites: knowing when it's time to commit. *Nature Reviews Microbiology*, *13*(9), pp.573-587.

Kamada, Y., Funakoshi, T., Shintani, T., Nagano, K., Ohsumi, M. and Ohsumi, Y., 2000. Tor-mediated induction of autophagy via an Apg1 protein kinase complex. *Cell Biology, 150*(6), pp.1507-1513.

Kanki, T., Wang, K., Baba, M., Bartholomew, C.R., Lynch-Day, M.A., Du, Z., Geng, J., Mao, K., Yang, Z., Yen, W.L. and Klionsky, D.J., 2009. A genomic screen for yeast mutants defective in selective mitochondria autophagy. *Molecular Biology of The Cell*, *20*(22), pp.4730-4738.

Kaslow, D.C. and Biernaux, S., 2015. RTS, S: Toward a first landmark on the Malaria Vaccine Technology Roadmap. *Vaccine*, *33*(52), pp.7425-7432.

Kaushik, S. and Cuervo, A.M., 2012. Chaperone-mediated autophagy: a unique way to enter the lysosome world. *Trends in Cell Biology*, *22*(8), pp.407-417.

Kawai, S., Kano, S., Chang, C. and Suzuki, M., 1996. The effects of pyronaridine on the morphology of *Plasmodium falciparum in Aotus trivirgatus*. *The American Journal of Tropical Medicine and Hygiene*, *55*(2), pp.223-229.

Kebaier, C., Voza, T. and Vanderberg, J., 2009. Kinetics of mosquito-injected *Plasmodium* sporozoites in mice: fewer sporozoites are injected into sporozoite-immunized mice. *PLoS Pathogens*, *5*(4), p.e1000399.

Kerr, J.F., Wyllie, A.H. and Currie, A.R., 1972. Apoptosis: a basic biological phenomenon with wide-ranging implications in tissue kinetics. *British Journal of Cancer*, *26*(4), pp.239-257.

Kim, J. and Klionsky, D.J., 2000. Autophagy, cytoplasm to vacuole targeting pathway and pexophagy in yeast and mammalian cells. *Annual Review of Biochemistry, 69*: pp.303-342.

Kitamura, K., Kishi-Itakura, C., Tsuboi, T., Sato, S., Kita, K., Ohta, N. and Mizushima, N., 2012. Autophagy-related Atg8 localizes to the apicoplast of the human malaria parasite *Plasmodium falciparum*. *PLoS One*, *7*(8), p.e42977.

Klionsky, D.J. and Schulman, B.A., 2014. Dynamic regulation of macroautophagy by distinctive ubiquitin-like proteins. *Nature Structural & Molecular Biology*, *21*(4), pp.336-345.

Klionsky, D.J., 2005. The molecular machinery of autophagy: unanswered questions. *Journal of Cell Science, 118*(1), pp.7-18.

Klionsky, D.J., 2008. Autophagy revisited: a conversation with Christian de Duve. *Autophagy*, *4*(6), pp.740-743.

Klonis, N., Del Pilar Crespo-Ortiz, M.P., Bottova, I., Abu-Bakar, N., Kenny, S., Rosenthal, P.J. and Tilley, L., 2011. Artemisinin activity against *Plasmodium falciparum* requires hemoglobin uptake and digestion. *Proceedings of the National Academy of Sciences*, *108*(28), pp.11405-11410.

Koyama-Honda, I., Itakura, E., Fujiwara, T.K. and Mizushima, N., 2013. Temporal analysis of recruitment of mammalian ATG proteins to the autophagosome formation site. *Autophagy*, *9*(10), pp.1491-1499.

Kraft, C., Reggiori, F. and Peter, M., 2009. Selective types of autophagy in yeast. *Biochimica et Biophysica Acta (BBA)-Molecular Cell Research*, *1793*(9), pp.1404-1412.

Krai, P.M., 2013. Investigations into the Nature of the Endosomal System in *Plasmodium falciparum*. (Doctoral dissertation, Virginia Tech) https://vtechworks.lib.vt.edu/handle

/10919/51537

Kroemer, G., Galluzzi, L., Vandenabeele, P., Abrams, J., Alnemri, E.S., Baehrecke, E.H., 2009. Classification of cell death: Recommendation of the Nomenclature Committee on Cell Death. *Cell Death and Differentiation, 16*: pp.3-11.

Kwenti, T.E., Kwenti, T.D.B., Njunda, L.A., Latz, A., Tufon, K.A. and Nkuo-Akenji, T., 2017. Identification of the *Plasmodium* species in clinical samples from children residing in five epidemiological strata of malaria in Cameroon. *Tropical medicine and health*, *45*(1), p.14.

Kyburz, D., Brentano, F. and Gay, S., 2006. Mode of action of hydroxychloroquine in RA—evidence of an inhibitory effect on Toll-like receptor signaling. *Nature clinical practice Rheumatology*, *2*(9), pp.458-459.

Kyes, S.A., Kraemer, S.M. and Smith, J.D., 2007. Antigenic variation in *Plasmodium falciparum*: gene organization and regulation of the var multigene family. *Eukaryotic Cell*, *6*(9), pp.1511-1520.

Lambros, C. and Vanderberg, J.P., 1979. Synchronization of *Plasmodium falciparum* erythrocytic stages in culture. *The Journal of Parasitology*, *65*(3), pp.418-420.

LaMonte, G., Lim, M.Y.X., Wree, M., Reimer, C., Nachon, M., Corey, V., Gedeck, P., Plouffe, D., Du, A., Figueroa, N. and Yeung, B., 2016. Mutations in the Plasmodium falciparum cyclic amine resistance locus (PfCARL) confer multidrug resistance. *American society for microbiology*, *7*(4), pp.e00696-16.

Langhorne, J., Gillard, S., Simon, B., Slade, S. and Eichmann, K., 1989. Frequencies of CD4+ T cells reactive with *Plasmodium chabaudi chabaudi*: distinct response kinetics for cells with Th1 and Th2 characteristics during infection. *International Immunology*, *1*(4), pp.416-424.

Langreth, S.G. and Peterson, E.L.I.Z.A.B.E.T.H., 1985. Pathogenicity, stability, and immunogenicity of a knobless clone of *Plasmodium falciparum* in Colombian owl monkeys. *Infection and Immunity*, *47*(3), pp.760-766.

Langsley, G., van Noort, V., Carret, C., Meissner, M., De Villiers, E.P., Bishop, R. and Pain, A., 2008. Comparative genomics of the Rib protein family in Apicomplexan parasites. *Microbes and Infection, 10*(5), pp.462-470.

Le Chat, L., Sinden, R.E. and Dessens, J.T., 2007. The role of metacaspase 1 in *Plasmodium berghei* development and apoptosis. *Molecular and Biochemical Parasitology*, *153*(1), pp.41-47.

Leed, A., DuBay, K., Ursos, L.M., Sears, D., de Dios, A.C. and Roepe, P.D., 2002. Solution structures of antimalarial drug− heme complexes. *Biochemistry*, *41*(32), pp.10245-10255.

Legakis, J.E., Yen, W.L. and Klionsky, D.J., 2007. A cycling protein complex required for selective autophagy. *Autophagy*, *3*(5), pp.422-432.

Leroy, D., Campo, B., Ding, X.C., Burrows, J.N. and Cherbuin, S., 2014. Defining the biology component of the drug discovery strategy for malaria eradication. *Trends in Parasitology*, *30*(10), pp.478-490.

Levine, B. and Kroemer, G., 2008. Autophagy in the pathogenesis of disease. *Cell*, *132*(1), pp.27-42.

Lew, V.L., Tiffert, T. and Ginsburg, H., 2003. Excess hemoglobin digestion and the osmotic stability of *Plasmodium falciparum*–infected red blood cells. *Blood*, *101*(10), pp.4189-4194.

Lim, L. and McFadden, G.I., 2010. The evolution, metabolism and functions of the apicoplast. *Philosophical Transactions of the Royal Society of London B: Biological Sciences*, *365*(1541), pp.749-763.

Lindblade, K.A., Steinhardt, L., Samuels, A., Kachur, S.P. and Slutsker, L., 2013. The silent threat: asymptomatic parasitemia and malaria transmission. *Expert review of anti-infective therapy*, *11*(6), pp.623-639.

Lipinski, C.A., Lombardo, F., Dominy, B.W. and Feeney, P.J., 1997. Experimental and Computational Approaches to Estimate Solubility and Permeability in Drug Discovery and Development Settings. Advanced Drug Delivery Review, *23*(1-3), pp. 3-25.

Liu, J., He, X. and Zhang, J.Z., 2013. Improving the scoring of protein–ligand binding affinity by including the effects of structural water and electronic polarization. *Journal of Chemical Information and Modelling*, *53*(6), pp.1306-1314.

Liu, J., Xia, H., Kim, M., Xu, L., Li, Y., Zhang, L., Cai, Y., Norberg, H.V., Zhang, T., Furuya, T. and Jin, M., 2011. Beclin1 controls the levels of p53 by regulating the deubiquitination activity of USP10 and USP13. *Cell*, *147*(1), pp.223-234.

Ljungström, I., Moll, K., Perlmann, H., Scherf, A. and Wahlgren, M. eds., 2008. *Methods in malaria research*. MR4/ATCC.

Loewith, R., Jacinto, E., Wullschleger, S., Lorberg, A., Crespo, J.L., Bonenfant, D., Oppliger, W., Jenoe, P. and Hall, M.N., 2002. Two TOR complexes, only one of which is rapamycin sensitive, have distinct roles in cell growth control. *Molecular Cell*, *10*(3), pp.457-468.

Lopes da Silva, M., Thieleke-Matos, C., Cabrita-Santos, L., Ramalho, J.S., Wavre-Shapton, S.T., Futter, C.E., Barral, D.C. and Seabra, M.C., 2012. The host endocytic pathway is essential for *Plasmodium berghei* late liver stage development. *Traffic*, *13*(10), pp.1351-1363.

Lum, J.J., Bauer, D.E., Kong, M., Harris, M.H., Li, C., Lindsten, T. and Thompson, C.B., 2005. Growth factor regulation of autophagy and cell survival in the absence of apoptosis. *Cell, 120*(2), pp.237-248.

Lynch-Day, M.A. and Klionsky, D.J., 2010. The Cvt pathway as a model for selective autophagy. *FEBS Letters*, *584*(7), pp.1359-1366.

MacPherson, G.G., Warrell, M.J., White, N.J., Looareesuwan, S.O.R.N.C.H.A.I. and Warrell, D.A., 1985. Human cerebral malaria. A quantitative ultrastructural analysis of parasitized erythrocyte sequestration. *The American Journal of Pathology*, *119*(3), p.385.

Ma, J.P., Xia, H.J., Zhang, G.H., Han, J.B., Zhang, L.G. and Zheng, Y.T., 2012. Inhibitory effects of chloroquine on the activation of plasmacytoid dendritic cells in SIVmac239-infected Chinese rhesus macaques. *Cellular & molecular immunology*, *9*(5), pp.410-416.

Manjithaya, R., Nazarko, T.Y., Farre, J.C. and Subramani, S., 2010. Molecular mechanism and physiological role of pexophagy. *FEBS Letters, 584*(7), pp.1367-1373.

Mata-Cantero, L., Cid, C., Gomez-Lorenzo, M.G., Xolalpa, W., Aillet, F., Martín, J.J. and Rodriguez, M.S., 2015. Development of two novel high-throughput assays to quantify ubiquitylated proteins in cell lysates: application to screening of new anti-malarials. *Malaria Journal*, *14*(1), p.200.

Matthews, H., Ali, M., Carter, V., Underhill, A., Hunt, J., Szor, H. and Hurd, H., 2012. Variation in apoptosis mechanisms employed by malaria parasites: the roles of inducers, dose dependence and parasite stages. *Malaria Journal*, *11*(1), p.297.

Maude, R.J., Woodrow, C.J. and White, L.J., 2010. Artemisinin antimalarials: preserving the “Magic Bullet”. *Drug Development Research*, *71*(1), pp.12-19.

McQueen, P.G. and McKenzie, F.E., 2004. Age-structured red blood cell susceptibility and the dynamics of malaria infections. *Proceedings of the National Academy of Sciences of the United States of America*, *101*(24), pp.9161-9166.

Medicine for Malaria Venture (MMV). avialble at: http://www.mmv.org/ [accessed: 01/06/2015].

Mein, R.M. (1951) Camoquin in the treatment of human malaria. *The American Journal of Tropical Medicine and Hygiene*, *31*(2), pp.212–217.

Meis, J.F.G.M., Verhave, J.P., Jap, P.H.K. and Meuwissen, J.T., 1985. Transformation of sporozoites of *Plasmodium berghei* into exoerythrocytic forms in the liver of its mammalian host. *Cell and Tissue Research*, *241*(2), pp.353-360.

Mendiratta, D.K., Bhutada, K., Narang, R. and Narang, P., 2006. Evaluation of different methods for diagnosis of *P. falciparum* malaria. *Indian Journal of Medical Microbiology*, *24*(1), p.49-51.

Meshnick, S.R., Yang, Y.Z., Lima, V., Kuypers, F., Kamchonwongpaisan, S.U. and Yuthavong, Y.O, 1993. Iron-dependent free radical generation from the antimalarial agent artemisinin (qinghaosu). *Antimicrobial Agents and Chemotherapy*, *37*(5), pp.1108-1114.

Meslin, B., Barnadas, C., Boni, V., Latour, C., De Monbrison, F., Kaiser, K. & Picot, S. (2007). Features of apoptosis in *Plasmodium falciparum* erythrocytic stage through a putative role of PfMCA1 metacaspase-like protein. *Journal of Infectious Diseases*, *195*(12), pp.1852-1859.

Meslin, B., Beavogui, A.H., Fasel, N. and Picot, S., 2011b. *Plasmodium falciparum* metacaspase PfMCA-1 triggers a z-VAD-fmk inhibitable protease to promote cell death. *PLoS One*, *6*(8), p.e23867.

Meslin, B., Zalila, H., Fasel, N., Picot, S. and Bienvenu, A.L., 2011a. Are protozoan metacaspases potential parasite killers?. *Parasites & Vectors*, *4*(1), p.26.

Miller, L.H. and Su, X., 2011. Artemisinin: discovery from the Chinese herbal garden. *Cell*, *146*(6), pp.855-858.

Mills, A., Lubell, Y. and Hanson, K., 2008. Malaria eradication: the economic, financial and institutional challenge. *Malaria Journal*, *7*(Supp 1), p.S11.

Mizushima, N. & Sahani, M. H., 2014. ATG8 localization in apicomplexan parasites: Apicoplast and more? *Autophagy*, *10*(9), 1487-1494.

Mizushima, N. and Levine, B., 2010. Autophagy in mammalian development and differentiation. *Nature Cell Biology*, *12*(9), pp.823-830.

Mizushima, N., Yamamoto, A., Hatano, M., Kobayashi, Y., Kabeya, Y., Suzuki, K., Tokuhisa, T., Ohsumi, Y. and Yoshimori, T., 2001. Dissection of autophagosome formation using Apg5-deficient mouse embryonic stem cells. *The Journal of Cell Biology*, *152*(4), pp.657-668.

Mogire, R.M., Akala, H.M., Macharia, R.W., Juma, D.W., Cheruiyot, A.C., Andagalu, B., Brown, M.L., El-Shemy, H.A. and Nyanjom, S.G., 2017. Target-similarity search using *Plasmodium falciparum* proteome identifies approved drugs with anti-malarial activity and their possible targets. *PloS One*, *12*(10), p.e0186364.

Mok, S., Ashley, E.A., Ferreira, P.E., Zhu, L., Lin, Z., Yeo, T., Chotivanich, K., Imwong, M., Pukrittayakamee, S., Dhorda, M. and Nguon, C., 2014. Population transcriptomics of human malaria parasites reveals the mechanism of artemisinin resistance. *Science*, *347*(6220) pp.431-435.

Montgomery, J., Mphande, F.A., Berriman, M., Pain, A., Rogerson, S.J., Taylor, T.E., Molyneux, M.E. and Craig, A., 2007. Differential var gene expression in the organs of patients dying of *falciparum* malaria. *Molecular Microbiology*, *65*(4), pp.959-967.

Mutai, B.K. and Waitumbi, J.N., 2010. Apoptosis stalks *Plasmodium falciparum* maintained in continuous culture condition. *Malaria Journal*, *9*(3), p.S6.

Na-Bangchang, K., Muhamad, P., Ruaengweerayut, R., Chaijaroenkul, W. and Karbwang, J., 2013. Identification of resistance of *Plasmodium falciparum* to artesunate-mefloquine combination in an area along the Thai-Myanmar border: integration of clinico-parasitological response, systemic drug exposure, and *in vitro* parasite sensitivity. *Malaria Journal*, *12*(1), p.263.

Nabben, M. and Glatz, J., 2015. Metabolically Relevant Cell Biology-Role of Intracellular Organelles for Cardiac Metabolism. *The scientist's Guide to Cardiac Metabolism*, pp.7-18.

Nair, U., Cao, Y., Xie, Z. and Klionsky, D.J., 2010. Roles of the lipid-binding motifs of Atg18 and Atg21 in the cytoplasm to vacuole targeting pathway and autophagy. *Journal of Biological Chemistry, 285*(15), pp.11476-11488.

Nakatogawa, H., 2013. Two ubiquitin-like conjugation systems that mediate membrane formation during autophagy. *Essays in Biochemistry*, *55*, pp.39-50.

Nakatogawa, H., Ichimura, Y. and Ohsumi, Y., 2007. ATG8, ubiquitin-like protein required for autophagosome formation, mediates membrane tethering and hemifusion. *Cell, 130*, pp.165-178.

Nakatogawa, H., Suzuki, K., Kamada, Y. and Ohsumi, Y., 2009. Dynamics and diversity in autophagy mechanisms: lessons from yeast. *Nature Reviews Molecular Cell Biology, 10*(7), 458-467.

Nankabirwa, J., Brooker, S.J., Clarke, S.E., Fernando, D., Gitonga, C.W., Schellenberg, D. and Greenwood, B., 2014. Malaria in school-age children in Africa: an increasingly important challenge. *Tropical Medicine & International Health*, *19*(11), pp.1294-1309.

Natalang, O., Bischoff, E., Deplaine, G., Proux, C., Dillies, M.A., Sismeiro, O., Guigon, G., Bonnefoy, S., Patarapotikul, J., Mercereau-Puijalon, O. and Coppée, J.Y., 2008. Dynamic RNA profiling in *Plasmodium falciparum* synchronized blood stages exposed to lethal doses of artesunate. *BMC genomics*, *9*(1), p.388.

Navale, R., Allanki, A.D. & Sijwali, P.S. (2014). Characterization of the Autophagy Marker Protein Atg8 Reveals Atypical Features of Autophagy in *Plasmodium falciparum. PloS one*, *9*(11), e113220.

Newton, C.R., Peshu, N., Kendall, B., Kirkham, F.J., Sowunmi, A., Waruiru, C., Mwangi, I., Murphy, S.A. and Marsh, K., 1994. Brain swelling and ischaemia in Kenyans with cerebral malaria. *Archives of Disease in Childhood*, *70*(4), pp.281-287.

Nguyen, H.M., El Hajj, H., El Hajj, R., Tawil, N., Berry, L., Lebrun, M., Bordat, Y. and Besteiro, S., 2017. *Toxoplasma gondii* autophagy-related protein ATG9 is crucial for the survival of parasites in their host. *Cellular Microbiology*, *19*(6), e12712.

Nunes, T., Bernardazzi, C. and de Souza, H.S., 2014. Cell death and inflammatory bowel diseases: apoptosis, necrosis, and autophagy in the intestinal epithelium. *BioMed Research International*.

Nyakeriga, A. M., Perlmann, H., Hagstedt, M., Berzins, K., Troye-Blomberg, M., Zhivotovsky, B. and Grandien, A., 2006. Drug-induced death of the asexual blood stages of *Plasmodium falciparum* occurs without typical signs of apoptosis. *Microbes and Infection, 8*(6), pp.1560-1568.

Oakley, M.S., Kumar, S., Anantharaman, V., Zheng, H., Mahajan, B., Haynes, J.D. and Aravind, L., 2007. Molecular factors and biochemical pathways induced by febrile temperature in intraerythrocytic *Plasmodium falciparum* parasites. *Infection and Immunity, 75*(4), pp.2012-2025.

Obara, K., Sekito, T., Niimi, K. and Ohsumi, Y., 2008. The Atg18-Atg2 complex is recruited to autophagic membranes via phosphatidylinositol 3-phosphate and exerts an essential function. *Journal of Biological Chemistry*, *283*(35), pp.23972-23980.

Okamoto, K., Kondo-Okamoto, N. and Ohsumi, Y., 2009. Mitochondria-anchored receptor Atg32 mediates degradation of mitochondria via selective autophagy. *Developmental Cell, 17*(1), pp.87-97.

Okonko, I.O., Soleye, F.A., Amusan, T.A., Ogun, A.A., Udeze, A.O., Nkang, A.O., Ejembi, J. and Faleye, T.O.C., 2009. Prevalence of malaria *Plasmodium* in Abeokuta, Nigeria. *Malaysian Journal of Microbiology*, *5*(2), pp.113-118.

Olivier, M., Van Den Ham, K., Shio, M.T., Kassa, F.A. and Fougeray, S., 2014. Malarial pigment hemozoin and the innate inflammatory response. *Frontiers in immunology*, *5*, p.25.

Omodeo-Sale, F., Cortelezzi, L., Basilico, N., Casagrande, M., Sparatore, A. and Taramelli, D., 2009. Novel antimalarial aminoquinolines: heme binding and effects on normal or *Plasmodium falciparum*-parasitized human erythrocytes. *Antimicrobial Agents and Chemotherapy*, *53*(10), pp.4339-4344.

Outchkourov, N.S., Roeffen, W., Kaan, A., Jansen, J., Luty, A., Schuiffel, D., van Gemert, G.J., van de Vegte-Bolmer, M., Sauerwein, R.W. and Stunnenberg, H.G., 2008. Correctly folded Pfs48/45 protein of *Plasmodium falciparum* elicits malaria transmission-blocking immunity in mice. *Proceedings of the National Academy of Sciences*, *105*(11), pp.4301-4305.

Packard, R.M., 2014. The origins of antimalarial-drug resistance. *New England Journal of Medicine*, *371*(5), pp.397-399.

Paguio, M.F., Bogle, K.L. and Roepe, P.D., 2011. *Plasmodium falciparum* resistance to cytocidal versus cytostatic effects of chloroquine. *Molecular and Biochemical Parasitology*, *178*(1), pp.1-6.

Pal, A., Hall, B.S., Nesbeth, D.N., Field, H.I. and Field, M.C., 2002. Differential Endocytic Functions of *Trypanosoma brucei* Rab5 Isoforms Reveal a Glycosylphosphatidylinositol-specific Endosomal Pathway. *Journal of Biological Chemistry*, *277*(11), pp.9529-9539.

Park, E.J., Min, K.J., Choi, K.S., Kubatka, P., Kruzliak, P., Kim, D.E. and Kwon, T.K., 2016. Chloroquine enhances TRAIL-mediated apoptosis through up-regulation of DR5 by stabilization of mRNA and protein in cancer cells. *Scientific reports*, *6*, p.22921.

Parroche, P., Lauw, F.N., Goutagny, N., Latz, E., Monks, B.G., Visintin, A., Halmen, K.A., Lamphier, M., Olivier, M., Bartholomeu, D.C. and Gazzinelli, R.T., 2007. Malaria haemozoin is immunologically inert but radically enhances innate responses by presenting malaria DNA to Toll-like receptor 9. *Proceedings of the National Academy of Sciences*, *104*(6), pp.1919-1924.

Pasini, E.M., Van den Ierssel, D., Vial, H.J. and Kocken, C.H., 2013. A novel live-dead staining methodology to study malaria parasite viability. *Malaria Journal*, *12*(1), p.190.

Pasternak, N.D. and Dzikowski, R., 2009. PfEMP1: an antigen that plays a key role in the pathogenicity and immune evasion of the malaria parasite *Plasmodium falciparum*. *The International Journal of Biochemistry & Cell Biology*, *41*(7), pp.1463-1466.

Patel, D.N., Pradeep, P., Surti, M.M. and Agarwal, S.B., 2003. Clinical manifestations of complicated malaria–an overview. *Journal, Indian Academy of Clinical Medicine*, *4*(4), pp.323-331.

Patel, N., Singh, S.B., Basu, S.K. and Mukhopadhyay, A., 2008. *Leishmania* requires Rab7-mediated degradation of endocytosed hemoglobin for their growth. *Proceedings of the National Academy of Sciences*, *105*(10), pp.3980-3985.

Pattanapanyasat, K., Sratongno, P., Chimma, P., Chitjamnongchai, S., Polsrila, K. and Chotivanich, K., 2010. Febrile temperature but not proinflammatory cytokines promotes phosphatidylserine expression on *Plasmodium falciparum* malaria-infected red blood cells during parasite maturation. *Cytometry Part A*, *77*(6), pp.515-523.

Periyasamy-Thandavan, S., Jiang, M., Schoenlein, P. and Dong, Z., 2009. Autophagy: molecular machinery, regulation, and implications for renal pathophysiology. *American Journal of Physiology-Renal Physiology*, *297*(2), pp.F244-F256.

Perkins, D.J., Were, T., Davenport, G.C., Kempaiah, P., Hittner, J.B. and Ong'echa, J.M., 2011. Severe malarial anemia: innate immunity and pathogenesis. *International Journal of Biological Sciences*, *7*(9), p.1427.

Petithory, J.C., Ardoin, F. and Ash, L.R., 2005. Rapid and inexpensive method of diluting Giemsa stain for diagnosis of malaria and other infestations by blood parasites. *Journal of clinical microbiology*, *43*(1), pp.528-528.

Picot, S., Burnod, J., Bracchi, V., Chumpitazi, B.F.F. and Ambroise-Thomas, P., 1997. Apoptosis related to chloroquine sensitivity of the human malaria parasite *Plasmodium*

falciparum. *Transactions of the Royal Society of Tropical Medicine and Hygiene*, *91*(5), pp.590-591.

Pindolia, D.K., Garcia, A.J., Huang, Z., Fik, T., Smith, D.L. and Tatem, A.J., 2014. Quantifying cross-border movements and migrations for guiding the strategic planning of malaria control and elimination. *Malaria Journal*, *13*(1), p.169.

Pingaew, R., Prachayasittikul, S., Ruchirawat, S. and Prachayasittikul, V., 2013. Synthesis and cytotoxicity of novel N-sulfonyl-1, 2, 3, 4-tetrahydroisoquinoline thiosemicarbazone derivatives. *Medicinal Chemistry Research*, *22*(1), pp.267-277.

Plowe, C.V., 2005. Antimalarial drug resistance in Africa: strategies for monitoring and deterrence. In *Malaria: Drugs, Disease and Post-genomic Biology* (pp. 55-79). Springer Berlin Heidelberg.

Porter, H., Gamette, M.J., Cortes-Hernandez, D.G. and Jensen, J.B., 2008. Asexual blood stages of *Plasmodium falciparum* exhibit signs of secondary necrosis, but not classical apoptosis after exposure to febrile temperature (40 C). *Journal of Parasitology*, *94*(2), pp.473-480.

Porter, H.S., 2007. The effect of febrile temperature on *Plasmodium falciparum*. Brigham Young University.

Powis, G., Bonjouklian, R., Berggren, M.M., Gallegos, A., Abraham, R., Ashendel, C., Zalkow, L., Matter, W.F., Dodge, J., Grindey, G. and Vlahos, C.J., 1994. Wortmannin, a potent and selective inhibitor of phosphatidylinositol-3-kinase. *Cancer Research*, *54*(9), pp.2419-2423.

Proto, W.R., Coombs, G.H. and Mottram, J.C., 2013. Cell death in parasitic protozoa: regulated or incidental? *Nature Reviews Microbiology*, *11*(1), p.58.

Puente, C., Hendrickson, R.C. and Jiang, X., 2016. Nutrient-regulated phosphorylation of ATG13 inhibits starvation-induced autophagy. *Journal of Biological Chemistry*, *291*(11), pp.6026-6035.

Quevillon, E., Spielmann, T., Brahimi, K., Chattopadhyay, D., Yeramian, E. and Langsley, G., 2003. The *Plasmodium falciparum* family of Rab GTPases. *Gene, 306*, pp.13-25.

Rampersad, S.N., 2012. Multiple Applications of Alamar Blue as an Indicator of Metabolic Function and Cellular Health in Cell Viability Bioassays. Sensors, *12*(9), pp.12347-12360.

Ranson, H., N'Guessan, R., Lines, J., Moiroux, N., Nkuni, Z. and Corbel, V., 2011. Pyrethroid resistance in African anopheline mosquitoes: what are the implications for malaria control? *Trends in Parasitology*, *27*(2), pp.91-98.

Rathore, S., Datta, G., Kaur, I., Malhotra, P. and Mohmmed, A., 2015. Disruption of cellular homeostasis induces organelle stress and triggers apoptosis like cell-death pathways in malaria parasite. *Cell Death & Disease*, *6*(7), p.e1803.

Rathore, S., Jain, S., Sinha, D., Gupta, M., Asad, M., Srivastava, A., Narayanan, M.S., Ramasamy, G., Chauhan, V.S., Gupta, D. and Mohmmed, A., 2011. Disruption of a

mitochondrial protease machinery in *Plasmodium falciparum* is an intrinsic signal for parasite cell death. *Cell Death & Disease*, *2*(11), p.e231.

Ravikumar, B., Moreau, K., Jahreiss, L., Puri, C. and Rubinsztein, D.C., 2010. Plasma membrane contributes to the formation of pre-autophagosomal structures. *Nature Cell Biology*, *12*(8), p.747.

Reuck, A.V.S. and Cameron, M.P., 1963. Giba Foundation symposium on lysosome. London: J.A. Churchill Ltd.

Ribeiro, S.C., Muratori, M., De Geyter, M. and De Geyter, C., 2017. TUNEL labeling with BrdUTP/anti-BrdUTP greatly underestimates the level of sperm DNA fragmentation in semen evaluation. *PloS One*, *12*(8), p.e0181802.

Rigden, D.J., Michael, P.A. and Ginger, M.L. (2009). Autophagy in protists. *Autophagy, 5*(6), 784-794.

Riglar, D.T., Richard, D., Wilson, D.W., Boyle, M.J., Dekiwadia, C., Turnbull, L., Angrisano, F., Marapana, D.S., Rogers, K.L., Whitchurch, C.B. and Beeson, J.G., 2011. Super-resolution dissection of coordinated events during malaria parasite invasion of the human erythrocyte. *Cell Host & Microbe*, *9*(1), pp.9-20.

Roberts, L., Egan, T.J., Joiner, K.A. and Hoppe, H.C., 2008. Differential effects of quinoline antimalarials on endocytosis in *Plasmodium falciparum*. *Antimicrobial Agents and Chemotherapy*, *52*(5), pp.1840-1842.

Robibaro, B., Stedman, T.T., Coppens, I., Ngô, H.M., Pypaert, M., Bivona, T., Nam, H.W. and Joiner, K.A., 2002. *Toxoplasma gondii* Rab5 enhances cholesterol acquisition from host cells. *Cellular Microbiology*, *4*(3), pp.139-152.

Roepe, P.D., 2014. To kill or not to kill, that is the question: cytocidal antimalarial drug resistance. *Trends in Parasitology*, *30*(3), pp.130-135.

Rose, T.L., Bonneau, L., Der, C., Marty-Mazars, D. and Marty, F., 2006. Starvation-induced expression of autophagy-related genes in Arabidopsis. *Biology of the Cell*, *98*(1), pp.53-67.

Rosenblatt, J.E., Reller, L.B. and Weinstein, M.P., 2009. Laboratory diagnosis of infections due to blood and tissue parasites. *Clinical infectious diseases*, *49*(7), pp.1103-1108.

Rubinsztein, D.C., Codogno, P. and Levine, B., 2012b. Autophagy modulation as a potential therapeutic target for diverse diseases. *Nature Reviews Drug Discovery*, *11*(9), pp.709-730.

Rubinsztein, D.C., Shpilka, T. and Elazar, Z., 2012a. Mechanisms of autophagosome biogenesis. *Current Biology*, *22*(1), pp.29-34.

Russell, R.C., Yuan, H.X. and Guan, K.L., 2014. Autophagy regulation by nutrient signalling. *Cell Research*, *24*(1), p.42.

Sable, R. and Jois, S., 2015. Surfing the protein-protein interaction surface using docking methods: application to the design of PPI inhibitors. *Molecules*, *20*(6), pp.11569-11603.

Sachanonta, N., Chotivanich, K., Chaisri, U., Turner, G.D., Ferguson, D.J., Day, N.P. and Pongponratn, E., 2011. Ultrastructural and real-time microscopic changes in *P. falciparum*-infected red blood cells following treatment with antimalarial drugs. *Ultrastructural Pathology*, *35*(5), pp.214-225.

Sagara, I., Fofana, B., Gaudart, J., Sidibe, B., Togo, A., Toure, S., Sanogo, K., Dembele, D., Dicko, A., Giorgi, R. and Doumbo, O.K., 2012. Repeated artemisinin-based combination therapies in a malaria hyperendemic area of Mali: efficacy, safety, and public health impact. *The American Journal of Tropical Medicine and Hygiene*, *87*(1), pp.50-56.

Sakano, T., Mahamood, M.I., Yamashita, T. and Fujitani, H., 2016. Molecular dynamics analysis to evaluate docking pose prediction. *Biophysics and Physicobiology*, *13*, pp.181-194.

Sanz, A.B., Santamaría, B., Ruiz-Ortega, M., Egido, J. and Ortiz, A., 2008. Mechanisms of renal apoptosis in health and disease. *Journal of the American Society of Nephrology*, *19*(9), pp.1634-1642.

Saunders, D.L., Vanachayangkul, P. and Lon, C., 2014. Dihydroartemisinin–piperaquine failure in Cambodia. *New England Journal of Medicine*, *371*(5), pp.484-485.

Scherz-Shouval, R., Shvets, E., Fass, E., Shorer, H., Gil, L. and Elazar, Z., 2007. Reactive oxygen species are essential for autophagy and specifically regulate the activity of Atg4. *The EMBO Journal, 26*(7), 1749-1760.

Schlagenhauf-Lawlor, P., 2007. Travelers' Malaria. Pub: Chapter 14, Clinical features of malaria in travellers and migrants, BC Decker, 271.

Schofield, L. and Mueller, I., 2006. Clinical immunity to malaria. *Current Molecular Medicine*, *6*(2), pp.205-221.

Scott, D.E., Bayly, A.R., Abell, C. and Skidmore, J., 2016. Small molecules, big targets: drug discovery faces the protein-protein interaction challenge. *Nature Reviews Drug Discovery*, *15*(8), pp.533-550.

Scott, S.V., Guan, J., Hutchins, M.U., Kim, J. and Klionsky, D.J., 2001. Cvt19 is a receptor for the cytoplasm-to-vacuole targeting pathway. *Molecular Cell*, *7*(6), pp.1131-1141.

Shao, S., Li, S., Qin, Y., Wang, X., Yang, Y., Bai, H., Zhou, L., Zhao, C. and Wang, C., 2014. Spautin-1, a novel autophagy inhibitor, enhances imatinib-induced apoptosis in chronic myeloid leukemia. *International Journal of Oncology*, *44*(5), pp.1661-1668.

Shaw, P.J., Chaotheing, S., Kaewprommal, P., Piriyapongsa, J., Wongsombat, C., Suwannakitti, N., Koonyosying, P., Uthaipibull, C., Yuthavong, Y. and Kamchonwongpaisan, S., 2015. *Plasmodium* parasites mount an arrest response to dihydroartemisinin, as revealed by whole transcriptome shotgun sequencing (RNA-seq) and microarray study. *BMC Genomics*, *16*(1), p.830.

Sherman, I.W., 2012. The Malaria Genome Projects: Promise, Progress, and Prospects. World Scientific, pp.195-267.

Shintani, T. and Klionsky, D.J., 2004. Autophagy in health and disease: a double-edged sword. *Science*, *306*(5698), pp.990-995.

Shpilka, T., Weidberg, H., Pietrokovski, S. and Elazar, Z., 2011. Atg8: an autophagy-related ubiquitin-like protein family. *Genome Biology*, *12*(7), p.226.

Siala, E., Khalfaoui, M., Bouratbine, A., Hamdi, S., Hili, K. and Aoun, K., 2005. Relapse of *Plasmodium malariae* malaria 20 years after living in an endemic area. *Presse Medicale (Paris, France: 1983)*, *34*(5), pp.371-372.

Simonsen, A. and Tooze, S.A., 2009. Coordination of membrane events during autophagy by multiple class-III PI3-Kinase complexes. *Journal of Cell Biology, 186*, 773-782.

Sinden, R., E., 1999. *Plasmodium* differentiation in the mosquito. *Parasitologia, 41,* pp. 139-148.

Singh, A.P., Buscaglia, C.A., Wang, Q., Levay, A., Nussenzweig, D.R., Walker, J.R., Winzeler, E.A., Fujii, H., Fontoura, B.M. and Nussenzweig, V., 2007. *Plasmodium* circumsporozoite protein promotes the development of the liver stages of the parasite. *Cell*, *131*(3), pp.492-504.

Slater, A.F., 1993. Chloroquine: mechanism of drug action and resistance in *Plasmodium falciparum*. *Pharmacology & Therapeutics*, *57*(2-3), pp.203-235.

Smilkstein, M., Sriwilaijaroen, N., Kelly, J.X., Wilairat, P. and Riscoe, M., 2004. Simple and inexpensive fluorescence-based technique for high-throughput antimalarial drug screening. *Antimicrobial Agents and Chemotherapy*, *48*(5), pp.1803-1806.

Sow, F., Nyonda, M., Bienvenu, A.L. and Picot, S., 2015. Wanted *Plasmodium falciparum*, dead or alive. *Microbial Cell*, *2*(7), pp.219-224.

Spielmann, T., Hawthorne, P.L., Dixon, M.W., Hannemann, M., Klotz, K., Kemp, D.J., Klonis, N., Tilley, L., Trenholme, K.R. and Gardiner, D.L., 2006. A cluster of ring stage–specific genes linked to a locus implicated in cytoadherence in *Plasmodium falciparum* codes for PEXEL-negative and PEXEL-positive proteins exported into the host cell. *Molecular Biology of the Cell*, *17*(8), pp.3613-3624.

Steketee, R.W., Nahlen, B.L., Parise, M.E. and Menendez, C., 2001. The burden of malaria in pregnancy in malaria-endemic areas. *The American Journal of Tropical Medicine and Hygiene*, *64*(1_suppl), pp.28-35.

Stoute, J.A., Slaoui, M., Heppner, D.G., Momin, P., Kester, K.E., Desmons, P., Wellde, B.T., Garçon, N., Krzych, U., Marchand, M. and Ballou, W.R., 1997. A preliminary evaluation of a recombinant circumsporozoite protein vaccine against *Plasmodium falciparum* malaria. *New England Journal of Medicine*, *336*(2), pp.86-91.

Sui, X., Chen, R., Wang, Z., Huang, Z., Kong, N., Zhang, M., Han, W., Lou, F., Yang, J., Zhang, Q. and Wang, X., 2013. Autophagy and chemotherapy resistance: a promising therapeutic target for cancer treatment. *Cell Death & Disease*, *4*(10), p.e838.

Sullivan, D.J., Gluzman, I.Y., Russell, D.G. and Goldberg, D.E., 1996. On the molecular mechanism of chloroquine's antimalarial action. *Proceedings of the National Academy of Sciences*, *93*(21), pp.11865-11870.

Sutherland, C.J., Tanomsing, N., Nolder, D., Oguike, M., Jennison, C., Pukrittayakamee, S., Dolecek, C., Hien, T.T., Do Rosário, V.E., Arez, A.P. and Pinto, J., 2010. Two

nonrecombining sympatric forms of the human malaria parasite *Plasmodium ovale* occur globally. *The Journal of Infectious Diseases*, *201*(10), pp.1544-1550.

Suzuki, K. and Ohsumi, Y., 2007. Molecular machinery of autophagosome formation in yeast, *Saccharomyces cerevisiae*. *FBES, 581*: pp.2156-2161.

Suzuki, K., Kamada, T., Mizushima, N., Noda, T. and Ohsumi, Y., 2001. The pre-autophagosomal structure organized by concerted functions of ATG gene is essential for autophagosome formation. *EMBO Journal, 20*, pp.5971-5981.

Szmitko, P.E., Kohn, M.L. and Simor, A.E., 2008. *Plasmodium falciparum* malaria occurring eight years after leaving an endemic area. *Diagn. Microbi Infect. Dis*, *61*(1), pp.105-107.

Takala, S.L., Coulibaly, D., Thera, M.A., Batchelor, A.H., Cummings, M.P., Escalante, A.A., Ouattara, A., Traoré, K., Niangaly, A., Djimdé, A.A. and Doumbo, O.K., 2009. Extreme polymorphism in a vaccine antigen and risk of clinical malaria: implications for vaccine development. *Science Translational Medicine*, *1*(2), pp.2ra5-2ra5.

Tanner, M. and Savigny, D.D., 2008. Malaria eradication back on the table. *Bulletin of the World Health Organization*, *86*(2), pp.82-82.

Taylor-Brown, E. and Hurd, H., 2013. The first suicides: a legacy inherited by parasitic protozoans from prokaryote ancestors. *Parasites & Vectors*, *6*(1), p.108.

Teter, S.A., Eggerton K.P., Scott S.V., Kim, J., Fischer, A.M. and Klionsky, D.J., 2001. Degradation of lipid vesicle in the yeast vacuole requires function of CVT 17, a putative lipase. *Journal of Biological Chemistry, 276*, pp.2083-2087.

Tewari, S.G., Prigge, S.T., Reifman, J. and Wallqvist, A., 2017. Using a genome-scale metabolic network model to elucidate the mechanism of chloroquine action in *Plasmodium falciparum*. *International Journal for Parasitology: Drugs and Drug Resistance*, *7*(2), pp.138-146.

Theunissen, C., Janssens, P., Demulder, A., Nouboussié, D., Van Esbroeck, M., Van Gompel, A. and Van den Ende, J., 2009. *Falciparum* malaria in patient 9 years after leaving malaria-endemic area. *Emerging Infectious Diseases*, *15*(1), p.115.

Tomlins, A.M., Ben-Rached, F., Williams, R.A., Proto, W.R., Coppens, I., Ruch, U. and Langsley, G., 2013. *Plasmodium falciparum* ATG8 implicated in both autophagy and apicoplast formation. *Autophagy, 9*(10), pp.1540-1552.

Totino, P.R., Daniel-Ribeiro, C.T., Corte-Real, S. and Ferreira-da-Cruz, M.D., 2008. *Plasmodium falciparum*: Erythrocytic stages die by autophagic-like cell death under drug pressure. *Experimental Parasitology, 118*(4), 478-486.

Totino, P.R.R., Daniel-Ribeiro, C.T. and de Fatima Ferreira-da-Cruz, M., 2011. Refractoriness of eryptotic red blood cells to *Plasmodium falciparum* infection: a putative host defense mechanism limiting parasitaemia. *PloS One*, *6*(10), p.e26575.

Trager, W. and Jensen, J.B., 1976. Human malaria parasites in continuous culture. *Science*, *193*(4254), pp.673-675.

Ullah, I., Sharma, R., Biagini, G.A., Horrocks, P., 2017. A validated bioluminescence-based assay for the rapid determination of the initial rate of kill for discovery antimalarials. *Journal of Antimicrobial Chemotherapy* 72(3), pp.717–726.

Uneke, C.J., 2007. Impact of placental *Plasmodium falciparum* malaria on pregnancy and perinatal outcome in sub-Saharan Africa: I: introduction to placental malaria. *The Yale Journal of Biology and Medicine*, *80*(2), pp.39-50.

Vaid, A., Ranjan, R., Smyth, W.A., Hoppe, H.C. and Sharma, P., 2010. PfPI3K, a phosphatidylinositol-3 kinase from *Plasmodium falciparum*, is exported to the host erythrocyte and is involved in haemoglobin trafficking. *Blood, 115*(12), pp.2500-2507.

Vaidya, A.B. and Mather, M.W., 2000. Atovaquone resistance in malaria parasites. *Drug Resistance Updates*, *3*(5), pp.283-287.

Valbuena, N., Rozalen, A.E. and Moreno, S., 2012. Fission yeast TORC1 prevents eIF2α phosphorylation in response to nitrogen and amino acids via Gcn2 kinase. *J Cell Sci*, *125*(24), pp.5955-5959.

Van den Bosch, H., 1980. Intracellular phospholipases A. *Biochimica et Biophysica Acta (BBA)-Biomembranes*, *604*(2), pp.191-246.

Veber, D.F., Johnson, S.R., Cheng, H.Y., Smith, B.R., Ward, K.W. and Kopple, K.D., 2002. Molecular Properties that Influence the Oral Bioavailability of Drug Candidates, *Journal of Medicinal Chemistry*, *45*(12), pp.2615-2623.

Vlahakis, A., Graef, M., Nunnari, J. and Powers, T., 2014. TOR complex 2-Ypk1 signalling is an essential positive regulator of the general amino acid control response and autophagy. *Proceedings of the National Academy of Sciences*, *111*(29), pp.10586-10591.

Waite, M., Griffin, H.D., Dingle, R.F.J. and Dean, R.T., 1976. Lysosomes in Biology and Pathology, *5*, 257-305.

Walczak, M. and Martens, S., 2013. Dissecting the role of the Atg12–Atg5-Atg16 complex during autophagosome formation. *Autophagy*, *9*(3), pp.424-425

Walczak, M., Ganesan, S.M., Niles, J.C. and Yeh, E., 2018. Atg8 is essential specifically for an autophagy-independent function in apicoplast biogenesis in blood-stage malaria parasites. *MBio*, *9*(1), pp.e02021-17.

Walker, D.M., Mahfooz, N., Kemme, K.A., Patel, V.C., Spangler, M. and Drew, M.E., 2013. *Plasmodium falciparum* erythrocytic stage parasites require the putative autophagy protein PfAtg7 for normal growth. *PloS One*, *8*(6), p.e67047.

Walther, M., Thompson, F.M., Dunachie, S., Keating, S., Todryk, S., Berthoud, T., Andrews, L., Andersen, R.F., Moore, A., Gilbert, S.C. and Poulton, I., 2006. Safety, immunogenicity, and efficacy of prime-boost immunization with recombinant poxvirus FP9 and modified vaccinia virus Ankara encoding the full-length *Plasmodium falciparum* circumsporozoite protein. *Infection and Immunity*, *74*(5), pp.2706-2716.

Wang, T., Ming, Z., Xiaochun, W. and Hong, W., 2011. Rab7: role of its protein interaction cascades in endo-lysosomal traffic. *Cellular Signalling, 23*(3), pp.516-521.

Wanzira, H., Katamba, H. and Rubahika, D., 2016. Use of long-lasting insecticide-treated bed nets in a population with universal coverage following a mass distribution campaign in Uganda. *Malaria Journal*, *15*(1), p.311.

Warhurst, D.C., Craig, J.C., Adagu, I.S., Guy, R.K., Madrid, P.B. and Fivelman, Q.L., 2007. Activity of piperaquine and other 4-aminoquinoline antiplasmodial drugs against chloroquine-sensitive and resistant blood-stages of *Plasmodium falciparum*: role of β-haematin inhibition and drug concentration in vacuolar water-and lipid-phases. *Biochemical pharmacology*, *73*(12), pp.1910-1926.

Webber, J.L., Young, A.R. and Tooze, S.A., 2007. Atg9 trafficking in mammalian cells. *Autophagy*, *3*(1), pp.54-56.

Wells, T.N., Van Huijsduijnen, R.H. and Van Voorhis, W.C., 2015. Malaria medicines: a glass half full?. *Nature Reviews Drug Discovery*, *14*(6), pp.424-442.

White NJ, 2009. Malaria. In: Manson's tropical diseases. Edited by Cook GC, Manson P, Zumla A. Twenty-second ed: Saunders; pp.1201-1300.

White NJ, Pukrittayakamee S, Hien TT, Faiz MA, Mokuolu OA, DondorP, A. M. 2014. Malaria. Lancet 383, pp.723–735.

WHO, 2006. Use of indoor residual spraying for scaling up global malaria control and elimination. *Geneva: Switzerland.*
http://apps.who.int/iris/bitstream/10665/69386/1/WHO_HTM_MAL_2006.1112_eng.pdf

WHO, 2016. Overview of malaria treatment. *Geneva: Switzerland.*http://www.who.int/malaria/areas/treatment/overview/en/

WHO, 2017. Malaria. *Geneva: Switzerland.* http://www.who.int/mediacentre/factsheets/fs094/en/

Willcox, M., Bodeker, G., Rasoanaivo, P. and Addae-Kyereme, J. eds., 2004. *Traditional Medicinal Plants and Malaria*. CRC Press.

Wong, E.H., Hasenkamp, S. and Horrocks, P., 2011. Analysis of the molecular mechanisms governing the stage-specific expression of a prototypical housekeeping gene during intraerythrocytic development of *P. falciparum*. *Journal of Molecular Biology*, *408*(2), pp.205-221.

Wright, M.H., Clough, B., Rackham, M.D., Rangachari, K., Brannigan, J.A., Grainger, M., Moss, D.K., Bottrill, A.R., Heal, W.P., Broncel, M. and Serwa, R.A., 2014. Validation of N-myristoyltransferase as an antimalarial drug target using an integrated chemical biology approach. *Nature Chemistry*, *6*(2), pp.112-121.

Wu, L., Feng, Z., Cui, S., Hou, K., Tang, L., Zhou, J., Cai, G., Xie, Y., Hong, Q., Fu, B. and Chen, X., 2013. Rapamycin upregulates autophagy by inhibiting the mTOR-ULK1 pathway, resulting in reduced podocyte injury. *PloS one*, *8*(5), p.e63799.

Wu, L.J., Rabbege, J.R., Nagasawa, H., Jacobs, G. and Aikawa, M., 1988. Morphological effects of pyronaridine on malarial parasites. *The American Journal of Tropical Medicine and Hygiene*, *38*(1), pp.30-36.

Wu, Y.T., Tan, H.L., Shui, G., Bauvy, C., Huang, Q., Wenk, M.R., Ong, C.N., Codogno, P. and Shen, H.M., 2010. Dual role of 3-methyladenine in modulation of autophagy via different temporal patterns of inhibition on class I and III phosphoinositide 3-kinase. *Journal of Biological Chemistry*, *285*(14), pp.10850-10861.

Xie, Z. and Klionsky, D.J., 2007. Autophagosome formation: core machinery and adaptations. *Nature cell Biology*, *9*(10), pp.1102-1109.

Yamaguchi, M., Noda, N.N., Nakatogawa, H., Kumeta, H., Ohsumi, Y. And Inagaki, F., 2010. Autophagy-related protein 8 (Atg8) family interacting motif in Atg3 mediates the Atg3-Atg8 interaction and is crucial for the cytoplasm-to-vacuole targeting pathway. *Journal of Biological Chemistry, 285*(38), pp.29599-29607.

Yang, Z., Huang, J., Geng, J., Nair, U. and Klionsky D.J., 2006. ATG22 recycle amino acids to link the derivative and recycling function of autophagy. *Molecular Biology of the Cell. 17*(12), pp.5094-5104.

Yayon, A. and Ginsburg, H., 1983. Chloroquine inhibits the degradation of endocytic vesicles in human malaria parasites. *Cell Biology International Reports*, *7*(11), p.895.

Yayon, A., Waa, J.A.V., Yayon, M., Geary, T.G. and Jensen, J.B., 1983. Stage-dependent effects of chloroquine on *Plasmodium falciparum in vitro*. *Journal of Eukaryotic Microbiology*, *30*(4), pp.642-647.

Yin, J., Angeline, J.J. and Tan, K.S., 2010. Autophagy is involved in starvation response and cell death in Blastocystis. *Microbiology*, *156*(3), pp.665-677.

Yu, L., Strandberg, L. and Lenardo, M.J., 2008. The selectivity of autophagy and its role in cell death and survival. *Autophagy*, *4*(5), pp.567-573.

Yu, Z.Q., Ni, T., Hong, B., Wang, H.Y., Jiang, F.J., Zou, S., Chen, Y., Zheng, X.L., Klionsky, D.J., Liang, Y. and Xie, Z., 2012. Dual roles of Atg8− PE deconjugation by Atg4 in autophagy. *Autophagy*, *8*(6), pp.883-892.

Zenz, W., Trop, M., Kollaritsch, H. and Reinthaler, F., 2000. Congenital malaria due to *Plasmodium falciparum* and *Plasmodium* malariae. *Wiener klinische Wochenschrift*, *112*(10), pp.459-461.

Zhang, Y. and Just, W.W., 1987. A comparative study on the effect of chloroquine and ammonium chloride on feeding process of *Plasmodium falciparum in vitro*. Parasitology Research, 73(5), pp.475-478.

Appendix 1 (Chapter 3)

Table shows compound ID, EC_{50} in both $Dd2^{luc}$ (CQR) and 3D7 (CQS) with chemical structures for 131 synthetic putative autophagy inhibitors.

Compound ID	EC_{50} (µM) in $Dd2^{luc}$ (95% Confidence intervals)	EC_{50} (µM) in 3D7 (95% Confidence intervals)	Chemical structure
SK1.49	1.1 (1.0 to 1.1)	0.8 (0.6 to 1.0)	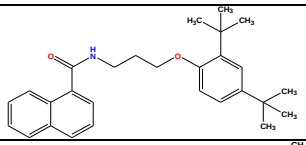
SK1.47	2.1 (1.7 to 2.6)	1.6 (1.3 to 2.0)	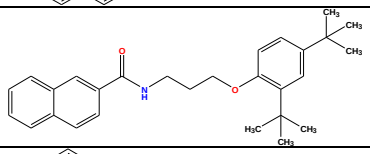
7315922	4.9 (3.6 to 6.5)	4.2 (3.3 to 5.3)	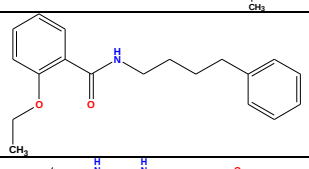
SK1-109	5.0 (4.0 to 6.0)	4.5 (3.5 to 5.6)	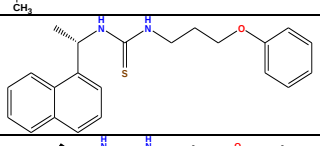
SK1.108	6.2 (5.4 to 7.1)	3.9 (3.0 to 5.0)	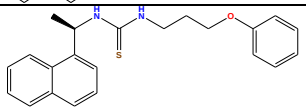
SK1.63	6.6 (5.9 to 7.3)	4.0 (3.0 to 5.2)	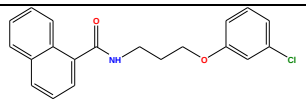
LO9	12.5 (10.9 to 14.2)	7.9 (7.0 to 8.9)	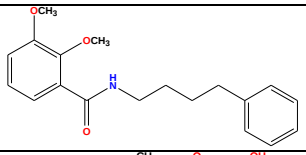
6596157	12.7 (10.5 to 15.2)	21.6 (19.1 to 24.4)	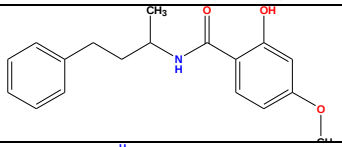
SK1.70	13.4 (11.5 to 15.4)	ND	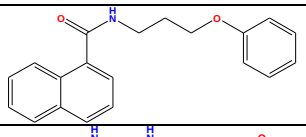
SK1.104	14.7 (13.7 to 15.6)	ND	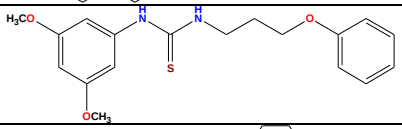
JM.16	15.0 (13.4 to 16.7)	ND	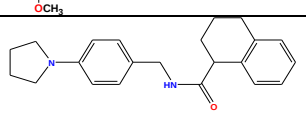
5217339	15.4 (11.8 to 20.0)	9.1 (8.6 to 9.5)	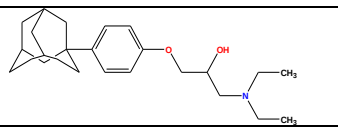

SK1.64	**17.0 (15.5 to 18.5)**	**ND**	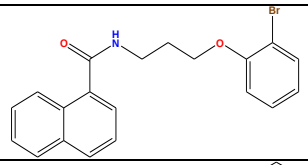
ke-4a	**17.1 (14.1 to 20.6)**	**ND**	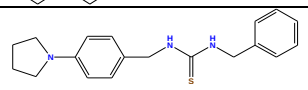
SK1.107	**17.9 (16.7 to 19.0)**	**ND**	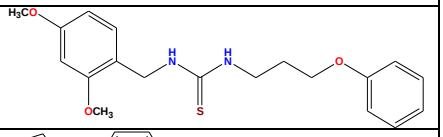
JM3	**18.4 (15.6 to 21.6)**	**ND**	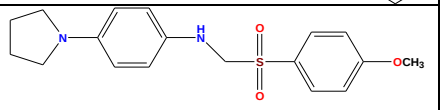
SK1.83	**18.6 (14.9 to 23.2)**	**ND**	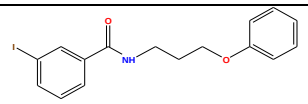
SK1.50	**18.7 (16.1 to 21.6)**	**ND**	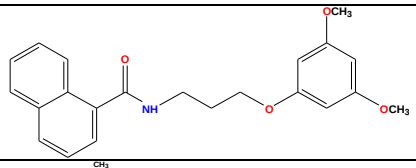
SK1.87	**18.8 (16.3 to 21.7)**	**ND**	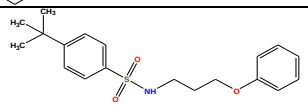
SK1.102	**18.9 (15.5 to 22.9)**	**ND**	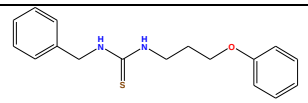
SK1.72	**19.0 (16.1 to 22.3)**	**ND**	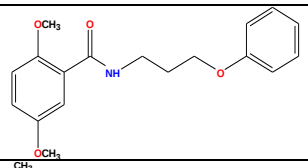
7221498	**19.6 (16.8 to 22.8)**	**10.6 (8.6 to 12.9)**	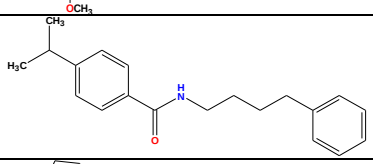
ke-4d	**19.9 (17.1 to 23.0)**	**ND**	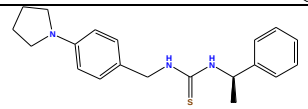
JM15	**20.5 (16.7 to 24.9)**	**ND**	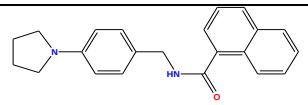
SK1.35	**21.1 (19.5 to 22.8)**	**ND**	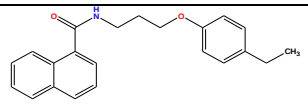
ke-4e	**22.3 (19.4 to 25.5)**	**ND**	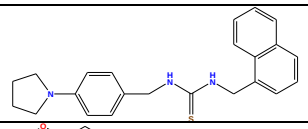
SK1.85	**24.6 (21.1 to 28.5)**	**ND**	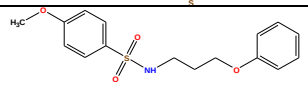

JM13	**25.6 (22.3 to 29.2)**	**ND**	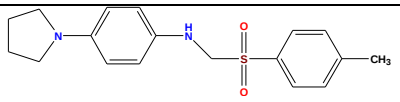
SK1.53	**26.1 (22.7 to 29.9)**	**ND**	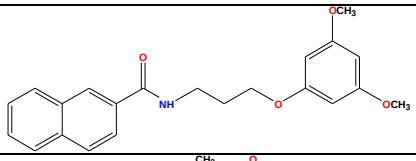
6555142	**26.4 (23.6 to 29.5)**	**10.9 (9.3 to 12.6)**	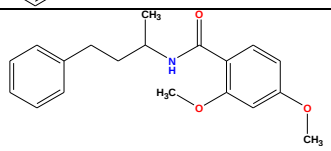
SK1.101	**29.9 (27.0 to 33.0)**	**ND**	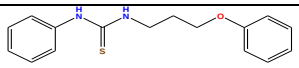
6115259	**32.0 (26.2 to 39.0)**	**42.3 (38.8 to 45.9)**	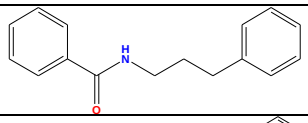
5522477	**32.5 (29.2 to 36.0)**	**ND**	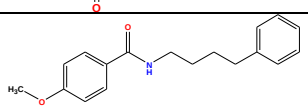
9108417	**35.7 (30.5 to 41.7)**	**ND**	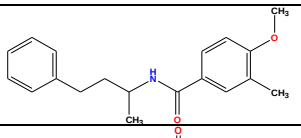
9090513	**39.3 (33.1 to 46.4)**	**ND**	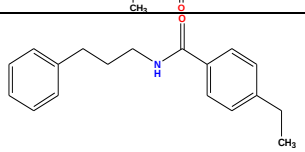
7737951	**39.3 (33.1 to 46.4)**	**ND**	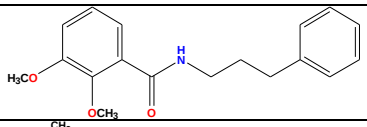
7311494	**42.2 (36.8 to 48.3)**	**ND**	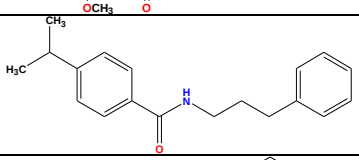
7962202	**66.4 (60.0 to 73.2)**	**ND**	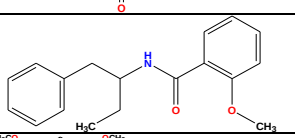
LO8	**69.1 (66.0 to 72.2)**	**57.0 (54.0 to 77.3)**	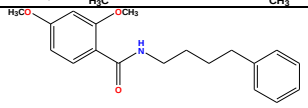
9148206	**149.2 (129.6 to 171.7)**	**ND**	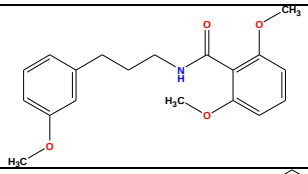
5335716	**ND**	**17.3 (15.7 to 18.9)**	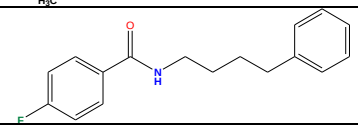

7661021	**ND**	**29.0 (26.7 to 31.5)**	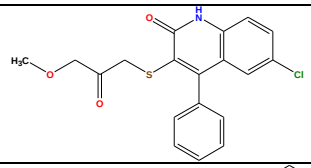
5337355	**ND**	**32.2 (33.1 to 46.4)**	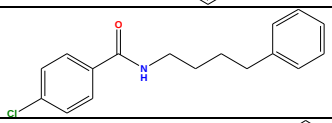
5334050	**ND**	**37.8 (27.6 to 51.5)**	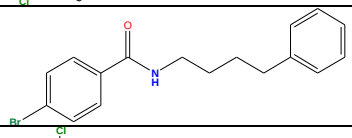
7226051	**ND**	**37.8 (28.7 to 49.5)**	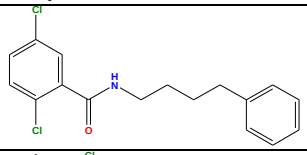
7264596	**ND**	**38.5 (35.3 to 41.8)**	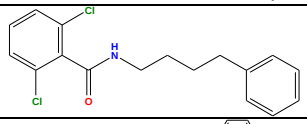
7668219	**ND**	**42.1 (37.7 to 46.8)**	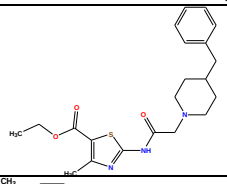
5361579	**ND**	**43.8 (42.0 to 45.5)**	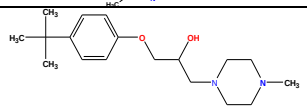
7260078	**ND**	**44.0 (36.6 to 52.6)**	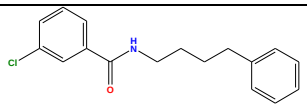
5557287	**ND**	**57.0 (50.7 to 63.8)**	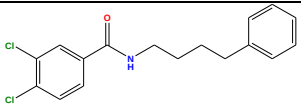
6525395	**ND**	**63.9 (58.5 to 69.7)**	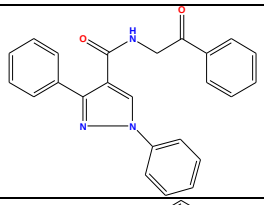
7669739	**ND**	**64.8 (56.7 to 74.0)**	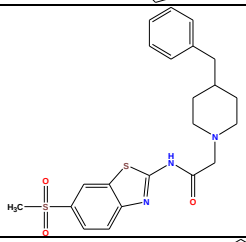
5334466	**ND**	**67.6 (50.3 to 90.8)**	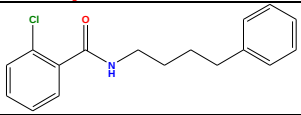
7685637	**ND**	**73.3 (59.8 to 89.6)**	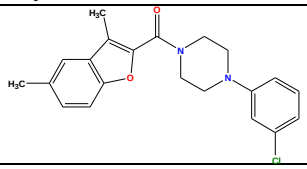

5334325	**ND**	**77.7 (64.6 to 93.2)**	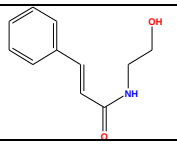
5329246	**ND**	**85.6 (72.6 to 100.8)**	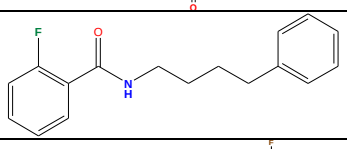
6067284	**ND**	**89.2 (57.5 to 138.2)**	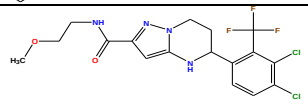
5106372	**ND**	**ND**	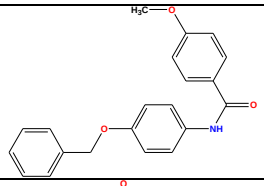
5229998	**ND**	**ND**	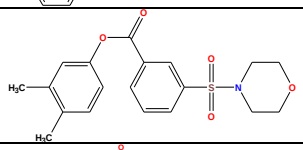
5529858	**ND**	**ND**	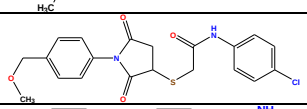
4012455	**ND**	**ND**	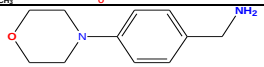
4013951	**ND**	**ND**	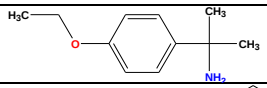
5330932	**ND**	**ND**	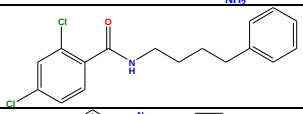
5528440	**ND**	**ND**	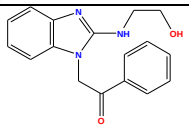
5328083	**ND**	**ND**	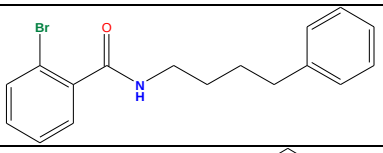
5328241	**ND**	**ND**	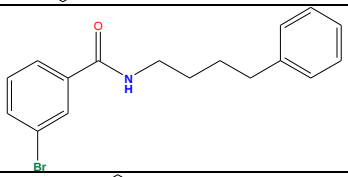
NKLA-98	**ND**	**ND**	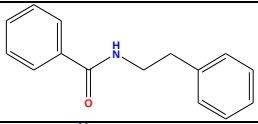
NKLA-104	**ND**	**ND**	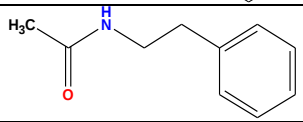
NKLA-106	**ND**	**ND**	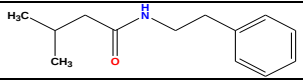

NKLA-110	**ND**	**ND**	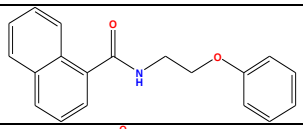
NKLA-112	**ND**	**ND**	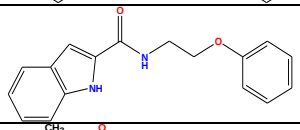
NKLA-114	**ND**	**ND**	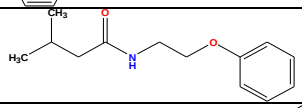
NKLA-122	**ND**	**ND**	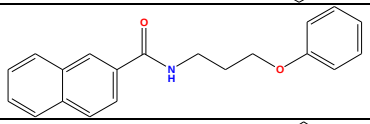
NKLA-124	**ND**	**ND**	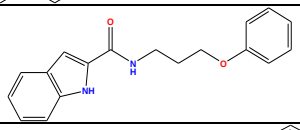
NKLA-128	**ND**	**ND**	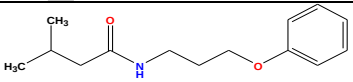
5274150	**ND**	**ND**	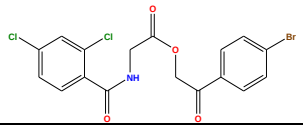
5349520	**ND**	**ND**	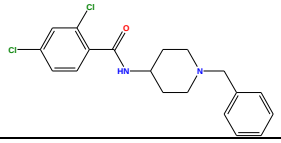
5378129	**ND**	**ND**	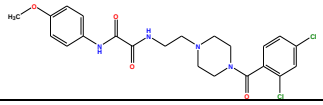
6045327	**ND**	**ND**	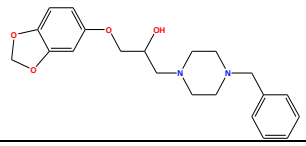
7643458	**ND**	**ND**	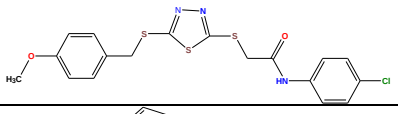
7680448	**ND**	**ND**	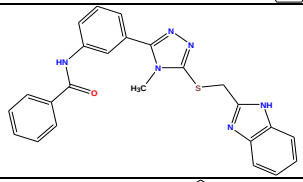
7689756	**ND**	**ND**	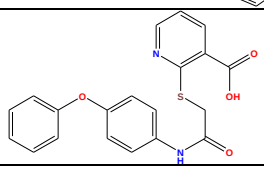

7755811	**ND**	**ND**	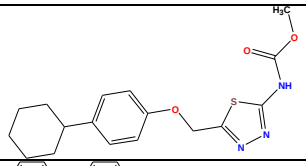
7804934	**ND**	**ND**	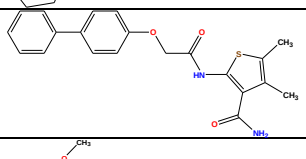
7971741	**ND**	**ND**	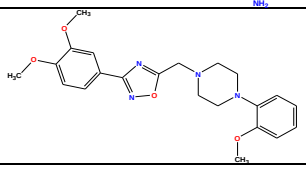
7981744	**ND**	**ND**	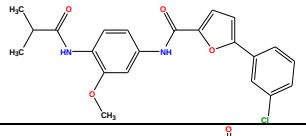
9008875	**ND**	**ND**	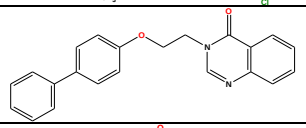
9017025	**ND**	**ND**	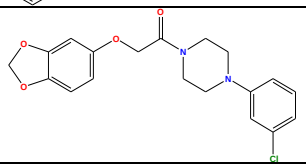
9038873	**ND**	**ND**	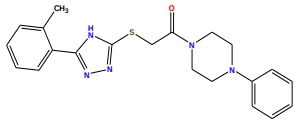
9079263	**ND**	**ND**	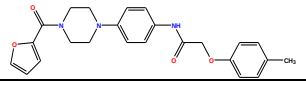
9138062	**ND**	**ND**	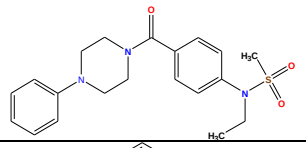
9149687	**ND**	**ND**	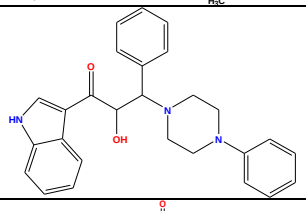
9154044	**ND**	**ND**	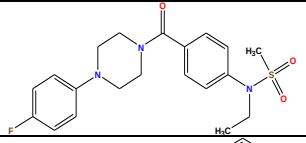
9155821	**ND**	**ND**	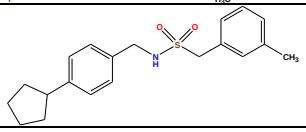

LO5	**ND**	**ND**	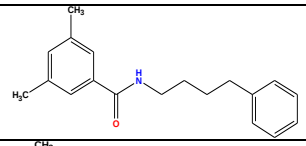
LO6	**ND**	**ND**	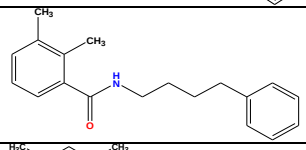
LO7	**ND**	**ND**	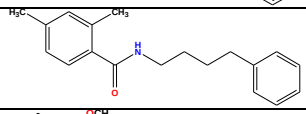
LO10	**ND**	**ND**	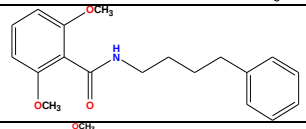
LO11	**ND**	**ND**	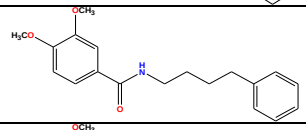
LO12	**ND**	**ND**	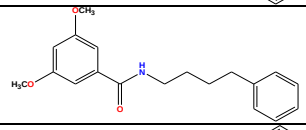
5334792	**ND**	**ND**	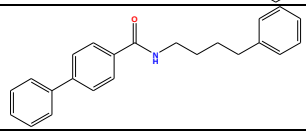
6576414	**ND**	**ND**	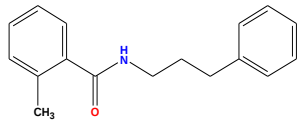
7240174	**ND**	**ND**	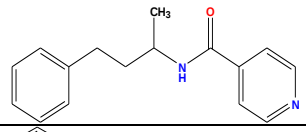
7242287	**ND**	**ND**	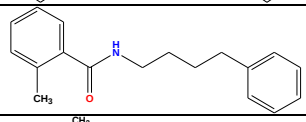
7723347	**ND**	**ND**	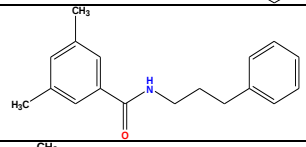
7769345	**ND**	**ND**	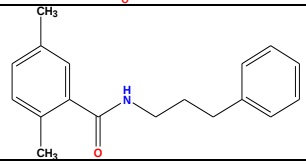
7774436	**ND**	**ND**	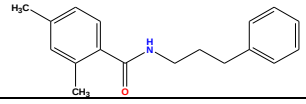

9138443	**ND**	**ND**	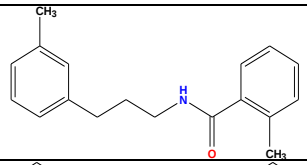
SK1.93	**ND**	**ND**	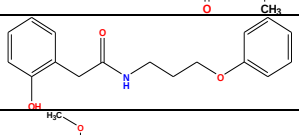
SK1.74	**ND**	**ND**	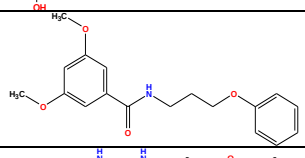
SK1.106	**ND**	**ND**	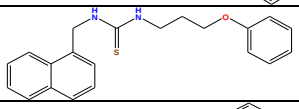
SK1.60	**ND**	**ND**	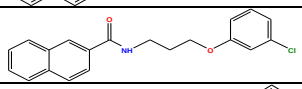
SK1.61	**ND**	**ND**	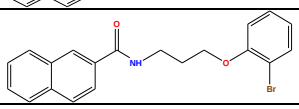
SK1.86	**ND**	**ND**	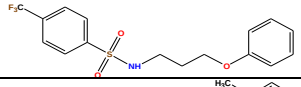
SK1.46	**ND**	**ND**	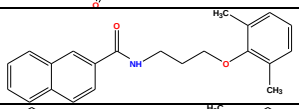
SK1.43	**ND**	**ND**	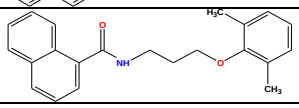
SK1.36	**ND**	**ND**	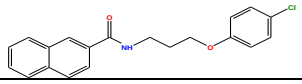
SK1.92	**ND**	**ND**	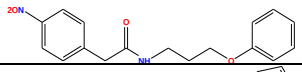
Ke-4f	**ND**	**ND**	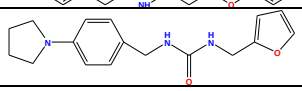
Ke-4c	**ND**	**ND**	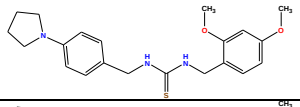
Ke-4b	**ND**	**ND**	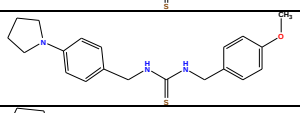
Ke-4g	**ND**	**ND**	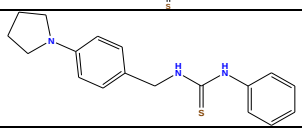
SK1.91	**ND**	**ND**	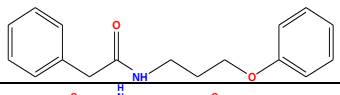
SK1.39	**ND**	**ND**	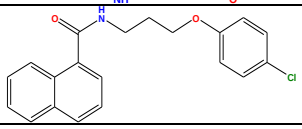

SK1.79	**ND**	**ND**	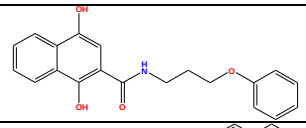
SK1.31	**ND**	**ND**	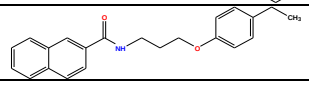
JM18	**ND**	**ND**	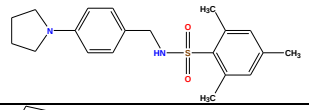
JM12	**ND**	**ND**	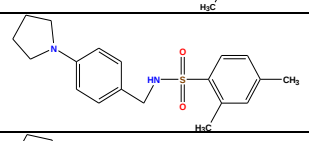
JM6	**ND**	**ND**	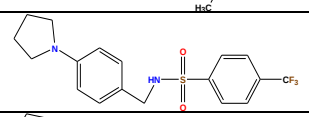
JM10	**ND**	**ND**	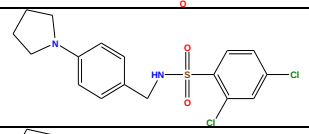
JM17	**ND**	**ND**	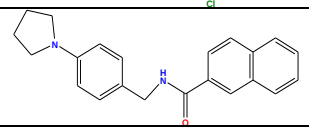

Appendix 2 (Chapter 3)

Illustrating EC_{50} values of library compounds in 3D7 (A) and $Dd2^{luc}$ (B) trophozoite stage of *P. falciparum* using malaria SYBR Green I Fluorescence assay.

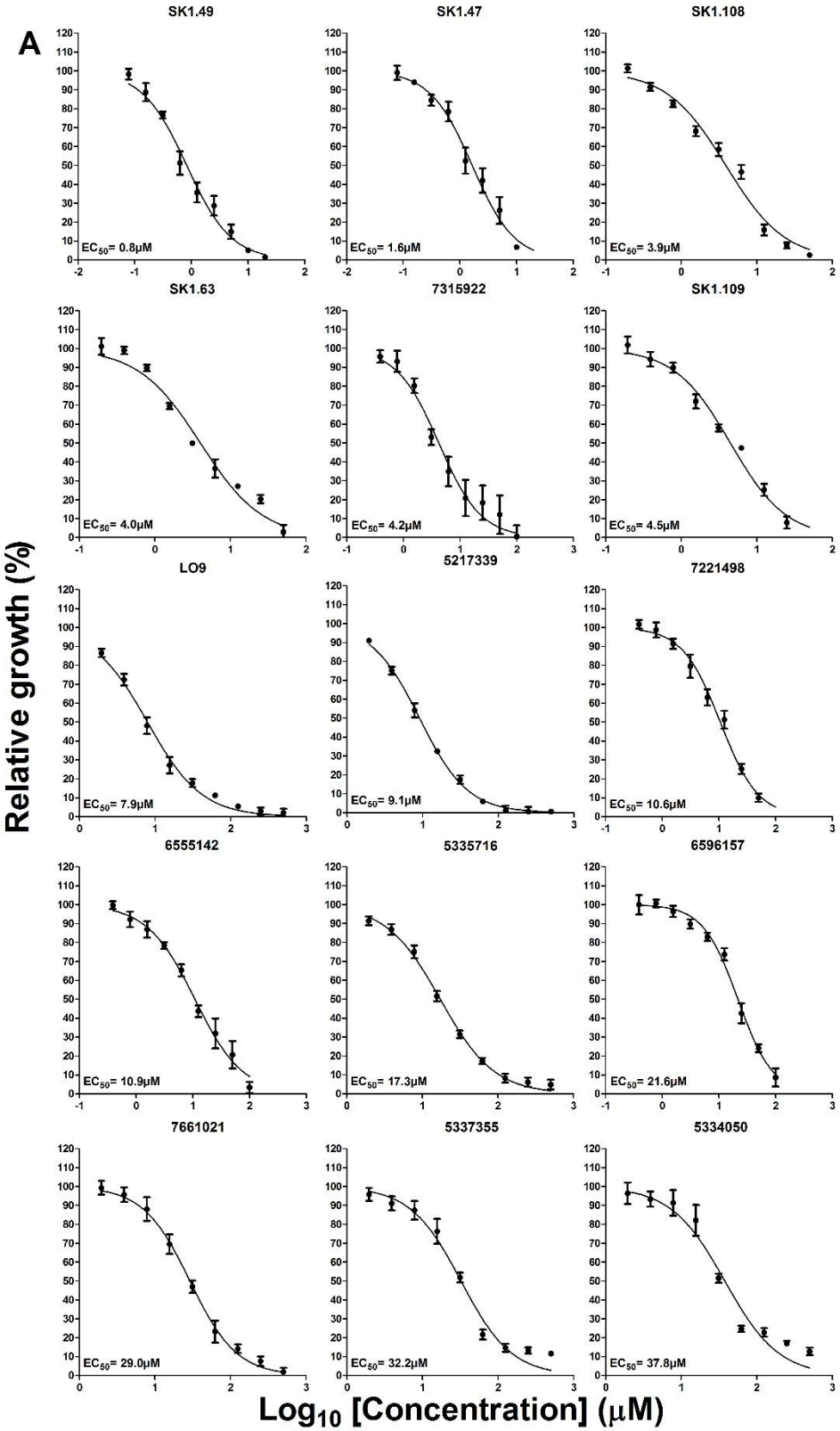

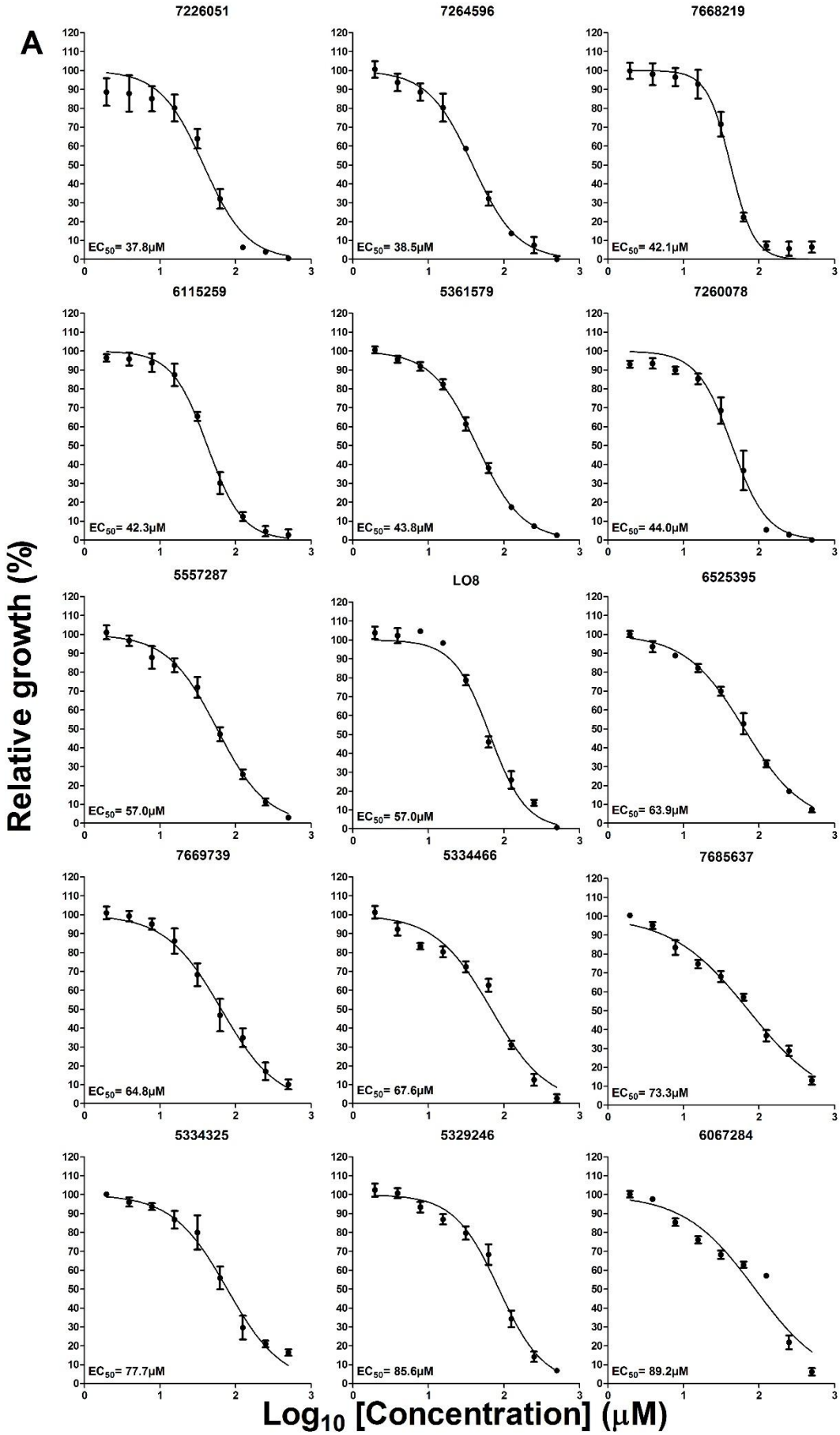
A
7226051
EC50= 37.8μM
7264596
EC50= 38.5μM
7668219
EC50= 42.1μM
6115259
EC50= 42.3μM
5361579
EC50= 43.8μM
7260078
EC50= 44.0μM
5557287
EC50= 57.0μM
LO8
EC50= 57.0μM
6525395
EC50= 63.9μM
7669739
EC50= 64.8μM
5334466
EC50= 67.6μM
7685637
EC50= 73.3μM
5334325
EC50= 77.7μM
5329246
EC50= 85.6μM
6067284
EC50= 89.2μM
Relative growth (%)
Log10 [Concentration] (μM)

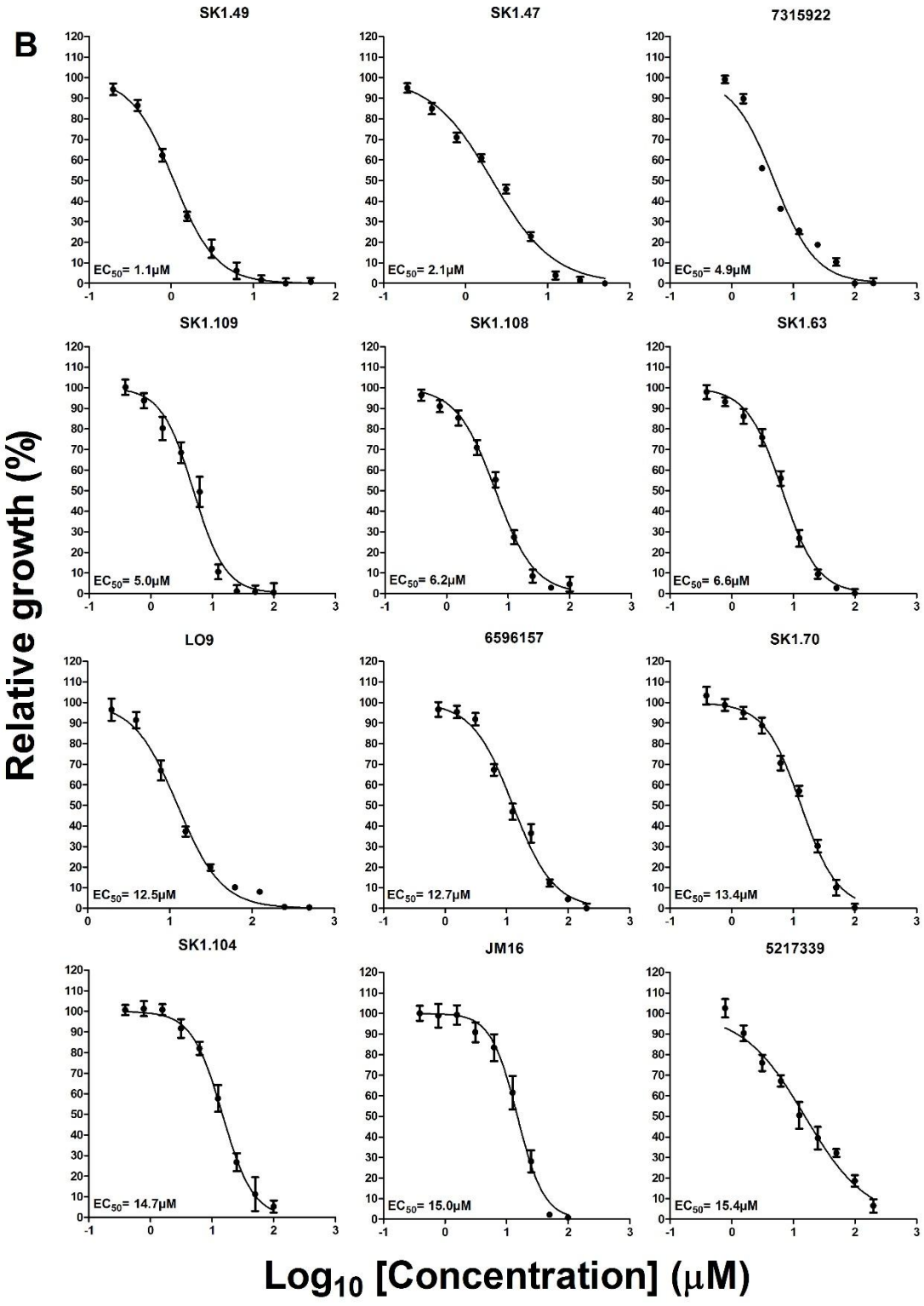
B
SK1.49
SK1.47
7315922
SK1.109
SK1.108
SK1.63
LO9
6596157
SK1.70
SK1.104
JM16
5217339
EC50= 1.1μM
EC50= 2.1μM
EC50= 4.9μM
EC50= 5.0μM
EC50= 6.2μM
EC50= 6.6μM
EC50= 12.5μM
EC50= 12.7μM
EC50= 13.4μM
EC50= 14.7μM
EC50= 15.0μM
EC50= 15.4μM
Relative growth (%)
Log10 [Concentration] (μM)

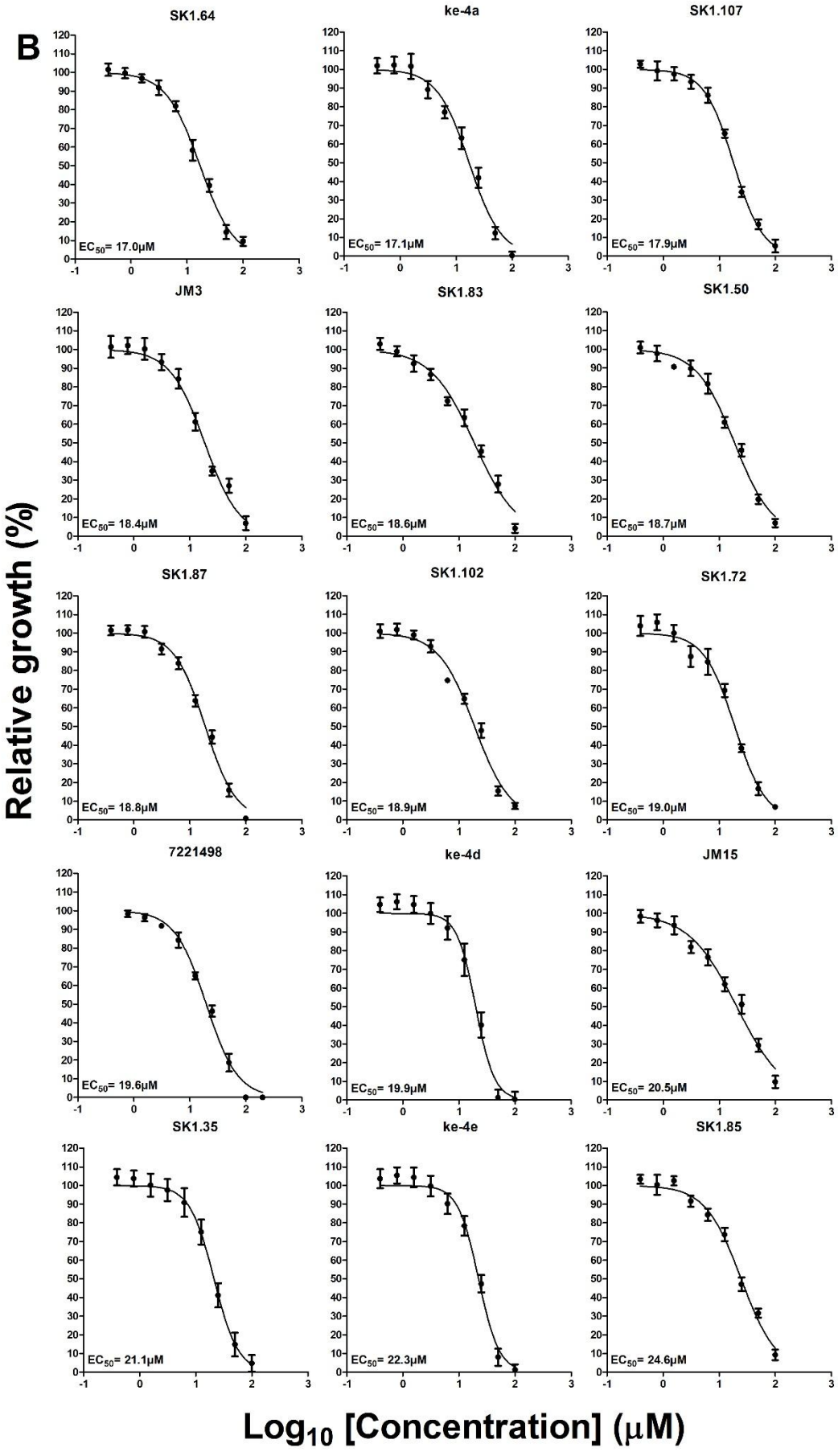
B
SK1.64
ke-4a
SK1.107
JM3
SK1.83
SK1.50
SK1.87
SK1.102
SK1.72
7221498
ke-4d
JM15
SK1.35
ke-4e
SK1.85
EC50= 17.0μM
EC50= 17.1μM
EC50= 17.9μM
EC50= 18.4μM
EC50= 18.6μM
EC50= 18.7μM
EC50= 18.8μM
EC50= 18.9μM
EC50= 19.0μM
EC50= 19.6μM
EC50= 19.9μM
EC50= 20.5μM
EC50= 21.1μM
EC50= 22.3μM
EC50= 24.6μM
Relative growth (%)
Log10 [Concentration] (μM)

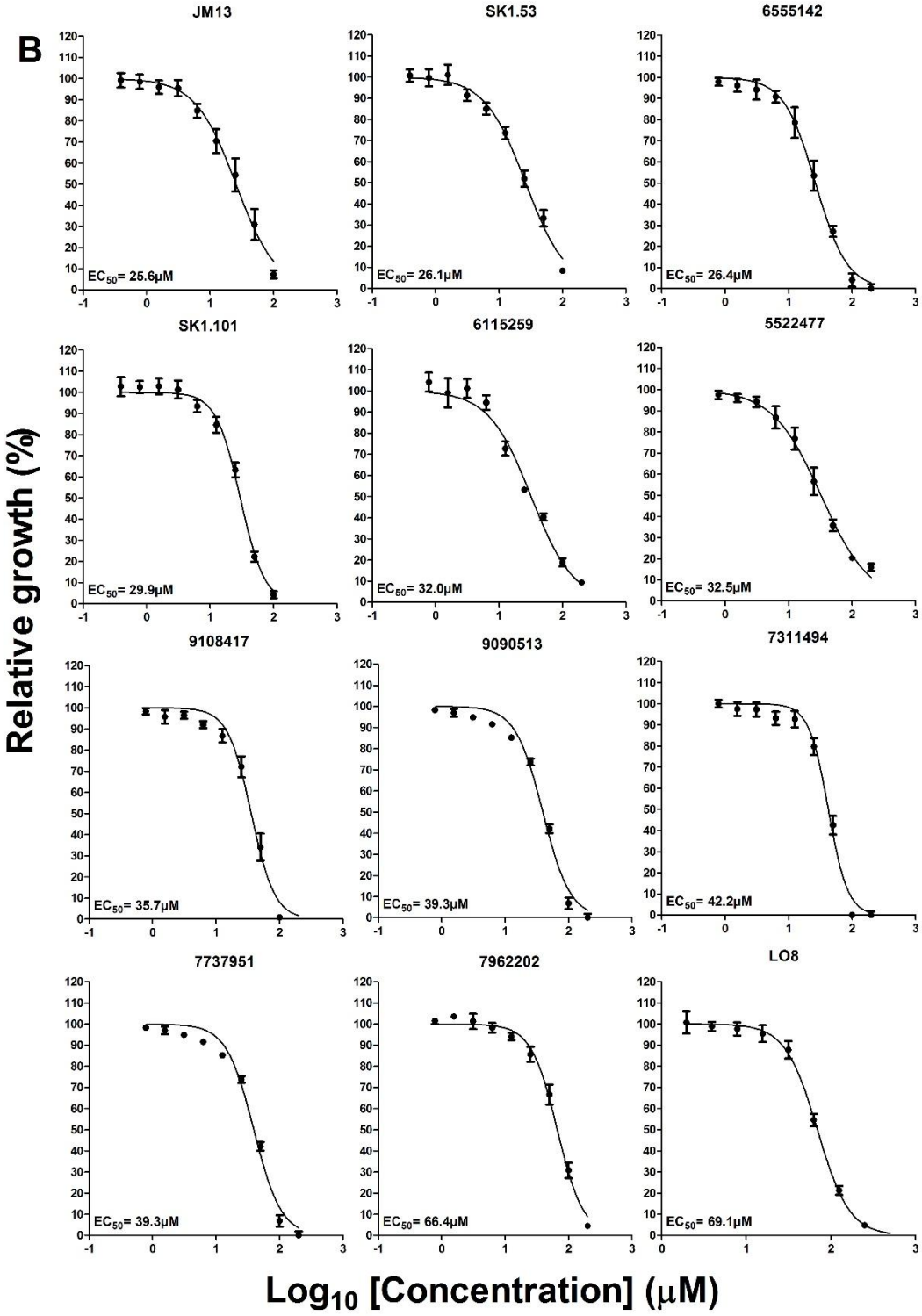
B
JM13
SK1.53
6555142
SK1.101
6115259
5522477
9108417
9090513
7311494
7737951
7962202
LO8
EC50= 25.6μM
EC50= 26.1μM
EC50= 26.4μM
EC50= 29.9μM
EC50= 32.0μM
EC50= 32.5μM
EC50= 35.7μM
EC50= 39.3μM
EC50= 42.2μM
EC50= 39.3μM
EC50= 66.4μM
EC50= 69.1μM
Relative growth (%)
Log10 [Concentration] (μM)

Appendix 3 (Chapter 4)

Table shows docking scores for compounds docked to three binding centres (LYS47, LYS48 and LEU50 within PfAtg8 and LYS49, LYS51 and LEU53 of hLC3) with 7-8 binding points for each one of these binding centres as well as indicated H-bond formation and whether docked (docking status) into W and/or L-pockets.

Comp. ID +target	Binding centre-binding points	Pose No.	Docking pose	Docking score	H-bond	Docking status
SK1.49 +PfAtg8	LYS48-N380	1	#1	-7.9		Docked
		2	#2	-7.1		Docked
		3	#3	-7.1		W-only
		4	#4	-6.9		L-only
	LYS48-C381		Nil			
			Nil			
			Nil			
			Nil			
	LYS48-C382	5	#1	-7.9		Docked
		6	#2	-7.7		W-only
		7	#3	-7.3		Docked
		8	#4	-7.0		W-only
	LYS48-O383	9	#1	-7.9		W-only
		10	#2	-7.5		W-only
		11	#3	-7.2		W-only
		12	#4	-7.2		W-only
	LYS48-C384	14	#1	-7.9		Docked
		15	#2	-7.5		Docked
		16	#3	-7.5		W-only
		17	#4	-7.3		W-only
	LYS48-C385	18	#1	-8.0		Docked
		19	#2	-7.6		Docked
		20	#3	-7.3		W-only
		21	#4	-7.2		W-only
	LYS48-C386	22	#1	-7.9		Docked
		23	#2	-7.7		W-only
		24	#3	-7.5		W-only
		25	#4	-7.3		W-only
	LYS48-C387	26	#1	-7.9		docked
		27	#2	-7.5		docked
		28	#3	-7.1		Docked
		29	#4	-6.9	H-bond	Docked
	LYS48-N388	30	#1	-7.9		W-only
		31	#2	-7.6		W-only
		32	#3	-7.5		W-only
		33	#4	-7.5		Docked

Comp. ID +target	Binding centre	Pose No.	Docking pose	Docking score	H-bond	Docking status
SK1.49 +PfAtg8	LEU50-N400	34	#1	-7.9		Docked
		35	#2	-7.5		W-only
		36	#3	-7.3		Docked
		37	#4	-7.1		W-only
	LEU50-C401		Nil			
			Nil			
			Nil			
			Nil			
	LEU50-C402	38	#1	-7.9		W-only
		39	#2	-7.5		Docked
		40	#3	-7.2		Docked
		41	#4	-7.1		Docked
	LEU50-O403	42	#1	-7.8		Docked
		43	#2	-7.2		Docked
		44	#3	-7.1		Docked
		45	#4	-6.9		Docked
	LEU50-C404	46	#1	-7.9		Docked
		47	#2	-7.7		Docked
		48	#3	-7.1		Docked
		49	#4	-6.5	H-bond	Docked
	LEU50-C405	50	#1	-7.9		Docked
		51	#2	-7.3		W-only
		52	#3	-6.6		Docked
		53	#4	-6.6		W-only
	LEU50-C406	54	#1	-8.0		Docked
		55	#2	-7.4		Docked
		56	#3	-7.0		Docked
		57	#4	-6.9		W-only
	LEU50-C407	58	#1	-8.0	H-bond	Docked
		59	#2	-7.6		W-only
		60	#3	-7.2		Docked
		61	#4	-6.7	H-bond	Docked

Comp. ID +target	Binding centre	Pose No.	Docking pose	Docking score	H-bond	Docking status
SK1.49 +PfAtg8	LYS47-N371	62	#1	-7.9		Docked
		63	#2	-7.4		Docked
		64	#3	-7.2		W-only
		65	#4	-6.8		Docked
	LYS47-C372		Nil			
			Nil			
			Nil			
			Nil			
	LYS47-C373	66	#1	-7.9		Docked
		67	#2	-7.2		W-only
		68	#3	-6.8	H-bond	W-only
		69	#4	-6.6		Docked
	LYS47-O374	70	#1	-7.9		W-only
		71	#2	-7.6		W-only
		72	#3	-7.5		Docked
		73	#4	-7.5		Docked
	LYS47-C375	74	#1	-7.7		Docked
		75	#2	-7.3		W-only
		76	#3	-7.0		Docked
		77	#4	-6.8		W-only
	LYS47-C376	78	#1	-7.9		Docked
		79	#2	-7.5		W-only
		80	#3	-7.3		W-only
		81	#4	-7.2		W-only
	LYS47-C377	82	#1	-7.6		W-only
		83	#2	-7.3	H-bond	W-only
		84	#3	-7.2		W-only
		85	#4	-6.7		Out
	LYS47-C378	86	#1	-7.1	H-bond	W-only
		87	#2	-7.1		W-only
		88	#3	-6.8		W-only
		89	#4	-6.8		W-only
	LYS47-N379	90	#1	-7.3		W-only
		91	#2	-7.2		W-only
		92	#3	-6.9		Out
		93	#4	-6.9		Out

Comp. ID +target	Binding centre	Pose No.	Docking pose	Docking score	H-bond	Docking status
SK1.47 +PfAtg8	LYS48-N380	94	#1	-8.3	H-bond	W-only
		95	#2	-8.3		Docked
		96	#3	-8.2	H-bond	Docked
		97	#4	-8.2		W-only
	LYS48-C381		Nil			
			Nil			
			Nil			
			Nil			
	LYS48-C382	98	#1	-8.3		W-only
		99	#2	-8.0		Docked
		100	#3	-6.2		W-only
		101	#4	5.9		L-only
	LYS48-O383	102	#1	-8.5		Docked
		103	#2	-8.4		Docked
		104	#3	-8.2		Docked
		105	#4	-7.6		Docked
	LYS48-C384	106	#1	-8.2		W-only
		107	#2	-7.0		W-only
		108	#3	-7.0		W-only
		109	#4	-6.7		W-only
	LYS48-C385	110	#1	-7.8		W-only
		111	#2	-7.6		Docked
		112	#3	-7.4		W-only
		113	#4	-7.3		Docked
	LYS48-C386	114	#1	-8.5		Docked
		115	#2	-8.3		Docked
		116	#3	-8.0		L-only
		117	#4	-7.4		W-only
	LYS48-C387	118	#1	-8.3		Docked
		119	#2	-8.3		Docked
		120	#3	-7.2		Docked
		121	#4	-6.9		W-only
	LYS48-N388	122	#1	-8.3		W-only
		123	#2	-7.7		W-only
		124	#3	-7.7		W-only
		125	#4	-7.4		W-only

Comp. ID +target	Binding centre	Pose No.	Docking pose	Docking score	H-bond	Docking status
SK1.47 +PfAtg8	LEU50-N400	126	#1	-8.5		W-only
		127	#2	-8.3		Docked
		128	#3	-7.7		Docked
		129	#4	-7.5		W-only
	LEU50-C401		Nil			
			Nil			
			Nil			
			Nil			
	LEU50-C402	130	#1	-8.0		W-only
		131	#2	-7.8		W-only
		132	#3	-7.7		Docked
		133	#4	-7.4		Docked
	LEU50-O403	134	#1	-8.1		Docked
		135	#2	-8.0		W-only
		136	#3	-7.7		Docked
		137	#4	-7.4		L-only
	LEU50-C404	138	#1	-8.5	H-bond	Docked
		139	#2	-8.4		Docked
		140	#3	-8.2		Docked
		141	#4	-7.6		W-only
	LEU50-C405	142	#1	-8.3		W-only
		143	#2	-7.7		W-only
		144	#3	-7.6		Docked
		145	#4	-7.6		W-only
	LEU50-C406	146	#1	-8.3		W-only
		147	#2	-7.5		Docked
		148	#3	-7.5		W-only
		149	#4	-7.2		W-only
	LEU50-C407	150	#1	-8.0		W-only
		151	#2	-7.9		Docked
		152	#3	-6.9		L-only
		153	#4	-6.8		Docked

Comp. ID +target	Binding centre	Pose No.	Docking pose	Docking score	H-bond	Docking status
SK1.47 +PfAtg8	LYS47-N371	154	#1	-8.3		W-only
		155	#2	-7.7		Docked
		156	#3	-7.4		W-only
		157	#4	-6.8		W-only
	LYS47-C372		Nil			
			Nil			
			Nil			
			Nil			
	LYS47-C373	158	#1	-8.3		W-only
		159	#2	-7.6		L-only
		160	#3	-7.5		Docked
		161	#4	-7.2		Docked
	LYS47-O374	162	#1	-8.3		W-only
		163	#2	-7.7		Docked
		164	#3	-7.4		Docked
		165	#4	-7.2		Docked
	LYS47-C375	166	#1	-8.4		Docked
		167	#2	-8.0		W-only
		168	#3	-8.0		Docked
		169	#4	-7.9		W-only
	LYS47-C376	170	#1	-8.3	H-bond	Docked
		171	#2	-7.9		W-only
		172	#3	-7.7		W-only
		173	#4	-7.1		W-only
	LYS47-C377	174	#1	-7.9		W-only
		175	#2	-7.5		W-only
		176	#3	-7.4		W-only
		177	#4	-6.9		Out
	LYS47-C378	178	#1	-7.5		W-only
		179	#2	-7.5	H-bond	W-only
		180	#3	-6.9		W-only
		181	#4	-6.7		W-only
	LYS47-N379	182	#1	-6.1		W-only
		183	#2	-5.6		Out
		184	#3	-5.5		Out
		185	#4	-5.5		W-only

Comp. ID +target	Binding centre	Pose No.	Docking pose	Docking score	H-bond	Docking status
SK1.109 +PfAtg8	LYS48-N380	186	#1	-7.0	H-bond	Docked
		187	#2	-7.0		Docked
		188	#3	-6.9		W-only
		189	#4	-6.8		W-only
	LYS48-C381		Nil			
			Nil			
			Nil			
			Nil			
	LYS48-C382	190	#1	-7.6	2H-bonds	Docked
		191	#2	-7.0		W-only
		192	#3	-6.8		Docked
		193	#4	-6.7	H-bond	Docked
	LYS48-O383	194	#1	-7.4	2H-bonds	Docked
		195	#2	-7.2		Docked
		196	#3	-6.7		Docked
		197	#4	-6.5		W-only
	LYS48-C384	198	#1	-7.2	H-bond	Docked
		199	#2	-7.1	H-bond	Docked
		200	#3	-7.1	H-bond	Docked
		201	#4	-6.8		W-only
	LYS48-C385	202	#1	-7.2	H-bond	Docked
		203	#2	-7.1		Docked
		204	#3	-6.6	H-bond	W-only
		205	#4	-6.6		W-only
	LYS48-C386	206	#1	-7.5		Docked
		207	#2	-6.5		W-only
		208	#3	-6.2		W-only
		209	#4	-6.2		W-only
	LYS48-C387	210	#1	-7.5	H-bond	Docked
		211	#2	-6.8	H-bond	W-only
		212	#3	-6.6		W-only
		213	#4	-6.4		W-only
	LYS48-N388	214	#1	-6.8		W-only
		215	#2	-6.6		W-only
		216	#3	-6.6		W-only
		217	#4	-6.4		W-only

Comp. ID +target	Binding centre	Pose No.	Docking pose	Docking score	H-bond	Docking status
SK1.109 +PfAtg8	LEU50-N400	218	#1	-7.2		Docked
		219	#2	-6.6		Docked
		220	#3	-6.5		W-only
		221	#4	-6.2		W-only
	LEU50-C401		Nil			
			Nil			
			Nil			
			Nil			
	LEU50-C402	222	#1	-7.2		Docked
		223	#2	-7.0		L-only
		224	#3	-6.3		W-only
		225	#4	-6.2		L-only
	LEU50-O403	226	#1	-7.5	H-bond	Docked
		227	#2	-7.2		Docked
		228	#3	-7.2		L-only
		229	#4	-6.9		L-only
	LEU50-C404	230	#1	-7.4		Docked
		231	#2	-7.1		Docked
		232	#3	-7.1	H-bond	W-only
		233	#4	-6.8	H-bond	Docked
	LEU50-C405	234	#1	-7.6	H-bond	Docked
		235	#2	-6.8	H-bond	W-only
		236	#3	-6.6		Docked
		237	#4	-6.6		W-only
	LEU50-C406	238	#1	-7.0	H-bond	Docked
		239	#2	-6.8		Docked
		240	#3	-6.6		L-only
		241	#4	-6.0		Docked
	LEU50-C407	242	#1	-7.4		Docked
		243	#2	-7.2	H-bond	Docked
		244	#3	-7.0		W-only
		245	#4	-6.8		W-only

Comp. ID +target	Binding centre	Pose No.	Docking pose	Docking score	H-bond	Docking status
SK1.109 +PfAtg8	LYS47-N371	246	#1	-7.2	H-bond	Docked
		247	#2	-6.8	H-bond	Docked
		248	#3	-6.6		Docked
		249	#4	-6.1		W-only
	LYS47-C372		Nil			
			Nil			
			Nil			
			Nil			
	LYS47-C373	250	#1	-7.5		W-only
		251	#2	-6.4	H-bond	W-only
		252	#3	-6.4	H-bond	W-only
		253	#4	-6.1		Docked
	LYS47-O374	254	#1	-7.1		Docked
		255	#2	-6.9		Docked
		256	#3	-6.2		W-only
		257	#4	-5.8		L-only
	LYS47-C375	258	#1	-7.5		Docked
		259	#2	-7.4		Docked
		260	#3	-6.2		W-only
		261	#4	-6.1	H-bond	Docked
	LYS47-C376	262	#1	-5.8		W-only
		263	#2	-5.6	H-bond	Docked
		264	#3	-5.3		W-only
		265	#4	-5.1		W-only
	LYS47-C377	266	#1	-5.6		W-only
		267	#2	-5.6		W-only
		268	#3	-5.3		W-only
		269	#4	-5.3		W-only
	LYS47-C378	270	#1	-5.9		W-only
		271	#2	-5.8		W-only
		272	#3	-5.3		W-only
		273	#4	-5.1		W-only
	LYS47-N379	274	#1	-6.8		W-only
		275	#2	-6.3		W-only
		276	#3	-6.2		W-only
		277	#4	-5.6		Out

Comp. ID +target	Binding centre	Pose No.	Docking pose	Docking score	H-bond	Docking status
SK1.108 +PfAtg8	LYS48-N380	278	#1	-7.2	H-bond	Docked
		279	#2	-7.2	H-bond	Docked
		280	#3	-7.0		Docked
		281	#4	-6.9		W-only
	LYS48-C381		Nil			
			Nil			
			Nil			
			Nil			
	LYS48-C382	282	#1	-7.6	H-bond	Docked
		283	#2	-7.2	2H-bonds	Docked
		284	#3	-6.8		W-only
		285	#4	-6.4		W-only
	LYS48-O383	286	#1	-7.4	H-bond	Docked
		287	#2	-7.3		Docked
		288	#3	-6.9		Out
		289	#4	-6.8		W-only
	LYS48-C384	290	#1	-7.3	H-bond	Docked
		291	#2	-7.1		W-only
		292	#3	-7.0	H-bond	W-only
		293	#4	-6.8		W-only
	LYS48-C385	294	#1	-7.4		Docked
		295	#2	-7.1		W-only
		296	#3	-7.1		Docked
		297	#4	-7.0	H-bond	Docked
	LYS48-C386	298	#1	-7.4	H-bond	Docked
		299	#2	-7.2		Docked
		300	#3	-7.0		W-only
		301	#4	-6.9		W-only
	LYS48-C387	302	#1	-7.4		Docked
		303	#2	-7.0		W-only
		304	#3	-6.8		W-only
		305	#4	-6.8		W-only
	LYS48-N388	306	#1	-6.8		W-only
		307	#2	-6.8		W-only
		308	#3	-6.6		W-only
		309	#4	-6.5		W-only

Comp. ID +target	Binding centre	Pose No.	Docking pose	Docking score	H-bond	Docking status
SK1.108 +PfAtg8	LEU50-N400	310	#1	-7.4	H-bond	Docked
		311	#2	-7.3		Docked
		312	#3	-6.8		W-only
		313	#4	-6.2		Docked
	LEU50-C401		Nil			
			Nil			
			Nil			
			Nil			
	LEU50-C402	314	#1	-7.0		Docked
		315	#2	-7.0		Docked
		316	#3	-6.9	H-bond	Docked
		317	#4	-6.7		W-only
	LEU50-O403	318	#1	-7.4	2H-bonds	Docked
		319	#2	-7.4		Docked
		320	#3	-7.2		Docked
		321	#4	-6.9		W-only
	LEU50-C404	322	#1	-7.3		Docked
		323	#2	-6.9	H-bond	Docked
		324	#3	-6.4		Docked
		325	#4	-6.3		W-only
	LEU50-C405	326	#1	-7.4	H-bond	Docked
		327	#2	-7.4		Docked
		328	#3	-6.8		W-only
		329	#4	-6.7		L-only
	LEU50-C406	330	#1	-6.8		Docked
		331	#2	-6.6		Docked
		332	#3	-6.4		W-only
		333	#4	-6.3		W-only
	LEU50-C407	334	#1	-7.3	2H-bonds	Docked
		335	#2	-7.0	H-bond	Docked
		336	#3	-6.4		W-only
		337	#4	-6.3		W-only

Comp. ID +target	Binding centre	Pose No.	Docking pose	Docking score	H-bond	Docking status
SK1.108 +PfAtg8	LYS47-N371	338	#1	-7.6		Docked
		339	#2	-7.5		Docked
		340	#3	-6.8		W-only
		341	#4	-6.5		Docked
	LYS47-C372		Nil			
			Nil			
			Nil			
			Nil			
	LYS47-C373	342	#1	-7.2		Docked
		343	#2	-7.1		Docked
		344	#3	-6.8		W-only
		345	#4	-6.5		W-only
	LYS47-O374	346	#1	-7.4		Docked
		347	#2	-7.0		Docked
		348	#3	-6.5		Docked
		349	#4	-6.6		Docked
	LYS47-C375	350	#1	-7.0		Docked
		351	#2	-6.8		W-only
		352	#3	-6.8	H-bond	Docked
		353	#4	-6.6	H-bond	Docked
	LYS47-C376	354	#1	-7.2		Docked
		355	#2	-7.2		Docked
		356	#3	-7.0		W-only
		357	#4	-6.4		Out
	LYS47-C377	358	#1	-7.1	H-bond	W-only
		359	#2	-6.6		W-only
		360	#3	-6.6		W-only
		361	#4	-6.2		W-only
	LYS47-C378	362	#1	-7.2		W-only
		363	#2	-6.7		W-only
		364	#3	-6.5		W-only
		365	#4	-6.4		W-only
	LYS47-N379	366	#1	-6.2		W-only
		367	#2	-6.2		Out
		368	#3	-6.2		W-only
		369	#4	-6.1		Out

Comp. ID +target	Binding centre	Pose No.	Docking pose	Docking score	H-bond	Docking status
SK1.63 +PfAtg8	LYS48-N380	370	#1	-6.7		W-only
		371	#2	-6.6		Docked
		372	#3	-6.4		W-only
		373	#4	-6.2		W-only
	LYS48-C381		Nil			
			Nil			
			Nil			
			Nil			
	LYS48-C382	374	#1	-6.7		W-only
		375	#2	-6.5	H-bond	Docked
		376	#3	-6.4		W-only
		377	#4	-6.4		W-only
	LYS48-O383	378	#1	-6.3		W-only
		379	#2	-6.1		W-only
		380	#3	-6.0		W-only
		381	#4	-5.8		W-only
	LYS48-C384	382	#1	-6.3		W-only
		383	#2	-6.0		W-only
		384	#3	-6.0		W-only
		385	#4	-5.9		W-only
	LYS48-C385	386	#1	-6.2		W-only
		387	#2	-5.8		W-only
		388	#3	-5.7		W-only
		389	#4	-5.7		W-only
	LYS48-C386	390	#1	-6.1		W-only
		391	#2	-6.1		W-only
		392	#3	-5.9	H-bond	W-only
		393	#4	-5.8		W-only
	LYS48-C387	394	#1	-6.2		W-only
		395	#2	-5.9		W-only
		396	#3	-5.7		W-only
		397	#4	-5.7		W-only
	LYS48-N388	398	#1	-6.1		W-only
		399	#2	-6.0		W-only
		400	#3	-6.0		W-only
		401	#4	-5.8		W-only

Comp. ID +target	Binding centre	Pose No.	Docking pose	Docking score	H-bond	Docking status
SK1.63 +PfAtg8	LEU50-N400	402	#1	-6.6		W-only
		403	#2	-6.5		W-only
		404	#3	-6.2		Docked
		405	#4	-6.0		W-only
	LEU50-C401		Nil			
			Nil			
			Nil			
			Nil			
	LEU50-C402	406	#1	-6.4		W-only
		407	#2	-6.3		Docked
		408	#3	-6.1		L-only
		409	#4	-6.1		L-only
	LEU50-O403	410	#1	-6.3		W-only
		411	#2	-6.2		W-only
		412	#3	-6.1		W-only
		413	#4	-6.1		W-only
	LEU50-C404	414	#1	-7.3	H-bond	Docked
		415	#2	-7.2		W-only
		416	#3	-7.1		L-only
		417	#4	-6.8		W-only
	LEU50-C405	418	#1	-6.2		W-only
		419	#2	-6.1		W-only
		420	#3	-6.1		Docked
		421	#4	-6.0		W-only
	LEU50-C406	422	#1	-6.3		W-only
		423	#2	-6.3		W-only
		424	#3	-6.2		W-only
		425	#4	-6.2		W-only
	LEU50-C407	426	#1	-6.2		W-only
		427	#2	-6.2		Docked
		428	#3	-6.0		W-only
		429	#4	-6.0		W-only

Comp. ID +target	Binding centre	Pose No.	Docking pose	Docking score	H-bond	Docking status
SK1.63 +PfAtg8	LYS47-N371	430	#1	-6.1		W-only
		431	#2	-6.0		W-only
		432	#3	-5.9		W-only
		433	#4	-5.7		W-only
	LYS47-C372		Nil			
			Nil			
			Nil			
			Nil			
	LYS47-C373	434	#1	-6.8		Docked
		435	#2	-6.8		W-only
		436	#3	-6.7		Docked
		437	#4	-6.5		W-only
	LYS47-O374	438	#1	-6.5		W-only
		439	#2	-6.5		W-only
		440	#3	-6.4		W-only
		441	#4	-6.3		W-only
	LYS47-C375	442	#1	-6.6		Docked
		443	#2	-6.5		W-only
		444	#3	-6.2		W-only
		445	#4	-6.0		W-only
	LYS47-C376	446	#1	-6.2		W-only
		447	#2	-6.1		W-only
		448	#3	-6.1		W-only
		449	#4	-6.0		W-only
	LYS47-C377	450	#1	-6.6		W-only
		451	#2	-6.5		W-only
		452	#3	-6.4		W-only
		453	#4	-6.3		W-only
	LYS47-C378	454	#1	-6.3		W-only
		455	#2	-6.1		W-only
		456	#3	-6.0		W-only
		457	#4	-6.0		W-only
	LYS47-N379	458	#1	-6.5		W-only
		459	#2	-6.4		W-only
		460	#3	-6.2		W-only
		461	#4	-6.1		Out

Comp. ID +target	Binding centre	Pose No.	Docking pose	Docking score	H-bond	Docking status
LO9 +PfAtg8	LYS48-N380	462	#1	-6.6		W-only
		463	#2	-5.8	H-bond	Docked
		464	#3	-5.8		W-only
		465	#4	-5.7		W-only
	LYS48-C381		Nil			
			Nil			
			Nil			
			Nil			
	LYS48-C382	466	#1	-6.5		Docked
		467	#2	-6.3		W-only
		468	#3	-6.2		W-only
		469	#4	-6.1		Docked
	LYS48-O383	470	#1	-6.4		Docked
		471	#2	-5.7		W-only
		472	#3	-5.7		W-only
		473	#4	-5.6		W-only
	LYS48-C384	474	#1	-6.6	H-bond	Docked
		475	#2	-6.5		W-only
		476	#3	-6.4	H-bond	W-only
		477	#4	-6.1		W-only
	LYS48-C385	478	#1	-6.6		W-only
		479	#2	-6.0		W-only
		480	#3	-5.6		W-only
		481	#4	-5.2		W-only
	LYS48-C386	482	#1	-6.6	H-bond	Docked
		483	#2	-6.6	H-bond	Docked
		484	#3	-6.5		W-only
		485	#4	-6.1		W-only
	LYS48-C387	486	#1	-6.6		Docked
		487	#2	-6.4		W-only
		488	#3	-6.3		W-only
		489	#4	-6.1	H-bond	Docked
	LYS48-N388	490	#1	-6.8	H-bond	Docked
		491	#2	-6.1		W-only
		492	#3	-5.9		W-only
		493	#4	-5.7		W-only

Comp. ID +target	Binding centre	Pose No.	Docking pose	Docking score	H-bond	Docking status
LO9 +PfAtg8	LEU50-N400	494	#1	-6.4		W-only
		495	#2	-6.4		W-only
		496	#3	-5.9		W-only
		497	#4	-5.8		W-only
	LEU50-C401		Nil			
			Nil			
			Nil			
			Nil			
	LEU50-C402	498	#1	-6.4		Docked
		499	#2	-6.2		W-only
		500	#3	-6.0		W-only
		501	#4	-5.8		Docked
	LEU50-O403	502	#1	-6.5		Docked
		503	#2	-6.5	H-bond	W-only
		504	#3	-6.3		W-only
		505	#4	-6.3		W-only
	LEU50-C404	506	#1	-6.1		Docked
		507	#2	-6.1		W-only
		508	#3	-6.0		W-only
		509	#4	-5.9		W-only
	LEU50-C405	510	#1	-6.8		W-only
		511	#2	-6.5	H-bond	Docked
		512	#3	-6.3	H-bond	Docked
		513	#4	-6.3	H-bond	Docked
	LEU50-C406	514	#1	-6.8	H-bond	Docked
		515	#2	-6.6		W-only
		516	#3	-6.3		W-only
		517	#4	-5.9		W-only
	LEU50-C407	518	#1	-6.2		Docked
		519	#2	-6.0		W-only
		520	#3	-5.9		W-only
		521	#4	-5.8	H-bond	W-only

Comp. ID +target	Binding centre	Pose No.	Docking pose	Docking score	H-bond	Docking status
LO9 +PfAtg8	LYS47-N371	522	#1	-6.5	H-bond	W-only
		523	#2	-6.1	H-bond	W-only
		524	#3	-6.1		W-only
		525	#4	-5.9		W-only
	LYS47-C372		Nil			
			Nil			
			Nil			
			Nil			
	LYS47-C373	526	#1	-6.6	H-bond	W-only
		527	#2	-6.5	H-bond	Docked
		528	#3	-6.3	H-bond	W-only
		529	#4	-5.9		W-only
	LYS47-O374	530	#1	-6.1	H-bond	Docked
		531	#2	-5.9		W-only
		532	#3	-5.4		W-only
		533	#4	-5.2		W-only
	LYS47-C375	534	#1	-6.0		W-only
		535	#2	-5.8		W-only
		536	#3	-5.7		W-only
		537	#4	-5.7		Docked
	LYS47-C376	538	#1	-6.0		W-only
		539	#2	-5.8		W-only
		540	#3	-5.6		W-only
		541	#4	-5.6		W-only
	LYS47-C377	542	#1	-6.1		W-only
		543	#2	-5.9		W-only
		544	#3	-5.7		W-only
		545	#4	-5.6		W-only
	LYS47-C378	546	#1	-6.4		W-only
		547	#2	-5.7		W-only
		548	#3	-5.5		W-only
		549	#4	-5.5		W-only
	LYS47-N379	550	#1	-6.2		W-only
		551	#2	-5.7		W-only
		552	#3	-5.4		W-only
		553	#4	-5.2		Out

Comp. ID +target	Binding centre	Pose No.	Docking pose	Docking score	H-bond	Docking status
LO8 +PfAtg8	LYS48-N380	554	#1	-5.6		W-only
		555	#2	-5.1		W-only
		556	#3	-5.0		W-only
		557	#4	-4.9		Docked
	LYS48-C381		Nil			
			Nil			
			Nil			
			Nil			
	LYS48-C382	558	#1	-6.2		W-only
		559	#2	-5.9		W-only
		560	#3	-5.9		Docked
		561	#4	-5.7		W-only
	LYS48-O383	562	#1	-6.2	H-bond	Docked
		563	#2	-6.2		W-only
		564	#3	-6.0		W-only
		565	#4	-5.8		Docked
	LYS48-C384	566	#1	-6.4		W-only
		567	#2	-6.2	H-bond	W-only
		568	#3	-6.0		W-only
		569	#4	-5.8		W-only
	LYS48-C385	570	#1	-6.2		W-only
		571	#2	-5.9		W-only
		572	#3	-5.7		W-only
		573	#4	-5.1		W-only
	LYS48-C386	574	#1	-5.8		W-only
		575	#2	-5.8		W-only
		576	#3	-5.5		W-only
		577	#4	-5.4		W-only
	LYS48-C387	578	#1	-6.2		Docked
		579	#2	-6.0		Docked
		580	#3	-5.8		W-only
		581	#4	-5.6		W-only
	LYS48-N388	582	#1	-5.2		Docked
		583	#2	-5.2		W-only
		584	#3	-5.0		W-only
		585	#4	-4.8		W-only

Comp. ID +target	Binding centre	Pose No.	Docking pose	Docking score	H-bond	Docking status
LO8 +PfAtg8	LEU50-N400	586	#1	-6.1		Docked
		587	#2	-6.1		Docked
		588	#3	-5.9		Docked
		589	#4	-5.8		W-only
	LEU50-C401		Nil			
			Nil			
			Nil			
			Nil			
	LEU50-C402	590	#1	-5.8		Docked
		591	#2	-5.8		Docked
		592	#3	-5.7		W-only
		593	#4	-5.5		W-only
	LEU50-O403	594	#1	-6.3		Docked
		595	#2	-6.2	H-bond	Docked
		596	#3	-5.3		W-only
		597	#4	-5.3		W-only
	LEU50-C404	598	#1	-6.1		Docked
		599	#2	-5.8		W-only
		600	#3	-5.7		W-only
		601	#4	-5.5		W-only
	LEU50-C405	602	#1	-6.4		Docked
		603	#2	-6.4	H-bond	W-only
		604	#3	-6.2		W-only
		605	#4	-6.2		W-only
	LEU50-C406	606	#1	-6.3		Docked
		607	#2	-6.1		W-only
		608	#3	-5.9		W-only
		609	#4	-5.8		W-only
	LEU50-C407	610	#1	-6.0		Docked
		611	#2	-5.4		W-only
		612	#3	-5.2		W-only
		613	#4	-5.0		W-only

Comp. ID +target	Binding centre	Pose No.	Docking pose	Docking score	H-bond	Docking status
LO8 +PfAtg8	LYS47-N371	614	#1	-6.3		W-only
		615	#2	-6.2		Docked
		616	#3	-6.0		W-only
		617	#4	-6.0		W-only
	LYS47-C372		Nil			
			Nil			
			Nil			
			Nil			
	LYS47-C373	618	#1	-5.8		W-only
		619	#2	-5.8		W-only
		620	#3	-5.7		W-only
		621	#4	-5.6		Docked
	LYS47-O374	622	#1	-6.0		W-only
		623	#2	-6.0		W-only
		624	#3	-5.8		W-only
		625	#4	-5.8		W-only
	LYS47-C375	626	#1	-6.0		Docked
		627	#2	-6.0		W-only
		628	#3	-5.8		W-only
		629	#4	-5.4		W-only
	LYS47-C376	630	#1	-5.2		Docked
		631	#2	-5.0		W-only
		632	#3	-4.8		W-only
		633	#4	-4.7		W-only
	LYS47-C377	634	#1	-6.0		W-only
		635	#2	-5.9		W-only
		636	#3	-5.0		Out
		637	#4	-5.0		Out
	LYS47-C378	638	#1	-5.4		W-only
		639	#2	-5.4		W-only
		640	#3	-5.2		W-only
		641	#4	-5.0		W-only
	LYS47-N379	642	#1	-5.2		W-only
		643	#2	-5.2		W-only
		644	#3	-5.1		W-only
		645	#4	-5.0		W-only

Comp. ID +target	Binding centre	Pose No.	Docking pose	Docking score	H-bond	Docking status
Comp.1 +PfAtg8	LYS48-N380	646	#1	-6.5		W-only
		647	#2	-6.0		W-only
		648	#3	-5.8	H-bond	W-only
		649	#4	-5.7		W-only
	LYS48-C381		Nil			
			Nil			
			Nil			
			Nil			
	LYS48-C382	650	#1	-6.3		W-only
		651	#2	-6.2		W-only
		652	#3	-5.7		W-only
		653	#4	-5.7		W-only
	LYS48-O383	654	#1	-6.3		W-only
		655	#2	-6.2		W-only
		656	#3	-6.2		W-only
		657	#4	-6.1		Docked
	LYS48-C384	658	#1	-6.3		W-only
		659	#2	-6.0		W-only
		660	#3	-5.9	H-bond	Docked
		661	#4	-5.7		W-only
	LYS48-C385	662	#1	-6.4		W-only
		663	#2	-5.9		W-only
		664	#3	-5.7		W-only
		665	#4	-5.4		W-only
	LYS48-C386	666	#1	-6.3		W-only
		667	#2	-6.0	H-bond	W-only
		668	#3	-5.9		W-only
		669	#4	-5.9	H-bond	W-only
	LYS48-C387	670	#1	-6.4		W-only
		671	#2	-6.0		W-only
		672	#3	-5.9		W-only
		673	#4	-5.9		Docked
	LYS48-N388	674	#1	-6.5		W-only
		675	#2	-6.1		Docked
		676	#3	-5.9		W-only
		677	#4	-5.7		W-only

Comp. ID +target	Binding centre	Pose No.	Docking pose	Docking score	H-bond	Docking status
Comp.1 +PfAtg8	LEU50-N400	678	#1	-6.4		W-only
		679	#2	-5.9		W-only
		680	#3	-5.9		W-only
		681	#4	-5.8		W-only
	LEU50-C401		Nil			
			Nil			
			Nil			
			Nil			
	LEU50-C402	682	#1	-6.0		W-only
		683	#2	-6.0		W-only
		684	#3	-5.9		W-only
		685	#4	-5.8		W-only
	LEU50-O403	686	#1	-5.9		W-only
		687	#2	-5.8	H-bond	Docked
		688	#3	-5.8		W-only
		689	#4	-5.7		W-only
	LEU50-C404	690	#1	-5.9		W-only
		691	#2	-5.9		W-only
		692	#3	-5.8		W-only
		693	#4	-5.8	H-bond	docked
	LEU50-C405	694	#1	-6.0		W-only
		695	#2	-5.9	H-bond	W-only
		696	#3	-5.7	2H-bond	Docked
		697	#4	-5.5		W-only
	LEU50-C406	698	#1	-5.9		W-only
		699	#2	-5.8		W-only
		700	#3	-5.8		W-only
		701	#4	-5.7	H-bond	W-only
	LEU50-C407	702	#1	-5.9		W-only
		703	#2	-5.9		W-only
		704	#3	-5.8		W-only
		705	#4	-5.8	H-bond	Docked

Comp. ID +target	Binding centre	Pose No.	Docking pose	Docking score	H-bond	Docking status
Comp.1 +PfAtg8	LYS47-N371	706	#1	-6.3		W-only
		707	#2	-6.1		W-only
		708	#3	-6.0		W-only
		709	#4	-5.8	H-bond	Docked
	LYS47-C372		Nil			
			Nil			
			Nil			
			Nil			
	LYS47-C373	710	#1	-6.4		W-only
		711	#2	-6.0		W-only
		712	#3	-5.6		W-only
		713	#4	-5.6		Out
	LYS47-O374	714	#1	-6.6		W-only
		715	#2	-6.1		W-only
		716	#3	-5.8	2 H-bond	Docked
		717	#4	-5.8	H-bond	Docked
	LYS47-C375	718	#1	-6.4		W-only
		719	#2	-5.8		W-only
		720	#3	-5.8		Docked
		721	#4	-5.6		Out
	LYS47-C376	722	#1	-6.4		W-only
		723	#2	-6.0		W-only
		724	#3	-5.9		Docked
		725	#4	-5.9		W-only
	LYS47-C377	726	#1	-6.0		W-only
		727	#2	-5.9		W-only
		728	#3	-5.9		W-only
		729	#4	-5.7		Out
	LYS47-C378	730	#1	-6.0		W-only
		731	#2	-5.9		W-only
		732	#3	-5.8		Docked
		733	#4	-5.6	H-bond	Out
	LYS47-N379	734	#1	-6.4		W-only
		735	#2	-6.0		W-only
		736	#3	-5.6		W-only
		737	#4	-5.4		Out

Comp. ID +target	Binding centre	Pose No.	Docking pose	Docking score	H-bond	Docking status
SK1.49 +hLC3	LYS51-N429	738	#1	-6.8		W-only
		739	#2	-6.6		W-only
		740	#3	-6.2		W-only
		741	#4	-6.1		W-only
	LYS51-C430		Nil			
			Nil			
			Nil			
			Nil			
	LYS51-C431	742	#1	-7.3		W-only
		743	#2	-7.2		Docked
		744	#3	-6.9		W-only
		745	#4	-6.8		W-only
	LYS51-O432	746	#1	-7.3		Docked
		747	#2	-7.2		W-only
		748	#3	-7.0		W-only
		749	#4	-6.8		W-only
	LYS51-C433	750	#1	-7.3		W-only
		751	#2	-7.2		W-only
		752	#3	-7.1		W-only
		753	#4	-7.0		W-only
	LYS51-C434	754	#1	-6.7		W-only
		755	#2	-6.6		W-only
		756	#3	-6.2		W-only
		757	#4	-6.0		W-only
	LYS51-C435	758	#1	-7.3		W-only
		759	#2	-7.0		W-only
		760	#3	-6.8		W-only
		761	#4	-6.6		W-only
	LYS51-C436	762	#1	-7.0		W-only
		763	#2	-7.0		W-only
		764	#3	-6.8		W-only
		765	#4	-6.5		W-only
	LYS51-N437	766	#1	-6.8		W-only
		767	#2	-6.5		W-only
		768	#3	-6.2		W-only
		769	#4	-5.9		W-only

Comp. ID +target	Binding centre	Pose No.	Docking pose	Docking score	H-bond	Docking status
SK1.49 +hLC3	LEU53-N449	770	#1	-7.6		Docked
		771	#2	-7.6		Docked
		772	#3	-7.2		W-only
		773	#4	-7.1		W-only
	LEU53-C450		Nil			
			Nil			
			Nil			
			Nil			
	LEU53-C451	774	#1	-7.6		Docked
		775	#2	-7.3		W-only
		776	#3	-7.3		W-only
		777	#4	-7.2		W-only
	LEU53-O452	778	#1	-7.5		W-only
		779	#2	-7.3		W-only
		780	#3	-7.3		W-only
		781	#4	-7.1		W-only
	LEU53-C453	782	#1	-7.3		W-only
		783	#2	-7.3	H-bond	W-only
		784	#3	-7.0		W-only
		785	#4	-6.8		W-only
	LEU53-C454	786	#1	-7.4		W-only
		787	#2	-7.3	H-bond	Docked
		788	#3	-7.2		Docked
		789	#4	-7.1		W-only
	LEU53-C455	790	#1	-7.0		W-only
		791	#2	-7	H-bond	W-only
		792	#3	-6.9		W-only
		793	#4	-6.7		Docked
	LEU53-C456	794	#1	-7.0		Docked
		795	#2	-7.0		Docked
		796	#3	-6.8		Docked
		797	#4	-6.4		Docked

Comp. ID +target	Binding centre	Pose No.	Docking pose	Docking score	H-bond	Docking status
SK1.49 +hLC3	LYS49-N413	798	#1	-7.0		W-only
		799	#2	-7.0		Out
		800	#3	-6.8		Out
		801	#4	-6.7		Out
	LYS49-C414		Nil			
			Nil			
			Nil			
			Nil			
	LYS49-C415	802	#1	-7.4		W-only
		803	#2	-7.2		Out
		804	#3	-6.9		Out
		805	#4	-6.8		Out
	LYS49-O416	806	#1	-6.6		Out
		807	#2	-6.5		W-only
		808	#3	-6.1		W-only
		809	#4	-5.7		Out
	LYS49-C417	810	#1	-7.3		Out
		811	#2	-7.1		W-only
		812	#3	-6.9		W-only
		813	#4	-6.6		Out
	LYS49-C418	814	#1	-7.3		W-only
		815	#2	-7.2		W-only
		816	#3	-7.1		W-only
		817	#4	-6.8		W-only
	LYS49-C419	818	#1	-7.2		W-only
		819	#2	-7.1		W-only
		820	#3	-7		W-only
		821	#4	-6.7		W-only
	LYS49-C420	822	#1	-6.6		W-only
		823	#2	-6.8		W-only
		824	#3	-6.6		Out
		825	#4	-6.3		Out
	LYS49-N421	826	#1	-6.4		L-only
		827	#2	-6.4		Out
		828	#3	-6.1		Out
		829	#4	-6		Out

Comp. ID +target	Binding centre	Pose No.	Docking pose	Docking score	H-bond	Docking status
Comp.1 +hLC3	LYS51-N429	830	#1	-6.8		W-only
		831	#2	-6.4		W-only
		832	#3	-5.8		Out
		833	#4	-5.8		W-only
	LYS51-C430		Nil			
			Nil			
			Nil			
			Nil			
	LYS51-C431	834	#1	-6.7	H-bond	Docked
		835	#2	-6.0		W-only
		836	#3	-6.0		W-only
		837	#4	-5.2		L-only
	LYS51-O432	838	#1	-6.8	H-bond	Docked
		839	#2	-6.5		W-only
		840	#3	-6.0		W-only
		841	#4	-5.9		W-only
	LYS51-C433	842	#1	-6.7		W-only
		843	#2	-6.2		W-only
		844	#3	-5.9		Out
		845	#4	-5.6		Out
	LYS51-C434	846	#1	-6.5		W-only
		847	#2	-6.1		Out
		848	#3	-6.0	H-bond	W-only
		849	#4	-5.9		W-only
	LYS51-C435	850	#1	-6.6		W-only
		851	#2	-6.2		Docked
		852	#3	-5.9		W-only
		853	#4	-5.8		W-only
	LYS51-C436	854	#1	-6.6		Docked
		855	#2	-6.2		W-only
		856	#3	-5.9	H-bond	W-only
		857	#4	-5.8		W-only
	LYS51-N437	858	#1	-6.7	H-bond	Docked
		859	#2	-6.5		Docked
		860	#3	-6.0		W-only
		861	#4	-6.0	H-bond	W-only

Comp. ID +target	Binding centre	Pose No.	Docking pose	Docking score	H-bond	Docking status
Comp.1 +hLC3	LEU53-N449	862	#1	-6.7	H-bond	Docked
		863	#2	-6.5	H-bond	W-only
		864	#3	-6.2		W-only
		865	#4	-6.0		W-only
	LEU53-C450		Nil			
			Nil			
			Nil			
			Nil			
	LEU53-C451	866	#1	-6.2	H-bond	Docked
		867	#2	-6.2		Docked
		868	#3	-6.0		W-only
		869	#4	-5.9	H-bond	Docked
	LEU53-O452	870	#1	-6.7		W-only
		871	#2	-6.1		W-only
		872	#3	-6.1		W-only
		873	#4	-5.8	H-bond	Docked
	LEU53-C453	874	#1	-6.4	H-bond	Docked
		875	#2	-6.2		W-only
		876	#3	-6.1		W-only
		877	#4	-5.9	H-bond	Docked
	LEU53-C454	878	#1	-6.7	H-bond	Docked
		879	#2	-6.0	H-bond	W-only
		880	#3	-5.9		Docked
		881	#4	-5.7		Docked
	LEU53-C455	882	#1	-6.7	H-bond	Docked
		883	#2	-6.5	H-bond	Docked
		884	#3	-6.0	H-bond	W-only
		885	#4	-6.0		W-only
	LEU53-C456	886	#1	-6.6	H-bond	Docked
		887	#2	-6.5	H-bond	Docked
		888	#3	-5.5		W-only
		889	#4	-5.0		L-only

Comp. ID +target	Binding centre	Pose No.	Docking pose	Docking score	H-bond	Docking status
Comp.1 +hLC3	LYS49-N413	890	#1	-6.7	H-bond	Docked
		891	#2	-6.0	H-bond	W-only
		892	#3	-5.8		Out
		893	#4	-5.6		Out
	LYS49-C414		Nil			
			Nil			
			Nil			
			Nil			
	LYS49-C415	894	#1	-6.4		Out
		895	#2	-6.1	H-bond	Out
		896	#3	-5.8	H-bond	Out
		897	#4	-5.6	H-bond	Out
	LYS49-O416	898	#1	-5.9		Out
		899	#2	-5.7	H-bond	Out
		900	#3	-5.6		Out
		901	#4	-5.4		Out
	LYS49-C417	902	#1	-6.7	H-bond	Docked
		903	#2	-6.1		W-only
		904	#3	-5.5		W-only
		905	#4	-5.5	H-bond	Out
	LYS49-C418	906	#1	-6.7	H-bond	Docked
		907	#2	-6.1		W-only
		908	#3	-5.7		W-only
		909	#4	-5.4		W-only
	LYS49-C419	910	#1	-6.6		W-only
		911	#2	-6.2		W-only
		912	#3	-6.0	H-bond	W-only
		913	#4	-5.5		Out
	LYS49-C420	914	#1	-5.5		Out
		915	#2	-5.5	H-bond	Docked
		916	#3	-5.4		Out
		917	#4	-4.9		Out
	LYS49-N421	918	#1	-5.5		Out
		919	#2	-5.4		Out
		920	#3	-5.3		Out
		921	#4	-5.3		Out

Comp. ID +target	Binding centre	Pose No.	Docking pose	Docking score	H-bond	Docking status
Comp.A +PfAtg8	LYS48-N380	996	#1	-8.9		Docked
		997	#2	-8.8		Docked
		998	#3	-8.4		W-only
		999	#4	-7.8		W-only
	LYS48-C381		Nil			
			Nil			
			Nil			
			Nil			
	LYS48-C382	1000	#1	-9.0	H-bond	Docked
		1001	#2	-8.8		Docked
		1002	#3	-8.4	H-bond	Docked
		1003	#4	-7.7		W-only
	LYS48-O383	1004	#1	-8.9	H-bond	Docked
		1005	#2	-8.8	H-bond	Docked
		1006	#3	-8.4		Docked
		1007	#4	-8.0	H-bond	W-only
	LYS48-C384	1008	#1	-8.9		Docked
		1009	#2	-8.7		Docked
		1010	#3	-8.3		Docked
		1011	#4	-8.3		Docked
	LYS48-C385	1012	#1	-8.9		Docked
		1013	#2	-8.8		Docked
		1014	#3	-8.2		W-only
		1015	#4	-8.1		W-only
	LYS48-C386	1016	#1	-8.8		Docked
		1017	#2	-8.5		Docked
		1018	#3	-8.3		Docked
		1019	#4	-7.9		Docked
	LYS48-C387	1020	#1	-8.6		Docked
		1021	#2	-8.4	H-bond	Docked
		1022	#3	-8.2	H-bond	Docked
		1023	#4	-8.0	H-bond	Docked
	LYS48-N388	1024	#1	-8.5	H-bond	W-only
		1025	#2	-8.2		W-only
		1026	#3	-7.8		W-only
		1027	#4	-7.8		W-only

Comp. ID +target	Binding centre	Pose No.	Docking pose	Docking score	H-bond	Docking status
Comp.B +PfAtg8	LYS48-N380	1028	#1	-8.8		Docked
		1029	#2	-8.5		Docked
		1030	#3	-8.2		W-only
		1031	#4	-7.9		Docked
	LYS48-C381		Nil			
			Nil			
			Nil			
			Nil			
	LYS48-C382	1032	#1	-8.6		Docked
		1033	#2	-8.4		Docked
		1034	#3	-8.3		Docked
		1035	#4	-8.2		Docked
	LYS48-O383	1036	#1	-8.8	H-bond	Docked
		1037	#2	-8.4		Docked
		1038	#3	-8.0		W-only
		1039	#4	-7.9	H-bond	W-only
	LYS48-C384	1040	#1	-8.5		Docked
		1041	#2	-8.5		Docked
		1042	#3	-8.4		Docked
		1043	#4	-7.7		W-only
	LYS48-C385	1044	#1	-8.6	H-bond	Docked
		1045	#2	-8.5		Docked
		1046	#3	-8.5	H-bond	Docked
		1047	#4	-8.3		Docked
	LYS48-C386	1048	#1	-8.7		Docked
		1049	#2	-8.4		Docked
		1050	#3	-7.8		W-only
		1051	#4	-7.7		W-only
	LYS48-C387	1052	#1	-8.3		W-only
		1053	#2	-8.1		W-only
		1054	#3	-8.1		Docked
		1055	#4	-8.0		Docked
	LYS48-N388	1056	#1	-8.2		W-only
		1057	#2	-7.7		W-only
		1058	#3	-7.5		W-only
		1059	#4	-7.5		Docked

Comp. ID +target	Binding centre	Pose No.	Docking pose	Docking score	H-bond	Docking Status
Comp.C +PfAtg8	LYS48-N380	1060	#1	-9.2	H-bond	Docked
		1061	#2	-8.6	H-bond	Docked
		1062	#3	-8.2		L-only
		1063	#4	-8.1		Docked
	LYS48-C381		Nil			
			Nil			
			Nil			
			Nil			
	LYS48-C382	1064	#1	-8.9		Docked
		1065	#2	-8.6		Docked
		1066	#3	-8.3	H-bond	Docked
		1067	#4	-8.2	H-bond	W-only
	LYS48-O383	1068	#1	-9.0		Docked
		1069	#2	-8.6		Docked
		1070	#3	-8.0		W-only
		1071	#4	-7.4	H-bond	W-only
	LYS48-C384	1072	#1	-9.2		Docked
		1073	#2	-8.8		Docked
		1074	#3	-8.2	H-bond	Docked
		1075	#4	-7.6		W-only
	LYS48-C385	1076	#1	-8.9		Docked
		1077	#2	-8.5		Docked
		1078	#3	-8.1		W-only
		1079	#4	-7.7		W-only
	LYS48-C386	1080	#1	-8.9		Docked
		1081	#2	-8.4		Docked
		1082	#3	-8.1		Docked
		1083	#4	-7.5		W-only
	LYS48-C387	1084	#1	-8.6	H-bond	Docked
		1085	#2	-8.4		W-only
		1086	#3	-7.9		Docked
		1087	#4	-7.7		W-only
	LYS48-N388	1088	#1	-8.5		Docked
		1089	#2	-7.9		W-only
		1090	#3	-7.8		W-only
		1091	#4	-7.8	H-bond	W-only

Comp. ID +target	Binding centre	Pose No.	Docking pose	Docking score	H-bond	Docking Status
Comp.D +PfAtg8	LYS48-N380	1092	#1	-7.6		Docked
		1093	#2	-7.6	H-bond	Docked
		1094	#3	-7.4		Docked
		1095	#4	-7.2		L-only
	LYS48-C381		Nil			
			Nil			
			Nil			
			Nil			
	LYS48-C382	1096	#1	-7.9		W-only
		1097	#2	-7.7	H-bond	Docked
		1098	#3	-7.4		W-only
		1099	#4	-7.1		W-only
	LYS48-O383	1100	#1	-7.8		Docked
		1101	#2	-7.7		W-only
		1102	#3	-7.6		Docked
		1103	#4	-7.0		Docked
	LYS48-C384	1104	#1	-7.7		Docked
		1105	#2	-7.6		W-only
		1106	#3	-7.4		W-only
		1107	#4	-7.4		W-only
	LYS48-C385	1108	#1	-7.6		Docked
		1109	#2	-7.3		W-only
		1110	#3	-7.0		W-only
		1111	#4	-6.8		W-only
	LYS48-C386	1112	#1	-7.9		Docked
		1113	#2	-7.6		Docked
		1114	#3	-7.5		W-only
		1115	#4	-7.1		W-only
	LYS48-C387	1116	#1	-7.5		Docked
		1117	#2	-7.4		W-only
		1118	#3	-7.1		W-only
		1119	#4	-7.1		W-only
	LYS48-N388	1120	#1	-7.6		W-only
		1121	#2	-7.4		W-only
		1122	#3	-7.2		W-only
		1123	#4	-6.8		W-only